

Proceedings
of
Symposium on Energy Engineering
in the 21st Century (SEE2000)

Volume 4

Edited by

Ping Cheng
Mechanical Engineering Department
The Hong Kong University of Science and Technology
Clear Water Bay, Kowloon, Hong Kong

Begell House
New York, Wallingford (U.K.)

DISTRIBUTION STATEMENT A
Approved for Public Release
Distribution Unlimited

DTIC QUALITY INSPECTED 1

20000223 144

Library of Congress Cataloging-in-Publication Data

Catalog record is available from the Library of Congress.

This book represents information obtained from authentic and highly regarded sources. Reprinted material is quoted with permission, and sources are indicated. A wide variety of references are listed. Every reasonable effort has been made to give reliable data and information, but the authors and the publisher cannot assume responsibility for the validity of all materials or for the consequences of their use.

All rights reserved. This book, or any parts thereof, may not be reproduced in any form without written consent from the publisher.

Direct all inquiries to Begell House, Inc., 79 Madison Avenue, New York, NY 10016.

© 2000 by Begell House, Inc.

ISBN 1-56700-132-7 (hard cover edition)

Printed in Hong Kong 1 2 3 4 5 6 7 8 9 0

REPORT DOCUMENTATION PAGE					Form Approved OMB No. 0704-0188	
<p>The public reporting burden for this collection of information is estimated to average 1 hour per response, including the time for reviewing instructions, searching existing data sources, gathering and maintaining the data needed, and completing and reviewing the collection of information. Send comments regarding this burden estimate or any other aspect of this collection of information, including suggestions for reducing the burden, to Department of Defense, Washington Headquarters Services, Directorate for Information Operations and Reports (0704-0188), 1215 Jefferson Davis Highway, Suite 1204, Arlington, VA 22202-4302. Respondents should be aware that notwithstanding any other provision of law, no person shall be subject to any penalty for failing to comply with a collection of information if it does not display a currently valid OMB control number.</p> <p>PLEASE DO NOT RETURN YOUR FORM TO THE ABOVE ADDRESS.</p>						
1. REPORT DATE (DD-MM-YYYY) 14-02-2000		2. REPORT TYPE Conference Proceedings			3. DATES COVERED (From - To) 9-13 Jan 00	
4. TITLE AND SUBTITLE Proceedings of Symposium on Energy Engineering in the 21 st Century (SEE 2000) (Four Volumes) Vol. 4				5a. CONTRACT NUMBER F6256299M9146		
				5b. GRANT NUMBER		
				5c. PROGRAM ELEMENT NUMBER		
				5d. PROJECT NUMBER		
				5e. TASK NUMBER		
6. AUTHOR(S) Conference Committee				5f. WORK UNIT NUMBER		
7. PERFORMING ORGANIZATION NAME(S) AND ADDRESS(ES) Hong Kong University of S&T Clear Water Bay Hong Kong Hong Kong					8. PERFORMING ORGANIZATION REPORT NUMBER N/A	
9. SPONSORING/MONITORING AGENCY NAME(S) AND ADDRESS(ES) AOARD UNIT 45002 APO AP 96337-5002					10. SPONSOR/MONITOR'S ACRONYM(S) AOARD	
					11. SPONSOR/MONITOR'S REPORT NUMBER(S) CSP-991002	
12. DISTRIBUTION/AVAILABILITY STATEMENT Approved for public release; distribution is unlimited.						
13. SUPPLEMENTARY NOTES						
14. ABSTRACT Volume 1, Page 1 – 406 Includes: Keynote Papers, Forced Convection, Natural Convection, and Boiling and Condensation Volume 2, Page 407 – 903 Includes: Two-Phase Flow, Porous Media, Heat Pipes and Thermosyphons, Conduction and Radiation, Microscale Heat Transfer, Heat Transfer Enhancement, Solar Energy & Nuclear Energy, Thermal Storage, Melting & Solidification Volume 3, Page 904 – 1,345 Includes: Drying & Food Processing, Heat Exchangers, Air-Conditioning and Refrigeration, Cryogenic Engineering, Energy and Environment, Combustion and Fire Volume 4, Page 1,346 – 1,734 Includes: Cycle Analysis, Engine Combustion, Waste Treatment by Thermal Methods, Fuel Cells, Clean Combustion Technology, Coal Combustion						
15. SUBJECT TERMS Fire Supression						
16. SECURITY CLASSIFICATION OF:			17. LIMITATION OF ABSTRACT	18. NUMBER OF PAGES 1,734	19a. NAME OF RESPONSIBLE PERSON Terence J. Lyons, M.D.	
a. REPORT	b. ABSTRACT	c. THIS PAGE			19b. TELEPHONE NUMBER (Include area code) +81-3-5410-4409	
U	U	U	UU			

FORWARD

The signing of the Montreal Protocol in 1987 and the Kyoto Protocol in 1997 by various nations serves as a reminder once again of the intimate relationship between energy and environment, which will no doubt remain one of the major issues in the 21st Century. This is particularly so in Southeast Asia, where industrial growth has taken place at such a rapid pace during the last two decades. At the same time, research in energy engineering is accelerating in this part of the world. At the Hong Kong University of Science and Technology (HKUST), the Center for Energy and Thermal Systems (CETS) was recently established for the research and development of energy efficient and environmentally benign thermal systems. Thus, it is a privilege for CETS to be able to host the Symposium on Energy Engineering in the 21st Century (SEE2000) on the HKUST campus between 9-13 January 2000, the first international energy engineering conference ever held in Hong Kong.

The aim of this Symposium is to provide a forum for technical interchange in various aspects of energy engineering. The 226 papers (including 11 keynote papers) presented in the 25 technical sessions of the Symposium are published in this proceedings which contains 4 volumes, covering a variety of topics from heat and mass transfer, various energy and thermal systems, to clean combustion technology.

It has been a great pleasure for me to work with Symposium Co-Chairmen Professor Kefa Cen of the Zhejiang University and Professor Patrick Takahashi of the University of Hawaii in the planning of this Symposium. I would like to express my sincere thanks to keynote speakers for their efforts in writing up-to-date review papers, to members of the International Advisory Committee and the Organizing Committee for their enthusiasm in promoting the Symposium, and to members of the Local Committee for their hard work in reviewing the manuscripts. Special thanks are due to Dr. H. H. Qiu (the Symposium Secretariat) and Ms. Lotta Tse for their help in making conference arrangements, as well as to Ms. Ellie Ho, Ms. Ronnie Tse and other clerical staff for their help in the typing of the manuscripts and for the preparation of the proceedings. The generous financial support from the K. C. Wong Education Foundation, U.S. Air Force Asian Office of Aerospace Research and Development, U.S. Army Research Office - Far East, U.S. Office of Naval Research - Asia, and the International Technic HVAC Company are gratefully acknowledged.

Ping Cheng
Symposium Chair

*Hong Kong
January 2000*

SYMPOSIUM CHAIRMAN

Professor Ping Cheng

Department of Mechanical Engineering
Hong Kong University of Science and Technology
Clear Water Bay, Kowloon, Hong Kong
Fax: (852) 2358-1543 E-mail: mepcheng@ust.hk

SYMPOSIUM CO-CHAIRMAN

Professor Kefa Cen

Institute for Thermal Power Engineering
Zhejiang University
Hangzhou 310027, China
Fax: (86) 571-595-1616
E-mail: kfcen@sun.zju.edu.cn

Professor Patrick Takahashi

Hawaii Natural Energy Institute
University of Hawaii
Honolulu, Hawaii 96822, U.S.A.
Fax: (808) 956-2336
E-mail: ptakaha@uhccmvs.uhcc.hawaii.edu

SYMPOSIUM SECRETARIAT

Dr. H. H. Qiu

Department of Mechanical Engineering
Hong Kong University of Science and Technology
Clear Water Bay, Kowloon, Hong Kong
Fax: (852) 2358-1543 E-mail: meqiu@ust.hk

INTERNATIONAL ADVISORY COMMITTEE

Tien, C. L., (Honorary Chairman), University of California, Berkeley
Bull, S. R., National Renewable Energy Laboratory, Golden
Chen, X. J., Xian Jiaotong University, Xian
Chiu, H. H., Cheng Kung University, Tainan
Cotta, R. Federal University of Rio de Janeiro, Rio de Janeiro
De Vahl Davis, G., University of New South Wales, Sydney
Fang, L. J., Industrial Technology Research Institute, Hsinchu
Fletcher, "Skip" L. S., Texas A & M University, College Station
Fujita, Y., Kyushu University, Fukuoka
Goldstein, R., University of Minnesota, Minneapolis
Gori, F., University of Rome, Rome
Hahne, E., University of Stuttgart, Stuttgart
Leontiev, A. I., Moscow State University, Moscow
Martenenko, O. G., Byelorussian Academy of Sciences, Minsk
Mayinger, F., Technical University of Munich, Munich
Mujumdar, A. S., McGill University, Montreal
Ro, S. T., Seoul National University, Seoul
Shi, S. X., Tianjin University, Tianjin
Sidemann, S., Israel Institute of Technology, Haifa
Tanasawa, I., Tokyo University of Agriculture & Technology, Tokyo
Viskanta, R., Purdue University, West Lafayette
Wang, B. X., Tsinghua University, Beijing
Yang, K. T., University of Notre Dame, Notre Dame

ORGANISING COMMITTEE

Auracher, H. L., Technical University of Berlin, Berlin
Cai, R. X., Institute of Engineering Thermophysics, Beijing
Chen, T. S., University of Missouri, Rolla
Faghri, A., University of Connecticut, Storrs
Fujii, T., Kobe University, Kobe
Fukusako, S., Hokkaido University, Sapporo
Groll, M., University of Stuttgart, Stuttgart
Guo, Z. Y., Tsinghua University, Beijing
Howell J., University of Texas, Austin
Inaba, H., Okayama University, Okayama
Kakac, S., University of Miami, Miami
Kashiwagi, T., Tokyo University of Agriculture & Technology, Tokyo
Kaviany, M., University of Michigan, Ann Arbor
Kennedy, L. A., The University of Illinois at Chicago, Chicago
Kim, Jong Hyun, EPRI, Palo Alto
Kurosaki, Y., University of Electro-Communications, Tokyo
Law, C. K., Princeton University, Princeton
Lee, J. S., Seoul National University, Seoul
Lloyd, A. C., Desert Research Institute, Reno
Lou, D. Y. S., University of Nebraska, Lincoln
Minkowycz, W. J., University of Illinois at Chicago, Chicago
Nelson, R. A., Los Alamos National Laboratory, Los Alamos
Ni, M. J., Zhejiang University, Hangzhou
Nishio, S., University of Tokyo, Tokyo
Peng, X. F., Tsinghua University, Beijing
Peterson, G. P., Texas A & M University, College Station
Radebaugh, R., National Institute of Standards and Technology, Boulder
Saitoh, T. S., Tohoku University, Sendai
Serizawa, A., Kyoto University, Kyoto
Shoji, M., University of Tokyo, Tokyo
Son, J. E., Korea Institute of Energy Research, Taejon
Straub, J., Technical University of Munich, Munich
Suzuki, K., Kyoto University, Kyoto
Tong, T. W., Colorado State University, Fort Collins
Wang, C. Y., Pennsylvania State University, College Park

LOCAL COMMITTEE

Hsu, C. T, HKUST
Chao, Y. H., HKUST
Chi, Y, Zhejiang University
Kot, S. C., HKUST
Lee, H. K., HKUST
Qiu, H. H., HKUST
Zhao, T. S., HKUST.

SPONSORS

American Society of Mechanical Engineers
Japanese Society of Mechanical Engineers
Chinese Society of Power Engineering
International Center of Heat and Mass Transfer
K. C. Wong Education Foundation
U.S. Air Force Asian Office of Aerospace Research and Development
U.S. Army Research Office-Far East
U.S. Office of Navy Research-Asia

SUMMARY OF TECHNICAL SESSIONS

Volume 1

- A. Keynote Papers
- B. Forced Convection
- C. Natural Convection
- D. Boiling and Condensation

Volume 2

- E. Two-Phase Flow
- F. Porous Media
- G. Heat Pipes and Thermosyphons
- H. Conduction and Radiation
- I. Microscale Heat Transfer
- J. Heat Transfer Enhancement
- K. Solar Energy & Nuclear Energy
- L. Thermal Storage
- M. Melting and Solidification

Volume 3

- N. Drying and Food Processing
- O. Heat Exchangers
- P. Air-Conditioning and Refrigeration
- Q. Cryogenic Engineering
- R. Energy and Environment
- S. Combustion and Fire

Volume 4

- T. Cycle Analysis
- U. Engine Combustion
- V. Waste Treatment by Thermal Methods
- W. Fuel Cells
- X. Clean Combustion Technology
- Y. Coal Combustion

CONTENTS OF VOLUME 4

Forward	iii
T. Cycle Analysis	1346
T1. Cheng Cycle Cogeneration for a Significantly Varying Demand of Heat and Power <i>D. Hein and K. Kwanka</i>	1347
T2. Thermodynamic Analysis and Sensitivity Studies on Braysson cycle Using an Intelligent Cai Software <i>S. Bhattacharyya</i>	1353
T3. Evaluation of Topping Cycle Performance in IGCC Systems <i>L. Zheng, R. Lin and Z. L. Liu</i>	1360
U. Engine Combustion	1365
U1. Investigations of Common-Rail Ruel Injection Technique in DI-Diesel-Engines <i>S. Eisen, B. Ofner and F. Mayinger</i>	1366
U2. Optimization of a Hydrogen Fueled Large Bore Compression Ignition Engine: Development of a New Variable Injection System for High Pressure Gas Injection <i>P. Prechtl and F. Mayinger</i>	1379
U3. Recent Focuses and Future Researches in Smart Engine Technology <i>F. Lin and Z. W. Li</i>	1388
U4. Simulation of In-cylinder Radiative Heat Transfer of Diesel Engine with Monte-Carlo Method <i>Z. D. Yan, Z. T. Liu, J. Chen, X. L. Yu and C. S. Cheung</i>	1397
V. Waste Treatment by Thermal Methods	1403
V1. Control and Sensing System Based on Fuzzy Logic for Domestic Refuse Incinerators <i>M. Fujiyoshi, W. C. Lam and S. J. Sun</i>	1404
V2. Novel Gas Technology for Treatment of Hazardous Aqueous Waste Streams <i>M. Benali, I. Hugron, M. Morin and C. Guy</i>	1412
V3. Compacting Municipal Solid Waste into "Logs" for Coal-Fired Combustion at Power Plants <i>H. Liu and Y. D. Li</i>	1420
V4. Experimental Study for Gasification of Scrap Tires <i>X. L. Yin, Z. L. Zhao, B. Y. Xu, C. Z. Wu, Y. Chen and D. Y. C. Leung</i>	1427
V5. Pyrolysis and Combustion Characteristics of Different Sludge <i>F. J. Tian, X. F. Guo, H. B. Li, Y. Chen, X. Y. Xu, X. L. Yang and B. Q. Li</i>	1433
V6. Performance Evaluation of The Two-Fluid Cycle in Municipal Solid Waste-Burnt Power Generation <i>T. Fujii, K. Sugimoto, T. Yamashita, H. Asano and N. Tsuchimoto</i>	1438
V7. Safe and Economical On-Farm Disposal of Animal Waste <i>S. C. Ling and H. P. Pao</i>	1446
W. Fuel Cells	1452
W1. Direct Liquid Water Injection and Interdigitated Flow Field for Reactant Gas, Water and Thermal Management in Proton Exchange Membrane Fuel Cells <i>Trung Van Nguyen</i>	1453
W2. Transport Phenomena in Proton Exchange membrane Fuel Cells <i>C. Y. Wang</i>	1460
W3. Mathematical Model Development for Pem Fuel Cells <i>H. T. Liu, L. X. You and T. H. Zhou</i>	1468
W4. Hydrogen Energy and Fuel Cell Power Packs <i>M. L. Ng and Y. C. Cheng</i>	1476

W5.	Development of Proton Conducting Membrances for High Temperature Direct Methanol Fuel Cells	1483
	<i>S. N. Lvov, X. Y. Zhou, L. Benning, X. J. Wei, M. V. Fedkin, H. R. Allcock, M. A. Hofmann, A. M. Cannon, E. C. Kellam and R. V. Morford</i>	
W6.	Optimization of SOFC Power Generation System with Chemical Looping Combustor	1489
	<i>X. Wang, L. F. Zhao and S.H. Zhang</i>	
X.	Clean Combustion Technology	1495
X1.	Study Combustion Model of Petroleum Cokes By TGA	1496
	<i>B. X. Shen, D. C. Liu and H. P. Chen</i>	
X2.	Environmental Update of Gas-Turbine MS-3002 Units Applied as Electrogenators	1500
	<i>A. Soudarev, E. Vinogradov, Y. Zakharov, S. Vesely, G. Poslushny, and K. H. Scholz</i>	
X3.	Numerical Modeling of Flow Pattern and Combustion in a Industrial Glass Melting Furnace	1508
	<i>Y. C. Guo, W. Y. Lin and C. K. Chan</i>	
X4.	Prediction of Gas-Particle Flows and Gas Combustion in a Cyclone Furnace	1515
	<i>Y. C. Guo and C. K. Chan</i>	
X5.	Stimulated Ignition of Natural Gas At Compression Ignition Conditions	1524
	<i>M. Mbarawa, B. E. Milton, and R. T. Casey</i>	
X6.	Unsteady Heat and Mass Transfer for multi-component Particle Deposition in the Modified Chemical Vapor Deposition	1532
	<i>K. S. Park, M. Choi and J. D. Chung</i>	
X7.	The Basic Study on Biogas by Use of Methane Clathrate	1540
	<i>I. Fujii and T. Kimura</i>	
X8.	Interferometric Measurements of Gas Diffusivity in Supercritical Water	1546
	<i>K. Kuge, K. Yokota, Y. Murayama, T. Honda, Y. Kato and Y. Yoshizawa</i>	
X9.	Biodiesel Production Using Waste Cooking Oil From Restaurant	1553
	<i>D. Y. C. Leung and G.Y.Chen</i>	
X10.	The Effects of CO ₂ Concentration on Limestone Desulfurization During O ₂ /CO ₂ Combustion	1560
	<i>J. R. Qiu, L. Z. Zhang, B. Feng, J. Wu and Q. H. Wang</i>	
X11.	Pyrolysis Characteristics of Straw on a Pilot-scale Gasificator	1566
	<i>J. S. Zhou, Z.Y. Luo, M. X. Fan, X. Gao, C. J. Yu, X.S. Guo, K.F. Cen, W.H.Luo, D. Yang and X.F. Xu</i>	
X12.	Aerodynamic Suppression of Combustion-Driven Pressure Oscillations in Technical Premixed Combustors	1573
	<i>H. Buchner, H. Bockhorn and S. Hoffmann</i>	
X13.	Combustion and Emission Characteristics of Residual Oil with Additive of Organic Barium	1581
	<i>T. S. Lee and M. J. Chen</i>	
X14.	Concentrated Primary Air Arrangement to Make Bituminite Burned Boiler Slagging-prevent and Low NO _x Release	1586
	<i>H. Zhou, Z.H. Chi, X. J. Jiang, K. F. Cen and G. J. Sun</i>	
X15.	Prediction of Carbon Combustion Rate in CO ₂ /O ₂ Environments and Its Relevance to Greenhouse Gas Recovery	1591
	<i>W. P. Yan and Y. F. Liu</i>	
X16.	A Desulfurization Mathematical Model and a Pilot Experiment by Spraying NaOH Solution into Downstream Flue Duct of a coal-fired Industrial Boiler	1595
	<i>H. S. Zhang, Y. P. Liu and D. Z. Chen</i>	
X17.	Experimental Study on Combustion Behaviors of Petroleum Coke Residual Oil Slurry	1603
	<i>X. Han, Z. Z. Li, J. W. Zhang, X. Y. Cao, and K. F. Cen</i>	
X18.	Precession Strouhal Numbers of a Self-Excited Precessing Jet	1609
	<i>J. Mi and G. J. Nathan</i>	
X19.	Research Method of Relative Contribution of Volatile-N and Char-N to N ₂ O Formation Based on Coal/Char Respective Combustion Experiment: Discussion on Experiment and Calculation	1615
	<i>Y. Liu, Q. Y. Li, J. M. Zhou and G. H. Li</i>	

X20.	Efficient Integration of Furnaces for Energy Saving in the Process Industry <i>P. Stehlik and Z. Jegla</i>	1624
X21.	The Biomass Pyrolysis for Liquids in CFB Reactor <i>X.W. Dai, Z.H. Xiong, C.Z. Wu and Y. Chen</i>	1632
X22.	Study on the Thermal Efficiency and Heat Transfer of Post Combustion for Smelting Reduction Furnace <i>H. C. Liu, T. S. Lee and H. H. Chiu, C. L. Yeh and L. C. Weng</i>	1640
X23.	Study on Fluid Dynamic Characteristic in the ESP <i>Y. Wang, Y. Zhang, Z. Z. Li and Z. X. Feng</i>	1646
X24.	A Study on the Electron-Emitting Characteristics in NHTHPEP <i>Z. Z. Gu, S. Cai, X. G. Liu, Q. D. Wei, Y. P. Yong and Z. H. Cao</i>	1651
X25.	A Study of the Moving Granular Bed Filter Removing Dust From Hot Gas for IGCC and PFBC-CC Systems <i>S. S. Xu</i>	1657
X26.	The Sensitivity of Pressurised Fluidized Bed Combustion of Char to In-bed Processes and Their Parameters <i>Y. B. Cui and J. F. Stubington</i>	1662
X27.	Carbon Elutriation from Pressurised Fluidized Bed Combustion of Australian Coals <i>Alan L. T. Wang and J. F. Stubington</i>	1669
X28.	Measures for Emission Control in Fluidized Bed Combustion of Sewage Sludge <i>M. Saenger, J. Werther and G. Hiller</i>	1677
Y.	Coal Combustion	1685
Y1.	Environmental Control of Toxic Metal Air Emissions From the Combustion of Coal and Wastes <i>J. O. L. Wendt, S. B. Davis, T. K. Gale, W. S. Seames and W. P. Linak</i>	1686
Y2.	Large Utility Boilers Burning Low Grade Coals with High Efficiency and Clean Environment <i>J. Zhou</i>	1694
Y3.	Application and Research of the Automatic Adjustable Pulverized Coal Distributor <i>W. D. Bai, Y. Yun, Z. D. Shu and Q. G. Zheng</i>	1703
Y4.	Study on Ash Deposition Characteristics of Different Types of Coals <i>M. Shimogori, N. Ooyatsu, N. Takarayama and A. Baba</i>	1710
Y5.	Advanced Technology on Coal-Fired Power Generation Systems <i>A. Tagishi and S. Nakamura</i>	1715
Y6.	Prospect of Coal Pyrolysis Under Hydrogen-Rich Gases <i>B. Q. Li and H. Q. Liao</i>	1722
Y7.	An Experimental Research on Influence of Coal Quality on Boiler Combustion Performance <i>J. Xiang, L. S. Sun, Z. Q. Zou, M. Li, X. H. Cheng and X. X. Sun</i>	1728

T. Cycle Analysis

CHENG CYCLE COGENERATION FOR A SIGNIFICANTLY VARYING DEMAND OF HEAT AND POWER

Dietmar Hein, Klaus Kwanka
Institute for Thermal Power Systems
Technische Universität München
Email: ltk@ltk.mw.tum.de; Fax: +49 89 289 16271

Keywords: gas turbine, cogeneration, exhaust heat recovery, Cheng Cycle, online control

ABSTRACT. To supply the campus site of the Technische Universität München at Garching with a significantly varying demand of heat and power a Cheng Cycle gas turbine cogeneration plant was installed. By injecting steam, produced by the heat recovered from the exhaust gases of the gas turbine, the electricity output can be increased by 50 % from 4 to 6 MWe within 2 minutes. To make full use of this flexibility an online load control system is essential. The combination of offline optimization by MILP-calculations and conversion with a neural controller during operation has proven as a simple but effective way to realize such a system.

1. INTRODUCTION

Combined production of heat and power allows to efficiently use fuels and to thereby reduce the burdens put on the environmental system. Fuel utilization factors of up to 90 % can be realized by combined heat and power plants (CHP).

In most applications the demand of heat is not simultaneous with the demand of electric power; the heat to power ratio will vary significantly. A boundary condition that also has to be kept in mind is that, in Germany, the costs for electricity are not exclusively based on the amount of electricity. They also depend on the peak power, which the utility company has to make available within a period of time specified in the contract.

A campus of university and research institutes is an excellent example for a consumer with a significantly varying demand of electricity and significant short-term power peaks. This is caused by connecting and disconnecting powerful test facilities and machinery.

These boundary conditions cause problems to efficiently and cost-effectively supply heat and power.

Due to these boundary conditions, common CHP plants (e.g. engine-based CHP, gas turbine with heat recovery steam generator) are not well suited to efficiently supply a significantly varying demand of heat and power. The situation asks for a plant allowing flexible, almost non-interdependent production of heat and power. This means that, in case of demand, more electric power can be made available, possibly by reducing the production of heat.

To supply the campus site of the Technische Universität München at Garching with electricity and heat, a new gasturbine cogeneration plant, based on the Cheng Cycle, has been installed.

2. THE CHENG CYCLE

Flexible production of heat and power can be realized with a Cheng Cycle. Steam produced by heat recovered from the flue gas of the gas turbine can either be used for supplying heat or be directly injected into the combustion chamber of the gas turbine (Fig. 1). In this case the expansion of the enhanced mass flow leads to an increased power output. The recovery of heat from the flue gas of the gas turbine ameliorates the electric efficiency. As part of the flue gas, the injected steam is emitted into the environment, the corresponding amount needs to be replaced by feed water.

The flexibility of a Cheng Cycle can be displayed with the help of a performance graph (Fig. 1). Line (1)-(2) resembles the operation of a simple gas turbine, with (2) showing the 100 % load point. The injection of steam into the combustion chamber reduces the output of heat, while enhancing the electric power along line (2)-(3).

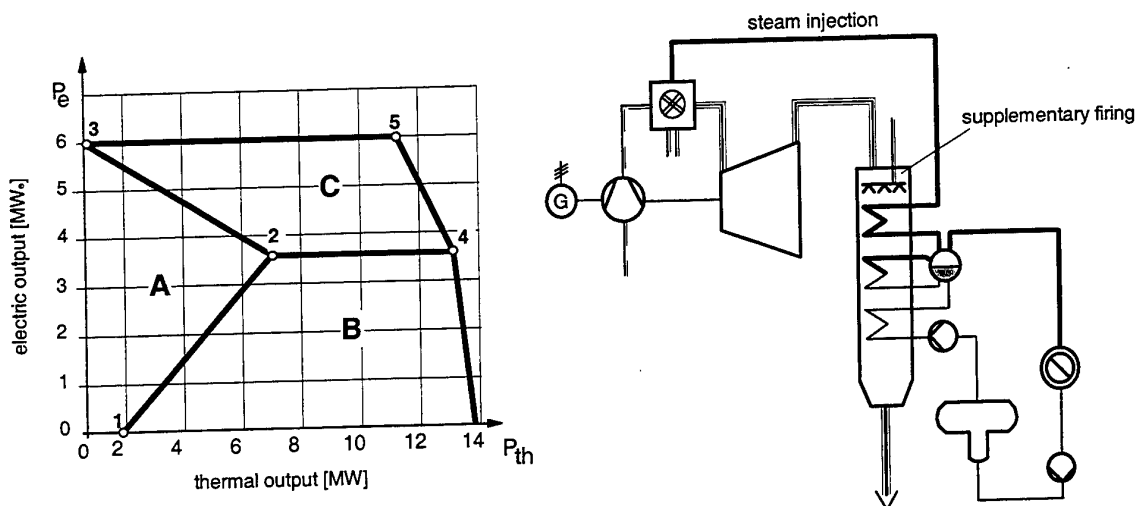


Fig. 1: Characteristic of Cheng Cycle Series 7

If the demand of heat exceeds the output associated with the 100 % load point (2), the supply can be realized by supplementary firing in the heat recovery steam generator. The oxygen content in the flue gas of the gas turbine allows to combust additional fuel, so that point (4) can be reached. The electric power and the heat output marked by point (5) can be reached by maximum injection of steam plus maximum additional firing. By operating at part load, in connection with supplementary firing, any point displayed in the performance graph can be realized. The plant built at the Garching research campus of the Technische Universität München is shown in Fig. 2.

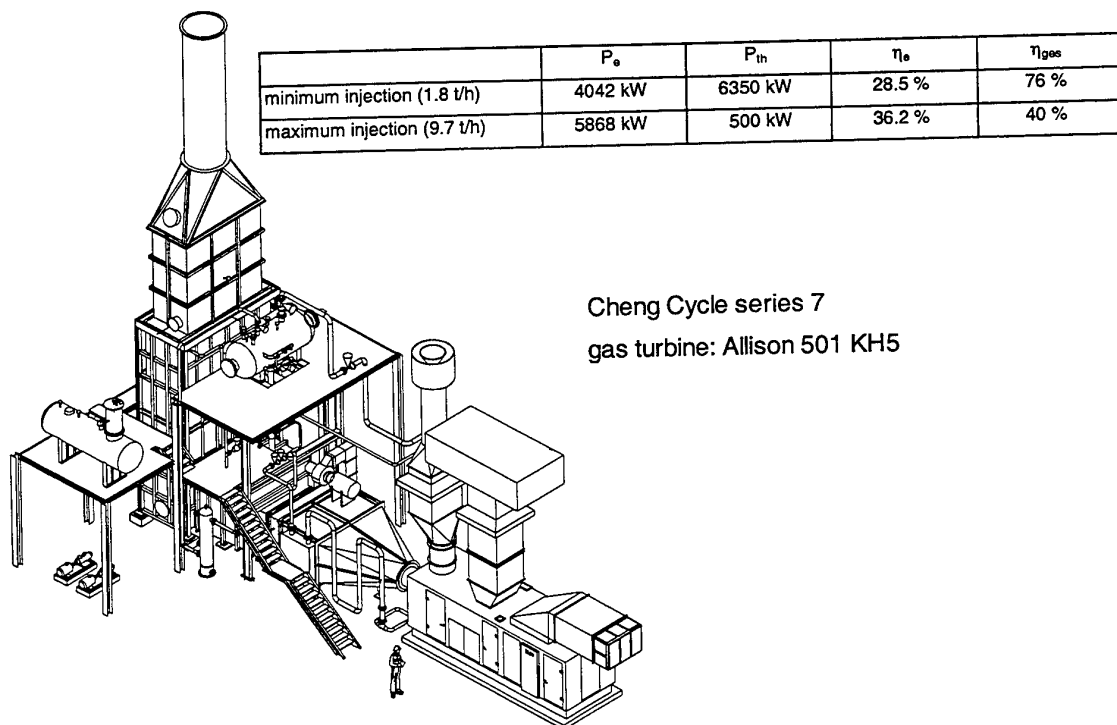


Fig. 2: Sketch of plant, characteristic values

3. OPERATION OF A CHENG CYCLE PLANT

Compared to a simple gas turbine plant with a heat recovery steam generator, economic advantages of a Cheng Cycle result from two factors:

- a higher number of full load operating hours per year, since the plant can be run at high load at times of a low demand of heat, but a high demand of electricity.
- reduction of peak power expenses by using the 50% increase in electric power, which can be achieved by the injection of steam into the gas turbine.

Combined heat and power plants can be operated based on the demand of heat or the demand of electricity. Heat-oriented operation leads to questions concerning the price of the electricity, that has to be purchased in times of low demand of heat. During high tariff periods point A in Fig 3 will be the operation point of choice, during low tariff periods, however, point B may be preferable. Electricity oriented operation aims at reducing peaks of electricity purchase by increasing the plant's power production. Therefore the heat must partly be supplied by supplementary firing.

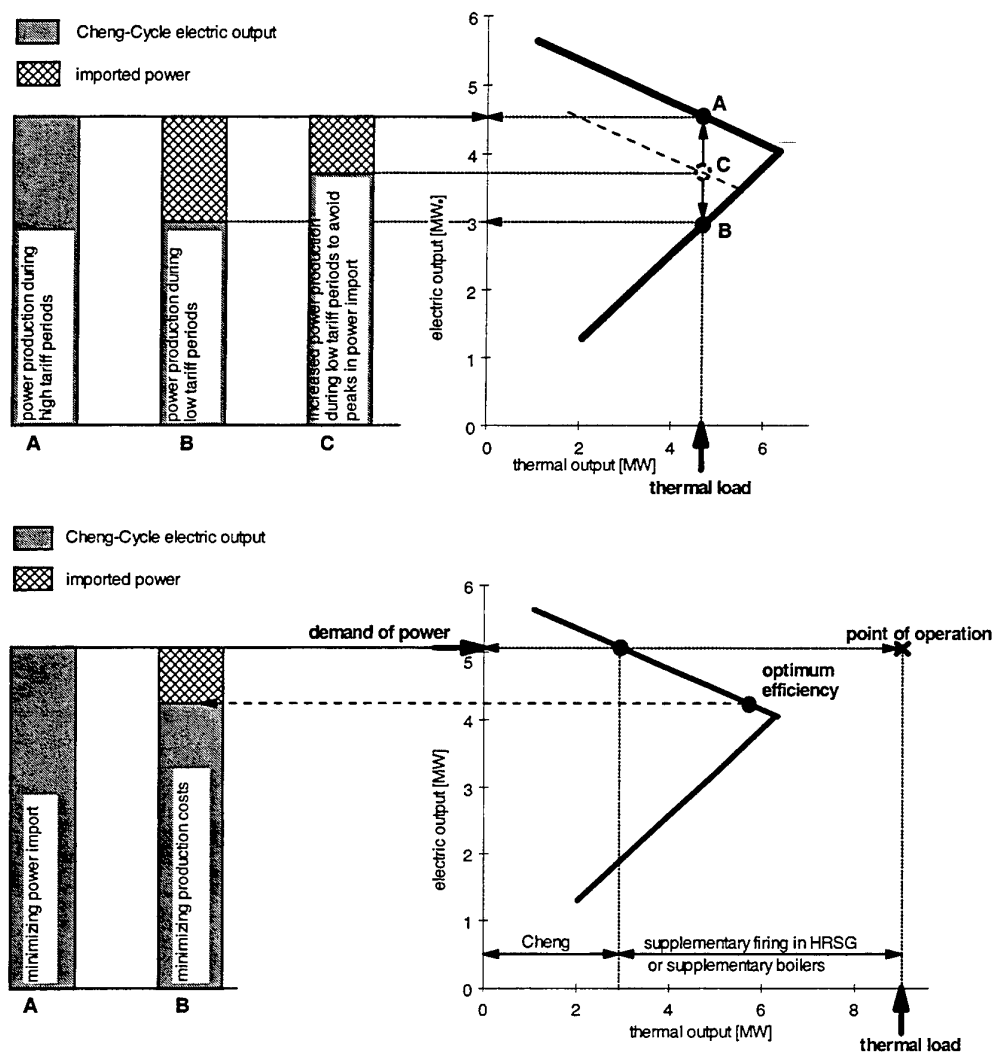


Fig. 3: modes of operation for different thermal loads

A precondition for cost-optimized operation of a CHP plant at the Garching campus is a characteristic allowing quick responses of power output to load changes, because it is necessary to reduce peaks of power purchase within the 15-minute period fixed in the contract. Fig. 4 shows measurements of plant conditions upon load changes. An increase in electric power can be realized with a transient of 1 MW/min. This means that the electric power can be raised from 4 to 6 MW_e within 2 minutes. The slower increase of heat output upon reducing the injection of steam is result of the sluggishness of the heating system. However, this has no influence on economic considerations.

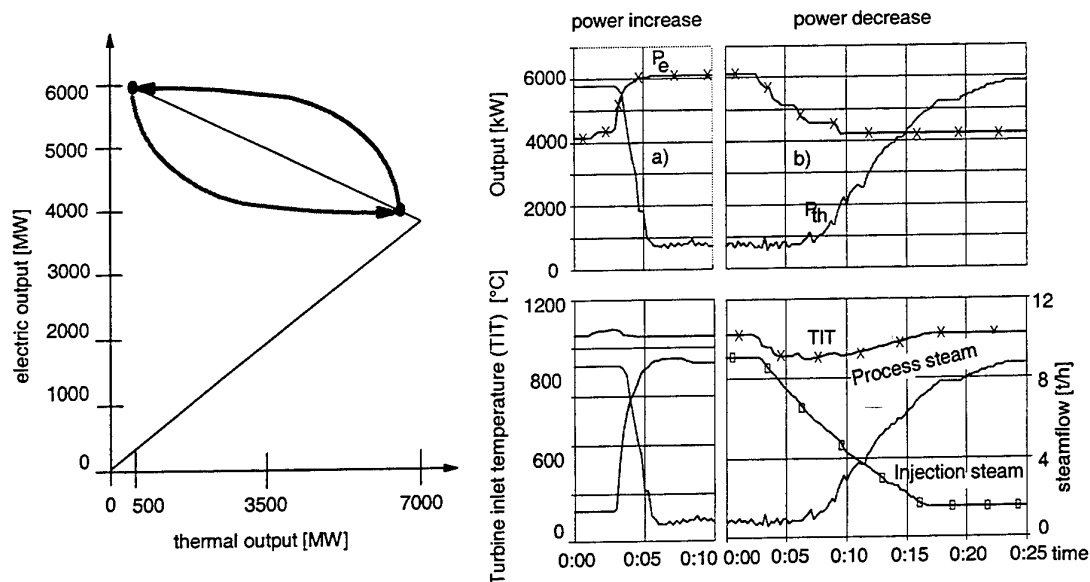


Fig. 4: Load alternation ability of a Cheng Cycle

4. PROCESS CALCULATION AND ONLINE CONTROL

For the calculation and optimization of power plants MILP-models (mixed integer linear programming models) are often used. The associated costs are used as linear parameters. The non-linear boundary conditions can be linearized in sections. During the planning phase of cogeneration power plants only optimization calculations allow to compare the economic advantages of different concepts (flexible or rigid coupling, use of storage device, etc). Otherwise the specific potential of each set-up would not be taken into account.

MILP-models have been developed and used for different scenarios to compare the economic advantage of a flexible Cheng Cycle against a simple gas turbine cycle. These models were based on linearized equations for the whole area of fuel consumption over the whole operation.

The advantage of a flexible cogeneration plant depends strongly on the thermal and electric load patterns. Fig.5 shows the reference load patterns used for the optimization calculations. It is a combination of a typical working day in summer, a typical working day in winter and halves of weekend days in summer and winter. The thermal power needed at the campus site in winter times is much higher than the maximum thermal output from the gas turbine. Therefore the load pattern is limited by the maximum thermal output of the gas turbine. The consideration of contracts with the regional utility and the gas company are of importance. Especially the agreements about the additional and reserve electric power supply are important economic factors for comparing different plant concepts.

In these contracts, the peak price is about 20 DM/kW_e month, 35 % of reserve power are included in the minimum amount of power to pay. A 50 % fine on the normal price is charged, if the used reserve power is higher than the contracted amount. The normal price for the electric power is about 102 DM/MWh during high

tariff periods and 88 DM/MWh during low tariff periods, the fuel price is about 3 DM/MWh (100 %). The price of the gas and electricity bought from the local supplier is split for different time zones.

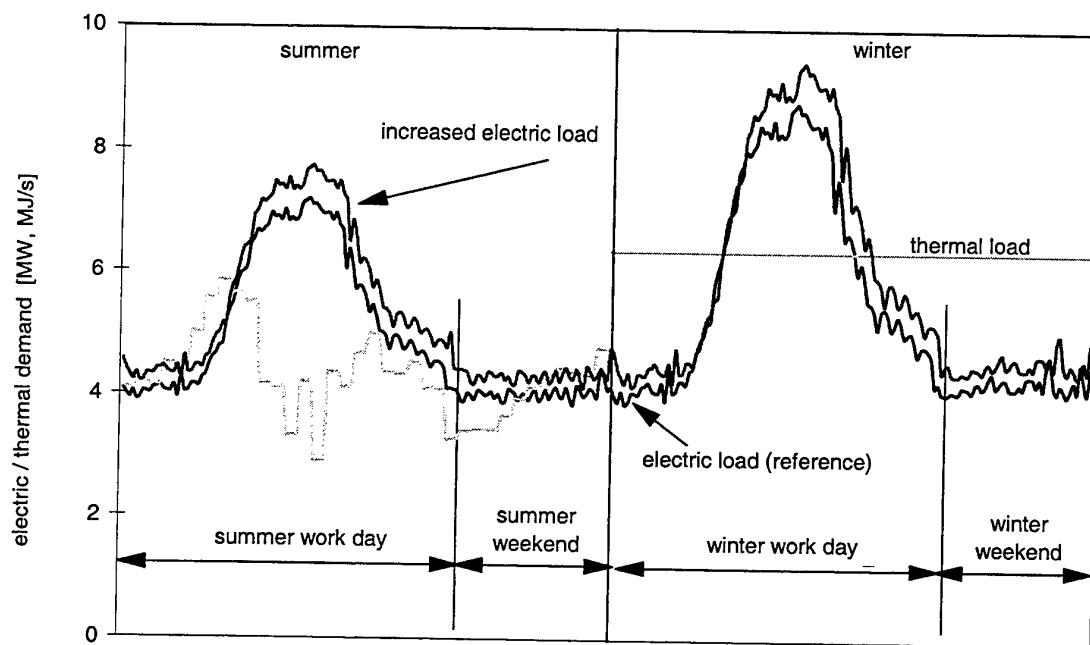


Fig. 5: Reference load patterns and variants

Fig. 6 shows the yearly savings with a Cheng Cycle unit – for heat oriented and cost optimized operation – compared to a simple, rigid-coupled gas turbine and HRSG plant (same gas turbine). By relinquishing the use of maximum thermal output whenever this helps to lower the electric power imported from the regional utility, the savings will increase further (Cheng, cost optimized operation). The additional investments necessary for the Cheng Cycle plant have to be refunded with those savings.

To use the advantages of a Cheng Cycle power plant as determined in the calculation, the point of operation has to be adjusted continuously depending on the actual load. For this purpose the results of the optimization calculation must be abstracted and adjusted to the actual load combinations. Neuronal grids are suitable to learn from the results of the MILP-calculation and can transfer the contained rules to modified situations. The structure of the problem is similar, but the actual load schedule differs from reference load patterns. The online control system of the Cheng Cycle plant in Garching takes advantage of neural grids and neural fuzzy controllers, to find the best operation point for the actual load. First a reference load pattern has to be optimized. Single operation points (thermal and electric power) are used as learning patterns for the neural controller. The calculated electric power in the optimization solution is the set point. The corresponding thermal power adjusts itself automatically. The controller must be trained again, if the shape of the load patterns or the contracts with the utility companies change significantly. The strategy enclosed in the optimum solution will be used by the controller. The controller is implemented in a control programme, transferring data from the process control system by using a DDE-connection. A prognosis module estimates the load schedule for the next 15-minute period. The load prognosis is the input variable for the load controller which calculates the next optimum point of operation.

From the two years operation up to June 1999 it can be concluded that the generalization of the strategy used in the MILP-solution works reliably and with good success. The imported power is limited to the optimized value, and the real load schedule is close to the calculated optimum. During the last months the Cheng Cycle plant was able to realize >95 % of the potential economic savings compared to a rigidly coupled gas turbine.

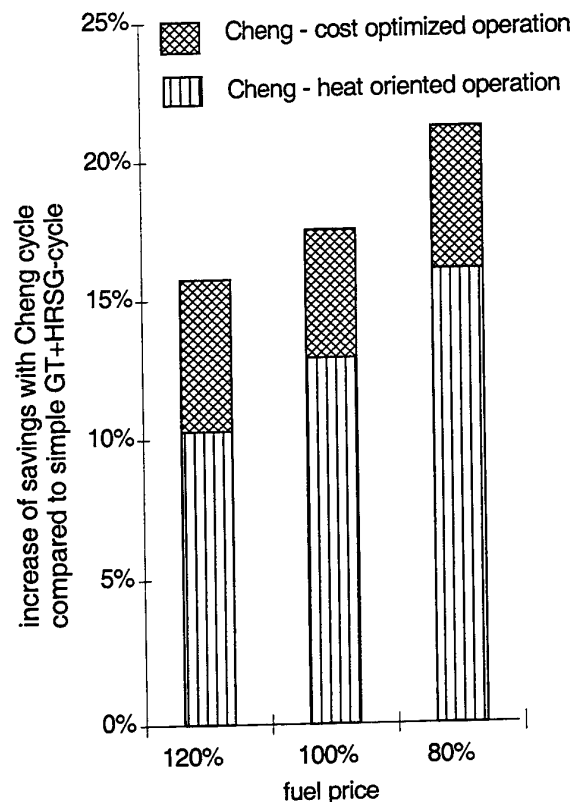


Fig. 6: Savings achievable by Cheng Cycle operation based on the load patterns displayed in Fig. 5

5. CONCLUSIONS

The Cheng Cycle plant of the Technische Universität München at its campus in Garching is now regular in operation for two years. During that period the time availability was high, but the peak availability has to be improved.

To make full use of the potential of flexibility of the Cheng Cycle plant an online load control system is needed: the optimal load point for electric power has to be set without any manual measure from the operator.

The combination of offline optimization by MILP-calculations and conversion with a neural controller is a simple and effective way to establish such a system. Post calculations showed that the online control system reached up to 98 % of the theoretical potential.

REFERENCES

1. Y. Cheng, "Regenerative Parallel Compound-Dual", *Fluid Heat Engine*, US Patent n. 4.128.994 (1978).
2. Kellerer, C. Spangenberg and D. Hein, "Lastfolgebetrieb mit einer Cheng Cycle-Anlage", *VDI-Bericht 1321*, Düsseldorf (1997).
3. Nauck, F. Klawonn and R. Kruse, *Neuronale Netze und Fuzzy-Systeme Vieweg*, Braunschweig/Wiesbaden (1994).
4. Spangenberg and D. Hein, "Gasturbinen mit Dampfinjektion zur Leistungssteigerung - Technik, Betrieb, Wirtschaftlichkeit", *VDI-Bericht 1182*, Düsseldorf (1995).

THERMODYNAMIC ANALYSIS AND SENSITIVITY STUDIES ON BRAYSSON CYCLE USING AN INTELLIGENT CAI SOFTWARE

Souvik Bhattacharyya

Department of Mechanical Engineering, University of Canterbury

Private Bag 4800, Christchurch, New Zealand

FAX: +64-3-364-2987 Email: souvik@mech.canterbury.ac.nz

Keywords: CyclePad, Braysson Cycle, thermodynamic analyses

ABSTRACT. A hybrid gas turbine cycle, Braysson cycle, has been recently proposed in the literature based on the conventional Brayton topping cycle while adopting the Ericsson cycle as the bottoming one. In this article thermodynamic analyses and sensitivity studies have been carried out employing an intelligent computer-aided instruction (CAI) software for power and energy systems design and analysis. Salient features and capabilities of the CAI tool have been discussed as well to extend assistance to the prospective users. Such tools can be effective means for conducting initial research studies on advanced novel cycles that are being suggested by researchers.

1. INTRODUCTION

Thermodynamic cycle analysis continues to arouse interest among both researchers and educators [1]. Thermodynamic behaviour of different options for power and refrigeration cycles along with characteristics of various working fluids is commonly carried out as part of thermodynamics instruction. Often, complex performance studies involving multiple design alternatives are left out because of the time and difficulty involved in the computations. Lately computer-aided learning has become popular and a few tools based on software platforms have become available. In addition to softwares for thermodynamic property computation for various substances, intelligent softwares which can guide the user in the design of a system without limiting itself to a mere analysis of it, have become available lately. These tools are opening up new opportunities for the educators since such design oriented exercises can now be undertaken as part of classroom instruction in the form of student assignments or design projects. Remote internet-based education is being offered to a greater extent today and such tools could be of immense utility under these configurations. The software platform is expected to augment the present curricula as a new paradigm rather than as a replacement module.

2. CYCLEPAD: AN INTELLIGENT ENVIRONMENT

A synergistic combination of qualitative physics and artificial intelligence techniques have been employed to develop CyclePad [2,3] to assist in teaching, design and research in applied thermodynamics and advanced energy conversion. This versatile freeware, available over the internet [4], introduces students to the concept of design as an open-ended process involving synthesis, analysis, and choices among design alternatives. It provides an articulate virtual laboratory [3], in terms of a software environment consisting of a set of parts, corresponding to physical components or important abstractions in the domains of interest, tools for assembling collections of these parts into designs, and facilities for analysing and testing designs. It enables the visualisation of schematic combination of a variety of thermodynamic cycles which enables the students to explore the sensitivity of key parameters on global behaviour of the cycle. Aside from their intrinsic interest, the conceptual design of thermodynamic cycles provides an extremely motivating context for students to learn fundamental principles more deeply than they would otherwise. This is strongly evident in several student and faculty surveys that have been undertaken in several universities [2] from which it transpires that such a tool is welcomed by the students. It does not replace the requirement of solving problems by hand but surely it supplements that activity quite effectively. For complex configurations, the students are not bogged down by routine calculations and in the mechanics of problem solving. CyclePad automates the numerical analysis of cycles so that one can devote more time and effort in thinking about the implications of a specific design or to explore what if options available to the designer. To assist in the investigations, CyclePad provides a hypertext-based query system, offering explanations of any parametric value, substance phase, or modelling assumption, that CyclePad has derived. Additionally a fairly detailed User's manual has been developed primarily for the students [5].

CyclePad allows one to specify the structure of the design, through sequential linking of components. The design is then analysed by assuming numerical values for parameters (eg. operating temperatures and pressures), and

making modelling assumptions (eg. whether or not to consider a device as isentropic) and choosing the working substances. Sensitivity analyses can be performed to understand how different parameters of a design contribute to its performance. For example, CyclePad can determine how the efficiency of a system changes as a function of other parameters. CyclePad performs steady-state analyses of both open and closed cycles while working in two phases, *build mode* and *analyse mode*. In the first phase (build), a graphical editor is employed to place components and to connect them with stuffs (component links) from the Component Palette (Figure 1). One can only proceed to the next phase (analysis) when every component is connected to another component via links or stuffs, and every stuff has been used as both an input and an output for components in the design. When there has been an erroneous data furnished or an impossible assumption made, the *contradiction* dialog box provides the assistance by identifying the item at fault and suggesting possible changes. In the analysis phase, items specified are: the working fluid, modelling assumptions used to analyse the design, and numerical values for the properties of components and stuffs. As soon as CyclePad receives some information from the user, it draws as many conclusions as it can about the design, based on everything we have told it so far. When we specify a working fluid, for instance, it knows whether to use property tables or an ideal gas approximation. When we specify numerical values, CyclePad sees if it can then calculate other numerical values. It displays the results of its calculations, and we are free to inquire about how values were derived and how one might proceed at any time, using a hypertext query system. As we provide more information, CyclePad deduces more about the physical system. At this juncture, one may want to investigate the relationship between a value that has been assumed and one that CyclePad has calculated in order to determine how to improve the design. The *Sensitivity Analysis* tool, from the Tools pull-down menu, is employed to do this using a dependent parameter and an independent parameter; this entire process is extremely interactive and user defined. There are many *what if* questions that can be asked for systems analysis in a preliminary design.

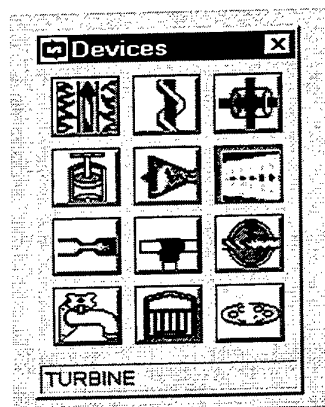


Figure 1. Component palette of CyclePad

3. BRAYSSON CYCLE

A hybrid gas turbine cycle [2] has been reported in the literature based on the conventional Brayton topping cycle while adopting the Ericsson cycle as the bottoming one. This combined cycle has been given a new name - Braysson cycle. In such a scheme, the irreversibilities of the boiler and the ancillaries of a conventional gas-steam turbine combined cycle is eliminated to give rise to improved performance parameters.

In the initial analyses reported here, ideal gas air standard cycles are assumed with turbines and compressors performing with a fixed isentropic efficiency of 90%. For subsequent studies, polytropic processes with base-line polytropic efficiency of 90% have been envisaged for all turbine and compressor stages - a level that is achieved in current ducted fan aero engines by careful blading design and sealing. For a fixed maximum-minimum temperature ratio the variables that affect the overall thermal efficiency and specific power of a practical Braysson cycle are the polytropic efficiency of compression and expansion, the pressure ratio of the basic Brayton cycle and the elevation of the minimum temperature during intercooled compression above the ambient temperature given by the ratio of the two. A maximum cycle temperature has also been assumed at realistic levels and the effect of raising it to higher levels as suggested by recent research (and currently achieved in only military aircraft engines) is also demonstrated. Effect of refrigerated inlet condition for compressor is also investigated.

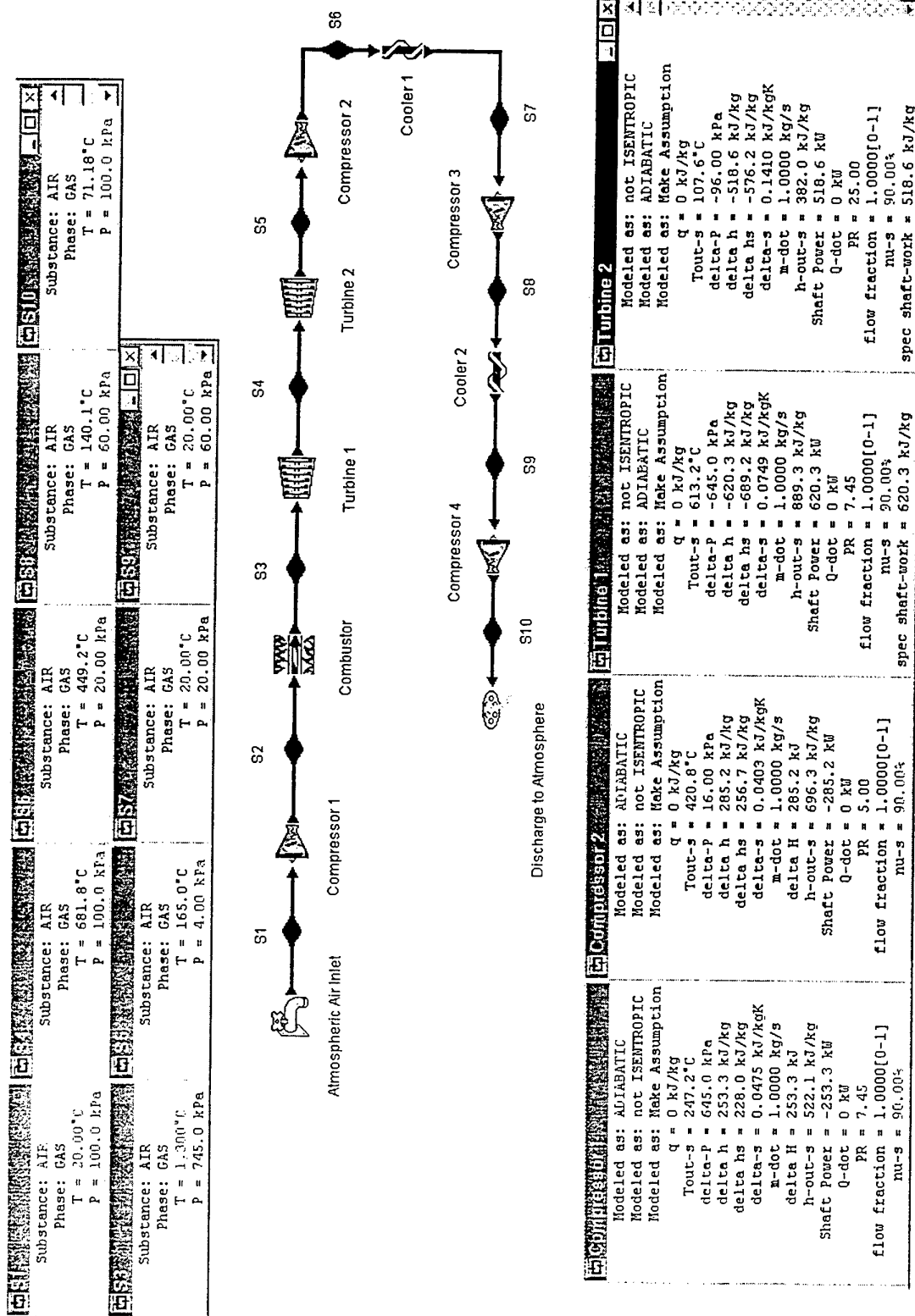


Figure 2. The Braysson Cycle as laid out on CyclePad with given states and equipment parameters.

The cycle being analysed operates under the following conditions: air enters the Brayton cycle compressor at 20°C and 100 kPa. The Brayton turbine inlet conditions are 1300 °C and 745 kPa. The second turbine in the cycle (Figure 2) belongs to the bottoming cycle (Ericsson cycle). Air enters this turbine at 100 kPa and exits at 4 kPa. A 3-stage intercooled compression is provided for this cycle with isobaric intercooling occurring with exit condition of 20 °C for each intercooler. Analysis of this combined cycle yields an overall thermal efficiency of 41.56% with a backwork ratio of 62.37%. The combustor heat input rate is 1.031 MW and the net power output is 428.6 kW.

4. SENSITIVITY ANALYSIS

Multiple sensitivity analyses have been carried out to optimise the Braysson cycle in terms of thermal efficiency and net work output as a function of various temperatures and pressures. Figure 3 illustrates how the topping cycle compressor (number 1) pressure ratio (which is the Brayton cycle pressure ratio) affects the net cycle power output in the combined cycle. So this gives us an opportunity to choose the optimum pressure ratio for maximum power output for the given conditions.

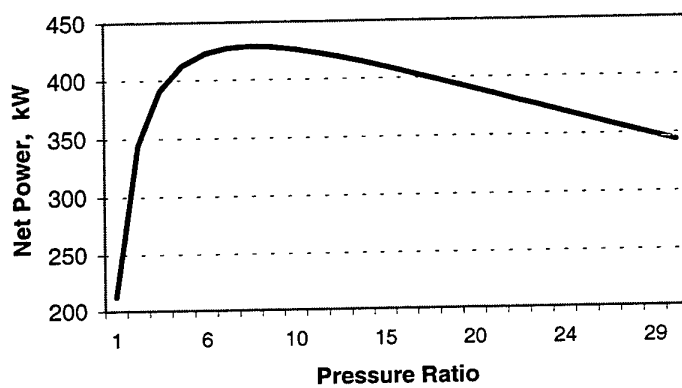


Figure 3. Influence of compressor (1) pressure ratio on net cycle power output

Figure 4 depicts a similar effect on cycle efficiency for varying pressure ratio values. It is interesting to note that the optimum pressure ratio for maximum net work output and for maximum cycle efficiency are not necessarily the same.

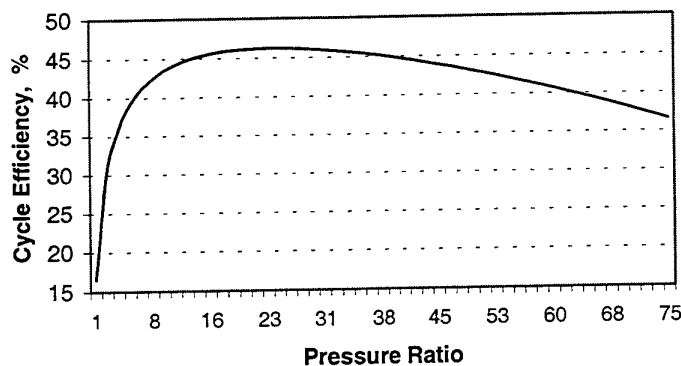


Figure 4. Influence of compressor (1) pressure ratio on cycle efficiency

Figure 5 shows the effect of having higher turbine inlet temperature on the cycle thermal efficiency; the results are intuitive, however, the prompt and easy sensitivity analysis tool of CyclePad is once more illustrated here. It may be observed that the gradient of the plot changes with temperature and one can choose the inlet temperature according to the return on extra investment for providing higher inlet temperatures for the Brayton turbine.

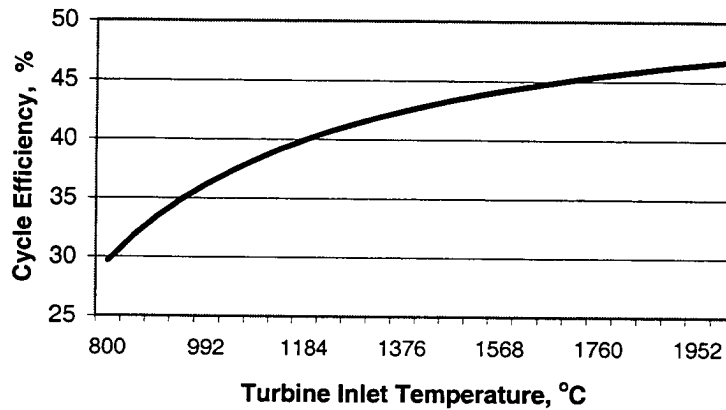


Figure 5. Influence of turbine inlet temperature on cycle efficiency

Power boosting of gas turbine cycles with compressor inlet air refrigeration has been suggested in the literature [7]. This has been explored as shown in Figure 6 where it can be observed that lowering of compressor inlet temperature causes a monotonous increase in net power output of the cycle. However, any decrease below the dew point will necessitate prevention of moisture and ice formation measures. Obviously the power gain seems quite attractive compared to the problems involved.

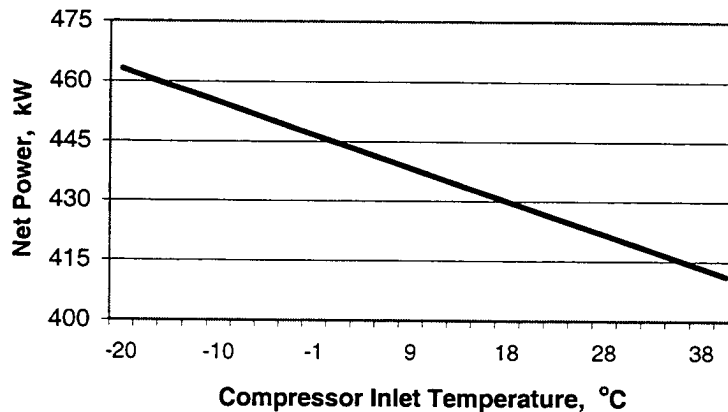


Figure 6. Variation of net power output of the cycle with compressor inlet air temperature

Figure 7 shows the effect of varying topping cycle turbine exhaust pressure on the overall cycle efficiency and again provides one with an opportunity to optimise the cycle for maximum efficiency. This pressure is the intermediate pressure between the Brayton and the Ericsson cycle. In Figure 8, it can be observed that there exists an optimum intercooler pressure which yield maximum cycle efficiency and it enables the designer to locate the intercooler optimally between the compressors.

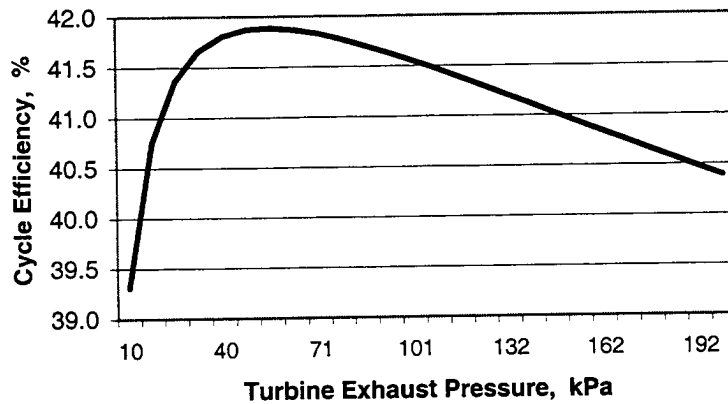


Figure 7. Variation of cycle efficiency with Brayton turbine exhaust pressure

5. CONCLUSIONS

A synergistic combination of qualitative physics and AI techniques have been employed to develop CyclePad to assist in teaching, design and research in applied thermodynamics and advanced energy conversion systems. It provides an articulate virtual laboratory, in terms of visualisation of the schematic combination of a variety of thermodynamic cycles. Believed to be the first attempt among Australasian Universities, CyclePad is being used in a second professional year course in thermodynamics in University of Canterbury with strong positive feedback from the students. The entire problem solving and assignment submission and evaluation process has been made paper-less and is conducted electronically.

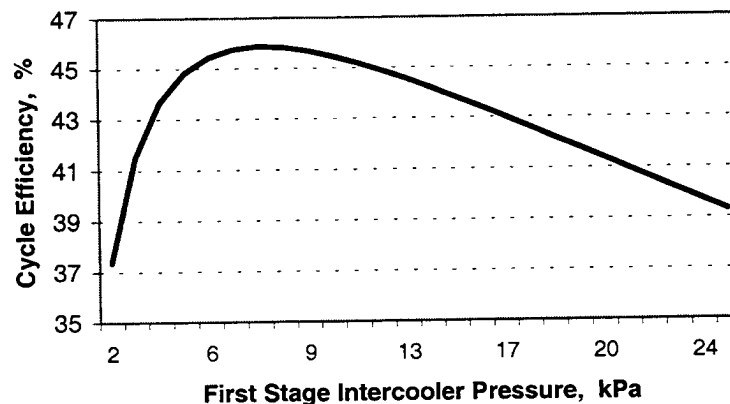


Figure 8. Optimisation of cycle with respect to intercooler pressure

A hybrid gas turbine cycle, called Braysson Cycle, has been recently proposed in the literature based on the conventional Brayton topping cycle while adopting the Ericsson cycle as the bottoming one. A thermodynamic analysis has been carried out employing an intelligent CAI software for power and process cycle design and analysis. Salient features and capabilities of the CAI tool, CyclePad, have been discussed as well to extend assistance to the prospective users. Sensitivity of key process parameters on global cycle performance have been explored. Such a design analysis will serve as a good insight into the performance of this novel combined cycle including information on parametric influences on its performance levels. Such studies demonstrate that analyses

of complex cycles can now be carried out as part of classroom instruction as well employing intelligent software environments. Sample sensitivity analyses have also been presented in the study to demonstrate the features of the software. CyclePad serves as an effective educational tool toward optimisation of energy conversion systems where fair amount of complexity is inherent in the design, especially when multiple possible variations of the related design parameters need to be studied.

REFERENCES

1. G.H.A. Cole, Multicycle approach to power cycle studies. *Int J Mech Engg Education*, **23**, pp. 129-141 (1995).
2. J. Baher, *Frontiers in Education Conference*. Tempe, Arizona, November 4-7 (1998).
3. K.D. Forbus and P.B. Whalley, *Proc. 12th National Conference on Artificial Intelligence*. AAAI-94, 1175-1182 (1994).
4. Internet site: <http://www.qrg.ils.nwu.edu/projects/NSF/Cyclepad/>
5. S. Bhattacharyya, *CyclePad 2.0 : A User's Manual*. Department of Mechanical Engineering, University of Canterbury, Christchurch, New Zealand (1999).
6. T.H. Frost, A. Anderson and B. Agnew, *Proc. of the Institution of Mechanical Engineers* v. 211, part A, pp. 121-131 (1997).
7. M.A. Ait-Ali, *ASME J. of Engg. For Gas Turbines and Power* v. 119, pp. 124-130 (1997).

EVALUATION OF TOPPING CYCLE PERFORMANCE IN IGCC SYSTEMS

Lily Zheng, Rumou Lin, Zelong Liu
Institute of Engineering Thermophysics
Chinese Academy of Sciences
Email: zlily@163.net; Fax: (8610)62575913

Keywords: IGCC, topping cycle, evaluation, optimize

ABSTRACT. Integrated Gasification Combined Cycle (IGCC) power system has attractive prospective well into the next century with its high efficiency and excellent environmental superiority. At present, many demonstration power plants have been built in the world. Research in this area is also actively carried on in China and a 400MW-demonstration power plant will be built in the next five years. The IGCC system commonly has two parts: the topping cycle and the bottom cycle (HRSG and Steam Turbines). The topping cycle consists of the gasifier, the syngas cooling and clean-up subsystem, the air separation unit (ASU) and the gas turbine. The gas turbine is the key component of the topping cycle as well as the total IGCC system. The purpose of this paper is to study the influence on IGCC topping cycle performance of different degree of ASU integration incorporated with gas turbine and proportion of the re-injecting nitrogen. In this paper, the key factors, which affect the topping cycle, are analyzed, a new idea—simultaneous optimization of the two opening variables—is presented and a mathematical model and the corresponding computing procedure are developed to realize the simultaneous optimization. This procedure is employed to calculate a typical commercial IGCC topping-cycle system, which is based on a slurry-feed gasifier, a low-temperature clean-up subsystem, a low-pressure ASU and a large gas turbine. The acquired results constitute useful information on the analysis and optimization of IGCC topping cycle performance during the system design phase.

1. WHICH FACTORS HAVE KEY EFFECTS ON TOPPING CYCLE PERFORMANCE

Fig.1. shows the IGCC topping cycle super-configuration scheme, which has two openings. One is the compressor extraction outlet; the other is the re-injecting nitrogen inlet. Followed are the key factors, which affect topping cycle performance most:

- The degree of ASU integration incorporated with gas turbine.
- The percentage of the total nitrogen available from ASU, which is re-injected into the combustor.
- The off-design performance of gas turbine when the expander inlet flow rate increases greatly due to the medium-Btu coal-derived syngas and the re-injection of nitrogen to the combustor.

2. HOW TO SIMULTANEOUSLY OPTIMIZE TOPPING CYCLE PERFORMANCE

Through the above analysis, we can find that it is very complex and difficult to evaluate and optimize the IGCC topping cycle performance. The traditional methods have many limits. They are usually used to analyze or optimize the specific IGCC configuration with only one variable coefficient. This paper presents a new idea—simultaneous optimization of the two opening variables—to analyze the topping cycle

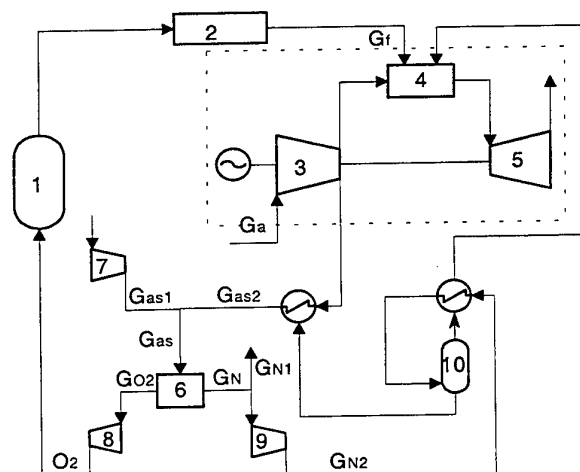


Fig.1. Topping cycle super-configuration scheme with two openings

1 Gasifier	2 Clean-up subsystem	3 Compressor
4 Combustor	5 Expander	6 ASU
7 Air-compressor	8 Oxygen-compressor	
9 Nitrogen-compressor	10 Nitrogen Saturator	

performance by employing an airside subsystem super-configuration. The intent is to demonstrate the effect on gas turbine output and overall system efficiency (LHV) of some of the key system variables such as ASU integration degree, the re-injecting nitrogen proportion, gas turbine firing temperature and compressor guide vane angle.

The approach of optimizing topping cycle is comprised of three steps. Firstly, we design an airside subsystem super-configuration, which may cover all possible types of airside integration technologies. The second step is the preparatory optimization of the topping cycle configuration using numerical analysis method, which is based on the elementary requirement and optimizing target. Thirdly, the topping cycle, whose process has been optimized, is accurately optimized both the parameters and configuration. To given optimizing target, we calculate the optimal key set of independent variables by means of numerical analyzing the crossed combination of five independent variable.

Fig.2. shows the optimization flow chart.

Two Opening Variables

- (1) ASU-integrated coefficient (Xas)

$$X_{as} = \frac{Gas_2}{Gas} \quad (1)$$

where: Gas₂----mass flow of air extracted from compressor
Gas-----mass flow of total air for ASU

- (2) Nitrogen-reinjected coefficient (Xgn)

$$X_{gn} = \frac{Gn_2}{Gn} \quad (2)$$

where: Gn₂----mass flow of reinjected nitrogen to combustor
Gn-----mass flow of total nitrogen available from ASU

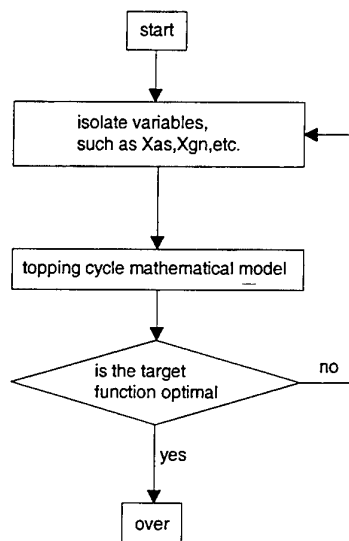


Fig.2. Topping cycle optimization flow chart

Target Variables

- (1) IGCC auxiliary power ratio is mainly influenced by the degree of ASU integration incorporated with gas turbine and the mass flow of reinjected nitrogen.

$$\eta_e = \frac{W_{los} + W_{asu}}{N_{gt} + N_{st}} \quad (3)$$

where: W_{los}----IGCC system other consumption power
W_{asu}----ASU consumption power
N_{gt}-----gas turbine output power
N_{st}-----steam turbine output power

- (2) IGCC overall efficiency indicates the synthetical effects of ASU wear-off power and gas turbine outlet temperature variation on the bottom cycle.

$$\eta_{is} = \frac{(N_{gt} + N_{st}) \times (1 - \eta_e)}{G_{cl} \times H_u} \quad (4)$$

where: G_{cl}-----mass flow of consumption fuel
H_u-----fuel low heat value

3. HOW TO SET UP MATHEMATICAL MODEL OF TOPPING CYCLE

The intent of building this model is to calculate the topping cycle performance coefficients with different variable combination for a typical IGCC system with given facilities such as gasifier, ASU and gas turbine and

to provide useful information to the system design.

Mathematical Model of Gasifier

Gasifier employs the black-box model. That is to say we only consider the input and output variables and raw syngas ingredient and don't concern the inner chemical reactions.

Mathematical Model of ASU

A cryogenic ASU process is used in this model because its technology is full-blown due to the prevalent use in chemical industry. The consuming works of the air-compressor, oxygen-compressor and nitrogen-compressor are calculated.

$$W_{ASU} = W_{Air} + W_{O_2} + W_{N_2} \quad (5)$$

where: W_{Air} -----special air-compressor consumption power
 W_{O_2} -----special oxygen-compressor consumption power
 W_{N_2} -----special nitrogen-compressor consumption power

Mathematical Model of Gas Turbine

Gas turbine is the key component of the topping cycle. Firstly, the mathematical models of compressor, combustor and expander should be built respectively. And then, the three models will be combined to get the balance-working point.

Compressor mathematical model A map is necessary to determine the off-design performance of the gas turbine when firing syngas. Actual compressor maps for modern gas turbine compressors are not available in the open literature. The compressor map used here is a typical one of advanced compressor, shown as Fig.3.. This map is translated to some equations with two given variables by means of a gridding method. The minimal surge margin of compressor is given as a constrained qualification.

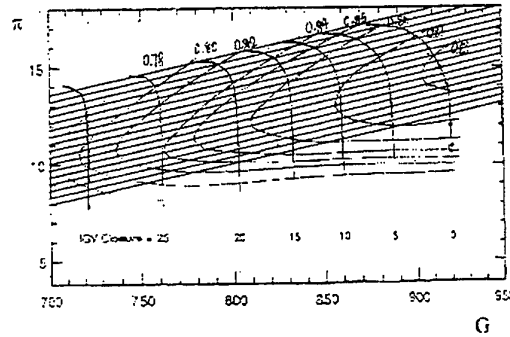


Fig.3. Compressor performance map and gridding

Expander mathematical model The expander off-design performance is described by the Quasi-ellipse Equation, which is applicable to the turbines with different number of stages under the condition of the certain rotate speed.

$$\frac{G_{g3} \sqrt{T_{g3}} / P_{g3}}{G_{g3}^0 \sqrt{T_{g3}^0} / P_{g3}^0} = \sqrt{\frac{(a_z + b_z \pi_t - \pi_t^2)}{(a_z + b_z \pi_{t0} - \pi_{t0}^2)}} \quad (6)$$

where: superscript 0 indicates the benchmark; a_z and b_z is up to the number of stages of expander, average degree of reaction and working-flow; G_{g3} is the mass flow of expander inlet; T_{g3} and P_{g3} are the temperature and the pressure of expander inlet; π_t is the expander expanding ratio.

Combustor mathematical model The combustor in IGCC system is not the same as the simple cycle for the medium-Btu syngas, compressor extraction air to ASU and nitrogen re-injection from ASU. The thermal equilibrium equation should consider all the above changes.

$$G_3 \times (H_3 - H_{g25}) = (G_2 + G_{11}) \times (H_a - H_{a25}) + G_f \times (H_u + Dh_f) \quad (7)$$

where: G_3 -----mass flow of expander inlet gas
 H_3, H_{g25} -----gas enthalpy at expander inlet and 25°C
 G_2, G_{11} -----air mass flow at combustor inlet and for expander cooling
 H_{a2}, H_{a25} -----air enthalpy at combustor inlet and 25°C
 H_u, Dh_f -----mixture gas low heat value and sensible heat

4. CASE STUDY AND RESULT ANALYSIS

Here a typical 400MW commercial IGCC power system, which is comprised of an entrained flow gasifier with feeding oxygen flow of 95% density, a low temperature clean-up subsystem, a large gas turbine and a cryogenic ASU. The intent is the gas turbine output and overall system efficiency. During the calculation, the compressor surge limit is carefully considered. Some results and curves are acquired, which provide useful information for system designer.

- (1) Fig.4. and Fig.5. show that the gas turbine output is larger and IGCC overall efficiency is higher when the degree of ASU integration incorporated with gas turbine is lower and the proportion of reinjected nitrogen is larger. Under the condition of the certain surge margin, the largest gas turbine output and highest IGCC overall efficiency available will be increased if the ASU-integrated coefficient is larger.
- (2) Fig.6. shows IGCC auxiliary power ratio is lower when the ASU-integrated coefficient is larger.
- (3) Fig.7. indicates that the gas turbine output, efficiency and pressure ratio are lower when the compressor guide vane angle is partially closed. So partially closing the compressor guide vane is one of the useful methods to avoid the system surge. At the same time, more nitrogen can be reinjected.
- (4) Fig. 8. and Fig.9. indicate that the gas turbine output and IGCC overall efficiency will be lowered with the expander inlet temperature declined. But more nitrogen can be reinjected under the condition of the same surge margin.

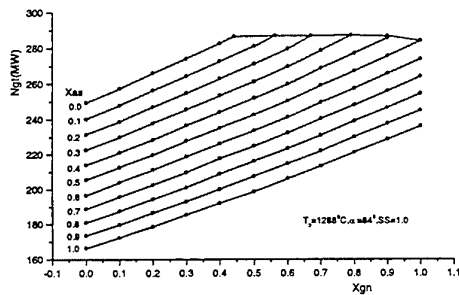


Fig.4. Gas turbine output power as a function of ASU-integrated coefficient and nitrogen-reinjected coefficient.

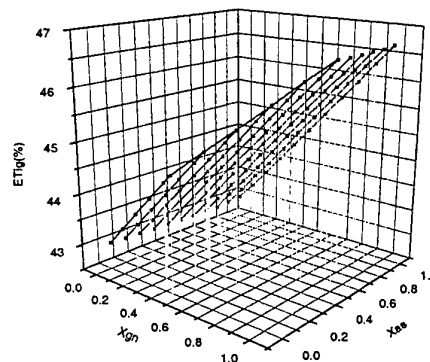


Fig.5. IGCC overall efficiency as a function of ASU-integrated coefficient and nitrogen-reinjected coefficient

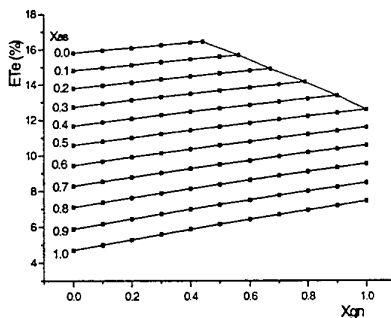


Fig.6. IGCC auxiliary power ratio as a function of ASU-integrated coefficient and nitrogen-reinjected coefficient

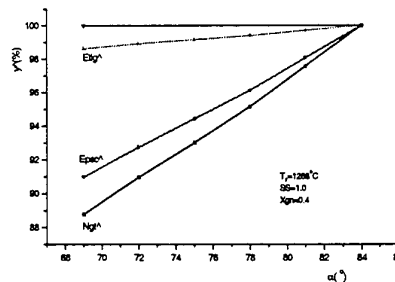


Fig.7. Gas turbine output power, efficiency and pressure ratio as a function of nitrogen-reinjected coefficient and compressor guide vane angle.

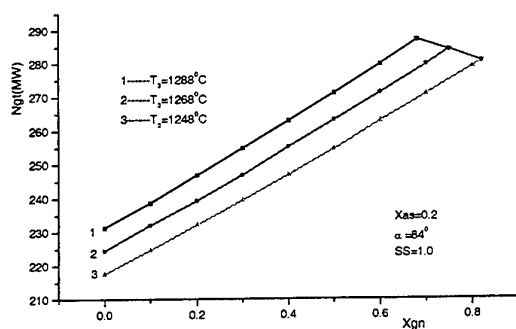


Fig.8. Gas turbine output power as a function of nitrogen-reinjected coefficient and expander inlet temperature.

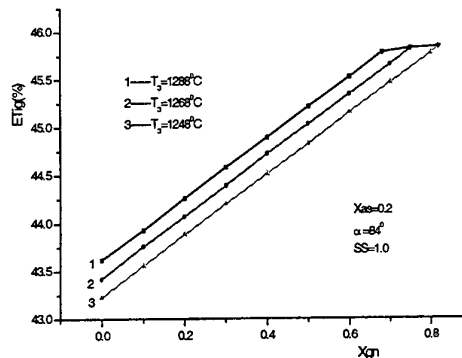


Fig.9. IGCC overall efficiency as a function of nitrogen-reinjected coefficient and expander inlet temperature.

5. CONCLUSIONS

This paper has described the key factors, which have effects on topping cycle performance, and the procedure to evaluate and optimize the topping cycle. A new idea— simultaneous optimization of the two opening variables—is presented and used to analyze a typical IGCC system. The resulting curves relating ASU integration coefficient, re-injecting nitrogen coefficient, gas turbine firing temperature, compressor guide vane angle and expander flow area are valuable for IGCC power plant design, analysis, or simulation.

REFERENCES

1. J.S. Kapat, A.K. Agrawal, T. Yang, "Air Extraction in a Gas Turbine for Integrated Gasification Combined Cycle (IGCC): Experiments and Analysis", Transactions of the ASME. Journal of Engineering for Gas Turbines and Power. (Journal Paper) ASME. Jan. 1997.
2. M.S. Johnson, "Prediction of Gas Turbine on- and off- Design Performance When Firing Coal-Derived Syngas", Transaction of the ASME, Vol.114, April 1992.
3. A.R. Smith, J. Klosek, D.W. Woodward, "Next-generation Integration Concepts for Air Separation Units and Gas Turbines", Transactions of the ASME. Journal of Engineering for Gas Turbines and Power. (Journal Paper) ASME. April 1997.
4. Z. Liu, R. Lin, "Technologies and Performance Prediction of Gas Turbine for IGCC", Journal of Engineering Thermophysics, Vol 18, 1997.

U. Engine Combustion

INVESTIGATIONS OF COMMON-RAIL FUEL INJECTION TECHNIQUE IN DI-DIESEL-ENGINES

S. Eisen, B. Ofner, F. Mayinger

Lehrstuhl A für Thermodynamik

Technische Universität München, Germany

Email: diesel@thermo-a.mw.tum.de; Fax: +49 89 289-16218

Keywords: combustion, diesel, Common-Rail, direct injection

ABSTRACT. The mixture formation and the combustion process of small direct-injection (DI) Diesel engines, equipped with high pressure common-rail fuel injection systems, was investigated by means of modern optical measurement techniques, such as digital high-speed cinematography and phase doppler particle analyzing (PDPA). The measurements were carried out in a high pressure chamber (HPC) and in a rapid compression machine (RCM). Several engine operating conditions with different boost pressures, injection pressures, and fuel quantities were examined. The influence of the injection and the swirl mode on the ignition delay and the flame propagation was analyzed. Different nozzle types (sac hole and VCO nozzles) with a variable number of holes and different injector types (electromagnetic/piezoelectric) were investigated. In order to observe the fuel injection, the ignition, and the combustion process simultaneously, a combined high-speed shadow graph and flame visualization technique was applied. The experimental analysis of the combustion process in the rapid compression machine yielded informations about the spray penetration and dispersing angle, the velocity, the distribution and the evaporation of the fuel droplets inside the piston bowl, the delay and the location of ignition as well as the progression of the whole combustion process including informations about the timedependent air flow during the compression and expansion stroke. The applied swirl did not show a significant influence on the spray penetration, but had a strong influence on the ignition and combustion process. Also a reducing effect on the swirl speed was observed, caused by the injected amount of high pressured fuel. PDPA measurements in the center of the spray show a characteristic and reproducible structure in the time series of droplet size and droplet velocity. The turbulence of the droplet velocity increases from the center to the edge of the spray while the mean velocity rapidly decreases.

1. INTRODUCTION

The growing international consciousness for environmental protection and the consequently ever more tightened emission legislation forces the automotive industry to reduce fuel consumption, and pollutant emission of Diesel engines. Since the injection method has a high influence on the combustion process, huge efforts have been made to improve current injection systems and to develop new technologies. Particularly the common-rail technology, which applies pressures up to 135 MPa, offers the advantage of a flexible sequential control of the injection process. In order to improve and to optimize the application of these systems, it is essential to get a better understanding of the complex processes inside the combustion engine. Therefore, modern optical measurement techniques have been applied to a high pressure chamber and a rapid compression machine to intensify the investigations on the system under conditions similar to a real engine.

The common rail technology offers several advantages, compared to conventional Diesel fuel injection systems:

- high injection pressures independant of the engine speed
- good fuel atomization also at the beginning and the end of each injection due to a constant rail pressure
- flexible and exact choice of injection begin and injection duration due to electronic control
- possibility of a pilot injection to reduce noise, particulates and NO_x emissions
- reduced need for swirl intensity at low engine speed due to high turbulence energy of the spray

- reduction of noise and material stress due to a silent high pressure pump with low torque oscillations and low torque peaks

2. EXPERIMENTAL SETUP

Fuel Injection System

The measurements were performed using a BOSCH common-rail fuel injection system, as shown in Fig.2. Variable nozzles, i.e. sac hole nozzles and VCO nozzles (see Fig.1), with five, six and seven holes were investigated. The VCO nozzles were equipped with two needle guidances to prevent a needle tip deviation from the needle seat.

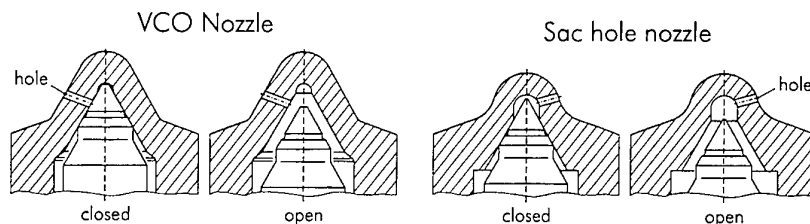


Figure 1: Diagrammatic section of the investigated nozzle types. The needle cone of a VCO nozzle itself occludes the nozzle hole whereas the sac hole needle seals the gap between the needle and the nozzle body

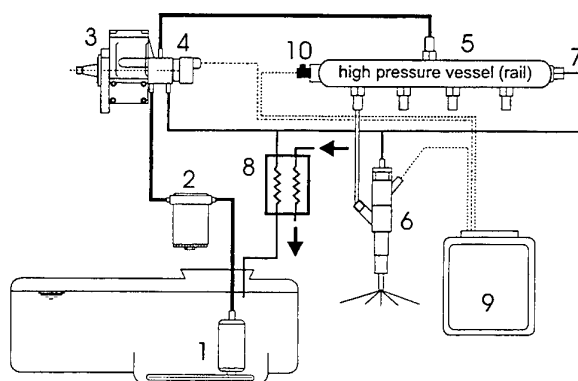


Figure 2: Setup of the common-rail system: 1: fuel tank with low pressure pump (0,15 MPa), 2: fuel filter, 3: high pressure pump (up to 135 MPa), 4: pressure regulating valve, 5: high pressure vessel (rail), 6: fuel injector with solenoid valve and nozzle, 7: safety valve, 8: heat exchanger, 9: control unit, 10: pressure transducer (0-160 MPa)

High Pressure Chamber

A high pressure chamber was used to investigate the fuel jet disintegration and the spray penetration under variable ambient pressure but constant ambient temperature conditions. The chamber provides an optical access to the nozzle from three different directions. It was designed for the application of several measurement techniques, such as the schlieren and the shadow imaging, the 2D Mie scattering as well as the 3D short time holography and the phase doppler particle analyzing technique.

Rapid Compression Machine

For experiments under conditions similar to those in a real engine, a rapid compression machine (RCM) was developed. This real scale RCM with a bore of 78.3 mm is based on a new driving concept. It offers optical access to the piston bowl from four directions, as shown in Fig.3. The RCM simulates one compression stroke of an engine with a speed of up to 3000 rpm.

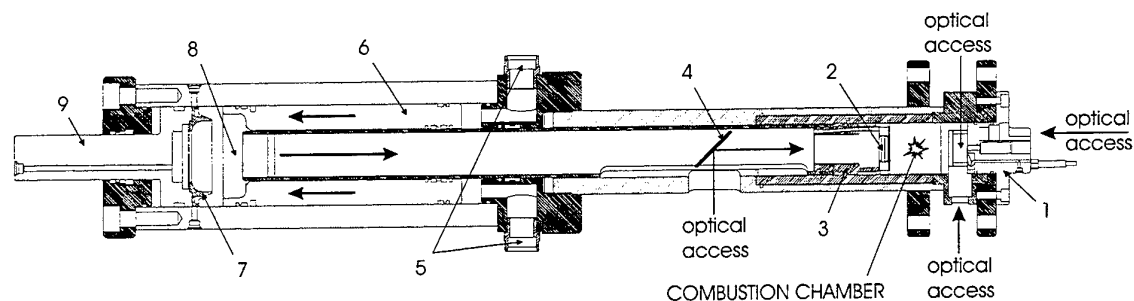


Figure 3: Halfsection of the Rapid Compression Machine shows the simple modular construction : 1: cylinder head, 2: piston bowl with windows, 3: piston, 4: mirror, 5: air pressure supply, 6: mass balance piston (also driving piston), 7: throttle aperture, 8: hydraulic oil filled volume, 9: adjustment piston for the compression ratio

Driven by pneumatic pressure, the maximum acceleration of the piston is 900 m/s^2 . The mass balance cylinder is located coaxial to a connecting pipe on which the piston itself is plugged on. Both, the mass balance cylinder and the connecting pipe, coupled with hydraulic oil, accomplish an opposite and concentric movement, which provides a 100% mass balance. This is especially important for optical measurements in order to avoid vibrations and to reduce measurement errors. The compression ratio of the RCM is continuously adjustable in a range of $\epsilon = 8$ to $\epsilon = 25$. The RCM also possesses a special shaped ring (forming the counterpart to the mass balance weight), mounted on top of the stroke-adjust piston (ref. No. 7 in Fig.3), which causes an orifice flow at the end of a stroke in the clearance between the mass balance weight and the ring. Close to the top dead centre this leads to a stroke adjustment equal to the motion of a crank mechanism.

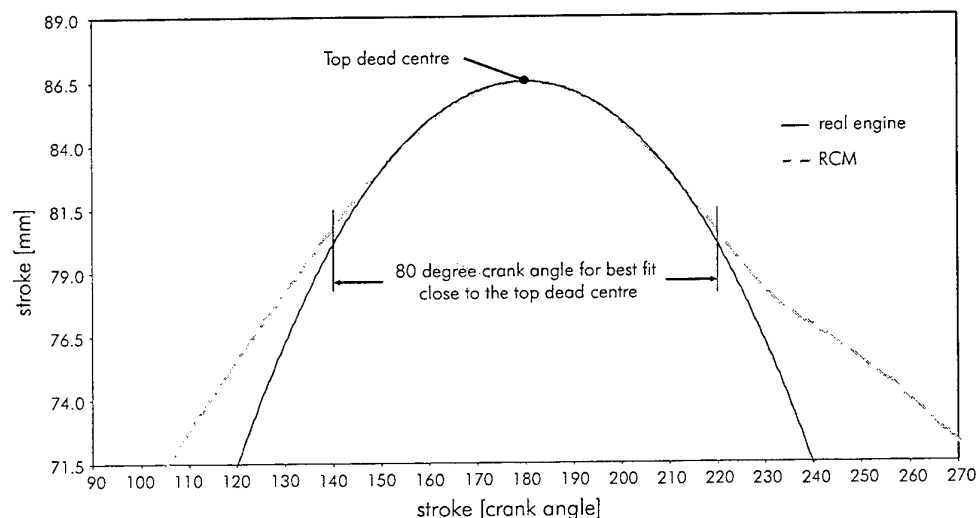


Figure 4: Comparison of the stroke movement between a real engine (100mm stroke length) and the RCM states an acceptable accordance over a range of 80 degree

Additionally the turbulence intensity, known for its strong influence on the mixing and the combustion process, can easily become adjusted by changing the swirl mode [11]. Finally the modular built up RCM with its screw plugged combustion chamber offers experimental rates up to 15/h since the transparent parts of the chamber have to become cleaned after each stroke in order to maintain the perfect optical access.

3. OPTICAL MEASUREMENT TECHNIQUES

High-Speed Cinematography

A sketch of the experimental setup can be seen in Fig.5. The injection, the ignition and the combustion process in the RCM was visualized by means of a digital high-speed camera with a framerate of up to 40.500 frames/sec. In contrast to single shot imaging techniques, this high-speed camera can record 1000 images, which provides a high resolution of complex transient processes.

In combination with a high power Argon-Ion-Laser (7.5 W), which was applied for a Schlieren and a shadow graph setup, the fuel injection and the spray penetration was observed together with the combustion process. This was realized by the usage of a filter combination with a high transmission for the light of the laser wavelength and a low transmission for the light spectrum of the flame. Due to the high velocity of the spray, the cw- Ar^+ -laser was chopped by means of an acoustic-optical-modulator to avoid a movement blur.

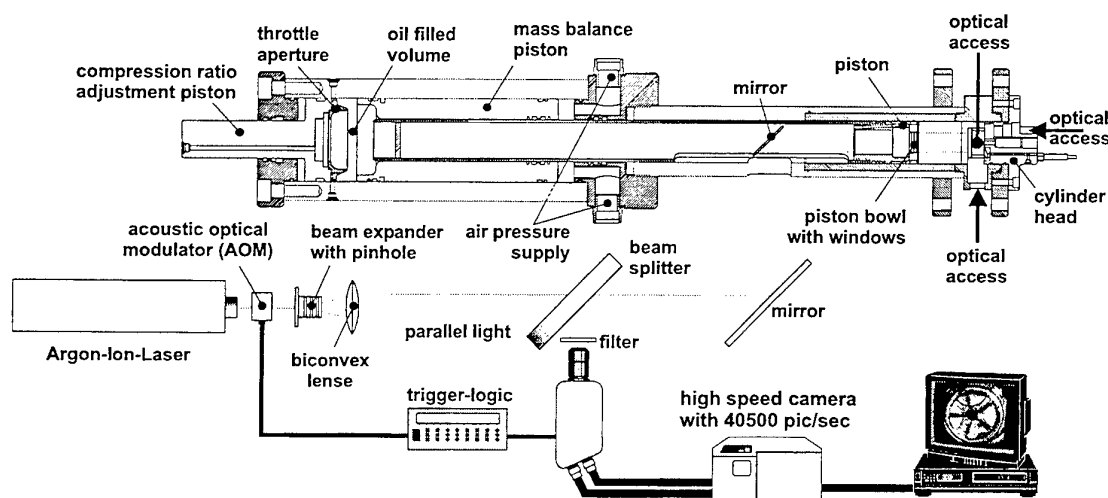


Figure 5: Half section of the rapid compression machine (RCM) and experimental setup for high-speed cinematography

Phase Doppler Particle Analysis

The principle of phase doppler particle analysis (PDPA) can be found elsewhere [2,3,5,10]. Therefore, only the application of this measurement technique will be described here. Due to the high droplet concentration a high laser power is required to ensure the laser beams penetration into the spray center. Moreover, the measurement volume must be as small as possible to avoid that several droplets pass the measuring volume at the same time. A small measurement volume decreases measurement errors due to the slit and the trajectory effect [1]. Furthermore it increases the intensity of the diffracted light, which raises the signal to noise ratio (SNR). The fact, that on the one hand the mean droplet diameter of the investigated sprays was smaller than $20\mu m$ and on the other hand the droplet velocity in the center of the spray reached more than 300 m/s forced to a compromise in the choice of the measurement setup.

To get a small measurement volume and a high spatial resolution in diameter, the focal length of the

transmitting probe has to be short and the beam separation must be large. The high velocity of the droplets, however, requires a large fringe spacing, which can only be realized by a narrow crossing angle of the laser beams, i.e. a large focal length and a small beam separation.

The best results were achieved with a configuration as shown in Table 1. Comparative measurements of the PDPA with a high speed camera proved that, with this configuration, the PDPA was capable of measuring droplet sizes and velocities, even in the very dense region of the spray tip center.

Table 1: Configuration of the PDPA for Measurements in a High Pressure Diesel Spray

Measuring volume			
diameter:	47	μm	
length:	1.96	mm	
fringe spacing:	10.6	μm	
laser power:	500	mW	
Measuring setup			
scattering mode:	refraction		
scattering angle:	27	degrees	
diameter range:	0.4 – 156	μm	
velocity range:	0 – 372	$\frac{m}{s}$	

Mie Scattering

In order to investigate the fuel jet disintegration and the spray penetration in quiescent air, the Mie scattering technique together with a high resolution CCD-Camera (1280 * 1024 Pixel, 12 bit colour) was applied to the high pressure chamber. The spray was illuminated with a flash light (NANOLIGHT). Although this measurement technique provides only one image of a single injection, it offers the advantage of short exposure, higher resolution and an easy measurement setup.

4. RESULTS AND DISCUSSION

Spray Properties

Spray penetration and spray structure. The penetration of the fuel jet of VCO nozzles at the beginning of the injection was visualized by means of the shadow graph imaging technique. The acceleration of the spray tip results from the decreasing pressure losses and throttle effects inside the nozzle, due to the needle stroke. Therefore, the later injected fuel passes and accelerates the spray tip (see Fig.6). These intense throttle effects at low needle lifts of VCO nozzles have significant influence on the spray penetration, the spray structure and the mixture formation. The spray angle of the VCO nozzles reached its maximum immediately after the needle opened and then decreased to a constant value of approximately 20° at the investigated engine operating conditions. At high injection pressures a reincrease of the spray angle during needle closure was observed. The sac hole nozzles, however, showed a constant spray angle during the whole injection. In contrast to the sac hole nozzles, most of the VCO nozzles, even if equipped with two needle guides, created a nonsymmetrical spray, as shown in Fig.7. This is caused by a deviation of the needle tip from the seat center, which leads to a strong throttle effect at the partly occluded holes and to an increase in the fuel jet velocity at opposite holes. This problem, which can occur at low needle lifts, is intensified by two facts. On the one hand the high pressure pump permanently delivers an injection pressure of up to 135 MPa. Therefore, small needle deviations already have a strong influence on the spray structure from the beginning of injection. On the other hand the solenoid controlled common-rail fuel injector has a slow needle opening velocity, so that the needle remains in a critical partial lift for a relatively long time. This effect plays an important role for the proportioning of small fuel quantities, as it is needed for the pilot injection.

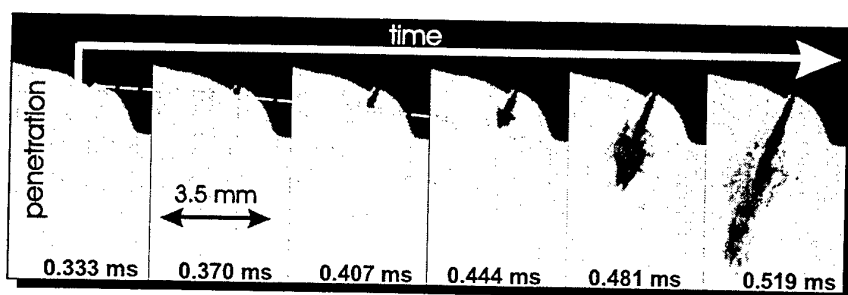


Figure 6: Acceleration of the spray tip at the beginning of the injection; VCO nozzle with five holes; a baffle plate was mounted for observation of one fuel jet

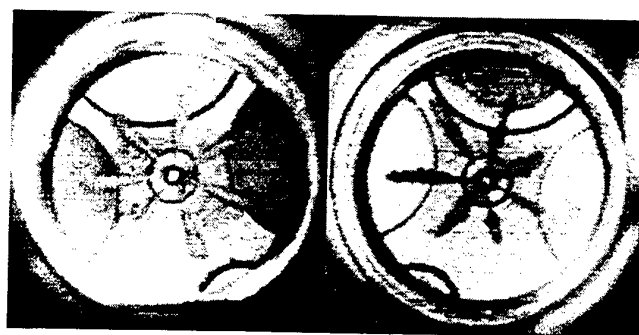


Figure 7: Spray structure of a sac hole nozzle (left image) and a VCO nozzle (right image)

Droplet size and droplet velocity. Modern Diesel fuel injection systems use high injection pressures and nozzles with a small hole diameter. This increases the turbulence energy of the spray and decreases the droplet diameter. Therefore the mixture formation as well as the evaporation of the droplets is accelerated.

PDPA measurements of the droplet sizes and the droplet velocities were carried out under room temperature conditions and variable ambient pressure (up to 2.0 MPa). About 200 injections were necessary to validate 20.000 droplets. In each spray 50 spots were analyzed, distributed over a plane perpendicular to the spray axis at distances of 20 mm from the nozzle. The collected data was post processed to calculate a time resolved arithmetical mean diameter (D_{10}), a Sauter mean diameter (D_{32}), and a mean velocity as well as the appropriate RMS value and a probability density function (PDF) of the droplet size and the droplet velocity distribution. The time resolved mean values were calculated within intervals of $200\mu s$, which were shifted by $50\mu s$, so that the intervals overlapped each other by $150\mu s$.

The results of the PDPA experiments show a characteristic and reproducible structure in the time series of the droplet size and the droplet velocity in the center of the spray (see Fig.8). With an increasing distance from the center of the spray, the turbulence and the RMS of the droplet velocity rises while the mean velocity decreases rapidly. This results from the fuel jet induced vortexes, the shear forces and the exchange of momentum with the ambient air.

The center of the spray tip covers a wide range of velocities from 80 m/s up to more than 300 m/s. The highest droplet velocities appear right behind the spray tip and remain at a constant level as long as the needle lift is constant. At the end of the injection the droplet velocity decreases rapidly.

One reason for this characteristic course is, that the spray was injected into quiescent air. The spray tip was decelerated while the air was accelerated due to an exchange of momentum. Therefore the air

was entrained and penetrated into the spray. This reduced the drag for the droplets behind the spray tip which had the highest velocity. Consequently these droplets caught up with and even passed the spray tip. This led to a rising droplet concentration in the region of the spray tip with an increased distance to the nozzle.

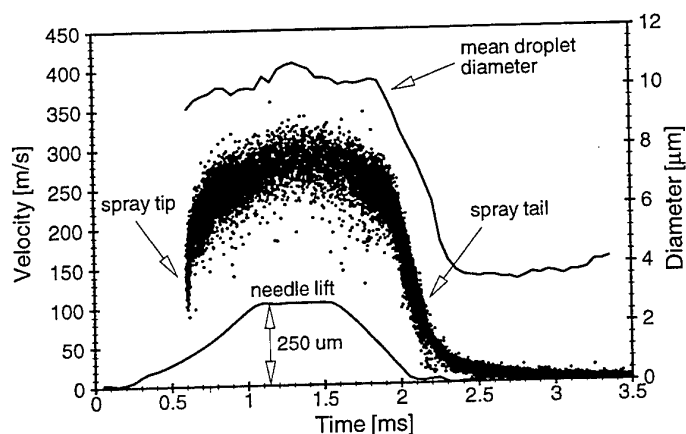


Figure 8: Time series of the droplet velocity and the mean droplet size (D_{10}) in the center of a high pressure Diesel spray (20.000 validated droplets)

At ambient pressures (0.1 MPa) the course of the time resolved mean droplet diameter (D_{10}) is similar to the course of the velocity, as shown in Fig.8. The smallest droplets have the lowest velocity and vice versa, which proves that the droplet size is correlated with the droplet velocity. Measurements at increased ambient air pressures but constant injection pressures, however, show an significant influence of the air density on the droplet velocity and the droplet size, see Fig.9.

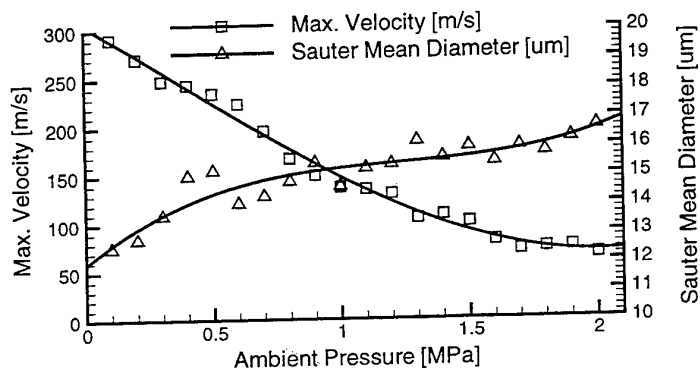


Figure 9: Influence of the air density on the size and the velocity of droplets in the center of the spray

At higher air densities, the maximum velocity decreases significantly and the range of the droplet velocities in the spray tip expands. Droplets with almost zero velocity were measured. At the same time, the droplet size in the spray tip decreases, while behind the spray tip the droplet size and consequently the Sauter mean diameter increases. Similar results were found by Payri et. al. (1996) [8]. The distribution of the mean droplet size and the mean velocity in a plane perpendicular to the spray axis is shown in Fig.10. The mean values were calculated in a time interval with constant needle lift. The highest velocities and biggest droplets appear in the center of the spray. The velocity distribution has a high gradient towards the edge of the spray with peak values of up to 260 m/s in the center and only 20 m/s at spots 1.5 mm away from there. The mean droplet diameter decreases from 10 μm in the center down to 4 μm at the edge of the spray.

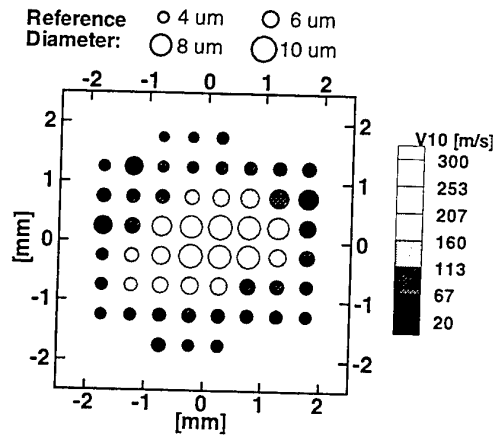


Figure 10: Distribution of the mean droplet diameter (D_{10}) and the mean droplet velocity in a plane perpendicular to the spray axis

Mixture Formation and Evaporation

The mixture formation and the evaporation without combustion was investigated in the RCM. Therefore the air inside the RCM was replaced by nitrogen. Images from a high-speed video of the fuel injection into the piston bowl are shown in Fig.11. In this case, a pilot injection of 2 mg fuel at an injection pressure of 80 MPa was realized. It can clearly be seen, that the spray of the pilot injection does not reach the wall of the piston bowl, due to its insufficient momentum, based on the strong throttle effects at low needle lifts.

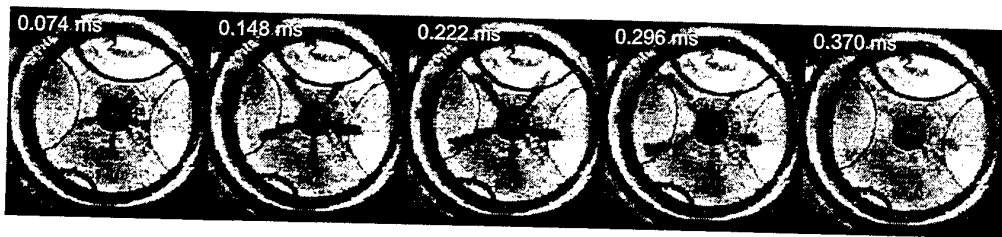


Figure 11: Evaporation of a pilot injection (2mg fuel mass, injection pressure 80 MPa). Time interval between two images is $74\mu\text{s}$.

However, the fuel of the main injection (15 mg) in Fig.12, which has a higher needle stroke and therefore a higher fuel jet speed, reaches the piston bowl wall after $300\mu\text{s}$. The swirl, which rotated counter clockwise at a speed of 580 rad/s, does not have a significant influence on the spray penetration. Only after the droplets are decelerated and partly evaporated, the swirl affects the spray motion. An essential increase in the momentum of the swirl, i.e. the swirl speed, would be necessary to improve the mixture formation. This, however, is difficult to achieve at a low engine speed. Therefore common-rail systems use high injection pressures to increase the turbulence energy of the spray, which reduces the need of swirl energy to produce the necessary mixture formation energy.

The fuel of the pilot injection (see Fig.11) evaporates completely within $400\mu\text{s}$ and the fuel of the main injection within $600\mu\text{s}$ (see Fig.12) after the begin of its injection. A significant difference in the evaporation processes of VCO nozzles and sac hole nozzles was not observed. Figure 13 illustrates a complete injection sequence including pilot and main injection (1mg/15mg) using a VCO nozzle with six holes (combustion suppressed by nitrogen).

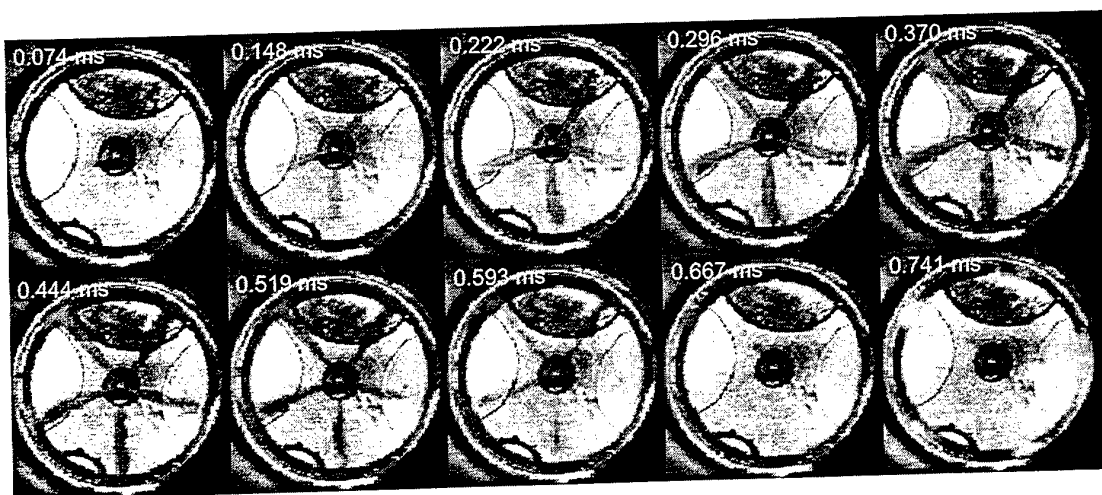


Figure 12: Evaporation of an underload main injection (15mg fuel mass, injection pressure 80 MPa). Time interval between two images is $74\mu\text{s}$.

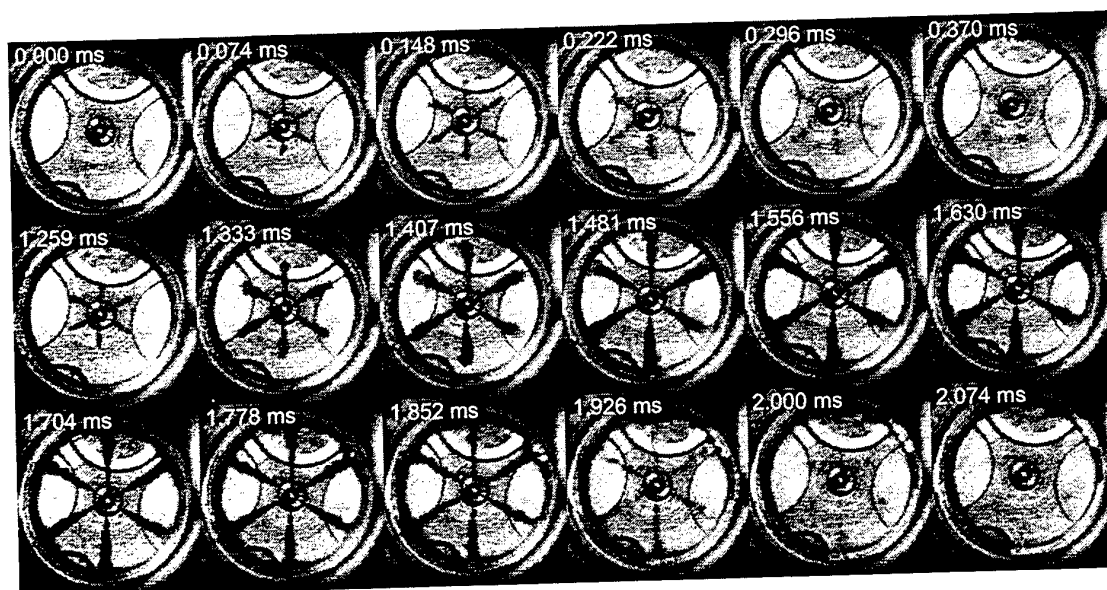


Figure 13: Evaporation of the spray — VCO nozzle with six holes; pilot injection: 2 mg; main injection: 15 mg; injection pressure: 80 MPa; time delay between pilot and main injection: 1 ms; swirl intensity: 80 rev/s; high-speed video of the fuel injection into the piston bowl in the RCM, recorded through the bottom of the piston; air replaced by nitrogen; framerate: 13500 pic/sec

Ignition and Combustion

The common-rail fuel injection system produces droplets of less than $20\mu\text{m}$, which evaporate rapidly. This led to a short ignition delay and a continued combustion of the fuel during the injection. Therefore, together with pilot injection, a significant reduction of the ignition delay of the main injection can be realized, especially when the fuel jet of the main injection penetrates through the flame of the pilot injection (see Fig.14).

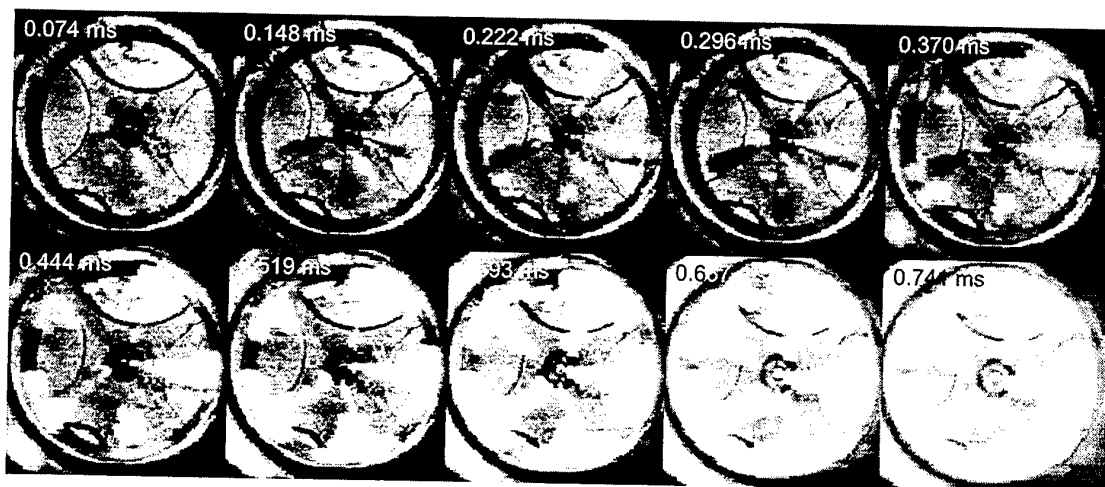


Figure 14: Ignition of a main injection with swirl penetrating the rest of a pilot flame (partly visible in the first picture). Typical for this kind of combustion is the ignition along the fuel jet from the center to the piston bowl wall. Due to the air motion the jet ignites at the averted side of the swirl.

Compared to conventional fuel injection systems, not the entire amount of heat is released at once, because the ignition and combustion starts while the fuel is still injected. This causes a smoother pressure and temperature gradient which generally reduces the noise and the NO_x emission. The ignition always started at the sprayside which was averted to the swirl, since the fuel vapor was washed out of the spray and formed an ignitable fuel/air mixture. This ignitable mixture remained in an eddy region behind the spray until the ignition started (see Fig.14). Though the swirl does not have a significant influence on the spray penetration, it has a strong influence on the ignition and the flame propagation and therefore improves the utilization of the air charge. In case of VCO nozzles experiments without swirl showed, that the ignition is frequently located nearby the nozzle.

The fuel, which is injected first, has a lack of momentum and therefore a short penetration depth. It evaporates and remains near the nozzle until the ignition delay passes. After the ignition nearby the nozzle, the flame propagates very fast along the fuel jets towards the wall of the piston bowl where it usually remains (see Fig.15/16/17). This is caused by the high momentum of the main injection. The spray interacted with the wall and wetted the wall, which had a too low temperature for instant evaporation of the fuel. The fuel evaporated slowly from the wall. Consequently, a heatable piston bowl was designed, which will be used for further investigations. The use of sac hole nozzles caused, given the same conditions, an ignition of the load along the later parts of the fuel jet closer to the wall. But the main combustion also took place nearby the piston bowl border.

Furthermore a reduction of the swirl speed was to be seen due to the fuel mass which was injected perpendicular to the air motion. Dependent on the fuel mass (underload fuel mass assumed) the swirl speed approximately becomes reduced by factor 0.8.

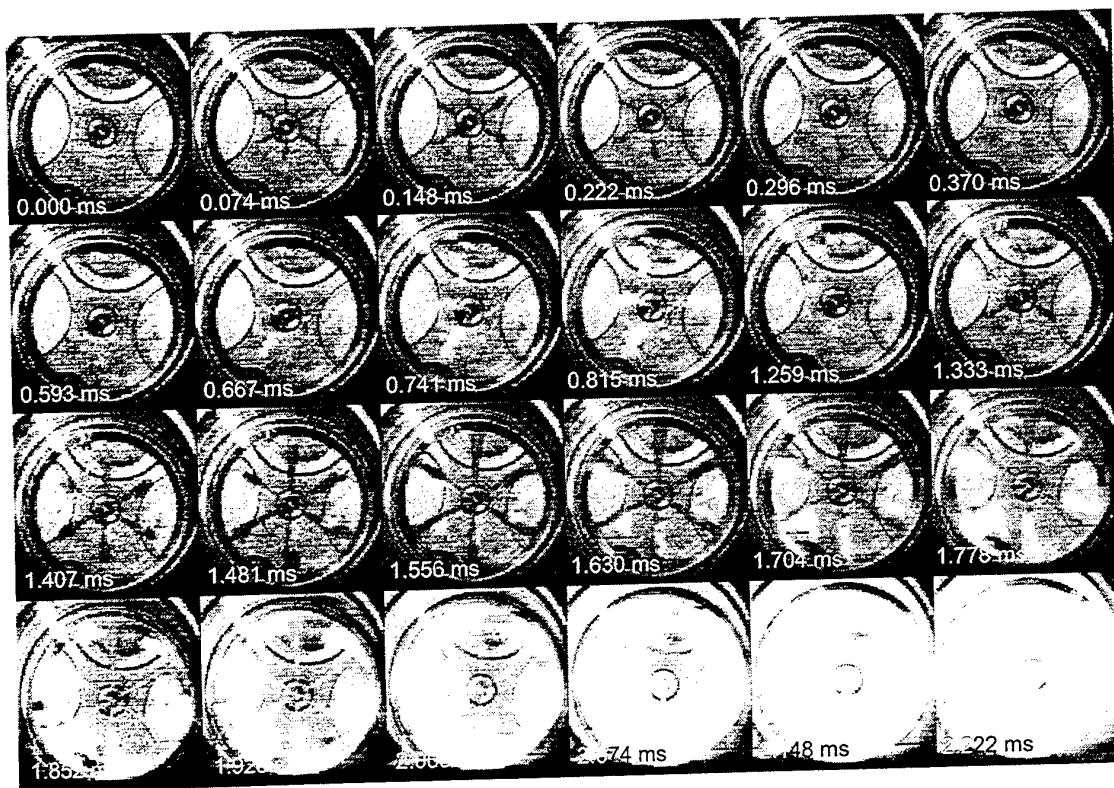


Figure 15: Evaporation of the spray and combustion of the fuel vapor — Measurement conditions are the same as in Fig.13 (but without nitrogen)

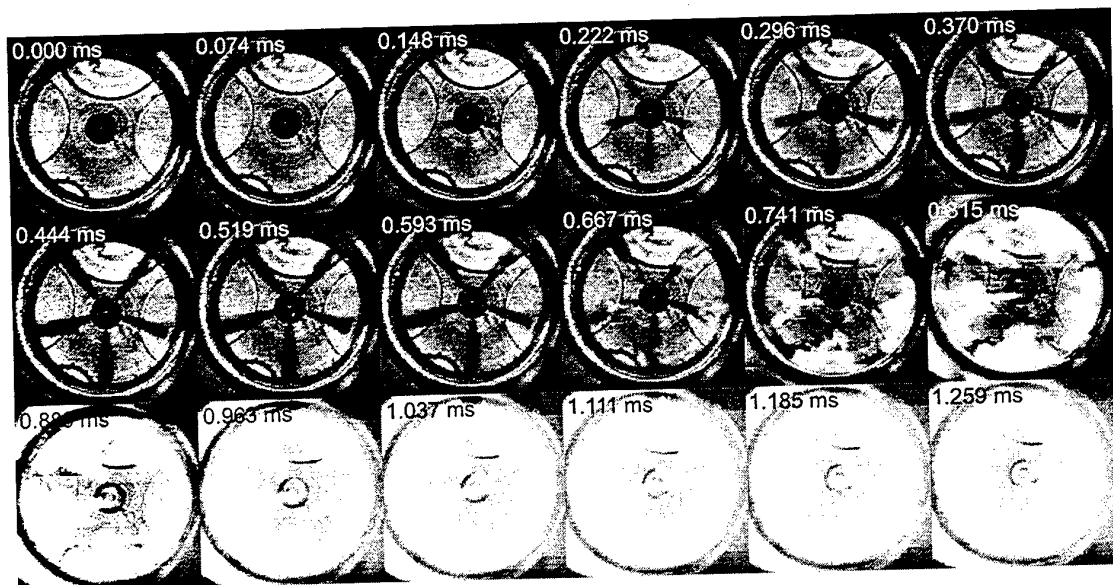


Figure 16: Evaporation of the spray and combustion of the fuel vapor without swirl and without pilot injection using a piezoelectric injector. Main injection: 15 mg; compression pressure: 8 MPa; injection pressure: 80 MPa;

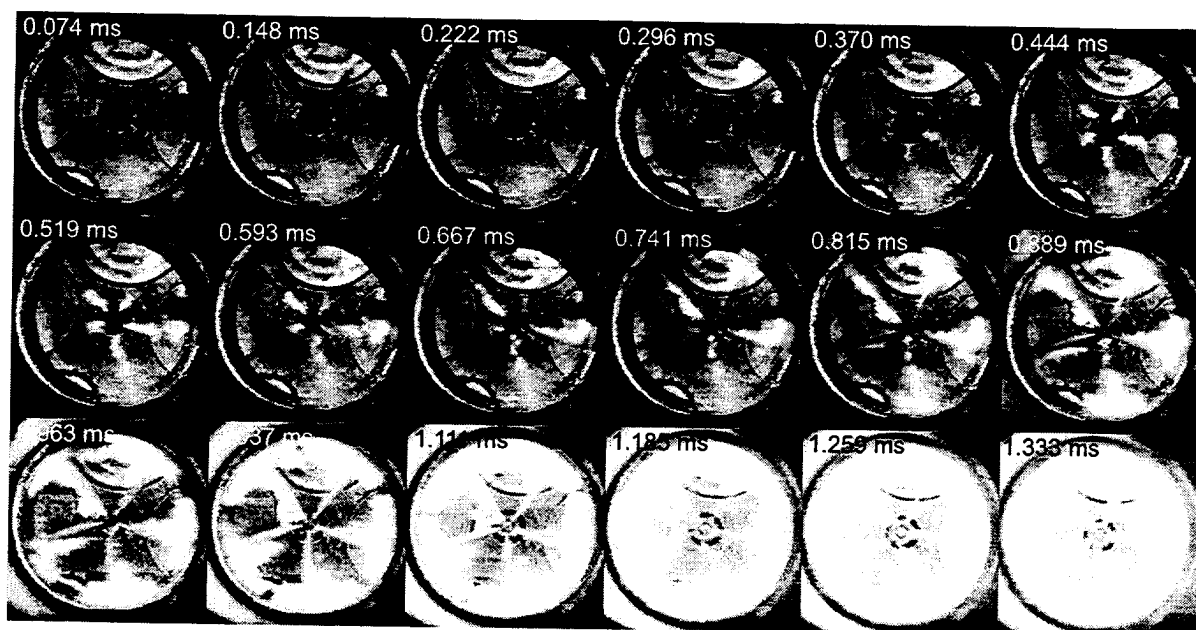


Figure 17: Evaporation of the spray and combustion of the fuel vapor with swirl and pilot injection using a piezoelectric injector. Chamber conditions are the same as in 16. Pilot injection: 1 mg; main injection: 15 mg; compression pressure: 8 MPa; injection pressure: 80 MPa;

One of the most promising developments concerning improvements of the spray behaviour aim to a new needle opening technique realized by using a piezo electrical crystal. This way throttle effects due to slow needle lifts become minimized based on the time for a needle lift of less than a third compared to a common magnetic driven injector. Combined with a Common Rail System it is conceivable to apply up to five pilot/post injections for each single compression stroke obtaining acceptable spray properties.

Exhaust gas recirculation (EGR) has been shown to be an effective means to control NO_x emission [6]. The exhaust gas dilutes the air by a reduction of the availability of oxygen, which lowers the flame temperature in rich regions and therefore reduces the formation of NO_x . For investigations of the ignition and the combustion process with EGR in the RCM, the exhaust gas of a Diesel engine was mixed with air until an EGR-rate of 40% was obtained. The first results of experiments with EGR showed an increase of the ignition delay as well as a smoother pressure rise and a weaker light emission of the flame. Further measurements concerning EGR are still in progress.

5. SUMMARY, CONCLUSIONS AND OUTLOOK

In this paper, the application of modern optical measurement techniques for investigations of the mixture formation and the combustion process in direct injecting Diesel engines is presented. The measurements were carried out in a rapid compression machine (RCM) and in a high pressure chamber in order to analyze the performance of solenoid controlled common-rail fuel injection systems.

Common-rail fuel injection systems have a high potential for the reduction of soot and NO_x to meet future emission legislation. The constant injection pressure of up to 135 MPa improves fuel atomization, also at the beginning and the end of injection, especially at low engine speed and under load condition. The high velocity of the fuel jet and the fuel droplets cause a high turbulence energy and therefore reduces the need of swirl energy to reach a necessary mixture formation. The flexible electronically control of the begin of injection and the possibility for multiple injections can lower the noise and NO_x as well as the particulates emission.

Beside the discussed advantages, there are still problems which have to be solved, such as an unsatisfied manufacturing accuracy of the nozzles leading to a nonsymmetrical spray structure and a difficult proportioning of small fuel quantities. This is also intensified by the relatively slow needle motion. This might be eliminated by the use of piezo-electrical controlled fuel injectors, which can open and close the needle up to three times faster than solenoid controlled fuel injectors. Therefore this promising new technology will be the subject of further investigations.

ACKNOWLEDGEMENT

The authors wish to thank the Bavarian Research Foundation (Bayerische Forschungstiftung) and the automotive companies AUDI, BMW and MAN for the financial support.

NOMENCLATURE

D_{10}	$\frac{1}{n} \sum_{i=1}^{i=n} D_i$	Arithmetical mean diameter	p_a	Ambient pressure
			p_{inj}	Injection pressure
D_{32}	$\frac{\sum_{i=1}^{i=n} D_i^3}{\sum_{i=1}^{i=n} D_i^2}$	Sauter mean diameter		

REFERENCES

1. Y. Aizu; F. Durst; G. Grehan; F. Onofri; T.-H. Xu; (1993); "PDA-system without Gaussian beam defects"; Proc. of the 3rd Int. Conf. on Optical Particle Sizing (OPS); Yokohama; Japan
2. W.D. Bachalo; (1994); "Experimental methods in multiphase flows"; Int. Journal of Multiphase Flow, Vol. 20, Suppl., pp.261-295;
3. J. Domnick; V. Dorfner; F. Durst; M. Yamashita; (1993); "Performance Evaluation of Different Phase Doppler Systems"; Proc. of the 3rd Int. Conf. on Optic. Part. Sizing (OPS); Yokohama; Japan
4. H. Hiroyasu; M. Arai; (1990); "Structures of Fuel Sprays in Diesel Engines"; University of Hiroshima; Japan; SAE-Paper 900475
5. F. Mayinger; (1999); "Optical Measurements - Techniques and Applications"; to be published in fall 1999; Springer Publishing Company; Germany
6. T. Murayama; (1989); "Simultaneous Reduction of NO_x and Smoke of Diesel Engines, without Sacrificing Thermal Efficiency"; JSME Int. Journal, Series B, 37, 1
7. J. Naber; L. Siebers; (1996); "Effects of Gas Density and Vaporization on Penetration and Dispersion of Diesel Sprays"; Sandia National Labs.; USA; SAE-Paper 960034
8. F. Payri; J.M. Desantes; J. Arregle; (1996); "Characterization of D.I. Diesel Sprays in High Density Conditions"; CMT-Universidad Politecnica de Valencia; Spain; SAE-Paper 960774
9. P. Precht; F. Dorer; B. Ofner; S. Eisen; F. Mayinger; (1998); "Modern Optical Measurement Techniques applied in a Rapid Compression Machine for the Investigation of Internal Combustion Engine Concepts"; ERCOFTAC Bulletin, No. 3; pp. 47-52; Switzerland
10. C. Tropea; T.H. Xu; F. Onofri; G. Grehan; P. Haugen; M. Stieglmeier; (1995); "Dual Mode phase Doppler anemometer"; Fourth Int. Congr. on Optical Particle Sizing (OPS); Nrnberg; Germany
11. B. Ofner; S. Eisen; Mayinger, F.; (1998); "Performance of Common-Rail Fuel Injection Systems in DI-Diesel-Engines"; to be published in fall 1999; International Conference on Engineering Thermophysics (ICET'99), Beijing

OPTIMIZATION OF A HYDROGEN FUELED LARGE BORE COMPRESSION IGNITION ENGINE: DEVELOPMENT OF A NEW VARIABLE INJECTION SYSTEM FOR HIGH PRESSURE GAS INJECTION

Peter Prechtel, Dorer, Franz Mayinger

Lehrstuhl A für Thermodynamik

Technische Universität München, Germany

Email: prechtel@thermo-a.mw.tu-muenchen.de; Fax: (+49)/89-289-16218

Keywords: hydrogen, large bore engine, diesel engine, compression ignition, high pressure injection system

ABSTRACT. In the research project "Directly Injecting Hydrogen Diesel Engine with High Power Density and Low Emissions", the basis for the use of a large bore diesel engine fueled with hydrogen was investigated. The project partners were the MAN B&W Diesel AG [1], the Lehrstuhl für Verbrennungskraftmaschinen und Kraftfahrzeuge (LVK) and the Lehrstuhl A für Thermodynamik (LAT). The LAT investigated mixture formation, ignition and combustion processes with modern optical measurement techniques, in a newly developed rapid compression machine (RCM) and with numerical simulations. The investigations delivered a set of suitable thermodynamic parameters for the operation of the engine. In addition, optimized geometries for the nozzle design were found out. A new concept for a high pressure hydrogen injection system with variable needle lift was setup and investigated.

1. INTRODUCTION

The development of new concepts for internal combustion (i.c.) engines with alternative fuels requires a detailed investigation of internal processes especially of the properties of the new fuel and necessary components. Thermodynamic and chemical properties of hydrogen, for use in compression ignition engines, are completely different compared to properties of diesel fuel. The autoignition temperature of hydrogen is with 850 K much higher compared to diesel with values of 520 K. In addition, hydrogen is gaseous down to very low temperatures of -253°C. Due to high pressure, it is impossible to liquefy hydrogen at room temperature. A high laminar combustion velocity (2.3 m/s for an equivalence ratio of 1) and wide ignition limits between $\lambda = 0.14 - 10$, lead to a different combustion behavior when compared to diesel fuel. The design of the engine concept was influenced by properties of hydrogen and the use in large bore engines with high power density. The engine is driven with late inner mixture formation and compression ignition. For the mixture formation a new electro-hydraulic controlled high pressure gas injection system was developed. The highly pressurized hydrogen is injected gaseously into the combustion chamber near top dead center (TDC).

2. EXPERIMENTEL SETUP

Optical measurement techniques allow a detailed study of the mixture formation, ignition and combustion process with high temporal and spatial resolution. A new type of rapid compression machine, which allows the investigation of the internal processes under realistic conditions was developed at LAT. The RCM allows an easy variation of the thermodynamic conditions, such as load pressure and temperature, and geometry such as the compression ratio ($\epsilon \leq 30$) and the form of the combustion chamber. In addition, it is possible to vary the flow conditions in the cylinder (swirl). The adaptation of the cylinder head for the application of different injection systems is possible with little expenses. The maximum combustion pressure is limited to 200 bar due to optical access through quartz windows.

In Fig. 1, a cross-section of the rapid compression machine is shown. A large window ($\varnothing=200$ mm, $d=100$ mm) in the piston allows a nearly complete look into the combustion chamber. Two additional windows at both sides give access to the combustion chamber for laser light sheets.

The operation of the machine is based on the opposite movement of two concentric pistons, a compression piston and a mass balance piston (outer piston). Both pistons are connected to an oil cushion. The pistons are driven by pressurized air (10 – 60 bar), supplied from three 50 liter bottles. The pressurized air accelerates the outer piston.

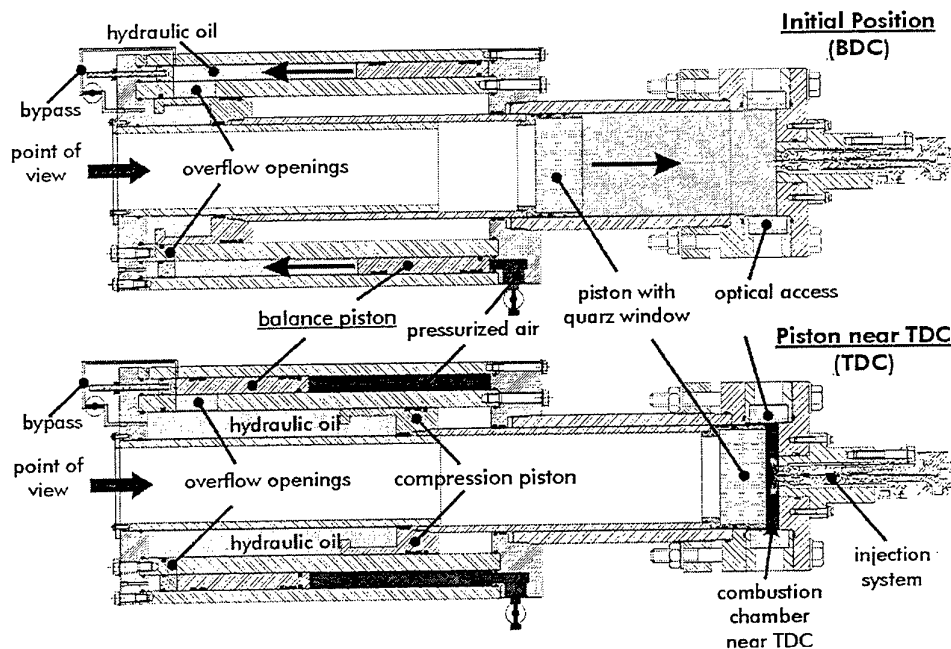


Fig. 1: Cross-section of the rapid compression machine with the pistons in two positions (top: initial position, bottom: top dead center)

Despite the high acceleration forces of about 270 kN, the machine nearly operates without any vibrations due to the total mass balance of the two pistons. At the beginning of the experiments, the pistons are in their initial positions (top of Fig. 1). The compression stroke is started by opening the small bypass valve, through which both pistons begin to move slowly. The compression piston functions as a large, fast switching valve. When the compression piston leaves the large sealing, the big overflow openings are opened and the pistons accelerate to velocities of 10 to 15 m/s. The air in the combustion chamber is compressed by the compression piston in realistic time. After the compression stroke, both pistons move back in direction of their initial positions, just as on an air spring. In Fig. 2, the piston position and pressure is shown for a single compression without injection and combustion. In the vicinity of TDC, the pressure of the RCM corresponds very well with the values of the single cylinder engine. The injection system can be electronically triggered, depending on the position of the piston.

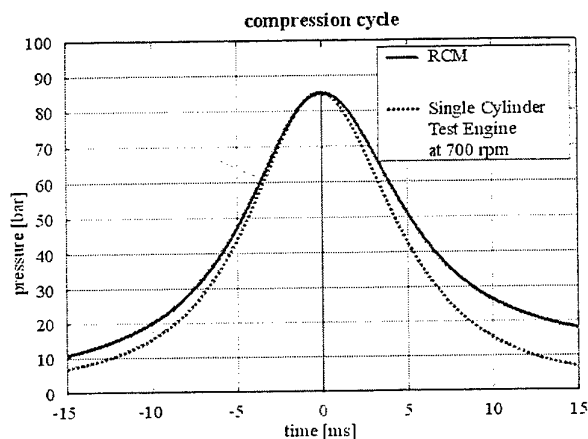


Fig. 2: Piston position and pressure during a compression and expansion stroke of the rapid compression machine compared to a single cylinder large bore test engine.

3. OPTICAL MEASUREMENT TECHNIQUES

For the experimental investigation with high temporal resolution, two setups [2] were used; a Schlieren/Shadow technique and a Fluorescence technique in combination with a digital high-speed camera. The Schlieren/Shadow-technique is necessary, to make the gaseous hydrogen visible during the injection process. This technique uses the effect of the distortion of the parallel laser light due to variations of the optical density (refraction index) on the light path through the combustion chamber. The setup for this technique is shown in Fig. 3 with the RCM and the optical equipment (Ar-Ion laser with an opto acoustic chopper, lenses, mirrors and the high-speed camera). For the investigation of the ignition and combustion process, the self fluorescence cinematography is used. The camera detects the light which is emitted during the hydrogen combustion. A large part of the light emission is located in the UV range around 308 nm which arrives from the OH-molecule. Therefore, the camera and the objective have to be sensitive in the UV-range. The combination of both techniques allow a simultaneous detection of the mixture formation and the ignition process. The experiments were carried out with frame rates between 4500 Hz and 40500 Hz.

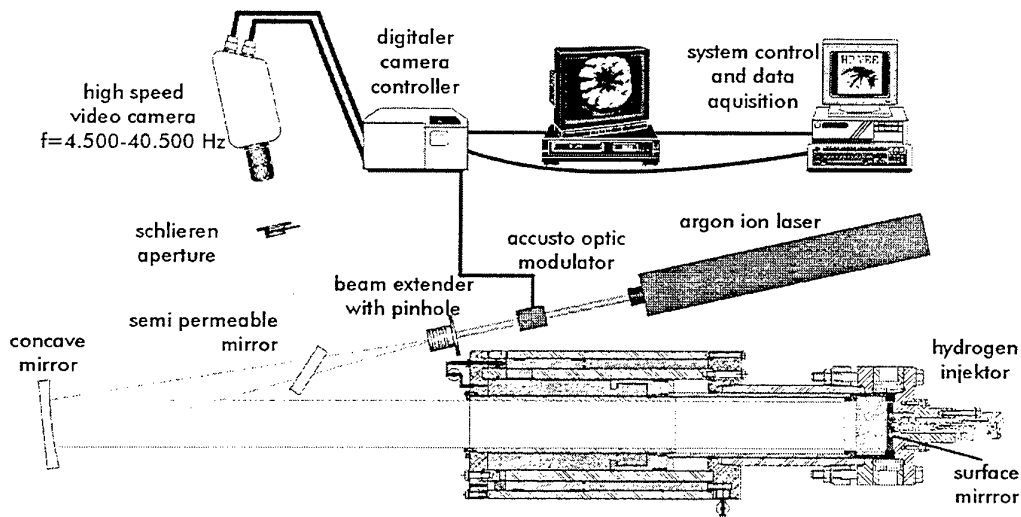


Fig. 3: Schlieren/Shadow setup with the rapid compression machine

4. MIXTURE FORMATION

The use of the Schlieren/Shadow setup as shown, allows an investigation of spatial and temporal behavior of high pressure injection of hydrogen into the combustion chamber. In Fig. 4, images of the mixture formation for different types of nozzles are shown. In the vicinity of the nozzle - at the beginning of the injection period - the hydrogen jet propagates with the highest velocity up to 160 m/s into the combustion chamber. Due to high density of compressed air near top dead center and a small momentum of the hydrogen jet, the penetration speed decreases, within a few centimeters from the nozzle, down to values of 10 to 20 m/s. Despite the high velocity of hydrogen in the smallest cross-section of the nozzle of 1400 m/s (speed of sound of hydrogen), the momentum of the jet is very low, due to the low mass density.

The experiments have been carried out with different geometries of the nozzles and bore diameters between 0,2 and 1,0 mm. Large bore diameters lead to higher propagation speeds and faster utilization of the whole combustion chamber, owing to a higher momentum of the hydrogen jet. A higher number of small bores, with an equivalent total cross-section leads to faster homogenization of hydrogen air mixture, especially at the beginning of the injection period.

Among the nozzle geometry, the pressure in the combustion chamber and the position of the piston play a decisive role referring to the mixture formation. It can be seen in Fig. 5 (top), that the hydrogen propagates very fast and unhindered, in form of narrow jets up to the cylinder walls.

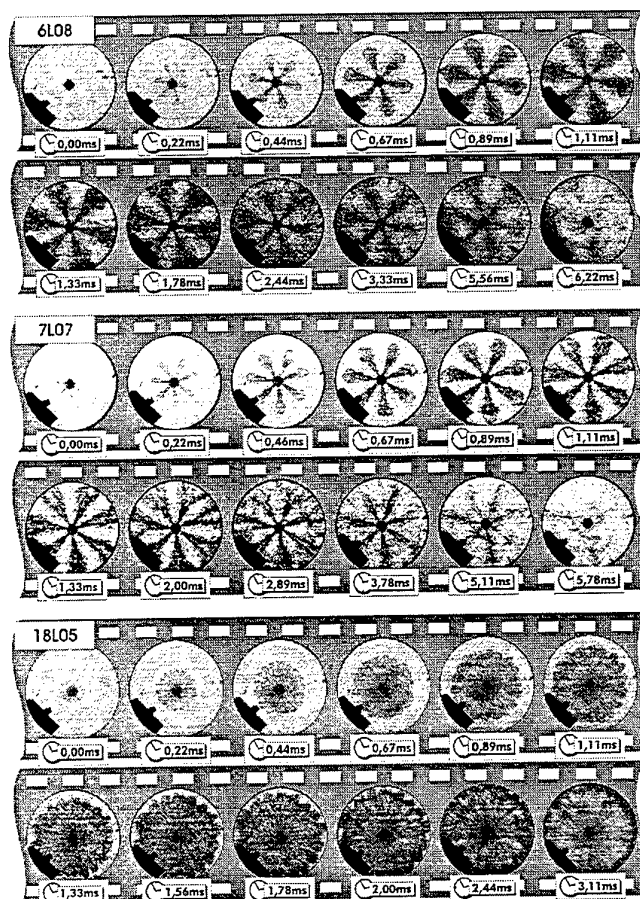


Fig. 4: Schlieren/Shadow images of the mixture formation for different types of nozzles (top: 6x0,8 mm, middle: 7x0,7 mm, bottom: 18x0,5 mm)

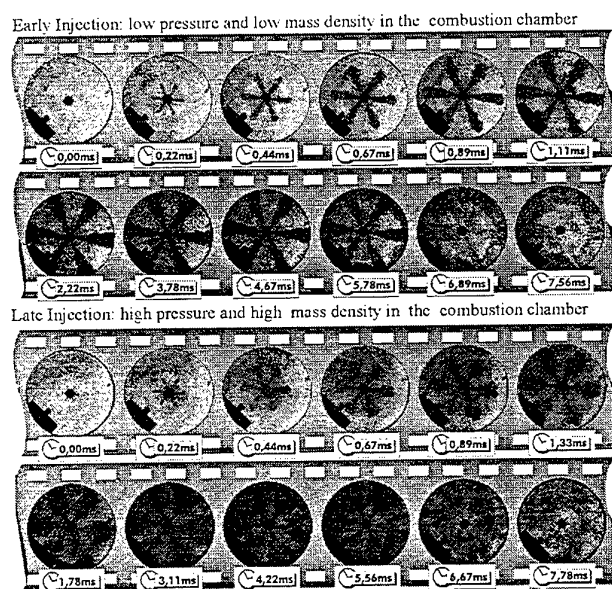


Fig. 5: Schlieren/Shadow images of the mixture formation for different conditions in the combustion chamber (top: Piston 40 mm before TDC, bottom: piston near TDC)

At a later injection, the hydrogen jet is slowed down significantly and expanded in diameter. A higher air density and effects of the vicinity of walls (layout of the piston, and cylinder walls) are the reason for the different behavior.

5. COMBUSTION

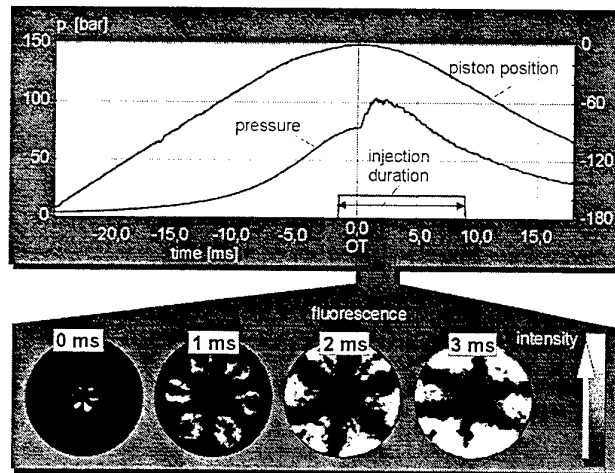


Fig. 6: Stable combustion with late internal mixture formation and compression ignition at high temperatures

The experiments showed that it is possible to achieve autoignition of hydrogen. In Fig. 6, a stable combustion with late internal mixture formation and compression ignition is shown. All jets are ignited symmetrically and immediately in the vicinity of the nozzle. In order to reach autoignition considerably higher temperatures are necessary for hydrogen in comparison to diesel. In the experiment shown, the compression ratio was about 25. Owing to different thermal conditions, it has to be taken into account that the compression ratio of the engine could be slightly reduced.

For lower compression ratios, respectively the compression end temperatures, the times for ignition delays are increased up to some milliseconds. In most cases, small variations of thermodynamic boundary conditions or spatial inhomogeneities at the beginning of the injection period lead to large variations in the combustion process, which cause cyclic variations of the pressure curves. In Fig. 7, an example for an irregular combustion is shown. Only four of six injected hydrogen jets are ignited. In other experiments, all possibilities of the ignition of one to all jets have been observed. A total miss fire was observed, too. The same results were found in the single cylinder test engine at LVK [3].

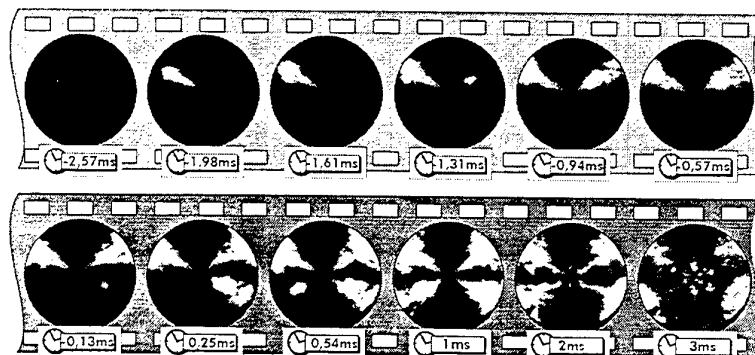
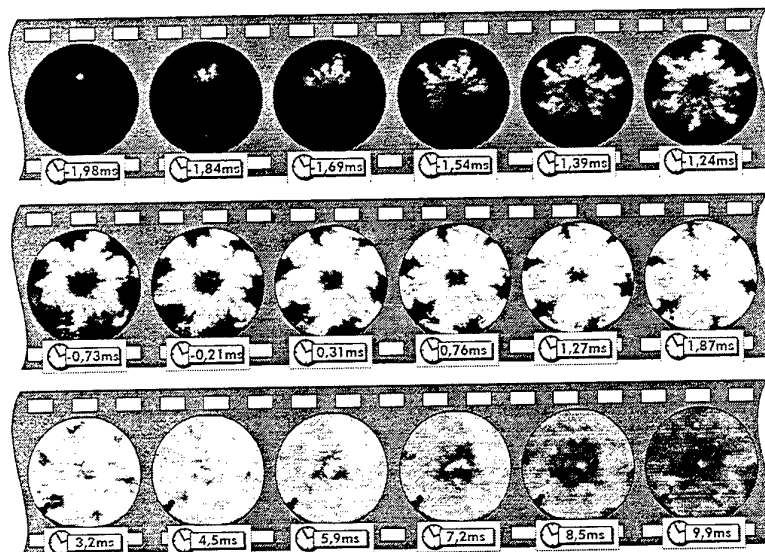


Fig. 7: Origin of cyclic variations: unstable ignition and insufficient flame propagation at low temperatures

A much better combustion behavior is observed with nozzles with a higher number of small bores. In these cases, better homogenization of the hydrogen air mixture and according spatial connected combustible regions occur immediately after injection begin. This is a requirement for a stable and reproducible combustion. The application of small bores caused a slower utilization of the whole combustion chamber. In order to improve the situation, an optimized combination nozzle was set up. This combines the positive properties of small and large bores. A typical combustion process of nozzles of that category can be seen in Fig. 8.



**Fig. 8: Optimized nozzle for a better ignition and utilization of the combustion chamber
(18 hole nozzle: 6x0.6 mm + 12x0.4 mm)**

The ignition occurs in a single position and propagates within a millisecond around the nozzle. The jets from the bigger holes improve the induced turbulence as well as the mixture formation, especially at the end of the injection and combustion period. In comparison to diesel engines, the combustion is finished earlier after the end of injection. Depending on the configuration, the combustion continues for about one millisecond after the end of injection.

6. NUMERICAL SIMULATIONS

From experiments it was observed, that the form of the injected hydrogen jets is kept for a long time and that they significantly influence the combustion process. During the research project, according to experimental investigations, numerical simulations of the mixture formation and the ignition process have been carried out. The calculations were done with the piston resting in the vicinity of TDC and with the take of the advantage of symmetry properties of the geometry.

An example of the mixture formation of a 8 hole nozzle with a bore diameter of 0.6 mm, is shown in Fig. 9. The viewpoint is chosen perpendicular to the vertical axis of symmetry. In the shown example, hydrogen was injected with 300 bar and 300 K into the combustion chamber with a pressure of 100 bar and a temperature of 1000 K. In Fig. 9, both, the temporal propagation of the concentration and the distribution of the temperature can be seen. The mixing of the injected cold hydrogen with the hot air causes a minimum temperature in the center of the jet. Owing to the great temperature gradient only in a small region around the jet, good ignition conditions with high enough temperature and hydrogen concentration are found. These ignitable areas are hatched in gray. The regions are found around the 10% (volume percent) isoline of the concentration profile. The reason for the short ignition delays in the lean regions ($\lambda \approx 3.8$) can be explained with the strong temperature dependence of the chemical reaction.

A careful analysis of the chemical processes during the ignition is possible with detailed reaction chemistry [4]. The calculations have been carried out in a zero dimensional "well stirred" reactor. It was assumed to simplify the problem that the hydrogen air mixture reacts in a closed container without any influence of walls and flow

condition. With this method, it is possible to separately study the influences of different thermodynamic conditions.

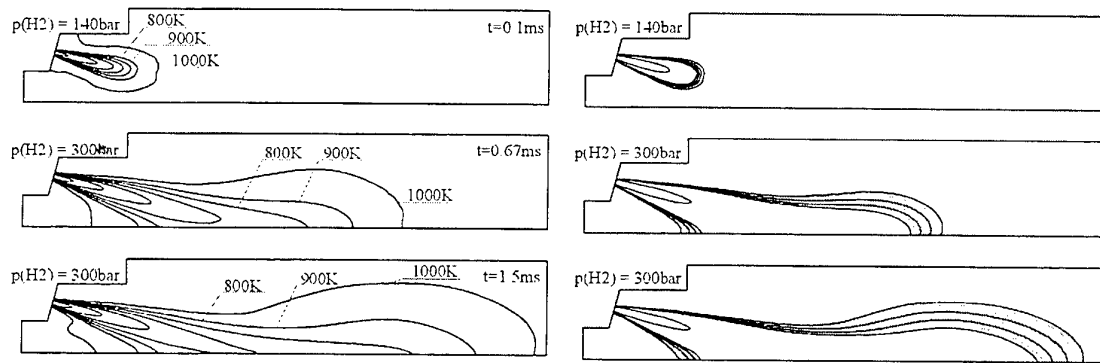


Fig. 9: Propagation of the concentration and temperature profiles during the injection process (without combustion)

In order to use this method for late internal mixture formation, the conditions for pressure and temperature of compressed air and injected hydrogen were fixed. The mixture of hot air and cold hydrogen leads to a mixing temperature depending on the hydrogen concentration. It can be found out that the mixing temperature is significantly lower than the compression end-temperature and has great influence on the temporal process of the chemical reaction. In Fig. 10, the influence of the compression end temperature TL on the ignition delay is shown. The ignition delay is plotted over the local hydrogen concentration. Obviously, for lower temperatures of TL, a clear minimum of ignition delay can be found in the range of 10 volume percent for the hydrogen concentration. The ignition occurs for an operation according to the diesel principle at much higher temperatures than the theoretical autoignition temperature of 850 K. The necessity of high temperatures is confirmed by own experiments and investigations by Siebers [5].

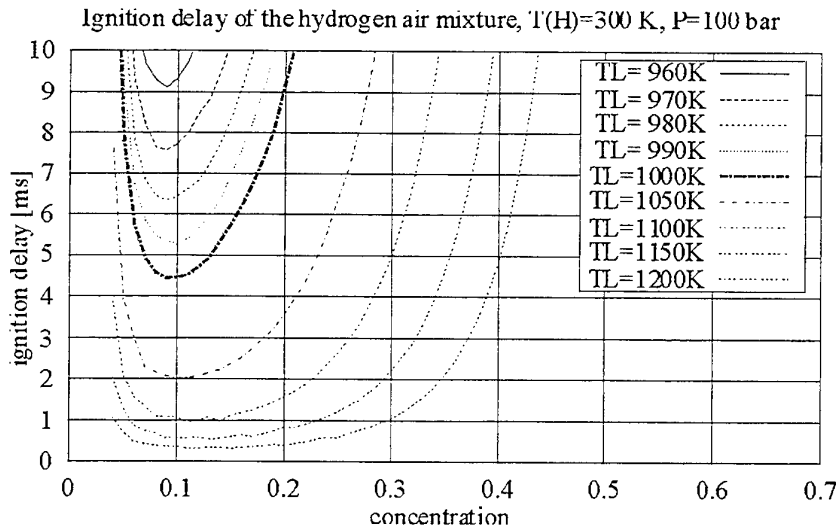


Fig. 10: Calculated ignition delay depending on compression end temperature and hydrogen concentration.

7. VARIABLE INJECTION SYSTEM

Long ignition delays, a high flow rate during injection, and a higher number of bore holes lead to a high pressure rise after ignition. With a new injection system, which was designed at LAT, it is possible to control the velocity of the needle lift. In Fig. 11 the principle of the injector and two plots of needle lifts with pre-injection and different opening characteristics are shown. With such a system it is possible to start the injection earlier before top dead center to improve the ignition behavior without risking the danger of knocking or hard combustion. Especially, the amount of hydrogen which is injected during pre-injection, can be reduced significantly, if a slow needle lift is possible. In both plots, the minimal pulse length, which is two milliseconds, was applied to the magnetic valve of the injection system.

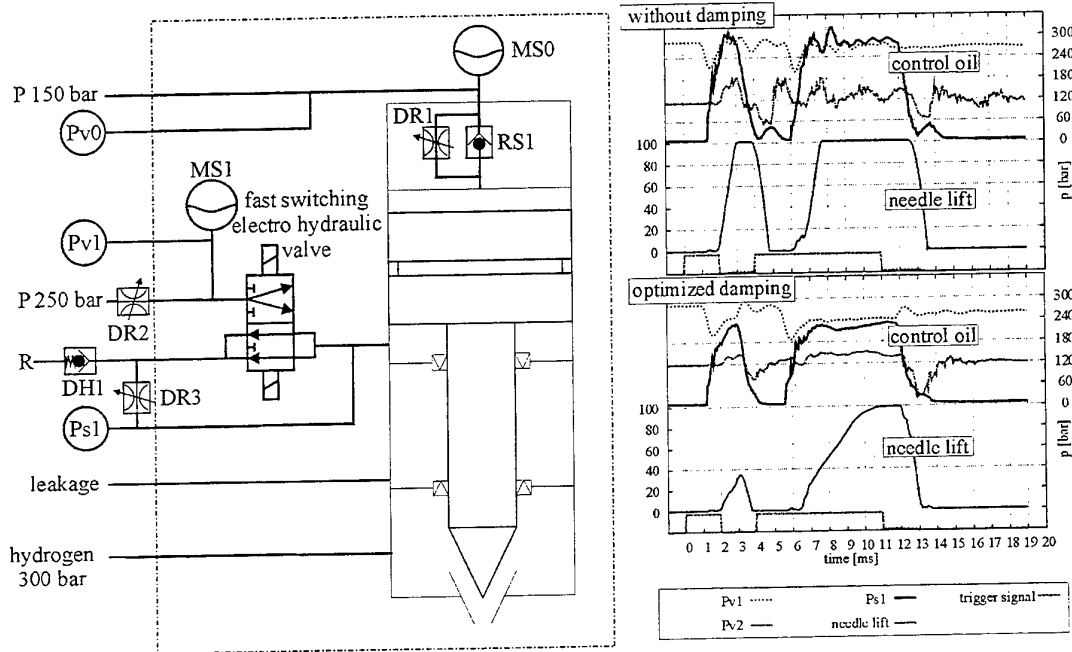


Fig. 11: Optimized injection system with variable needle lift.

8. SUMMARY AND OUTLOOK

The properties and phenomenon's of the internal processes of hydrogen engine, were investigated at the Lehrstuhl A für Thermodynamik within the scope of the research project, "Directly Injecting Hydrogen Diesel Engine with High Power Density and Low Emissions". For the investigations, a newly developed experimental setup with optical access as well as numerical simulations are used.

The recoil free architecture of the RCM allows realistic imitation of the compression and expansion stroke of a large bore diesel engine, and the simultaneous observation of the mixture formation, ignition, and combustion with high spatial and temporal resolution. With the digital image capture system frame rates between 4500 and 40500 pictures per second were achieved. The mixture formation was analyzed with Schlieren/Shadow cinematography. For the investigation of the combustion process the light of the self fluorescence was detected. According to experimental investigations, the mixture formation was simulated with three dimensional numerical flow calculations. The ignition delay of the hydrogen air mixture was analyzed with zero dimensional simulations of the detailed chemistry.

The experiments proved the possibility of compression ignition of hydrogen in a large bore engine. In comparison to diesel, significantly higher temperatures are necessary. Temperatures over 1000 K are necessary to get

autoignition in combination with late internal mixture formation. Ignition delays under one millisecond can be achieved with temperatures over 1100 K.

The experimental and numerical investigations of the mixture formation and ignition process deliver different reasonable combinations of nozzle geometries and piston layouts. It has to be considered that the temporal control of injection depends on the applied configuration.

With regard to a successful implementation of a method for hydrogen combustion in large bore diesel engines, the injection system plays a significant role. Therefore, the electromagnetic and hydraulic controlled injection system used, was significantly improved and redesigned at LAT for better control of needle lift (variable opening speed of the needle) and the possibility of multiple injection.

Both, the experimental and theoretical investigations, and the new developed components are the basic elements for future developments of large bore hydrogen engines.

REFERENCES

1. C.Vogel, *Motortechnische Zeitschrift MTZ* 10 (1999), Nr. 10, "Direkteinspritzender Wasserstoffmotor hoher Leistungsdichte und geringer Abgasemission" (1999).
2. F. Mayinger, *Optical Measurements: Techniques and Applications*, Springer-Verlag, (1994).
3. Z. Woschni, and R. Wiebicke, "Hydrogen C.I. Large Bore Ship Engine", Proceedings, XII World Hydrogen Energy Conference, pp. 1515-1536, Buenos Aires, Argentina (1998)
4. U. Maas, J. Warnatz, "Ignition Processes in Hydrogen-Oxygen Mixtures" *Combustion and Flame*, Nr. 74, pp. 53-69 (1988).
5. J. D.Naber, and D. L. Siebers, "Hydrogen Combustion under Diesel Engine Conditions", Proceedings, XI World Hydrogen Energy Conference, Stuttgart, Germany (1996).

RECENT FOCUSES AND FUTURE RESEARCHES IN SMART ENGINE TECHNOLOGY

Feng Lin¹

Dept. of Mechanical Engineering
Indiana Institute of Technology
Fort Wayne, Indiana, USA
Email: Lin@indtech.edu

Zhongwei Li²

Gas Turbine Laboratory
Massachusetts Institute of Technology
Cambridge, Massachusetts, USA
Email: zwli@mit.edu

Keywords: compressors, rotating stall, surge, active control, nonlinear dynamics

ABSTRACT. Smart engine technology (SET) attracts a great deal of attentions from researchers and engineers around the world in recent ten years. A "smart engine" utilizes modern control technologies to increase the performance of its components. The researches involve multiple disciplines including fluid mechanics, heat transfer, control, nonlinear sciences, computational dynamics, and even statistics. While ideally every engine component could be made "smart", the recent focuses are on compressor stability and control and combustion control. In this paper, recently developed ideas on compressor stability control are compared with each other. The criteria of comparison include not only the performance improvement but also the affordability, reliability and supportability, all of which are very important from an implementation point of view. The projects for future research are suggested as the comparisons are concluded. Since SET is still under development and many ideas are subject to the test of time, it is in some sense too premature to be reviewed or surveyed. With this in mind, this article is not trying to cover the whole spectrum of this rich research mix. Instead, the comparisons and suggestions are made to draw some useful outlines of current progresses and highlight the important areas that need more resolution. The author is in hope that the information in this article can benefit China in starting systematic SET researches for its power industry.

1. INTRODUCTION

The technology progresses not only create many new exciting disciplines but also revitalizes traditional engineering fields. Often, applications of new technology release the design constraints imposed by traditional design tools and approach and therefore improve the performance of the engineering systems. In return, the huge benefit one thus obtains stimulates the further development of new technologies. As a matter of fact, revitalization of traditional engineering fields is always one of the major driving forces for new technology development. For instance, the space exploration program leads to not only successful lunar launches but also invention of electronic computers. It is the latter that profoundly changes the history of mankind. The research of *smart engine technology* (SET) contributes to new technology development in a similar fashion. If successful, it not only revolutionizes gas turbines, which brings huge benefit to the industry and its customers, but also stimulates the development of modern linear/nonlinear control theories and practices, Micro-Electro-Mechanical Systems (MEMS), digital signal processing (DSP), and many more.

A "smart" engine means its components are being actively controlled so that their performance improves. For instance, rotating stall and surge, the two modes of compressor instability limits the efficiency improvement of the entire engine. Traditionally, one has to design the compression system operating in a margin from the surge boundary (figure 1) to accommodate all the disturbances, which in turn means an expensive price is paid in exchange of safety. Przybylko [1] indicates that for an aircraft engine, if one stage in the compressor would be eliminated due to margin-reduction technologies, 5% increase in thrust-to-weight ratio, 1.5% decrease in fuel

¹ Assistant Professor, Member of AIAA and ASME.

² Visiting Professor, on leaving from DSP Center of Northwestern Polytechnical University, Xi'an, China.

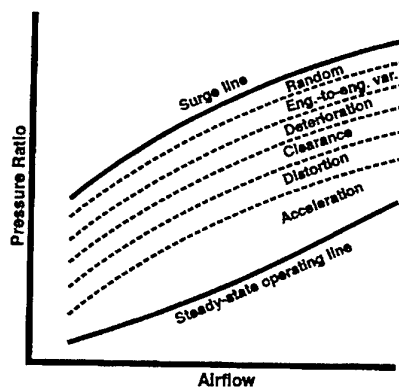


Figure 1. Surge margin to accommodate all disturbances, from [1]

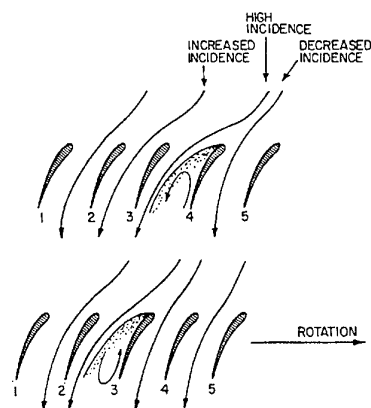


Figure 2. Emmon's model for stall propagation

consumption (sfc), 3.2% and 1% reduce in acquisition and operating cost would be achieved. To illustrate the significance of these figures, assume a modern commercial airplane needs 4 engines with 244640 N (55000 lbf) thrust each and current sfc for them is 0.5 kg/hour/10N (0.49 lbm/hour/lbf). A simple calculation leads to the fact that a 1.5% decrease in sfc means 734 kg/hour (1617 lbm/hour) of saving in fuel for this airplane only.

The scope of this paper will be limited to active control of rotating stall and surge, as it is the one that so far receives most extensive studies. Readers should be aware that active combustion control and high-cycle-fatigue researches are also important part of SET and draw more and more attentions lately. While a historic remark is provided at next session, the focus of this paper is on recent and future researches. The published researches are grouped into two categories: dynamic models of the system and control demonstration. Sensing and actuation techniques will be discussed in the context of controls. Brief reviews and comparisons between various ideas and practices will be given. As the review concludes, future researches will be suggested and their impact to science and technology will be foreseen.

2. HISTORIC REMARKS

Fluid Mechanics Modeling

In 50's, rotating stall and surge are only investigated from fluid mechanics point of view. From his experiments in Princeton University, Emmon et al [2] conclude that a stall cell is actually a flow blockage caused by flow separation in blade passages and traveling around the compressor annulus. Figure 2 illustrates Emmon's stall model. Due to flow non-uniformity or external disturbance, such as inlet distortion, the angle of attack of a blade may be significantly increase so that flow separates in that blade passage. Once a blade is blocked this way, all incoming streamlines will be diverted. On one side of the blockage, streamline diversion will cause increased angle of attack, and on the other side decreased angle of attack. The blade passage subjected to increased angle of attack will therefore stalled. As the new one stalled, the angle of attack of the blade passage already stalled decreases and the passage becomes unstalled. The stall cell will thus propagate from blade to blade around the compressor. The Emmon's model is well received in industry. It is still the most insightful model in terms of fluid physics. It explains well how a stall cell may form and why it propagates around the compressor. However, it cannot explain why sometimes a minor flow irregularity causes rotating stall and sometimes does not. Neither can it explain sometimes there are more than one stall cell and predict how fast a stall cell propagates. Unfortunately, these questions are still not completely answered and remain to be investigated.

Dynamic Modeling

Starting from 70s, it is recognized that compressor instability is not only related to flow structure in the blade passages but also the dynamic connection between the components of a system. Hence, researchers looked for dynamic models that can reveal such connection. Various models were produced. Among them, parallel compressor model for inlet distortion, Greitzer's surge model [3], Moore's rotating stall model [4], and later,

Moore-Greitzer model for both stall and surge [5] are the most popular ones. A common approach is that to study the dynamic instability, a compression system is simplified as a lumped parameter system, that is, the detail flow structure is neglected. Instead, the compressor is replaced with a "black box" with its performance curves obtained from experiments. Greitzer [3] uses a mass-spring-damper mechanical analogue to illustrate the dynamics of surge. The analysis shows that for a given compressor characteristic, plenum volume, compressor length, etc., there is an important non-dimensional parameter on which the system response depends. This parameter is later denoted as Greitzer's B parameter:

$$B = \frac{U}{2\omega L_c} = \frac{\text{The magnitude of pressure difference across the compression system}}{\text{The magnitude of the inertial forces that arise due to local fluid accelerations}},$$

where ω is the Helmholtz resonator frequency of the system, L_c is an "effective length" of the compressor duct, and U is the rotor speed. The capability to accelerate the fluid in the duct is increased as B increases. Hence, as B becomes larger one would expect greater excursions in axial velocity and thus a general trend towards surge rather than rotating stall.

Moore-Greitzer model [5] is the most successful model to date in qualitatively capturing the post stall behavior of a compression system. It is a combination of Greitzer's surge model and Moore's stall model. Bifurcation analysis [6] shows that even the first-mode truncated MG model can capture the rich dynamics of the system and the results are in accord with experiments. MG model heavily relies on its basic assumption, that is, the axisymmetric compressor characteristic, which describes performance of a compressor in steady axisymmetric flows, is applicable to unsteady state and nonuniform flow. When compressor stalls, the pressure rise across a blade row varies locally and in time. Hoying et al. [7] verified numerically that the unsteady compressor performance does not deviate substantially from the steady performance, which allows the unsteady performance to be described adequately as a linear functions of the inlet conditions with the first order differential lag. However, there is no experimental report in validation of this basic assumption.

Control of Stall and Surge

As to the authors' knowledge, the earliest attempt in active stall control was reported by Ludwig et al. in 1979 [8]. The extensive researches do not start until 1990s. In 1989, Epstein *et al.* [9] proposed to linearly extend surge boundary to unstable region using a technique similar to active noise suppression. The basic idea was that rotating stall and surge are the mature forms of small amplitude disturbances that are the natural modes of oscillation in the compression system. Feedback control operating on these small disturbances can change the dynamics of the system so that they would not grow into rotating stall or surge. Ffowcs Williams and Huang [10] and Paduano [11] demonstrated the success of this idea in active surge and rotating stall control respectively. For details, please refer to [12] where Greitzer presents a comprehensive review of the originality of the researches of smart jet engines. Alternatively, Liaw and Abed [13] proposed a bifurcation-theoretic approach for active stall suppression. Instead of linearly extending stall limit, nonlinear control is used to reduce the stall margin by enlarging the domain of attraction of an operating point. Badmus *et al.* [14] applied this control philosophy in their experiments. In the recent ten years, a large number of papers have been published. Fluid mechanicians, control specialists, nonlinear dynamicists, and mathematicians have all contributed ideas to the overall research mixes.

3. RECENT DEVELOPMENT

Modeling The Dynamics

As in any control problem, creating appropriate models is the first challenge. The fundamental requirement is to understand the key physical phenomena which drive the dynamic behavior. The basic questions being investigated include: 1) how many types of stall precursor there exist; 2) which precursor would occur at a given operation condition; 3) how compressor pumps energy into the stall precursors; 4) which mechanism drives the hysteresis associated to rotating stall; 5) under which condition the system stalls or surges; and 6) what makes high-speed compressor different from its low-speed counterpart. In this section, the most recent development will be reviewed in category rather than chronically.

Prestall dynamics. For the stability of any compression system, the stall process is classified into two stages in this paper — prestall and poststall. As opposed to poststall that refers to the fully-developed, large-amplitude

rotating stall, prestall refers to the period of time immediately prior to the moment when stall amplitude rapidly grows, during which the compressor operation is steady but may exhibit small amplitude dynamics. The importance of investigation of prestall dynamics to active control is obvious. No matter which control scheme is chosen, the stall perturbation must be suppressed before it grows into fully developed stall or surge.

Since the basic idea of active stall control was to eliminate small amplitude flow disturbances, it was postulated that there exist modal waves as the stall precursor which later grows into fully developed rotating stall [9]. This type of long-scale modal wave is later observed in experiments [15, 16]. However, detection of such a stall precursor is not trivial. Tryfonidis *et al* [15] developed a method called traveling wave energy. The philosophy is to take a time window of signals from a number of sensors located evenly around the compressor annulus and then transfer the data into spatial spectra. The stall precursor is recognized if one or more growing peaks in the spectra can be found as the time windows slide towards the stall inception point. Similar to this idea, Le *et al* [17] applied wavelet analysis to their engine for the same purpose. While wavelet analysis is more formal and mathematically correct, both methods work well for the data presented in their papers. However, the real challenge is how to detect stall precursors in real time, namely sensing, processing and feeding back information within the time frame between the first precursor being identified and the moment of its rapid growing. The signal-noise ratio during the prestall is so low due to strong turbulence and other disturbances that the modal waves, even though it exists, may be corrupted by noise. More advanced sensing and digital signal processing techniques are needed for real time stall precursor detection.

In parallel to the above research, a group of researchers in Cambridge University found another route that leads to stall inception, short length-scale spikes. While the long length-scale modes exist, stall inception does not occur until the local mass flow, at some spatial location, is low enough that a small region of the annulus experiences flow separation in the blade passage. This region then propagates, rapidly spreading into a fully developed stall or surge event [18-20, 26]. Day [18] gives a typical example where the modal waves, while exist, does not lead to instability. In this example, the stall cell does not appear to be a continuous development of the modal wave, but rather a separate disturbance which appears despite the presence of the modal wave. The presence of spikes significantly complicates the active control technology because spikes always happen locally and grow rapidly without much warning time and they are highly nonlinear. Researchers therefore seek to determine the conditions under which waves or spikes occur. Camp and Day [21] studied a four-stage low-speed experimental compressor and found that the first stage rotor had an identifiable "critical incidence" above which spikes occurred prior to stall inception. Hoving [22] used a three-dimensional computation model of a single blade row to reveal fluid dynamics mechanism of stall inception. This mechanism involves the stability properties of the tip leakage vortex. Interested readers please refer to their original papers for details.

Due to the existence of both modal waves and spikes and the fact that it is very difficult to predict which would occur *in prior*, a question is naturally raised: how does a compressor pump its energy into fully developed stall cells or surge? To understand how compressor interacts with initial stall disturbance regardless spikes or waves, Lin [23] numerically studied the full MG model, using the first 64 spatial modes, and found that the shape of the compressor characteristic plays an important role in pumping energy into stall cells. When the slope of the compressor characteristic corresponding to the local mass flow is negative, the work done by the compressor on this local disturbance would be negative and the disturbance would be suppressed. Otherwise, it would be amplified. Hence, for overall effects, when the average work done by the compressor on the disturbances is positive, the compressor pumps energy into initial stall disturbances and makes them grow into fully developed stall or surge.

It still remains a challenge to design a control that works for both waves and spikes. One possible solution is to incorporate both spikes and waves into a model for control law development and testing. Another is to develop a control philosophy that would work regardless which type of stall inception. More researches are needed in these aspects.

Poststall dynamics. Study of post-stall dynamics is to understand nonlinear aspects of the system performance. Such understanding leads to development of a control strategy completely different from the one that arises from linear dynamics. McCaughan [6] applied bifurcation theory to analyze the three-state MG model. This model is an approximation of the full mode MG model by truncating all modes higher than the first

mode when a Galerkin process is applied to the MG model. The rotating stall corresponds to a set of steady state solutions in which the amplitude of the first mode is not zero. The analysis reveals the nonlinear mechanism of

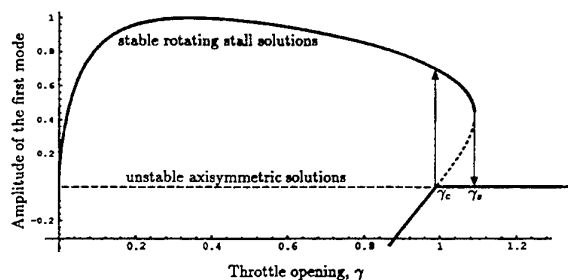


Figure 3. Hysteresis of rotating stall is qualitatively captured with the three-state MG model, from [6].

hysteresis associated with rotating stall. Figure 3 shows one result of bifurcation analysis. In this figure, there exists a region over which the rotating stall equilibria overlap with steady axisymmetric equilibria, separated by a set of unstable stall equilibria. When one closes the throttle, the steady axisymmetric equilibria would not lose their stability until the throttle coefficient γ reaches γ_c . However, to recover from stall, one has to reopen γ to γ_s which is larger than γ_c . Hysteresis is therefore a consequence of the nonlinearity of the system.

The MG model heavily relies on the correctness of the compressor characteristic. Ideally, one expects that by collecting the compressor characteristic experimentally, such characteristic would account for all the effects created by complicated flow structures in blade passages, such as viscosity, compressibility, and even tip vortices. Although this approach is widely accepted, the authors believe higher resolution is needed in obtaining such characteristic, especially for high-speed compressors.

The MG model is successful in modeling low-speed compressors. Its ability in modeling high-speed compressors is still questionable. Hendricks *et al.* [24] and Feulner *et al.* [25] incorporate compressibility into their model of multi-stage high-speed compressors. But their works actually focus on describing how the modal waves grow when the compressibility is present. The key question here is for a high-speed compressor whether a simple performance curve can be used in representing the compressor or a compressor stage in the MG model. At least, such representation needs to be validated experimentally.

Demonstration of Active Control Schemes

A successful active control scheme consists of an appropriate dynamic model, control law design, as well as effective and realistic sensing and actuation. Although Ludwig *et al.* in 1979 made their first attempt in active stall control, the work suffered from lack of theoretical base and shortcoming of testing equipment. It takes more than one decade to fill in the theoretical and technological foundation. In recent ten years after the MG model was built, significant progresses have been made in linear/nonlinear control theory, sensor and actuator technology, computer, digital signal processing, and many more, which pave the way towards smart engine technology.

Paduano [11] reported the first attempt in active stall control after Ludwig. The work is followed soon after by Haynes *et al.* [27] with a three-stage low-speed compressor, and later by Weigl *et al.* [28] with a single-stage, high speed compressor. The control philosophy of their work is linear extension of surge line, namely extending the surge limit to the original unstable region by suppressing prestall modal waves when the amplitude is small and the dynamics is linear (figure 4a). Paduano and Haynes sensed flow velocity in the inlet and used adjustable inlet guide vanes as the actuators. Weigl's approach is more practical. The sensors are an array of high-response pressure sensors distributed circumferentially and the actuators are specially designed air injection valves, which are capable of delivering 5.8% of the design compressor mass flow when supplied with 100 psi air. The signal bandwidth is 400 Hz. Table 1 shows part of the results obtained by Weigl.

Table 1: Summary of Steady Blowing and Control Experiments, from [28]

Configuration	Mass Flow at Stall	% Decrease Mass Flow at Stall	Pressure Ratio at Stall	Stall Margin %
100% Speed Solid Casing	18.73	—	1.9010	12.2
3.6% Blowing, no control	17.92	4.3	1.8850	17.9
5.8% blowing, no control	16.86	10.0	1.8910	24.0
3.6% blowing, 0 th , 1 st , 2 nd control	17.27	7.8	1.8650	19.4
3.6% blowing, 1-sided actuation	17.26	8.4	1.8670	20.3

Alternatively, a competing control philosophy is to enlarge domain of attraction of operating points so that they are stable enough to reject various disturbances. Ideally, if this type of active control can success, then operability of the engine has been functionally enhanced at more desirable performance levels. For instance, the open-loop surge line could be transferred by active control into the operating line by eliminating the tendency to surge along that line (figure 4b). If such performance enhancement can be taken into account when designing compressors, the designers can then set the design operating point, normally also the best efficiency point, at a lower mass flow and with less surge margin. This philosophy is different from the linear region extension and therefore has its own language and culture. Liaw and Abed [13] numerically illustrated their idea of altering the bifurcation property of the compression system modeled with the three-state MG model. Badmus *et al.* [14] demonstrated this could be done experimentally using a 1D actuation, a plenum bleeding valve. Eveker *et al.* [29-30] further revised this control scheme and applied it to a low-speed and later a high-speed compressor. Following the same control philosophy, D'Andrea *et al.* [31], Behnken *et al.* [32], Wang and Murray [33], and Yeung and Murray [34] achieved similar success in their low-speed compressor test rig with 2D actuation. The limitation of bifurcation control, under the constraints of actuator rate limits, saturation of the actuators, and noise, was also studied in [33].

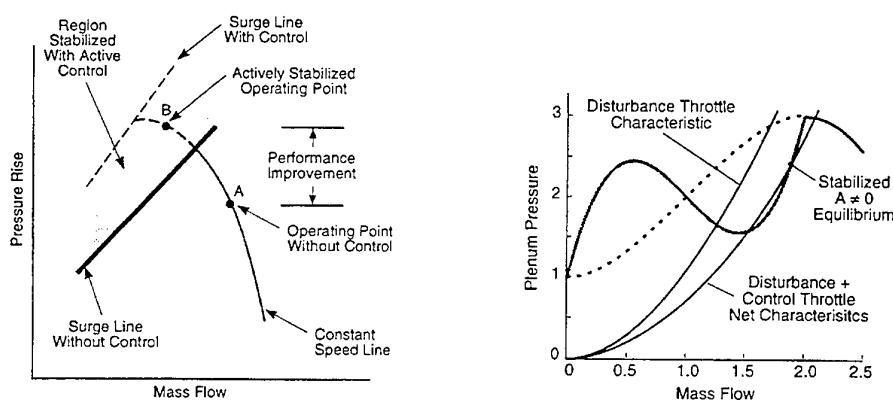


Figure 4. Comparison of the two popular control strategies: (a) linear range extension (left), from [9, 11], and (b) nonlinear disturbance rejection (right), from [14].

Although there are some success in active control of compressors under clean and well-organized laboratory conditions, it still goes a long way to apply these techniques to real engines. Weigl's effort shows that linear extension of surge line does work but with an expensive price tag. Further research is needed to investigate the trade-offs between steady blowing and active control. Steady blowing requires a large amount of injected air. Active stabilization requires a feedback control law with high-bandwidth sensing and actuation and the high-bandwidth actuators are not cheap. The reliability of many sensors (at least 8 of them in each axial location), which are needed to allow decomposition of perturbations into harmonics, is also of practical concerns. What if one of them breaks down and provides false information to the controller? On the other hand, the disturbance rejection control schemes need to be refined, although they claim that they would provide robustness of compressor operation with lower bandwidth requirement. The common theoretical foundation for these approaches is the three-state MG model, which is significantly simplified from its origins. The important physics that is neglected in the three-state model is the nonlinear interaction between the spatial modes. As for

the actuators, the plenum-bleeding valve, as used in Eveker's experiment, is not realistic in practical applications despite of its simplicity. The air injection valves for nonlinear control, as used in [31-34], are subjected to be tested in a more realistic environment, especially in large-scale, high-speed machines as such machines challenge the correctness of the three-state MG model.

Lin [23, 35-36] proposes to use a Lyapunov-based stability concept, call "practical stability" to describe the stability of compression systems. Practical stability is used to describe two types of phenomena that cannot be described with normal stability concepts. On one hand, an operating point that is normally stable may not be acceptable in practice. For instance, a compressor operating close to the surge line but without sufficient surge margin may be unstable in a practical sense. On the other hand, a linearly unstable point may be acceptable as long as the trajectory of the system is within a limited range around the unstable point. For instance, the performance of a rocket that slightly oscillates around its design trajectory is well acceptable. According to practical stability, the performance of a control scheme can thus be designed, which theoretically requires less sensors and lower high-bandwidth actuators. Since the theory is based on Lyapunov function that was invented in Russia and is not so popular in the western world, the practical stability concept is not well received by now. The control scheme thus designed remains to be experimentally tested.

In a recent study by Freeman *et al.* [38], a recirculation mechanism was tested, which allowed bleed air from either the exit of the fourth stage or the last stage to be injected either at the fourth stage or the inlet of the compressor. Six circumferentially distributed pipes recirculated the flow, actuated by high-response (300Hz) hydraulic valves. Various control schemes were tested. The most interesting result to the authors of this paper is the performance of the 1D 'nonlinear' approach, which increased the stable operating range by up to 25% in pressure rise, and was able to extend the stable operating range at all speeds and with each method they used to induce stall. This 1D approach is to sense stall inception and subsequently clears the stall cell before it fully developed, with a uniform recirculation. This kind of 1D actuation is similar to the one proposed by Lin in [36]. The latter is a direct result from the nonlinear theory of Lyapunov, while the former is almost purely empirical.

It is worth to note that both dynamical analysis [37] and experiments [28, 34, 38] shows that the best performance is usually achieved by introducing a stabilizing flow that would influence the flow structure inside the blade passages. However, the price paid for such surge margin improvement techniques is that either the bleed or inlet injection involves bleeding high-pressure air from downstream of the compressor. The trade-off between efficiency, surge margin, and technical complexity is difficult to justify, which requires implementing active control through very careful design and implementation.

4. FUTURE RESEARCHES

In previous sections, the areas that need higher resolution are indicated in the context. For convenience, we summarize the major points as below:

1. Set up models that incorporate both fluid mechanics in the blade passages and dynamics connection between components.
2. Develop real time stall precursor detection systems. This research involves: distributed sensing technology using MEMS; digit signal processing algorithm that works both for waves and spikes; a fast response system that can detect the stall precursors and activate the actuators before the stall precursors grow.
3. Develop more realistic and advanced control schemes, including test of practical stability; tip clearance control using magnetic bearings or tailored flexible structures that involves piezo-electric materials; flow separation control on individual blades (MEMS again), and many more.
4. Study the trade-offs between efficiency, surge margin, and technical complexity for any active control schemes.
5. Perform other researches in smart engine technology (SET), such as active combustion control, active noise control, and active flutter control. In MIT, the methods developed for rotating stall and surge control are currently being applied to rotor flutter / high cycle fatigue (HCF) control research. A research concept, active rotor for HCF identification and control, is under development. The active rotor or "articulated" rotor is a transonic compressor with "smart structures". Blades are independently actuated by adaptive material like piezos, and can dynamically change shape and stiffness. Currently, the blades are designed and tested. The spin rig test facility with a multiple channel real time DSP system is being built. The rig might be used

for aerodynamics damping measurement, flutter control, investigation of optimal mistuning, change of efficiency, and noise.

5. IMPACT TO SCIENCE AND TECHNOLOGY PROGRESSES

The impacts of SET researches are in two folds. Directly, the technology thus developed brings great benefits to the gas turbine industry, as stated in the first section of this paper. Indirectly, the researches stimulate the developments of related fields, such as DSP, control theory, MEMS, etc., which may have much broader and deeper impacts on improving technology levels for a country's industry. For instance, the harsh requirement of real time stall precursor detection would simulate development of sensor technology and linear/nonlinear signal processing techniques. Another great benefit of SET research is that it requires forming a cross-discipline team, which is completely different from the way a traditional research project is organized and will bring new challenges to administration systems for science and technology. At last, SET researches will educate a lot of students with ability of cross-discipline researches, which will provides leaders of science and technology development in a country for the next century.

REFERENCES

- 1 S. J. Przybylko, AIAA 97-2769, 33rd Joint Propulsion Conference & Exhibit, July 1997.
- 2 H. W. Emmons, C. E. Pearson, and H. P. Grant, *Transaction of ASME*, Vol. 79, pp455-469, 1955.
- 3 E. M. Greitzer, *ASME J. Of Engineering for Power*, Vol. 98, pp190-217, Apr., 1976.
- 4 F. K. Moore, *J. Of Engineering for Gas Turbine and Power*, Vol. 106, pp313-336, Apr., 1984.
- 5 F. K. Moore and E. M. Greitzer, *ASME J. Of Engineering for Gas Turbines and Power*, Vol. 108, pp. 68-76, 1986.
- 6 F. E. McCaughan, *SIAM J. Appl. Math.*, Vol. 50, No. 5, pp. 1232-1253, Oct., 1989.
- 7 D. A. Hoying, E. M. Greitzer and C. S. Tan, AIAA 97-2771, 33rd Joint Propulsion Conference & Exhibit, July 1997.
- 8 G. R. Ludwig, J. P. Nenni, *J. of Engineering for Power*, Vol. 101, pp305-314, 1979.
- 9 A. H., Epstein, J. E. Ffowcs Williams, and E. M. Greitzer, *AIAA J. of Propulsion and Power*, Vol. 5, No. 2, pp. 204-211, 1989.
- 10 J. E. Ffowcs Williams and X. Huang, *J. of Fluid Mechanics*, Vol. 20, pp. 245-262, 1989.
- 11 J. D. Paduano, *Ph.D. Dissertation, GTL Report #208*, MIT, Cambridge, 1992.
- 12 E. M. Greitzer, *JSME International Journal*, Series B, Vol 41, No. 1, 1998.
- 13 D.C. Liaw and E. H. Abed, *Second IFAC Nonlinear Control Symposium*, Borfeaux, France, 1992.
- 14 O. O. Badmus, S. Chowdhury, K. M. Eveker, C. N. Nett, and C. J. Rivera, AIAA 93-0229 and AIAA 93-2234, 29th Joint Propulsion Conference, Monterey, 1993.
- 15 M. Tryfonidis, O. Etchevers, J. D. Paduano, A. H. Epstein, G. J. Hendricks, *ASME J. of Turbomachinery*, Vol. 117, pp.62-80, 1995.
- 16 V. H. Garnier, A. H. Epstein, and E. M. Greitzer, *ASME J. of Turbomachinery*, Vol. 113, pp. 290-301, 1991.
- 17 D. K. Le, A. K. Owen, and D. L. Mattern, AIAA 96-3174, 1996.
- 18 I. J. Day, 91-GT-87, *ASME Turbo Expo'91*, Orlando, FL, 1991.
- 19 I. J. Day, T. Breuer, J. Escuret, M. Cherrett, A. Wilson, 97-GT-281, *ASME Turbo Expo'97*, Orlando, FL, 1997.
- 20 I. J. Day, and C. Freeman, *ASME J. of Turbomachinery*, Vol. 116, No. 2, pp217-225, 1994.
- 21 T. R. Camp, and I. J. Day, 97-GT-526, *ASME Turbo Expo'97*, Orlando, 1997.
- 22 D. A. Hoying, *AIAA/ASME/SAE/ASEE 29th Joint Propulsion Conference*, Monterey, 1993.
- 23 F. Lin, AIAA 97-2773, 33rd Joint Propulsion Conference and Exhibit, Seattle, 1997.
- 24 G. J. Hendrick, L. P. Bonnaure, J. P. Longley, E. M. Greitzer, A. H. Epstein, AIAA 93-2233, 29th Joint Propulsion Conference, Monterey, 1993.
- 25 M. R. Feulner, G. J. Hendricks, and J. D. Paduano, 94-GT-200, *ASME Turbo Expo'94*, The Hague, Netherlands, 1994.
- 26 J. F. Escuret, and V. Garnier, *J. of Turbomachinery*, Vol. 118, pp690-696, Oct., 1996.
- 27 J. M. Haynes, G. J. Hendricks, and A. H. Epstein, *J. Turbomachinery*, Vol. 116, pp. 226-239, 1994.
- 28 H. J. Weigl, J. D. Paduano, L. G. Frechette, A. H. Epstein, E. M. Greitzer, M. M. Bright, and A. J. Strazasar, 97-GT-411, *ASME Turbo Expo'97*, Orlando, 1997.

- 29 K. M. Eveker, D. L. Gysling, C. N. Nett, and O. P. Sharma, *Proceedings of SPIE*, Vol. 2494, Orlando, pp152-165, 1995.
- 30 K. M. Eveker, D. L. Gysling, C. N. Nett, and O. P. Sharma, 97-GT-352, *ASME Turbo Expo'97*, Orlando, 1997.
- 31 R. D'Andrea, R. L. Behnken, R. M. Murray, "Active Control of Rotating Stall via Pulsed Air Injection: A Parametric Study on a Low Speed, Axial Flow Compressor", <http://avalon.caltech.edu/~murray>.
- 32 R. L. Behnken, M. Leung, and R. M. Murray, 97-GT-316, *ASME Turbo Expo'97*, Orlando, 1997.
- 33 Y. Wang, and R. M. Murray, "Effects of Noise, Magnitude Saturation, and Rate Limits on Rotating Stall Control", *36th IEEE Conference on Decision and Control*, 1997.
- 34 S. Yeung, and R. M. Murray, "Reduction of Bleed Valve Bandwidth Requirements for Control of Rotating Stall Using Continuous Air Injection", <http://avalon.caltech.edu/~murray>.
- 35 F. Lin, *China-Russia Joint Propulsion Conference*, Nanjing, 1997
- 36 F. Lin, 96-GT-512, *ASME TurboExpo'96*, Birmingham, UK
- 37 G. J. Hendricks, and D. L. Gysling, AIAA 92-3486, *28th Joint Propulsion Conference and Exhibit*, Nashville, 1992.
- 38 C. Freeman, A. G. Wilson, I. J. Day, and M. A. Swinbanks, 97-GT-280, *ASME Turbo Expo'97*, Orlando, 1997.

SIMULATION OF IN-CYLINDER RADIATIVE HEAT TRANSFER OF DIESEL ENGINE WITH MONTE-CARLO METHOD*

Yan Zhaoda Liu Zhentao Chen Jie Yu Xiaoli

Dept. of Energy Engineering ,Zhejiang University

Fax:(086)-0571-7951874

Cheung C.S

Dept. of Mechanical Engineering

Hong Kong Polytechnic University

Keywords: simulation,radiative heat transfer,monte-carlo method

ABSTRACT. A multi-zone (multi-dimensional) is used to model the in-cylinder radiative heat transfer of a direct injection diesel engine. The space and the surface of the ω - combustion chamber are approximated by simple geometric shapes and discretized. Taking into consideration of the complexity of the structure of the combustion chamber and the non-uniform distribution of the radiation medium, the Monte-Carlo method is used to simulate the in-cylinder radiative heat transfer.

1. INTRODUCTION

Following the progress in research in the in-cylinder heat transfer processes of diesel engines, the analytical evaluation of the radiative heat transfer is becoming more and more important. Many researchers have proposed their models and developed their corresponding approaches in evaluating the in-cylinder radiative heat transfer of diesel engine [1-8]. But till now, there is still few studies on the multi-dimensional modeling of in-cylinder radiative heat transfer.

In this paper, the multi-zone (multi-dimensional) radiative heat transfer model developed in [1] is adopted. The effect of the complex structure of the combustion chamber, and the effect of non-uniform distribution of radiative medium, on the surface heat flux in the cylinder of the engine are taken into consideration. The combustion chamber and surface are approximated by simple geometrical shapes and discretized into a number of volume and surface elements. The Monte-Carlo method is able to deal with both non-uniform radiation media and the complex structure of the combustion chamber, it is chosen for simulating and analyzing the in-cylinder radiative heat flux of a G4135 direct injection diesel engine.

2. MONTE-CARLO METHOD [9,10]

The Monte-Carlo method is a kind of probability simulation method, in which the object of investigation is specified as a probability model and solved with a probability method. For the radiative heat transfer processes in the combustion chamber, the probability model assumes that the radiative energy emitted by an element of the radiating medium is composed of many energy bundles. The direction of radiation each energy bundle is random, and can be characterized by three random quantities with a definite distribution density function. By tracing each of the energy bundles until all of them have been absorbed, the number of energy bundles absorbed by each of the surface elements can be obtained.

The radiative heat flux Q_{Aj} at the surface element A_j of the combustion chamber can be defined as below:

$$Q_{Aj} = \int_{A_j} \int_V \frac{k_{ai}}{\pi r^2} \exp(-\int_0^r k_{ai} r dr) \sigma T_g^4 dV_i dA_j$$

$$+ \int_{A_j} \int_A \frac{\cos \eta_i \cos \eta_j}{\pi r^2} \exp(-\int_0^r k_{ai} r dr) \epsilon_{si} \sigma T_{si}^4 dA_i dA_j$$
(1)

* Supported by Foundation of National Engine Combustion Lab. Tianjin University

In the Eq.(1), the first term is the radiative heat transfer between all volume elements V and the surface element A_j , while the second term is the radiative heat transfer between all surface element and the surface elements A_j ; K_{ai} is the absorption coefficient of a volume element, η is the angle between the normal to the surface and the direction of radiation, ϵ is the absorption coefficient of a surface element, r is the distance from the radiation source to the surface, σ is the Boltzmann's constant and T the temperature of an element. The subscripts i and j refer to the zones, g to a volume element and s a surface element.

If the volume element dV_i emits n energy bundles of which n_i are absorbed by dA_j , then the fraction of the energy bundles emitted by dV and absorbed by dA_j is:

$$P_{gij} = n_i / n$$

Similarly, P_{sij} represents the fraction of the energy bundles emitted by all surface elements absorbed by dA_j . Then Eq.(1) can be rewritten as:

$$Q_{Aj} = \sum_{i=1}^{M_g} P_{gij} Q_{gi} + \sum_{i=1}^{M_s} P_{sij} Q_{si} \quad (2)$$

Where M_g and M_s are the number of volume elements and the number of surface elements respectively, while Q_{gi} and Q_{si} are the energy emitted by the volume element and the surface element respectively.

The steps for evaluating the radiative heat flux to the cylinder head, the cylinder liner surface, the piston bowl and the global radiative heat flux are shown below.

- 1.) At any crank angle during the stage of diffusion combustion, the combustion chamber is divided into M_g volume elements and M_s surface elements.
- 2.) Determine the extinction coefficient, radiation temperature, absorption coefficient and emission coefficient(or the emissivity ϵ) of the volume elements and the surface elements based on the diesel engine multi- zone (multi- dimensional) in-cylinder radiation model developed in .^[1]
- 3.) The radiation energy emitted by each element is divided into N energy bundles. Apply the Monte-Carlo method to simulate the direction and the trajectory(including the refraction part) of each energy bundle and determine the position at which it is absorbed.
- 4.) Sum up the number of energy bundles absorbed by each surface element. From Eq.(2), the distribution of radiative heat flux through the surfaces can be calculated and hence the averaged global radiative heat flux.

3. DISCRETIZATION OF THE COMBUSTION CHAMBER

3.1 Geometrical Description of the Combustion Chamber

The G4135 direct injection diesel engine has a ω -combustion chamber. For the convenient of computation, the piston bowl is divided into a cylindrical section $d'd$ and two connecting conical sections dc and cb , as shown in Fig. 1. The values of $\tan\beta_4$, $\tan\beta_5$, $\tan\beta_6$, lc_4 , lc_5 , lc_6 can be calculated accordingly. Due to the movement of the piston, the geometrical boundaries vary with time, so the relative boundary conditions have to be established. These surfaces and boundary conditions directly affect the directions and the paths of the energy bundles.

3.2 Discretization of the Combustion Chamber

To apply the Monte-Carlo method for calculating the radiative heat flux, the space and the surfaces of the combustion chamber need to be discretized into a number of volume elements and surface elements. Since the space geometry and values of the parameters (such as the shapes of the burned zone and the unburned zone, the distribution of soot concentration) of the radiating medium vary with time, the zonal division of the volume

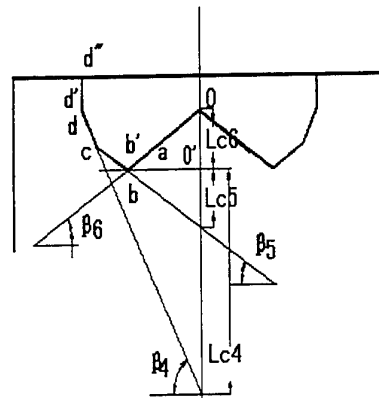


Fig.1 Schematic of the ω combustion chamber geometric shapes

cavity should also vary with time. Except for the cylinder liner surface, other surface elements will not change with time. The surface elements of the cylinder head and the piston surface are hence fixed in size. Thus the volume elements and the surface elements are independent of each other.

The combustion chamber is divided into seven independent surfaces, numbered from 0 to 6, as shown in Fig. 2. The surfaces 0,2,3,4,5,6 are fixed surfaces, whose surface elements are numbered 0-12, 25-29, 23-24, 21-22, 19-20, 13-18 respectively. Actually surface 0 refers to the cylinder cover, surface 2 refers to the piston crown and the other surfaces, 3,4,5 and 6, refer to the piston bowl surface. Surface 1 refers to the cylinder liner, whose elements are numbered 38-47, while the length of an element is determined by the piston stroke. The space of the combustion chamber is divide into 8 volume elements, numbered 30-37. They are either solid or hollow cylinders.

3.3 Determination of Zonal Radiation Parameters

Based on the multi-zone (multi-dimensional) radiative heat transfer model [1], the burning zone is divided into a fuel core zone, two combustible mixing zones B_1, B_2 and an air zone A, as shown in Fig. 3. Element 30 is located in the fuel core zone, elements 31 and 32 are located in the rich mixture zones B_1 , elements 33 and 34 are located in the lean mixture zones B_2 , while the rest are air zones. The values of the characteristic parameters of each zone are shown in table 1.

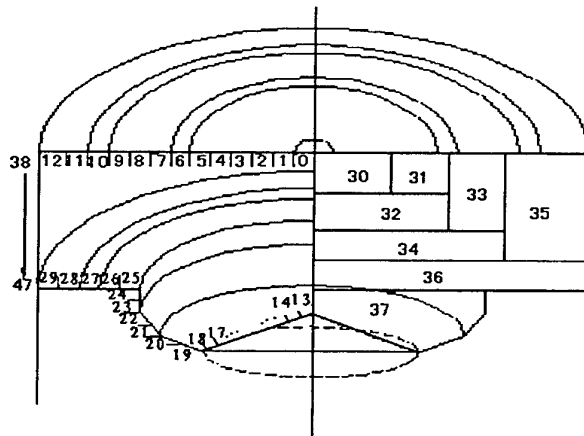


Fig.2 Division of the volume elements and surface elements of the combustion chamber

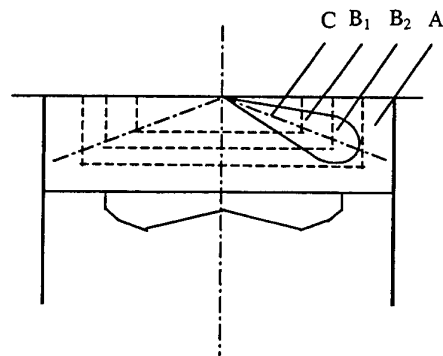


Fig.3 Division of combustion model zones

Table 1 Characteristic parameters of each zone

ATDC °CA	extinction coef.(1/m)				Radiation temp.(K)			
	C	B_1	B_2	A	C	B_1	B_2	A
10U	600	380	450	0	1980	1980	2450	2450
10S	680	380	450	0	1980	1980	2450	2450
20U	100	180	240	0	2300	2700	2600	2600
30U	80	20	120	0	2500	2800	2600	2600
30S	110	20	120	0	2500	2800	2600	2600

U—unscattering , S—sacttering

4. SIMULATED RESULTS AND ANALYSES

- 4.1 The heat release rate of a diesel engine with ω -combustion chamber shows that in general the heat release occurs from 8-10°CA BTDC to 40-60°CA ATDC. The initial period is a stage of premixed combustion, which rises to a peak value near the TDC. After the TDC, diffusion combustion begins and the amount of

heat released in this stage is 70-80 percent of the total amount of heat released. Fig. 4 and Fig.5 show that the peak radiative heat flux on the bottom of cylinder head and the top of the piston occurs at 20°C A TDC. At 10°C A TDC, diffusion combustion is not yet fully developed, hence the radiative heat flux at this crank angle is lower than that at 20°C A TDC. While at 30°C A TDC, diffusion combustion is nearly completed, causing the radiative heat flux to drop significantly. In-cylinder radiative heat flux is directly related to the temperature and soot concentration. Experimental data of the G4135 engine[11] show that the peak flame temperature and soot concentration occurs around 20°C A TDC, which agree with the simulated results.

4. 2 At any crank angle, the peak radiative heat flux on the piston crown come into contact with the flame front first. The peak radiative heat flux always occurs at the apex of the bowl of the ω -combustion chamber, element 13. The simulation indicates that this location can absorb more energy bundles coming from all directions. On the other hand, the peak radiative heat flux on the cylinder head does not appear at its center, but close to element 5. The reason is that at the center of the cylinder head, which is the location of the fuel injector and the fuel core zone C, the temperature is relatively low. Combustion starts at the combustible fuel-air mixture zone B, which is at the tip of the spray bundles around element 5. As the optical thickness from the flame to the center of the cylinder head is large and the unburned fuel droplets tend to reduce the radiation energy of the energy bundles, the radiative heat flux is relatively low. As shown in the curve 2 of figure 4, at 20°C A TDC, there is a significant increase in the radiative heat flux at center of the cylinder head due to the intense diffusion combustion. This figure also shows that there is fluctuation in the distribution of radiative heat flux, which is due to the difference in the values of the various parameters in the different zones.

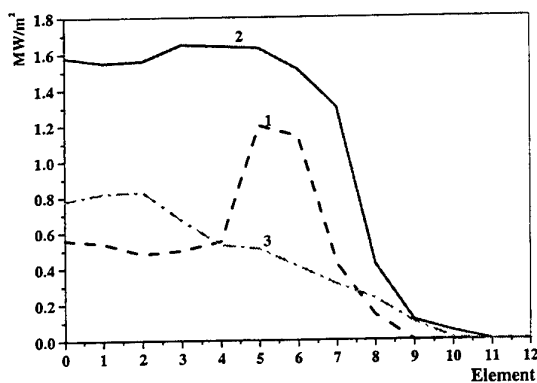


Fig.4 Radiative heat flux on the bottom of cylinder head
1—10°C A TDC 2—20°C A TDC
3—30°C A TDC

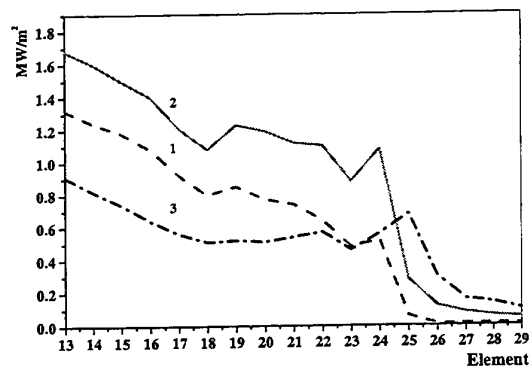


Fig.5 Radiative heat flux on the top of piston
1—10°C A TDC 2—20°C A TDC
3—30°C A TDC

4. 3 As shown in Fig. 5, the radiative heat flux bounces at the edges joining the piston crown and the piston bowl of the ω -combustion chamber, elements 24 and 25. The main reason is that when the radiation energy bundles emitted by the soot and the gas radiation sources arrive at these elements, most of them are absorbed and few of them reflected. On the other surfaces, there is reflection of the energy bundles. So the bounce occurs. As the piston moves, the distances and directions of the energy bundles to these elements also change, the level of bounce in the radiative heat flux at these elements hence changes with crank angle.
4. 4 As shown in Fig. 6, the radiative heat flux on the cylinder liner is always lower than that on the piston crown and the cylinder head. This is due to the larger area in absorbing the energy bundles than those of the other two surfaces. Influenced by the position of the piston, the radiative heat flux at the element 47, which is close to the piston crown, is always higher than that at the element 38, which is close to the cylinder head. The radiative heat flux also peaks at 20°C A TDC. The pattern of distribution of radiative heat flux is similar to the results obtained by Meguc et al. [12] with a spherical harmonics approximation

method. The magnitudes of the heat flux shown in table 2 also agree with experimental data obtained from similar engines. Hence, the mathematical model established in this paper can be used for predicting the radiative heat flux of similar engines.

Table2 Radiative heat flux(MW/m²)

ATDC	Radiative heat flux peak value on top of piston	Radiative heat flux peak value on the bottom of cyl. head	Average radiative heat flux of whole surface
10°C A	1.35	1.19	0.34
20°C A	1.70	1.62	0.60
30°C A	0.92	0.84	0.25

- 4.5 The scattering effect of the fuel droplet on radiative heat transfer is controversial. In this paper, the scattering effect of fuel droplet is taken into consideration. The simulated results with and without fuel droplet scattering are shown in Fig. 7. The effect on radiative heat flux is not significant, except around the fuel core region where the fuel droplet density is high.

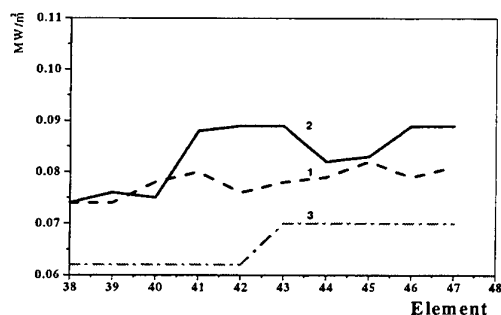


Fig.6 Radiative heat flux of cylinder liner

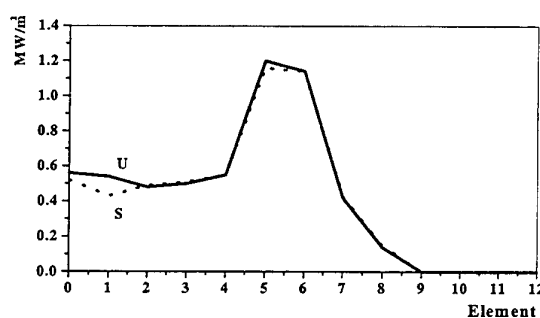


Fig.7 Scattering effect of fuel droplet on cyl. head radiative heat flux at 10°C A ATDC
(U—unscattering , S—sacttering)

5. CONCLUSIONS

Based on a multi-zone spray combustion model and a multi-zone (multi-dimensional) radiation model, the in-cylinder radiative heat flux of a diesel engine has been calculated with the Monte-Carlo method. The combustion chamber and the surfaces are geometrically simplified and discretized into a number of elements. The effect of non-uniform distribution of the radiation medium is taken into account. The numerical results indicate that the pattern of distribution and magnitude of the radiative heat flux agree with the combustion processes and with experimental data. The results also match with those obtained by Menguc and Spicher. The scattering effect of fuel droplet on radiative heat flux has also been investigated. It can be concluded that the probability model of describing the radiation mechanism can be an effective method for simulating the in-cylinder radiative heat flux of similar diesel engines.

6. REFERENCE

1. H. Chen, Investigation on Multi-zone and Multi-dimensional Heat Radiative Transfer Model in a D.I. Diesel Engine Cylinder. *Ph.D. thesis, Zhejiang Univ. 1998.*
2. W.J.D. Annand, Heat Transfer from Flames in Internal Combustion Engine. *International Symposium on Heat transfer from Flames, Trogir(1963)*
3. T Kunitomo, et al, Prediction of Radiative Heat Flux in a Diseal Engine. *SAE Trans.*,841908.

4. M. Chapman, et al, A Time-dependant Spatial Model for Radiant Heat Transfer in Diesel Engine. SAE 831725.
5. S.L. Chang, et al, Computation of Radiation Heat Transfer in Diesel Combustion . SAE 831332.
6. N.D. Whitehouse, et al.,Radiative Heat Transfer Calculations from Soot Clouds for a Quiescent Combustion Chamber Diesel Engine. ASME Symp. FED-20 on Flows in I.C. engine,84.
7. O. Zhou, et.al., A Mathematical Method to Study the Soot Emission and the Heat Radiation Transfer in D.I. Diesel Engine Cylinder. Trans. of CSICE,900040
8. Z. Zhang, et.al., Evaluation of Global Radiative Heat Flux from Heat Release Rate. Trans. of CSICE,940041
9. M. Xie, Internal Combustion Engine Combustion Modeling , Dalian University of Technology press 1995
10. R. Siegel, et al, Thermal Radiant Heat Transfer. 2nd Edition, M.C. Graw-hill Book Company, Newyork,1981.
11. S. Xu, et.al., Study on Flame Temperature and Soot Formation in Combustion Chamber of D.I. Diesel Engine by Multi-optical Poly-color Method. Trans. of CSICE 960042
12. M. Mengul,et al, Multidimentional Modeling of Radiative Heat Transfer in Diesel Engine. SAE 850503.

V. Waste Treatment by Thermal Methods

CONTROL AND SENSING SYSTEM BASED ON FUZZY LOGIC FOR DOMESTIC REFUSE INCINERATORS

Makoto Fujiyoshi, Wan Chung Lam

Hitachi Zosen Corporation

Email: fuiyoshim@elec.lab.hitachizosen.co.jp, lamw@elec.lab.hitachizosen.co.jp

Fax: (81)-6-6551-9876

ShiJie Sun

I. CON Co. Ltd.

Email: icon-f@db3.so-net.ne.jp; Fax: (81)-726-86-3233

Keywords: refuse incinerator, fuzzy logic, control and sensing system, dioxin, domestic refuse

ABSTRACT. In refuse incineration, controller design is a matter of trade-off between poorly defined control objectives under poorly defined conditions, in the sense that real time measurement of dioxin production is impossible and the quality of refuse feed to the incinerator is difficult to define, since its content is usually inhomogeneous and its calorific value not measured. The critical requirement for refuse incineration is clean and thorough thermal decomposition of refuse so that production of dioxin is minimized. In Hitachi Zosen Corporation, we have developed a control and sensing system for these incinerators based on fuzzy logic. In the sensor part of the system, the quality of combustion inside the furnace is evaluated by means of 3 parameters – the Combustion Center Point (CCP), the Refuse Mass Energy (RME) and the Air Balance in Furnace (ABF) – which are determined based on fuzzy logic from a range of measurements. In the control part of the system, control input such as the amount of air injection, refuse feed rate, etc., to the furnace are controlled using a fuzzy controller which use the current control input and the quality of combustion as input parameters. This sensing and control system has been implemented and tested in domestic refuse incinerators built by Hitachi Zosen Corporation.

1. INTRODUCTION

Refuse incineration as a means of domestic waste disposal has several advantages. Firstly, incineration is an efficient and rapid way to reduce the volume, weight and odor of domestic refuse. When carried out in high temperature in properly designed incinerator, organic toxic material (such as PCB) and biological hazard (such as virus and bacteria) can be removed, and the heat generated can be used for heating and electricity generation. As a result, domestic refuse incineration are adopted by many European countries as well as Japan where population density and other factors make landfill unattractive. According to Japanese government statistics, 49.66 million tons (75.5% of all domestic refuse collected) of domestic refuse was disposed by incineration in 1994[1]. In Japan, 1892 incinerators (those operated by municipal governments) are in operation. Comparatively figures for other countries are summarized in table 1.

Table 1. Refuse Incineration in Several European and American Countries

Countries (year when statistics is collected)	Germany (1993)	Netherlands (1993)	Sweden (1991)	USA (1993)
Annual Domestic Refuse Generation (million tons)	43.5	12.0	3.2	207.0
Annual amount incinerated	11.0	2.8	1.7	32.9
Percentage incinerated	25%	23%	55%	16%
Number of incinerator plants	53	11	21	148
Average capacity of incinerator plants (kilo tons)	208	255	81	223
Allowable dioxin concentration in exhaust (ngTEQ/Nm ³)	0.1	0.1	0.1	0.14 – 0.21

Technologies for domestic refuse incinerator are developed to meet tighter and tighter regulations on the amount of toxic material that can be released in the form of exhaust gas and ash. When incinerators in its present form

was first built in Japan in the 1950s, the only regulation on exhaust gas release is on dust and suspended particle content. Over the years, regulations have been subsequently imposed on SOx concentration, HCl concentration and NOx concentration in the exhaust. From 1997, the new guidelines issued by the Japan government state that all new incinerator plants are to be built to release less than 0.1ngTEQ/Nm³ of dioxin in its exhaust – which is also the standards adopted by many developed countries. A variety of technologies is being pursued to achieve this standard. One of which is the control of the incineration process within the furnace so that complete and stable thermal decomposition of refuse can be achieved in high temperature, a condition essential to suppress the generation of dioxin. In Hitachi Zosen Corporation, we have developed a control and sensing system for incinerators based on fuzzy logic. This system has been developed with the aim of achieving clean combustion, i.e. thorough thermal decomposition of hydrocarbon, inside the furnace of the incinerator, so that production of dioxin is minimized.

2. REFUSE INCINERATOR

The layout of a domestic refuse incinerator plant is shown in Figure 1. Refuse is first dumped into the receive pit (1) where it is mixed and fed to the furnace (2). In the stoker design shown in this figure, the furnace bed is inclined with movable grating at the bottom of the bed, which acts to break slag which may form at the bottom, and forces the refuse layer down the furnace bed. Eventually the refuse is decomposed into ash completely, which is collected, treated and removed. Inside the furnace, combustion is basically controlled by:

1. Refuse feed rate
2. Air injection rate
3. Air temperature

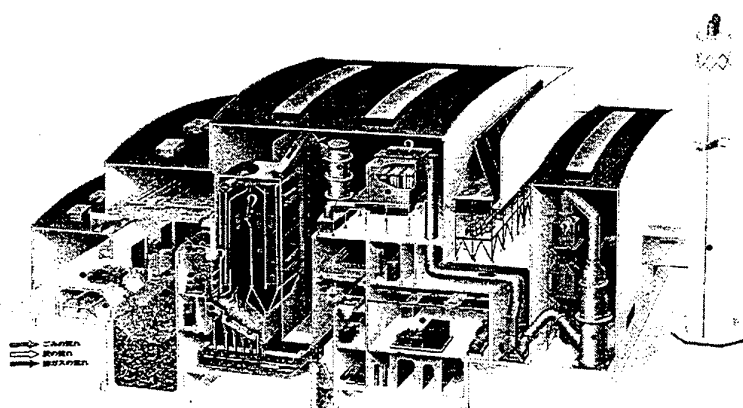


Fig. 1. Domestic refuse incinerator

The exhaust gas from the furnace is passed first through the exhaust heat boiler (3) where heat energy is collected for electricity generation or heating purpose. Then it is passed to the bag filter (4) where suspended particles are removed. Eventually the gas is washed and chemically treated (5) to remove the remaining toxic gas and released into the atmosphere.

In any refuse incinerator, dioxin is inevitably produced and released into the exhaust gas. As summarized in Figure 2, when the exhaust gas temperature is at least 850 degree Celsius and has a resident time of at least 2 seconds, most the dioxin is decomposed before reaching the exit of the furnace. At the same time, air is injected inside the furnace as secondary air so that oxygen concentration is high enough for complete combustion of suspended particles, and turbulence resulted from air injection works to remove cool air pocket inside the furnace where dioxin may not be decomposed.

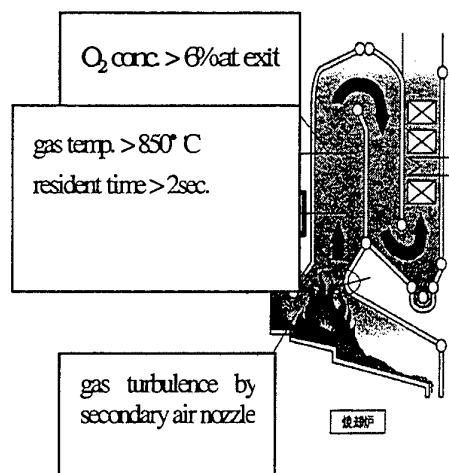


Fig.2. Conditions needed to suppress dioxin

3. INCINERATION PROCESS

The most common designs for the furnace of incinerators are stoker, fluidized bed and rotary kiln. The furnace for stoker type of incinerator is shown in Figure 3. Compared with other types of incinerators such as rotary kiln or fluidized bed, stoker is robust and well established for large scale domestic refuse incineration. Refuse is fed by means of overhead crane from refuse pit into the refuse hopper. From there, the refuse is transported by the movable grate down the furnace. The grate is divided into 3 region:

1. Drying grate, where refuse is preheated to remove excess water
2. Combustion grate, where high temperature incineration occurs
3. Burnout grate, where refuse are allowed to burnout and ash is discharged into the ash pit

As shown in Figure 4, air boxes are installed under the grates from which preheated primary air is delivered. Secondary air is introduced directly into the furnace. Temperature and pressure sensors are also installed inside the furnace to monitor the conditions inside the furnace. Together with the flow sensors for primary air and secondary air, camera is also installed inside the furnace so that operators can monitor the internal condition of the furnace. Therefore, the measurements that can be used as control input can be summarized as follows:

1. refuse feed rate (grate movement speed)
2. furnace temperature
3. furnace pressure
4. primary air flow rate
5. secondary air flow rate
6. visual image

4. PROCESS MODELING

To design an effective controller for incinerator, it is first necessary to construct a mathematical model for the process inside the furnace. For conventional PID controller design, it is usual practice to use linear model to simulate the process. When the process is complicated, additional parameters are used to account for additional input/output relationship.

Although various measurements are obtained during the operation of an incinerator, it has been very difficult to model the combustion process inside the furnace with high accuracy. The most important reason is that the calorific value of the refuse cannot be determined easily – and is in fact not sampled for control purpose in most cases.

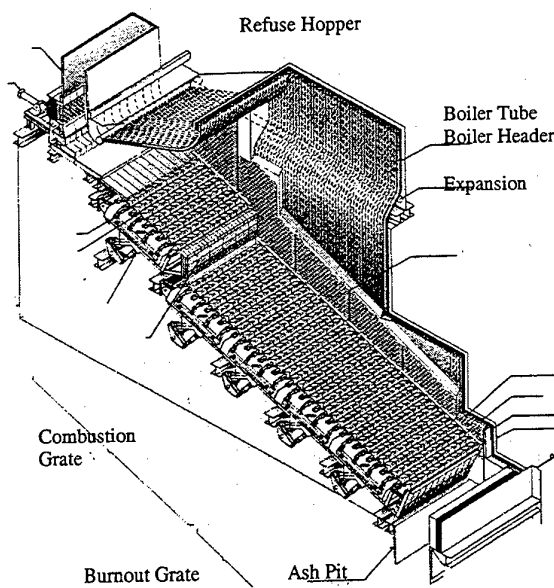


Fig. 3. Stoker furnace

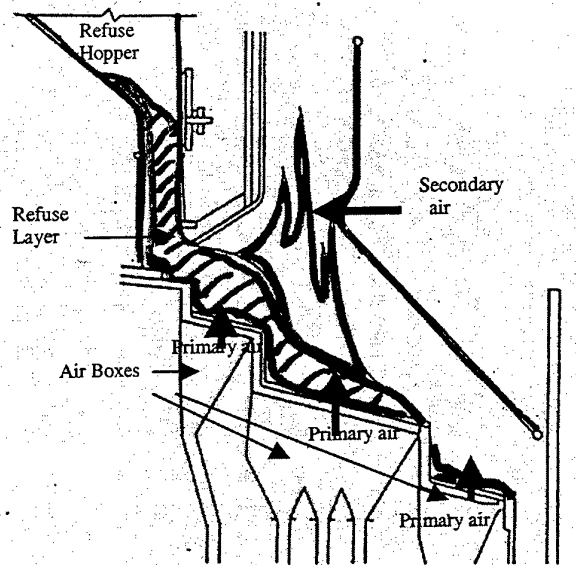


Fig. 4. Control of combustion in stoker

Furthermore, depending on that state of refuse the combustion process can vary a lot – but it is simply impossible to parameterized all changes in the quality of the refuse. Another difficulties in deriving a precise combustion model for controller design is that there is a long reaction time for the process. Typically, refuse stays inside the furnace for about 2 hours before fully incinerated and discharged into the ash pit. Therefore any change in parameters, such as large change in the calorific value of the refuse feed, may be observed only after a long time delay. By that time it is already too late to take action to control the process. Knowing that it is difficult to construct a physical model for the incineration process, we have made use of the flexibility provided by fuzzy logic to represent the properties of the process. While the model is deterministic, the membership function in the model can be adjusted to absorb the deviation of the model from the physical process. This is analogous to the control and monitoring of incinerators by experienced operators. In most case, operators have no complete knowledge of the combustion process, the quality of the refuse, etc. But his/her fragmented know-how in the operation and collection of scenario-reaction rules are usually valuable in the day-to-day operation of incinerator.

In our fuzzy process model, the state of the incinerator are characterized by 3 fuzzy parameters:

1. Combustion Center Point (CCP) – which indicate the center of combustion within the furnace. There is an optimal CCP within the furnace that make complete combustion of refuse more likely. Examples are shown in figure 5. In figure 5(a), the primary air is inefficient in the combustion grate but abundant in the burnout grate. Therefore the CCP is upstream. In figure 5(b), the refuse feed rate is too low, resulting in CCP moving upstream. In figure 5(c), the conditions are optimal and so the CCP is at the proper position.

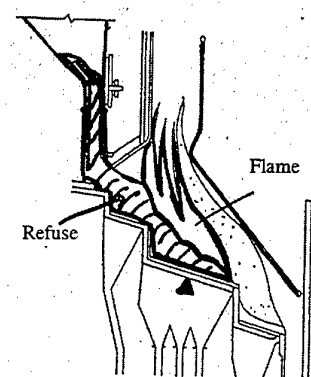


Fig. 5(a)

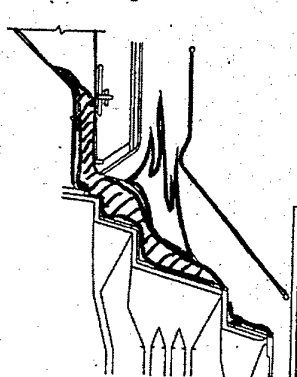


Fig. 5(b)

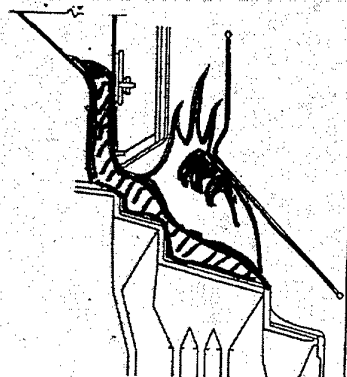


Fig. 5(c)

Fig. 5. The concept of CCP

2. Refuse Mass Energy (RME) – which measures the thermal energy possessed by refuse. If RME decreases, heat release during combustion tends to decrease.
3. Air Balance in Furnace (ABF) – which measures the balance of combustion air within the furnace. A steady ABF indicates that combustion air supply is sufficient and combustion is stable.

These fuzzy parameters are deduced from physical measurements as shown in Figure 6. CCP is deduced by fuzzy logic from the image of furnace flame obtained by camera placed to capture the view inside the furnace, and temperature measurements within the furnace. RME is deduced from the flow of combustion air, temperature within the furnace and thickness of the refuse layer. ADB is deduced from flow rate of cooling air, combustion air and secondary air. While measurements are deterministic, CCP, RME and ADB are all fuzzy concept. Based on this 'fuzzy sensor' process model, control system for refuse incinerator is designed.

5. CONTROL SYSTEM

In designing the controller system for domestic refuse incinerators, the objective is to achieve dioxin free incineration. However, the concentration of dioxin in the exhaust gas is extremely low and analysis of dioxin

concentration is extremely complicated and time consuming. Real time monitoring and control is not possible.

It is found that dioxin production is minimized if the conditions summarized in Figure 2 is achieved. These same conditions strongly influence CO production in the incinerator. In fact, it is found that there is a strong statistical correspondence between CO production and dioxin production. A typical CO concentration measurement collected during incinerator operation is shown in Figure 10. Sudden increase in CO concentration corresponding to incomplete combustion shows up from time to time. This may occurs when bulky refuse is fed, air is temporarily run out, etc. When these peaks of CO occurs, production of dioxin is found to be maximum. Since CO concentration can be measured in real time, CO is usually measured in place of dioxin to monitor incinerator condition.

As expected, PID control strategy is by far the most common technique used in incinerator controller design. Since combustion process is extremely difficult to model and predict, PID techniques have been useful in providing well understood and robust design for controller.

However, as the regulation on dioxin release becomes tight, more precise control of the combustion process is needed. There are attempts to model and identify the dynamics of incinerator more precisely so that predictive control can be implemented[2]. On the other hand, identification of the complicated combustion process by non-linear, 'black-box' techniques such as neuro networks is also reported[3].

As mentioned in section 5, we have found fuzzy logic a useful technique to model the combustion process of a refuse incinerator, in the sense that we can use all the available measurements to evaluate the state of the combustion process to obtain a robust and stable model which can also take into account the fuzzy know-how of operators to tune the model. The fuzzy states of CCP, RME and ABF can

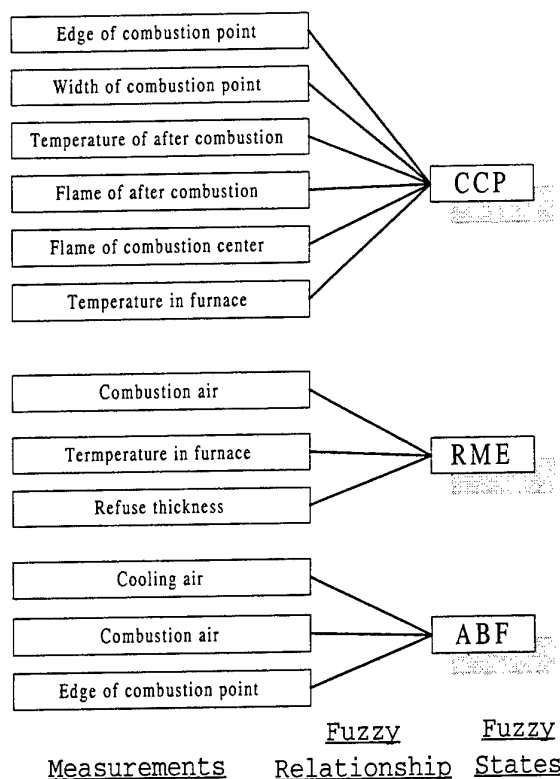


Fig. 6. Fuzzy Sensor Process Model

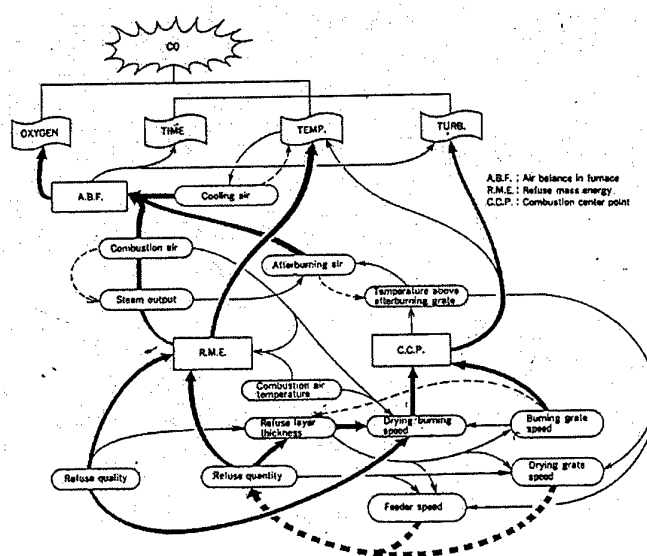


Fig. 7. Cause and effect relationship between combustion process and CO generation

be used to predict CO concentration by fuzzy relationship as shown in Figure 8.

This CO prediction is in term used to modify the control input to the incinerator. Based on CO prediction, fuzzy controller produces output that reduce CO production. On the other hand, non-fuzzy, conventional PID controller has been developed and used in refuse incinerators. These PID controllers are used as regulators to maintain the flow rate and temperature of primary air and secondary air constant, and to regulate the refuse layer thickness on the grate constant by controlling the feed rate (movement speed) of the movable grate. The output from the PID controller and the output from the fuzzy controller is combined to give final control input to the incinerator. In this way, the experience gained in the development of traditional PID controller is fully utilized in the final configuration of the controller software (Figure 9)[4,5].

During the experimentation stage, an in house developed fuzzy controller was used for the implementation of the fuzzy logic. A new hybrid intelligent multi-programmable controller developed by Icon Corporation is used for present and future development and deployment. It consist of not only pure fuzzy control, but also fuzzy PID control and PID control so that both fuzzy control or PID control or fuzzy PID control can be chosen during installation, experimentation and operation. The hybrid controller is equipped with a powerful software tool so that users can construct/programm control system with ease under the Windows environment (95/98/NT).

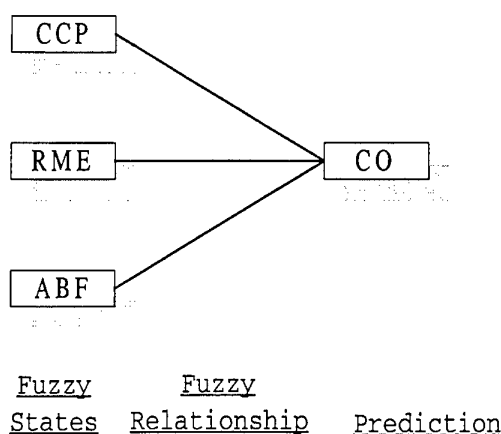


Fig. 8. Fuzzy prediction of CO concentration

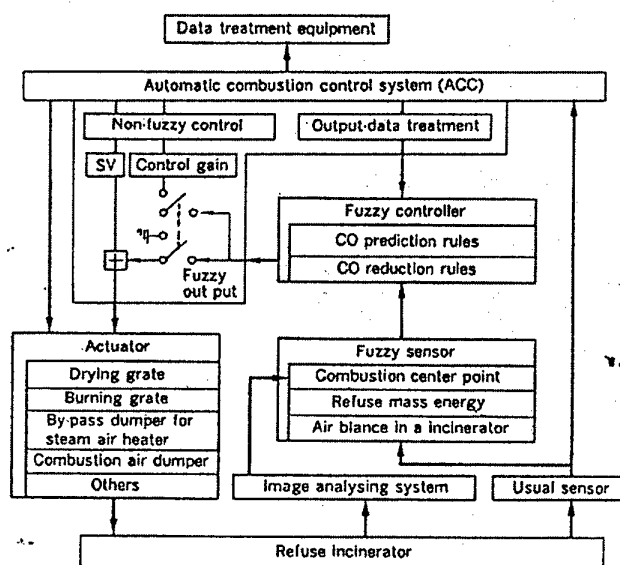


Fig. 9. Fuzzy ACC for refuse incinerator

6. EXPERIMENTAL RESULTS

The fuzzy controller has been implemented in an operational refuse incinerator in Osaka, Japan and data has been collected and analyzed during normal operation when ordinary domestic refuse was incinerated. In Figure 10, CO concentration was measured for a time span of 4.5 hours, and is plotted against the value of RME. During the operation, fuzzy ACC (Automatic Combustion Control) system was used in the first half, while the fuzzy part was switched off during the second half of the operation. When CO concentration is used as a barometer for dioxin production, instead of its absolute concentration it is the CO peak (which occurs the most prominently at 13:11 in Figure 10) that indicates incomplete combustion and therefore high dioxin production. Data in Figure 10 shows that with the fuzzy controller, CO concentration was kept more or less even at a low concentration less than 50ppm. When the fuzzy part of the controller was switched off (only the conventional PID regulators in use), not only the absolute concentration of CO was increased, there were also numerous CO peaks above 50ppm observed.

Since CO peaks are important barometer for incomplete combustion and dioxin production, the number of CO peaks were counted during a 24 hour operation cycle. The results are summarized in figure 11 and 12. With fuzzy ACC we had a count of 8 times, while the count for conventional PID controller is 59 times. The number of CO peaks above 50 ppm is cut by 85%. Another important parameter is combustion control is oxygen concentration, since a minimum concentration of 8% is required for stable

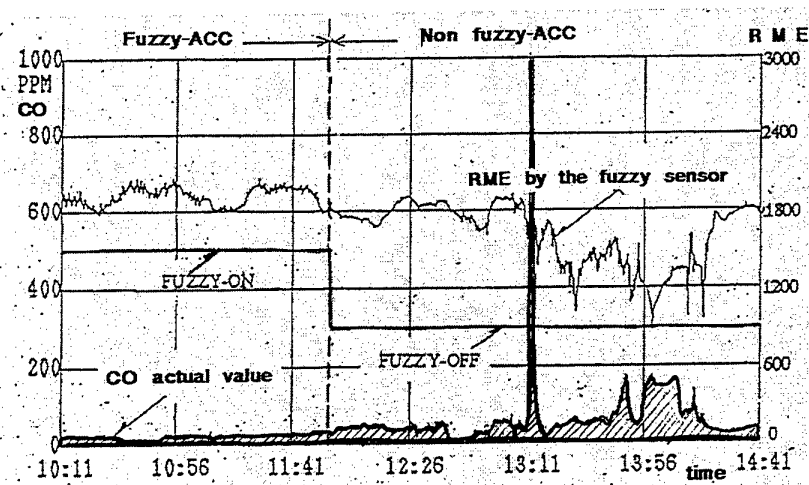


Fig. 10. Variation of CO concentration during an experiment

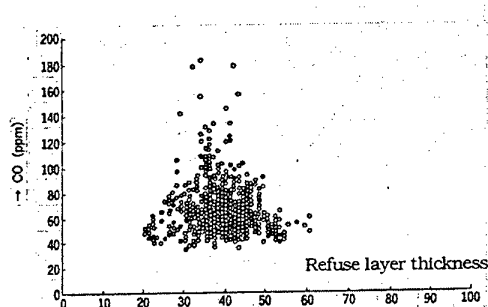


Fig. 11(a) CO conc. peak - PID controller

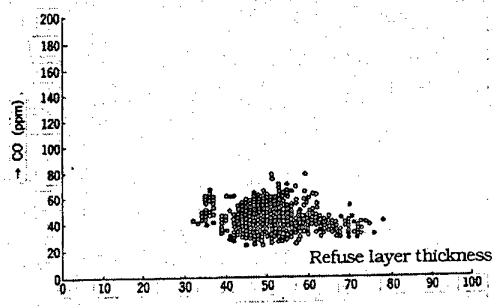


Fig. 11(b) CO conc. peaks - fuzzy controller

and complete combustion. Oxygen concentration and CO concentration data were collected and compared in Figure 13. From Figure 13, it is found that CO concentration is distributed towards the lower end when fuzzy ACC is used. Operation at 10ppm or lower is about 50% of the time with conventional PID regulator. In the case of Fuzzy ACC it is about 62%. The average CO concentration of 14ppm is extremely low when PID regulator is used. With fuzzy ACC the concentration is even lower. For oxygen concentration, the histogram shows that when fuzzy ACC is used the distribution is centered around 7.8% to 8.5%. The mean and standard deviation is slightly lower than the case of conventional PID regulator, which means that a more stable and efficient combustion is achieved. In short, we found that the fuzzy logic based sensing system and controller is effectively in providing a stable combustion in the furnace and in reducing CO peaks, and so production of dioxin is expected to reduce. Further R&D on the application of fuzzy controller for fluidized bed incinerator and new gasification melting incinerator is now being developed in Hitachi Zosen Corporation.

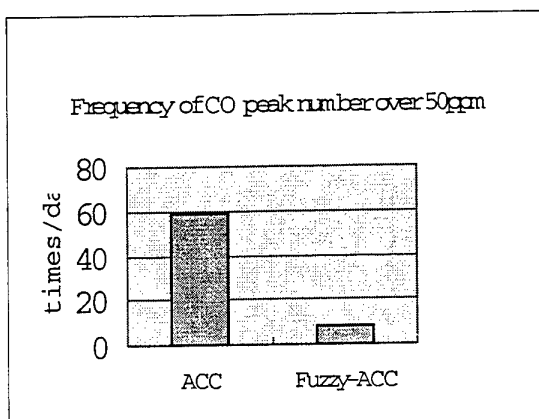


Fig. 12. Count of CO peaks

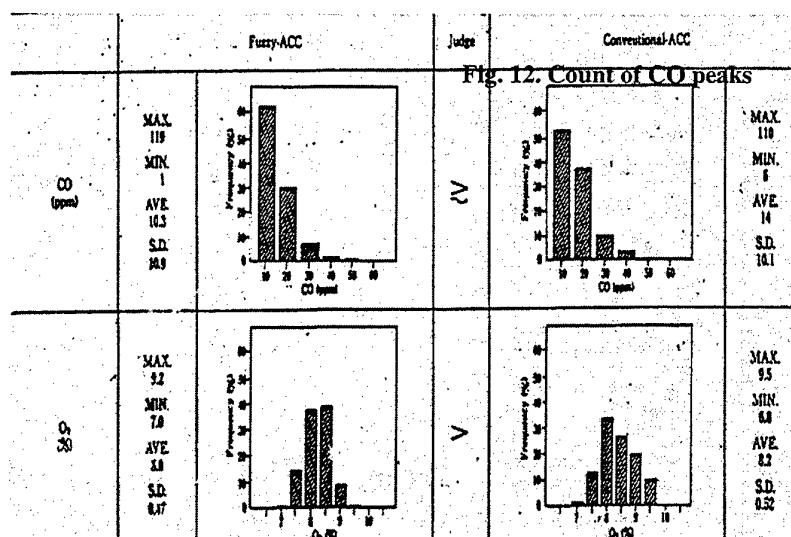


Fig. 13. Comparison of CO and oxygen concentration measurement

7. CONCLUSION

Due to various environmental problems associated with landfill, scarcity of land resource, and the maturity of incinerator technology, more and more countries in Europe and Asia are turning to incineration as the means of refuse disposal. Stringent dioxin release limit as low as 0.1 ngTEQ/Nm^3 is common in the international community. In order to meet this limit, it is necessary to take every precaution in the design and operation in the whole process of refuse incineration from waste collection to ash disposal. It is therefore necessary to improve the design of incinerator controller so that production of dioxin within the furnace is kept to a minimum. In the case of incinerators, controller design is a matter of trade-off between poorly defined control objectives under poorly defined conditions. We have defined 3 fuzzy parameters to quantify the combustion process – CCP, RME and ABF. The values of these parameters are evaluated based on fuzzy logic from a number of sensor measurements as well as results from image processing. These fuzzy model of the combustion process is then used in the fuzzy controller for the incinerator, where the prediction value of CO concentration is used to adjust refuse feed rate, air flow rate and grate movement, etc. In implementation and experimentation, CO concentration peak count is used as barometer of dioxin production. Experimental results shows that satisfactory reduction in CO peaks can be achieved with the fuzzy controller design.

REFERENCES

1. "Nihon no haikibutsu shori" published by Japanese government Ministry of Health and Welfare, Environmental Health Bureau (1997).
2. Y. Miyamoto, et al., "Development of On-line Identification and Model Predictive Control for a Fluidized Bed Incinerator", Kawasaki Technical Review, vol. 136 (January 1998, in Japanese).
3. H. Kidohsho, et al., "Application of Neurocontrol to Fluidized Bed Incinerators", Transaction C of the Japan Society of Mechanical Engineers, vol. 61, No. 591, pp 160-166 (November 1995, in Japanese).
4. K. Kaketa, M. Fujiyoshi, "The Fuzzy Automatic Combustion Control System on the refuse incinerator plant," vol. 51, no. 2, Technical Report of Hitachi Zosen. (February 1994 in Japanese).
5. M. Fujiyoshi, T. Shiraki, "A Fuzzy Automatic Combustion Control System of Refuse Incineration Plant," IIZUKA'92 International Conference, Proceeding Vol. 1, July 17-22, 1992.

NOVEL GAS TECHNOLOGY FOR TREATMENT OF HAZARDOUS AQUEOUS WASTE STREAMS

Marzouk Benali¹

Natural Resources Canada – CANMET/Energy Diversification Research Laboratory
1615, Lionel-Boulet Boulevard, P.O. Box 4800, Varennes (Quebec) J3X 1S6 Canada
Email: mbenali@nrcan.gc.ca; Fax: (450) 652-5994

Isabelle Hugron, Marie-Ève Morin and Christophe Guy

Ecole Polytechnique, Chemical Engineering Department, P.O. Box 6079, Stat. Centre-Ville
Montreal (Quebec) H3C 3A7 Canada

Keywords: free radicals, gas flame, chemical oxidation, direct contact, liquid effluents

ABSTRACT. The principle of the novel treatment technology of liquid waste treatment is based on free radicals from natural gas flame to destroy organic pollutants through a chemical oxidation process and oxidizes the organic substance in aqueous phase. Its original concept is based on a direct contact between a contaminated liquid stream and the flame of a gas-fired burner containing free radicals such as OH^* , H^* , CH_3^* and CHO^* . The high temperature of the flame enables completion of the oxidation of the organic substance, in aqueous phase, by means of the oxygen excess present in flame. Experimental results obtained on a 50kW-test bench shows a pollutant destruction efficiency of 75 to 99% for wastewater contaminated by phenol, toluene, xylenes (ortho, meta and para), or acetone having a concentration varying between 180 and 82,000 ppm. The cumulative specific energy consumption varies from 0.4 to 0.5 kWh/L of treated liquid waste stream.

INTRODUCTION

Hazardous organic substances such as phenol, benzene, toluene, chloro- or nitro-benzene, methanol, xylene, styrene, and other volatile or halogenated organic compounds often contaminate industrial liquid waste streams. The main sources of such waste streams are: treatment/disposal processes for industrial waste waters and liquid wastes, oil refineries and petrochemical plants, pulp and paper mills, foundries and metal refineries, metal/plastic product manufacturing, organic chemicals plants, tanneries, food industry and mineral industry. The numerous, available processes for treating such liquid waste streams can be divided into three types of processes: biological, physical and chemical (Table 1). A combination of biological, physical and/or chemical processes may also be used. The efficiency of the biological processes in destroying organic substances can be as high as 97%. However, certain factors such as a concentration of organic matter higher than 500 mg/L or lower than 5 mg/L, and/or a temperature lower than 10°C may adversely affect the efficiency of such biological processes. This is also the case in the presence of halogenated contaminants. The basic concept of the physical processes is to transfer one organic substance toward another one. These physical processes present two drawbacks: they are selective in the treatment of the liquid effluent, and they require storage and/or disposal of the eliminated contaminants. The chemical processes use conventional oxidation agents such as chlorine, chlorine dioxide, potassium permanganate, hydrogen peroxide, ozone, ultraviolet radiations, sulphite ions, and others. They are often limited with respect to the volume of liquid waste to be treated. Wet oxidation which uses air (or pure oxygen) as oxidant shows high efficiencies but is restricted by severe operation conditions: pressures of the order of 2 to 25 MPa [1].

The above brief analysis of treatment methods suggests that pollution prevention requires a change in "philosophy" so that the generation of contaminated wastes has to be viewed as an inefficient production process rather than as an inevitable environmental problem. Many chemical process industries are working toward a goal of "zero discharge" which, in many cases, means the elimination of certain priority pollutants or toxic substances in the liquid waste streams from a facility.

¹ Author to whom correspondence should be addressed.

The main selection criteria either for destruction or recovery process are:

1. Flowrate of the contaminated liquid waste stream to be treated;
2. Flowrate variability of the contaminated liquid waste stream to be treated;
3. Chemical composition of the liquid waste stream to be treated;
4. Concentration of the organic pollutants, and
5. Limitations and constraints of the production process.

Table 1. Major Sources of Liquid Waste Streams

Category	Effluent flowrate (m ³ /day/plant)	Treatment mode
Organic chemicals plants	30 to 200,000	- Physico-chemical - Chemical
Oil refineries and petrochemical plants	1000 to 192,000	- Physical - Physico-chemical
Pulp and paper mills	500 to 175,000	- Chemical - Biological
Treatment/disposal processes for industrial waste-waters and liquid wastes	≥ 500, generally variable	- Chemical - Physical - Underground injection

The new treatment method presented in this paper, the Direct Contact Thermal Treatment (DiCTT) Technology [2,3] provides a decontamination process capable of substantially eliminating the above discussed drawbacks of the prior art. Table 2 shows the principal competing commercial technologies of the DiCTT process.

Table 2. Principal Competing Technologies of DiCTT Technology

Technology	Advantages	Disadvantages
Wet Air Oxidation (WAO)	well known technical process	costly
Electric Plasma Oxidation (EPO)	well known technical process	very costly
Photochemical Process	none	small scale only
Dilution and biological Treatment	less costly	Under specific conditions

DESCRIPTION OF THE "DiCTT" TECHNOLOGY

The principle of the DiCTT technology (Fig. 1) is based on a direct contact between the contaminated liquid, containing at least one organic pollutant, and a natural gas flame. It consists of (Fig. 2):

1. a vertical stainless steel reactor;
2. a gas-fired burner to produce in this reactor a flame centred on the geometrical axis which provides free radicals and oxygen;
3. a means for producing a flow of liquid effluent on the inner wall of the reactor to cause a direct contact between (a) the flame containing free radicals and oxygen, and (b) the organic substance contaminating the liquid effluent;

4. a liquid/gas separator for separating liquid from gaseous products exiting the outlet of the reactor;
5. a stainless steel reservoir containing the contaminated wastewater;
6. a stainless steel reservoir containing hydrogen peroxide as an auxiliary oxidizing agent.

The liquid effluent may contain an organic mixture of a first easily oxidized species and a second recalcitrant species, so that aqueous-phase oxidation reactions occur in the reactor, proceeding according to a free-radical mechanism and being characterized by an induction period followed by a rapid reaction phase.

Fig. 1 and 2 are schematic views of the DiCTT concept and a pilot-scale experimental installation for decontaminating a liquid effluent located at Energy Diversification Research Laboratory's facilities (Varennes, Canada). As illustrated in Fig. 1 and 2, the reactor and its geometrical axis may be generally horizontal or vertical. The contaminated liquid effluent is injected tangentially in the reactor through a tangentially oriented orifice so as to produce a helical flow of contaminated liquid effluent on the cylindrical inner wall of the reactor.

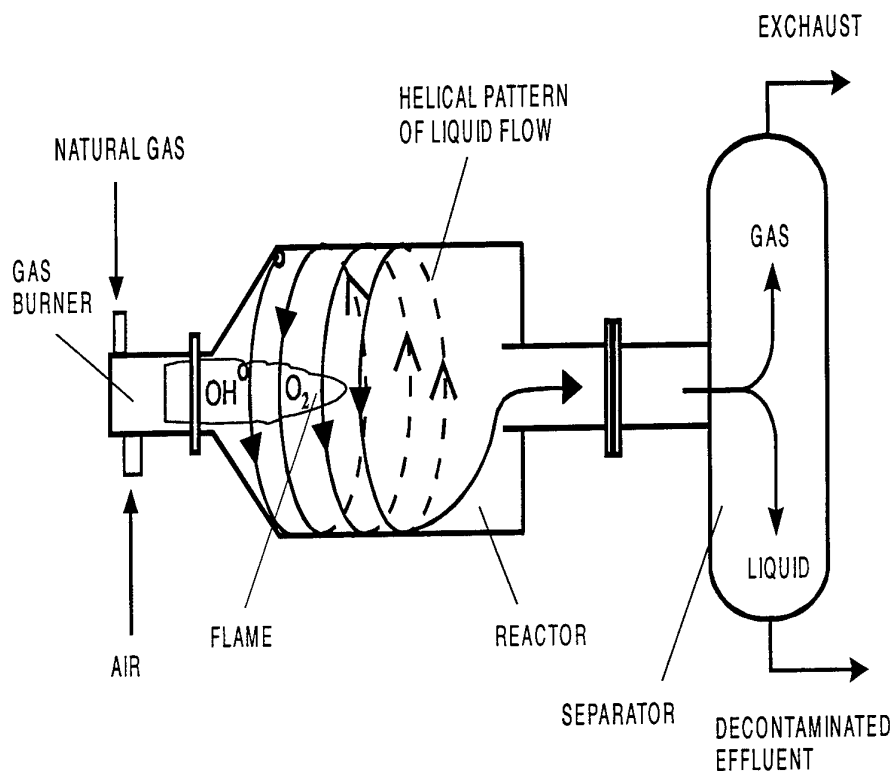


Fig.1. Principle of DiCTT technology concept

With the geometry of the arrangement of Fig. 1 and 2, the helical flow produces a direct and intimate contact of the liquid effluent with the free radicals such as OH^* of the flame to cause oxidation, in liquid phase. The helical flow also increases the surface of contact between the free radicals and the flame. The high temperature of the flame contributes to the performance of this free radical oxidation reaction. Simultaneously, the high temperature of the flame enables completion of the process of oxidation, in liquid phase, by means of the excess oxygen present in the flame. Also, an auxiliary liquid oxidizing agent (hydrogen peroxide) is added in the reactor to further improve the performance of the free radical oxidation reaction of the organic pollutants such as phenol.

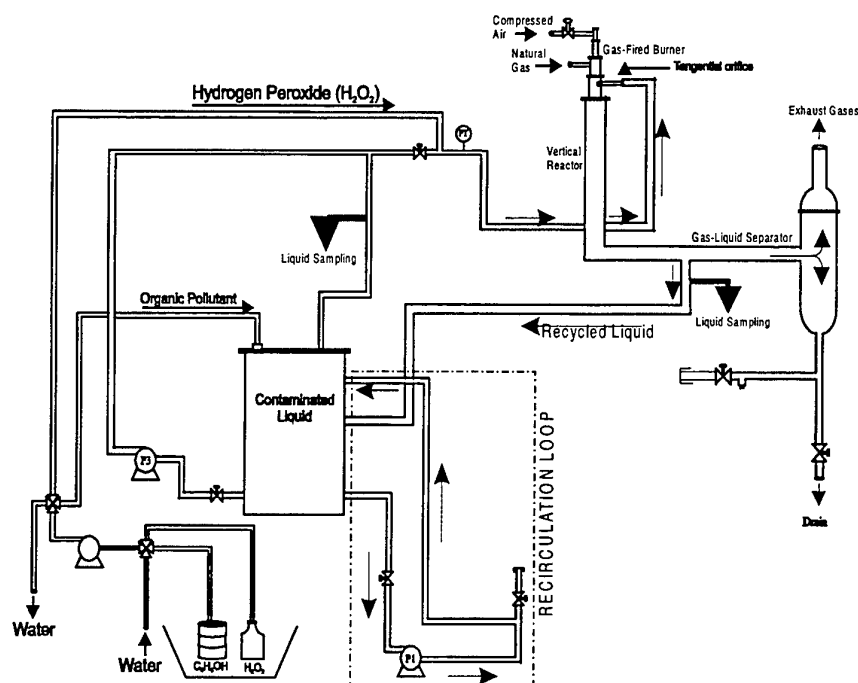


Fig. 2. Flow diagram of 50 kW-DiCTT test-bench

LIQUID-PHASE OXIDATION OF PHENOL

It is generally believed that two steps control the complete phenol aqueous-phase oxidation process:

1. the mass transfer of oxygen and free-radicals from the gaseous phase (gas-fired flame) to the liquid phase,
2. the reaction between dissolved oxygen and the phenols.

Our experiments indicate that the aqueous phase oxidation of phenol proceeds according to a complex free-radical mechanism. Consequently, the reaction rate is initially slow over an induction period, and is followed by a fast reaction phase during which most of the phenol degradation occurs. During the induction period, initiation reactions gradually increase the concentration of free radicals until propagation becomes the dominant process. The addition of free-radical initiators reduces the length of the induction period. The length of the induction period is inversely proportional to the concentration of dissolved oxygen. At high temperatures, in the aqueous phase, the form in which oxygen participates in chemical reactions is complex. O^* radicals are formed and can react with water and oxygen, giving peroxide (H_2O_2) and ozone (O_3). These four species, O^* , O_2 , O_3 and H_2O_2 , are capable of oxidizing phenols and so reducing the induction period. At high temperatures and in the presence of water, oxygen is capable of three different oxidation reactions. It may substitute an oxygen atom into an aromatic ring to form a dihydric phenol or quinone. It is also capable of attacking carbon-to-carbon double bonds to form carbonyl compounds. Finally, it may oxidize alcohols and carbonyl groups to form carboxylic acids. It has been shown that the oxidation of phenol by hydrogen peroxide implies the intermediate formation of catechol and hydroquinone in the presence of ferrous salts. These products are in turn oxidized to produce quinone, and then carboxylic acid and, finally, carbon dioxide [4].

During the combustion of natural gas free radicals are formed in the reaction zone of the flame and may be used to initiate phenol degradation reactions. Thus the fuel is subject to a series of simple reactions during which hydrogen is

removed from the hydrocarbon molecules, mainly thanks to the OH^* radicals [5]. Phenol is more reactive in an oxidizing system where attack by hydroxyl radicals (OH^*) predominates, rather than in pyrolysis situations, where attack by hydrogen atoms is dominant.

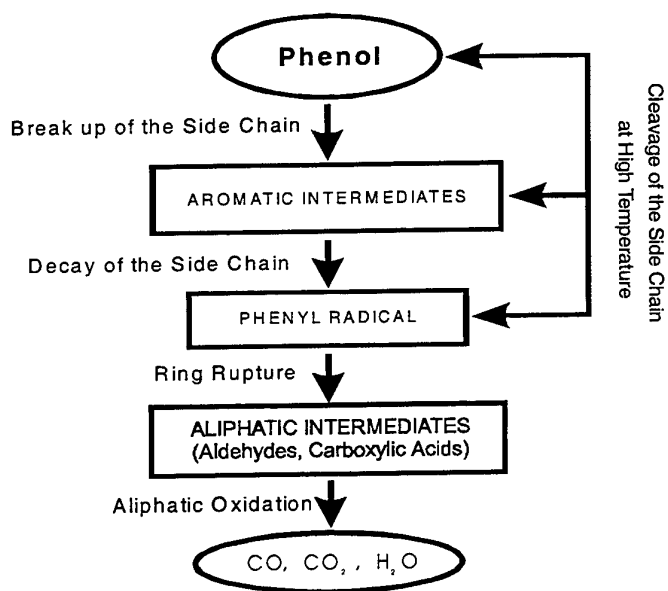


Fig.3. Mechanism ruling the free-radical oxidation of phenol

Fig. 3 shows the main steps involved in the mechanism ruling the oxidation of phenol. At high temperature, the side chain of phenol is decayed; this decay is characterized by the rupture of the bond O-H, and leads to the formation of a phenyl radical in passing by a sequence of formation of unstable aromatic intermediates. The oxidation reaction propagates and leads to the rupture of the ring. Accordingly, as phenol disappears, carbon monoxide is produced. Carbon dioxide is formed after a substantial increase of the concentration of carbon monoxide accompanied by a rapid increase of temperature. The formation of these carbon oxides is preceded, in particular, by the formation of aliphatic intermediates including aldehydes and carboxylic acids, mainly oxalic acid.

EXPERIMENTAL RESULTS

Table 3 summarizes the major results obtained on the 50kW-DiCTT-test bench. In the mentioned experiments, the incoming liquid waste stream is preheated up to 70-75°C before oxidation occurs in the reactor. Table 3 demonstrates clearly the effect of the hydrogen peroxide (H_2O_2), used as an auxiliary oxidizing agent, in increasing the destruction efficiency of the refractory pollutants: H_2O_2 concentration was varied from 10 to 80% of stoichiometric oxidation reaction and 50% was the optimum value, and the average residence time varied between 20 and 90 minutes, depending on the operating conditions. Test 5 is based on an industrial effluent, provided by a photochemical company, which is contaminated with acetone, acetic and oxalic acids, and phenolic compounds.

For all tests, the maximum evaporation rate was about 5% and the outlet gas stream is composed mainly of CO , NO_x , CO_2 : NO_x concentration varied from 5 to 40 ppm while CO emissions varied from 15 to 250 ppm.

Table 3. Experimental Results

Test No.	Burner Power (kW on HHV basis)*	Excess Air (%)	Inlet Liquid Flowrate (L/h)	Type of Organic Pollutant/Concentration	Hydrogen Peroxide Concentration (% of Stoichiometric)	Pollutant Destruction Efficiency (%)
1	42	30	235	Phenol/500 ppm	50	90.0
2	41	37	245	Phenol/500 ppm	50	95.0
3	40	36	243	Phenol/500 ppm	50	98.0
4	42	36	235	Phenol/3,900 ppm	50	97.0
5	40	33	254	Acetone/82,000 ppm + phenol/250 ppm	50	Acet. = 92.0 Phe. > 99.9
6	42	30	245	Phenol/500 ppm	50	92.0
7	40	30	250	Toluene/220 ppm	0	98.0
8	42	30	240	Phenol/600 ppm	0	75.0
9	42	30	250	Xylenes/180 ppm	0	95.0
10	43	30	245	Phenol/11,500 ppm	50	99.0

* HHV means Higher Heating Value.

COST ESTIMATION OF THE DiCTT TECHNOLOGY

In Canada, three industrial sectors represent about 80% of the whole market of the hazardous aqueous wastes: treatment/disposal processes for industrial wastewater and liquid wastes, oil refineries and petrochemical plants, and pulp and paper mills. Cost estimation of the DiCTT technology includes operating and capital costs. The capital cost shown in Table 4 represents the fixed-capital investment necessary for the installed DiCTT equipment with all auxiliaries that are needed for complete DiCTT operation.

The operating labour cost may vary due to the company labour policy, the multiplicity of units, and the amount of instrumentation and control for the process.

Annual costs for equipment maintenance and repairs may range from as low as 2% of the capital cost if operating conditions are light to 20% for cases in which there are severe operating conditions. For example, for the complicated processes with severe corrosive conditions or extensive instrumentation, maintenance and repair costs may be as high as 7 to 11% [5]. For the purposes of the DiCTT technology, the average maintenance and repair cost will be taken as 15% of the overall capital cost. The major assumptions used in Table 4 are as follows:

1. The incoming liquid waste stream is contaminated by phenol.
2. The flowrate of liquid effluent to be treated is 2000 litres/h with 4 hours/day, 5 days/week and 48 weeks/year.
3. The initial concentration of phenol is 500 ppm.
4. Higher heating value of natural gas is 38.6 MJ/m³ and its cost is 0.1 \$/m³ (std).
5. The cost of hydrogen peroxide is 1000 US\$/ton (metric).
6. The electricity cost is 0.04 \$/kWh.

Table 4. Operating and Capital Costs of DiCTT Technology (all costs are in Canadian dollars)

Type of Costs	Consumption	Costs
Operating Costs:		
• Natural Gas	89,534 m ³ /year	8,953\$/year
• Hydrogen Peroxide	76 kg/year	76 \$/year
• Electricity	53,750 kWh/year	2,153\$/year
• Preheating of liquid/Natural Gas	14,554 m ³ /year	1,455\$/year
• Other costs due new technology instabilities	20% of overall energy consumption	2,512\$/year
• Operating labour	1 worker/unit/shift	24,000\$/year
• Maintenance and Repairs	15% of fixed-capital costs	20,700\$/year
	-----	59,849 \$/year (≈60,000\$/year)
OVERALL OPERATING COSTS		
Capital Costs:		
• Materials/Equipments	-----	15,000\$
• Burner+Gas Train	-----	25,000\$
• Reactor	-----	8,000\$
• Gas-Liquid Separator	-----	5,000\$
• Feeding Pump	-----	8,500\$
• Recirculation Pump	-----	1,500\$
• Controllers	-----	10,000\$
• Buffer Reservoir	-----	10,000\$
• Tubular Heat Exchanger	-----	15,000\$
• Installation	-----	40,000\$
	-----	138,000\$
OVERALL CAPITAL COSTS		
	-----	198,000\$
TOTAL COSTS		

COST COMPARISON WITH WAO AND EPO TECHNOLOGIES

The capital costs for Wet Air Oxidation (WAO) units depend primarily on the flow and oxygen demand of the waste, the severity of the oxidation conditions, and the materials of construction. The operating costs are almost entirely for the power to compress air to the required high pressure.

Table 5 presents a cost comparison of the WAO and DiCTT technologies for the same contaminated waste water flowrate. This cost comparison is based on a WAO operating pressure of 2 to 3 MPa.

Electro-Plasma Oxidation (EPO), used for many years in the metal industry, is starting to be used in a new application, for the treatment of contaminated effluents. A plasma is a partially ionized gas, electrically neutral overall, containing molecules, atoms, ions, electrons and free radicals in movement [6]. Plasmas are generated by electrical discharge in a gas, either between high-voltage electrodes, or induced by microwave or radio radiation. The pressure of the gas

involved determines the temperature and transport properties of each plasma. With temperatures of up to 10,000°C, plasmas break down toxic compounds in a few milliseconds, avoiding the formation of secondary combustion products. These processes are very expensive, since the equipment must withstand very high temperatures, the electrical energy demand is enormous, and the scale-up is complicated. This process would be used to handle complex waste problems. Moreover, the capacity of facilities for plasma treatment of liquid organic materials is limited to 800 Litres/hour. Data in Table 5 show that operating and capital costs of DiCTT technology are significantly lower.

Table 5. Cost Comparison Between DiCTT, WAO and EPO Technologies (all costs are in Canadian dollars)

<i>Technology</i>	<i>Operating Costs (\$/year)</i>	<i>Capital Costs (\$/year)</i>
DiCTT	60,000	138,000
WAO	136,000	390,000
EPO	250,000	550,000
WAO/DiCTT (%)	2.3	2.8
EPO/DiCTT (%)	4.2	4.0

CONCLUSION

The novel liquid wastewater treatment presented in this paper, as a new processing technology for aqueous hazardous waste streams, was designed, fabricated and tested for high concentrations of organic contaminants. It is shown that its efficiency is high for destruction of phenol and other organic contaminants. Moreover, a cost estimation demonstrates that our technology is more cost effective than wet air oxidation technology and other chemical oxidation processes.

ACKNOWLEDGMENTS

The authors would like to thank *Gas Technology Canada* for their financial support.

REFERENCES

1. T. L. Randall and P. V. Knoll, "Detoxification of Specific Organic Substances by Wet Oxidation", *Jour. Water Poll. Control Fed.*, V.52 (8), pp. 2117-2130 (1990).
2. C. Guy, M. Benali and E. Ostiguy, "Free Radical Oxidation Process and Installation for treating Liquid Effluents Contaminated by Organic Substances", *US Patent, 5,641,412* (1997).
3. E. Ostiguy, C. Guy and M. Benali, "Direct Contact Thermal Treatment of Contaminated Waste-Waters", 1995, *Proceedings of the 1995 International Gas Research Conference*, Cannes, France, 567-573.
4. R.S. Willms, D.D. Reible, D.M. Wetzel and D.P. Harrison, "Aqueous-Phase Oxidation: Rate Enhancement Studies", *Ind. Eng. Chem. Res.*, v.26, pp. 606-612 (1987).
5. M.S. Peters and K. D. Timmerhaus, "Cost Estimation", Chapter 5, in *Plant Design and Economic for Chemical Engineers* 3th ed., McGraw-Hill, New York (1980).
6. M. Thorpe, "Plasma Energy: The Ultimate in Heat Transfer", *Chem. Eng. Prog.*, pp. 43-53 (1990).

COMPACTING MUNICIPAL SOLID WASTE INTO "LOGS" FOR COMBUSTION AT COAL-FIRED POWER PLANTS

Henry Liu and Yadong Li

Capsule Pipeline Research Center

College of Engineering

University of Missouri-Columbia

Email: liuh@missouri.edu; Fax: (573) 884-4888

Keywords: compaction; fuel; logs; high-pressure; solid waste

ABSTRACT. This paper is based on the findings of a research project entitled "Compacting Biomass and Municipal Solid Wastes to Form an Upgraded Fuel," sponsored by the Federal Energy Technology Center (FETC), U.S. Department of Energy. High-pressure compaction of various types of waste paper and plastics found in municipal solid waste were studied. A piston-and-mold (punch-and-die) process was used and compaction was performed without binder under room temperature and at pressures ranging from 69 to 138 MPa. The waste materials were compacted into 49-mm-diameter logs both separately and in mixtures. The effects of compaction pressure, moisture content and composition of the feedstock on the product – logs were studied. The density, abrasion resistance, impact resistance, and combustion characteristics of the logs made were tested. It was found that all the papers can be compacted into good logs under pressure of 100 MPa. Paper mixture with moisture content ranging from 5% to 20% can be easily compacted into logs of good quality under pressures above 70 MPa. When the pressure is above 100 MPa and the moisture content of the waste paper is lower than 10%, logs with dry densities greater than 1 g/cm³ can be produced. The optimum moisture content for making abrasion-resistant and impact-resistant logs is in the neighborhood of 15%. Although plastics are difficult to compact into good logs, by mixing plastics with waste paper, good logs can be made. It was found that a mixture of paper and plastic film containing up to 15% LDPE or HDPE film can be compacted into good logs with dry densities above 0.8g/cm³ and high abrasion and impact resistance.

1. INTRODUCTION

Paper, yard waste, and plastics are the three components of municipal solid waste (MSW) generated in the United States. Although the recovery rate of paper products is the highest (41%) compared to all other materials in MSW [1], the discarded waste paper still constitutes the largest component in the waste stream. The recovery rate for plastics is only 5.3%. Most of the states have banned yard waste from landfilling and are promoting yard waste composting program. Therefore, paper and plastic products are the largest components entering landfills. On the other hand, paper and plastics have very high heating values and can be use as alternate fuel if properly processed. The utilization of waste paper and plastics as fuel can effectively lower emissions of CO₂, SO₂, NO_x, and metals compared to the use of coal. Refuse-derived fuel (RDF) is a well-known alternative fuel produced from the combustibles in MSW which are composed of waste paper and many other materials such as plastics, textiles, wood, etc. Co-firing RDF with coal in existing boilers is a common practice. The boilers with traveling grate commonly used in a spreader stoker appears to be most suitable for burning RDF [2]. The dissimilarity between RDF and coal in both physical and combustion characteristics may cause problems in co-firing. The difference in density is often a problem, which makes the energy density of the two fuels different, and causes difficulties in feeding the fuel into the boiler. Ordinary densified refused-derived fuel (d-RDF) in the form of pellets has a relative high density ranging from 0.4 to 0.7 g/cm³ [3], but it is much lower than that of coal. High density also makes it more economical to transport, store, and handle the fuel. The most common densification process to manufacture d-RDF is pelletizing using rotary die pelletizers [4]. Since the pressure is developed in a similar manner as the extrusion process, high pressure is difficult to achieve [5]. Therefore, the density of the product is limited to about 0.7 g/cm³. Another type of densification equipment is baler, which is used to produce dense bales of recovered materials from MSW. The typical pressure of balers is from 0.7 MPa to 1.4 MPa. In early 1970s, a study of high-pressure compaction and baling of MSW was conducted using a three-stroke press [6]. The highest pressure used was 24 MPa.

This study was aimed at optimizing the process for producing high-density binderless fuel from waste paper and plastics using high-pressure piston-and-mold (punch-and-die) press. The physical properties, abrasion resistance,

impact resistance, and combustion properties of the fuel in the form of log were tested to assess the process and the products.

2. MATERIALS AND METHODS

The types of paper products studied include corrugated board, newsprint, office paper, commercial printing (magazine, brochure, and advertisement), and non-corrugated box board, which make up over 70% of all the paper products in ordinary MSW [1]. The initial moisture contents of the papers were measured to be 5.3%, 7.5%, 4.7%, 3.7%, and 5.9%, respectively for the five types mentioned above. Plastic products made of five types of plastic resins that make up 78% of the total plastics found in MSW were tested. These products include low density polyethylene (LDPE) film, high density polyethylene (HDPE) – both film and hard products (milk jars, detergent bottles, etc.), polypropylene (PP) hard products (mainly containers), polystyrene (PS) – both foamed and hard products, and polyethylene terephthalate (PET) bottles. The papers were shredded into pieces (flakes) of 6 mm by 25 mm using a heavy-duty office paper shredder. The plastics were shredded into pieces with maximum size of ½ inch by scissors. The feedstock with desired moisture content was achieved by adding calculated amount of water into the shredded material in an air-tight bag, storing for at least three days with periodically turning of the bag to insure a uniform distribution of the moisture.

A 48.5-mm-diameter cylindrical mold (die) with length of 300 mm was used to make logs from the waste papers. The upper and lower pistons (punches) are both movable relative to the mold. A hydraulic press (Baldwin Locomotive Works, Inc.) with maximum load of 267 kN was used for the compaction. The maximum pressure that the machine could achieve for this mold was 145 MPa.

Since the compaction ratios of the materials were as high as 8 to 10 for the feedstock set in a container freely, to make logs with sufficient length, the material had to be pushed into the mold manually by a plunger. After the pistons and mold were well aligned, pressure was applied uniformly at a rate of approximately 1.7 ± 0.2 MPa per second. When the pressure reached the desired value, it was either held for a certain time (holding time) or released immediately depending on whether or not the holding pressure was needed. All the tests were conducted under room temperature.

The abrasion resistance and impact resistance of the logs made were tested by adapting the ASTM standard methods of tumbler test D 441-86 [7] and drop shatter test D440-86 [8] for coal. For the tumbler test, three logs with diameter and length of about 49 mm and 50 mm respectively were placed in a porcelain jar in each test. The jar was rotated at 60 rpm for 40 minutes. The total number of revolutions during a test is approximately 2400. For drop test, the logs were dropped twice from 6 feet (1.83 m) onto a concrete floor instead of a steel plate as recommended by the ASTM standard. The weights of the logs before and after the tumbler test or drop test were measured and the percent weight loss were calculated as an indicator of the friability of the logs. All the property tests were conducted 24 hours after the logs were made and stored in air-tight bags. Higher heating values of the paper materials used in this study were tested using an Automatic Calorimeter (Model AC-300 by LECO Corporation), and proximate analysis was conducted using a Proximate Analyzer (Model MAC-400 by LECO Corporation).

3. RESULTS AND DISCUSSION

Compaction of Waste Paper

Individual types of papers. The effect of pressure on the integrity and density of the logs made from individual types of papers was tested. The moisture contents of the papers were as-received as given in Section 2 above. The pressure was applied without any holding time. It was found that corrugated board and office paper are relatively easy to be compacted into good logs. A compaction pressure of 70 MPa can make good logs. When the pressure was raised to 100 MPa, all the papers can be compacted into good logs with density close to or higher than 1 g/cm^3 .

Effect of pressure holding time. A mixture of the five types of papers containing equal weight for each was used to examine the effect of pressure holding time under various pressures. Three moisture contents, 5.4% (as-received), 17%, and 24% were used. Under the same pressure, the material was compacted both without and

with 10-second pressure holding time. The dry densities measured 2 minutes after the ejection of the logs were used to verify the differences since the most rapid expansion occurred within the first 2 minutes. The results as shown in Fig. 1 indicate that a 10-second holding time increases the density of the logs made under the same pressure. The lower the pressure, the more significant the effect of the holding time is. At the highest pressure used in this study (138 MPa), holding time no longer has any noticeable influence on log density. The effect of holding time was also related to the moisture content; it has less effect on the material with lower moisture content than those with high moisture contents such as 24% or higher.

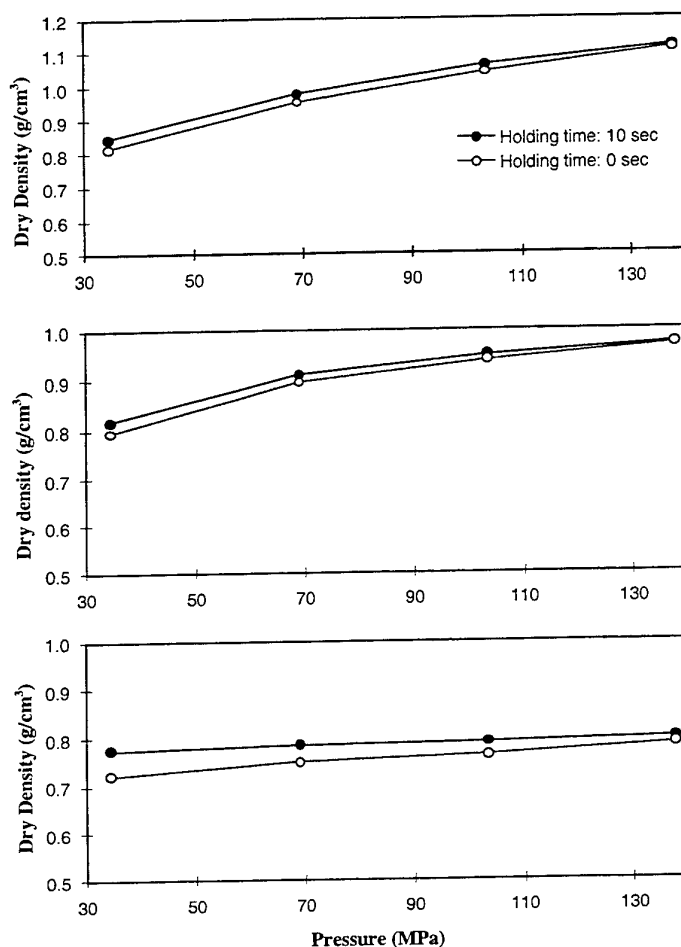


Fig. 1. Effects of compaction pressure and holding time on the dry densities (measured 2 minutes after ejection) of logs made of paper mixture.

Effect of moisture content and pressure on log properties. The density, abrasion resistance, and impact resistance of the logs made of paper mixture compacted at various pressures and moisture contents are shown in Fig. 2. The logs expanded rapidly within the first 2 minutes. The expansion reached a peak at about 24 hours, then the logs started shrinking due to the evaporation of moisture in the logs. A steady state was reached after 7 days and densities at the steady state were close to the densities at 2 minutes after the ejection of the logs were used to indicate the physical property of the logs. The tumbler and drop tests were conducted 24 hours after the logs were made. It can be seen from Fig. 2(a) that the higher the pressure, the higher the density of the logs produced. Pressure has more effect on the density of the logs when the mixture moisture is low. When the moisture was higher than 17%, it became difficult to make the density of the logs near 1 g/cm³ even when 138 MPa pressure was employed. Considering the results from the tumbler tests and the drop tests, it can be concluded that the optimum moisture content for compaction is in the neighborhood of 15%. High quality logs with high density (near 1

g/cm^3), and good abrasion and impact resistance properties can be produced when the moisture is in the range between 10% and 17% and when compaction pressure is above 69 MPa. Photos of logs made of paper mixture at 138 MPa with various moisture contents are shown in Fig. 3.

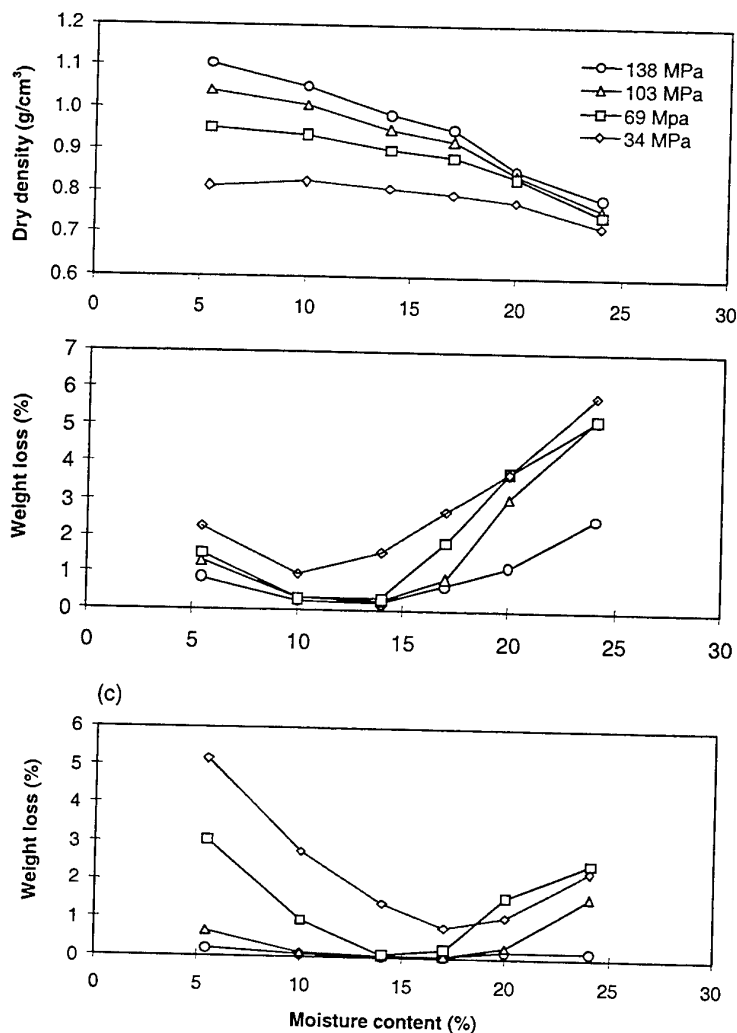


Fig. 2. Effects of moisture content and compaction pressure on properties of logs made of mixed paper. (a) Dry density; (b) tumbler test results; (c) drop test results.

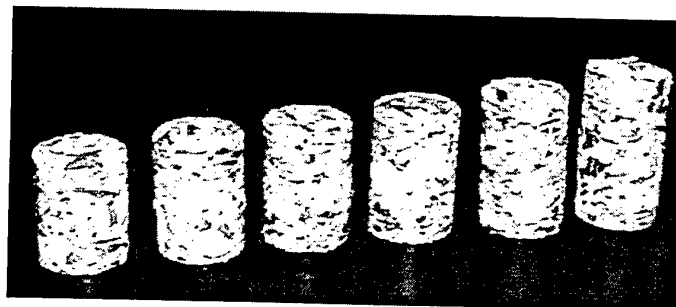


Fig. 3. Logs of mixed paper compacted at 138 MPa pressure with moisture contents of 5.4% (leftmost), 10%, 14%, 17%, 21%, and 24% (rightmost).

Compaction of Plastics

All the plastic products mentioned in Section 2 were compacted separately. Except for foamed PS which could be compacted to form good logs under pressure greater than 70 MPa, all the other plastics could not be compacted into good logs even at 138 MPa. LDPE film is the most difficult one to form logs. It expanded rapidly as in the case of a squeezed sponge upon rejection from the mold. The logs made from others plastics could stand for a short period of time, but disintegrated when subject to a small handling force.

Compaction of Mixture of Paper and Plastics

LDPE film or HDPE film was mixed with paper mixture containing equal amount of the five types of papers mentioned in Section 2. LDPE film makes up 71% of the total plastic film products in MSW [9]. Mixtures of the mixed paper and LDPE film containing 5%, 10%, 15%, and 20% of LDPE film by dry weight were compacted under pressure of 138 MPa and moisture content of 15%. By the same token, mixtures of mixed paper and HDPE film were compacted. The logs expanded upon ejection from the mold. The higher the film content, the more expansion the logs underwent. After 7 days, a steady state was reached. The dried densities of the logs at the steady state were measured and the results are listed in Table 1. Also listed in Table 1 are the results of the tumbler and the drop tests of the logs. It can be seen that the higher the film content, the lower the quality of the logs was.

Table 1. Tested Properties of the Logs Made of Mixed Paper and LDPE or HDPE Film with Different Contents Under 138 MPa and 15% Moisture Content.

Film type	Film content (%)	Dry density (g/cm ³)	Weight loss after tumbler test (%)	Weight loss after drop test (%)
LDPE	5	0.92	0.1	0.1
	10	0.85	1.1	0.1
	15	0.79	1.6	0.4
	20	0.71	3.8	Broke into 2 pieces
HDPE	5	0.94	0.2	0.1
	10	0.89	1.2	0.1
	15	0.81	1.4	0.15
	20	0.77	1.7	Broke into 2 pieces

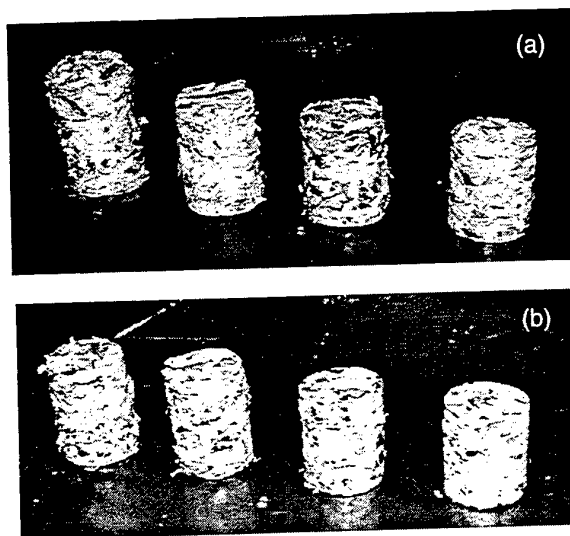


Fig. 4. Logs made of mixed paper and film under 138 MPa and 15% moisture content. The film contents were 5% (rightmost), 10%, 15%, and 20% (leftmost). (a) Mixed paper and LDPE film; (b) mixed paper with HDPE film.

For the same film content, logs with HDPE film had higher densities than those with LDPE film. Overall, good quality logs could be made as long as the LDPE or HDPE film content was less than 15%. Weight losses of the logs after the tumbler tests were all less than 2%, and less than 0.4% after the drop tests. Photos of the logs made of mixed paper and LDPE film and mixed paper with HDPE film with various film contents are shown in Fig. 4.

Combustion Characteristics of the Logs

The higher heating values (HHV) and proximate analysis results for each type of the papers and plastics were determined and listed in Table 2.

Table 2. Combustion Characteristics of the Tested Waste Papers (Dry Basis)

Material	HHV (kJ/kg)	Volatile matter (%)	Fixed carbon (%)	Ash content (%)
Office paper	151,00	79.9	11.3	8.8
Newsprint	18,900	80.4	14.2	5.4
Corrugated board	17,300	79.8	15.4	4.8
Commercial printing	12,300	70.2	7.0	22.8
Box board	17,700	79.0	14.7	6.3
Polyethylene film	19,730	98.5	0.1	1.2
Logs of mixed paper	16,300	77.9	12.5	9.6
Logs of paper and 5% LDPE/HDPE film	17,800	78.9	11.9	9.2
Logs of paper and 10% LDPE/HDPE film	19,200	79.9	11.3	8.8
Logs of paper and 15% LDPE/HDPE film	20,700	81.0	10.7	8.4
Logs of paper and 20% LDPE/HDPE film	22,200	82.0	10.0	7.9

For the logs made of paper mixture, the HHV was calculated to be 15,400 kJ/kg based on the tested results for each type of the papers. The volatile matter, fixed carbon, and ash contents of the paper mix were also calculated to be 77.9%, 12.5%, and 9.6%, respectively, based on the proximate analysis results of each paper. The heating value of the paper mixture is equivalent to that of the lignite fuels and the ash content is equivalent to that of most of the bituminous and subbituminous coal [10]. For the logs with 20% LDPE/HDPE film, the HHV is near that of subbituminous coals. Although it has a very high heating value, plastic film is not an ideal fuel because it has a very low combustion efficiency. The low efficiency is due to the difficulty of obtaining adequate oxygen mixing with the combustible gases given off by plastic film that is highly volatile. Using a mixture of paper and plastic film as fuel can overcome the problem of low combustion efficiency of the plastic and make use of its high heating value. Therefore, the logs made of mixed paper and LDPE/HDPE film make an acceptable fuel.

4. CONCLUSIONS

High-quality waste paper logs with high density, high abrasion, and impact resistance have been produced by the piston-and-mold process at room temperature without having to use any binder. It was found that the waste paper with moisture content ranging from 5% to 20% can be easily compacted into logs of good quality under pressures above 70 MPa. When the pressure is higher than 100 MPa and the moisture content of the waste paper is lower than 10%, logs with dry densities greater than 1 g/cm³ can be produced. As far as the mechanical properties of the logs are concerned, the optimum is achieved when the mixture moisture is in the neighborhood of 15%.

Although plastic films can not be compacted to form good logs even by using 138 MPa pressure, mixtures of paper and LDPE or HDPE films containing up to 15% of the films can be compacted into good logs with dry densities above 0.8g/cm³ and high abrasion and impact resistance. Plastic film and paper are relatively easy to separate from MSW because they are both lightweight fractions. Air classification can be readily used to accomplish this task. This makes the findings in this study practical in commercial applications.

5. FUTURE WORK

Compaction of mixtures containing more combustible components in MSW including hard plastics, textiles, wood, etc. will be conducted in the near future.

ACKNOWLEDGEMENTS

This study is a part of the research project entitled "Compacting Biomass and Municipal Solid Wastes to Form an Upgraded Fuel," sponsored by the Federal Energy Technology Center (FETC), U.S. Department of Energy.

REFERENCES

1. U.S. EPA, Characterization of Municipal Solid Waste in the United States: 1997 Update, EPA 530-R-98-007 (1998).
2. S. F. Castle, *Energy Progress*, v.7, pp.115-118 (1987).
3. O.O. Ohlsson, D.K. Walters, and B.J. Goodman, "An overview of RDF processing systems: current status, design features, and future trends", *Refuse-Derived Fuel (RDF) - Quality, Standards, and Processing, FACT-Vol. 13*, pp.1-8, edited by C. Saltiel, American Society of Mechanical Engineers (1991).
4. A.G.R. Manser and A.A. Keeling, *Practical Handbook of Processing and Recycling Municipal Waste*, CRC Press (1996)
5. Q.W. Deng and H. Liu, *Powder Technology*, v.91, pp.31-41 (1997).
6. K.W. Wolf and C.H. Sosnovsky, "High-pressure compaction and baling of solid waste", *Handbook of Solid Waste Management*, pp.136-149, edited by D. G. Wilson, Wan Nostrand Reinhold Company (1977).
7. ASTM D 441-86, "Standard test method of tumbler test for coal", *Annual book of ASTM Standards*, v.05.05, pp.192-194 (1998).
8. ASTM D 441-86, "Standard test method of drop shatter test for coal", *Annual book of ASTM Standards*, v.05.05, pp.188-191 (1998).
9. American Plastics Council, *Understanding Plastic Film: Its Uses, Benefits and Waste Management Options, Technical Report* (1996).
10. J.G. Speight, *The Chemistry and Technology of Coal*, 2nd Ed, Marcel Dekker, Inc. (1994).

EXPERIMENTAL STUDY FOR GASIFICATION OF SCRAP TIRES

Xiu-Li Yin, Zeng-Li Zhao, Bing-Yan Xu, Chuang-Zhi Wu, Yong Chen

Division of Clean Fuel, Guangzhou Institute of Energy Conversion

Chinese Academy of Sciences

Email: yinxl@ms.giec.ac.cn; Fax: (86)-20-87608586

D.Y.C. Leung

Department of Mechanical Engineering

University of Hong Kong

E-mail: ycleung@hkucc.hku.hk; Fax: (852)2858 5415

Keywords: pyrolysis, gasification, scrap tires, biomass

ABSTRACT. A set of laboratory apparatus with feature of fast pyrolysis and capability of continuously measuring and recording of parameters was designed and constructed. Powder of ground automotive tire was pyrolysed with the apparatus in a N_2 atmosphere. The composition and properties of derived gases were determined in relation to pyrolysis temperature from 500-1000°C and different gas phase residence time. As pyrolysis temperature and gas phase residence time was increased, the mass percentage of solid char decreased, while gas productivity increased. The tires produced 41% oil, 24% gas and 35 % char approximately and calorific value of the gases was about 36000kJ/Nm³ at 800°C. The gases were identified as H_2 , CO, CO_2 , CH_4 , C_2H_4 , C_2H_6 and C_3H_6 in addition to lower concentrations of H_2S and other hydrocarbon gases. Test results of tire pyrolysis are compared with data obtained by biomass gasification.

1. INTRODUCTION

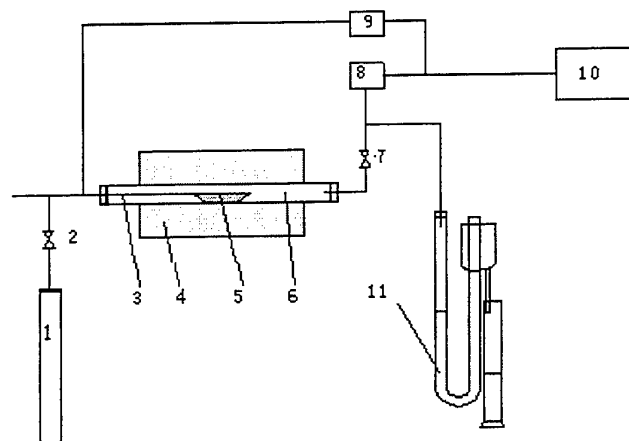
It has been estimated that about 250 million used automotive tires are discarded annually in the United States[1] and 100 million in China. Also, 15 million tons per year in European Union, 2.5 in North America and 2.4 in UK.[2]. Disposal of the used tires has caused many environmental and economic problems, and a great deal of research on recovering energy from scrap tires has been performed [3,4]. It is well-known that scrap tires possess high volatile and low ash contents with heating value reaching 38MJ/kg, which is greater than that of coal and biomass. This makes it an ideal material for pyrolysis, combustion and gasification. Among many methods of recovering energy, scrap tire gasification is the only one that has not been applied successfully. The gaseous fuel produced by gasification can be stored, transported and easily fueled for existing boilers and various combustors with little modification. It has been proved a beneficial way in recovering energy from biomass gasification[5]. Main objectives of present work are to examine feasibility of producing gas from scrap tires by fast pyrolysis, and to examine effect of reactor temperature and gas phase residence time on deriving gas composition and yield. Test results of tire pyrolysis are compared with data obtained from biomass pyrolysis at the same condition.

2. EXPERIMENTAL

2.1 Facilities

Experimental apparatus is shown schematically in Fig.1. A tubular reactor was installed inside a furnace. Tire samples were pushed into hot zone from cold terminal of the reactor once temperature of hot zone reached the expected value, therefore heating rate was much higher than typical Thermogravimetry (TG); Different residence time of gas phase could be obtained when length of hot zone changed.

The derived gases were sampled through a gas syringe and off-line analyzed by Gas Chromatography (GC). The gases were identified as H_2 , CO, CO_2 , N_2 and O_2 using a molecular sieve SA60-80 column with argon as carrier gas and a Thermal Conductivity Detector (TCD). Gaseous hydrocarbon CH_4 , C_2H_4 , C_2H_6 up to C_6 were determined on Al_2O_3 capillary column with nitrogen as carrier gas using a Flame Ionization Detector (FID). After pyrolysis the solid char was removed and weighed. The quantity of total evolved liquids was obtained by minus method.



1. N₂ supply 2,7. valve 3. thermocouple 4. furnace 5. sample boat 6. reactor
8. pressure transmitter 9. temperature transmitter 10. computer 11. gas collecting system

Fig.1 Schematic illustration of experimental apparatus

2.2 Feedstock Characteristics

Tires contain vulcanized rubber in addition to rubberized fabric with reinforcing textile cords, steel or fabric belts and steel-wire reinforcing bead. A typical composition of tire rubber is shown in Table 1.

Table 1. Tires Compounding Composition

Composition	Rubber	Carbon black	Extender oil	Zinc oxide	Stearic acid	Sulpher	Accelerator
Wt%	62.1	31	1.9	1.9	1.2	1.1	0.7

The elemental composition, proximate analysis and calorific value of the scrap tires on a metal core freebasis are shown in Table 2. Comparison with a typical biomass, namely wood, shows lower volatile and moisture content, higher calorific value and ash content.

Table 2. Composition of Feedstock.

	Elemental composition (%)					Proximate analysis(%)				Q _{b,ad}
	C _{ad}	H _{ad}	O _{ad}	N _{ad}	S _{ad}	V _{ad}	FC _{ad}	M _{ad}	A _{ad}	kJ/kg
Tire	76.89	7.08	4.79	0.34	1.67	67.5	25.2	2	5.3	37328.4
Wood	42.92	5.76	40.24	1.14	0.91	73.7	17.3	8.2	0.8	17390.9

3. RESULTS AND DISCUSSION

3.1 Temperature Effect on Pyrolysis Rate

Tire pyrolysis curves at 700°C and 900°C are shown in Fig.2 and Fig.3. Pyrolysis spending time from the beginning of gas appearing to end was counted. It was found that heating rate was much higher and time needed to complete pyrolysis was much shorter than that of TG. Fig.4 shows that the time decreases while temperature increases linearly. At 500°C, it took 54s, but at 1000°C, only 8s to complete the reaction. For the purpose of comparison, the data of biomass pyrolysis are figured out hereafter with broken lines. Fig.4 also indicates the changing trends of wood and tire are similar, but the pyrolysis rate of wood is faster than that of tires.

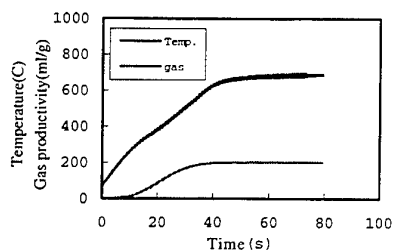


Fig.2 Tire pyrolysis curve at 700°C

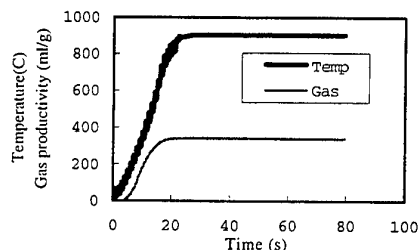


Fig.3 Tire pyrolysis curve at 900°C

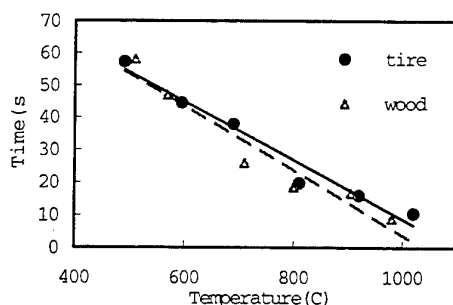


Fig. 4 Time of completing pyrolysis vs. temperature

3.2 Temperature Effect on Gas and Char Productivity

Yield of char decreases slowly and yield of gas increases quickly as temperature is increased. As shown in Fig.5 and Fig.6, gas productivity is 358ml/g at 1000°C, 95ml/g at 500°C, almost 3.8 times difference, the char productivity has no obvious loss with increasing temperature. It indicates that reaction at higher temperature breaks down the higher molecular mass species of pyrolysis, viz. tar into gaseous products. The trends of wood pyrolysis are similar, but the gas productivity is 1.8 times of that of tire.

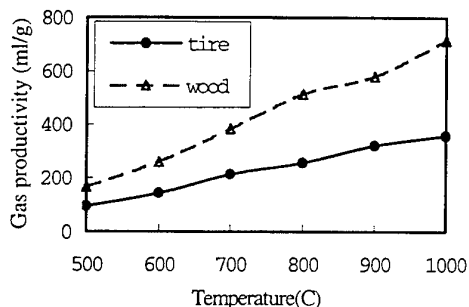


Fig.5 Gas productivity vs. temperature

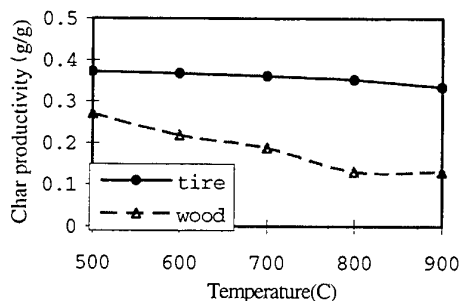


Fig.6 Char productivity vs. temperature

3.3 Temperature Influence on Gas Composition

Detailed analysis of gas composition from pyrolysis of tire revealed main gases were hydrogen, carbon dioxide, carbon monoxide, methane, ethane, ethylene, propylene, in addition to a few other hydrocarbon gases etc, which were composed of high molecular hydrocarbon gas and H_2S . A little of these gases failed to be detected or identified due to limits of GC. C1-C6 hydrocarbon gases at 800°C and 1000°C are shown in Fig.7 and Fig.8.

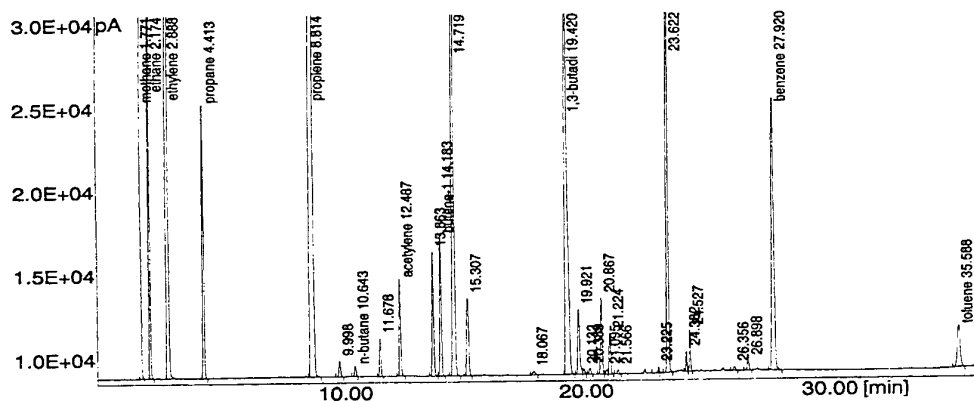


Fig. 7 Gas chromatogram of C1-C6 hydrocarbon gases at 800°C

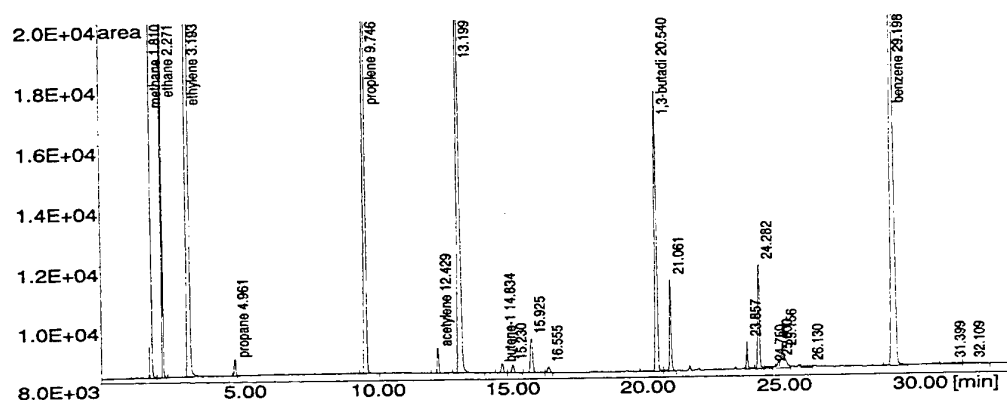


Fig.8 Gas chromatogram of C1-C6 hydrocarbon gases at 1000°C

It is obvious that kinds of high molecular hydrogen gases at 800°C are more than that of 1000°C. Fig.9 shows the relationship between main gas composition and temperature. Percentage of H_2 increased and percentage of

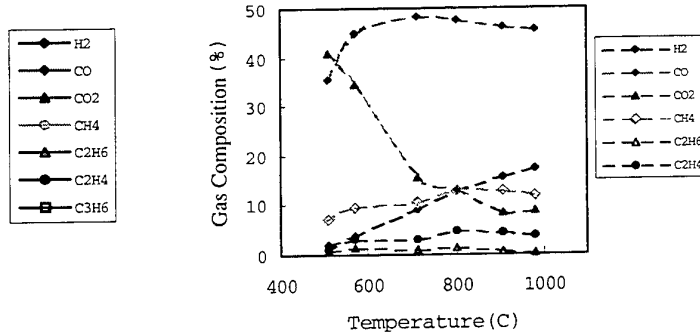
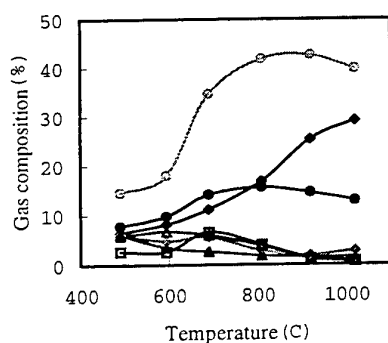


Fig.9 Main gas composition vs. temperature(tire) Fig.10 Main gas composition vs. temperature(wood)

CO , CO_2 decreased correspondingly while temperature was increased from 500 to 1000°C. The percentage of CH_4 , C_2H_4 , C_2H_6 and C_3H_6 increased while reactor temperature increasing up to their critical band of about 900°C, 800°C, 700°C and 700°C respectively, and then decreased slowly. Fig.10 shows the relationship between main gas composition and temperature of wood pyrolysis. It is found that there are similar trends in gas composition changing, but comparison with tire shows higher CO , CO_2 and lower H_2 and some hydrocarbon

gases.

3.4 Pyrolysis Product Profile

Table 3 shows the pyrolysis products profile at 800°C. Compared with wood, the generated gases from tire pyrolysis have a higher calorific value, higher productivity of char and tar, and lower gas productivity. The calorific value of gases is dependent on gas composition. Too high temperature may induce decreasing of the calorific value because of higher molecule hydrocarbon gases being cracked. From present work, we find the critical band of calorific value is between 700 to 800°C.

Table 3 Yield of Pyrolysis Product (800°C)

	Tires	Wood
Gas productivity ml/g	262	513
Gas productivity g/g	0.24	0.54
Gas heating value kJ/Nm ³	36000	17123
Char productivity g/g	0.35	0.13
Liquid productivity g/g	0.41	0.32

3.5 Effect of Residence Time of Gas Phase on Secondary Reaction

Residence time of gas phase at higher temperature strongly influences products profile. Longer residence time causes more tar to crack and more permanent gas to be produced. Thus, the influence of residence time on secondary reaction can be expressed by the increment of gas productivity. Primary vapours are first produced in pyrolysis process, the characteristics of which are mostly influenced by temperature and heating rate. These primary vapours then degrade secondary tar and gases. The proportion and characteristics of which are a function of temperature and time. Fig.11 shows the relationship between gas productivity and temperature at different residence time. Fig.12 shows main gas composition of different residence time at 800°C. Therefore, to maximize gas yield, the primary products should be remained in hot zone to continue secondary reactions. However, too much residence time also causes gas calorific value to decrease.

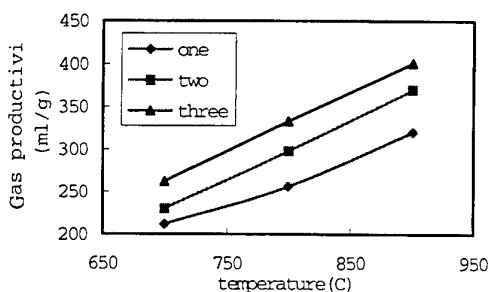


Fig.11 Gas productivity vs. Temperature at different residence time

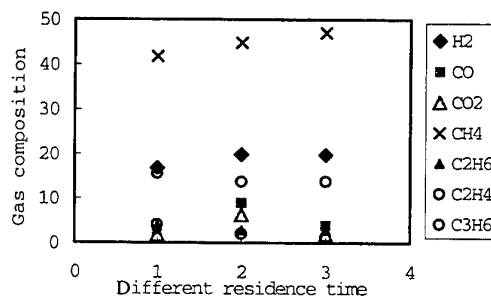


Fig.12. Gas composition vs. residence time (800°C)

4. CONCLUSION

1. The gas productivity increases if temperature is increased and/or gas phase residence time is lengthened at temperature 700-900°C. The gases have a significant calorific value, which is dependent on gas composition. Too high temperature and/or too much residence time may make it to decrease.
2. The tires can be produced 41% oil, 24% gas and 35% char approximately at 800°C. The calorific value of gases is about 36MJ/Nm³ at 800°C.
3. The gases were identified as H₂, CO, CO₂, CH₄, C₂H₄, C₂H₆ and C₃H₆, in addition to smaller concentrations of H₂S and other hydrocarbon gases.

REFERENCES

1. A. Atal and Y.A. Levendis, "Comparison of the combustion behaviour of pulverized waste tyres and coal.", *FUEL*, V.74, pp1570-1581(1995).
2. P. T. Williams, S. Besler, D. T. Taylor, "The pyrolysis of automotive tyre waste", *J. Institute Energy* 68, pp.11-21 (1995).
3. P. T. Williams, S. Besler and David T. Taylor, "The Pyrolysis of Scrap Automotive Tyres", *FUEL*, v.69, pp.1474-1482 (1990).
4. J.A. Conesa, R. Font, and A. Marcilla, "Gas from the Pyrolysis of Scrap Tires In a Fluidized Bed Reactor", *Energy & Fuels*, v.10, pp134-140 (1996).
5. B. Xu, Kinetic study on biomass gasification, *Solar Energy*, 1992, 49(3), pp99-204.

PYROLYSIS AND COMBUSTION CHARACTERISTICS OF DIFFERENT SLUDGE

Fu-Jun Tian Xiao-Fen Guo Hai-Bin Li

Yong Chen Xue-ying Xu Xue-Lian Yang

Guangzhou Institute of Energy Conversion

Chinese Academy of Sciences

Email: tianfj@ms.giec.ac.cn; Fax: (020)-8778-7136

Bao-Qing Li

Institute of Coal Chemistry

Chinese Academy of Sciences

Email: libq@ms.sxicc.ac.cn; Fax: (0351)-4048-967

Keywords: sludge, pyrolysis, combustion

ABSTRACT. There have been a great deal of interest to dispose sludge through the combustion technology. The water content of sludge has a critical effect on its combustion and it is important to study the combustion mechanism of dewatered sludge. In addition, pyrolysis is regarded as the initial step of the whole combustion of solid fuels such as coal, sludge, RDF (Refuse Derived Fuel) and et. al. So it is necessary to investigate pyrolysis behavior of sludge in order to deeply investigate its combustion behavior. This paper presents the pyrolysis and combustion behaviors of sewage sludge and paper-making sludge. Tests were carried out using WCT-2 thermal balance which can perform experiments such as TG, DTG and DTA at the same time. The primary constituents and heating value of aforementioned sludges were also analyzed. Based on the TG data of sludge, kinetics parameters of combustion of sludge were obtained. The results indicate that the different sludge has distinctive kinetic parameters.

1. INTRODUCTION

The disposal of sludge from waste water treatment continues to be a major concern because of the very large amounts generated and the associated hazard with wastes. The reduction in landfill sites and the second pollutions to soil and underground water have limited the utilization of the conventional treatment methods such as landfill, compost and dispose to the marine [1]. Studies on combustion characteristics and NO_x emission of different sludge indicate that combustion offers an environmentally attractive method to dispose lots of sludge [2, 3]. However, the high moisture of sludge not only makes its spontaneous combustion difficult but also largely increases its treatment cost. According to high heat value and moisture of sludge, Chen et. al. [4] put forward the co-briquette of coal with sludge to obtain solid fuel and dispose sludge. The advantages of this process are: 1) to use sludge as cohesive material; 2) to use the energy in sludge efficiently; 3) not to add water into feedstock during the preparation of co-briquette due to the high moisture content of sludge. In order to study the combustion characteristics of briquette, it is also important to study the combustion mechanism of dewatered sludge. In addition, pyrolysis is regarded as the initial step of the whole combustion of solid fuels such as coal, sludge, RDF (Refuse Derived Fuel) and et. al. So it is necessary to investigate pyrolysis behavior of sludge in order to deeply understand its combustion behavior.

This paper presents the pyrolysis and combustion behaviors of wastewater sludge and paper-making sludge. Tests were carried out using WCT-2 thermal balance which can perform experiments such as TG, DTG and DTA at the same time. The primary constituents and heat value of aforementioned sludges were also analyzed. Based on the TG data of sludge, kinetics parameters of combustion of sludge were obtained.

2. EXPERIMENT

2.1 Samples

Sewage sludge was collected from Da-tan-sha Sewage-treating Factory, and paper-making sludge was offered by Guangzhou Paper Co. The proximate and ultimate analysis of these sludges are summarized in Table 1. Except for their high moisture, other properties are obtained from the dry-based samples. Each sludge was separately dried and ground to a mean diameter of less than 0.125 mm for TG of pyrolysis and combustion. Since the heat values of them equal approximately to that of low rank coals, lots of sludge is regarded as the potential energy.

Table 1. Analysis of Samples

Sample	Proximate Analysis/ w%			Ultimate Analysis/ w% ar					Heat Value/ kJ/kg
	M	A _{ar}	V _{ar}	C	H	N	S	O	
Sewage Sludge	83.60	43.29	47.18	29.54	5.09	5.06	1.56	25.59	13878.9
Paper-making Sludge	77.86	23.49	56.02	32.25	4.67	0.57	0.88	31.85	13810.4

2.2 TG-DTG-DTA

The TG-DTA system (WCT-2, Beijing) was used to investigate the pyrolysis and combustion behaviors of sewage sludge and paper-making sludge. The pyrolysis and combustion were carried out under an atmosphere of nitrogen and air respectively. The gas flow rate was 30 cm³/min. The samples of about 10mg were loaded on the sample holder and were heated from room temperature to 1273.5K at the heating rate of 20K/min. Profiles of TG, DTG and DTA of each sample were recorded together.

3. RESULTS AND DISCUSSIONS

3.1 TG/DTG/DTA Results

Comparisons of the TG and DTA curves for sewage sludge and paper-making sludge are shown in Fig. 1. Combustion characteristics of the two kinds of sludge are summarized in Table 2. Comparisons DTG curves of pyrolysis and combustion for them are shown in Fig. 2. The results reveal some distinguishing characteristics of the two sludges:

- As can be seen from Fig. 1A, the TG curves of the sewage sludge contain an initial weight loss due to the moisture released up to about 500K. After that, it is found that the TG behavior of combustion is basically similar to that of pyrolysis during the second weight loss between 400 and 730K, which indicates that the second weight loss is mainly due to the devolatilization and the gas-phase combustion of volatiles. And then the last weight loss between 730 and 825K is due to the solid-phase combustion of carbon residues.
- As can be seen from Fig. 1B, the TG curves of the paper-making sludge also contain an initial weight loss due to the moisture released up to about 500K. But the combustion TG has a shift from the pyrolysis one during the second weight loss between 500 and 670K. The reason may be due to the partial solid-phase combustion besides the gas-phase combustion of volatiles. Finally the weight loss between 670 and 770K is due to the solid-phase combustion of carbon residues.

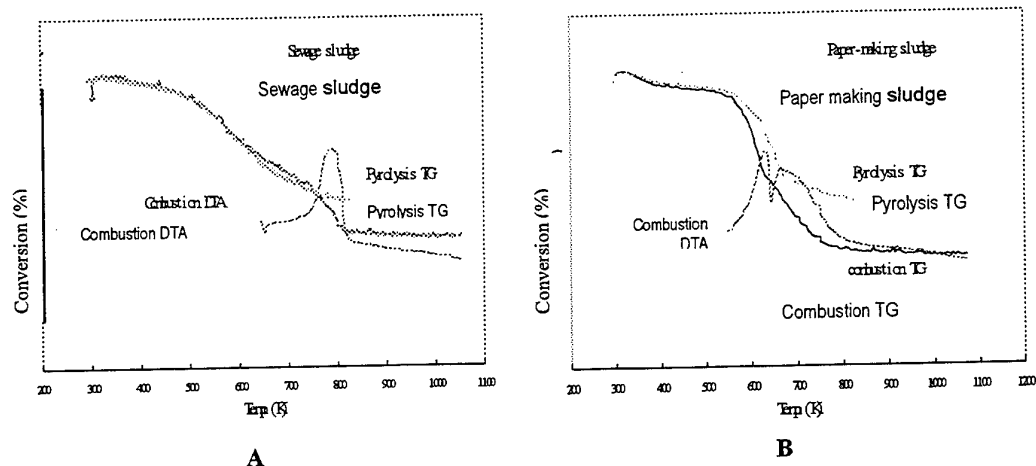


Fig. 1. TG and DTA curves of different sludges

- Comparisons of combustion parameters for the two sludges (Table 2) indicate that their combustion behaviors are different. DTG curves of their combustion (Fig. 2) also show the difference. DTG curve of paper-making sludge contains one sharp peak with a shoulder, which can be attributed to its simple components, mainly consisting of cellulose. But that of sewage sludge contains two blunt peaks, which can

be due to its complex components consisting of protein, grease, cellulose and so on.

(iv) Sewage sludge has a larger temperature range of combustion than paper-making sludge does.

Table 2. Parameters of Sludge Combustion

Sample	Ignition Temp. / K	End Temp. of ignition/ K	Process of weight loss	Temp. of DTG peak/ K	Value of DTG peak / mg/min
Sewage sludge	500.5	825.5	3	773.5	0.44
Paper-making sludge	510.5	770.5	2	603.5	1.27

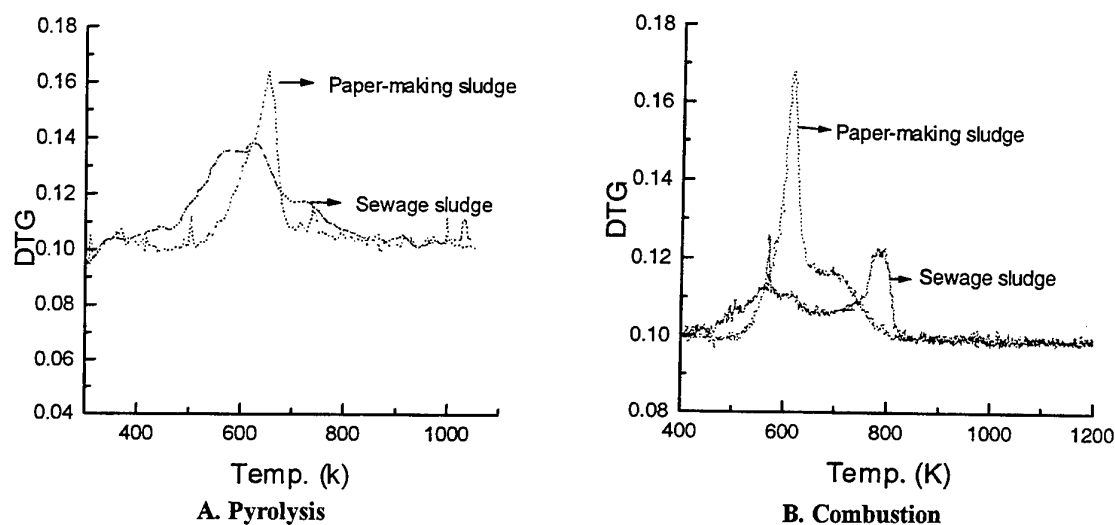


Fig. 2. DTG curves of different sludges

3.2 Determination of Kinetic Parameters

The rate expression for the solid fuel combustion is

$$\frac{d\alpha}{dt} = K(1 - \alpha)^n \quad (1)$$

where α is conversion of combustion, K is the reaction rate constant, n is the reaction order. The reaction rate constant follows the Arrhenius expression:

$$K = Ae^{-E/RT} \quad (2)$$

where E represents the apparent activation energy, and A is pre-exponential factor.

The heating rate is:

$$\Phi = \frac{dT}{dt} \quad (3)$$

Inserting the reaction rate constant (K) and the heating rate (ϕ) into Equation 1, we obtain

$$\frac{d\alpha}{dT} = \frac{A}{\phi} e^{-E/RT} (1 - \alpha)^n \quad (4)$$

In the determination of the kinetic parameters by use of the above equations, various analysis methods [5-7] have been suggested. In the present study, the non-isothermal analysis method proposed by Ito et. al. [7] was used. Taking the natural logarithm of Equation 4, we obtain

$$\ln\left(\frac{\phi \frac{d\alpha}{dT}}{(1-\alpha)^n}\right) = \ln A - \frac{E}{RT} \quad (5)$$

The values of $d\alpha/dT$ and α can be calculated from the TG curves. To determine the kinetic parameters in eq 5, the solid fuel combustion is generally analyzed as a first order reaction. Assuming n equals 1, the calculated results of the left-hand term in eq 5 are plotted against the reciprocal of corresponding temperature. It shows a straight line in $\ln((1-\alpha)^{-n}(d\alpha/dT)\phi)$ vs. $1/T$, and then the activation energy E and pre-exponential factor A are obtained from the intercept and the slope of the straight line.

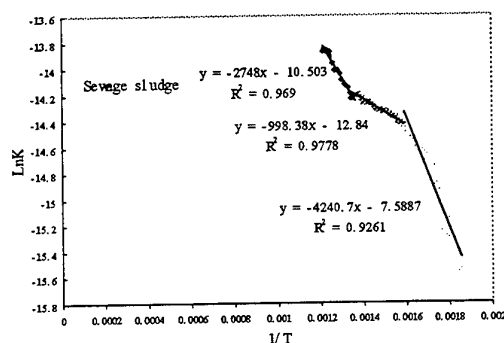
Fig 3 shows that the combustion processes of paper-making sludge and sewage sludge respectively contain two and three independent first-order reactions, whose kinetic parameters are very different (Table 3). The activation energy (E_i) of each first-order reaction mainly depends on the reaction temperature and reactants. In order to understand the contribution of E_i to the general reaction, Coming et. al. put forward the conception of average activation energy (E_m):

$$E_m = F_1 E_1 + F_2 E_2 + \dots + F_n E_n$$

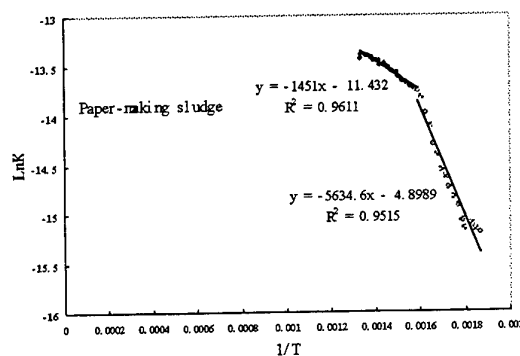
where F_1 --- F_n represents the range of conversion for every independent first-order reaction. The calculated values of E_m are also listed in Table 3.

Table 3. Kinetic Parameters of Sludge Combustion

Sample	Range of temp./ K	Activation energy/ kJ(mol) ⁻¹	Pre-exponention factor/ s ⁻¹	Correlation coefficient	Interval of conversion/ %	Range of conversion / %	Apparent activation energy/ KJ(mol) ⁻¹
Sewage	539.5-628.5	35.26	42.93	0.926	5.02-19.04	14.02	
sludge	628.5-732.5	8.3	0.05	0.978	19.04-30.41	11.37	9.79
	732.5-825.5	22.85	1.51	0.969	30.41-47.50	17.09	
Paper-making	536.5-628.5	46.85	840.09	0.951	6.96-34.30	27.37	15.43
sludge	628.5-737.5	12.06	0.32	0.961	34.30-55.91	21.61	



A



B

Fig. 3. $\ln K \sim 1/T$ spectra of sludge combustion

4. CONCLUSIONS

1. The TG behavior of combustion for sewage sludge is basically similar to that of pyrolysis during the second weight loss between 400 and 730K, which indicates that the second weight loss is mainly due to the

devolatilization and the gas-phase combustion of volatiles. But the combustion TG for paper-making sludge has a shift from the pyrolysis one during the second weight loss between 500 and 670K. The reason may be due to the partial solid-phase combustion besides the gas-phase combustion of volatiles.

2. Sewage sludge has a larger temperature range of combustion than paper-making sludge does.
3. The combustion processes of paper-making sludge and sewage sludge respectively contain two and three independent first-order reactions, whose kinetic parameters are very different.

REFERENCES

1. W. Towers, and P. Horne, *Water Environ. Management*, v. 11, pp. 126 (1997).
2. J. Werther, "Sewage Sludge Combustion in the FB Comparison of Stationary and CFB Techniques", *Proceedings of the 13th International Conference on FBC*, pp. 951, edited by K.J. Heinschel, N.Y. USA (1995).
3. Z. N. Yu and T.H. Zeng, *Enviro. Protection (Chinese)*, No. 2, pp. 36 (1998).
4. Y. Chen, F.J. Tian, H.B. Li and C.Z. Wu, *Patent (China)*, No. 99 1 17010.5, "Preparation of sludge briquette".
5. A. W. Coat, J. P. Redfern, *Nature*, v. 201, pp. 68 (1964).
6. C.D. Doyle, *J. Appl. Polymer Sci.*, v. 5, pp. 285 (1961).
7. N. Ito, K. Obata, T. Hakuta, Yoshitome, H. Kagaku Jikogaku Ronbunshu, v. 9, pp. 434 (1983).
8. J. W. Coming, *Fuel*, v. 63, pp. 1436 (1984).

PERFORMANCE EVALUATION OF THE TWO-FLUID CYCLE IN MUNICIPAL SOLID WASTE-BURNT POWER GENERATION

Terushige Fujii, Katsumi Sugimoto, Tomoya Yamashita, Hitoshi Asano

Faculty of Engineering, Kobe University
1-1, Rokkodai-cho, Nada-ku, Kobe 657-8501, Japan.
E-mail: fujii@mech.kobe-u.ac.jp ; Fax.078-803-6122,

Nobutaka Tsuchimoto

Takuma Co., Ltd.
2-33, Kinrakuji-cho 2-chome, Amagasaki, Hyogo 660-0806, Japan.
E-mail: tutimoto@takuma.co.jp ; Fax.06-6483-2763

Keywords: municipal solid waste, two-fluid cycle, MSW-burnt power generation,
working fluids, performance characteristics

ABSTRACT. An improvement of energy conversion efficiency is important for energy saving and for solving the global environmental problems. The two-fluid cycle is dealt with for municipal solid waste(MSW)-burnt electric power generation, using 6 kinds of fluid such as NH_3 , C_5H_{12} , C_6H_6 , and H_2O as the working fluid at the bottoming cycle against water on the topping cycle. The performance characteristics of the two-fluid cycle are calculated and the optimum cycle conditions, which maximize the plant's thermal efficiency, are determined for the respective working fluid. As a result, it is shown that the plant's thermal efficiency was increased from 17.6 % to 21.3 % for the single Rankine cycle by the adoption of the two-fluid cycle, using C_6H_6 as the working fluid under a constant condition of the topping steam temperature of 295°C.

NOMENCLATURE

L : power [kW]
m : mass flowrate [kg/s]
P : pressure [MPa]
 ΔT : terminal temperature difference of heat exchanger [°C]
Q : heat quantity [kW]
q : heat drop(=Q/m) [kJ/kg]
T : temperature [°C]
x : quality [-]
 η : efficiency [%]

Subscripts

0 : conventional , 1, top : topping
2, bot : bottoming , B : boiler
E : exhaust or heat exchanger ,
G : generator , M : mechanical
n : net , p : plant or pump
s : saturated , super : superheated
T : turbine

1. INTRODUCTION

In Japan, more than 90 % of the primary energy resources are imported, and more than 60 % of the energy converted is not utilized and abandoned into the atmosphere and the sea. Further improvement of energy conversion performance and useful utilization of the energy which has been abandoned unused so far are not only a matter of economy of the primary energy resources but also are of great help for the solution of the global environmental problems. In this paper, the performance characteristics of the municipal solid waste(MSW)-burnt power generation plant are investigated to further increase its thermal efficiency for adoption of the two-fluid cycle. In Japan, 50 million tons per year (137 thousand tons per day) of municipal solid wastes is discarded and more than 70 % of them is burnt. There are about 160 MSW-burnt power generation plants in Japan, where about 70,000 tons of municipal solid wastes is burnt, generating a total electric power of 560,000 kW as at the end of 1995. In the year 2010, the number of its facilities will be increased to about 400 and the total electrical power generated is expected to attain 4 million kW. However, the thermal efficiency of the MSW-burnt power plants was 5 to 15 %. For this reason, the system called "the super rubbish-burnt power generation system", which is combined with the gas turbine and/or further burns ordinary fuel after the MSW-burnt boiler, has been proposed so far and has already been realized in part. Here, an improvement of the thermal efficiency is made by using the two-fluid cycle for the MSW-burnt power generation plant, which the bottoming cycle is added to the

conventional cycle. Various working fluids such as NH_3 , C_5H_{12} , and C_6H_6 are selected as those of the bottoming cycle, while the topping cycle uses water as the working fluid. The two-fluid cycle has been studied up to date [1]-[4] for i) large-capacity thermal power generation plants using organic fluids as the working fluids of the bottoming cycle in order to make the lower-pressure stage of the turbine compact, and/or ii) mercury or potassium-water two-fluid cycle. Also, for an effective utilization of geothermal heat and the heat exhausted from factories and so on at the middle-and low-temperature level, a number of investigations have been made for the binary cycle using a low-boiling medium as the working fluid. However, its performance characteristics are different from those of the two-fluid cycle consisting of both the topping and the bottoming cycle. There are few reports on the investigation of the two-fluid cycle consisting of two Rankine cycles as the objective of the MSW-burnt power generation plant. In this paper, under a constant condition of the maximum steam temperature of 295°C , which is the same as that of the conventional MSW-burnt plant in Japan, the performance characteristics of the two-fluid cycle are investigated using 6 kinds of fluids such as NH_3 , C_5H_{12} , C_6H_6 , and H_2O on the bottoming cycle. Lastly, an optimum heat balance for the maximum steam temperature of $T_1=395^\circ\text{C}$ will be. The case of using the mixture medium such as water- NH_3 as the working fluid of the bottoming cycle will be presented in another paper.

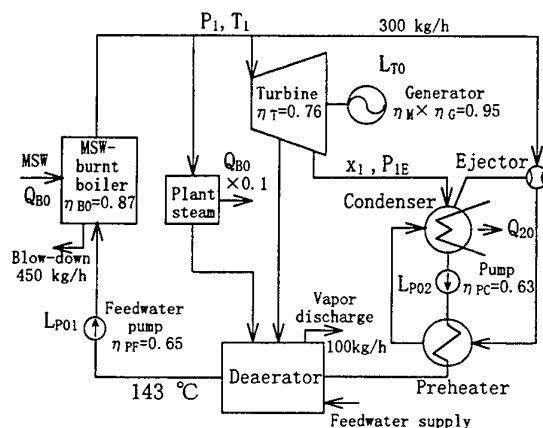


Fig.1 Flowsheet of conventional MSW-burnt Power plant

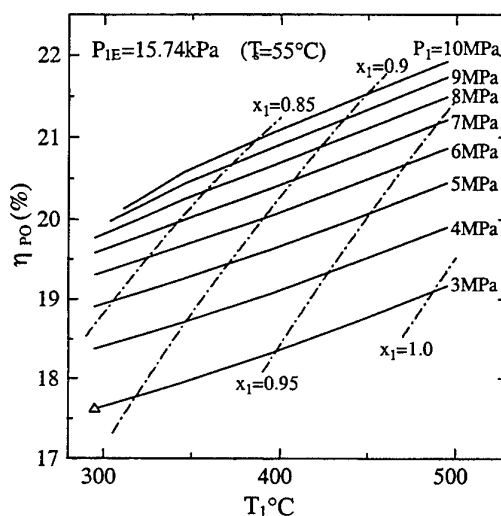


Fig.2. Thermal efficiency of conventional MSW-burnt plant

2. CYCLE CONFIGURATION

2.1 Conventional Cycle

A general flowsheet of the conventional MSW-burnt power generation plant is shown in Fig. 1. The input quantity of the MSW of 300 t/day, whose total heat quantity Q_{BO} is 34,896 kW by assuming the lower calorific value to be 10,050 kJ/kg, is selected as the object of the calculation. The respective efficiencies of the components such as the MSW-burnt boiler and the turbines are constant, for example $\eta_{BO}=0.87$, $\eta_T=0.76$, being independent of the plant condition, as shown in the figure. In this system, 10 % of the total heat quantity Q_{BO} is used for domestic steam such as for the prevention of the white smoke exhausted from the chimney and the steam for the air-preheater from the main steam line. The 450 kg/h hot water of the blow-down and the 100 kg/h steam are both abandoned unused respectively from the MSW-burnt boiler and the deaerator. Furthermore, the 300 kg/h ejector steam is used for gas removal in the condenser. The pressure loss and the heat loss are considered to be constant at 100 kPa and 5°C only for the main steam line from the boiler exit to the turbine inlet. All the pump work is calculated as 1.15 times the rated pressure at the exit of the pump. The plant's thermal efficiency η_{PO} is shown against the main steam temperature T_1 in Fig. 2 as a parameter of the main steam pressure P_1 under constant conditions of a condensation temperature of 55°C and a boiler feedwater temperature of 143°C . The dot-dash-line in the figure denotes the constant steam quality x_1 at the exit of the

turbine. The steam condition of the conventional MSW-burnt power generation plant in Japan is generally a main steam temperature T_1 of 295 °C and a boiler inlet feedwater temperature of 143 °C, considering the higher- and lower-temperature corrosion due to the chloride in the flue gas. Assuming that the main steam pressure is 3 MPa owing to the limit of the steam quality of $x_1 = 0.88$ at the turbine exit and that the turbine back-pressure of P_{1E} is 15.74 kPa corresponding to the saturation pressure of 55 °C in the air-cooled type condenser, the plant's thermal efficiency η_{p0} is 17.6 % as shown by the symbol Δ in Fig. 2. The specific power output of the turbine is 571.6 kW·s /kg, and the power output is 6,220 kW for the MSW of 300 t/day. Here, the main steam pressure may be increased, leading to an improvement of the plant's thermal efficiency, by applying the two-fluid cycle instead of the single-fluid Rankine cycle.

2.2 Two-Fluid Cycle

The flowsheet of the two-fluid cycle is shown in Fig. 3, which adds a Rankine cycle using a different fluid as the working fluid at the bottoming side of the conventional Rankine cycle (Fig. 1) using water as the working fluid. Here, the main steam temperature T_1 and the dryness quality x_1 at the turbine exit are constant at 295 °C and 0.88, respectively, for the topping side. In the heat exchanger between the topping and the bottoming cycle, the fluid exhausted from the heat exchanger at the topping side is assumed to be saturated vapor of $x=1$. Its temperature T_2 is determined by fixing the temperature difference ΔT_1 (between 10 and 40 °C) from the exhausted temperature T_{1E} of the topping turbine. Accordingly, its pressure P_2 denotes saturation related to T_2 . The condensation temperature at the bottoming side is assumed to be 55 °C owing to the adoption of the air-cooled type condenser. The respective component efficiencies are the same as the case of Fig.1 as shown in Fig. 3. Further, the domestic steam and the discarded steam from the boiler and the deaerator are considered in a way similar to the conventional cycle of Fig. 1.

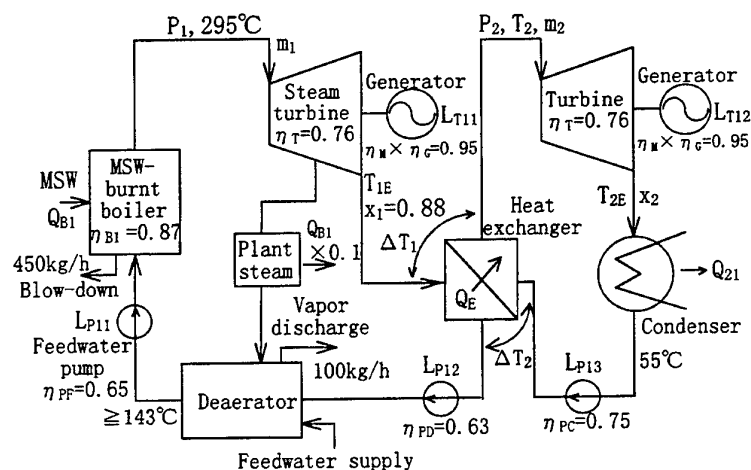


Fig.3 Flowsheet of two-fluid cycle power plant

3. WORKING FLUID

Water is used as the topping working fluid. On the other hand, six kinds of fluid, [ammonia (NH_3), propylene (C_3H_6), isobutane (C_4H_{10}), pentane (C_5H_{12}), benzene (C_6H_6), and water (H_2O)] were selected as the bottoming working fluid. The T - s diagram of the respective working fluids and the P - T curves are shown in Figs. 4 (a) and (b), respectively. Here, the T - s diagram of the respective fluids is shown by normalizing as $s=0$ for $T=0$. The saturation pressure related to the same temperature is greater for NH_3 and C_3H_6 , and lower for C_6H_6 and H_2O .

4. CALCULATION RESULTS

The calculation of the performance characteristics of the two-fluid cycle is made based on the analysis of Section 3. The calculation results are shown below. The thermophysical properties of the working fluids are those given in the ASME table for water and are based on Peng Robinson [7] for the other fluids.

4.1 Topping and Bottoming Main Pressures P_1 and P_2

The steam temperature exhausted from the topping turbine T_{1E} and the main vapor pressure at the bottoming side P_2 are shown against the topping steam pressure P_1 in Fig. 5 for a topping steam temperature T_1 of 295 °C (the saturation pressure $P_s = 8.0$ MPa). The pressure P_2 denotes the saturation pressure corresponding to the temperature ($T_{1E} - \Delta T_1$). In the figure, respective symbols denote the calculation results. The empty symbols are for $\Delta T_1 = 10$ °C and the full symbols are for $\Delta T_1 = 40$ °C for five kinds of the working fluid excluding water and the symbol \times indicates the critical point. With an increase of P_1 , the temperature at the topping turbine exit T_{1E} increases, leading to an increase of T_2 , whose saturation pressure P_2 also increases. The bottoming pressure P_2 for NH_3 is the greatest (3 to 11 MPa) of all the working fluids selected, compared with the pressure below 1.7 MPa for C_6H_6 in the range of $P_1 = 4$ to 8 MPa.

4.2 Plant's Thermal Efficiency η_{P1}

The plant's thermal efficiency η_{P1} is shown against the topping steam pressure P_1 in Fig. 6 for the respective working fluids under a constant condition of $\Delta T_1 = 10$ °C. Here, the bottoming vapor pressure P_2 is obtained from the preceding figure (Fig. 5). The numerical values in the figure denote the exit temperature T_{2E} of the bottoming turbine or the dryness quality x_2 , depending on whether the exit vapor of the bottoming turbine is in the region of superheat or wetness. The full symbols (∇, \diamond) in the figure correspond to the case where the feed-liquid at the bottoming side is preheated by the superheated vapor which is exhausted from the bottoming turbine and is cooled to 60 °C. Also, the symbol \odot denotes the value ($\eta_{P0} = 17.6$ %) of the conventional plant's thermal efficiency shown in the preceding section 2.1. It is clarified that the curves have concave shapes and that the optimum pressure P_1 , which maximizes the plant's thermal efficiency η_{P1} , exists, except for H_2O and the preheating of C_6H_6 . For H_2O and the preheating of C_6H_6 shown by the symbols $+$ and \diamond , the plant's thermal efficiency η_{P1} increases with an increase of P_1 up to the saturation pressure 8 MPa corresponding to 295 °C. It is shown from this figure that η_{P1} of H_2O is the greatest of the six working fluids selected and attains to about 20 % at $P_1 = 7\text{--}8$ MPa ($P_2 = 0.7\text{--}1.5$ MPa), while η_{P1} of C_6H_6 takes 19.7 % at $P_1 = 8$ MPa ($P_2 = 1.5$ MPa) in the case of preheating the feed-liquid at the bottoming side.

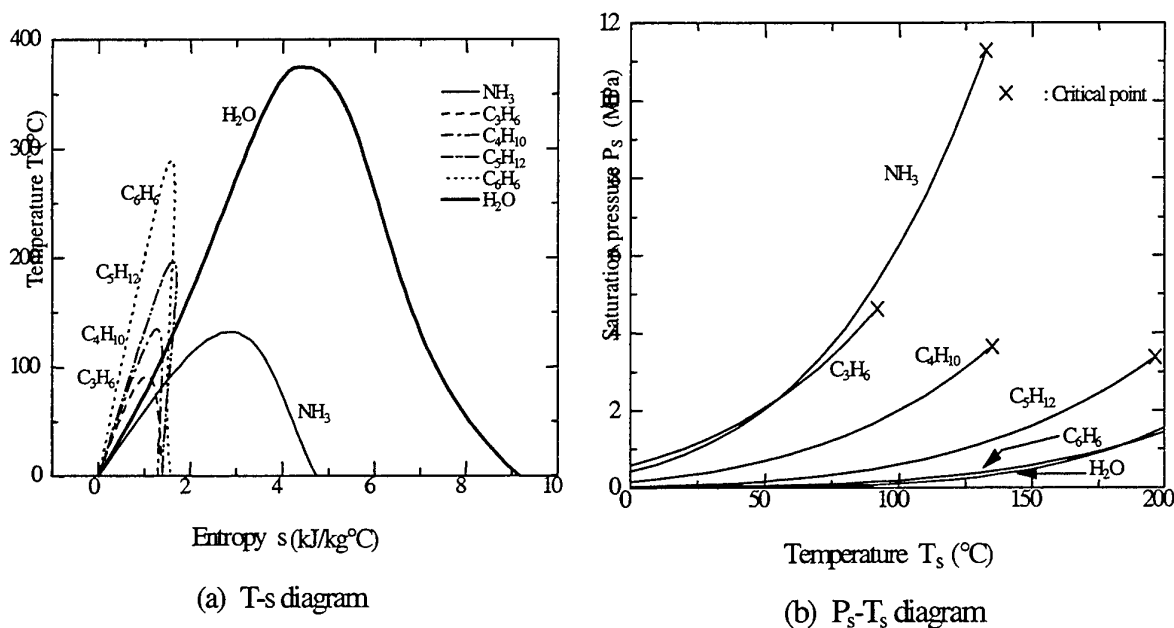


Fig.4 Working fluids

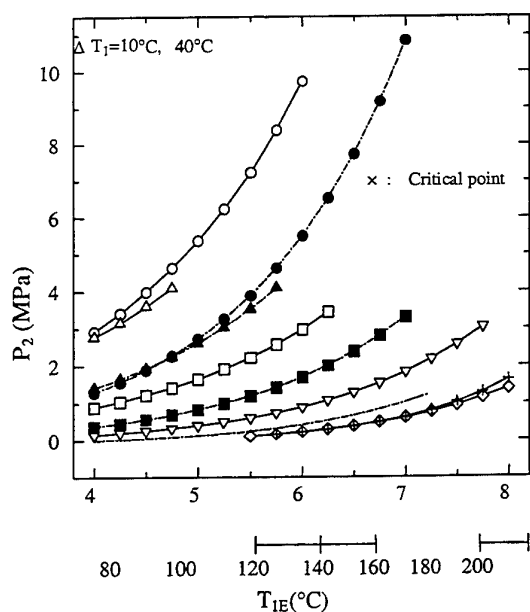


Fig.5 Bottoming turbine inlet pressure P_2

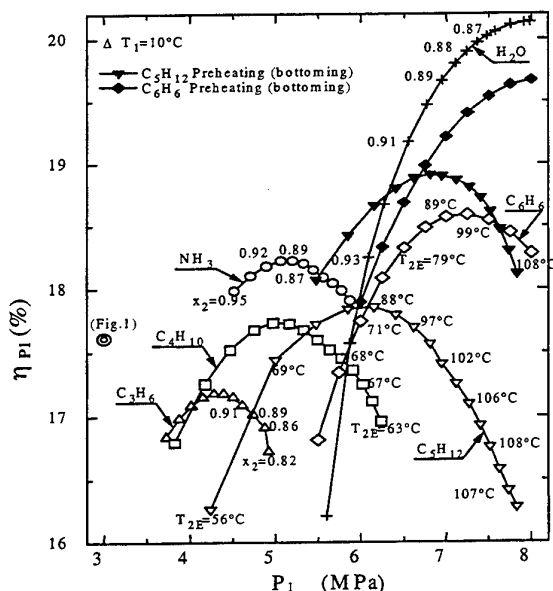


Fig.6 Plant's thermal efficiency of two-fluid cycle

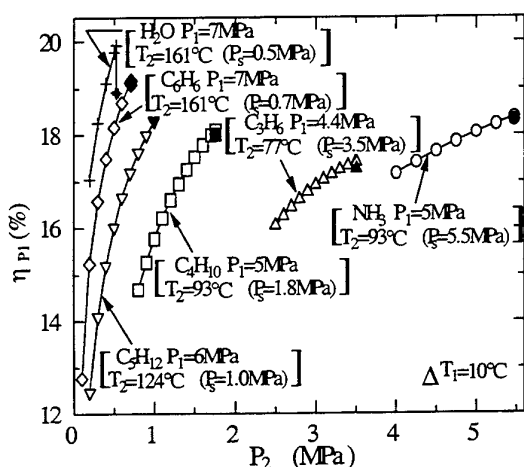


Fig.7 The effect of P_2 on η_{P1}

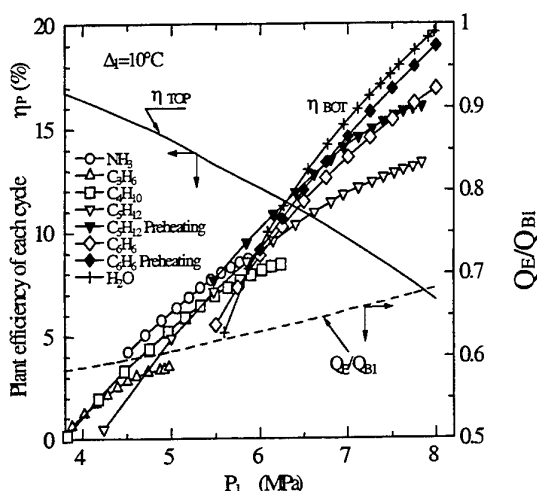


Fig.8 Plant thermal's efficiency of each cycle

Next, the effect of the bottoming vapor pressure P_2 below the saturation pressure P_S corresponding to T_2 on η_{P1} is shown in Fig. 7 for $\Delta T_1=10^\circ\text{C}$. In this case, the turbine inlet vapor is in the superheated state for the same T_2 . The full symbols in the figure denotes the case of the vapor quality $x=0.9$ at the bottoming turbine inlet for the saturation pressure P_S related to T_2 , which is shown by $(P_S=)$ in the figure. It is shown that η_{P1} decreases with P_2 and that η_{P1} in the saturation state of $x=1$ at the bottoming turbine inlet is greater than that below the saturation pressure P_S . The individual thermal efficiencies, η_{TOP} and η_{BOT} , which constitute η_{P1} , are shown in Fig. 8, where the relationship among them is expressed as $\eta_{P1} = \eta_{TOP} + \eta_{BOT} \cdot Q_E/Q_{B1}$, where Q_E is the heat quantity exchanged in the heat exchanger between the topping and bottoming sides. As P_1 increases, η_{TOP} decreases but

η_{BOT} increases. The degree of their contribution to η_{P1} depends on the heat quantity ratio Q_E/Q_{B1} , which is shown on the right vertical axis in Fig. 8. It increases with P_1 .

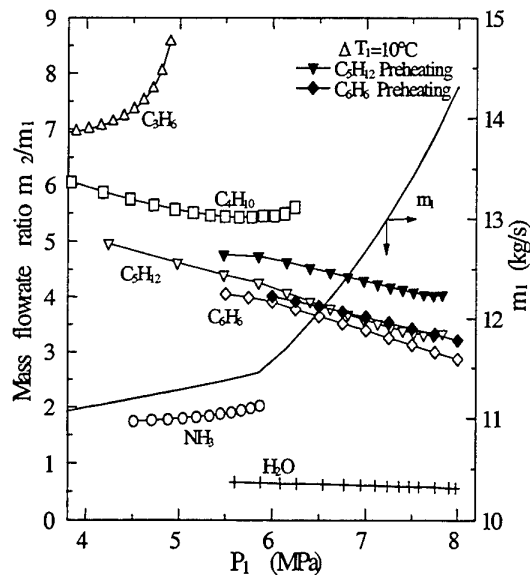


Fig.9 Mass flowrate ratio m_2/m_1

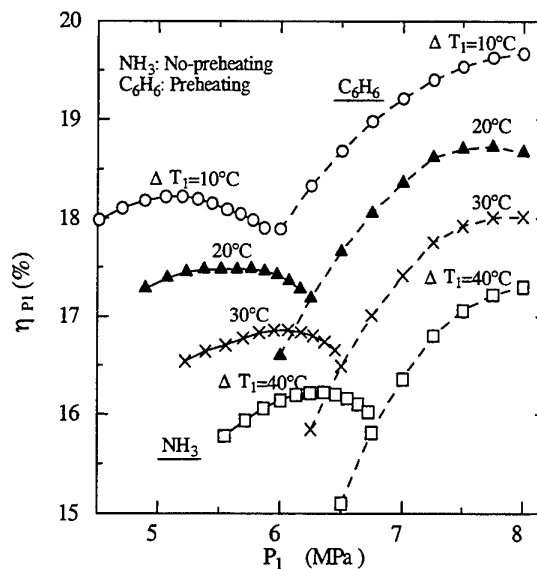


Fig.10 Effect of terminal temperature difference (ΔT_1)

4.3 Flowrate and Power Output

The flowrate at the inlet of the topping turbine (m_1) and the ratio of the bottoming flowrate m_2 to m_1 (m_2/m_1) for $\Delta T_1 = 10^\circ\text{C}$ is shown in Fig. 9. The value m_1 corresponds to the case for the input quantity of the M.S.W. of 300 t/day. The flowrate ratio m_2/m_1 is inversely proportional to the width of the saturation limit line in Fig. 4(a). It is shown that the values of m_2/m_1 are 0.5 to 0.7 for H_2O , 1.7 to 2.1 for NH_3 , 3.0 to 4.0 for C_6H_6 , 3.7 to 5.0 for C_3H_{12} , 5.5 to 6.0 for C_4H_{10} , and 7.0 to 8.5 for C_3H_6 .

4.4 The Effect of Terminal Temperature Difference ΔT_1 in Heat Exchanger

The effect of the terminal temperature difference between the two higher temperature sides ΔT_1 on η_{P1} is shown in Fig. 10 for NH_3 and C_6H_6 . For NH_3 , without the feed-liquid preheating due to the vapor exhausted from the bottoming turbine, the topping steam pressure P_1 , which maximizes η_{P1} , increases with an increase of ΔT_1 . On the other hand, for C_6H_6 , with the preheating regeneration of the feed-liquid at the bottoming side, a pressure of 8 MPa, which corresponds to a saturation temperature of 295°C , nearly shows the upper limit of η_{P1} . Next, without the preheating regeneration, the optimum value of P_1 , which maximizes η_{P1} , is shown against ΔT_1 in Fig. 11. It is shown that the optimum value of P_1 increases in proportion to an increase of ΔT_1 . It is shown that the optimum value of P_1 for C_6H_6 is almost the same as that of H_2O .

4.5 The Effect of Subcooling of Condensed Water at Topping Side

The effect of subcooling of the condensed water at the topping side in the heat exchanger on η_{P1} is shown in Fig. 12 as a parameter of ΔT_2 (10 to 40°C), which is the temperature difference between the inlet temperature of 55°C of the feed-liquid at the bottoming side and the exit temperature of the heat exchanger at the topping side as shown in the figure. The solid line connecting the symbol \bullet shows the case where the outlet temperature of the heat exchanger at the topping side is the saturation temperature of $x=0$ shown in parentheses (T_{1E}) in the figure. The four lines below the $x=0$ line correspond to the case of $\Delta T_2=10$ to 40°C . It is clarified that η_{P1} is greater with lower subcooling. Also, the symbol \odot shows the case where the feed-liquid for the bottoming cycle is preheated by using the bleeding vapor of the bottoming turbine, which is bled from a half of the turbine heat drop and a terminal high temperature difference of 10°C . It is seen that η_{P1} is improved by 0.2% .

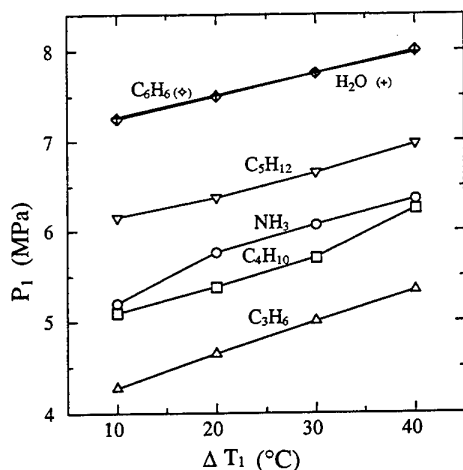


Fig.11 The optimum P_1 for ΔT_1 without preheating

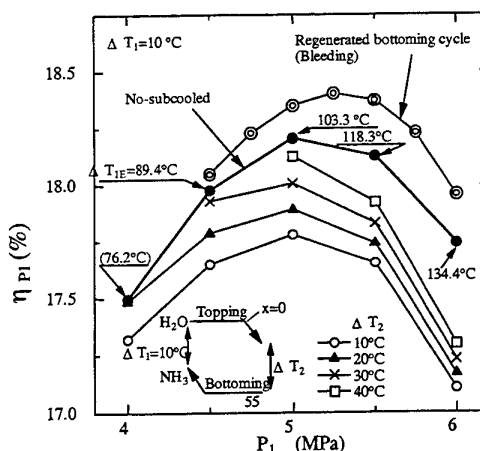


Fig.12 Plant's thermal efficiency for subcooling and bleeding regeneration (NH_3)

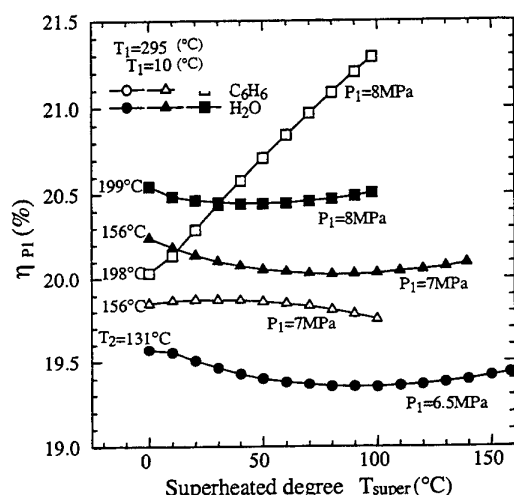


Fig.13 Plant's thermal efficiency for superheated two-fluid cycle

4.6 The Effect of Turbine Exhaust-Regeneration

The feed-liquid of 55 °C at the bottoming side is preheated by the superheated vapor exhausted from the bottoming turbine until the superheated temperature becomes 60 °C. The plant's thermal efficiency η_{P1} is improved as shown by the full symbols in Fig. 6 for C_5H_{12} and C_6H_6 because of the heat recovery of the turbine exit vapor.

4.7 The Effect of Superheating at Bottoming Side

The relationship between the superheated vapor temperature T_2 at the bottoming side and the plant's thermal efficiency η_{P2} is shown in Fig.13 for C_6H_6 and H_2O . The values of the temperature T_2 at the left side of the figure denote the main vapor temperature without superheating. Superheating is done in the MSW-burnt boiler of $\eta_B = 0.76$ at the topping side. The total heat quantity, which is the sum of the boiler heat quantity at both the topping and the bottoming side, is 34,896 kW at the rate of MSW 300 t/day. The plant's thermal efficiency η_{P2} is improved at $P_1 = 8$ MPa for C_6H_6 .

4.8 Higher Temperature of T_1 in the Future

In case the higher temperature of the maximum steam temperature T_1 is realized owing to the development of the tube material and so on to solve the high-temperature corrosion problem in the MSW-burnt boiler, the plant's

thermal efficiency must be improved further. Here, the results of the heat balance is shown in Fig. 14 under a maximum steam temperature of $T_1=395^\circ\text{C}$, using C_6H_6 as the working fluid for the MSW of 300 tons/day. The total net power output is 8,820 kW and the plant's thermal efficiency is improved greatly to 25.28 % from 19.0 % for the single Rankine cycle under conditions of $P_1=4\text{ MPa}$ and $T_1=395^\circ\text{C}$. Also, the flowrate ratio m_2/m_1 between the topping and the bottoming cycle is about 3.9.

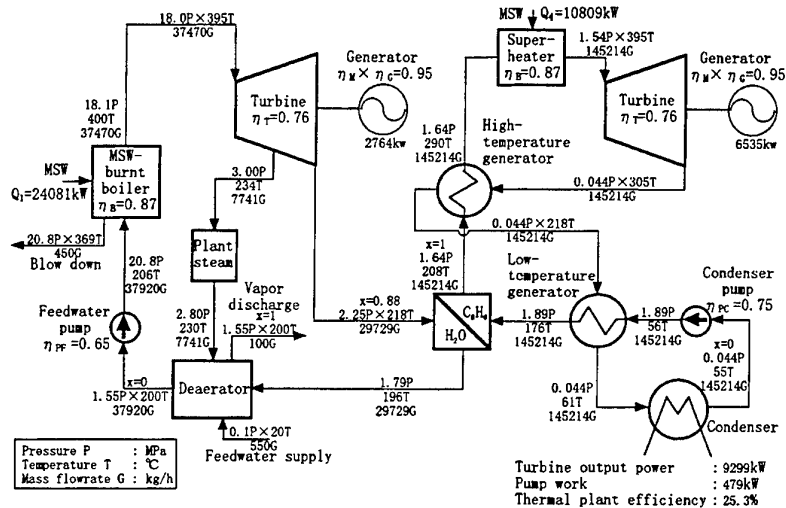


Fig. 14 Flowsheet of two-fluid cycle power plant ($\text{H}_2\text{O}-\text{C}_6\text{H}_6$, $T_1, T_2=395^\circ\text{C}$)

5. CONCLUSIONS

The performance characteristics of the two-fluid cycle due to an increase of the steam pressure were investigated, using 6 kinds of liquid as the working fluid including water, for the bottoming cycle under a constant condition of the topping steam temperature of 295°C . The conclusions are as follows.

- 1) The fluid having a good thermal efficiency is C_6H_6 and/or H_2O . The plant's thermal efficiency of C_6H_6 is 19.7 % under a topping steam pressure of 8 MPa, while the conventional thermal efficiency is 17.6 %. Further, an improvement of the thermal efficiency, 21.3 %, is anticipated by superheating the bottoming vapor for C_6H_6 .
- 2) When the bottoming working fluid is superheated, the degree of improvement of the thermal efficiency is different owing to the kind of working fluid and the plant condition. There are some cases of lower thermal efficiency.
- 3) When the topping liquid is subcooled in the heat exchanger, the thermal efficiency is higher as the subcooling of the condensed water is less. Finally, the plant's thermal efficiency is anticipated to be 25.3 % for C_6H_6 for a higher steam temperature of $T_1=395^\circ\text{C}$ in the future. However, in further studies, the economy of the above plant and the properties of the fluids such as the corrosion and the toxicity, including the other working fluids will be discussed.

REFERENCES

1. G. Horn, T.D. Norris and J.F.T. Whybrow, "Turbine Flow Problems of Binary Cycle employing High Density Fluids," Proc. Inst. Mech. Eng., 183-8, pp.165-178 (1969).
2. A.P. Fraas, "A Potassium-Steam Binary Vapor Cycle for a Molten-Salt Reactor Power Plant," Trans. ASME, J. Eng. Power, pp.355-366 (1966).
3. D.G. Shepherd, "Pick up Energy from Low Heat Sources," Hydrocarbon Processing, pp.141-149 (1977).
4. T. Terayama, H. Sekiya, et al., "Heat Recovery Power Generation and their Evaluation (in Japanese)," J. of Thermal and Nuclear Power, Vol.29, No.10, pp.63-76 (1978).
5. T. Sugiura, T. Tanaka, et al., "Experimental Study of Rankine Cycle using Ammonia Water Mixture as Working Fluid (in Japanese)," J. of Industry Machinery, pp.64-71 (1994).
6. The Institute of Applied Energy, "Municipal Solid Waste Incineration Power Generation (in Japanese)," pp.1-43 (1996).
7. Hyprotech, "Property Methods and Calculations," HYSYS Version 1.0 Reference, pp.207 (1995).

SAFE AND ECONOMICAL ON-FARM DISPOSAL OF ANIMAL WASTE

Sung C. Ling

Department of Mechanical Engineering
The Catholic University of America
Email: sling20901@aol.com; Fax: (301) 593-3026

Hsien P. Pao

Department of Civil Engineering
The Catholic university of America
Email: pao@cua.edu; Fax: (202) 319-6677

Keywords: on-farm incineration, pre-carbonization, animal wastes, public health

ABSTRACT. Present wastes from high density animal-farming have created serious environmental and public health problems. Hence there is an urgent need for the development of a safe on-farm animal-wastes incineration system. For wastes that contain high vapor-pressure hydrocarbon-components, improved incineration can be achieved through a low temperature pre-carbonization process. The resulting pre-carbonized products can be burnt in conventional ways to greatly minimize ground and air pollution problems and to improve the sanitary condition for the animal-farming operation.

1. INTRODUCTION

Large-scale and high density production of poultry and hogs on rural farms is presently an economically significant trend throughout the world. A critical environmental and health problem has resulted due to the inability of these operations to handle the massive quantities of animal wastes in an ecologically and economically sound manner. Pollution of ground and surface water due to mismanagement of animal wastes is now posing threats not only to the marine life but also to the health of people working and living along major watersheds; as evidenced by recent publicity about the outbreaks of highly toxic organisms (Barker, 1997) in rivers, estuaries, and coastal water along Mid-Atlantic seaboard of USA. Even more serious is the yearly outbreak of new strains of flu viruses in England, Spain, Japan, China, Taiwan, Malaysia, and Australia. This is also due in part to high-density animal farming that has greatly enhanced the probability for genetic mutation of viruses. It is generally believed that new strains of avian viruses are first transmitted to hogs, and in turn the new hog viruses are transmitted by mosquitoes to human beings. Recent studies have indicated evidence for a possible reverse transmission process. Similar virus mutations are suspected in past influenza pandemics that killed over 20 million people in 1918, 1957 and 1968. These outbreaks affect not only the health of world population but also the price of food and world economy. It should be noted that the overall waste production rate from high-density animal farming is 100 times more than that produced by human beings, and there is presently almost no sanitary sewage treatment for the animal waste. It is, therefore, most urgent that one should devise means to solve the problem at its source.

Ironically, high-density animal farming is operated under the high-tech control of very large corporations in conjunction with their affiliated cooperative farms. The cooperative farmers earn their income by pinching every penny in raising the animals for the corporations. Hence, there is great reluctance by the farmers to solve the waste problem as it will greatly affect their narrow profit margin. The problem has now become a tough political struggle between large financial interest against public health interest. Because high-density animal farming is generally located far apart in rural areas, it is not economical to transport the wastes to a central processing plant. Moreover in doing so, there is the danger for spreading new viruses from one farm to the other. Hence, treatment of animal farm wastes must be performed in situ. Various biological degrading techniques have been tried without success in the past decades, because the quantity of waste production simply overwhelms the relatively slow biodegrading and composting processes. This has resulted in serious pollution to both the surface and underground water, and extreme foul-smell to the surrounding air. The only workable solution left is to incinerate the waste on site. The objective of this paper is to find a new means to incinerate the waste with

minimum pollution to the environment and cost to implement. We identify this technology as a pre-carbonization incineration process.

2. PRE-CARBONIZATION INCINERATION TECHNIQUE

The low temperature pre-carbonization technology, also known as the charcoal process, was discovered and used by man since Stone Age. It is known that burning charcoal is much cleaner than burning wood. The technology for incineration of animal wastes is originated as a solution for the safe and economical disposal of municipal combustible garbage and sewage sludge. The technique is ideally applicable as a solution for safe disposal of animal farm-wastes. These wastes include deceased animal carcasses and used-plastic products. Additionally, the recaptured waste heat can be utilized to provide fresh heated or cooled air in the animal housing areas. The benefits include a much healthier environment for the animals, which in turn promote better growth and reduce morbidity loss; thus keeping the proliferation of dangerous viruses in check. Compared with other incineration processes, this low temperature pre-carbonization technology produces the least amount of toxic NO_x , SO_x , CO and micro fly-ash. Due to special composition of animal feeds, the residual ash of incineration is chemically neutral with pH of approximately 7.0. Hence, the ash can be safely spread into the soil of a farm to improve both its mineral content and texture. The process has no additional waste products that could cause further problems. Under proper implementation, it is believed that the technique will improve the profitability of a farm rather than an added financial burden to both the farmer and the public.

Since ancient time, man discovered that if solid fuels were pre-carbonized at a low temperature, the resulting char provided cleaner and more efficient combustion. Unfortunately, this technology has received very little attention in modern time. Due to many unresolvable problems facing the present combustion technologies, in particular the problems of air pollution and system fouling, we have re-examined the low-temperature pre-carbonization process. For example, through the extrapolation of existing pyrolysis data for coal, we have found that in the low-temperature pre-carbonization process at a temperature range of $350^\circ\text{--}400^\circ\text{C}$, a large percentage of hydrocarbon compounds in solid fuels can be pre-carbonized with only a minimal loss of high-vapor-pressure combustible constituents. Our literature search has revealed no published data for the preceding stated range of pre-carbonization temperatures. In this paper we shall present the results of our studies concerning slow and low temperature carbonization of various solid fuels: such as different ranks of coal, rubber tire, animal-farm wastes, sewage sludge, and plastic. The study was performed by methods of thermal-gravimetric analysis (Carpenter and Skorupska, 1993) and by larger sample batches in a temperature-controlled oven, from which the rate constants for pre-carbonization of various solid fuels were determined.

From a molecular point of view, both the present forms of combustion for solid fuels by chain stoker, powdered spray, or fluidized bed are physically non-steady and non-uniform processes of chemical oxidation. The fact that it is necessary to improve complete combustion for these processes by a second or even a third combustion cycle speaks for itself. That is, all turbulent mixing processes are too large in physical scale and too short in time scale to achieve the required molecular scale of mixing and reaction. The very fact that there is a visible bright flame in all these combustion processes indicates non-homogeneity in the oxidation of carbon. That is, before a liquid or solid fuel particle can be oxidized it will first go through a strong outgassing (pyrolysis) stage. This causes the oxygen surrounding the fuel particle to be displaced away from the expanding gas. Hence combustion can take place only through a molecular-diffusion process at the very boundary of the expanding gas. At the ideal combustion temperature of $1200^\circ\text{--}1400^\circ\text{K}$, greater than 99% of the combustion energy should be emitted as invisible infrared radiation. The visible yellow flames are carbon atoms within the expanding gas that are being irradiated to incandescent by the external infrared-radiation, and are not yet oxidized due to the local deficiency in oxygen.

Our solution to the "unresolvable problems" associated with the present-day combustion technologies is to employ the ancient technology of pre-carbonization for solid fuels. For example, fast pyrolysis for coal as a function of high carbonization temperature (Smoot, 1985) is shown on the right-hand side of Fig. 1. One notes that at high temperatures a large percentage of coal is converted into liquid tar and gas fractions. As the carbonization temperature is decreased more fractions of hydrocarbons in the coal can be carbonized with smaller loss of combustible constituents. Most of all, less tar fraction is produced. Our data for slow and low-

temperature carbonization of bituminous coal of different rank is shown on the left-hand side of Fig. 1. In this process, there is only minimal loss of combustible products by weight.

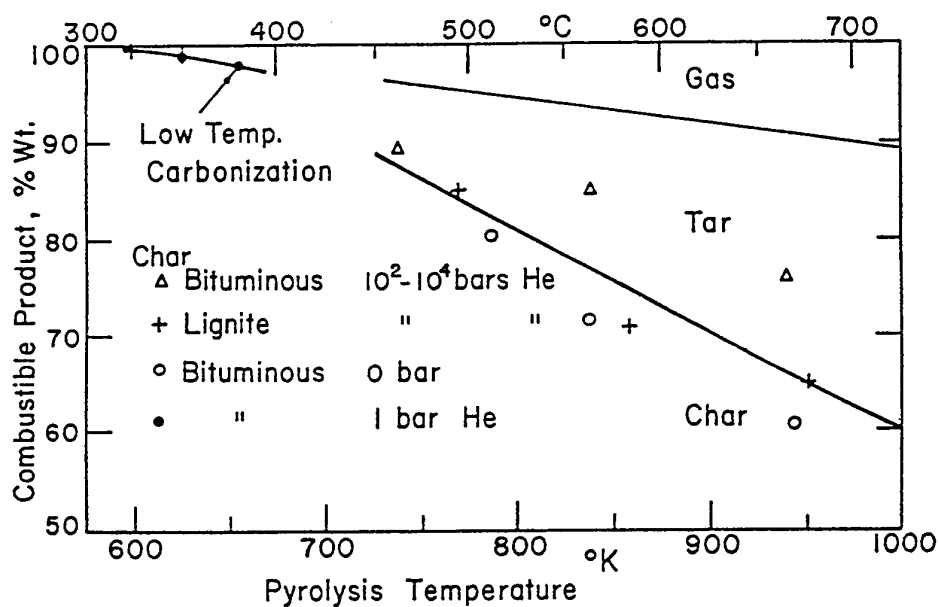


Fig. 1. Distribution of pyrolysis products at various pre-carbonization temperatures.

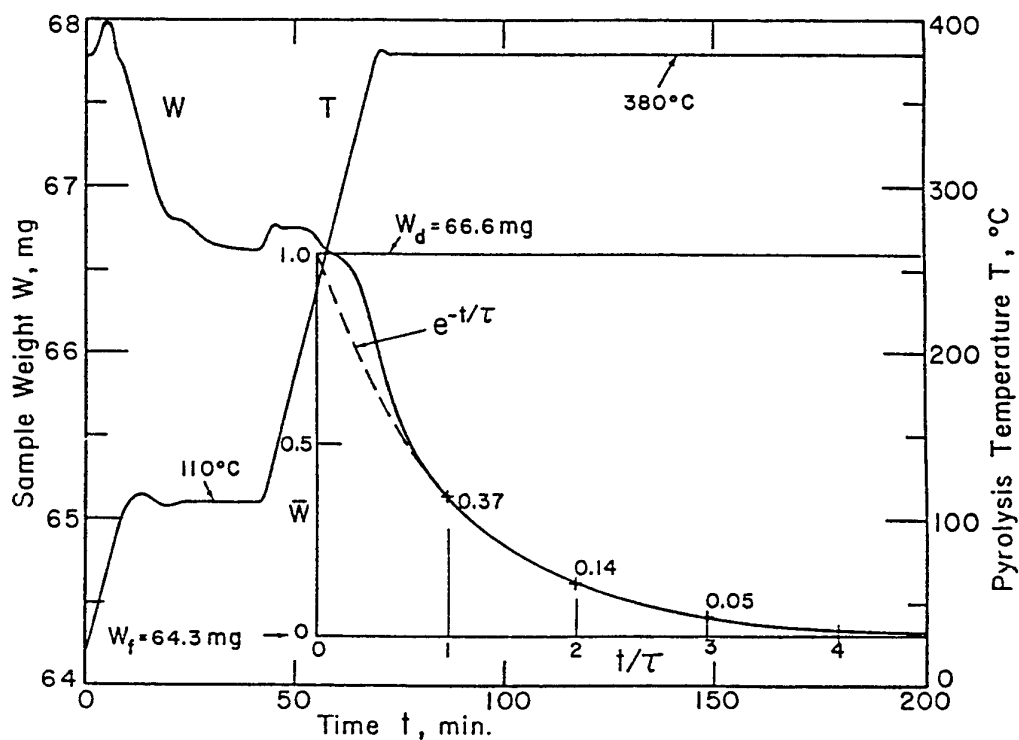


Fig. 2. Pre-carbonization of Virginia bituminous-coal by thermal-gravimetric analysis.

Figure 2 shows a typical result of thermal-gravimetric analysis for pre-carbonization of Virginia bituminous coal. In this study, 67.8 mg of coal sample particles, 0.1 to 0.5 mm in size, is placed in a crucible. The sample is first dried for 30 minutes at 110°C. It is then placed in a helium atmosphere of 1 bar pressure, and heated at a rate of 10°C/min to a constant pre-carbonization temperature of 380°C. The recording of loss of weight W with the time of carbonization t is noted to be exponential in nature. To obtain the rate constant k for the carbonization process, the initial dried sample weight of $W_d = 66.6$ mg and the final pre-carbonization weight of $W_f = 64.3$ mg are noted from Fig. 2. A corresponding normalized weight-scale defined as $W = (W - W_f)/(W_d - W_f)$ is plotted in Fig. 2. The value of W is noted to range from 0 to 1. The points along the $W(t)$ curve, at which the normalized weight is $W = 0.37, 0.14$, and 0.05 are marked with +. These points are assumed to correspond to 1, 2, and 3 times the time constant τ , respectively; where $W = e^{-t/\tau}$. Based on the equal time intervals found between these points, the normalized time-scale of t/τ is established in Fig. 2. The time constant τ for this case is noted to be 31 min. Hence the pre-carbonization process is 95% complete in $3\tau = 93$ min. The rate constant for carbonization is defined as

$$k = -dW/dt \big|_{t/\tau=0} = 1/\tau. \quad (1)$$

One may consider the value of τ defined by the above analysis as a good approximation for the rate constant of the low temperature pre-carbonization process, $k = 1/\tau = 0.032 \text{ min}^{-1}$. Hence, the rate constant for pre-carbonization of different solid fuels can be defined by a similar analysis. We have found the corresponding rate constant for rubber tire to be $k = 0.025 \text{ min}^{-1}$, for animal wastes and sewage sludge 0.06 min^{-1} , and for vinyl plastic 0.5 min^{-1} .

Based on the preceding analysis, we have produced large batches of combustible solid-fuel in a steel rotating-drum filled with steel pullets. The drum is placed inside an electric oven in which the temperature is maintained at a constant temperature of 375°C. The gas that evolves during the carbonization process is directed into a porous sintered-alumina closed-end tubing, having a wall thickness of 1 cm, for combustion in an adjacent oven that is maintained at a temperature above 800°C. Combustion of the gas is designed to take place inside the wall of the porous tube. This provides a very uniform and complete combustion for the gas with a minimum production of pollution products.

3. DESIGN OF A PRE-CARBONIZATION INCINERATOR

In the United States, each chicken farmer typically raises a total of 90,000 chickens that are housed in three batches according to their different stages of growth. The growth period for each batch is 6 weeks. The bedding material of wood chip or straw containing all animals wastes is renewed after a few growth cycles. The waste is bulldozed into a storage shed for subsequent disposal. In hog farms, each farm typically raises a total of several thousand pigs in long open sheds, with each shed designed for different stages of growth. Open-grate flooring is often used to collect wastes by an underground pit, where the waste materials are pumped into a 6 meters deep by 400 meters long open pit called a lagoon. The stench from such an operation is more than overwhelming. Spillage and mishandling of the wastes, as mentioned before, are presently a very serious public-health problem.

Presented in the following is a preliminary incinerator design for a poultry housing unit. The litters after separation from metal and stone is screw fed at a small steady rate from the storage bin to the top of the incinerator. See Fig. 3. The litter is then fed slowly down the large central feed-screw of the incinerator for pre-carbonization. The total travel time for the litter to reach the bottom of the screw feed is 15 minutes, during which the litter is subjected to pre-carbonization at a controlled uniform temperature of 370°C. The heating effect is supplied by the pre-heated combustion air of 400°C moving down the central tube of the feed-screw, and by the 800°C combusting gas on the outer tube surface of the feed-screw. The combustible gas, released from the pre-carbonization process, after mixing with the preheated air is directed upward into eight long porous ceramic tubing shown in Fig. 3. The porous ceramic tubes provide large heated surface area for promoting complete uniform combustion of hydrocarbon gas within the porous wall. If necessary, the porous ceramic

tubing can be coated with a micro layer of platinum to serve as a catalytic surface, much like the catalytic converter of a motor car, for the ultimate dissociation of all toxic gases.

The temperature of combustion in the incinerator can be easily regulated by controlling the pre-heated temperature of the air supply. The pre-carbonized char leaving the central feed-screw is first pulverized by steel rollers to increase its surface area for combustion on a series of rotating pans, see Fig. 3. The residual ash from the final combustion process is free of unburned carbon, and is also chemically neutral as mentioned before. Finally, the ash is screw fed to a storage bin for subsequent spreading and mixing with soil in the farm.

The heat derived from the incineration process is more than sufficient for heating or cooling the farm building with fresh air. Electric power will be used for starting up the incinerator as well as for subsequent control of the system when needed. Details for the automatic-control system and heat-exchange system are considered to be standard air conditioning technology and are not discussed herewith.

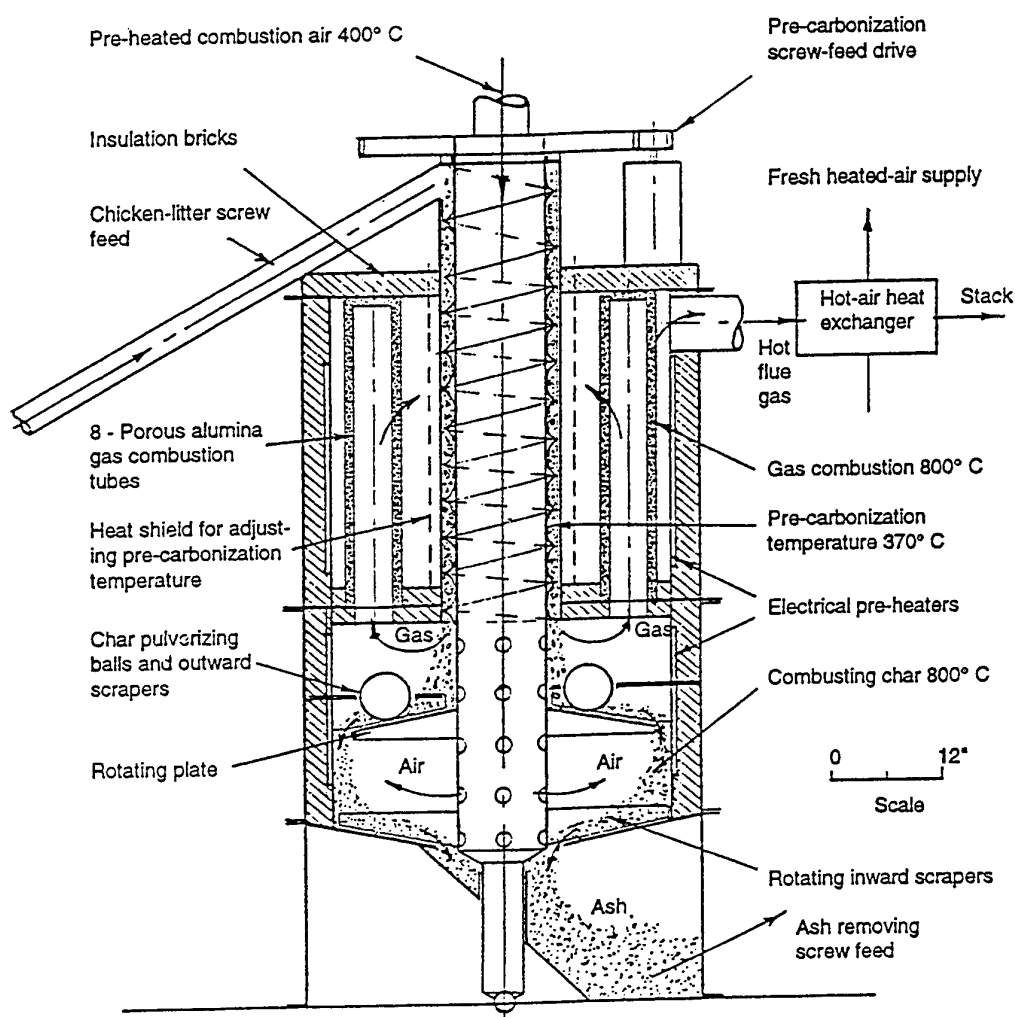


Fig. 3. Chicken-litter incinerator and hot-air heating supply.

In the incineration of pig waste, the litter may at time contain much water used for flashing the litter floor. In this case, the liquid that is first separated from the solid is fed as fine spray directly into the incinerator for combustion. The feed rate is limited so as not to affect the basic combustion process.

REFERENCES

1. R. Barker, *And the Waters Turned to Blood*, Simon & Schuster, New York (1997).
2. A.M.Carpenter and N.M. Skorupska, *Coal Combustion-Analysis and Testing*, IEACR/64, IEA Coal Research, London, pp.17-32 (1993).
3. L.D. Smoot and P.J. Smith, *Coal Combustion and Gasification*, Plenum Press, New York, p. 58 (1985).

W. Fuel Cells

DIRECT LIQUID WATER INJECTION AND INTERDIGITATED FLOW FIELD FOR REACTANT GAS, WATER AND THERMAL MANAGEMENT IN PROTON EXCHANGE MEMBRANE FUEL CELLS

Trung Van Nguyen

Department of Chemical & Petroleum Engineering

The University of Kansas

Lawrence, Kansas 66045, USA

E-mail: cptvn@ukans.edu; Fax: (785) 864-4967

Keywords: PEM fuel cells; liquid water injection; gas, water and thermal management

ABSTRACT. Proper gas, water and thermal management is vital to the successful operation of proton-exchange-membrane fuel cells. The effectiveness of the direct liquid water injection scheme and the interdigitated flow field design towards providing optimal gas distribution, membrane hydration, and heat removal and alleviating the mass transport limitations of the reactants and electrode flooding was investigated. It was found that the direct liquid water injection used in conjunction with the interdigitated flow fields is an extremely effective method of gas, water and thermal management. When used in the anode, the forced flow-through-the-electrode characteristic of the interdigitated flow field provides higher transport rates of reactant from the flow channels to the inner catalyst layer, increases the hydration state and conductivity of the membrane by bringing its anode/membrane interface in direct contact with liquid water, and increases the cell tolerance limits for excess injected liquid water, which could be used to provide simultaneous evaporative cooling for the cell. When used in the cathode, in addition to the enhanced transport rate of gaseous reactant and product, the shear force of gas flow through the electrode helps to remove the liquid water that is entrapped in the inner layers of the electrode, thereby significantly reducing the electrode flooding problem.

1. INTRODUCTION

Environmental concerns and our increasing dependence on imported fuels call for alternative energy sources and better utilization of existing energy sources. Fuel cells that convert chemical energy directly into electrical energy offer much better conversion efficiency than most existing energy conversion devices; and when fuel systems such as hydrogen/oxygen or hydrogen/air are used, fuel cells are totally pollution free. Of various existing fuel cell systems, the proton exchange membrane (PEM) fuel cell system shows greatest promise in future applications such as stationary and mobile power generation because of its high efficiency and ease of construction and operation. The attractiveness of this fuel cell system has increased significantly within the past several years because of the following improvements. The catalyst loading has decreased significantly, and membranes with improved conductivity, water permeability and thermal stability have been developed. Electrode/membrane contact area has increased and materials processing and preparation cost has decreased. However, before this system can become economically competitive with existing technologies, its performance must be improved further. Recent work has shown that optimal reactant gas distribution and proper water and thermal management are the keys to achieving improvements in this area.

To address these problems directly, a new flow field called the interdigitated flow field was developed. By forcing the gas to flow through the electrodes in order to exit as compared to flowing over the surface of the electrodes in a "conventional" flow field, the transport of the reactant and product gases to and from the catalyst layers are converted from a pure diffusion mechanism to a forced convection/diffusion mechanism. See Fig. 1. As a result, the diffusion layer is greatly reduced from the whole electrode thickness consisting of the catalyst layer and the macro-porous backing layer to a much-thinner combined catalyst and stagnant layer. Furthermore, the shear force of this gas flow helps to remove any liquid water that is entrapped in the inner layers of the electrode, thus eliminating the electrode flooding problem [1,2]. The forced-flow-through characteristic created by the interdigitated flow field also enables the cell to handle two-phase (liquid water and reactant gas) flow allowing the direct liquid water injection scheme to be used effectively. By introducing liquid water directly into the anode and allowing it to contact the anode and membrane interface, higher membrane hydration and consequently higher conductivity can be achieved [3]. This paper discusses the effectiveness of the direct liquid water injection scheme and the interdigitated flow field towards providing optimal membrane hydration and alleviating the mass transport limitations of the reactant gases and electrode flooding.

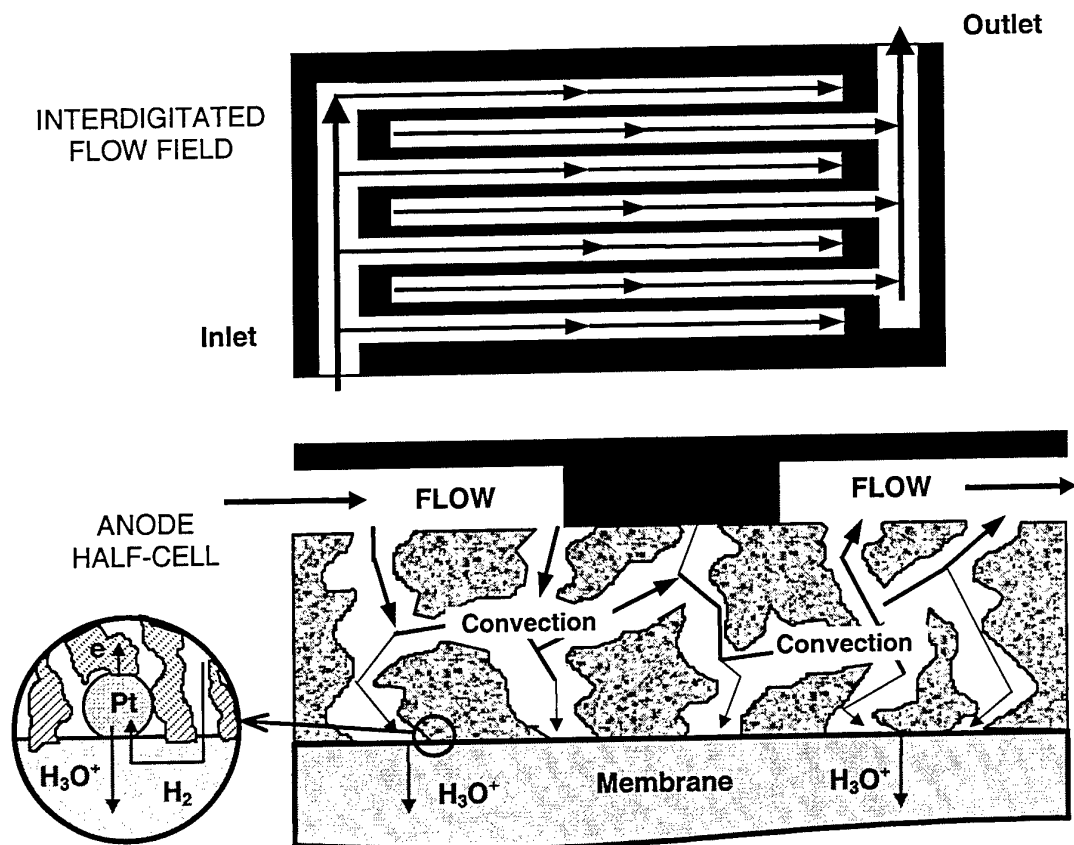


Figure 1. Schematic of an anode half-cell with an interdigitated flow field.

It is important to point out that the effectiveness of the direct liquid water injection scheme has been theoretically evaluated and proven by mathematical models [4,5]. Mathematical models of a PEM fuel cell system with the interdigitated flow fields have also been recently presented [6-8].

2. EXPERIMENTAL

The fuel cell used in this study consists of graphite plates with machined flow fields for gas distribution and pre-gasketed membrane and electrode assemblies (MEA's) provided by W.L. Gore and Associates. Except for the last results presented in Figure 6 where a 20- μm membrane was used, the MEA's used had a 40 μm -thick GORE-SELECT™ membrane with an equivalent weight of 950 and a catalyst loading of 0.3 mg Pt/cm²/electrode. The cell had an active surface area of 100 cm² per electrode. The macro-porous diffusion layers were made of carbon fiber cloths. Metering pumps were used to inject liquid water directly into the gas streams. Unless otherwise stated, cell pressures reported were outlet pressures. Pressure drops across the cell were measured with water manometers, and gas flow was controlled by mass flow controllers. Heater cartridges imbedded in stainless steel blocks placed next to the cell were used to control the cell temperature. Gas flow rates were held constant during the entire experiment, and for quick comparison purpose all flow rates are reported in A/cm² equivalent.

Different amounts of liquid water were injected into both the anode and cathode gas streams of a PEM cell having either the conventional or interdigitated flow fields. By holding the amount of water injected into one electrode constant while varying the amount injected into the other, the effects of liquid water injection into each electrode can be investigated. The results from these runs were used to evaluate the effectiveness of the

combined direct liquid water injection and interdigitated flow fields as a method of gas, water and thermal management for PEM fuel cells.

3. RESULTS AND DISCUSSION

Oxygen Operation

Effects on anode. In this study, the anode and cathode gas flow rates and water-to-oxygen ratio were held constant at 2.5 A/cm^2 , 3.0 A/cm^2 and $0.64 \text{ mol H}_2\text{O/mol O}_2$, respectively, and the water-to-hydrogen ratio was varied from 0 to $2.03 \text{ mol H}_2\text{O/mol H}_2$. Note that at 80°C a saturated gas has a water-to-gas ratio of approximately $0.88 \text{ mol H}_2\text{O/mol}$. From the results presented in Figure 2 the following observations can be made. With no anode water, both flow field designs gave poor performance with that of the conventional flow field being poorer. As water is added to the cell, the performance of both cells increased with that with the interdigitated flow fields increasing more. This is attributed to the fact that in the cell with interdigitated flow fields liquid water is brought into direct contact with the catalyst membrane interface resulting in higher membrane hydration and conductivity. On the other hand, in the cell with conventional flow fields, water has to diffuse from the channels to the catalyst membrane interface resulting in slower water transport rate to the membrane to maintain adequate hydration. Next, as the amount of water was increased further, from 1.16 to $2.03 \text{ mol H}_2\text{O/mol O}_2$, the performance of the cell with interdigitated flow fields continued to increase while that of the cell with conventional flow fields decreased. This decrease in performance in the cell with conventional flow field is attributed to liquid water flooding of the macro-porous backing layer. These results confirm the effectiveness of the combined system of direct liquid water injection and interdigitated flow field design as a water management method. Furthermore, the ability to tolerate excess liquid water allows this system to use the inherent evaporative cooling characteristic for thermal management.

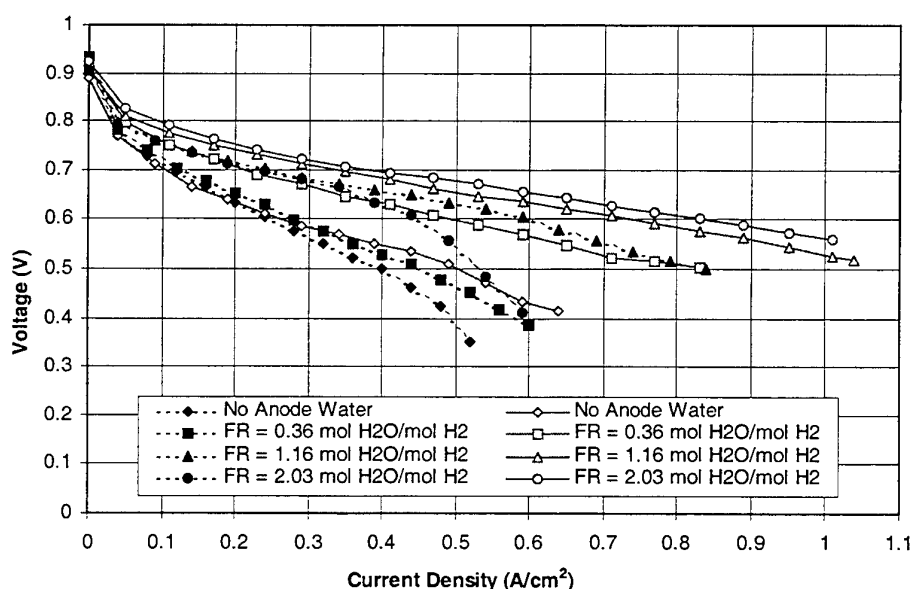


Figure 2. Performance comparison between flow fields for oxygen operation at various anode water injection levels. [$T_{\text{cell}} = 80^\circ\text{C}$, $P_a = P_c = 1 \text{ atm}$, $40 \mu\text{m}$ membrane, H_2 flow rate $= 2.5 \text{ A/cm}^2$, O_2 flow rate $= 3.0 \text{ A/cm}^2$, cathode water $= 0.64 \text{ mol H}_2\text{O/mol O}_2$, solid lines = Interdigitated, Dashed lines = Conventional.]

Effects of thin membrane on anode humidification. In this study, MEA's with thinner ($20 \mu\text{m}$ vs. $40 \mu\text{m}$) membranes were used to evaluate the effect of water back diffusion on anode humidification. Except for a cell temperature of 60°C , all other operating conditions were similar to those used in the previous case. The results given in Fig. 3 show that by having a thinner membrane to promote higher water back diffusion rate from the cathode to the anode, as well as lower ionic resistance, the effect of anode humidification on the cell performance is reduced. These two cells with either interdigitated or conventional flow fields performed better

than the two cells with thicker membranes at the same operating conditions. However, the cell with interdigitated flow fields still performed better than that with conventional flow fields.

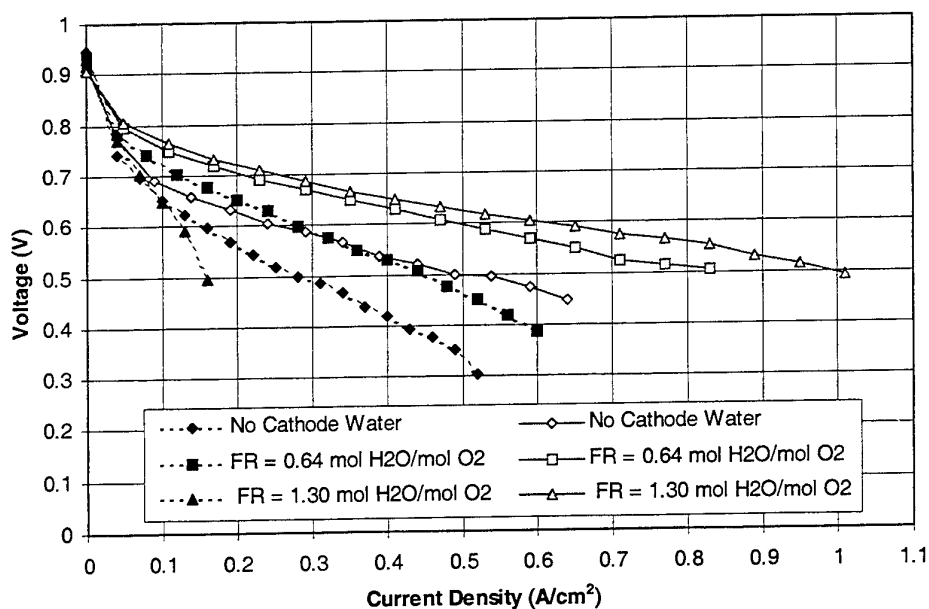


Figure 3. Performance comparison at 60°C between flow fields for oxygen operation with thinner (20mm) membranes. [$P_a=P_c=1\text{atm}$, H_2 flow rate= $2.5\text{A}/\text{cm}^2$, O_2 flow rate= $3.0\text{A}/\text{cm}^2$, cathode water= $0.64\text{mol H}_2\text{O}/\text{mol O}_2$, solid lines=Interdigitated, Dashed lines=Conventional.]

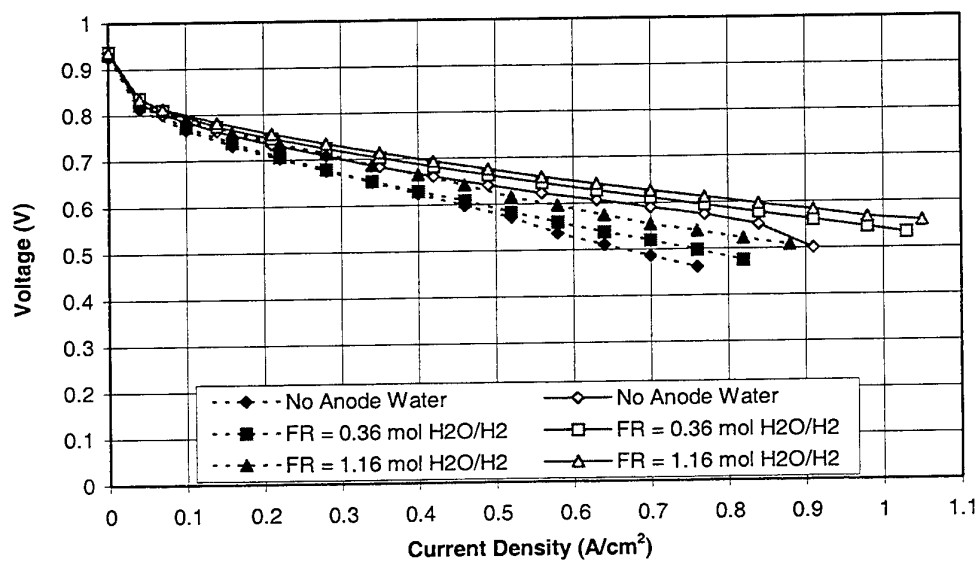


Figure 4. Performance comparison between flow fields for oxygen operation at various cathode water injection levels. [$T_{\text{cell}}=80^\circ\text{C}$, $P_a=P_c=1\text{atm}$, $40\mu\text{m}$ membrane, H_2 flow rate= $2.5\text{A}/\text{cm}^2$, O_2 flow rate= $3.0\text{A}/\text{cm}^2$, anode water= $0.36\text{mol H}_2\text{O}/\text{mol H}_2$, solid lines=Interdigitated, Dashed lines=Conventional.]

Effects on cathode. In this study, the anode and cathode gas flow rates were set at the same values as those in the previous study. The water-to-hydrogen ratio was now held constant at 0.36 mol H₂O/mol H₂, and the water-to-oxygen ratio was varied from 0 to 1.3 mol H₂O/mol O₂. The results are presented in Fig. 4. Again as in the previous case, the cell with interdigitated flow fields consistently performed better than that with conventional flow fields. In this case, the cell with interdigitated flow fields benefited from 1) higher mass transport rate of oxygen to the catalyst layer, 2) better membrane hydration and 3) more effective water removal from the electrode as a result of the forced flow-through-the-electrode characteristic of the dead-ended channel design. Without these benefits of the interdigitated flow fields, the cathode of the cell with conventional flow fields became quickly flooded with liquid water. The situation worsened as more liquid water was injected into the cathode.

Air Operation

When air is used as the cathode reactant, the performance of a PEM fuel cell is affected in two ways. First, lower oxygen concentration in air reduces the reactivity of the cathode reaction resulting in higher cell overpotential. Second, higher gas flow, which is needed because of the lower oxygen concentration, leads to higher pressure drop and therefore higher parasitic power loss. Furthermore, higher cathode gas flow rate could exacerbate the membrane dehydration problem. With more water transported out of the cathode, water transport across the membrane could change from the back-diffusion of water from the cathode to the anode to diffusion in the same direction as electro-osmosis (towards the cathode). This would put a higher demand on anode humidification or lead to more severe membrane dehydration. Liquid injection into both the anode and cathode gas streams was again conducted to evaluate the effectiveness of the combined liquid water injection and interdigitated flow field strategy.

Effects on anode. In this study, the anode and cathode gas flow rates and water-to-oxygen ratio were held constant at 2.5 A/cm², 2.0 A/cm² and 0.20 mol H₂O/mol O₂, respectively, and the water-to-hydrogen ratio was varied from 0 to 1.2 mol H₂O/mol H₂. Lower cathode gas stoichiometric flow rate was used to minimize pressure drop in the cell. The results presented in Fig. 5 show behaviors similar as those in Fig. 2 for oxygen

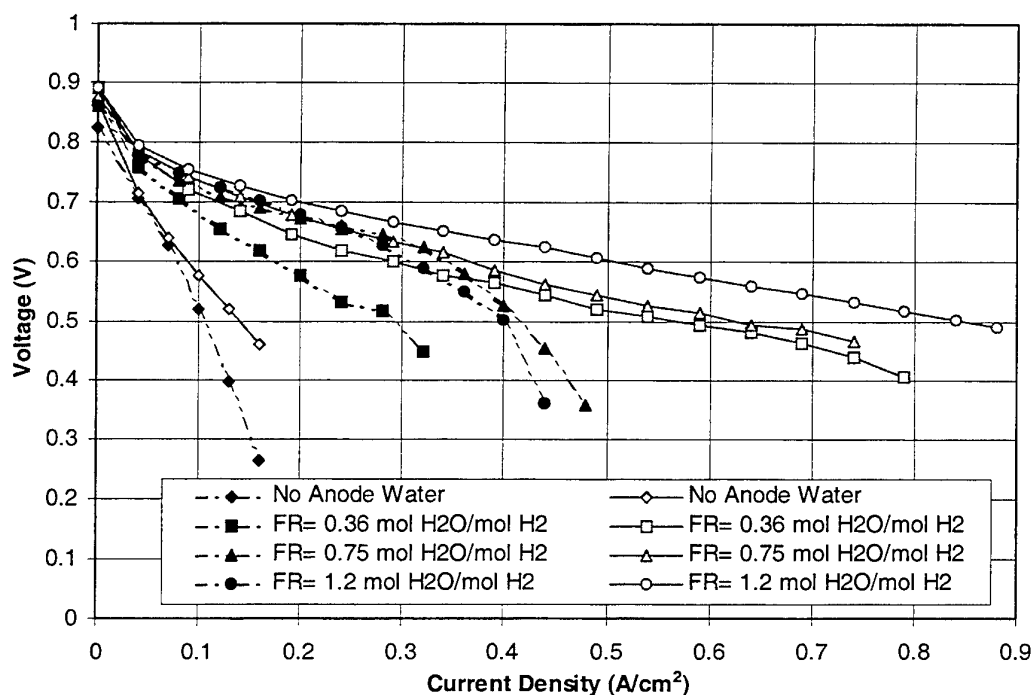


Figure 5. Performance comparison between flow fields for air operation at various anode water injection levels. [$T_{\text{cell}}=80^{\circ}\text{C}$, $P_a=P_c=1\text{atm}$, $40\mu\text{m}$ membrane, H_2 flow rate= $2.5\text{A}/\text{cm}^2$, Air flow rate= $2.0\text{A}/\text{cm}^2$, cathode water= $0.20\text{mol H}_2\text{O}/\text{mol O}_2$, solid lines=Interdigitated, Dashed lines=Conventional.]

operation. First, with no anode water both flow field designs gave poor performance. Second, the performance increased greatly when water was added to the anode gas streams. Finally, the cell with conventional flow fields became flooded as the amount of water injected into the anode gas stream increased beyond a certain level. In addition to these observations, these results also showed that the effect of dehydration was more severe when no water was added to the anode, and when water was added the increase in performance was more pronounced for both flow field designs. Finally, the cell performance obtained with air was not as good as that with oxygen as expected because of the lower oxygen concentration.

Effects on cathode. In this study, the anode and cathode gas flow rates were set at the same values as those in the previous study. The water-to-hydrogen ratio was now held constant at 0.36 mol H₂O/mol H₂, and the water-to-oxygen ratio was varied from 0 to 0.41 mol H₂O/mol O₂. The results are presented in Fig. 6. Note that adding water into the cathode gas stream increased the performance of cells of both flow field designs. The effect on the cell with interdigitated flow fields is more pronounced. At 0.41 mol H₂O/mol O₂, one could see the mass transport limitation behavior (sharp drop in performance at high current densities) for the cell with conventional flow fields. This is the sign of cathode flooding, which could highly hinder the transport of oxygen to the active sites. Finally, note that the performance of the cell with interdigitated flow fields with no anode water was much worse than that of the cell with conventional flow fields. This is attributed to the fact that having dry gas flowing much closer to the catalyst layer, as a result of the forced flow-through-the-electrode characteristic of the interdigitated flow field, leads to more severe dehydration of the anode and membrane interface.

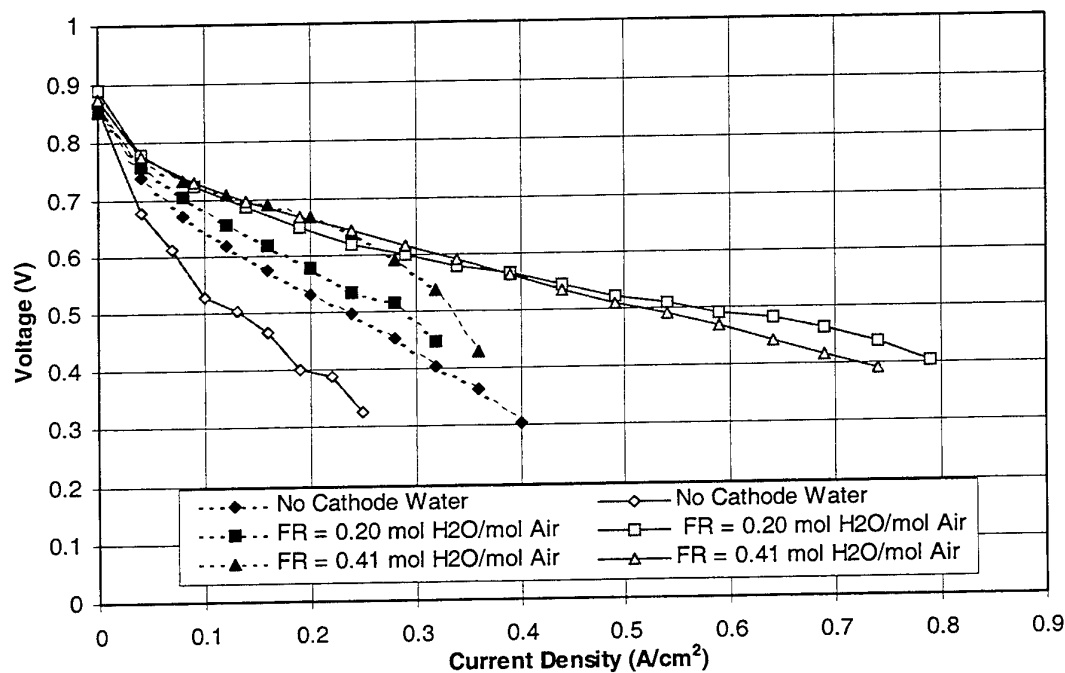


Figure 6. Performance comparison between flow fields for air operation at various cathode water injection levels. [$T_{\text{cell}}=80^{\circ}\text{C}$, $P_a=P_c=1\text{atm}$, $40\mu\text{m}$ membrane, H_2 flow rate= $2.5\text{A}/\text{cm}^2$, Air flow rate= $2.0\text{A}/\text{cm}^2$, anode water= $0.36\text{ mol H}_2\text{O}/\text{mol H}_2$, solid lines=Interdigitated, Dashed lines=Conventional.]

4. CONCLUSIONS

The interdigitated flow field design shows superior performance over the conventional flow field design due to its enhanced transport capabilities. Liquid water injection when used with the interdigitated flow field design is an extremely effective gas, water and thermal management strategy. Using the higher liquid water tolerance levels offered by the interdigitated flow fields, excess injected liquid water could be used as a heat removal method for PEM fuel cells.

5. ACKNOWLEDGEMENTS

The author would like to acknowledge the support of the University of Kansas (under Award No. 3578-20-0003-1101) and the National Science Foundation (under Grant No. CTS-9803364).

6. REFERENCES

1. T.V. Nguyen, "A Gas Distributor Design for Proton Exchange Membrane Fuel Cells," *Journal of the Electrochemical Society*, v.143, L103-L105 (1996).
2. D. Wood, III, J.S. Yi and T.V. Nguyen, "Effect of Direct Liquid Water Injection and Interdigitated Flow Field on the Performance of Proton Exchange Membrane Fuel Cells," *Electrochimica Acta*, v.43, 3795 (1998).
3. T.A. Zawodzinski, Jr., T.E. Springer, J. Davey, R. Jestel, C. Lopez, J. Valerio and S. Gottesfeld, "A Comparative Study of Water Uptake by and Transport Through Ionomeric Fuel Cell Membranes," *J. Electrochem. Soc.*, v.140, 1981 (1993).
4. T.V. Nguyen and R.E. White, "A Heat and Water Management Model for Proton-Exchange-Membrane Fuel Cells," *Journal of the Electrochemical Society*, v.140, 2178-2186 (1993).
5. J.S. Yi and T.V. Nguyen, "An Along-the-Channel Model of Proton Exchange Membrane Fuel Cells," *Journal of the Electrochemical Society*, v.145, 1149-1159 (1998).
6. J.S. Yi and T.V. Nguyen, "Multi-Component Transport in the Porous Electrodes of PEM Fuel Cells with Interdigitated Gas Distributors," *Journal of the Electrochemical Society*, v.146, 38-45 (1999).
7. V. Gurau, H. Liu, and S. Kalac, "Two-Dimensional Model for Proton Exchange Membrane Fuel Cells," *AIChE Journal*, v.44, 2410-2422 (1998).
8. T.V. Nguyen, "Modeling Two-Phase Flow in the Porous Electrodes of Proton Exchange Membrane Fuel Cells Using the Interdigitated Flow Fields," *Proceedings Volume of the Symposium on Tutorials in Electrochemical Engineering – Mathematical Modeling*, The Electrochemical Society, Inc., Pennington, NJ, 1999.

TRANSPORT PHENOMENA IN PROTON EXCHANGE MEMBRANE FUEL CELLS

C.Y. Wang

Electrochemical Engine Laboratory
Department of Mechanical Engineering
Pennsylvania State University
University Park, PA 16802, USA
Email: cxw31@psu.edu Fax: (814) 863-4762

Keywords: PEM fuel cells, transport phenomena, heat and water management, computational fluid dynamics

ABSTRACT. Proton exchange membrane (PEM) fuel cells have emerged as a viable technology for power generation and energy conversion. Fuel cell engines for transportation applications possess many attributes such as high fuel efficiency, low emission, quiet and low temperature operation, and modularity. This paper provides a tutorial overview of critical transport phenomena occurring in PEM fuel cells and their impacts on the cell performance. Both hydrogen and direct-methanol fuel cells are discussed. Coupled experimental and modeling efforts ongoing at Penn State Electrochemical Engine (EC-Engine) Lab are described. Recent progress in modeling the multi-dimensional fluid dynamics and multi-component species transport with electrochemical kinetics, understanding the two-phase transport in porous electrodes, and developing detailed validation experiments is reviewed. Areas where future theoretical and experimental research is needed are identified.

1. INTRODUCTION

Fuel cell engines can potentially replace the internal combustion engine because they are clean, energy-efficient, quiet, fuel-flexible, and quickly starting up due to low-temperature operation. Figure 1 schematically shows a PEM fuel cell consisting of an anode, a membrane, and a cathode. The membrane, typically a few hundred μm thick, is also the electrolyte and is made of ion-exchange polymers. The anode and cathode are prepared by applying a small amount of catalyst, typically platinum black or a supported platinum, to one surface of a thin sheet of porous electrode materials. The polymer electrolyte membrane is then sandwiched between the anode and cathode, as shown in Fig.1, and the three components are sealed together to produce an integral membrane/electrode assembly (MEA). The anode and cathode are contacted on the back side by flow plates in which mini-channels have been machined. The anode flow channel supplies either gaseous fuel (hydrogen) or liquid fuel (methanol), whereas air or oxygen is fed into the cathode flow plate. Both types of fuel flowing through the anode channel dissociate at the catalyst layer into protons and free electrons. The protons migrate through the membrane electrolyte to the cathode where they combine oxygen from air and electrons from the external circuit to form pure water.

The performance of a fuel cell is measured by its current-voltage relation (i.e. the polarization curve). Under an applied current the voltage drop is mainly caused by: (1) overpotentials of electrochemical reactions occurring on anode and cathode; (2) the ohmic drop across the membrane; and (3) the transport limitations of reactants and products (particularly on the air cathode). At high current densities of special interest to vehicular applications, excessive water is produced within the air cathode in the form of liquid thus leading to a gas-liquid two-phase flow in the porous electrode. The ensuing two-phase transport of gaseous reactants to the reaction surface, i.e. the cathode/membrane interface, becomes a limiting mechanism for cell performance, particularly at high current densities (e.g. $>1 \text{ A/cm}^2$).

Two-phase flow and transport also occur in the direct methanol fuel cell, e.g. in flow channels and porous electrodes. In the anode flow channel the liquid phase consists of the aqueous methanol solution and the gas phase is carbon dioxide produced by the anodic reaction and released from the porous anode. The formation of CO_2 bubbles in the porous anode and their subsequent transport in the adjacent flow plate directly determine the activity of the catalyst surface and hence impact the fuel cell performance. The transport of the liquid water and methanol to the catalytic reaction sites also controls the rate of anodic reaction. On the cathode side, water is transported from the anode side via electro-osmotic drag and diffusion as well as produced *in situ* by the cathodic reaction. The presence of excessive water will flood the cathode and prevent the oxidant from reaching the reaction sites. Therefore, the formation of water droplets in the porous cathode and their evaporation into

the cathode flow channel are important processes to keep the porous cathode unsaturated and operative. These two-phase transport phenomena play a paramount role in the development of a fuel-efficient DMFC.

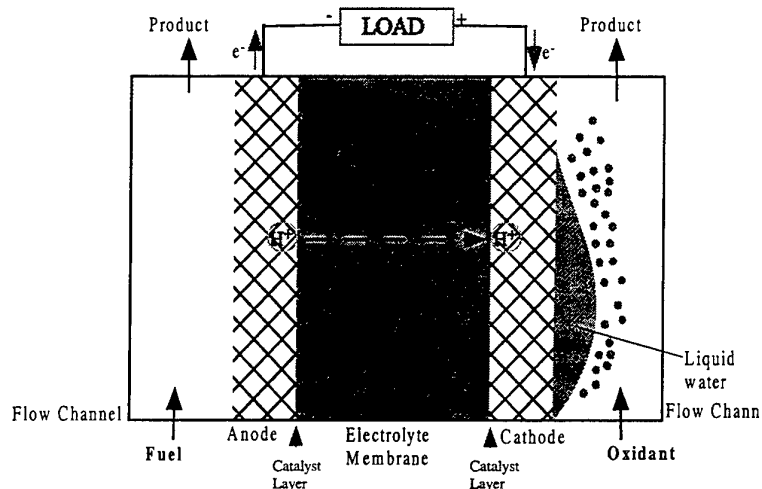


Figure 1. Schematic of a proton exchange membrane (PEM) fuel cell where the fuel can be hydrogen gas or liquid methanol.

Thermal management emerges as a critical issue in high-power fuel cell stacks. Heat generation in PEM fuel cells stems from the irreversibility of the electrochemical reactions, ohmic resistance, and mass-transport overpotentials. The resulting temperature distribution has a profound impact on the fuel cell performance because it affects water management via spontaneous vaporization/condensation, alters the transport characteristics of gaseous species through thermal buoyancy and thermocapillary forces, and accelerates the electrochemical reactions. If there is insufficient cooling, heat generation may give rise to excessive cell temperature and, consequently, membrane dehydration, shrinkage or rupture may occur. Therefore, the thermal management of a fuel cell is inherently coupled with the water management, and the two combine to ensure high performance and efficiency of the PEM fuel cell.

Much prior work has been done on hydrogen PEM fuel cells due to their recent promise for transportation applications. Prater [1] and Gottesfeld [2] presented excellent reviews of the hydrogen fuel cell research up to mid-1990s; Substantial experimental studies were reported by Gottesfeld and co-workers [3] and advances are continuing to be made worldwide, e.g. at Los Alamos National Laboratory [4] and Texas A&M University [5]. Modeling and computer simulation of hydrogen fuel cells have also been attempted by a large number of groups with the goal of better understanding and hence optimizing fuel cell systems [3, 6-11]. However, all these prior models are single-phase in nature, thus failing to consider the two-phase flow and transport with capillary effects inside the porous cathode although its importance was repeatedly stressed in the literature (e.g. [3]). Only most recently, two-phase flow and transport in the air cathode of hydrogen fuel cells began to receive some research attention [12,13].

Studies on direct methanol PEM fuel cells are of most recent origin, and DMFC systems are relatively less understood than hydrogen fuel cells despite their great potential as a power plant for transportation applications. Preliminary studies have been performed by Surampudi et al. [14] and Halpert et al. [15] at the Jet Propulsion Laboratory, Ren et al. [16] at Los Alamos, and Weng et al. [17] at Case Western Reserve University. Halpert et al. [15] demonstrated a 34% thermal efficiency of a DMFC stack and found that the methanol crossover is as high as 20%. Weng et al. [17] and Ren et al. [18] measured the electro-osmotic drag coefficient, a major index to quantify the methanol crossover and the ensuing reduction in the fuel efficiency of DMFC. While these initial studies have begun to look into the methanol crossover issue, a systematic and fundamental understanding of the flow and transport processes of liquid methanol and gaseous oxidant in DMFCs is absent, thus inhibiting the further improvement of the fuel cell technology for mobile applications.

The present paper describes both experimental and modeling efforts ongoing at Penn State EC-Engine Lab and reviews the current status of research on transport processes in PEM fuel cells. Section 2 will discuss experimental investigation on both hydrogen and direct-methanol fuel cells that aims at providing benchmark-quality data for validating fuel cell models based on computational fluid dynamics (CFD). Section 3 will summarize our work on modeling multi-dimensional fluid dynamics and multi-component transport coupled with electrochemical kinetics as well as a fundamental study of two-phase transport phenomena in the air cathode of a hydrogen fuel cell. The concluding section discusses future directions of the research on transport phenomena in PEM fuel cells.

2. EXPERIMENTAL

In an attempt to fully validate detailed fuel cell engine CFD models, several test rigs have been developed in our laboratory. Figure 2 presents various cell components typically composed of a single PEM fuel cell. A single cell test rig is shown in Fig.3, which can be used to test either hydrogen or direct-methanol fuel cells with the effective area of about 5 cm^2 . The test apparatus allows for full control and measurements of fuel and oxidant flow rates, operating temperature and pressure, as well as current and voltage. Hydrogen gas is pre-humidified by a heated humidifier bottle before entering the fuel cell, and the humidity is controlled by adjusting the bottle temperature.

Most recently, we also developed a larger single-cell test rig for direct-methanol fuel cells (with the effective area of $\sim 50 \text{ cm}^2$). This new experimental apparatus provides not only global measurements but also detailed diagnostics including:

1. spatial distribution of species compositions along the flow path via syringe sampling and Fourier Transform Infrared (FTIR) spectrometer,
2. visualization windows together with a Video Microprobe system (with 900x magnification) to observe and classify two-phase flow patterns in flow channels, and
3. a segmented cell design to enable measurement of the local current density distribution.

It is expected that this new apparatus will provide first detailed data for validation of a DMFC engine model being developed in parallel. Finally, a one-kilowatt hydrogen fuel cell stack custom-designed is also available as a research tool to address stack engineering issues such as active cooling. Test data are to be presented in a future publication.

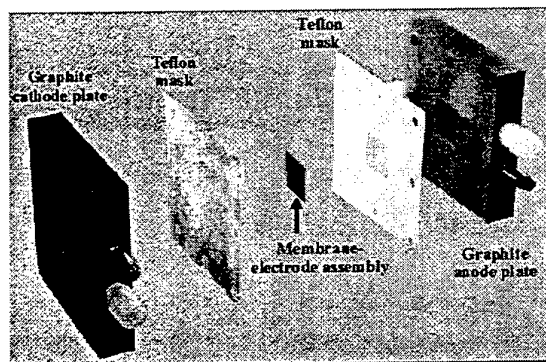


Figure 2. Structure of a PEM fuel cell.

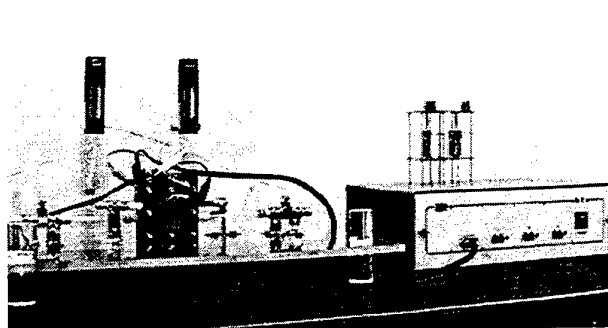


Figure 3. A single-cell experimental setup.

3. COMPUTATIONAL FLUID DYNAMICS MODELING

Replacing internal combustion engines places unprecedented stringent demands on fuel cell engine performance. Computer modeling and simulation promise to reduce the number of trial-and-error iterations in FC engine design, scale-up, and optimization. In the following, efforts to develop a computer-aided design system for hydrogen fuel cells are described.

3.1 Multi-Dimensional Transport Phenomena in PEM Fuel Cells

This subsection presents a comprehensive model of hydrogen PEM fuel cells which simultaneously accounts for multi-dimensional fluid flow in channels and porous electrodes, multi-component species transport in porous electrodes, charge transfer kinetics in catalyst layers, and charge transfer in the membrane and catalyst layers. The model can be used to predict steady-state performance of fuel cell engines as well as the transient response to fluctuations in operating conditions, to evaluate various flow field designs, and to upscale fuel cell systems. A schematic illustration of the modeled PEM fuel cell is shown in Fig.4.

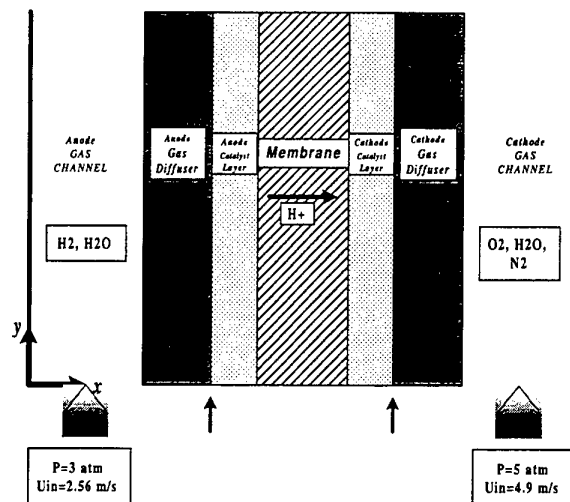


Figure 4. Schematic diagram of the PEM fuel cell model.

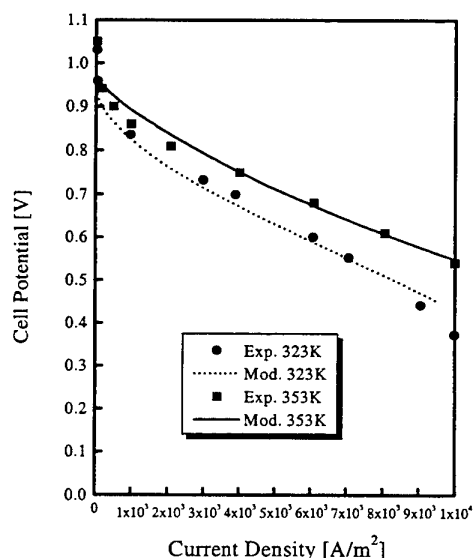


Figure 5. Model comparison with experimental data of Ticianelli et al. (1988).

Details of this model have been described elsewhere by Um et al. [19] and thus are not repeated here. Figure 5 shows a comparison of the model predictions with the experimental data of Ticianelli et al. [20] at two different operating temperatures. Excellent agreement can be seen. Figure 6 displays sample calculations of the velocity vector fields in both anode and cathode flow channels, the water vapor mole fraction distribution throughout the cell, and the oxygen mole fraction distribution in the cathode and its flow channel. These results provide much insight into how a PEM fuel cell operates, what are the steps limiting the cell performance, and what are innovative means to relax the present limitations.

3.2 Two-Phase Transport in Air Cathode

A fundamental study of two-phase flow and transport in the air cathode under high current densities has recently been carried out by Wang et al. [13]. We focused on a two-dimensional, steady-state and isothermal system of a porous cathode along with its adjacent flow channel. As a first approximation, the porous cathode is treated as a homogeneous medium with constant properties. We allow water in the electrode to exist as liquid and vapor depending upon whether the partial pressure of water vapor in air exceeds its saturation pressure. The governing equations for this two-phase, multi-component system in a porous electrode were developed based on the multiphase mixture model of Wang and co-workers [21-25]. The coupled governing equations were then solved by a control-volume based finite-difference method [26]. Details of computer simulations performed can be found in Wang et al. [13].

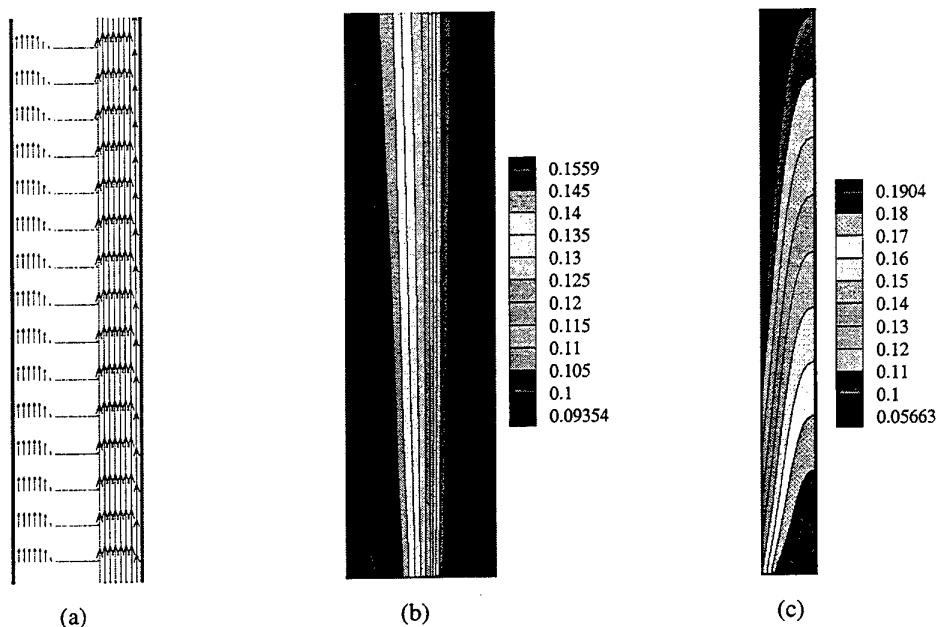


Figure 6. Sample model results of (a) flow fields in anode and cathode gas channels, (b) water vapor mole fraction, and (c) oxygen mole fraction for $I_{avg} = 8151 \text{ A/m}^2$, $V_{oc} = 0.6 \text{ V}$ and $T = 353 \text{ K}$.

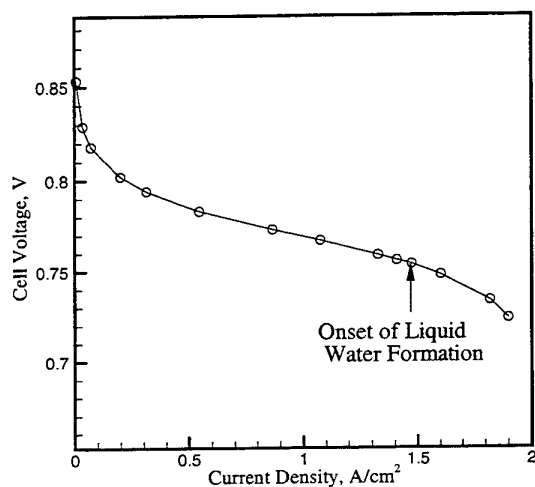


Figure 7a. Polarization curve of the air cathode.

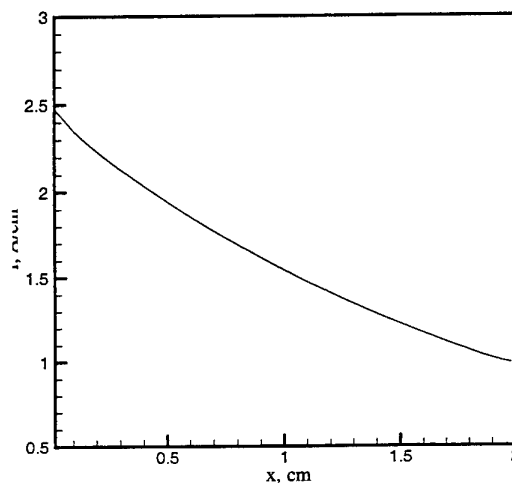


Figure 7b. Current density distribution with the average current density of 1.6 A/cm^2 .

Figure 7a shows a simulated polarization curve for an air cathode operated at 80°C. The curve compares well with experiment observations. At low current densities, the cathode activation overpotential is solely responsible for the potential losses of the cell. At higher current densities, more oxygen is consumed and more water is generated at the cathode/membrane interface due to both the electrochemical reaction and the water transport across the membrane from the anode. The cell polarization then begins to be limited by the transport of O_2 . As the current density rises beyond a threshold value, i.e. 1.47 A/cm^2 in the present case, so much water is produced that exceeds the capability to be removed by air from the electrode, and liquid water starts to form in the vicinity of the cathode/membrane interface. The presence of liquid water reduces the pore spaces for oxygen transport to the reaction surface as well as renders part of the surface electrochemically inactive. Clearly, a two-phase model is warranted for fuel cells operated at such high current densities, an operating range of special interest for transportation applications. An advantage of the present two-phase model is not only providing a unified formulation for both single-phase analysis at low current densities and two-phase analysis at higher values, but also forecasting and ensuring a smooth transition from the single- to two-phase region automatically. The predicted onset of two-phase regime is in accordance with experimental observations [3]. This threshold current density may vary with operating conditions for a given fuel cell, in particular, the cell pressure and cathode porosity. Figure 7b shows an appreciable current density distribution developed along the flow channel due to the depleting oxygen and increasing water vapor content in exhaust air.

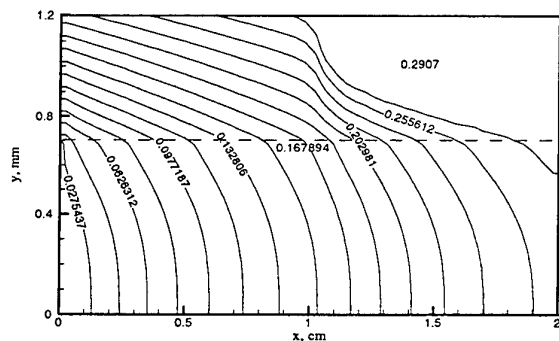


Figure 8. Water vapor mass fraction distribution in air cathode and channel at 1.6 A/cm^2 .

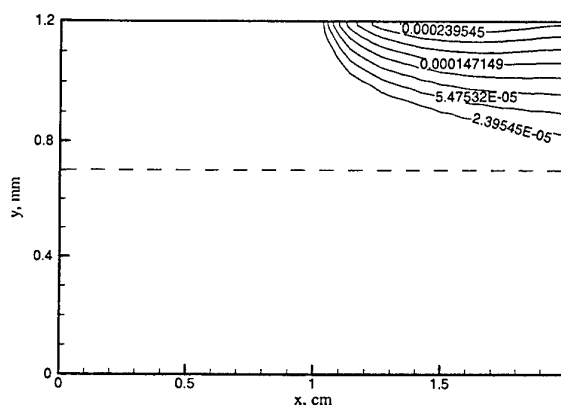


Figure 9. Liquid water saturation distribution in air cathode and channel at 1.6 A/cm^2 .

The possibility to form liquid water in the cathode is dependent on two competing rates: vapor transport rate within the cathode and the water generation rate at the cathode/membrane interface. No liquid water will appear if water vapor can be sufficiently removed out of the cathode before the water vapor density reaches its saturated value, 0.2907 kg/m^3 , in air at 80°C. Figure 8 displays the water vapor mass fraction contours in the cathode and gas channel. As the air flows through the gas channel, water vapor is added to air from the cathode resulting in an increased water vapor concentration down the channel. This leads to a decreased concentration gradient in water vapor and hence a lower water vapor diffusion rate from the cathode/membrane surface to the gas channel. As a result, liquid water may first appear in the vicinity of the cathode/membrane interface near the channel outlet. A two-phase zone at this location is indeed predicted in the present simulation shown in Fig. 8 where the water vapor concentration is seen to be constant at the saturated value. However, the liquid island does not have to always appear near the outlet because the local current density there is lower and hence the water production rate also lower. Figure 9 shows the liquid water saturation contours in the same case. In accordance with Fig. 8, liquid water is seen in the upper-right corner to coexist with the saturated water vapor. The predicted liquid amount is lower than that reported experimentally. This is likely because the present study simulates a single channel whereas experimental fuel cell fixtures usually use series-connected channels. With the effective channel length extended, a higher liquid water saturation will result. In the two-phase zone, liquid water is transported mainly by capillary action - since the flow is largely absent in the porous cathode - to the interface between the two- and single-phase regions. This interface is an evaporation front where liquid water is evaporated into the gas phase and then carried away via gas phase transport.

4. CONCLUSIONS AND OUTLOOK

The present paper review the integrated experimental and modeling efforts currently being made at Penn State EC-Engine Lab to understand and hence predict transport phenomena coupled with electrochemistry in PEM fuel cells. A multi-dimensional CFD model to comprehensively simulate cell performance has been created, and a basic study of two-phase flow and multi-component transport in air cathodes at high current densities was also carried out. This two-phase model is equally applicable to the air cathode of a direct-methanol fuel cell (DMFC) where the two-phase region is even more extensive due to large electro-osmotic and diffusion fluxes of liquid water from the DMFC anode. Similarly, the DMFC anode, where the liquid phase is methanol aqueous mixture and the gas phase is product carbon dioxide, can be treated by the present model.

Future work will include:

- (i) Integrate the two-phase cathode model into the three-dimensional full-cell CFD model to examine overall cell performance at high current densities. This integration will also permit addressing the coupling between the water content and the water activity determined by state of water at the membrane/cathode interface. In other words, the liquid water formation within the cathode will in turn affect the water transport within the membrane and hence its ionic conductivity and ohmic potential drop.
- (ii) Combine the two-phase model and three-dimensional CFD model to properly assess the beneficial effects of an interdigitated flow field design on cell performance in the high current density regime.
- (iii) Perform quantitative comparisons between the numerical predictions and experimental data of species composition and current density distributions being obtained at our laboratory.
- (iv) Develop a two-phase flow model for a whole direct-methanol fuel cell.

ACKNOWLEDGMENTS

This paper was prepared with the support from DOE Office of Advanced Automotive Technologies under cooperative agreement No. DE-FC02-98CH10954, Sandia National Laboratories under Contract No. BF-6597, Commonwealth of Pennsylvania, and Penn State University. The author is also grateful to his research associates and students, Z.H. Wang, Sukkee Um, W.B. Gu, and X.O. Chen for their help.

REFERENCES

1. K.B. Prater, *J Power Sources*, Vol.51, pp.129-144 (1994).
2. S. Gottesfeld, "Polymer Electrolyte Fuel Cells," in *Advances in Electrochemical Science and Engineering*, C. Tobias et al. eds., Vol.5, pp.195-301, John Wiley and Sons, New York (1997).
3. T.E. Springer, M.S. Wilson, and S. Gottesfeld, *J. Electrochem. Soc.*, Vol.140, pp.3513-3526 (1993).
4. S. Gottesfeld, T. Rockward, T.E. Springer and T.A. Zawodzinski, Abstract No.882, *193rd Mtg. of Electrochemical Society*, San Diego (1998).
5. F.N. Buchi and S. Srinivasan, *J. Electrochem. Soc.*, Vol.144, pp.2767-2772 (1997).
6. D.M. Bernardi and M.W. Verbrugge, *J. Electrochem. Soc.*, Vol.139, pp.2477-2491 (1992).
7. J.-T. Wang and R.F. Savinell, *Electrochimica Acta*, Vol.37, pp.2737-2745 (1992).
8. T.F. Fuller and J. Newman, *J. Electrochem. Soc.*, Vol.140, pp.1218-1225 (1993).
9. T.V. Nguyen and R.E. White, *J. Electrochem. Soc.*, Vol.140, pp.2178-2186 (1993).
10. V. Gurau, H. Liu and S. Kakac, *AIChE J.*, Vol.44, pp.2410-2422 (1998).
11. J.S. Yi and T.V. Nguyen, *J. Electrochem. Soc.*, Vol.146, pp.38-45 (1999).
12. T.V. Nguyen, presented at *195th Mtg. of Electrochemical Society*, May 4-7, Seattle (1999).
13. C.Y. Wang, Z.H. Wang and Y. Pan, in *Proc. of IMECE99*, ASME, New York (1999).
14. S. Surampudi, S.R. Narayanan, E. Vamos, H. Frank, G. Halpert, A. Laconti, J. Kosek, G.K. Surya, and G.A. Olah, *J. Power Sources*, Vol.47, pp.377 (1994).
15. G. Halpert, S.R. Narayanan, T. Valdez, W. Chun, H. Frank, A. Kinder and S. Surampudi, "Progress with the Direct Methanol Liquid-Feed Fuel Cell System," in *Proc. of 32nd IECEC-97*, Vol.2, pp.774-778 (1997).
16. X. Ren, M.S. Wilson and S. Gottesfeld, *J. Electrochem. Soc.*, Vol.143, pp.L12-L15 (1996).
17. D. Weng, J.S. Wainright, U. Laudau and R.F. Savinell, *J. Electrochem. Soc.*, Vol.143, pp.1260-1263 (1996).
18. X. Ren, W. Henderson and S. Gottesfeld, *J. Electrochem. Soc.*, Vol.144, pp.L267-L270 (1997).
19. S. Um, C.Y. Wang and K.S. Chen, *J. Electrochem. Soc.*, submitted for publication (1999).

20. E.A. Ticianelli, C.R. Derouin, A. Redondo and S. Srinivasan, *J. Electrochem. Soc.*, Vol.135, pp.2209 (1988); E.A. Ticianelli, C.R. Derouin and S. Srinivasan, *J. Electroanal. Chem.*, Vol.251, pp.275 (1988).
21. C.Y. Wang and C. Beckermann, *Int. J. Heat Mass Transfer*, Vol.36, pp.2747-2758 (1993).
22. C.Y. Wang and P. Cheng, *Int. J. Heat Mass Transfer*, Vol.39, pp.3607-3618 (1996).
23. C.Y. Wang, *Numerical Heat Transfer B, Fundamentals*, Vol.31, pp.85-105 (1997).
24. C.Y. Wang and P. Cheng, "Multiphase Flow and Heat Transfer in Porous Media," *Advances in Heat Transfer*, Vol.30, pp.93-196, Academic Press (1997).
25. C.Y. Wang, "Modeling Multiphase Flow and Transport in Porous Media," in *Transport Phenomena in Porous Media*, eds. by D.B. Ingham and I. Pop, pp.383-410, Elsevier Science (1998).
26. S.V. Patankar, *Numerical Heat Transfer and Fluid Flow*, Hemisphere Publishing Corporation (1980).

MATHEMATICAL MODEL DEVELOPMENT FOR PEM FUEL CELLS

Hongtan Liu, Lixin You and Tianhong Zhou

Department of Mechanical Engineering

University of Miami

Email: hliu@miami.edu; Fax (305) 284-2580

Keywords: PEM fuel cells, fuel cell models, proton exchange membrane, polymer electrolyte membrane

ABSTRACT. This paper summarizes the recent PEM fuel cell models developed at the University of Miami. In the last a few years, several mathematical models for PEM fuel cells have been developed at the University of Miami. The main thrust has been the development of models that are capable of simulating fuel cell performance without prescribing arbitrary/approximate boundary conditions at the interfaces between the different layers of the fuel cell sandwich. By solving transport equations and the equations for electrochemical reactions and current density with membrane phase potential in unified domains, polarization curves under various operating conditions were obtained. The modeling results also show the variations of species concentration and current density in the directions of the channels and across the channels.

1. INTRODUCTION AND BACKGROUND

Recently, several mathematical models for fuel cell performance simulation have been developed. One of the first models was developed by Springer *et al.* [1]. It is an isothermal one-dimensional steady-state model. This model provided useful insight into the fuel cell's water transport mechanisms and their effect on cell performance. Later they developed a model to study the behavior of the cathode over the whole range of current density [2]. Bernardi and Verbrugge [3] developed a model that takes into account of many of the important phenomena. There are various other one-dimensional models, such as the models developed by Bernardi and Verbrugge [4], Ridge and White [5], Verbrugge and Hill [6,7], *etc.* These models provided valuable information and the first step toward fuel cell modeling.

Based on the one-dimensional models, some two-dimensional models have been developed. The 2-D models deal mostly with the transport phenomena in the domain consisting of membrane, catalyst layers and the gas diffusers. The concentrations/partial pressures in the gas channels are assumed more or less arbitrarily, or averaged values are used as boundary conditions at the interface with the gas diffusers. The work of Singh *et al.* [8] assumed linear variations of the chemical species at the gas channel-gas diffuser interfaces, and the model describes phenomena exclusively in the domain consisting of the membrane, catalyst layers and the gas diffusers. Fuller and Newman [9] solved the equations for the transport phenomena across the fuel cell sandwich at certain locations along the gas channel, while the gas outside the gas diffusers is assumed to be uniform composition in the direction across the cell. Nguyen and White [10] used algebraic expressions for the concentrations along the electrodes, while Amphlett *et al.* [11], in their modeling of the Ballard IV fuel cell assume averaged partial pressures along the gas channels.

Most of the models deal with the processes in the membrane, the catalyst layers and the diffusion layers. They prove to be very useful for prediction some phenomena in fuel cells and provided valuable insight information on the fundamental mechanisms of some of the processes. However all the previous models have their limitations due to the approximate boundary conditions prescribed at the interfaces between the gas diffuser and the gas channels, or between the catalyst layer and the gas diffusers.

In order to facilitate our discussion, two schematic drawings are provides here in Fig.1. Figure 1 (a) shows the PEM fuel cell sandwich in the gas channel direction and Figure 1 (b) shows the sandwich in the direction across the gas channels. The fuel cell sandwich consists of two collector plates, two gas channels, two diffusion layers, two catalyst layers, and a membrane.

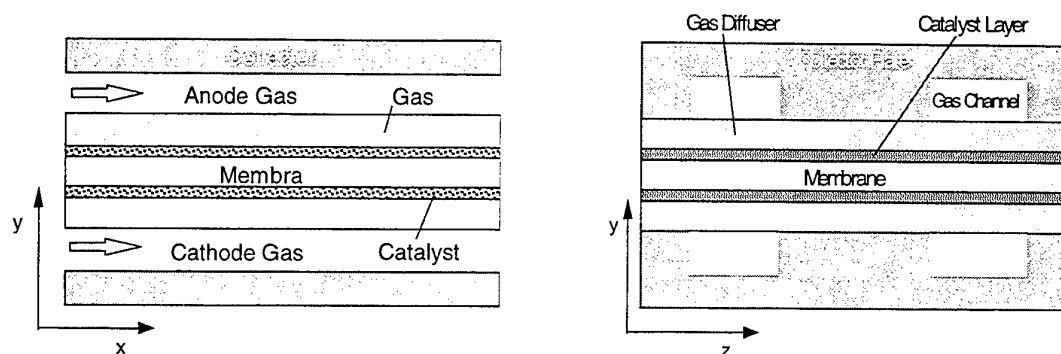


Fig. 1. Schematic of the PEM fuel cell sandwich. (a) in gas channel direction; (b) across the channel direction.

All the earlier models used some artificial boundary conditions at the interface between the gas diffusers and the gas channels. It is obvious that the concentrations of the reactants along the interfaces at any point $x \neq 0$, depend on the reaction rate in the catalyst layers from the entrance to the point x . Imposing some artificial values along the interface will obviously introduce errors and these errors become very significant when the models are used to simulate large fuel cells.

Two-dimensional models will introduce significant errors when applied to real-life-size fuel cells. The dimensions in most the 2-D models are the x - and y -directions (Fig. 1-a). In these models the effects of the third dimension (the z -direction) are neglected. The reaction rate at any location depends on the partial pressure of the reactants in the catalyst layer. Thus the current density in the z -direction will not be uniform. From Fig. 1-b, it is evident that the concentration of reactants in the catalyst layers can not be uniform. The concentration of the reactants at a point under the collector's "land area" will definitely be lower than the point directly under the gas channels due to greater diffusion barrier.

The reaction rate in the catalyst layer mainly depends on the reactant adsorption interaction with the catalyst and the active surface area of the catalyst. The adsorption rate in turn depends on the reactant concentrations in the catalyst layer, and thus depends on the concentrations at the interface between the diffusion layer and the gas channel. On the other hand, the concentrations at this interface depend on the reaction rate in the catalyst layer. As mentioned above, in all the published models, either constant values or some predetermined variations of the concentrations were imposed at this interface. This obviously introduced some subjective arbitrariness.

In order to eliminate the arbitrary, or approximate boundary conditions, the governing equations (continuity equation, momentum equations, species concentration equations, and the electrochemical reaction equations) have to be solved in unified domains consisting of the gas channels, the porous diffusion layers, the catalyst layers, and the membrane. The only independent variables for specified geometry and material should be the mass flow rates, temperature, humidity and the partial pressures of the species at the gas channel inlets, the external circuit resistance, and the temperature and flow rate of the cooling (or heating) agent. These are actually the parameters that can be controlled in real-life fuel cell operations or in laboratory experiments.

2. MATHEMATICAL MODELS

In recent years several mathematical models for PEM fuel cells have been developed at University of Miami. These models include a two-dimensional model in the channel direction and across the fuel cell sandwich (x - y directions in Fig.1-a), a model perpendicular to the channel and across the fuel cell sandwich (z - y directions in Fig.1-b), a two-phase flow model and a three-dimensional model. The details of model development and results for the first model was presented in a recent paper in the *AIChE Journal* [12], and the second model was presented in a paper to appear in the *J. Applied Electrochemistry* [13]. The results of the two-phase flow model and the three-dimensional model have not been published yet. In this presentation, we will not present any of the models in detail, but rather provide a very brief discussion on how the unified approach was implemented in the models.

At this stage, the crossover of oxygen and hydrogen through the membrane and liquid water in the flow channels are neglected. Thus we can divide the fuel cell into three unified domains: (a) the cathode channel, gas diffuser and the

catalyst layer for the humid air and oxygen; (b) the anode channel, gas diffuser and catalyst layer for hydrogen and (c) the membrane and the two catalyst layers for liquid water and proton. Considering isothermal condition, the main governing equations are the continuity equation, momentum equation and the species concentration equations, and they can be presented as follows,

$$\nabla \cdot \mathbf{V} = 0 \quad (1)$$

$$\rho \mathbf{V}(\nabla \mathbf{V}) = -\nabla P + \mu \Delta \mathbf{V} + \mathbf{S}_1 \quad (2)$$

$$\rho \mathbf{V}(\nabla X_k) = D_{\text{eff}} \Delta X_k + \mathbf{S}_2 \quad (3)$$

where \mathbf{S}_1 is the source term in the momentum equation and equals the force exerted by the porous medium on the fluid; \mathbf{S}_2 is the source term in species equation. At the cathode, the source terms for the oxygen, liquid water and protons are:

$$-\frac{1}{4F} j_c, \frac{1}{2F} j_c, -\frac{1}{F} j_c \quad (4)$$

and at the anode, the source terms for hydrogen and protons are:

$$-\frac{1}{2F} j_a, \frac{1}{F} j_a \quad (5)$$

where :

$$j_a = a j_0^{\text{ref}} \left(\frac{X_{\text{H}_2}}{X_{\text{H}_2\text{ref}}} \right)^{\frac{1}{2}} \left[e^{\frac{\alpha_a F}{RT} \eta} - \frac{1}{e^{\frac{\alpha_c F}{RT} \eta}} \right] \quad (6)$$

$$j_c = a j_0^{\text{ref}} \left(\frac{X_{\text{O}_2}}{X_{\text{O}_2\text{ref}}} \right) \left[e^{\frac{\alpha_a F}{RT} \eta} - \frac{1}{e^{\frac{\alpha_c F}{RT} \eta}} \right] \quad (7)$$

It is evident that the governing equations at different parts of a unified domain have the same general forms and the only difference lies in the source terms. Thus we can solve the equations in the coupled domains without prescribing boundary conditions at the various interfaces.

3. TYPICAL MODELING RESULTS

Figure 2 shows a typical result of the oxygen molar fraction distribution at the interface between the cathode gas channel and gas diffuser at different operation current densities. It is obvious that the oxygen concentration is neither constant nor linear along the channel as assumed by other models. The earlier fuel cell models use oxygen mole fraction or partial pressure distribution as input data. As stated earlier, reaction rate depends on oxygen concentration, and thus the "guessed" oxygen distribution will obviously result in current density distribution dependent on the "guessed" boundary conditions. Our coupled approach enabled us to *calculate*, rather than *prescribe* the oxygen concentration distributions, thus eliminate errors introduced by the approximate boundary conditions.

Figure 3 shows a typical result of current density variations along the flow direction. It can be seen that current density decreases along the flow direction, and the variation is not linear. If we had prescribed oxygen concentration boundary condition at the interface, the current density variation would then artificially mimic the boundary condition provided.

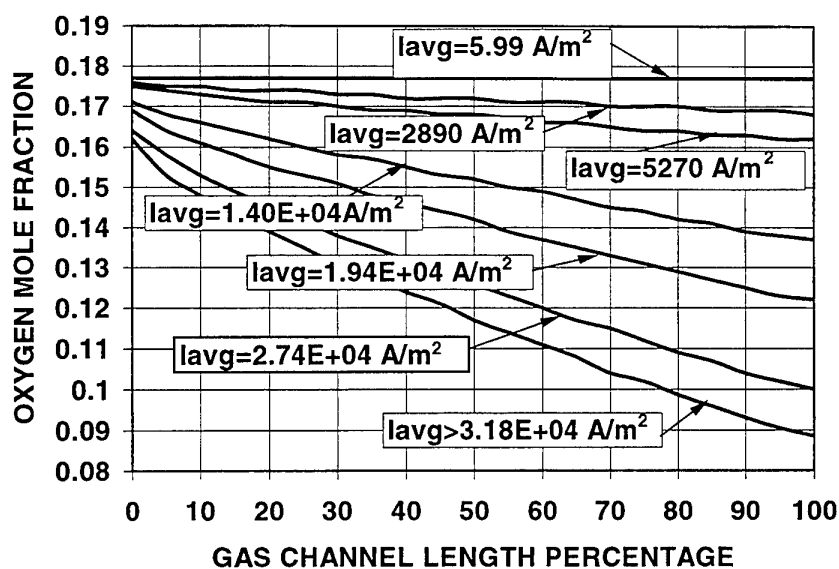


Figure 2. A typical result of oxygen molar fraction variation at the interface between the cathode channel and the gas diffuser [12]

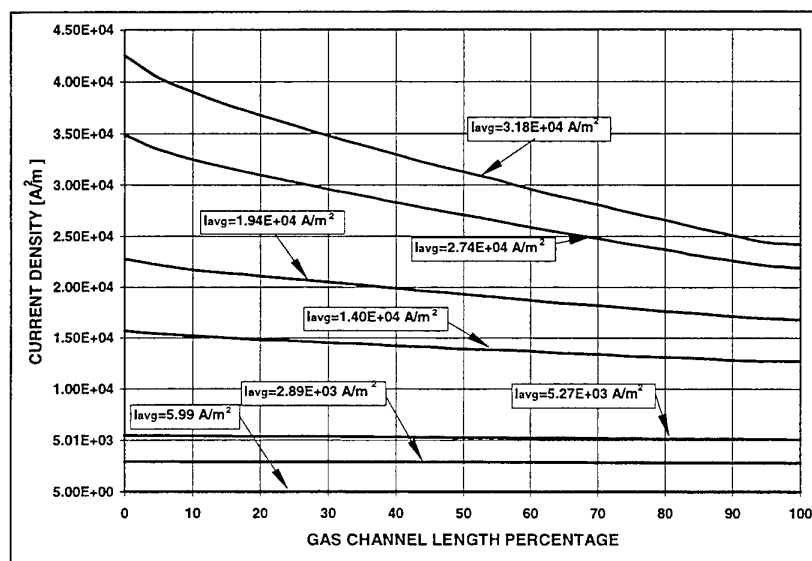


Figure 3. Current density variations along the flow direction at different average current densities [12]

Figure 4 is a typical result when the two-dimensional model in the across the flow direction is used to study the effects of flow field designs. Figure 4-a is the oxygen concentration distribution for straight-channel flow field, and Figure 4-b is for interdigitated flow field. The result clearly shows the effect of the third dimension and the performance enhancement of the interdigitated flow fields.

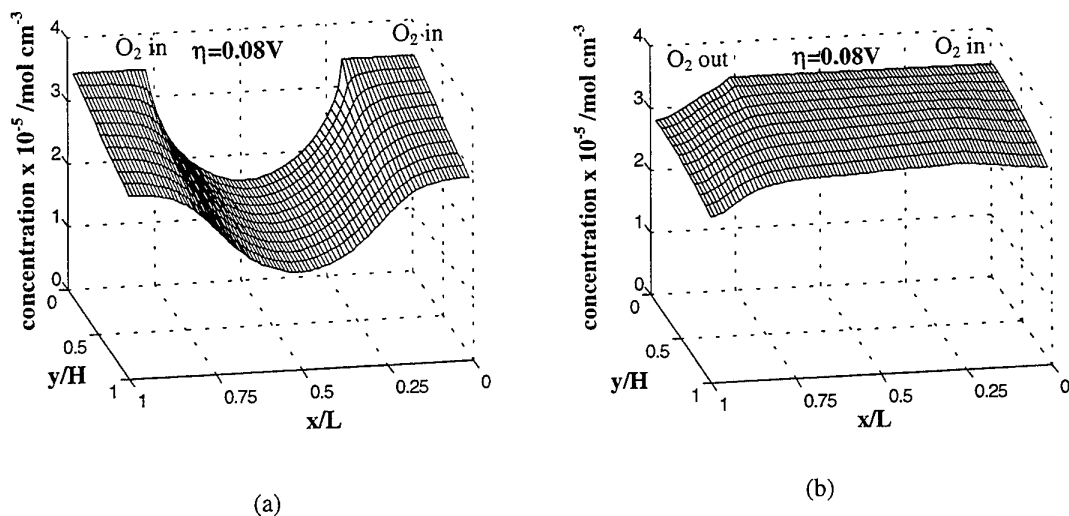


Figure 4. Comparison of oxygen concentration distribution in the gas diffuser. (a) Conventional flow field; (b) interdigitated flow field [13]

Figure 5 is a comparison between the performance of fuel cells with conventional flow fields and interdigitated flow fields. It is obvious that the interdigitated flow field significantly outperforms the conventional one. In this case, the limit current density for a fuel cell with interdigitated flow fields is approximately three times that for a fuel cell with a conventional flow field. The modeling result shows that the enhancement of mass transfer of the interdigitated flow field has a significant effect on fuel cell performance. This obviously is very important in fuel cell applications, especially for automotive applications, where specific power and power density are of primary importance.

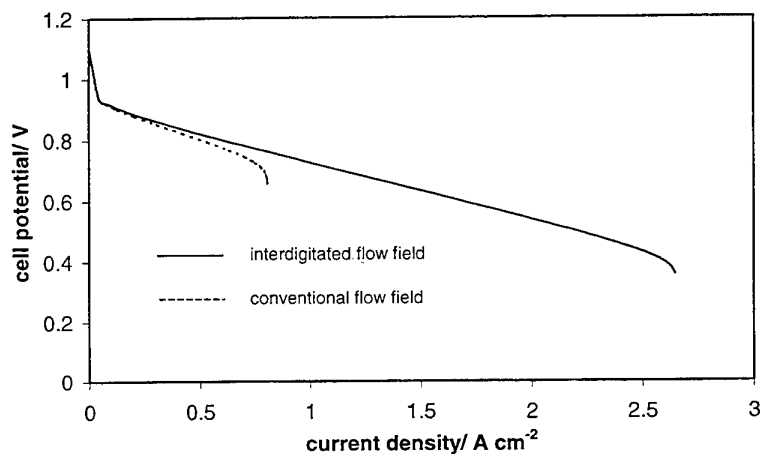


Figure 5. Polarization curves of fuel cells with conventional and interdigitated flow fields [13]

Figure 6 shows a set of two-phase flow modeling results of oxygen, nitrogen and water vapor concentrations. Figure 6-a shows the oxygen concentration field. The oxygen concentration decreases towards the boundary due to electrochemical reaction occurred at the boundary (catalyst layer). It can be seen that in the gas diffuser, the influence of convection is low and the concentration field is dominated by diffusion. Figure 6-b shows water vapor

concentration is higher at the catalyst boundary than at the diffuser-channel boundary. This is clearly due to water generation in the catalyst layer. Figure 6-c shows the nitrogen concentration increases toward the boundary, and the concentration gradient is also large, which can be easily explained by the consumption of oxygen. When the partial pressure of oxygen decreases, the partial pressure of nitrogen must increase to keep the total pressure almost constant. Please note that the partial pressure of vapor also plays a role, though a minor one.

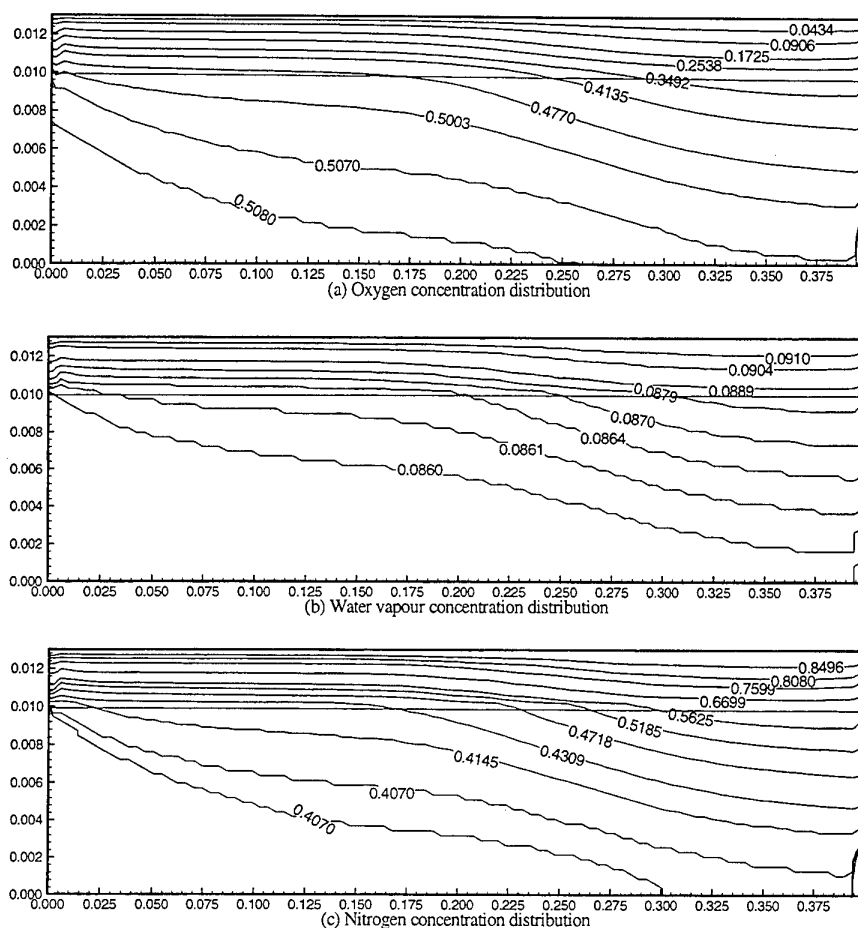


Figure 6. Typical result of the two-phase flow model: species concentration field.

Figure 7 is a typical oxygen concentration profile along the longitudinal section (x - y in Figure 1) obtained by the 3-D model. Figure 8 is produced here to show the oxygen concentration distribution at different current densities. It is clearly shown from these two figures that the oxygen concentration changes in the three different sub-domains: the flow channel, the gas diffuser and the catalyst layer. In the channel, the oxygen concentration changes gradually due to convection mixing. In the gas diffuser, the dominant mass transfer mechanism is diffusion (for single-phase flow model), so the profiles are straight lines. The steep slope is due to the higher mass transfer resistance of the porous media. In the catalyst layer, oxygen is consumed. It is clear that the slope is higher close to the interface due to higher reaction rate and lower close the membrane where reaction rate is lower. It is also clear from the figures that oxygen is consumed along the flow direction. If one examine the graph closely, one can find that the spaces between the lines at different x values decreases. This is due to the fact that reaction rate is higher close to the inlet of the channel and decreases along the channel.

In Figure 8, we see large changes of oxygen concentration across each of the layers of fuel cell sandwich at large current densities. In the very earlier models, constant oxygen concentration was prescribed at the interface between

the gas diffuser and the catalyst layer. Figure 8 shows that the concentration can decrease to only 25% of the bulk value. In the later models, the gas diffuser was taken as part of the solution domain, thus the concentration at the interface between the channel and the gas diffuser was assumed constant. It is evident from Figure 8 that such assumptions also certainly introduce significant errors at large current densities.

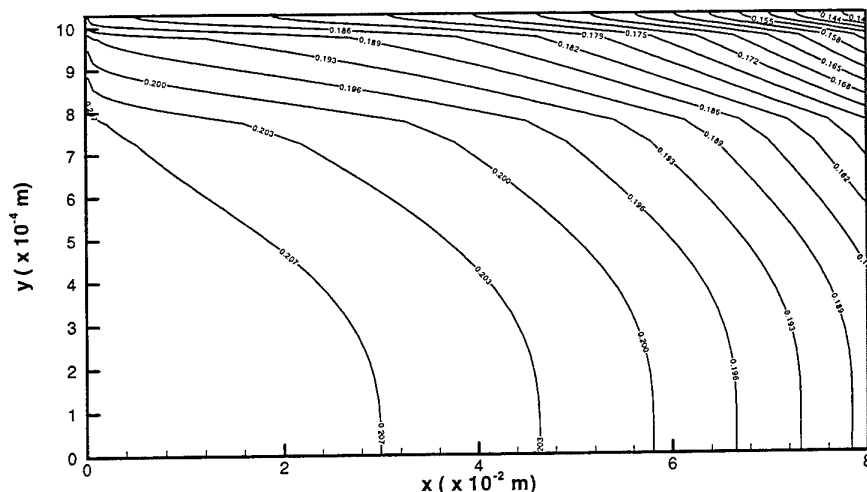


Figure 7. Typical oxygen concentration contours across the cathode gas channel, gas diffuser and catalyst layer. Base operating condition: gas diffuser porosity $\varepsilon = 0.4$, isothermal temperature $T = 353\text{ K}$, inlet air velocity $U_i = 0.35\text{ m/s}$, inlet pressure $= 3\text{ atm}$, current density $= 820\text{ A/m}^2$, stoichiometric ratios $= 3.195$.

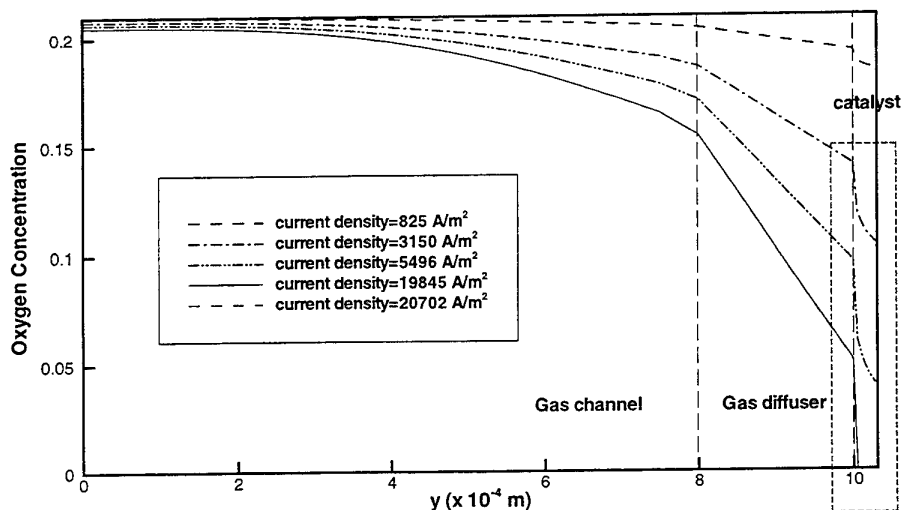


Figure 8. Typical oxygen concentration profiles with different current densities. Base operating condition: gas diffuser porosity $\varepsilon = 0.4$, isothermal temperature $T = 353\text{ K}$, inlet air velocity $U_i = 0.35\text{ m/s}$, inlet pressure $= 3\text{ atm}$.

Figure 9 shows a result of current density distribution obtained by the 3-D model. This figure shows the current variations both in the channel direction and in the cross flow direction. In the channel direction, oxygen concentration decreases, and so does the current density. In the cross the channel direction, the “land area” of the collector plate blocks the oxygen transfer to the reaction site under it, so the current density is lower there. The

current density obtained in any experiments is the average value of the across the whole active area of a fuel cell. Figure 9 shows that for a large fuel cell, one-dimensional and two-dimensional models can not provide realistic performance simulations without using some "guessed" average parameter values.

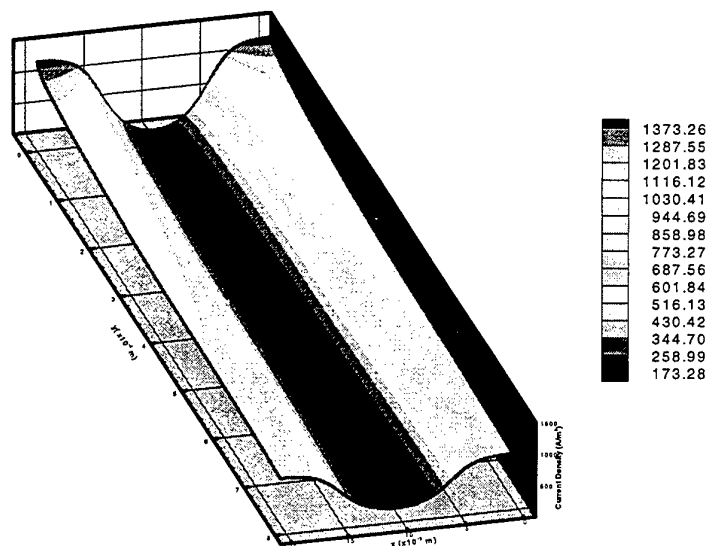


Figure 9. Typical current density contour across the oxz plane (in Figure 2). Base operating condition: gas diffuser porosity $\varepsilon = 0.4$, isothermal temperature $T = 353$ K, inlet air velocity $U_i = 0.35$ m/s, inlet pressure = 3 atm.

4. CONCLUSIONS

In the last a few years, several mathematical models for PEM fuel cells have been developed at the University of Miami. By a unified approach, we were able to use the models to simulate fuel cell performance without prescribing arbitrary/approximate boundary conditions at the interfaces between the different layers of the fuel cell sandwich. This approach eliminates the errors introduced by approximate boundary conditions. By solving transport equations and the equations for electrochemical reactions and current density with membrane phase potential in unified domains, we obtained reactant concentration distribution in each layer of the fuel cell sandwich. Current density variations in both along the channel and across the channel directions were also obtained.

REFERENCES

1. Springer, FE, Zawodzinski, TA & Gottesfeld, S, *J. Electrochem. Soc.*, v.138, 2334-2342, (1991).
2. Springer, FE, Wilson, MS & Gottesfeld, S, *J. Electrochem. Soc.*, v.140, 2178, (1993).
3. Bernardi, DM & Verbrugge, MW, *J. Electrochem. Soc.*, v.139, 2477-2491, (1992).
4. Bernardi, DM & Verbrugge, MW, *AIChE Journal*, v.37, 1151-1163, (1991).
5. Ridge, SJ, White, RE, Tsou, Y et al, *J. Electrochem Soc.* v.136, 1902 (1989).
6. Verbrugge, MW & Hill, RF, *J. Electrochem Soc.* v.137, 886 (1990).
7. Verbrugge, MW & Hill, RF, *J. Electrochem Soc.* v.137, 3770 (1990).
8. Singh, D, Lu, DM & Djilali, N, *Proc. of the First International Energy and Environment Symposium*, Karadeniz Technical University, Trabzon, Turkey, 615 (1996)
9. Fuller, TF & Newman, J, *J. Electrochem Soc.* v.140, 1218, (1993).
10. Nguyen, TV & White, RE, *J. Electrochem Soc.* v. 140, 2178, (1993).
11. Amphlett, JC, Baumert, RM & Mann, BA et al, *J. Electrochem Soc.* v.142, 1, (1995).
12. Gurau, V., Liu, H.T. & Kakac, S., *AIChE Journal*, v.44, 2410-2422, (1997).
13. Kazim, A., Liu, H. T. & Forges, P., Modeling of Performance of PEM Fuel Cells with Conventional and Interdigitated Flow Fields, *J. of Applied Electrochemistry*, accepted. (1999).

HYDROGEN ENERGY AND FUEL CELL POWER PACKS

Moses L. Ng

Energy and Resources Laboratories
Industrial Technology Research Institute
E-mail: F761211@erl.itri.org.tw; Fax (886)-3-582-0435

Yaw-Chung Cheng

Energy and Resources Laboratories
Industrial Technology Research Institute
E-mail: F690256@erl.itri.org.tw; Fax (886)-3-582-0435

Keywords: hydrogen energy, fuel cell power packs, PEM, rechargeable batteries

ABSTRACT. Fuel cells have been used as the prime power generators in space missions and are currently pursued in terrestrial applications because of their high efficiency and low intrusion to the environments. In spite of their success in power plant demonstration projects, fuel cells remain as pre-commercial products although they have better performance in on-site applications. The combination of hydrogen stored in cartridges with or without adsorbing materials and PEM fuel cells called fuel cell power packs may be used to replace the rechargeable batteries currently in use.

1. INTRODUCTION

In recent years, fuel cells have generated great interests among scientists, engineers, industrial developers as well as educators perhaps because of the innovation and yet not far from traditional methods of power generation. Above all, fuel cells offer much improvement both in energy conversion efficiency and in environmental benefits. Hence, ever since their success in space missions in the 60's, there have been a lot of efforts trying to bring this technology to terrestrial applications. However, like every new technology, there are more problems than anticipated which make fuel cells hard to be realized, although several demonstration projects have been successfully performed to show the feasibility of their principles of operations. Among these success are the 4.5 MW and 11 MW phosphoric acid fuel cell power plants in Goi of the Tokyo Electric Power Company, the 2 MW molten carbonate fuel cell power plant by the Energy Research Corporation, and several power plants with smaller capacity such as the 250 kW molten carbonate fuel cells by M-C Power Company and the 100 kW solid oxide fuel cells by the Westinghouse Corporation. By far, the most notable program to date is the fleet of 200 kW on-site power plants using phosphoric acid fuel cells built by ONSI Corporation of the International Fuel Cells, and the program is currently under worldwide demonstration/evaluation. Experimentation of one of such products was performed by a collaboration of the Power Research Institute of the Taiwan Power Company and the Energy and Resources Laboratories of the Industrial Technology Research Institute [1] and the results have been reported elsewhere [2].

The high power density exhibited by the recently developed Proton Exchange Membrane (PEM) fuel cells has attracted a lot of attention for their use in mobile applications such as traction in automobiles and as portable power generators. But the low tolerance of carbon monoxide limits the use of this kind of fuel cells on the energy source commonly available. At present, hydrogen stored in pressurized cylinders is demonstrated to fuel PEM fuel cells for powering buses in the cities of Chicago and Vancouver. On a smaller scale, hydrogen adsorbed in the form of metal hydrides has been shown to power PEM fuel cells in simple and safe design and operations that can be used in the future as a replacement of rechargeable batteries. Here, the power generation and the energy storage mechanisms are separately conducted by fuel cells and hydrogen cartridges respectively. Hence, the combination of hydrogen storage and PEM fuel cells which is sometimes called the fuel cell power pack offers shorter time of recharge and longer time of usage between charges. On reviewing the state-of-the-art of fuel cells, as well as the production, the storage and transportation of hydrogen, this paper reports a study of the make of fuel cell power packs in Taiwan.

2. PRINCIPLES OF FUEL CELLS

Fuel cells are direct energy conversion devices that convert the chemical energy of fuels into electricity through

electrochemical reactions without the complicated combustion and electromechanical processes. Hence, their energy conversion efficiency is high and they are relatively benign to the environment. Like batteries, fuel cells consist of two electrodes separated by an ion-conducting electrolyte. Electrons and ions are generated by electrochemical reactions on one of the electrodes. Electrons are conducted through an external conduit and ions flow through the electrolyte, both destined to the opposite electrode where they are combined, thus completing the oxidation-reduction process. But unlike batteries, these electrons and ions are continuously generated as long as fuel is continuously fed, hence the power generating and energy storage mechanisms are separated, as mentioned above. To date, five major types of fuel cells are developed. Their materials of construction and the operating conditions are different and thus find different applications. Tables 1 and 2 summarize the characteristics and the major application of these fuel cells.

Table 1: Characteristics and Applications of Various Types of Fuel Cells

TYPE	Alkaline (AFC)	Proton Exchange Membrane (PEMFC)	Phosphoric Acid (PAFC)	Molten Carbonate (MCFC)	Solid Oxide (SOFC)
Electrolyte	Potassium hydroxide	Polymer	Phosphoric acid	Molten carbonate	Stabilized zirconia
Anode	Pt/C	Pt/C	Ni/Cr Al	Ni Zr	Pt/C
Charge Carrier	OH^-	H^+	CO_3^{2-}	O_2^{2-}	H^+
Cell Voltage	< 0.97 v	< 0.80 v	< 0.85 v	< 0.90 v	< 0.80 v
Cell Material	Synthetic resin	Carbon	Carbon	Steel	Ceramic
Operating Temp	60 ~ 100 °C	80 ~ 100 °C	180 ~ 200 °C	~ 650 °C	~ 1000 °C
Working Pressure	< 4 atm	< 2 atm	< 8 atm	< 8 atm	Atmospheric
System Efficiency	~ 60 %	~ 60 %	34 ~ 45 %	45 ~ 60 %	> 50 %
Reactant	H_2/O_2	H_2/O_2	H_2/O_2	H_2/CO_2	H_2/O_2
Raw Fuel or Fuel Treatment System	Pure hydrogen only	Pure hydrogen, methanol	Natural gas, LPG, Methanol, naphtha and light oil	Natural gas, LPG, methanol, coal and petroleum gas	Natural gas, LPG, methanol, coal and petroleum gas
Major Potential Applications	Space, transportation	Space, transportation	Cogeneration, Disperse electric, transportation	Cogeneration, Disperse electric, Central power	Cogeneration, Disperse electric, Central power
Development Status	80 kW	10 kW	11 MW	2 MW	100 kW
Expected Commercial Use	Hydrogen energy era	after 2000	in 1990s	around 2000	after 2000

Among the five major types of fuel cells, alkaline fuel cells are the most matured and is routinely used in space missions at present. However, their use in terrestrial applications are, at the very least not convenient, as carbon dioxide in the air will neutralize the alkaline electrolyte and finally causing the failure of power generation. As can be seen later, most hydrogen is generated from fossil fuels currently, where carbon dioxide is inevitably produced as byproducts. Hence, using this kind of fuel cells would require additional procedure to treat the carbon dioxide both in the fuel gas as well as in the oxidant. Phosphoric acid fuel cells on the other hand, are the most developed fuel cells used in terrestrial power plants. However, because of the relative low power density as well as the amount of platinum used, this kind of fuel cells is not anticipated to be used as power generators in medium or large power plants. In addition, carbon monoxide, which reduces the performance of power generation in this kind of fuel cells, is also produced along with hydrogen generated from fossil fuels such as coal, petroleum or natural gas. This concern limits the use of phosphoric acid fuel cells as the power generators for centralized power plants. Molten carbonate and solid oxide fuel cells are intrinsically more adaptable to fuel gases from coal, petroleum or natural gas because of their material of construction as well as the operating temperature, and are thus more likely to replace the large thermal power plants in the future. The

high operation temperature also makes these fuel cells good candidates for cogeneration of both electricity and heat. However, because of tremendous problems associated, these fuel cells technologies are far from practicality at this stage.

Table 2. Comparison of Applications of Different Kinds of Fuel Cells

POWER PLANT TYPES	UTILIZATION	CAPACITY	AFC	PEMFC	PAFC	MCFC	SOFC
Centralized	Based Load	300 - 900 MW	×	×	×	○	○
	Peak or Swing Load	100 - 300 MW	×	△	△	○	○
Dispersed	Customer Site	10 - 30 MW	×	△	○	○	○
On-site	Factory (By-product Gas and Cogeneration)	100 - 10,000 kW	×	△	○	○	○
	Community (Cogeneration)	500 - 10,000 kW	×	△	○	△	△
	Commercial Buildings (Hotels and Hospitals)	50 - 1,000 kW	×	△	○	×	△
Space	Rockets and Space Shuttle	5 - 50 kW	○	○	×	×	×

○ applicable; △ marginal; × inappropriate

The low operating temperature and high power density makes PEM fuel cells the prime candidate for automobile application for quick startup and compactness. However, the low operating temperature also favors the undesired bonding of carbon monoxide to the catalyst platinum, which in turn tempers the performance on power generation. Hence, until there is improvement of this tolerance of carbon monoxide, and in the method of producing hydrogen for quick response in variation of quantity needed, the pure hydrogen presently used is of limited popularity in large scale applications. On the other hand, using pure hydrogen stored in cylinders with or without hydrogen adsorption materials, fuel cell power packs can replace rechargeable batteries as mentioned above. The challenge now lies in searching more efficient method of hydrogen storage that the energy density of the fuel cell power packs can be extended to compete for the vast market of rechargeable batteries currently in use.

3. HYDROGEN AS AN ENERGY CARRIER

Strictly speaking, hydrogen is not an energy source, but acts as an energy carrier. As in the case of carbon in the carbon-energy cycle, hydrogen combines with oxygen to form water in the case of combustion, thus releasing energy in the form of heat. Alternatively, hydrogen may be passed into the anodes of phosphoric acid or PEM fuel cells, and together with oxygen in the cathodes, the chemical energy in hydrogen turns into electricity directly through electrochemical reactions with high conversion efficiency and low intrusion to the environments. The research in hydrogen used as energy is usually categorized into production, storage/handling and utilization [3]. Most work has been devoted into the production of hydrogen as an alternative energy source. But in fact, equally important are the latter two problems, which in solving them will definitely prompt hydrogen as one of the major constituents in the total energy situation.

Although much effort has been focussed on developing future technology of hydrogen production, currently there is a general surplus of hydrogen in the world market. However, its price is about three times as much as that of natural gas per unit heating value. Most hydrogen currently produced comes from fossil fuels such as natural gas, oil or coal, or as byproducts of petrochemical or chloro-alkaline industries, although hydrogen of high purity is produced by electrolyses of water with low energy conversion efficiency. As fossil fuels are doomed to be extinct in the future, this perhaps prompts the development of electrolysis of water using electricity generated from alternative energy sources such as solar, OTEC, wind, biomass, etc. Other methods includes improvements on traditional method of production of hydrogen from coal and partial oxidation from oil or gas, as well as advanced methods such as radiolysis, thermolysis, high-temperature steam-electrolysis, photo-

electrolysis, catalytic photolysis, biophotolysis, etc [3].

The general perception of the public on hydrogen is clean but unsafe perhaps because of the impression left from the mishap of Hindenburg, the first hydrogen airship. Given proper engineering, hydrogen can be used in the same level of safety comparable to other fuels such as diesel and gasoline, as reflected in the operation of fuel cell buses in Vancouver and Chicago currently. In fact, it is a daily routine that hydrogen is being transported from one place to another in piping of many chemical and petrochemical plants. With less frequent or stand alone usage, hydrogen is usually stored and transported either in pressurized cylinders with or without hydrogen adsorbing materials, or in cryogenic liquid form depending on the quantity in use. There is an added advantage of safety for hydrogen being stored in cylinders in the form of metal hydrides. Because the process of releasing hydrogen from metal hydrides is endothermic and the rate of hydrogen will be reduced as the temperature is lowered, the risk of explosion in the case of leakage is thus drastically reduced. However, the weight fraction of hydrogen adsorbed in many metal hydrides under current development is so low that its practical use is very much limited. Recently, light-weighted materials that adsorb large amount of hydrogen per unit weight such as nanofiber graphite have been developed [4]. This raises the hope of storing hydrogen more effectively, and is especially beneficial to the transportation sector where weight consideration is one of the most important concerns.

4. FUEL CELL POWER PACKS

Metal Hydride Cartridge for Hydrogen Storage

The material chosen for storing hydrogen in this study is an alloy composed of the metal lanthanum and nickel prepared by arc-welding in the ratio of 32.1 to 67.9 by weight giving the molecular formula LaNi_5 . The bulk density is 8.4 g/cc and the hydride becomes $\text{LaNi}_5\text{H}_{6.7}$ after adsorbing hydrogen, giving a theoretical amount of hydrogen adsorbed as 1.53 wt %. Using a Sievert's type vacuum system, the P-C-T diagram showing the performance of hydrogen adsorption and desorption at constant temperature of this metal hydride is shown in Figure 1. It can be seen that the maximum value of H/M is 1.09 and there is a plateau region in the pressure ranging between 0.2 to 0.5 MPa (2 to 5 atmospheric pressure) where it is the main target for adsorbing and desorbing hydrogen using this alloy. It is also noted that there is a hysteresis of pressure during hydrogen adsorption and desorption processes. Hence, hydrogen can be filled under the pressure of about 6 atm and released at around 1 to 2.5 atm. Details of this experimentation can be found elsewhere [5].

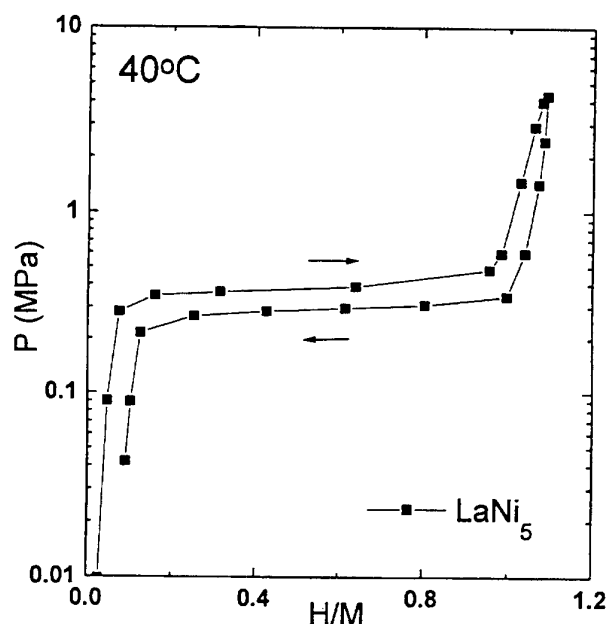


Figure 1. P-C-T diagram of LaNi_5

It is seen that hydrogen adsorption is an exothermic process while desorption is an endothermic one and the flow rate and pressure of these processes is very sensitive to the temperature of operation. Hence, different metals including aluminum and copper were tested to be used as the material for holding the metal hydrides. Aluminum is chosen for its light weight, good heat transfer characteristics and its ease of fabrication while copper for its excellent heat conductive quality. Experiments of releasing hydrogen from these cartridges were performed in the air at ambient temperature of approximately 20 °C, and at 40 °C in water bath. Both hydrogen flow rate and the pressure of the cartridge were measured at regular time intervals and the results of the copper cartridge are summarized in Figures 2 and 3. It is seen that the results of aluminum and copper cartridges are similar, and the hydrogen flow rate is drastically reduced when hydrogen is released in the air at the relative low ambient temperature compared to that released in water bath at elevated temperature. This preliminary result shows that the heat transfer problem is worth further investigation for better designing the hydrogen storage system in the fuel cell power packs.

Experimentation on Prototypes

It can be seen in Figures 2 and 3 that the cartridge pressure is very close to atmospheric and even falls below 1 atm when operated at elevated temperature. Hence, the metal hydrides used in commercial hydrogen storage cartridges are usually in the form of AB_2 where the operating pressure is in the range of 5 to 7 atm for easier flow of hydrogen in the channels of fuel cell stacks. With an aluminum cartridge of 5 cm in diameter and 13.5 cm in length weighing 953 g including the metal hydride inside, the whole package is approximately 21 cm x 13 cm x 33 cm totaling a volume close to 9 liters and weighs approximately 3.8 kg. The hydrogen flows from the cartridge to the input of fuel cell stack where its outlet is shut for reasons of economizing hydrogen utilization and safety. Using an electronic load and with a fan force feeding air into the cathodes, the package delivered a net output of 36 Wh operated at a constant voltage of 10.8 v while the gross output is estimated to be 41.5 Wh. Figure 4 shows the power of this fuel cell power pack delivered at constant voltage for close to 180 minutes of operation. Hence the specific energy is calculated as 10.8 Wh/kg and the energy density being 4 Wh/l. It is interesting to note that this fuel cell power pack is able to power a notebook personal computer for a maximum of 90 minutes of continuous operation.

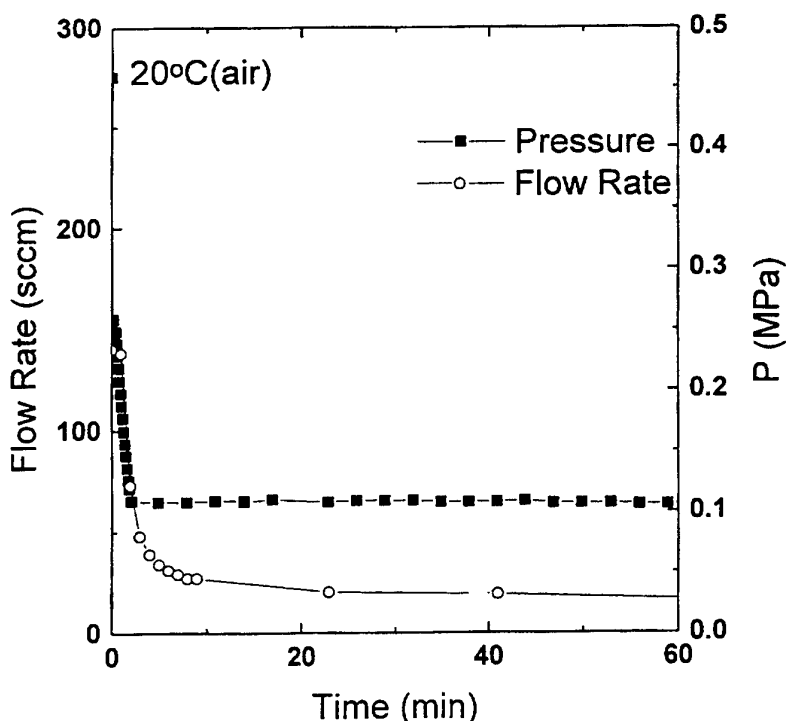


Figure 2. Flow rate and pressure of hydrogen released from copper cartridge in air at 20 °C

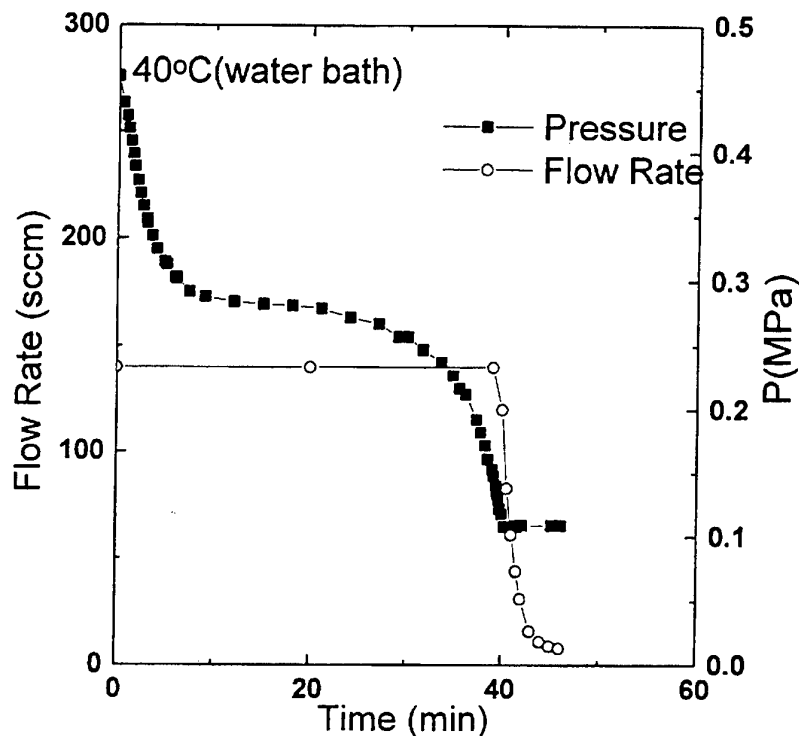


Figure 3. Flow rate and pressure of hydrogen released from copper cartridge in water bath at 40 °C

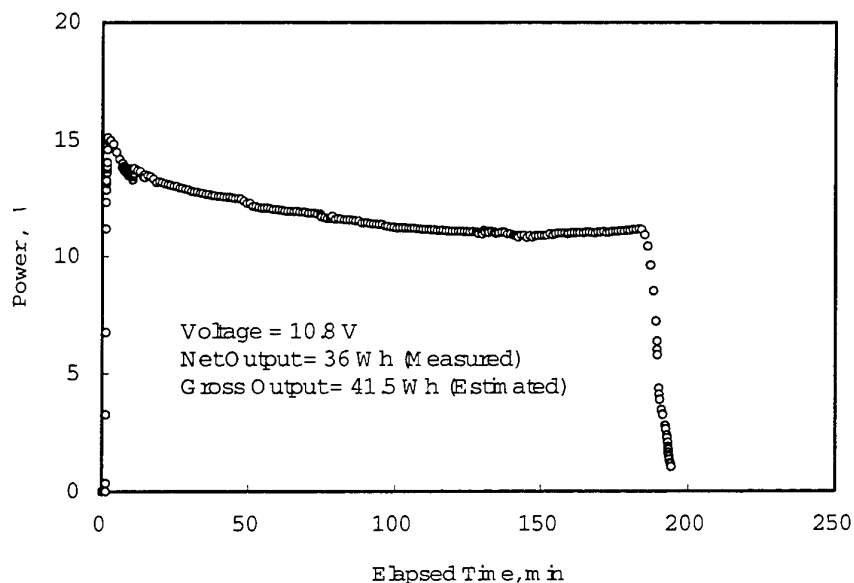


Figure 4. Power delivered from a fuel cell power pack at constant voltage of 10.8 v.

Using two similar cartridges to operate an improved prototype fuel cell stack, a total of 650 minutes of power was generated under similar condition of 10.8 v. With improved packaging, the system is about 18 cm x 15 cm x 24.5 cm totaling a volume of approximately 6.6 liters and weighs approximately 5 kg. A total of net 123 Wh of energy was delivered yielding a specific energy of 24.5 Wh/kg and an energy density of 18.6 Wh/l. It can be seen that the time of operation is markedly increased with even more improvement on the energy density.

5. CONCLUSIONS

1. The principles of fuel cells have been successfully demonstrated both in space and in terrestrial applications. Different fuel cells find their respective applications according to their operating conditions and materials of construction. Because of their high power density and low operating temperature, PEM fuel cells are particularly attractive in mobile applications.
2. Unlike rechargeable batteries, the power generation and energy storage mechanisms are separate in the fuel cell power packs, which makes them possible for extended life of usage and less time of recharge.
3. Although proven in principles, much research has to be done for better design the fuel cell power packs in raising their energy density.

ACKNOWLEDGEMENTS

This study is funded by the Energy Commission of the Ministry of Economic Affairs through its grant 884LK7200. The authors also wish to acknowledge the help from their colleagues Messrs. Chien-Liang Lin and Yao-Sheng Hsu for performing the experimentation mentioned in the paper.

REFEREMNCES

1. Moses L. Ng, "FUEL CELLS – ITRI's Collaborative Program on Clean and Efficient Power Generators", *ITRI Today*, v. 9, pp. 1-4 (1997).
2. Moses. L. Ng, Chien-Liang Lin and Ya-Tang Cheng, "Operation of an On-Site Fuel Cell Power Plant Using Natural Gas with Excess Carbon Dioxide", *J. Power Sources*, v. 74, pp. 159-168 (1998).
3. Carl-Jochen Winter and Joachim Nitsch (eds), *Hydrogen as an Energy Carrier*, Springer-Verlag (1988)
4. A. Chambers, Colin Park, R. Terry K. Baker and Nelly M. Rodriguez, "Hydrogen Storage in Graphite Nanofibers", *The Journal of Physical Chemistry B*, v. 102(22), pp. 4253-4256 (1998).
5. C.P. Chu, *Hydrogenation Properties of LaNi₅-based Multi-Component Alloys and the Application of Metal Hydrides to the Proton Exchange Membrane Fuel Cell*, M.S. Thesis, National Tsing Hua University (1998).

DEVELOPMENT OF PROTON CONDUCTING MEMBRANES FOR HIGH TEMPERATURE DIRECT METHANOL FUEL CELLS

S.N. Lvov¹, X.Y. Zhou², L. Benning², X.J. Wei², M.V. Fedkin²

⁽¹⁾Department of Energy and Geo-Environmental Engineering

⁽²⁾The Energy Institute

The Pennsylvania State University

Email: lvov@psu.edu, Fax: 8148653248

H.R. Allcock, M.A. Hofmann, A.M. Cannon, E.C. Kellam, R.V. Morford

Department of Chemistry

The Pennsylvania State University

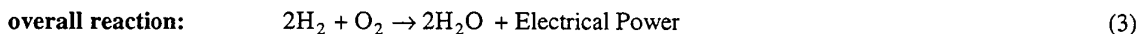
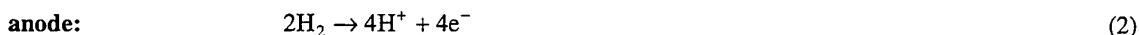
Email: hra@chem.psu.edu, Fax: 8148653314

Keywords: proton conducting membrane, direct methanol fuel cell, methanol crossover

ABSTRACT. Recent development of direct methanol fuel cells operating at elevated temperatures are reviewed emphasizing research on membranes which are suitable for high temperature conditions. Current research on this topic in our laboratory is also described. The most important result is the development of a family of proton conducting membranes based on polyphosphazane polymers. Experimental work has been conducted to characterize these membranes, in particular, in terms of conductivity and methanol crossover. It was found that polyphosphazane membranes can have much smaller methanol cross-over than Nafion 117.

1. DIRECT METHANOL FUEL CELLS

Direct methanol fuel cells present an attractive alternative to hydrogen systems as high energy density electric power sources for portable and transportation applications. The motivation to develop a direct methanol fuel cell is mainly based on three reasons: 1) methanol can be more easily and safely transported, handled and stored than hydrogen; 2) direct methanol systems are more compact and lighter than H₂/O₂ fuel cells; 3) the current infrastructure built for gasoline can be used for methanol. In the case of H₂/O₂ fuel cell [1, 2, 3], the cell reaction can be divided into two parts: a cathode reaction and an anode reaction as follows:



For a direct methanol fuel cell, methanol is oxidized at the anode producing CO₂ and the hydrogen ion:



The direct methanol fuel cell assembly consist of two electrodes, two electrocatalysts, and an ion exchange membrane. The membrane serves three purposes: (1) separation of two half cells, (2) support for the electrocatalyst, and (3) as an electrolyte. There are two technical obstacles impeding the development of direct methanol fuel cells. The first one is the non-availability of a less costly, but sufficiently active, anodic electrocatalyst as an alternative to the most commonly used Pt-Ru alloy. The second problem is that the membranes that are being currently employed, such as Nafion, have a substantial methanol crossover. If methanol diffuses across the membrane and arrives readily at the cathode it seriously decreases the cathode performance, and hence, decreases the overall fuel cell efficiency. The crossover reaction is given by:



Because the crossover reaction competes with the oxygen reduction reaction (1) at cathode, the rate of the crossover reaction is equivalent to the loss of current density.

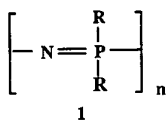
To overcome the first problem, Savinell et al. [4] proposed to increase the cell operating temperature up to 200°C. Operating a fuel cell at elevated temperatures can accelerate the electrochemical reactions and depress the electrode poisoning. Thus, the quantity of precious alloys such as Pt/Ru loaded on the electrodes can be reduced or nonprecious alloys can be used instead of Pt/Ru alloy.

Zelenay et al. [5] and Ren et al. [6] at Los Alamos National Laboratory investigated raising the temperature of direct methanol fuel cells with Nafion membranes. They tested the fuel cells at temperatures up to 100°C and found improved performance of the fuel cells due to high operation temperatures. However, it has been found that perfluorosulfonic acid polymer electrolytes, such as Nafion, lose conductivity and mechanical strength at temperatures higher than 100°C. In addition, the methanol crossover of Nafion membranes increases with temperature [4, 7] offsetting the benefit of elevated temperature in terms of faster electrochemical kinetics.

The conductivity of Nafion membranes, used in fuel cells, depends on the presence of water to solvate the protons generated by the ionization of the sulfonic acid group. Thus, permeation of water and methanol is inherent for these membranes. Moreover, when these membranes are at temperatures above 100°C and at atmospheric pressure, significant dehydration occurs and the membrane conductance decreases significantly. Wainright et al. [8] and Wang et al. [9] proposed to use polybenzimidazoles (PBI) as proton conducting membranes in fuel cells. They found that PBI membranes are thermally stable at temperatures higher than 200°C [9] and were not permeable to water and much less permeable to methanol than Nafion [8, 9, 10, 11, 12]. In contrast to Nafion, the conductivity of the PBI membranes increased with increasing temperature [8]. Fuel cells were operated at elevated temperatures up to 200°C and atmospheric pressure demonstrating significant increase in the power output. The authors also explored the use of ethanol, 1-propanol, 2-propanol, and trimethoxymethane as alternative fuels to methanol [13, 14]. However, there are other polymer materials that could be better than PBI in terms of thermal stability, mechanic strength, production cost, high temperature conductivity, and methanol crossover.

2. POLYPHOSPHAZENE MEMBRANES

We have synthesized and developed new proton transport membranes based on an advanced polymer system, the polyphosphazenes. Polyphosphazenes are macromolecules with the basic structure shown in **1**, in which the backbone contains alternating phosphorous and nitrogen atoms, with two side groups (R) attached to every phosphorus.



More than 700 different polyphosphazenes are known with different R groups and with different combinations of side groups linked to the polymer chain. Certain underlying attributes are associated with the inorganic backbone, especially oxidative, reductive, thermal, and general chemical stability, resistance to high energy radiation, and materials toughness or flexibility. Moreover, different side groups alter the properties over a wide range and allow both molecular and materials characteristics to be tuned to generate specific combinations of properties. In this respect, polyphosphazenes have many advantages over the classical organic polymers [15-17].

Although fluorinated side groups attached to an organic polymer backbone provide good thermal stability, the strongly hydrophobic nature of organo-fluorine groups favors dehydration of the membranes at temperatures somewhere above 80°C. The use of polyphosphazenes for proton conduction allows the materials microstructure to be tailored in order to stabilize water within the polymer framework. This should allow the membranes to be used at temperatures above 100°C and perhaps as high as 200°C.

Incorporation of inorganic elements into a polymer backbone increases the thermo -oxidative and -reductive stability. Thermogravimetric analysis results have shown that a variety of polyphosphazenes are thermally stable at temperatures above 200°C [18]. Based on these data, a polyphosphazene proton-conducting membrane should be able to withstand temperatures in excess of 200°C for long periods of time. Operation at temperatures

this high may allow the use of unreformed fuels, such as methanol. Polyphosphazenes also have an impressive resistance to free radical breakdown because the P-N bond energy is significantly higher than the C-C bond energy in organic polymers and the P-N bond resists homolytic cleavage into free radicals.

In addition to the advantages provided by the inorganic backbone, other attributes can be designed into the polymers by the judicious choice of different side groups. Variations in the types and combinations of different side groups allow the system to be tuned to optimize crystallinity or amorphous character, elasticity or rigidity, hydrophilicity, hydrophobicity, ion conduction, and the domain structure of the material. The balance of hydrophobic and hydrophilic character (i.e., the amphiphilicity) of the polymer can be easily tailored easily by variations in the ratios of hydrophilic and hydrophobic cosubstituent groups. Moreover, the choice of specific side groups can lead to a polymer that undergoes ionic clustering. These hydrophilic ionic aggregation domains will retain water molecules. The hydrophobic groups will also tend to separate into domains and will provide overall physical and thermal stability.

One of the strengths of the polyphosphazenes is the ease with which a wide variety of side groups can be incorporated into the structure. This is accomplished by a macromolecular substitution process based on a reactive polymeric intermediate, poly(dichlorophosphazene). Replacement of the chlorine atoms in the intermediate by organic groups generate a broad range of structures. Cosubstitution to introduce two or more different side groups allows the properties of these polymers to be fine-tuned for many different applications.

The methods of synthesis and post-synthesis modification available for polyphosphazenes also allow high loadings of acidic units throughout the polymeric material. This is an important advantage over polymers that are, for example, sulfonated only on the surface of particles or inside the pores.

3. MEMBRANE CHARACTERIZATION

Conductivity Measurements.

As shown in Figure 1, the system for measuring the ionic conductivity of polymeric membranes employs two external, potential sensing Ag|AgCl electrodes connected to the methanol aqueous solution containing chlorides, such as HCl, NaCl, KCl, and LiCl. The capillaries of the salt bridges were made from very fine PTFE tubes. The influence of the capillaries on the distribution of current density in the conductivity cell was negligible. One end of each of these two capillaries was placed as close as possible to the surfaces of the membrane to minimize the error due to the IR drop. It was found that the fluctuation and drift of the potential drop between the two external electrodes was less than one-thousandth of the average value. It was found that the conductivity values measured in different solutions were different but they were of the same order of magnitude. Since we always wanted to compare the conductivity of the polyphosphazane membranes with Nafion membranes, we were seeking the conductivity values of polyphosphazane membranes with respect to the conductivity of Nafion, rather than the absolute values.

The first obtained results for seven differently prepared aryloxyphosphazenes are summarized in Table 1. The ionic conductivities of these membranes were either very close to or slightly lower than that of a Nafion 117 membrane. The ionic conductivity of the Nafion 117 film was found to be 0.0110 S/cm, which was within the range of published values by other groups, i.e. from 1×10^{-3} to 10^{-1} S/cm

Methanol Crossover Evaluation.

Methanol crossover in polymeric membranes was evaluated with a specially designed, closed-volume vacuum cell (Figure 2). The cell was separated by the polymeric membrane to be tested in two chambers. The upper chamber was filled with air or a mixture of methanol and de-ionized water. The lower chamber was then held evacuated at the beginning of an experiment. The pressure in the vacuum chamber was monitored using a pressure transducer. To distinguish methanol crossover from water crossover, it is required to set the initial vacuum pressure between the vapor pressure of water and the vapor pressure of methanol. Thus, if there is methanol crossover, the pressure in the vacuum chamber increases. If, however, there is only water crossover, the water must exist in the form of liquid and hence the water crossover will not lead to pressure increase. The tests were started with the upper chamber being filled with air. If the pressure of the vacuum chamber did not increase and hence a sealing free of leakage was assured, a mixture of methanol and water was injected into the upper chamber.

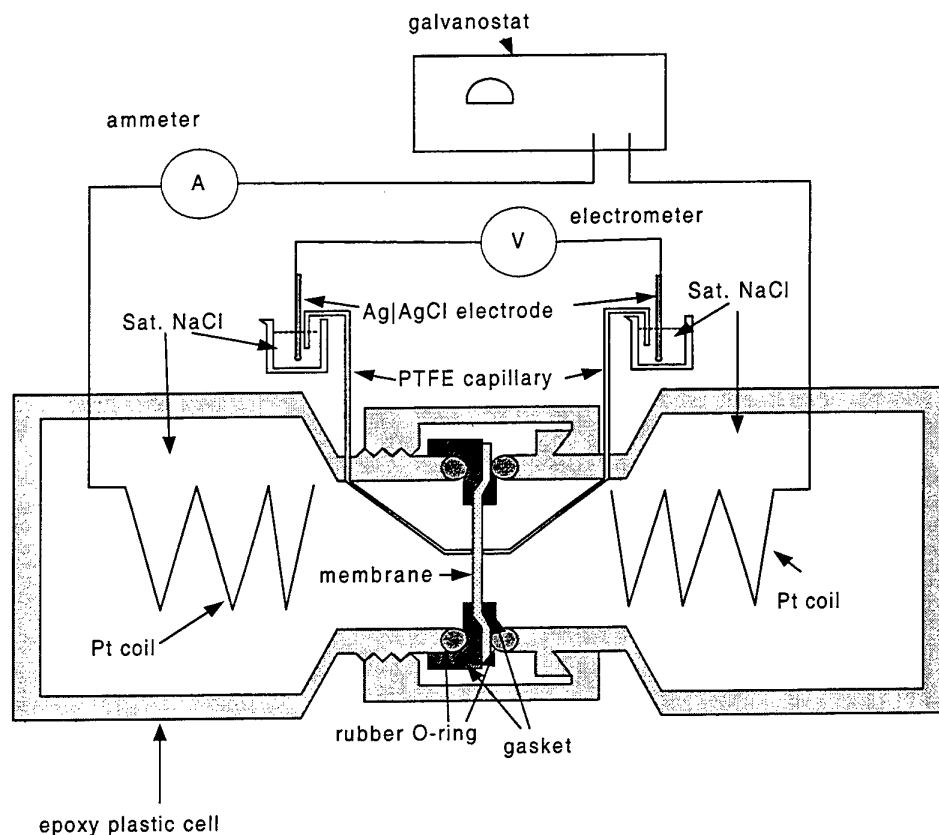


Figure 1. Schematic of the electrochemical cell for measuring proton conductivity of polymeric membranes

Assuming that the vapor of methanol is an ideal gas, the relationship between the rate of methanol entering the vacuum chamber from the upper chamber and the pressure increase can be expressed as:

$$\frac{dn}{dt} = \frac{V_0}{RT} \frac{dp}{dt} \quad (6)$$

where n is the amount of methanol vapor (in moles), V_0 is the volume of the lower chamber, R is the gas constant, and p is the pressure in the initially-evacuated chamber. Typical methanol crossover measurements are presented in Figure 3. The data show that the average methanol crossover rate of the best polyphosphazene membrane is less than 10% of that of the Nafion 117 membrane.

Table 1. Conductivities of Polyphosphazene Membranes Compared to the Conductivity of Acommercial Nafion 117 Membrane.

Membrane Code	Ionic conductivity (S/cm)	Ionic Conductivity of Nafion 117 (S/cm)
Polyphosphazane I	3.27×10^{-3}	1.10×10^{-2}
Polyphosphazane II	4.34×10^{-3}	
Polyphosphazane III	2.29×10^{-3}	
Polyphosphazane IV	3.76×10^{-3}	
Polyphosphazane V	1.36×10^{-3}	
Polyphosphazane VI	1.63×10^{-2}	
Polyphosphazane VII	6.79×10^{-3}	

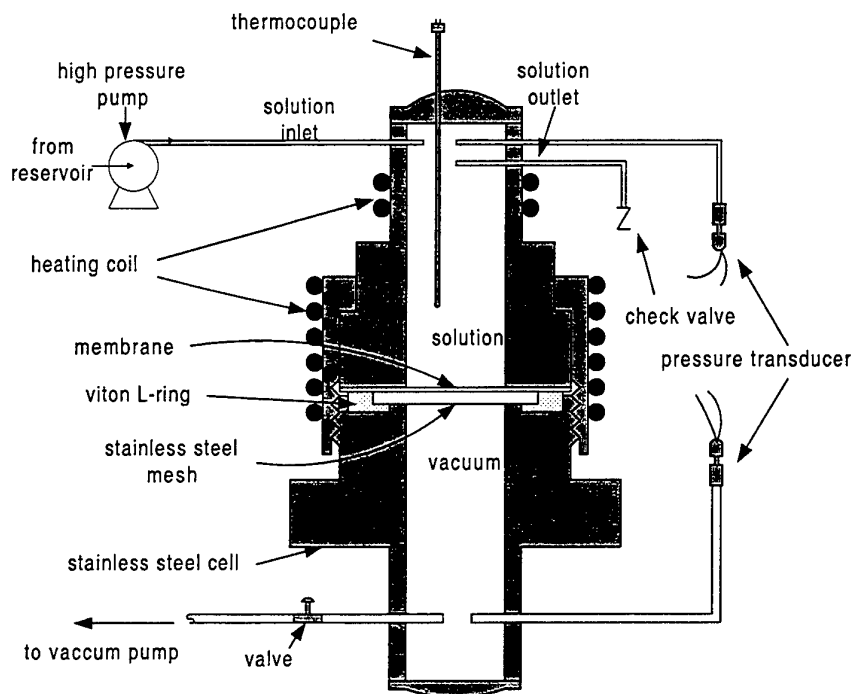


Figure 2. Schematic of the experimental system for measuring methanol crossover.

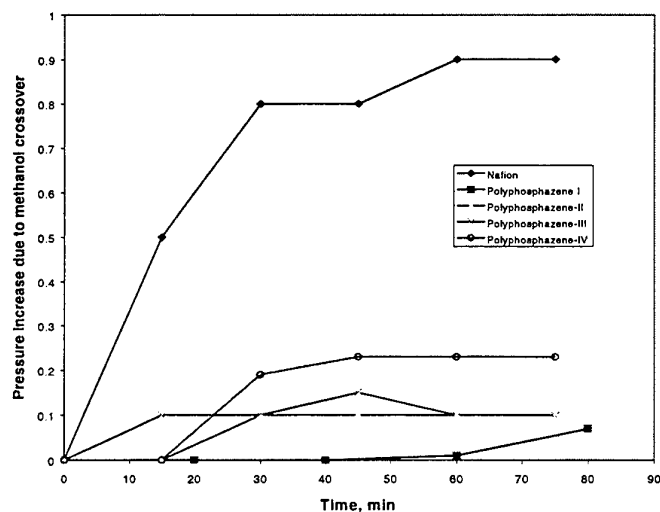


Figure 3. Methanol crossover of a Nafion 117 membrane and polyphosphazene membranes as indicated by pressure increase in a vacuum chamber that was separated from air or methanol solution by these membranes: Nafion: h (thickness) = 0.029 cm, Polyphosphazene-I: h = 0.030 cm, Polyphosphazene-II: h = 0.022 cm, Polyphosphazene-III: h =0.030 cm, Polyphosphazene-IV: h = 0.025 cm.

4. DISCUSSION

We are exploring to employ the recently synthesized and evaluated proton-conducting membranes for direct-

methanol fuel cells. Current membranes based on Nafion have upper temperatures of operation of about 80°C. At higher temperatures, the assembled membranes dehydrate, resulting in a substantial increase in resistivity and loss of mechanical stability. Moreover, Nafion membranes have an unacceptable permeability to methanol. In this work, we are using acidic polymers based on the polyphosphazene system, that will allow fuel cell operation at elevated temperatures up to 200°C. These polymers can be used because of the thermo-oxidative and reductive stability of the phosphorus-nitrogen backbone, and because of the ability of this system to permit large or subtle changes to be made in side group structure in order to optimize membrane properties. The rationale for exploring the higher temperature regime (100-200°C) is that: (1) Faster reaction rates may decrease or even eliminate the need for noble metal catalysts, and may yield greater tolerance to CO poisoning at the anode, (2) higher proton mobility will decrease the membrane resistivity, and (3) higher temperatures will enhance the prospects for developing direct-fueled fuel cells (i.e., cells that do not require the reforming of fuel to hydrogen). The principal challenges include the design and synthesis of polymer assemblies that are thermally and electrochemically stable at elevated temperatures and at the minimization of fuel (e.g., methanol) carry-over. The developed electrochemical systems allow us to measure the electrochemical properties (i.e., current-voltage curve, proton conductivity, and methanol crossover) of the above membranes at elevated temperatures.

ACKNOWLEDGEMENTS

The authors gratefully acknowledge the support of this work by the Department of Energy (DE-PS02-98EE504493) and thank D.D. Macdonald for helpful discussions during the course of this study.

REFERENCES

1. J.H. Hirschenhofer, D.B. Stauffer, R.R. Engleman, and M.G. Klett, *Fuel Cell Handbook*, Parsons Corporation, Pennsylvania (1999).
2. A.J. Appleby, *Fuel Cells - Trends in Research and Application*, Hemisphere Publishing Corp., Washington, D.C. (1987).
3. J. Ahn and R. Holze, *J. Applied Electrochemistry*, v.22, pp.1167-1178 (1992).
4. R. Savinell, E. Yeager, D. Tryk, U. Landau, J. Wainright, D. Weng, K. Lux, M. Litt, and C. Rogers, *J. Electrochem. Soc.* v.141, L46-48 (1994).
5. P. Zelenay, Sc. Thomas, and S. Gottesfeld, "Direct methanol fuel cells: recent progress in fuel cell efficiency, cell performance, and performance stability", *Proton Conducting Membranes-Fuel Cells II*, pp. 300-315, edited by S. Gottesfeld and T.F. Fuller, EIS, Pennington, NJ (1998).
6. X. Ren, P. Zelenay, and S. Gottesfeld, "Direct methanol fuel cells: transport properties of polymer electrolyte membrane and fuel efficiency", *Proceedings of the 194th Meeting of the Electrochemical Society, EIS, 1998*.
7. T.I. Valdez and S.R. Narayanan, "Recent Study on Methanol Crossover in Liquid-feed Direct Methanol Fuel Cells", *Proton Conducting Membranes-Fuel Cells II*, pp.380-387, edited by S. Gottesfeld and T.F. Fuller, EIS, Pennington, NJ (1998).
8. J.S. Wainright, J.-T. Wang, D. Weng, R.F. Savinell, and M. Litt, *J. Electrochem. Soc.*, v.142, L121-123 (1995).
9. J.-T. Wang, J.S. Wainright, R.F. Savinell, and M. Litt, *J. Appl. Electrochem.* v.26, pp.751-756 (1996).
10. D. Weng, J.S. Wainright, U. Landau, and R. F. Savinell, *J. Electrochem. Soc.* v.143, pp.1260-1263 (1994).
11. S.R. Samms, S. Wasmus, and R.F. Savinell, *J. Electrochem. Soc.* v.143, pp.1225-1232 (1996).
12. J.-T. Wang, S. Wasmus, and R.F. Savinell, *J. Electrochem. Soc.* v.143, pp.1233-1239 (1996).
13. J.-T. Wang, S. Wasmus, and R.F. Savinell, *J. Electrochem. Soc.* v.142, pp.4218-4224 (1996).
14. J.-T. Wang, W.F. Lin, M. Weber, S. Wasmus, and R.F. Savinell, *Electrochimica Acta*, v.43, pp.3821-3828 (1998).
15. H.R. Allcock, *Inorganic Polymers*, Ch. 3, Mark, Allcock, and West, Prentice Hall, Englewood Cliffs, NJ (1992).
16. H.R. Allcock, *Chem. Materials Review*, v.6, p.1476-1489 (1994).
17. R. Wycisk, P.N. Pintauro, *J. Membrane Science*, v.119, p.155-162 (1996).
18. H.R. Allcock, *Chem. Mater.*, v.2, p.425-436 (1990).

OPTIMIZATION OF SOFC POWER GENERATION SYSTEM WITH CHEMICAL LOOPING COMBUSTOR

Xun Wang Lifeng Zhao Shizheng Zhang

Institute of Engineering Thermophysics, Chinese Academy of Sciences
Beijing 100080, China

E-mail: ZSZ@etpserver.etp.ac.cn Fax: 86-10-6255-5581

Keywords: solid oxide fuel cell, chemical looping combustion, optimization

ABSTRACT. In a previous paper, a kind of solid oxide fuel cell combined cycle—SOFC power generation system with chemical looping combustor (CL-FCCC) has been studied. This cycle is made up of chemical looping combustor, solid oxide fuel cell, intercooling compressors, gas turbine, steam turbine, HRSG, and other auxiliary facilities. The key difference between other SOFC power systems and this one is the adoption of chemical looping combustor which can help to increase system's average temperature and pressure while provides energy for fuel and air preheating in the same time. But this configuration might not be the best one. So an optimization both of flowsheet and parameters was initiated in order to improve the performance of CL-FCCC. Both optimal flowsheet and fundamental parameters can be obtained by doing non-linear optimization of a more comprehensive system. The results achieved up to now are presented in the following.

1. INTRODUCTION

In order to solve the problem caused by the fossil fuel power plants radically, it is important to carry out studies on clean fuel. As an efficient, clean and renewable fuel, hydrogen energy is a prospective alternative to traditional fossil fuel.

Fuel cell, which is expected as on site power generating device in the future, provides a new way to hydrogen utilization[1,2,3]. It has many features, such as high energy conversion efficiency, low noise and vibration levels, modular structure, etc., that make it attractive for utility and industrial applications. A great deal of research is currently being undertaken to develop high temperature fuel cell for large scale power generation. Solid oxide fuel cell operates at high temperature and consequently the heat produced is useful for additional production for electricity by a turbine generator. But on the other hand, its operation temperature is high (SOFC: ~1000°C), which means reactants of anode and cathode should be preheated to high temperature.

With the adoption of chemical looping combustor[4], one kind of solid oxide fuel cell power generation system "Solid Oxide Fuel Cell Power Generation System with Chemical Looping Combustor (CL-FCCC)" can be constructed[5]. In chemical looping combustor, fuel and air go through different reactors without flame, which makes it convenient to connect with SOFC. Also the nitrogen oxide formation can be effectively suppressed. This system is made up of chemical looping combustor, solid oxide fuel cell, intercooling compressors, gas turbine, steam turbine, HRSG, and other auxiliary facilities. The key difference between other SOFC power systems and this one is that in this new cycle, fuel and oxidizer of fuel cell are preheated to SOFC working temperature by chemical looping combustor. Due to the limitation of material, the maximum working temperature of solid oxide fuel cell is about 1273K, which restricts the increase of system's average temperature and pressure. On the other hand, the inlet temperature of gas turbine has exceeded 1400°C. Chemical looping combustor is capable of working at very high temperature. Thus when it is set in front of solid oxide fuel cell, the hot fluid at high temperature and pressure can be expanded through a topping gas turbine and then flows into solid oxide fuel cell. Chemical looping combustor accompanied with a topping gas turbine can be taken as an additional topping cycle, which can help to increase system's average temperature and pressure while provides energy for fuel and air preheating in the same time. A theoretical efficiency 0.62 is achieved for this cycle when fuel cell is operated at 1000K and air is used as oxidizer.

However, it was felt that this configuration might not be the best one. The operation parameters of chemical looping combustor are highly dependent on fuel cell operation parameters, which hinder further increase of thermal efficiency. So a more comprehensive flowsheet is proposed. It contains more possible structures and its parameters that can be varied more freely. An optimization both of flowsheet and parameters was initiated in order to improve the performance of CL-FCCC. The results achieved up to now are presented in the following.

2. CYCLE PRESENTATION

The proposed flowsheet schematic (System A) is shown in figure 1. In the previous system (Base cycle [5]), the hydrogen and air are heated to fuel cell operation temperature entirely by chemical looping combustor. This might be a restriction of further efficiency increase. So a series of heat exchangers HE-H1, HE-H2, HE-A1, HE-A2 (dotted rectangles) are included into CL-FCCC[5] to form system A. Fuel and air in this system are preheated both by chemical looping combustor and by heat exchangers.

In figure 1, the symbol "[X]" represents mass flow fraction. "(X,Y)" stands for pressure and temperature respectively. (X) means temperature. Do adjustment on flow chart and parameters to determine the optimal system's configuration and parameters. If the value of one branch can be neglected, it is reasonable to cut this branch from system A. For example, if optimal results show that $[a]=[b]=[c]=[d]=0$ and $[e]=[f]=1$, then optimal system becomes the cycle in reference[5]. With optimization of flowsheet and parameters, the cycle performance is expected to be improved.

In system A, hydrogen at ambient state is compressed up to fuel cell operation pressure (PFC) and then divided into two parts. One part flows into chemical looping combustor. Another part flows into two heat exchangers (HE-H1 and HE-H2), in which it is heated up to high temperature (T6). Air at ambient state is also divided into two parts. One part is compressed up to oxidation reactor operation pressure (P4) and enters into oxidation reactor. The other part is heated to temperature T7 in heat exchangers HE-A1 and HE-A2 connected in series.

In the reduction reactor of chemical looping combustor[4], NiO reacts with the fuel stream (hydrogen). The hydrogen is then oxidized, and the NiO is reduced to Ni. The reduced solid Ni is then circulated to the oxidation reactor, where it is contacted with air and reoxidized to NiO. The regenerated NiO is then recirculated towards the reduction chamber. Since the only substances being circulated between the chambers are solids, the two reactors can run at different pressure and temperature determined by chemical kinetics, mass and energy balance. A series of fundamental experiments has been done in reference[4]. The study of reaction kinetics demonstrates that NiO/YSZ and NiO/NiAl₂O₄ have good properties with respect to the reaction rate, conversion and physics strength.

reduction reactor: $\text{H}_2 + \text{NiO} \rightarrow \text{H}_2\text{O} + \text{Ni}$

oxidation reactor: $\text{Ni} + 0.5 \text{O}_2 \rightarrow \text{NiO}$

In order to coordinate with fuel cell, only part of hydrogen in reduction reactor reacts with NiO and the operation pressure of oxidation reactor is higher than that of reduction reactor, which make the CL in this system different from its original concept in reference[4]. With heat released during indirect reaction of hydrogen and air, mixture of hydrogen and steam at temperature T3 and pressure PFC can be obtained in reduction reactor. And in the same time, mixture of oxygen and nitrogen at higher temperature T4 and pressure P4 are obtained in oxidation reactor. In view of the extremely brittle nature of the ceramic materials used in planar solid oxide fuel cells, it is impossible to operate the fuel cell with large pressure difference between the air and fuel channels. So the mixture of oxygen and nitrogen at temperature T4 and pressure P4 will first expanded through a gas turbine GT-1, which operates on the pressure difference between P4 and PFC, and then mixed with air at temperature T7 to reach fuel cell operation temperature TFC. Mixture of hydrogen and steam at temperature T3 is mixed with pure hydrogen at temperature T6 to attain fuel cell operation temperature TFC.

So the fuel cell anode is supplied with the mixture of hydrogen and steam, which is oxidized with the mixture of oxygen and nitrogen. The fuel cell unit is built with arrays (building blocks) each one having N cells connected in series from the point of view of both the fuel /oxidizer and the electric current. The unit consists of L branches connected in parallel, each branch having K arrays connected in series from the point of view of voltage. Thus the required voltage and current are obtained.

Two parts of the hot gases exiting the fuel cell anode and cathode [a] and [b] are used to heat hydrogen and air in heat exchanger HE-H1 and HE-A1. The left part of exhaust gases [e] will flow into combustion chamber directly without releasing heat. Due to oxidation, the content of hydrogen in anode exhaust gas is decreased. For the same reason, the oxidizer flow becomes smaller along fuel cell. But there is still hydrogen and oxidizer left

in exhaust gas. So an auxiliary combustor is placed in which surplus hydrogen combusts with oxidizer. The hydrogen oxidation reaction is completed in this conventional combustion chamber. After combustion, the hot gases are used to drive a gas turbine. The exhaust gases exiting GT-2 is also divided into three parts. One part [c] is used to heat hydrogen in heat exchanger HE-H2. The other part [d] provides the heat needed to heat air in heat exchangers HE-A2. The exhaust gases exiting HE-H2 and HE-A2 together with the left part [f] of exhaust gases exiting GT-2 are used to heat working fluid of steam bottoming cycle in a heat recovery boiler HRSG.

Fig 1 Flow chart of system A

Fig 2 T—Q diagram in HRSG

4. OPTIMIZATION MODEL

Thermal efficiency is chosen as objective function of this optimization problem. The total power output of this system is consist of four parts: W_{FC} , W_{GT-1} , W_{GT-2} , W_{ST} . The parasitic power is mainly consumed by compressors. So objective function can be written as:

$$\text{Max } \eta = (W_{FC} + W_{GT-1} + W_{GT-2} + W_{ST} - W_C) / (\Delta H \cdot N_{\text{tot}})$$

2. Design variables

1. δ : the mole fraction of hydrogen reacting with NiO in CL. $\delta = N_{re}/N_{in}$
2. X: the mole fraction of hydrogen entering CL. $X = N_{in}/N_{\text{tot}}$ So, $Y = 1 - X$
3. a: the mole fraction of fuel cell exhaust gases flowing into heat exchanger HE-H1
4. e: the mole fraction of fuel cell exhaust gases flowing directly into combustion chamber.
So, $b = 1 - a - e$ b: the mole fraction of fuel cell exhaust gases flowing into heat exchanger HE-A1.
5. c: the mole fraction of gas turbine exhaust gases flowing into heat exchanger HE-H2.
6. f: the mole fraction of gas turbine exhaust gases flowing directly into heat recovery boiler HRSG.
So, $d = 1 - c - f$ d: the mole fraction of gas turbine exhaust gases flowing into heat exchanger HE-A2.
7. T3: the temperature of mixture H_2 - H_2O exiting reduction reactor.
8. P4: the operation pressure of oxidation reactor.

3. Restrictions

- | | |
|--|---|
| 1. HE-H1: $T_8 - T_6 \geq \Delta T_{\min}$ | 5. HRSG: $T_{23} - T_{\text{BOT}} \geq \Delta T_{\min}$ |
| $T_{10} - T_9 \geq \Delta T_{\min}$ | $T_{17} - T_s \geq \Delta T_{\min}$ |
| $T_8 \geq T_{10}$ | $T_{14} - T_{\text{do}} \geq \Delta T_{\min}$ |
| 2. HE-H2: $T_{13} - T_9 \geq \Delta T_{\min}$ | 6. CL: $T_3 \leq T_{3\text{MAX}}$ |
| $T_{20} - T_1 \geq \Delta T_{\min}$ | $T_4 \leq T_{4\text{MAX}}$ |
| $T_{13} \geq T_{20}$ | $P_4 \geq P_{FC}$ |
| 3. HE-A1: $T_8 - T_7 \geq \Delta T_{\min}$ | 7. $0 \leq a \leq 1$ |
| $T_{11} - T_{12} \geq \Delta T_{\min}$ | 8. $0 \leq e \leq 1$ |
| $T_8 \geq T_{11}$ | 9. $0 \leq a + e \leq 1$ |
| 4. HE-A2: $T_{13} - T_{12} \geq \Delta T_{\min}$ | 10. $0 \leq c \leq 1$ |
| $T_{21} - T_{70} \geq \Delta T_{\min}$ | 11. $0 \leq f \leq 1$ |
| $T_{13} \geq T_{21}$ | 12. $0 \leq c + f \leq 1$ |

Optimization Procedure

1. Do optimization of parameters of system A.
2. If the value of one branch can be neglected (or equals to zero), then this branch can be removed from system A.
3. Do optimization of this new flowsheet again.
4. Repeat the above procedures until both the optimal flowsheet and parameters are obtained simultaneously.

5. RESULTS

Tables 1 and 2 show the comparison results of base cycle[5] and optimal system at fuel cell operation temperature (TFC) 1000K and 1100K. Thermal efficiency η_{opt} , δ_{opt} and optimal mole fraction X_{opt} of reduction reactor, operation pressure P4 of oxidation reactor are listed. The optimal system optimized from system A has the advantages over base system in the following aspects:

1. With the optimization of flowsheet and parameters, the thermal efficiency has been increased from 62.3% to 65.8% at TFC=1000K and 62.1% to 65.1% at TFC=1100K.
2. One drawback of base cycle is its high operation pressure (P4) of oxidation reactor. But in optimal system, P4 is decreased from 2.2MPa to 1.78MPa at TFC=1000K and 2.115MPa to 1.545MPa at TFC=1100K, which makes the cycle easier to be developed.

Table 1 Comparison Result at TFC=1000 K

	BASE SYSTEM[5]	OPTIMAL SYSTEM
δ_{opt}	0.29	0.27
X_{opt}	1	0.6537
$P4_{opt}$	2.2	1.78
η_{opt}	0.623	0.658

Table 2 Comparison Result at TFC=1100 K

	BASE SYSTEM[5]	OPTIMAL SYSTEM
δ_{opt}	0.34	0.44
X_{opt}	1	0.531
$P4_{opt}$	2.115	1.545
η_{opt}	0.62	0.651

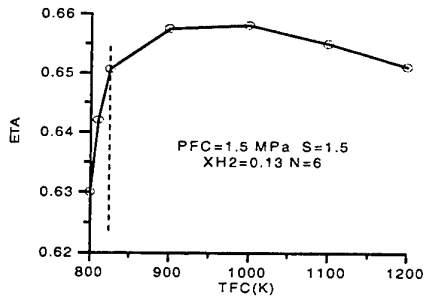


Fig. 3 Fuel Cell Operation Temperature TFC versus efficiency η_{opt}

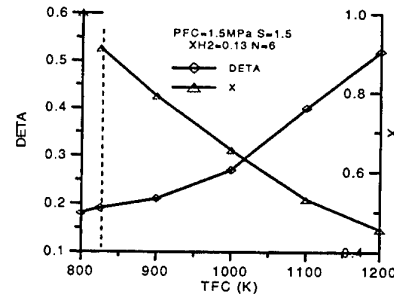


Fig. 4 Fuel Cell Operation Temperature TFC versus X_{opt} and δ_{opt} (DETA)

Optimal results illustrate that different fuel cell operation temperature TFC correspond to different optimal cycle configurations. In Figure 3 and Figure 4, the two sides of the dotted line are of different regulations because of different optimal flowsheet. Figure 3 shows fuel cell operation temperature TFC versus the optimal results of efficiency. From optimization of system A, it has been found that at lower fuel cell operation temperature, the optimal values of X , e , f are very close to "1", and the value of a , b , c , d are close to "0", which hint that heat exchangers (HE-H1, HE-H2, HE-A1, HE-A2) placed behind fuel cell are unnecessary. So branches related with heat exchangers are cut to form a new flowsheet and then do parameter optimization of it till optimal cycle configuration and parameters can be obtained. But at higher fuel cell operation temperatures, these branches are helpful for the improvement of cycle performance. Heat exchangers are included into optimal cycle configuration. At the left side of dotted line, hydrogen and air are heated to fuel cell operation temperature entirely by chemical looping combustor. So X equals "1" (Fig 4). But at the right side of dotted line, hydrogen and air are heated both by chemical looping combustor and by a series of heat exchangers. So X is less than "1" (Fig 4). The optimal value of X decreases with TFC (Fig 4). Parameter δ increases with TFC (Fig 4). So with optimization of a more comprehensive cycle (system A), flowsheet and parameters can be optimized simultaneously. Figure 5 is the ratio of hydrogen to oxygen utilization fraction S versus the optimal efficiency. In this case, fuel cell operation temperature TFC, operation pressure PFC and fuel utilization fraction $X_{H_2}^1$, are fixed. Optimization results show that the efficiency is maximal when hydrogen and oxygen are of same utilization fraction.

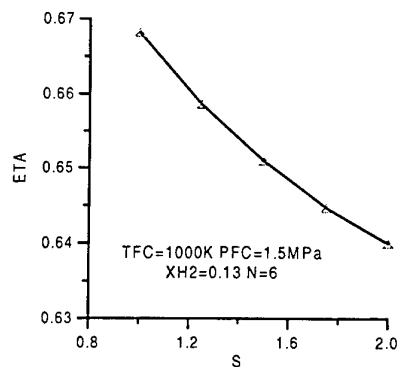


Fig 5 Ratio of Hydrogen to Oxygen Utilization Fraction S versus Efficiency η_{opt} (ETA)

6. CLOSURE

The present work is mainly concerned with optimization of system configuration and parameters. It has been illustrated that the application of this procedure is feasible to improve system performance. Different fuel cell operation temperatures correspond to different optimal cycle configurations. The thermal efficiency can be raised about 3.5 percentage points at fuel cell operation temperature 1000K. The operation pressure of oxidation chamber can also be decreased, which makes the system easier to be developed. Further work will include 1) Perform optimization of a more comprehensive system in which more possible structures are embraced, and 2) Do optimization from the point of view of economic and environment.

7. NOMENCLATURE

a,b,c,d,e,f: the mass flow fraction of exhaust gases in each branch	S: ratio of hydrogen to oxygen utilization fraction
C: compressor	ST: steam turbine
CL: chemical looping combustor	T3 _{MAX} : the maximum allowable temperature
FC: fuel cell	T4 _{MAX} : the maximum allowable temperature
GT: gas turbine	TFC: fuel cell operation temperature
N: number of fuel cell per array	V: voltage
N _{in} : amount of hydrogen entering reduction reactor	WFC: power output of fuel cell
N _{re} : amount of hydrogen reacting with NiO	X _{H₂} ¹ (XH ₂): utilization fraction of hydrogen(N=1)
N _{tot} : the total amount of hydrogen	ΔH: difference of enthalpy
PFC: fuel cell operation pressure	η (ETA): thermal efficiency
R _{ci} : resistance	

8. REFERENCE

1. C.A. Frangopoulos and N.C. Monantheras, "Performance Evaluation of A Fuel Cell Based Plant Producing Its Own Fuel by Solar Energy", Proc. Of Thermodynamic Analysis and Improvement of Energy System, Beijing, 573 (1997).
2. N.C. Monantheras and C.A. Frangopoulos, "Toward Synthesis optimization of a fuel cell based plant", ECOS98, FRANCE (1998).
3. S.P. Harvey and H.J. Richter, "A High Efficiency Gas Turbine Power Generation Cycle with Solid Oxide Fuel Cell Technology and Chemical Looping Fuel Combustion".
4. M. Ishida and J. Hongguang, "Hydrogen Fueled Gas Turbine Cycle with Chemical-Looping Combustion", Proc. of International Conference of New Energy System and Conference, Russia, (1997).
5. X. Wang and S.Z. Zhang, "Conceptual Study And Analysis Of Hydrogen Fired Power Plants", IECEC-98-419, 33rd Intersociety Engineering Conference on Energy Conversion Colorado Springs, CO, (1998).

X. Clean Combustion Technology

STUDY COMBUSTION MODEL OF PETROLEUM COKES BY TGA

Bo-Xiong Shen, De-Chang Liu, Han-Ping Chen
National Laboratory of Coal Combustion
Huazhong University of Science and Technology
Wuhan, China, 430074

Keywords: petroleum coke, combustion model, reaction order, kinetics parameters, combustion characters

ABSTRACT. It is found that combustion of some petroleum cokes agrees with one step model (with 1.5 reaction order), while combustion of other petroleum cokes agrees with two steps model (with 7.0, 2.0 reaction order) by thermogravimetric analysis (TGA). Several petroleum cokes kinetics parameters have been obtained and some combustion characters have been indicated at the same time.

1. INTRODUCTION

Petroleum coke is the final production of oil refinery [1, 2, 3]. Petroleum coke can be used as carbonaceous materials and alternative fuel of power boiler. Mechanism of petroleum coke combustion is very important to the utility of petroleum coke, but the mechanism of petroleum coke combustion is not clear because of few papers about it. In this paper, the mechanism of petroleum coke combustion is studied by TGA, whose measurement is accurate and continuous. From Table 1, we can find that petroleum coke contains few volatiles and high level of carbon, which closes to that of anthracite. Coal combustion is always considering as one step model with reaction order about 1.0, for petroleum coke combustion which model can be adapt to? In this paper, different petroleum cokes are used to study the mechanism of their combustion. In order to select a good model, different reaction orders are assumed to adapt to the experiments.

2. EXPERIMENTS

2.1 Experiments Samples

Petroleum coke samples came from Wuhan Chemical Oil Plant (WH), Guanzhou Chemical Oil Plant (GZ), Jingmen Chemical Oil Plant (JM) and Zhenhai Chemical Oil Plant (ZH2). The soft coal (YM) and anthracite (WYM) are used to compare with petroleum coke. The samples are skived and milled. The diameters of the samples are between 0.100-0.154 mm. The weights of samples in TGA experiments are in the same (10.2 mg). Proximate analysis and ultimate analysis of different samples appear in Table 1. From Table 1, we can find that petroleum coke is high in fixed carbon, low in volatiles, internal water and ash.

2.2 Experimental Apparatus and Conditions

The experimental apparatus, LCT-2B mid-temperature thermogravimetric scale, was made in China. The thermogravimetric scale consists of heating furnace, balance, measure and control system, signals processing system, data acquisition and processing system. The temperature is heated to certain value by the control system in linearity. The electric signals coming from the signals processing are collected and saved by computer. The data are dealt with by program, which is to determine combustion mechanism and kinetics parameters. The experiments are under conditions of 110 ml/min air flux and 20 °C/min heating rate.

Table 1. Proximate And Ultimate Analysis Of Petroleum Coke And Coal

Item	WH	GZ	JM	Z2	YM	WYM
Water %	1.03	0.78	0.97	0.71	2.1	4.12
Vol. %	11.85	11.96	13.82	11.01	22.32	6.35
Ash %	0.12	0.07	0.09	0.16	36.10	26.7
carbon %	88.00	87.19	85.13	88.12	39.48	63.26

3. ANALYSIS AND RESULTS

The combustion rule of solid fuel is generally considered to agree with the following equation,

$$-\frac{dw}{dt} = Kw^n = A \exp\left(-\frac{E}{RT}\right) w^n \quad (1)$$

where w is the weight of the solid in different time (mg), t is time (min), A is factor constant, E is the active energy (J/mol), n is reaction order, R is the universal gas constant (J/mol*K), T is absolute temperature (K). By seeking logarithm to both sides of Equation (1), Equation (2) can be obtained as follows:

$$\ln \left[\frac{\left(-\frac{dw}{dt} \right)}{w^n} \right] = \ln A - \frac{E}{RT} \quad (2)$$

Different reaction orders are select to agree with the linearity of Equation (2) by LMS (Least Square Method) (with reaction orders 0, 0.5, 2/3, 1, 1.5, 2.0, 2.5, 3.0, 3.5, 4.0, 4.5, 5.0, 5.5, 6.0, 7.0, 8.0, 9.0), so the mechanism of combustion can be determined. The results of the Least Square Method of Equation (2) indicate that different petroleum cokes agree with different model: GZ and ZH2 agree with one step model (with reaction order 1.5), WH and JM agree with two step model (with reaction order 7.0 and 2.0).

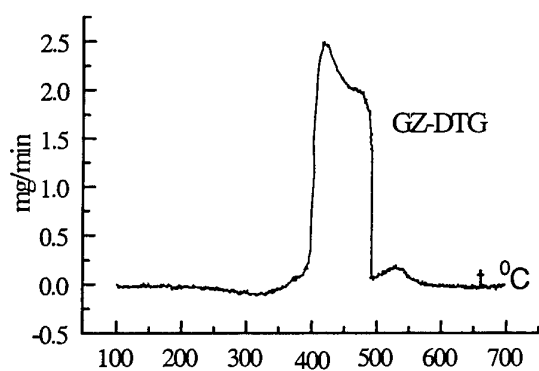


Figure 1. DTG value of GZ combustion

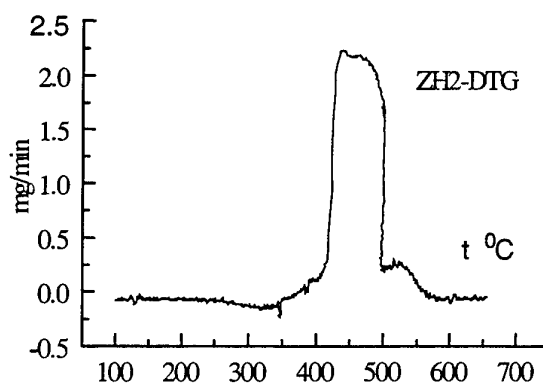


Figure 2. DTG value of ZH2 combustion

From Figure 1 to Figure 4, we can find that the combustion of GZ and ZH2 with only one peak value and those of WH and JM with two peak values. From Figure 5 and Figure 6, we can find that the combustion of the two coals agrees with one step model.

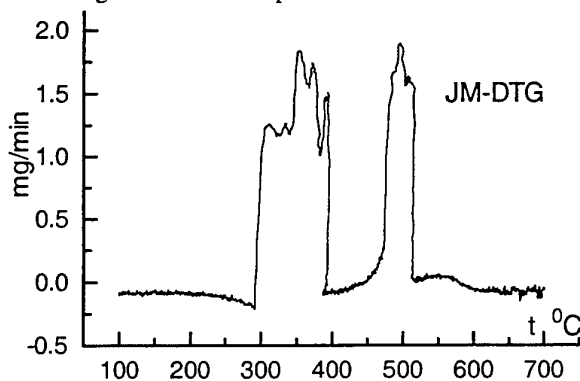


Figure 3. DTG value of JM combustion

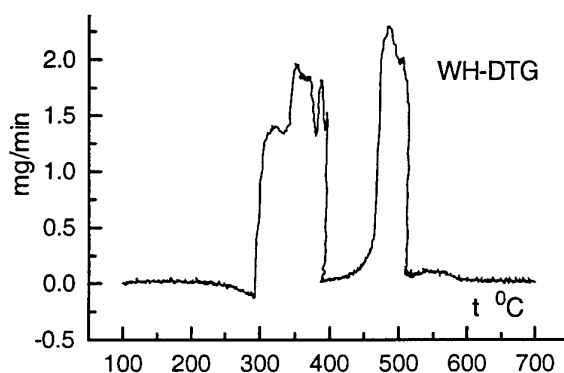


Figure 4. DTG value of WH combustion

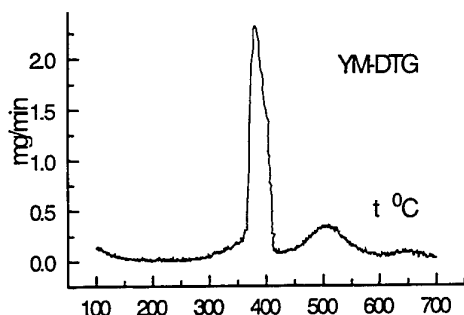


Figure 5. DTG value of YM combustion

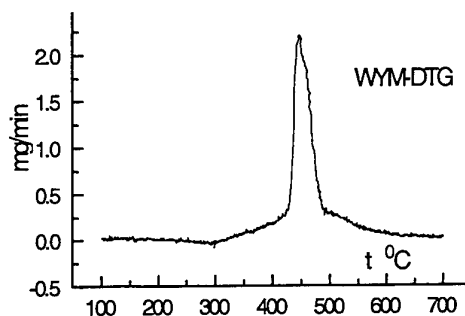


Figure 6. DTG value of WYM combustion

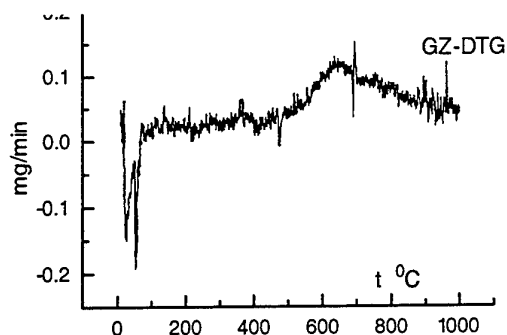


Figure 7. DTG value of GZ pyrolysis

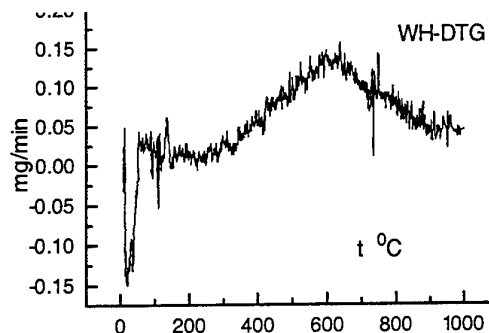


Figure 8. DTG value of WH pyrolysis

The sample of GZ is ignited at about 400 °C and burned out at about 500 °C. The sample of ZH2 is ignited at about 420 °C and burned out at about 500 °C. The samples of WH and JM are ignited at about 300 °C. The first steps of WH and JM are burned out at about 400 °C and the second steps are burned out at about 500 °C. Anthracite is ignited at about 430 °C and burned out at about 600 °C. The soft coal is ignited at about 350 °C and burned out at about 600 °C. From the DTG figures, we can find that the ignition temperatures of petroleum cokes are less than that of anthracite but not all the ignition temperatures of petroleum coke are higher than that of soft coal. The ignition temperature of WH and JM samples are less than that of soft coal but those of GZ and JM samples are higher than that of soft coal. Not all of burning out temperatures of petroleum cokes are higher than those of coals. Once the petroleum cokes are ignited, their weight loss speeds become rapid (especially for WH and JM samples). In the initial combustion the weight loss due to pyrolysis is small. DTG values of the petroleum cokes samples reach the peak value quickly after the samples are ignited. This indicates that the samples of petroleum cokes are ignited heterogeneously [3]. The DTG of GZ and WH samples pyrolysis appear in Figure 7 and Figure 8. The initial pyrolysis temperature of GZ sample is about 400 °C, which almost equals to the initial combustion temperature. The initial pyrolysis temperature of WH sample is about 300°C, which equals to the initial combustion temperature. The low concentration of the pyrolysis gas in the initial pyrolysis is not high enough to ignite the petroleum coke. This validates that the petroleum cokes are ignited heterogeneously again. The LMS results of petroleum cokes appear in Figure 9, Figure 10, Figure 11 and Figure 12. The reaction orders and kinetics parameters of the four kinds of petroleum cokes appear in Table 2.

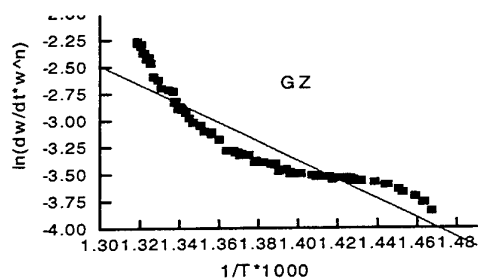


Figure 9. LMS of GZ

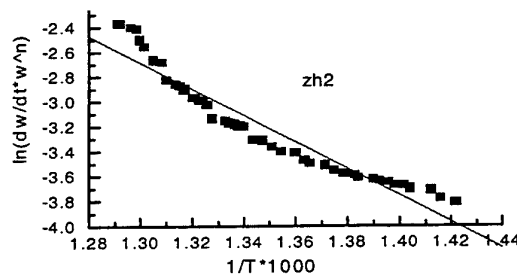


Figure 10. LMS of ZH2

Table 2. Reaction Order And Kinetics Parameters Of Petroleum Coke Combustion

Samples		N	A	E	Relative coefficient
GZ		1.5	8250.336	73557.43	0.9217436
ZH2		1.5	49345.441	84959.12	0.9639225
WH	The first step	7.0	1.1985×10^8	176445.84	0.9659883
	The second step	2.0	1.6519×10^{24}	367256.82	0.9695785
JM	The first step	7.0	5.2873×10^9	193412.40	0.9628462
	The second step	2.0	1.0946×10^{23}	353356.94	0.9707165

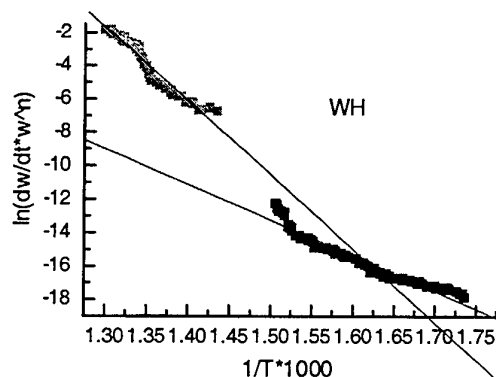


Figure 11. LMS of WH

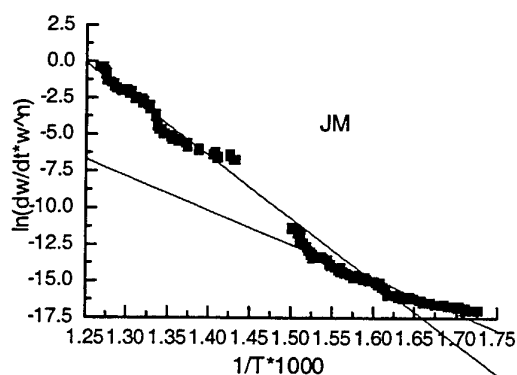


Figure 12. LMS of JM

4. CONCLUSIONS

1. The combustion of some petroleum cokes agrees with one step model (with reaction order of 1.5) and the combustion of other petroleum cokes agrees with two steps model (with reaction orders of 7.0 and 2.0).
2. The ignition temperatures of petroleum coke are between those of soft coal and anthracite. The burning out temperatures of petroleum cokes are less than those of soft coal and anthracite.
3. Petroleum cokes are ignited heterogeneously under the experimental conditions.
4. The reaction orders and kinetics parameters of four kinds of petroleum cokes are obtained.

REFERENCES

1. S.J. Goidich, A.R. McGee, K. Richardson, In Proceedings of 1991 International Conference On FBC, Montreal, Canada, April 21-24, pp. 57-64 (1991).
2. D.W. Tharpe, Iqbal Abdulally, 1997 FBC, Volume 1, ASME (1997).
3. J.B. Howard, and R.H. Essenhigh, Eleventh Symposium (Int.) on Combustion, pp. 399-408, the Combustion Institute, Pittsburgh (1967).

ENVIRONMENTAL UPDATE OF MS-3002 GAS-TURBINE PLANT APPLIED TO DRIVE ELECTROGENERATORS

A.Soudarev, E.Vinogradov, Yu.Zakharov
"EST", Russia

Email: flame@mail.admiral.ru; Fax: 7-812-265-0067

S.Vesely, G.Poslushny
"EKOL", Czech Republic

Email: ekolsro@brno.comp.cz; Fax: 420-5-43242912

K.-H.Scholz

"Ruhrgas", Germany

Ruhrgas Aktiengesellschaft Huttropstraße 60 D-45138 Essen

Fax: 0201/184-4164/3766

Keywords: combustor, update, emissions, test bed, compressor station

ABSTRACT. There are at present around 1,000 MS3002 General Electric gas-turbine units in service all over the world though the environmental characteristics of these machines, in particular, NO_x emissions, do not meet the current environmental norms. A relatively inexpensive and simple combustor update has been carried out, the salient features thereof are increased flow of air supplied to the primary zone, its accurate dosing and strict orientation of the air jets to be supplied into maximum temperature zones. The full-scale combustor model tests were carried out in the NPP "EST" test bed in Russia. The trial-commercial tests of the combustor as a part of a FRAME-3 unit were accomplished at an enterprise of the Ruhrgas in Germany. It has been operated over one year. The completed complex of tests demonstrated that the NO_x emissions from the updated combustor are 1.6 time below that from a standard one and do not exceed 150 mg/Nm³ (converted to 15% O₂ concentration) at all unit operating conditions. The CO emissions, at the same time, at GPU rating do not exceed 50 mg/Nm³, while within the 70 to 100% load range of the turbine unit rated output, the CO emissions are below the level of 100 mg/Nm³.

1. INTRODUCTION

Due to its robust design, the MS3002 gas-turbine plant of the General Electric production, called FRAME-3 as well, excels in a high operating reliability, appropriate operating qualities and has been widely applied all over the world. There are around 1000 machines of this series in service nowadays, the bulk thereof operates as a part of power stations to drive the electrogenerators.

At the same time, the environmental records of these machines, particularly the nitrogen oxide emissions, do not meet the current environmental requirements. Keeping in mind that the FRAME-3 life much exceeds 100,000 hours, it necessitates units with reasonably considerable residual life to have their NO_x emissions reduced to the level of the current toxic emissions norms.

The low-NO_x fuel combustion systems of DLN type, proposed by General Electric, and based on the technique of premixed lean combustion, are distinguished by having a complex control system and fairly costly (around 1 mln.dollars of USA per a unit). For units which have been in service for a long time and which life has been already partially depleted, application of such costly systems is not economically justified. For these purposes, cheaper and more simple engineering approaches must be developed.

By the order of "Ruhrgas" (Germany), the Research-Manufacture Enterprise "EST" (Russia) in tandem with "EKOL" (Czech Republic) developed a simple, produceable and comparatively inexpensive engineering approach to update environmentally the FRAME-3 unit.

The development of the engineering approach included the following main stages:

- analysis of design and operating process in standard combustor;
- design and manufacture of versions of full-scale prototypes of low-NO_x combustors;
- bed tests of models and option for an optimum version;
- design and manufacture of full-scale combustor;
- tests of updated combustor as a part of the unit on the compressor station to identify its main characteristics;
- trial-commercial operation of updated combustor to verify its reliability.

The most significant aspects of separate development stages will be discussed below.

2. PECULIAR FEATURES OF DESIGN AND OPERATING PROCESS IN THE STANDARD COMBUSTOR

The MS3002 unit combustor consists of tube sections placed in separate parallel casings with three sections on each side of the machine normal to its centerline. The combustion air is delivered as the counterflow by the annular channel formed by the liner and casing. The liner design is typical for combustors with the staged air supply into the combustion zone (see Fig.1). The liner has 5 rows of openings (2 rows to supply the primary air, 2 rows of afterburning openings and 1 row of mixer openings) located at various distances from the dome. The dome is the taper with developed perforation as scaly stamp-outs of louver type for cooling. A similar cooling system is applied on the liner within the dome-to-mixer area. The gas burner is secured on the casing cover and has the gas-distributing headpiece of jet type placed along the centerline.

The operating process in the combustors with the staged air supply is sufficiently studied and has a number of characteristic features. The combustion process intensity and fuel burn-out length in the given combustors are essentially dependent on the diameter and location of the primary air supply openings and afterburning openings in the liner.

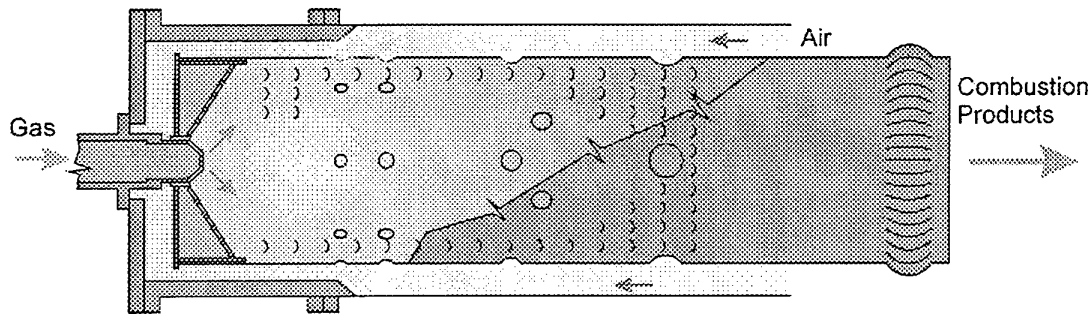


Fig. 1. Standard combustor.

The combustor in discussion is distinguished by the low flow velocities and small, close to one, excess-air coefficients within the head area, larger reverse currents zone volume which causes a lengthy time of combustion products residence within the high temperature zone and results in a higher NO_x emissions.

The main characteristics of the MS3142 unit combustor are shown in Table 1

Table 1

No	Characteristics	Dimension	Numerical value
1.	Air flow per a combustor	kg/sec	51
2.	Fuel gas flow per a combustor	kg/sec	0.792
3.	Pressure in combustor	MPa	0.72
4.	Gas temperature downstream of combustor	°C	943

5.	Air temperature upstream of combustor	°C	270
6.	Excess-air coefficient	-	3.60
7.	NO _x concentration (in dry combustion products at 15% O ₂)	mg/Nm ³	232
8.	CO concentration (in dry combustion products at 15%)	mg/Nm ³	58

3. DEVELOPMENT OF PROTOTYPE VERSIONS

As it was noted out above, the temperature within the combustion zone and residence time for combustion products within the high temperature zone are the principal factors determining NO_x formation. It is also known that these factors affect CO emissions as well but with the reverse effect.

So, a straightforward approach which comes down to a simple increasing the excess-air coefficient in the primary zone at the expense of variation of the number and diameter of the liner openings looks to be unpromising since it results in the increase in the CO emissions and, also, a likely deterioration of the combustion stability, emergence of pressure pulsations, lowering of combustion reliability and other unpalatable subsequences.

On the other hand, use of such effective techniques of NO_x emissions lowering as premix "lean" combustion, variable geometry of combustor paths or multi-stage fuel combustion are associated with considerable variations in the fuel supply systems, automatic control and governing, alterations of the combustor casing design which is inadmissible considering the set targets.

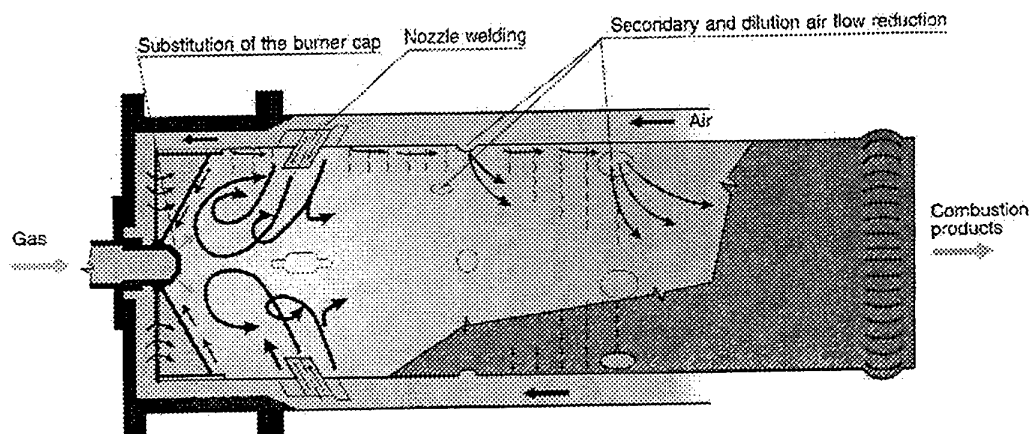


Fig. 2. Combustor - list of updated elements.

At the same time, the experience, gained by the Research-Manufacture Enterprise "EST" within the field of environmental update of combustors of gas turbines produced by various companies (GT-750-6 and GTK-10 of the "Nevsky Zavod" production, GTG-1500 of the "Proletarsky Zavod" production, GT-100 of the "Leningrad Metal Works" production, KWU VR-438 of the "Siemens" production, etc) indicates that in many cases a considerable NO_x emissions reduction could be achieved by minimum design variations of the combustor allowing to build up the operating process in the combustor in a rational way.

Thus, a reduction of the NO_x concentration in the waste gases from the gas-pumping units of GT-750-6 and GTK-10 on an average from 750-850 mg/Nm³ to 135-150 mg/Nm³ (at conversion to NO₂ at 15% O₂) was achieved by the technique of directed and dosed air blow into the local high temperature zones of the head areas of the combustor. The CO emissions level at the same time remained actually within the current norms limits.

By now, around 350 machines of GTK-10-4 type have been updated in Russia and over 150 units of GT-750-6 have been updated in Czech and Slovak Republics.

The technique of local dosed air blow-in was admitted to be the basis at design of versions of the prototypes of the low- NO_x MS-3002 combustor. The optimum version (as follows from the experimental elaboration findings) is shown in Fig.2.

The newly developed combustor (Fig.2) has the following salient features: increased air flow to the primary zone, its accurate dosing and strict orientation of the air jets to be supplied to the local high-temperature zones. This was achieved by installation of a special purpose system of the air-guide pipings welded to the liner (Fig.3). Furthermore, some changes were introduced into the system of separation of air supplied to various liner zones and the angle of the gas outflow from the burner was altered as well.

The above changes result in formation of the high-turbulent toroidal vortex in the primary zone which favours as follows:

- faster fuel/air mixing;
- lowering the mean flame temperature;
- increasing the flow velocity within the recirculation zone and, therefore, decreasing the time of combustion products residence within the high-temperature zones;
- enhancement of the fuel combustion process.

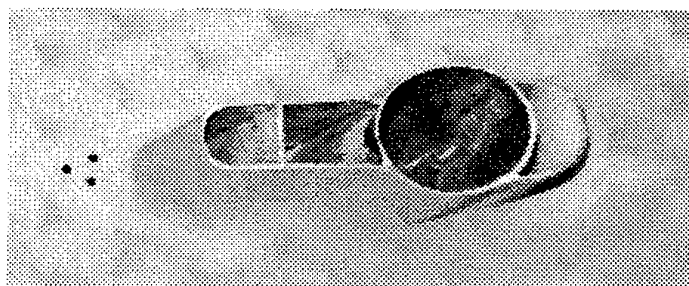


Fig. 3. Piping part.

Totally, 8 various models of low- NO_x combustors were designed, manufactured and tested in the test bed; all these were distinct from one another by their location, direction, quantity and configuration of the air-guide pipings, angle of fuel jets outflow from the burner openings, diameters of the afterburning and mixing openings.

4. BED TESTS OF MODELS

Tests of the full-scale models of low- NO_x MS-3002 combustors were carried out in the experimental test bed of the NPP "EST" in St.Petersburg. The test bed (see Fig.4) includes the air compressor experimental section where the combustor model under study is located, double-stage system of air preheating with the combustion products, exhaust system with the noise-silensor, fuel system with three independent circuits of fuel supply (one circuit was employed). The test bed was equipped with the automated measuring system allowing to keep records and carry out processing of all required parameters directly during the process of conducting the experiment. Some characteristics of the experimental test bed are shown in Table 2.

Table 2

Maximum air pressure, abs, Mpa	0.6
Maximum air mass flow, kg/sec	4.0
Maximum air temperature at combustor inlet, °C	500
Fuel type	gaseous; liquid
Maximum fuel gas pressure, Mpa	0.6

The bed tests of the low- NO_x MS-3002 combustor models were carried out at the air pressures close to the atmospheric ones. The rated air flow through the combustor for the test bed conditions was determined on the basis of the requirement to ensure equality of Mach numbers for the under-scale and full-scale models.

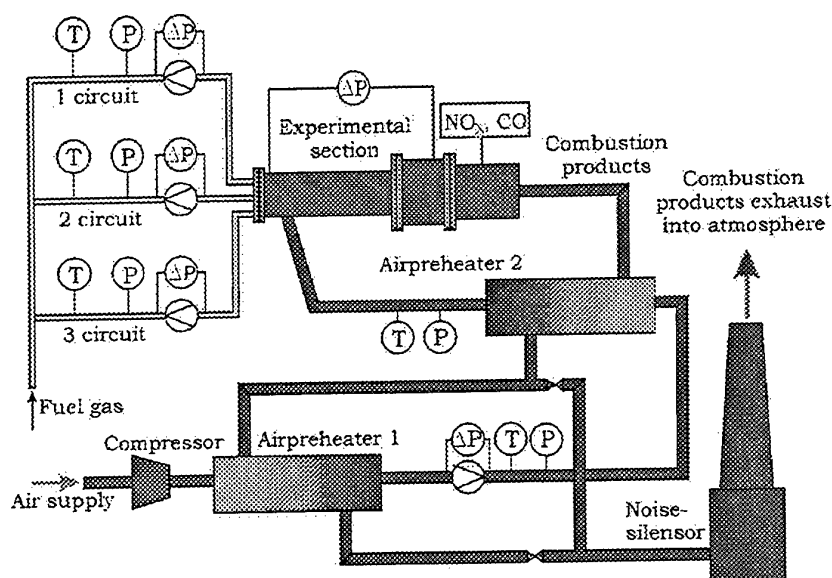


Fig. 4. Test bed

In the process of the bed tests, the following characteristics were identified for each studied version:

- boundaries of combustion stability in terms of "lean" and "rich" turn-down;
- relative hydraulic resistance;
- fuel-air mixture ignition conditions;
- heat state of the liner;
- dependence of NO_x and CO concentrations in the combustion products on variation of the excess-air coefficient;
- non-uniformity of the gas pattern factor at the combustor outlet.

Conversion of the NO_x concentration values in the test bed to full-scale pressure was implemented using the fraction-linear approximation of the form [1]

$$NO_x^M = NO_x^M \frac{16P^H - 0.23}{16P^M - 0.23} \cdot \frac{6P^M + 0.77}{6P^H + 0.77} \quad (1)$$

where NO_x^M is the NO_x concentration measured in the test bed;
 P^M, P^H are the pressures in the under-scale and full-scale combustor, MPa.

On the basis of the findings of tests of 8 versions of the combustor models, an optimum low- NO_x combustor design was chosen (see Fig.2) allowing to reduce the NO_x emissions by 1.8 time as compared with the standard combustor. The CO emissions, at the same time, at the rating remained close to 0.

5. TEST OF UPDATED COMBUSTOR AS A PART OF THE UNIT

In compliance with the project completed by the NPP "EST", the "EKOL" company manufactured and mounted a low- NO_x combustor on the MS-3002 unit at a "Ruhrgas" compressor station.

Complex tests of the combustor as a part of the unit confirmed conclusions drawn on the basis of the test bed elaboration of the combustor design results, in particular:

- 100% reliability of ignition and functioning of the cross-fire tube at the start-up;
- high flame stability and reliable functioning of the flame detectors within the entire operating conditions range;
- high fuel combustion completeness which exceeded 99.9% as in the original combustor;
- absence of working media pressure fluctuations;
- considerable pressure losses reduction in the combustor which led to a fuel flow reduction (Fig.5).

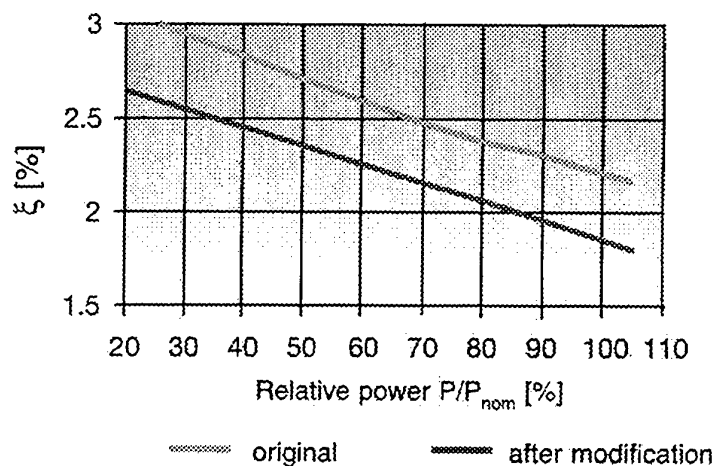


Fig. 5. Relative pressure losses ξ in the combustor.

A special attention was paid to the pattern factor of the combustion products and the liner metal temperature. Fig.6 and 7 show the photos of the inside surface of the liner after the tests carried out using a thermopaint susceptible to the temperature level. The maximum liner metal temperature (800°C) of the low- NO_x combustor did not exceed the temperatures measured on the standard combustor.

Comparison of the standard combustor emissions with the low- NO_x updated combustor emissions are shown in Fig.8.

The tests indicated that the NO_x emissions from the updated combustor is 1.6 time below that from the standard combustor and does not exceed 140 mg/Nm³ (converted to 15% O₂) over the unit's entire operating

conditions range. The CO emissions, at the same time, at the GPU rated loading are close to 0 while with loads making up 55-100% of the rated turbounit output, the CO emissions are below the level of 100 mg/Nm³. These characteristics meet the requirements of the Germany's environmental norms TA Luft.

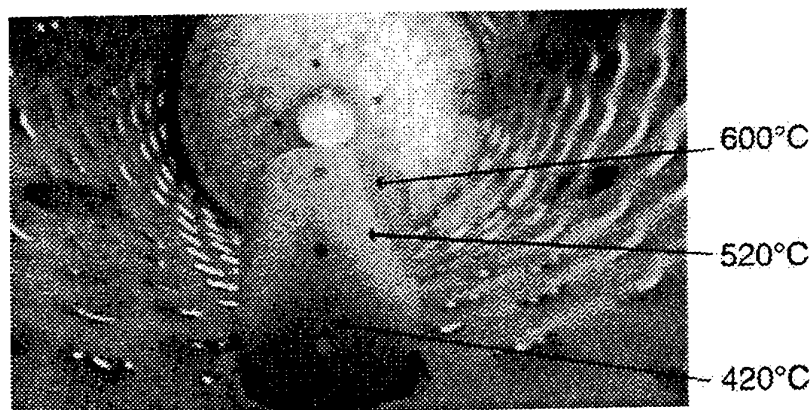


Fig. 6. Inside liner surface.

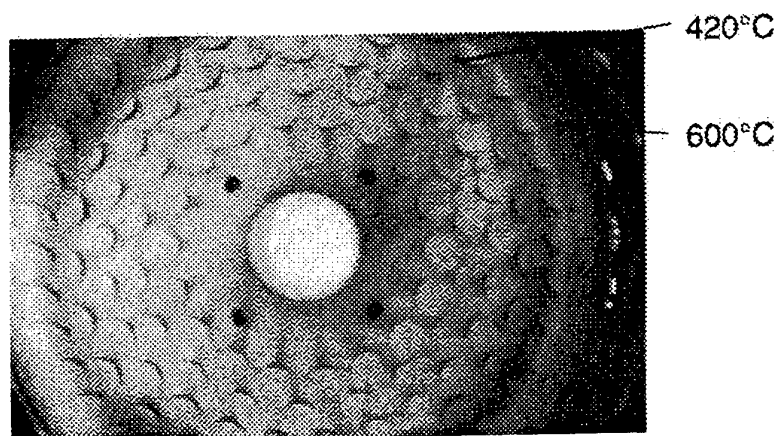


Fig.7. Inside liner dome surface.

The analysis of the complex test findings for the low-NO_x combustor indicated that its main operation characteristics are not inferior to those of the standard combustor or even superior to them.

After completion of the short-term complex tests, trial-commercial running of the low-NO_x combustor was started. By now, its operating hours are around 1,000 and operating of the updated combustor is being successfully continued.

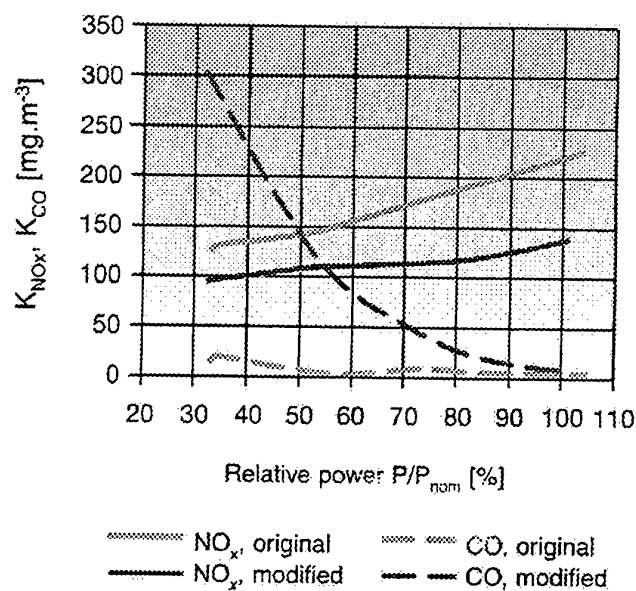


Fig. 8 NO_x and CO concentrations in the combustion products.

6. CONCLUSION

Feasibility of carrying-out environmental combustor update within short periods of time without involving other components and systems of the turbounit is a substantial advantage of the proposed engineering approach. The fuel system, control and governing systems, igniter and flame detector remain actually the same.

Update includes on-site replacement of the liners and burner headpieces. Terms of carrying out mounting and, therefore, the outage of the machine do not exceed 24 hours. The life of the components and parts replaced at carrying out the combustor update remained the same both for the appropriate standard components and parts supplied by the turbounit manufacturer.

At present, a similar engineering approach is being developed for the FRAME-3R unit, operating by the regenerative cycle. In the middle of 1999, the tests of the low- NO_x combustor as a part of the unit will be launched.

REFERENCES

1. V.A. Khristich, A.G. Tumanovsky, *Gas turbine engines and environmental protection*, Kiev Tekhnika, 1983, 144p.

NUMERICAL MODELING OF FLOW PATTERN AND COMBUSTION IN A INDUSTRIAL GLASS MELTING FURNACE

Yin-cheng Guo Wen-yi Lin

Department of Engineering Mechanics, Tsinghua University
Beijing, 100084, China

Email: guoyc@mail.tsinghua.edu.cn; Fax: (8610)62785569

Cheong-ki Chan

Department of Applied Mathematics, The Hong Kong Polytechnic University
Hung Kom, Kowloon, Hong Kong

Email: mackchan@polyu.edu.hk; Fax: (852)23629045

Keywords: glass melting furnace, combustion, heat transfer, numerical simulation

ABSTRACT. Heat transfer from the flame in a glass furnace is important for the efficient operation of any glass melting furnace. Numerical simulations of three-dimensional turbulent combustion with radiation heat transfer in the glass melting furnace are carried out in this paper. The comprehensive mathematical model is developed for simulating gas combustion and heat transfer. The standard k- ϵ turbulence model and EBU-Arrhenius model are incorporated into the comprehensive model. For radiation heat transfer, conventional six heat-flux model are used. On the basis of the above mathematical model, general numerical solution for the differential equations and computer codes have been successfully developed. Predicted results show that there is a diffusion flame at the centre of the pre-combustor which has remarkable effect on the combustion process in the glass melting furnace. Compared with the calculations under uniform inlet parameters, the results show that the flame becomes longer, while the temperature and the velocity become higher.

1. INTRODUCTION

The glass melting furnace is an important engineering unit in which there are complex physical, chemical, heat and mass transfer process. The glass melting furnace typically consists of a melting glass tank and a combustion chamber. The heat transfer from the combustion chamber to the surface of molten glass has significant effects on the flow pattern of molten glass. It affects the glass quality and productivity and energy consuming, therefore it is of the utmost importance to furnace designers and operators. Heat release from the combustion chamber not only provides the heat for batch melting, but also provides the driving force for molten glass flow. The molten glass flow in the glass tank is typical heat driven while the temperature gradient is the driving force. In the glass tank, the molten glass can be divided into two re-circulating flow regions according to the position of hot spots. One of the re-circulating flow regions is in the batch melting zone. It is called the melting re-circulating region. The other re-circulating flow region is in the molten glass cleaning zone which is called the cleaning re-circulating region. The size of each re-circulating region affects the glass quality. If the melting re-circulating region is too small, the batch melting process is not be complete and causes stripe drawback of glass production. On the other hand, if the cleaning re-circulating region is too small, bubbles formed in the batch melting process do not have sufficient time to escape from the molten. Bubbles entering the working tank following the molten glass will cause the bubble drawback of glass production. Therefore, these two re-circulating regions have important effects on the quality of glass production. The clarify of these two re-circulating regions mainly depend on the position of the hot spots whose positions depend on the shape and the temperature of the combustion fire in the furnace chamber. It is thus necessary to investigate the combustion process in the glass melting furnace combustion chamber.

Existing technology for designing industrial glass melting furnace is primarily empirical and cannot be logically extended to study different effects, such as inlet conditions, effects of pre-combustor or chamber geometry, on furnace performance. In the past two decades, with the development of computer technology and the development of the numerical methods of heat transfer, fluid dynamics and combustion, computational methods in fluid flow and heat transfer have been applied to the simulation of complex and practical combustion system. As for glass melting furnace, the primary numerical modeling of glass furnace mainly focused on the molten glass flow in the tank [1]. Zhao [2] developed a heat transfer model and batch model of melting glass flow. As for numerical simulation of combustion chamber, Gosman et al [3] developed a mathematical model for

modeling the flow field and heat transfer in the combustion chamber of a glass furnace. Carvalho et al [4,5] recently proposed a comprehensive model incorporating combustion model, molten glass flow and heat transfer model, batch model and pollution model for soot formation and nitric oxide (NO) emission together to solve the internal process in a glass tank and combustion chamber.

2. MATHEMATICAL MODEL

In this paper, numerical modeling of flow pattern and heat transfer in a combustion chamber of horseshoe-fire shape melting glass furnace is presented. The comprehensive mathematical model is developed for simulating turbulent gas combustion. The two-equation k- ϵ turbulence model and EBU-Arrhenius combustion model were incorporated into the comprehensive model. As for radiation heat transfer model, the six heat-flux model [6] were used. In Cartesian coordinates, the time-averaged three dimensional gas phase equations can be written in the following generalized form

$$\frac{\partial}{\partial x}(\rho u\phi) + \frac{\partial}{\partial y}(\rho v\phi) + \frac{\partial}{\partial z}(\rho w\phi) = \frac{\partial}{\partial x}\left(\Gamma_\phi \frac{\partial \phi}{\partial x}\right) + \frac{\partial}{\partial y}\left(\Gamma_\phi \frac{\partial \phi}{\partial y}\right) + \frac{\partial}{\partial z}\left(\Gamma_\phi \frac{\partial \phi}{\partial z}\right) + S_\phi, \quad (1)$$

where ϕ is the dependent variable, Γ_ϕ is the effective diffusion coefficient, S_ϕ is the source term of gas phase, $\phi, \Gamma_\phi, S_\phi$ are given in Table 1.

Table 1. Source Terms in Gas Phase Governing Equations

Equations	ϕ	Γ_ϕ	S_ϕ
continuity equation	1	0	0
x - direction momentum	u	μ_e	$-\frac{\partial p}{\partial x} + \frac{\partial}{\partial x}\left(\mu_e \frac{\partial u}{\partial x}\right) + \frac{\partial}{\partial y}\left(\mu_e \frac{\partial v}{\partial x}\right) + \frac{\partial}{\partial z}\left(\mu_e \frac{\partial w}{\partial x}\right) + \rho g_x$
y - direction momentum	v	μ_e	$-\frac{\partial p}{\partial y} + \frac{\partial}{\partial x}\left(\mu_e \frac{\partial u}{\partial y}\right) + \frac{\partial}{\partial y}\left(\mu_e \frac{\partial v}{\partial y}\right) + \frac{\partial}{\partial z}\left(\mu_e \frac{\partial w}{\partial y}\right) + \rho g_y$
z - direction momentum	w	μ_e	$-\frac{\partial p}{\partial z} + \frac{\partial}{\partial x}\left(\mu_e \frac{\partial u}{\partial z}\right) + \frac{\partial}{\partial y}\left(\mu_e \frac{\partial v}{\partial z}\right) + \frac{\partial}{\partial z}\left(\mu_e \frac{\partial w}{\partial z}\right) + \rho g_z$
turbulent kinetic energy	k	$\frac{\mu_e}{\sigma_k}$	$G_k - \rho \epsilon$
turbulent kinetic energy dissipation rate	ϵ	$\frac{\mu_e}{\sigma_\epsilon}$	$\frac{\epsilon}{k}(C_1 G_k - C_2 \rho \epsilon)$
thermal enthalpy	$C_p T$	$\frac{\mu_e}{\sigma_h}$	$2a_g(q_x + q_r + q_\theta - 3E_{bg}) + W_s Q_s$
gas phase species	Y_s	$\frac{\mu_e}{\sigma_Y}$	W_s

The generalized governing equations of radiation heat flux q_{rx}, q_{ry}, q_{rz} are given as follows

$$\frac{\partial}{\partial x}(\alpha \rho u\phi) + \frac{\partial}{\partial y}(\alpha \rho v\phi) + \frac{\partial}{\partial z}(\alpha \rho w\phi) = \frac{\partial}{\partial x}\left(\Gamma_{\phi x} \frac{\partial \phi}{\partial x}\right) + \frac{\partial}{\partial y}\left(\Gamma_{\phi y} \frac{\partial \phi}{\partial y}\right) + \frac{\partial}{\partial z}\left(\Gamma_{\phi z} \frac{\partial \phi}{\partial z}\right) + S_\phi, \quad (2)$$

where $\alpha, \varphi, \Gamma_{\varphi x}, \Gamma_{\varphi y}, \Gamma_{\varphi z}, S_{\varphi}$ are given in Table 2.

Table 2. Source Terms in Radiation Heat Transfer Equations

Equations	α	φ	$\Gamma_{\varphi x}$	$\Gamma_{\varphi y}$	$\Gamma_{\varphi z}$	S_{φ}
x - direction radiation heat flux	0	q_x	$\frac{1}{a+s}$	0	0	$-a_g(q_x - E_{bg}) - \frac{s}{3}(2q_x - q_y - q_z)$
y - direction radiation heat flux	0	q_y	0	$\frac{1}{a+s}$	0	$-a_g(q_y - E_{bg}) - \frac{s}{3}(2q_y - q_x - q_z)$
z - direction radiation heat flux	0	q_z	0	0	$\frac{1}{a+s}$	$-a_g(q_z - E_{bg}) - \frac{s}{3}(2q_z - q_x - q_y)$

Both gas phase conservation equations and radiation heat transfer flux governing equations have the same form where the convection term is the sum of the diffusion term and the source term. Finite difference numerical method is used for solving the above equations. A staggered grid system with upwind-difference scheme is employed, while integrating the above equations in the computational cell. The generalized finite-difference equation can be written as

$$a_p \varphi_p = a_E \varphi_E + a_W \varphi_W + a_N \varphi_N + a_S \varphi_S + a_T \varphi_T + a_B \varphi_B + b \quad (3)$$

The gas phase is solved using the SIMPLE algorithm, i.e. p-v corrections with TDMA line-by-line iterations. In Table 1, where G_k is the production term in the transport equation of turbulent kinetic energy, which can be

expressed as $G_k = \mu_T \left(\frac{\partial v_i}{\partial x_j} + \frac{\partial v_j}{\partial x_i} \right) \frac{\partial v_i}{\partial x_j}$, and μ_T is gas phase turbulent viscosity, the effective viscosity μ_e is

defined as $\mu + \mu_T$, where $\mu_T = C_\mu \rho k^2 / \epsilon$. For turbulent gas combustion, the conventional EBU-Arrhenius

model is used with $W_s = \min(W_{s,EBU}, W_{s,Arr})$, $W_{s,EBU} = C_R \rho \frac{k}{\epsilon} \min\left(Y_F, \frac{Y_{ox}}{\beta}\right)$ and

$$W_{s,Arr} = B_s Y_F Y_{ox} \exp\left(-\frac{E_s}{RT}\right).$$

In Table 2, a is absorption coefficient for gas phase, s is the scattering coefficient of the gas phase. In the calculation of gas phase combustion, the values of a and s are set as 0.1 and 0.01 respectively. The absorption coefficient ϵ_w for the chamber wall is 0.85.

3. PREDICTED RESULTS IN PRE-COMBUSTOR

Fig.1 shows a schematic diagram of the pre-combustor of the melting glass furnace combustion chamber. The chamber is of horseshoe-fired regenerative kind. Air is preheated to 1050°C, and fuel is preheated to 1080°C. The preheated air is injected with a velocity of 10.2 m/s into the pre-combustor at the upper inlet. The upper inlet is at an angle of 20° with the horizontal plane. The fuel inlet has a angle of 45° in the lower part of the pre-combustor. The pre-combustor is 1400 mm long, 357.9 mm high and 870 mm wide. Flow rate of the fuel is set at 1800 Nm³/h. Fuel composition and inlet conditions are given in Table 3.

Fig.2 shows the velocity vectors in the pre-combustor. Predicted results show that there is a low velocity region in the head of the pre-combustor. Above and below this low velocity region are air inlet and fuel inlet respectively. The air and fuel begin to mix and combustion takes place in this region. This low velocity region

enhances stabilization of the diffusion flame. Air velocity at the inlet is set at 10.2 m/s and fuel velocity is set at 7.28 m/s. Flow direction is therefore towards the lower part of the pre-combustor due to the high velocity of air jet. Results show that the gas phase velocity is non-uniform at the exit of the pre-combustor. At the lower part of the pre-combustor, maximum gas velocity is 26.1m/s, while at the upper part of the pre-combustor, gas velocity is only 15.9m/s.

Fig.3 shows the temperature distribution in the pre-combustor. As the air and the fuel mix at the head of the pre-combustor forming a typical diffusion flame towards the lower part of the pre-combustor. At the exit of the pre-combustor, the temperature distribution is non-uniform with maximum gas temperature of 1800K, which is much higher than the value of preheating temperature of 1050°C.

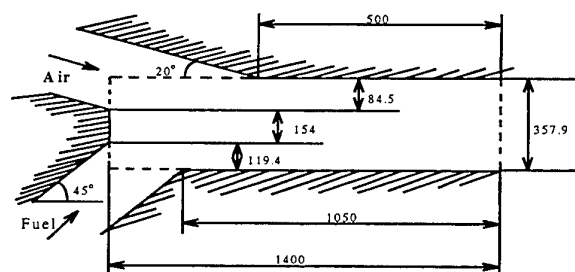


Fig.1. Configuration of the pre-combustor

Table 3. Composition and Inlet Conditions of Generator Gas

CH ₄ (%)	CO (%)	CO ₂ (%)	H ₂ (%)	N ₂ (%)	Temperature (°C)	Velocity (m/s)
3.58	21.08	3.22	2.38	69.74	1080	7.28

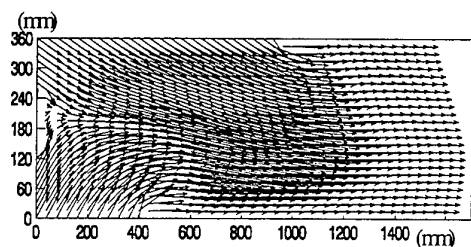


Fig.2. Velocity vectors in pre-combustor

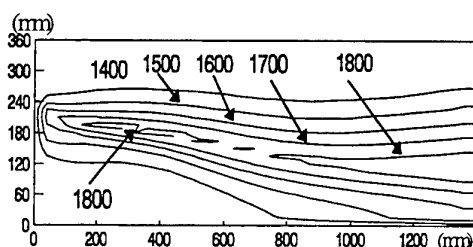


Fig.3. Temperature distribution in the precombustor

Fig.4 gives the concentration distribution of methane (CH₄) and the mass fraction of methane is 3.58% at the inlet. It can be seen that the concentration of methane is about 3.0% in the lower part of the pre-combustor, while it is less than 0.002 in the upper part of the pre-combustor. This indicates that the diffusion and mixing is not complete due to the short residence time. In the upper part of the pre-combustor, there is a lean-fuel zone, while in the lower part of the pre-combustor there is a rich-fuel zone. This kind of distribution can also be found in the concentrations of carbon monoxide (Fig.5) and hydrogen (Fig.6).

Fig.7 shows the concentration distribution of oxygen as the air is injected into the pre-combustor from the upper inlet. Oxygen concentration is higher in the upper region of the pre-combustor having a value of about 20%. In general, the species concentration at the exit of the pre-combustor is non-uniform, which indicate that the inlet condition of the combustion chamber cannot be assumed to be uniform. In fact, the flame formed in the combustion chamber is the development of diffusion flame in the pre-combustor.

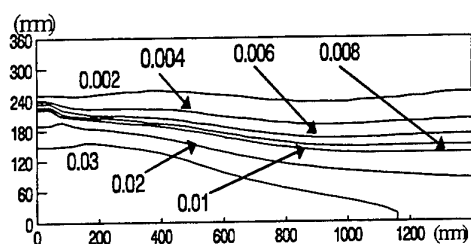


Fig.4. Concentration of Methane (CH_4)

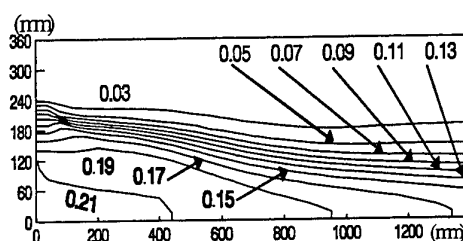


Fig.5. Concentration of CO

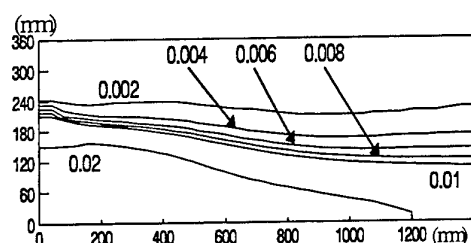


Fig.6. Concentration of Hydrogen

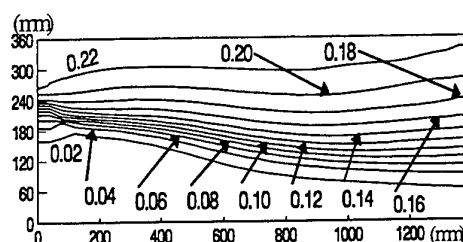


Fig.7. Concentration of Oxygen

4. PREDICTED RESULT IN GLASS MELTING FURNACE CHAMBER

On the basis of numerical results of the pre-combustor, numerical simulations of glass melting furnace combustion chamber was carried out. Fig.8 shows the configuration of the melting glass furnace combustion chamber. The inlet and exit are all arranged at the end of the combustion chamber with the inlet of the chamber being the exit of the pre-combustor.

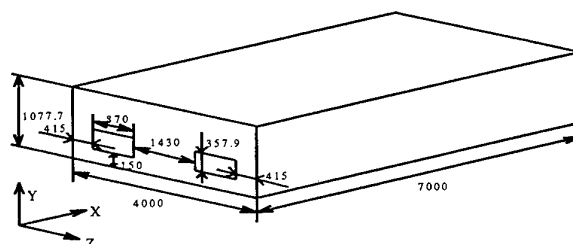


Fig.8. Configuration of glass melting furnace combustion chamber

Two cases of inlet conditions are investigated. One case is the so-called uniform inlet condition which assumes that the air and generator gas are well-stirred. The species concentration, gas temperature and velocity are assumed uniform at the inlet. Another case is non-uniform inlet condition in which the inlet temperature, species concentration and velocities are given by the calculation of the pre-combustor. Values at the exit of the pre-combustor are used as values at the inlet of the combustion chamber.

Fig.9 shows the velocity vectors in the X-Y plane of the combustion chamber. Fig.9 (a) gives predicted results at uniform inlet conditions. At the inlet of the chamber, mean gas velocity is taken to be 18.5 m/s. It can be seen that there is a re-circulating zone in the upper part of the chamber. Ahead of the chamber, there is a reverse-flow zone with length of about 2 metres. The main injection flow zone is about 5 metres long. Fig.9 (b) gives results at non-uniform conditions. At the inlet of the chamber, the maximum velocity is 26.1 m/s and the minimum velocity is 16.1 m/s with mean velocity at the inlet of the combustion chamber of 23.5 m/s which is higher than the mean velocity of the uniform inlet condition. Compared with results under uniform conditions, the main injection flow zone is longer, the upper re-circulating zone is also larger and stronger, and the reverse flow zone smaller and weaker. Fig.10 shows the concentration of carbon monoxide (CO) in the X-Z plane of

combustion chamber. Fig.10 (a) and Fig.10 (b) give results at uniform and non-uniform conditions respectively. Results indicate that the length of carbon monoxide combustion region is shorter with non-uniform inlet condition than with uniform inlet condition in this central inlet section. With uniform inlet conditions, gas combustion begins at the inlet of the chamber, while with non-uniform inlet conditions, gas combustion begins in the pre-combustor.

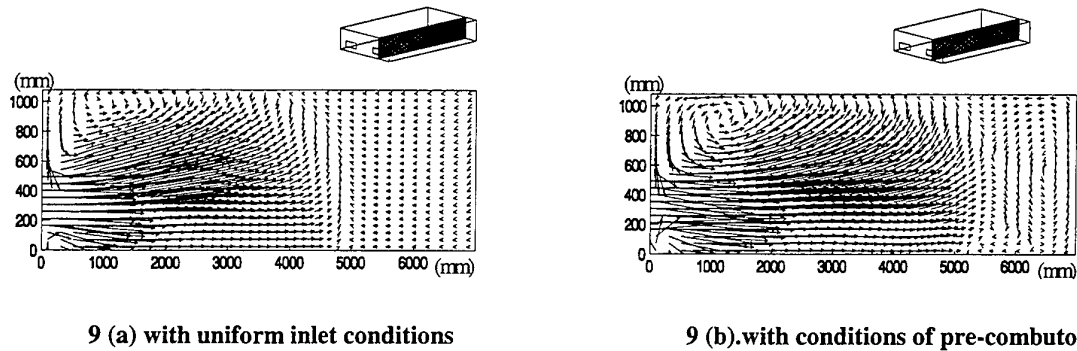


Fig.9. Velocity vectors distribution in the X-Y plane of the combustion chamber

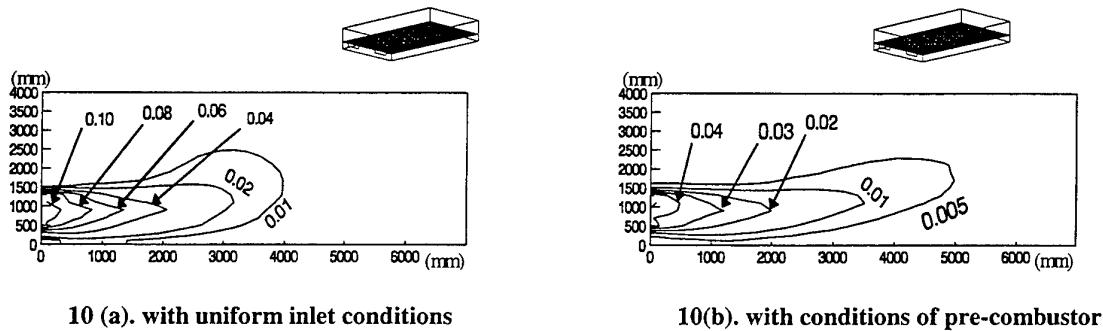


Fig.10. Concentration of carbon monoxide(CO) in the X-Z plane of the combustion chamber

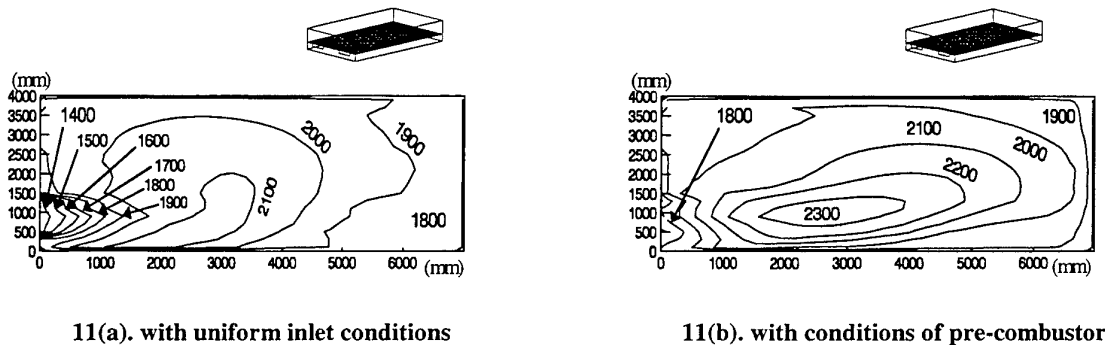


Fig.11. Temperature distributions in the X-Z plane of the combustion chamber

Fig.11 shows the temperature distribution in the X-Z plane of combustion chamber. Fig.11 (a) and Fig.11 (b) give results with uniform and non-uniform conditions respectively. It can be seen that the existing combustion flame is near the inlet side. Compared with the uniform inlet conditions, the predicted temperature is higher

with non-uniform inlet conditions having a maximum temperature is about 2300K. The flame also becomes longer and the high temperature region extends to the head of the chamber.

5. CONCLUSIONS

Results show that the gas phase velocity distribution, temperature distribution and species concentration distributions are non-uniform at the exit of the pre-combustor. There is a diffusion flame at the centre of the pre-combustor. Velocity and temperature have maximum values along the centre line of the pre-combustor. Compared with calculations under uniform inlet parameters and considering the non-uniform inlet condition calculated from the pre-combustor, the predicted results of combustion chamber show that the flame becomes longer while the temperature and velocity become larger, the high temperature region extends to the head of the combustion chamber.

ACKNOWLEDGEMENT

This work was partially supported by the Research Committee of The Hong Kong Polytechnic University under Grant No.A.63.37.PA81.

REFERENCES

1. T. Chen and R. E. Goodson, Glass Tech. Vol.13 (6), pp.161-167 (1972).
2. G. C. Zhao, Numerical Simulation and Model Experiment for Flow and Heat Transfer of Melt in Glass Tank Furnace, Ph. D. Thesis, Tsinghua University (1994).
3. A. D. Gosman, F. C. Lockwood, I. E. A. Megahed and N. G. Shan, "The Prediction of the Flow Reaction and Heat Transfer in the Combustion Chamber of a Glass Melting Furnace", *AIAA 18th Meeting on Aerospace Science*, California (1980).
4. M. G. Carvalho, P. Oliveira and V. S. Semiao, J. Institute of Energy Vol. 61 (448), pp.143-156 (1988).
5. M. G. Carvalho, V. S. Semiao and P. J. Coelho, J. Eng. for Industry Vol.114 (4), pp.514-523 (1992).
6. W. C. Fan and Y. P. Wan, *Model and Calculation of Flow and Combustion*, China Science and Technology University Press (1992).

PREDICTION OF GAS-PARTICLE FLOWS AND GAS COMBUSTION IN A CYCLONE FURNACE

Yin-cheng Guo

Department of Engineering Mechanics, Tsinghua University
Beijing, 100084, China

Email: guoyc@mail.tsinghua.edu.cn; Fax: (8610)62785569

Cheong-ki Chan

Department of Applied Mathematics, The Hong Kong Polytechnic University
Hung Kom, Kowloon, Hong Kong

Email: mackchan@polyu.edu.hk; Fax: (852)23629045

Keywords. cyclone furnace, turbulent gas combustion, two-phase flow, numerical modeling

ABSTRACT: On the basis of the pure two-fluid model for turbulent reacting gas-particle flows with combusting pulverized coal particles, a new comprehensive model for pulverized coal combustion was developed by incorporating a modified k- ϵ -kp model, a general model of pulverized coal devolatilization and a general model of char combustion. Both gas-phase and particle-phase conservation equations are described in the Eulerian coordinates, and these equations are integrated in the computational cell to obtain finite-difference equations. As the first stage of numerical modeling of pulverized coal combustion in the cyclone furnace, three dimensional simulation of turbulent gas combustion and gas-particle flows have been made. Predicted results show that there is a near wall re-circulating zone at the bottom of the cyclone furnace, and the re-circulating zone enhances ignition and flame stabilization. Results of tangential velocity distribution of both gas phase and particle phase are similar to those of the Rankine vortex.

1. INTRODUCTION

Simulation of pulverized coal combustion process involves modeling a number of complex simultaneous interdependent processes. The comprehensive model must account for turbulent gas-particle flow, gas phase combustion, coal particle mass change due to moisture evaporation, devolatilization and char combustion, NO_x formation, and radiative heat transfer. It is most difficult to model the reacting coal particles and their effect on the gas phase. In treating the particle phase for modeling pulverized coal combustion, most of current models adopt Lagrangian treatment of particles (Lockwood et al [1], Papadakis and Bergeles [2], Coimbra et al.[3]). In using particle trajectory model, it is easy to simulate the combusting coal particle history, despite requiring a large amount of particle trajectories for comparing with experimental data. Fiveland and Wessel [4] developed an Eulerian model for pulverized coal combustion by neglecting the velocity slip between the gas phase and coal particle phase. They also assumed that the temperature of coal particle phase is equal to the temperature of gas phase. The temperature of the gas-particle mixture can be obtained by solving the overall energy equation.

In this paper, a pure two-fluid model for reacting gas-particle flows is developed, using unified Eulerian treatment for both gas phase and particle phase. Both velocity slip and temperature slip between coal particles and gas phase are calculated by solving momentum equations and energy equations of gas phase and particle phase respectively. Besides, a modified k- ϵ -kp two-phase turbulence model, a second-order moment turbulence-chemistry model for NO_x formation, and a general model of pulverized coal devolatilization and a general model of char combustion were incorporated into the comprehensive model. For volatile and CO combustion and radiative heat transfer, conventional EBU-Arrhenius model and six heat-flux model were used.

2. GOVERNING EQUATIONS AND CLOSURE MODELS

The basic idea of the pure two-fluid model is to consider the particle phase as a pseudo-fluid interpenetrating with the gas phase. The basic assumptions are:

- (1) at each location of the flow field, particle phase and gas phase coexist and interpenetrate into each other, each having its own velocity and temperature.

- (2) each particle phase is identified by its initial size distribution which has its own continuous velocity and temperature distribution in space.
- (3) besides the mass, momentum and energy interaction with the gas phase, each particle phase has its own turbulent fluctuation resulting in particle turbulent transport of mass, momentum and energy. This particle fluctuation is determined by convection, diffusion, production and interaction with gas phase turbulence.
- (4) for dilute particulate suspensions the particle-particle collision effect can be neglected.

Based on the above assumptions, adopting a modified k- ϵ -kp two-phase turbulence model, the time-averaged equations of gas phase and particle phase in Eulerian coordinate can be obtained as the following.

Gas phase continuity equation

$$\frac{\partial}{\partial x_j}(\rho v_j) = -\sum_k n_k \dot{m}_k \quad (1)$$

The term on the right-hand side of Eq.(1) expresses the coal particle mass change due to moisture evaporation, daf (dry and free) coal devolatilization and char combustion.

Gas phase momentum equation

$$\frac{\partial}{\partial x_j}(\rho v_j v_i) = -\frac{\partial p}{\partial x_i} + \frac{\partial}{\partial x_j} \left(\mu_e \frac{\partial v_j}{\partial x_i} \right) + \frac{\partial}{\partial x_j} \left(\mu_e \frac{\partial v_i}{\partial x_j} \right) + \rho g_i - \sum_k \frac{\rho_k}{\tau_{rk}} (v_i - v_{ki}) - v_i \sum_k n_k \dot{m}_k \quad (2)$$

The last two terms on the right-hand side of Eq.(2) are source terms due to interaction between the gas phase and particle phase, the fifth term is volume-averaged particle drag force, where ρ_k is bulk density of raw-coal particle phase, and τ_{rk} is the relaxation time for particle mean motion, which can be expressed as

$$\tau_{rk} = \frac{d_k^2 \rho_p}{18\mu} \left(1 + \frac{Re_k^{0.6667}}{6} \right)^{-1} \quad (3)$$

d_k is the diameter of k-group coal particles, ρ_p is material density of raw-coal particle phase and Re_k is the Reynolds number of particle-gas relative motion, which can be expressed as

$$Re_k = \frac{|\bar{v} - \bar{v}_k| d_k}{\nu} \quad (4)$$

Gas phase turbulent kinetic energy equation

$$\frac{\partial}{\partial x_j}(\rho v_j k) = \frac{\partial}{\partial x_j} \left(\frac{\mu_e}{\sigma_k} \frac{\partial k}{\partial x_j} \right) + G_k - \rho \epsilon + G_p + G_R \quad (5)$$

where G_k is the production term, which can be expressed as: $G_k = \mu_T \left(\frac{\partial v_i}{\partial x_j} + \frac{\partial v_j}{\partial x_i} \right) \frac{\partial v_i}{\partial x_j}$, and μ_e is the

effective viscosity defined as $\mu + \mu_T$ where $\mu_T = C_\mu \rho k^2 / \epsilon$ is the gas phase turbulence viscosity. The last two terms on the right-hand side of Eq.(5) are source terms due to interaction between the gas phase and particle phase, $G_p = \sum_k \frac{2\rho_k}{\tau_{rk}} (C_p^k \sqrt{k k_k} - k)$, where k_k is k-group particle phase turbulent kinetic energy, and C_p^k is

empirical modeling constant which has the value of 0.75, the last term $G_R = -k \sum_k n_k \dot{m}_k$ is the production term due to mass change of coal particles.

Gas phase turbulent kinetic energy dissipation rate equation:

$$\frac{\partial}{\partial x_j} (\rho v_j \epsilon) = \frac{\partial}{\partial x_j} \left(\frac{\mu_e}{\sigma_\epsilon} \frac{\partial \epsilon}{\partial x_j} \right) + \frac{\epsilon}{k} [C_1 G_k - C_2 (1 - C_{gs} R_{igs}) \rho \epsilon] + \frac{\epsilon}{k} C_1 (G_p + G_R) \quad (6)$$

For strongly swirling flows, it is necessary to modify the ϵ -equation using a modified source term, adopting the treatment suggested by Launder et al [5], where $R_{igs} = \frac{k^2}{\epsilon^2} \frac{w}{r} \left(\frac{\partial w}{\partial r} + \frac{w}{r} \right)$.

Gas phase thermal enthalpy equation

$$\frac{\partial}{\partial x_j} (\rho v_j h) = \frac{\partial}{\partial x_j} \left(\frac{\mu_e}{\sigma_h} \frac{\partial h}{\partial x_j} \right) + W_s Q_s + 2a_g \left(\sum_j q_{rj} - 3E_{bj} \right) - \sum_k n_k Q_k - \sum_k n_k \dot{m}_k C_{pk} T_k. \quad (7)$$

In the right-hand side of Eq.(7), there are diffusion term of thermal enthalpy, heat release from gas phase turbulent combustion, radiative heat transfer of gas phase, convective heat transfer between coal particles and gas phase, and energy source term of phase change due to evaporation, devolatilization and char combustion.

where $Q_k = \pi d_k Nu_k \lambda_s (T - T_k) \frac{B_k}{\exp(B_k) - 1}$, $B_k = \frac{-\dot{m}_k C_{ps}}{\pi d_k Nu_k \lambda_s}$, and $Nu_k = 2 + 0.5 Re_k^{0.5}$. In the case where coal particle temperature is different from that of the gas phase, the so-called 1/3 Law is used for calculating the thermoconductivity λ_s and specific heat C_{ps} near the boundary layer of coal particles. As for radiative heat transfer, six heat-flux model is used, the governing equation for the radiative heat flux in the I-th direction q_{ri} is given as

$$\frac{d}{dx_i} \left(\frac{1}{a + s} \frac{dq_{ri}}{dx_i} \right) = a_g (q_{ri} - E_{bg}) + \frac{s}{3} (2q_{ri} - q_{rj} - q_{rk}) + a_k (q_{ri} - E_{bk}) \quad (8)$$

where $a = a_g + a_k$, $s = s_g + s_k$, $a_k = Q_{ak} \frac{\pi}{4} n_k d_k^2$, $s_k = Q_{sk} \frac{\pi}{4} n_k d_k^2$. a_g and a_k are absorption coefficient for the gas phase and particle phase respectively, s_g and s_k are scattering coefficient of the gas phase and particle phase, Q_{ak} is efficiency factor for absorption of particle radiation and Q_{sk} is efficiency factor for scattering of particles.

Gas phase species mass fraction equation:

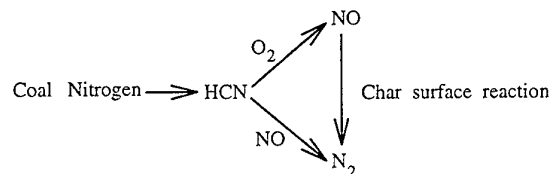
$$\frac{\partial}{\partial x_j} (\rho v_j Y_s) = \frac{\partial}{\partial x_j} \left(\frac{\mu_e}{\sigma_Y} \frac{\partial Y_s}{\partial x_j} \right) - W_s - \alpha_s \sum_k n_k \dot{m}_k \quad (9)$$

For volatile (assuming that the volatile is Methane) and CO combustion, the conventional EBU-Arrhenius model is used and $W_s = \min(W_{s,EBU}, W_{s,A\pi})$, where

$$W_{s,EBU} = C_R \rho \frac{k}{\epsilon} \min \left(Y_F, \frac{Y_{ox}}{\beta} \right), W_{s,A\pi} = B_s Y_F Y_{ox} \exp \left(-\frac{E_s}{RT} \right).$$

The last term on the right-hand side of Eq.(9) is the source term due to mass change of coal particles, α_s is the fraction of contribution of s-species in phase change.

As for NO_x formation, most of the nitrogen oxides emitted to the atmosphere by combustion are in form of nitric oxide (NO). Two mechanisms of nitric oxide formation are considered, thermal NO and fuel NO. Thermal NO is predicted using the Zeldovich mechanism. The fuel NO formation is described by a global mechanism explicit only in HCN, NO, and N_2 . The fuel NO formation mechanism is shown as follows



The reaction rate for HCN is $W_{\text{HCN}} = (W_0 - W_1 - W_2)M_{\text{HCN}}$, and the source term for NO can be written as $W_{\text{NO}} = (W_1 - W_2 - W_3)M_{\text{NO}} + W_4$, where $W_0 = \alpha_N \dot{m}_k / M_N$.

$$W_1 = \rho (1 \times 10^{11}) \frac{Y_{\text{HCN}} M_M}{M_{\text{HCN}}} \left(\frac{Y_{\text{O}_2} M_M}{M_{\text{O}_2}} \right)^b \exp \left(-\frac{67.0 \text{ kcal}}{RT} \right) (1 + F_1) \quad (10)$$

$$W_2 = \rho (3 \times 10^{12}) \frac{Y_{\text{HCN}} M_M}{M_{\text{HCN}}} \left(\frac{Y_{\text{NO}} M_M}{M_{\text{NO}}} \right) \exp \left(-\frac{60.0 \text{ kcal}}{RT} \right) (1 + F_2) \quad (11)$$

$$W_3 = 4.18 \times 10 n_k m_k A_E P_{\text{NO}} \exp \left(-\frac{34.7 \text{ kcal}}{RT} \right) \quad (12)$$

$$W_4 = 8.39 \times 10^{16} \rho^{1.5} T^{-0.5} Y_{\text{N}_2} Y_{\text{O}_2}^{0.5} \exp \left(-\frac{134.9 \text{ kcal}}{RT} \right) (1 + F_3) \quad (13)$$

Using a second-order moment to account for turbulence-chemistry interaction for NO_x formation, the time-averaged reaction for thermal NO, F_3 can be modeled as:

$$F_3 = \frac{\overline{Y_{\text{N}_2} Y_{\text{O}_2}}}{Y_{\text{N}_2} Y_{\text{O}_2}} + \frac{E}{RT} \left[\left(\frac{1}{2} \frac{E}{RT} - 1 \right) \left(\frac{\sqrt{T'}}{T} \right)^2 + \frac{\overline{T' Y_{\text{O}_2}}}{T Y_{\text{O}_2}} + \frac{\overline{T' Y_{\text{N}_2}}}{T Y_{\text{N}_2}} \right] \quad (14)$$

The correlations are modeled using gradient assumptions. The algebraic expressions can be written as

$$\overline{Y_{\text{N}_2} Y_{\text{O}_2}} = C_Y \frac{k^3}{\epsilon^2} \frac{\partial Y_{\text{N}_2}}{\partial x_j} \frac{\partial Y_{\text{O}_2}}{\partial x_j}, \quad \overline{T' Y_{\text{O}_2}} = C_Y \frac{k^3}{\epsilon^2} \frac{\partial T}{\partial x_j} \frac{\partial Y_{\text{O}_2}}{\partial x_j},$$

$$\overline{T' Y_{\text{N}_2}} = C_Y \frac{k^3}{\epsilon^2} \frac{\partial T}{\partial x_j} \frac{\partial Y_{\text{N}_2}}{\partial x_j}, \quad \overline{T'^2} = C_Y \frac{k^3}{\epsilon^2} \left(\frac{\partial T}{\partial x_j} \right)^2$$

The terms F_1 and F_2 can be modeled in a similar way. The heterogeneous char/NO reaction rate is not fast,

therefore effects of turbulence on char surface reaction rate is neglected.

Particle phase number density equation:

$$\frac{\partial}{\partial x_j} (n_k v_{kj}) = \frac{\partial}{\partial x_j} \left(\frac{\gamma_k}{\sigma_p} \frac{\partial n_k}{\partial x_j} \right) \quad (15)$$

Particle phase (raw coal) bulk density equation:

$$\frac{\partial}{\partial x_j} (\rho_k v_{kj}) = \frac{\partial}{\partial x_j} \left(\frac{\gamma_k}{\sigma_p} \frac{\partial \rho_k}{\partial x_j} \right) + n_k \dot{m}_k \quad (16)$$

Daf coal bulk density equation:

$$\frac{\partial}{\partial x_j} (\rho_{dk} v_{kj}) = \frac{\partial}{\partial x_j} \left(\frac{\gamma_k}{\sigma_p} \frac{\partial \rho_{dk}}{\partial x_j} \right) + n_k \dot{m}_{dk} \quad (17)$$

coal particle moisture bulk density equation:

$$\frac{\partial}{\partial x_j} (\rho_{wk} v_{kj}) = \frac{\partial}{\partial x_j} \left(\frac{\gamma_k}{\sigma_p} \frac{\partial \rho_{wk}}{\partial x_j} \right) + n_k \dot{m}_{wk} \quad (18)$$

As the bulk density of coal particle phase, $\rho_k = n_k m_k$, by solving Eq.(15) and Eq.(16), the mass m_k of a single coal particle can be obtained. Similarly, by solving Eq.(17) and Eq.(18), the daf coal mass and moisture content can be calculated. Therefore, Eq.(15) to Eq.(18) reveal the mass change due to moisture evaporation, daf coal devolatilization and char combustion. The total rate of change of mass is the sum of the devolatilization rate, the char reaction rate and the moisture evaporation rate and can be expressed as

$$\dot{m}_k = \dot{m}_{dk} + \dot{m}_{ck} + \dot{m}_{wk} \quad (19)$$

where \dot{m}_{wk} is moisture evaporation rate, which can be determined as $\dot{m}_{wk} = -\pi d_k Nu_k D_p \ln \left(1 + \frac{Y_{ws} - Y_{wg}}{1 - Y_{ws}} \right)$.

$Y_{ws} = B_w \exp \left(-\frac{E_w}{RT_k} \right)$ is mass fraction of vapor at the surface of coal particles Y_{wg} is the mass fraction of vapor in the calculation grid.

Using the general model of pulverized coal devolatilization suggested by Fu et al.[6], the devolatilization rate of daf coal can be obtained as:

$$\dot{m}_{dk} = -m_{daf,0} K_0 \left(V_{\infty} - \frac{m_{daf,0} - m_{daf}}{m_{daf,0}} \right) \exp \left(-\frac{E_v}{RT_k} \right). \quad (20)$$

The general devolatilization model assumes that the kinetic parameters, E_v and K_0 are independent of coal type and depend only on the final temperature of coal particles. The final temperature can be taken as

$$V_{\infty} = 1.2 V_{daf}^{0.8} \exp \left(-\frac{2 \times 10^6}{R(T_g - T_0)^2} \right) \quad (21)$$

The heterogeneous reaction rate of char can also be determined using a general model developed by Fu and Zhang [7]. The overall rate of char combustion is

$$\dot{m}_{ck} = -\pi d_k^2 K_{0, ch} \rho_s Y_{O_2, s} \exp(-E/RT_k) \quad (22)$$

in which the activation energy, E , is independent of coal properties and only varies with the temperature of the char particle. However, the frequency factor of char oxidation, $K_{0, ch}$, is dependent on coal properties during combustion. A value of $E = 180 \text{ kJ/mol}$, a constant in the oxidation of coal char in air is used.

Particle phase momentum equation:

$$\frac{\partial}{\partial x_j} (\rho_k v_{kj} v_{ki}) = \frac{\partial}{\partial x_j} \left(\mu_k \frac{\partial v_{kj}}{\partial x_i} \right) + \frac{\partial}{\partial x_j} \left(\mu_k \frac{v_{ki}}{x_j} \right) + \frac{\rho_k}{\tau_{rk}} (v_i - v_{ki}) + \frac{\partial}{\partial x_j} \left(v_{kj} \frac{\gamma_k}{\sigma_p} \frac{\rho_k}{x_i} + v_{ki} \frac{\gamma_k}{\sigma_p} \frac{\rho_k}{\partial x_j} \right) + v_i n_k \dot{m}_k + \rho_k g_i \quad (23)$$

Particle phase thermal enthalpy equation:

$$\frac{\partial}{\partial x_j} (\rho_k v_{kj} h_k) = \frac{\partial}{\partial x_j} \left(\frac{\mu_k}{\sigma_p} \frac{\partial h_k}{\partial x_j} \right) + Q_{rk} + n_k Q_{ck} + n_k Q_k + h_k n_k \dot{m}_k \quad (24)$$

where $h_k = C_{pk} T_k$ and Q_{rk} is the radiative heat transfer, $Q_{rk} = 2a_k \left(\sum_j q_{rj} - 3E_{bk} \right)$, Q_{ck} is the heat released by heterogeneous reaction on the coal particle surface.

Particle phase turbulent kinetic energy equation

$$\frac{\partial}{\partial x_j} (\rho_k v_{kj} k_k) = \frac{\partial}{\partial x_j} \left(\frac{\mu_k}{\sigma_p} \frac{\partial k_k}{\partial x_j} \right) + \frac{\partial}{\partial x_j} \left(k_k \frac{\gamma_k}{\sigma_p} \frac{\partial \rho_k}{\partial x_j} \right) + G_{pk} + G_{gk} \quad (25)$$

The particle phase turbulent kinetic energy is determined by convection, diffusion, production and the interaction with gas phase turbulence. G_{pk} is the production term of particle phase, which can be expressed as:

$$G_{pk} = \mu_k \left(\frac{\partial v_{ki}}{\partial x_j} + \frac{\partial v_{kj}}{\partial x_i} \right) \frac{\partial v_{ki}}{\partial x_j} . \text{ Using the kp model to model the particle phase turbulence, the particle phase}$$

turbulent viscosity is determined as $\mu_k = C_{\mu p} \rho_k k_k^{0.5} k_k^{1.5} / \epsilon$. The last term on the right-hand side of Eq.(25) is the source terms due to interaction between the gas phase and particle phase.

$$G_{gk} = \frac{2\rho_k}{\tau_{rk}} \left(C_p^k \sqrt{k k_k} - k_k \right) + \left(2C_p^k \sqrt{k k_k} - k_k \right) n_k \dot{m}_k + \left(\frac{1}{\tau_{rk}} + \frac{\dot{m}_k}{m_k} \right) \frac{v_k}{\sigma_p} (v_j - v_{kj}) \frac{\partial \rho_k}{\partial x_j} \quad (26)$$

For the pure two-fluid model, the gas phase and particle phase have separate momentum equations, thermal enthalpy equations and turbulent kinetic energy equations. Velocity slip and temperature slip between the gas phase and particle phase can be predicted. Each particle phase has a set of governing equations describing particle mass, momentum and energy diffusion.

3. NUMERICAL SOLUTION PROCEDURE

Both gas-phase and particle-phase conservation equations in the Eulerian coordinates are integrated in the computational cell to obtained finite-difference equations. The gas-phase equations are solved using the SIMPLE algorithm, i.e. p-v corrections with TDMA line-by-line iterations and under-relaxations. Similar

procedure is used for the particle phase, but without p-v corrections. Multiple iterations between gas phase and particle phase are adopted based on two-way coupling between Eulerian gas and Eulerian particles.

4. PREDICTED RESULT AND DISCUSSION

As the first stage of numerical modeling of pulverized coal combustion in the cyclone furnace, three dimensional simulation of turbulent gas combustion and gas-particle flows have been made. The configuration of cyclone furnace and the inlet conditions are shown in Fig.1. The inlet temperature of primary air and secondary air is 300K and the inlet velocity is along the tangential direction of the furnace. A single group coal particles with the diameter of $60\text{ }\mu\text{m}$ are calculated. The mass flow rate of particle phase to gas phase is taken as 0.09. Five species are considered in turbulent gas combustion, there are CH_4 , O_2 , CO , CO_2 and H_2O .

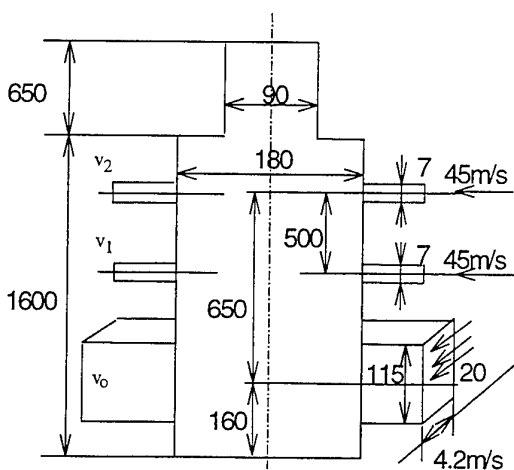


Fig. 1. Configuration of cyclone furnace

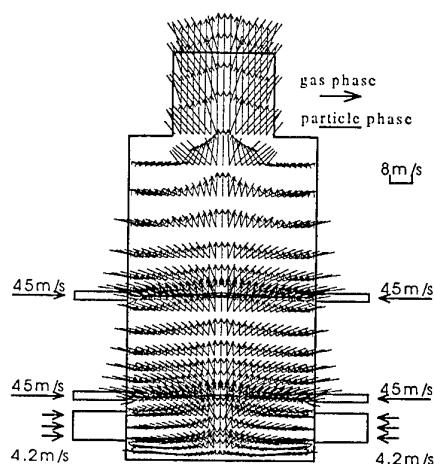


Fig. 2. Gas and particle phase velocity vectors

Fig.2 is the gas phase and particle phase velocity vector distribution under the condition of the gas phase combustion. It can be seen that both the gas phase and particle phase have large axial velocities in the centre of the furnace compare with the near wall region. For isothermal flow, axial velocities of gas phase and particle phase are all small in the centre of the furnace. From the distribution of gas phase and particle phase velocity vectors, it can also be seen that there is a large velocity slip between the gas phase and particle, especially in the radial direction. Compared with the gas phase radial velocity, the particle phase radial velocity is much larger due to the centrifugal force. At the bottom of the cyclone furnace, results show that there is a re-circulating zone near the wall, this re-circulating zone enhances ignition and flame stabilization. Fig.3 shows the axial velocities of gas phase and particle phase. It can be seen that the particle phase axial velocity distribution is similar to that of gas phase, indicating that the velocity slip in the axial direction is small.

Fig.4 gives the tangential velocity distribution of gas phase and particle phase. Results show that the tangential velocity distribution of both gas phase and particle phase was similar to those of the Rankine vortex. Comparing with the particle phase, the gas phase has larger values of tangential velocities. Fig.5 shows the bulk density distribution of particle phase. Results show that the particle phase concentration is much higher in the region near the wall of the furnace due to the centrifugal force. In the central upper part of the furnace, the particle concentration is nearly zero, which is a characteristic swirling gas-particle flows.

Fig.6 shows the gas phase temperature distribution. The temperature changes rapidly near the wall of the furnace. At the central region of the furnace, gas phase temperature is nearly uniform at about 1700K. Fig.7 gives the methane (CH_4) concentration profile. At the inlet, the mass fraction of methane concentration is 0.03 when it is injected into the furnace at the primary air inlet located at the bottom of the furnace. Velocity of primary air is 4.2 m/s. From Fig.7, it can be seen that methane combustion is rapid and complete at the lower part of the furnace.

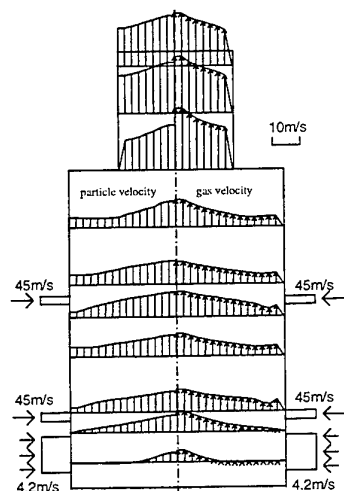


Fig. 3. Gas and particle phase axial velocity

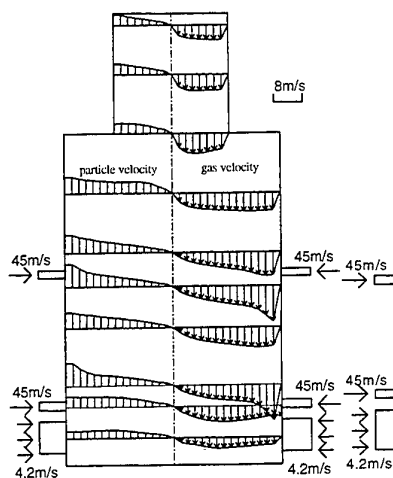


Fig. 4. Gas and particle phase tangential velocity

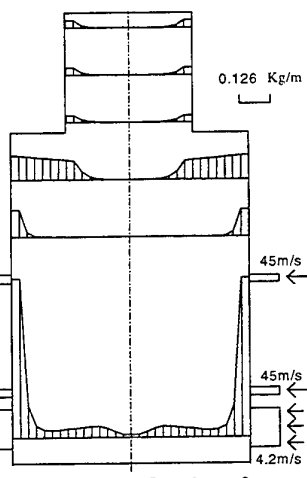


Fig. 5. Bulk density of particle phase

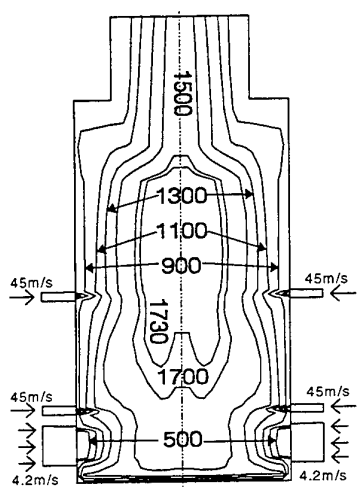


Fig. 6. Gas phase temperature

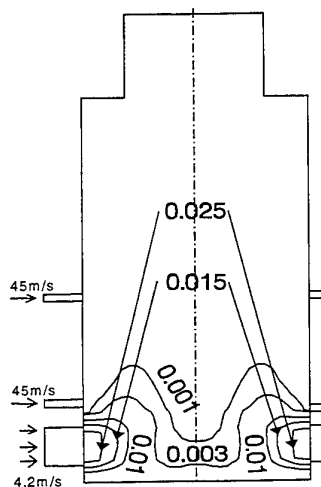


Fig. 7. CH₄ concentration

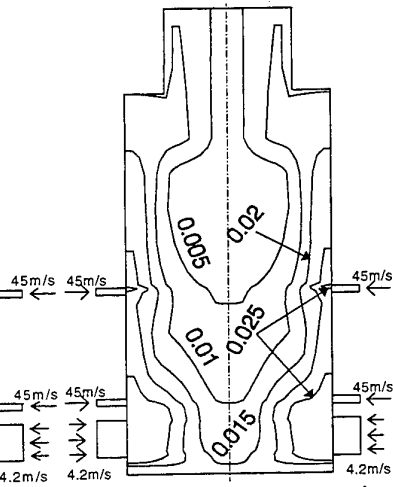


Fig. 8. CO concentration

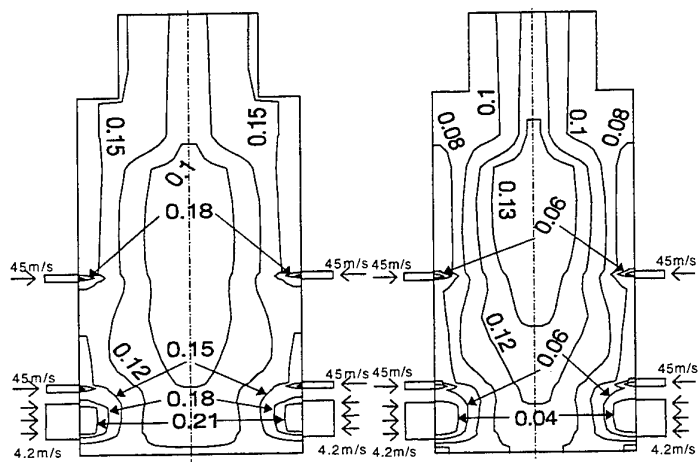


Fig. 9. O₂ concentration map

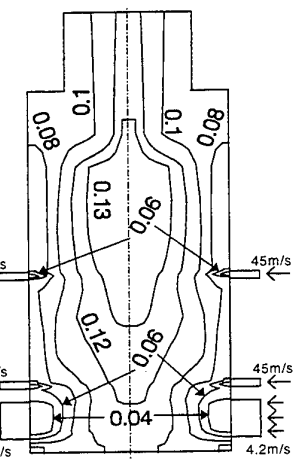


Fig. 10. CO₂ concentration

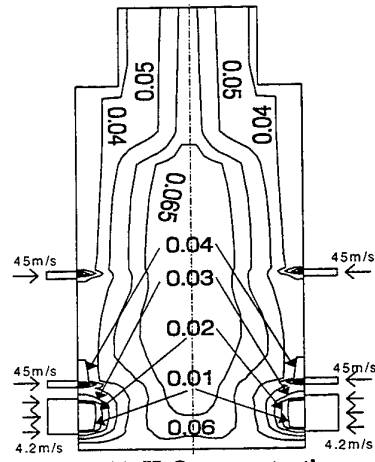


Fig. 11. H₂O concentration

Fig.8 shows the carbon monoxide (CO) concentration. At the inlet, the mass fraction of carbon monoxide is 0.03 when it is injected into the furnace not only at the primary air inlet located at the bottom of the furnace, but also at the upper secondary air inlets. It can be seen that the rate of carbon monoxide combustion is slow. At the exit of the furnace, the carbon monoxide concentration is still about 0.005, indicating that the combustion process is not complete. Fig.9 shows the oxygen (O₂) concentration distribution. The mass fraction of oxygen in the central region of the furnace is reduced due to methane and carbon monoxide combustion, whereas it is nearly uniform at the exit of the furnace at about 0.10. Fig.10 and Fig.11 show the combustion productions carbon dioxide and water vapor concentration distributions.

5. CONCLUSIONS

A comprehensive numerical model for pulverized coal combustion has been developed on the basis of pure two-fluid model for reacting gas-particle flows. As the first stage of numerical modeling of pulverized coal combustion, this model has been applied to the simulation of turbulent gas combustion and gas-particle flows in a cyclone furnace. Results show that there is large velocity slip between the gas phase and particle phase, especially in the radial direction. Particle velocities are much larger than gas phase velocities due to the centrifugal force. In the annular wall region of the cyclone furnace, the particle phase reaches its concentration peak. Predicted results show that there is a near wall re-circulating zone at the bottom of the cyclone furnace, and the re-circulating zone enhances ignition and flame stabilization.

ACKNOWLEDGEMENT

This work was partially supported by the Research Committee of The Hong Kong Polytechnic University under Grant No.A.63.37.PA81.

REFERENCES

1. C. Lockwood, C. Papadopoulos and A. S. Abbas, Combust. Sci. Tech. Vol.58, pp5-23 (1988).
2. G. Papadakis and G. Bergeles, J. of the Institute of Energy Vol.67, pp.156-167 (1994).
3. C. F. M. Coimbra, J. L. T. Azevedo and M. G. Carvalho, Fuel Vol.73, pp1128-1134 (1994).
4. W. A. Fiveland and R. A. Wessel, J. Eng. for Gas Turb. and Power Vol.110, pp.117-126 (1988).
5. B. E. Launder, C. H. Priddin and B. I. Sharma, J. Fluid Engng Vol.99, pp.363-374 (1979).
6. W. Fu, Y. Zhang, H. Han and D. Wang, Fuel Vol.68, pp505-510 (1989).
7. W. Fu and B. Zhang, J. of Combustion Science and Technology Vol.3, No.1, pp.1-14 (1997)

STIMULATED IGNITION OF NATURAL GAS AT COMPRESSION IGNITION CONDITIONS

M. Mbarawa, B.E. Milton, R.T. Casey
School of Mechanical and Manufacturing Engineering
The University of NSW, Australia
Email: b.milton@unsw.edu.au; Fax (61) 2 9663-1222

Keywords: dual-fuelling, natural gas engines, alternative diesel fuels

ABSTRACT. Most alternative fuels for internal combustion engines have low cetane numbers. This is particularly true of natural gas (NG) which has excellent clean burning characteristics and low greenhouse gas production. Compression ignition (CI) engines supply an increasing amount of the world's power because of their very high efficiency and suitability for large units. However, low cetane number fuels such as NG are not suited to compression ignition because their long ignition delay causes severe engine knock. Nevertheless, they can be used in CI engines by adopting a mixed combustion process called dual-fuelling (DF). Here, ignition of the alternative fuel is stimulated by a pilot distillate spray. When compared with NG spark ignition engines, the DF process has the added advantage of fuel flexibility during the development of an alternative fuel distribution system. Engine tests have highlighted many DF combustion problems. In this research program, a constant volume combustion bomb and an associated 3D numerical model have been used to examine the DF combustion of NG/air mixtures. The numerical model gives pressure traces which compare well with experiment. Using it, parametric studies illustrate the importance of the injection process on the subsequent NG combustion.

1. DUAL-FUEL ENGINES AND THEIR COMBUSTION PROBLEMS

There is currently a renewed interest in the practical application of alternative fuels, particularly natural gas (NG), in commercial transport vehicles. This is not only because NG is, compared to petroleum fuels, a cheap and abundant fuel, but also because it helps to reduce both local and global emissions. Compression ignition (CI) engines have become the main prime movers for commercial vehicle transport and small to medium scale on-site power generation where high efficiency is required. However, while NG has excellent clean burning characteristics and low greenhouse gas emissions, it has a number of combustion problems which prevents its direct use in these engines. These include inadequate ignition and possible severe "diesel knock" due to its long ignition delay (from its low cetane number) and poor flame propagation and possible flame quench in the pre-mixed fuel/air regions because of its slow burning characteristics at low NG/air equivalence ratios. These last occur when diesel type, "fuel/air ratio" governing is used. Thus, throttle controlled, spark ignition (SI) NG engines have been the preferred solution but these have lower efficiency and cylinder size limitations compared with diesels. They also experience fuelling supply problems on many routes due to the lack of a fuelling infrastructure and cannot easily provide a retro-fit solution to existing equipment. However, there is another solution which has the potential to solve these problems. For this, NG (or any other low cetane number fuel) can be used in CI engines as a pre-mixed primary fuel with an additional pilot diesel spray to provide ignition and, where necessary, stimulate the burning. Such engines are commonly known as dual-fuel (DF) types. While they have existed for a considerable period of time in stationary installations, they have potential for commercial road transport. While the DF system allows a NG CI type engine to operate, the mixed DF combustion process is complex and requires an improved understanding to aid in optimising performance, maximising NG substitution levels, raising efficiency and lowering emissions, particularly at light load operation.

In a DF engine, the NG fuel is normally introduced with the intake air in such a proportion that it is outside the auto-ignition limits at the conditions prevailing in the cylinder at the end compression. Admission is normally into the intake manifold but it may be through a timed injector directly into the cylinder. The former method is simpler and is far more common as no modifications are required to the cylinder head. In that system, substantial mixing occurs prior to the inlet valve and, while exceptions exist, a homogeneous NG/air mixture may be assumed to exist throughout any cylinder at ignition. However, at high NG levels, pre-mixing can lead to end-gas auto ignition (SI type) knock which was originally assumed to be the sole knock problem [1] and, on

very large bore stationary engines was likely to dominate.. However, there is evidence that the NG increases the diesel ignition delay [2,3,4] which can then exacerbate the normal CI type knock found in conventional diesel engines. Other problems such as ignition failure, incomplete combustion and direct short-circuiting of the fuel from the intake to exhaust occur. Direct NG injection allows improved control of gas losses to the exhaust (this being of particular importance with two-strokes), can give better air capacity as there is no displacement in the manifold and may reduce end-zone gas and hence SI knock and flame quench. However, it is much more complex. This paper is therefore concerned with the more usual manifold pre-mixed DF combustion.

The research reported here has concentrated on fundamental DF studies by use of a constant volume combustion bomb and a 3D numerical simulation code which has been developed for the bomb conditions. The conditions studied are, within the limits of the experimental apparatus, approaching those of naturally aspirated CI engines but without the swirl and turbulence generated by the intake and compression processes. The experimental results obtained from the combustion bomb tests were used to validate the numerical model. This was followed by a parametric analysis of the DF process to examine trends which were difficult to obtain experimentally. Both global and spatial effects of the pilot injector characteristics were considered.

2. THE EXPERIMENTAL EQUIPMENT

The constant volume combustion bomb and injection equipment used for this research has been described previously [5,6]. The bomb consists of an inner pressure cylinder (the test chamber) electrically heated by a surrounding 1.5 kW, 240 V electrical element wrapped with a ceramic fibre blanket to ensure minimum external heat loss. The unit is enclosed by an outer pressure casing. This, together with pressurisation of the chosen NG/air mixture allowed the required pre-ignition conditions to be obtained in a quiescent condition for the combustion study. The pre-ignition conditions could be varied over a wide range. Some limitations on the conditions existed. In particular, the pre-ignition temperature was a little below normal CI levels as it was found that higher temperatures could spontaneously ignite the pre-mixed NG fuel. The inner cylinder dimensions were: bore, 108 mm, depth, 30 mm. The pilot fuel injection system was based on a multi-cylinder Caterpillar pump with a solenoid valve installed between the pump and injector. Fuel normally by-passed the injector. When the valve was triggered by a timing pulse, the solenoid valve provided a single shot of pilot fuel to the injector. The injector opening pressure was normally 20 MPa giving a maximum injection pressure of 30 MPa through a vertical, central, 4 hole, pencil type injector, the spray from each orifice being oriented 15° below the horizontal. The opening pressure could be adjusted downwards with a consequent reduction in maximum pressure. Details of the experimental set-up and procedures are described in [6,7,8]. The pilot fuel injection system has a maximum capability of 57 mg/shot.

3 MODELLING THE DUAL-FUEL COMBUSTION PROCESS

Description of the Model

A simplified 3D, finite volume model has been developed [6,9] for simulation of the DF combustion in the cylindrical constant volume combustion bomb. For the former, the central location of the injector with its four equally-spaced holes enabled the computation to be performed for the quarter chamber only. In the model, two modes of NG introduction are possible, either pre-mixed with air [6] or injected in a separate spray near the diesel injector [9]. In this study, only the former was studied. The diesel injection simulation sub-model is similar to that of a normal CI system but, for DF operation, is reduced in quantity.

The numerical solution of the diesel spray, evaporation, ignition and subsequent gas phase combustion process follows the procedure described previously. It is based on the conservation equations of mass, enthalpy and momentum with the injection stimulated turbulence described by the κ - ϵ eddy diffusivity model. The general governing equation [9] in cylindrical coordinates is:

$$\frac{\partial(\rho_g \phi)}{\partial t} + \frac{1}{r} \frac{\partial(\rho_g r U_r \phi)}{\partial r} + \frac{1}{r} \frac{\partial(\rho_g U_\theta \phi)}{\partial \theta} + \frac{\partial(\rho_g U_z \phi)}{\partial z} - \frac{1}{r} \frac{\partial}{\partial r} \left(r \Gamma_\phi \frac{\partial \phi}{\partial r} \right) - \frac{1}{r} \frac{\partial}{\partial \theta} \left(\frac{\Gamma_\phi}{r} \frac{\partial \phi}{\partial \theta} \right) - \frac{\partial}{\partial z} \left(\Gamma_\phi \frac{\partial \phi}{\partial z} \right) = S_\phi \quad (1)$$

The dependent variable (ϕ) denotes the mass fractions of chemical species, specific enthalpy and gas momentum. Diesel fuel is simplified to a single component because of its low proportions compared to the NG. In the pre-mixed model, 16 chemical species, the diesel vapour, $C_{12}H_{26}$, the NG components, CH_4 , C_2H_6 , C_3H_8 , and 12 dissociated combustion product species H , O , N , H_2 , OH , CO , NO , O_2 , H_2O , CO_2 , H_2 , N_2 , Ar are considered.. The uniform (at any one time) chamber pressure is calculated using the ideal gas equation from the known volume and the temperature, different in each cell, mass averaged across all cells. Sub-models described previously of the diesel injection, NG injection, DF burning and heat transfer serve as the source or sink terms in the diffusion model. These in summary (for more detail, see [11]) are:

1. Diesel injection and spray trajectory, [12].
2. Liquid fuel spray tip penetration, [13].
3. Sauter Mean Diameter [14].
4. Linear momentum sharing model for droplet collision, [15].
5. Evaporation modelled from quasi-steady analysis of a single droplet, [16].
6. Spray impingement on the chamber wall, [17].
7. Mixed burning of distillate and NG by use of a "reaction spread factor", [6] using the simplified global reaction model of Westbrook and Dryer, [18] for each of the fuel species.
8. Equilibrium combustion products can be calculated [19].

The heat release rate then follows depending on either the growth of a kernel of pilot distillate flame in the computational cell under consideration or diffusion of flame sources into neighbouring cells. The flame propagation of NG then proceeds subject to local flammability limits within the cells with ignition sources or spontaneously as the temperature rises in other cells to a sufficient level to increase the NG reaction rate.

Refining the Model

Before proceeding with the simulation of the combustion process, a refinement study was carried out. This will be reported in more detail separately. The chamber is cylindrical and hence the grid is based on r , θ , z coordinates. The solution is a time-marching procedure and hence both spatial and temporal effects were considered. The spatial grid refinement was achieved by employing a relatively coarse spacing and successively replacing it with a finer grid in one coordinate at a time until the solution converged. This was repeated with the other coordinates. Finally, the time step was considered for the spatially refined grid. The same physical conditions (ie initial pressure, temperature, NG equivalence ratio, mass and other characteristics of diesel injection) were used throughout. The results show that the accuracy of the solution depends most strongly upon the spacing in the θ -direction, with the r , z directions being slightly less significant. Only the θ -direction effect is illustrated here. Figures 1 and 2 show the effect of different (θ -direction) grids on the rise in pressure and temperature respectively with time for the early part of combustion. Note that temperature, unlike pressure which is uniform across the chamber, was checked at three specific locations because it varies between cells.

That shown here is at the half-radius on the spray centreline. The convergence is shown on Figures 3 and 4 where the variation of the time taken to reach designated pressure and temperature levels is plotted against the

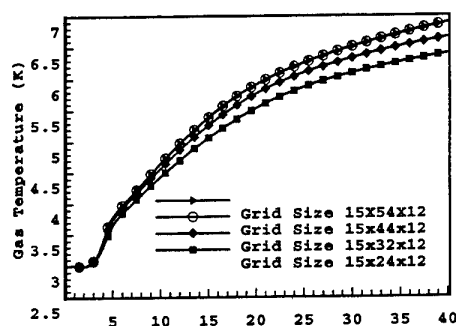


Fig. 1 Effect of grid Size (θ - direction) on the bomb pressure,

$P_o = 3 \text{ MPa}$, $T_o = 800 \text{ K}$, $\phi_{\text{gas}} = 0.7$, $m_{\text{inj}} = 32.67 \text{ mg}$

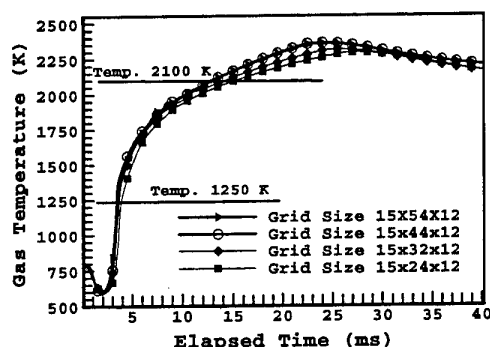


Fig 2. Effect of grid size (θ - direction) on gas temperature,

$P_o = 3 \text{ MPa}$, $T_o = 800 \text{ K}$, $\phi_{\text{gas}} = 0.7$, $m_{\text{inj}} = 32.67 \text{ mg}$

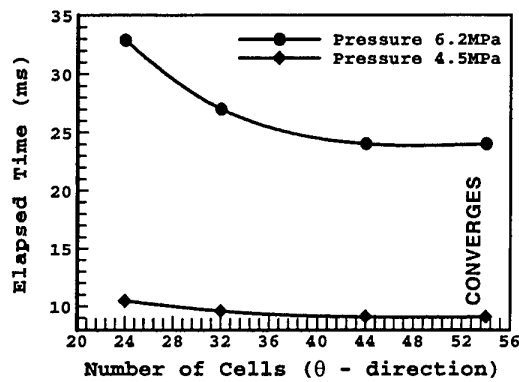


Fig. 3 Variation of elapsed time to designated pressure with number of cells

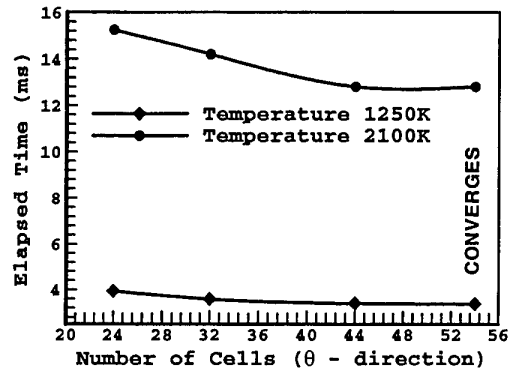


Fig. 4 Variation of elapsed time to designated temperatures with number of cells

number N_θ of θ -direction cells. As indicated by the graph, the solution of the differential equation on the θ -direction converges at $N_\theta = 44$. Using a similar analysis, the other grid directions N_r , N_z were found to converge 40- and 24 cells respectively. Again, following a similar procedure, a time step of 0.02 ms was found to be optimal.

4. COMBUSTION TESTS IN THE BOMB

Experimental pressure traces obtained from combustion bomb for both sole diesel and DF combustion have been used to analyse combustion modes, minimum DF ignition conditions and the DF ignition delay [5, 20]. They have been also used to calibrate the numerical models [6,9] which have been developed and for comparison with the numerical results of the combustion process with different injection characteristics.

Combustion Modes Analysed from Pressure Traces

A typical pressure trace can be seen on Figure 5 for sole diesel and pre-mixed NG/air mixture combustion. Note that this will differ from the trace obtained in an engine test due to lower ignition conditions, the quiescent nature of the combustion as there is no inlet or piston motion generated turbulence and no volumetric changes occurs from the start of injection as the combustion progresses. Differences can be detected between the pressure traces of pre-mixed DF and one for diesel fuel only (not shown here). The pressure trace of pre-mixed DF combustion has a longer ignition delay, takes a long time to reach the maximum pressure and is a two stage

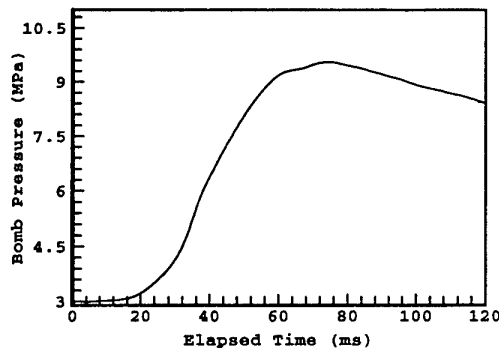


Fig.5 Pressure trace of pre-mixed of NG/air combustion.
 $P_o = 3$ MPa, $T_o = 623$ K, $P_g = 0.15$ MPa,
 $m_{inj} = 0.15$ MPa

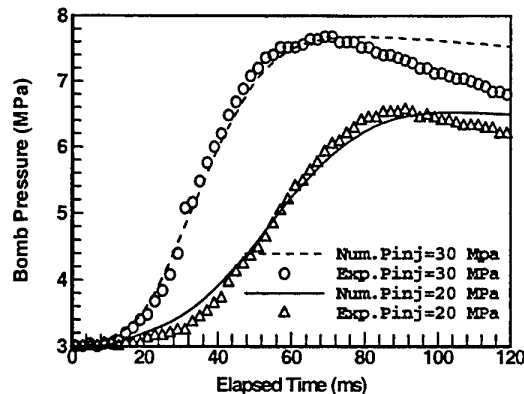


Fig.6 Comparison of simulation and experiment for pre-mixed combustion.
 $P_o = 3$ MPa, $T_o = 623$ K, $P_g = 0.15$ MPa,
 $m_{inj} = 0.15$ MPa

process, where the heat release rate changes from about the quarter maximum pressure position. This is likely to be the point where the NG conditions become such as to support a flame development through the unburnt mixture away from the spray zone. This is different from the diesel traces where a short ignition delay is followed by a sharp pressure rise.

Validation of the 3D Diffusion Model

The validation of the model was obtained by comparing the output of the model and the combustion bomb experimental results as shown in Figure 6. It can be seen that the simulation compares well until the peak pressure is reached. Beyond that point, the trends are slightly different. This may be due to decay of the piezoelectric transducer amplifier charge and heat transfer after the combustion.

5. PARAMETRIC STUDIES USING THE NUMERICAL MODEL

A number of parametric studies have been carried out. Those of significance here are:

1. Injection pressure effects on the combustion process.
2. Injector insertion depth.
3. Number of nozzle holes.

For these studies, the dimensions of the combustion chamber were taken as those of the experimental constant volume combustion bomb but the pre-ignition conditions of the charge were simulated at the higher values more typical of actual CI engine operation (ie 3 MPa, 800 K). The partial pressure of natural gas was taken as 2 MPa; this giving a NG/air equivalence ratio ϕ_{NG} of 0.72. In general, because the computing time is long, the results reported here were continued for only part of the combustion period (40 ms), it generally taking about 2.5 times (see Figure 6) this value to reach maximum pressure. It should be noted that the pressure across the chamber is, in reality uniform at any instant where other parameters (temperature, mass of distillate, combustion products, CO, NO) vary with location and time. All these can be graphed on spatial contour plots as required.

Pilot Injection Pressure Effects on the Combustion.

Four different injection pressures were examined, the nozzle diameter being varied to maintain a constant mass of fuel injected for the different injection velocities. For the fixed mass of diesel fuel at 26.7 mg, the pressures/hole size combinations were 120MPa/0.123 mm, 60 MPa/0.148 mm, 30 MPa/0.178 mm and 20 MPa/0.20 mm respectively.

Figure 7 shows the effect of pilot injection on the chamber pressure. The combustion process of the NG/air mixture is illustrated on Figure 8 which shows the major NG component, the unburnt methane. The gas temperature contours 16 ms after injection are shown on Figure 9. During the early stage of combustion, the burning of the gaseous fuel is spatially limited for all four injection pressures. This is due to the high combustion

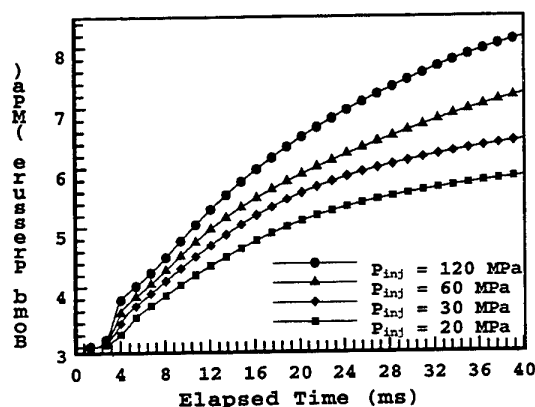


Fig. 7 Effects of injection pressure on bomb pressure.

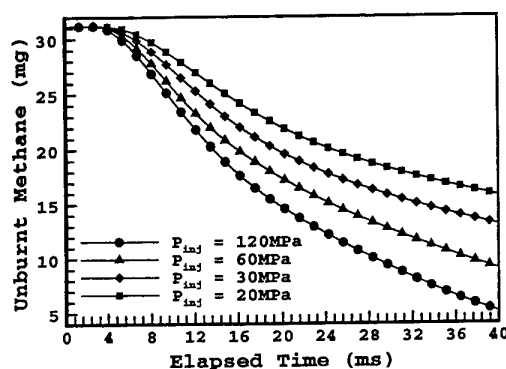


Fig.8 Effects of injection pressure on unburnt methane.

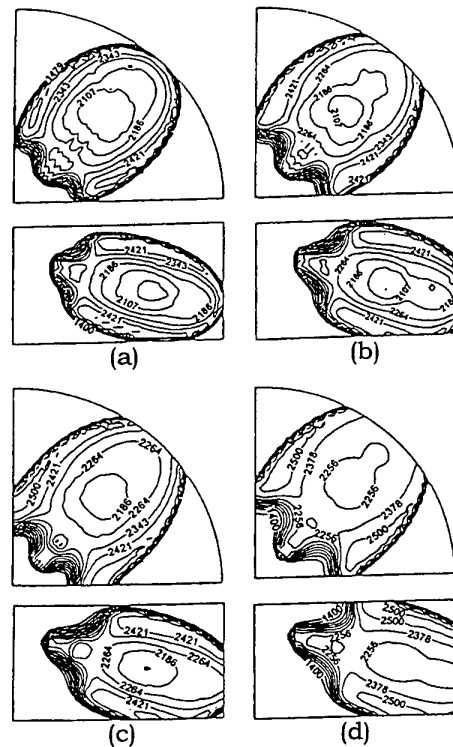


Fig. 9 Spatial variation of gas temperature

- a) Injection pressure: 20 MPa, b) Injection pressure: 30 MPa,
 b) c) Injection pressure: 60 MPa, d) Injection pressure: 120 MPa

temperature resulting from the initial rapid combustion which tends to vaporise the fuel spray. Hence, there is little penetration deep into the combustion chamber, particularly at low injection pressures. The initial NG combustion within the spray is restricted to a small region near the injector and the flame propagates only slowly through the pre-mixed NG outside the spray. The overall consumption of the gaseous fuel is therefore slow. The methane starts to burn between 1 and 2 ms after the diesel injection ignition delay is completed. Following this, the flame from the various ignition centres originating from the pilot distillate fuel propagates through the chamber. The burning rate of methane rises faster for higher pilot distillate pressures. This is due to the fact that the outlet velocity and spray penetration increase, providing a greater multiplicity centres and a larger combustion zone with an increased temperature and a higher activity of the oxidation reactions. The contours of Figure 9 shows that the burning propagates into the inner region of the spray plume and outwards through the combustion chamber.

Number of Nozzle Holes

Three nozzles with the same flow area but different diameters/ numbers of holes were used to investigate the influence of the spray distribution for a constant diesel delivery and injection pressure. In order to maintain constant diesel flow rate, the nozzle diameter was reduced with increase in the number of holes. The number of holes/diameter (mm) combinations used were 8/0.14 mm, 4/0.2 mm and 2/0.28 mm. The results of the simulation show that the greater number of smaller diameter holes distributes the spray over a wider range, changing the ignition and burning characteristics of the NG/air mixture and increasing the burning rate of NG. This can be seen by the overall pressure rise rate and diesel oil consumption as shown on Figures 10 and 11.

Insertion Depth of the Injector

The location of the origin of the spray is also likely to influence the combustion. To examine this, the injector was maintained in its original orientation central in the chamber upper wall but with different insertion depths,

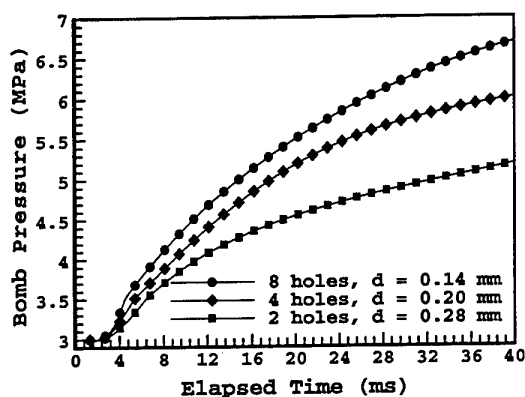


Fig.10 Effect of number of nozzle holes on combustion pressure

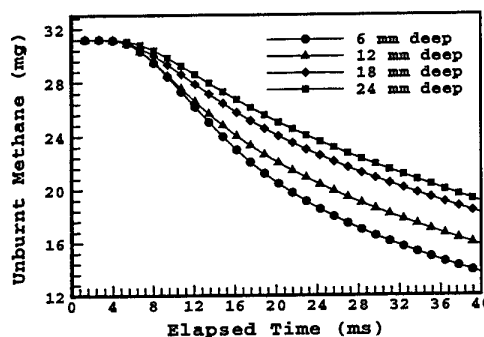


Fig.11 Effect of number of nozzle holes on mass of diesel vapour

below the top wall, these being 6 mm, 12 mm, 18 mm, and 24 mm respectively. The insertion depth changes the distribution of the diesel fuel, a deeper location moving the initial spray more towards the centre of the chamber. The centre line of the spray is directed downwards at 15° from the horizontal. For the above mentioned dimensions of the chamber, the centreline of the spray intersects with side wall at progressively lower points for the first two locations, near to the bottom corner for third and onto the bottom wall for lowest injector location. These positions may be modified by the evaporation and charge motion induced by the spray and combustion process if the latter commences prior to wall impact. The impact area is subject to the spray cone and local wall shape. The wall impact limits the fuel distribution in the gas space, greater wall impact decreasing the initial combustion zone. Figure 12 shows the effects of the injector location on the combustion bomb pressure. At short times after ignition, a higher pressure is reached at the 6 mm and 12 mm depths which are similar to each other. Thereafter, the least depth provides a greater pressure. As shown in Fig.13, the ignition of methane starts at the same time for all injector locations. This shows that there is sufficient ignition energy early in the process regardless of the free length of the spray. The mass of unburnt methane is greater as the injector depth increases, although only a small difference is apparent between the higher two positions. The slower consumption rate of methane at the deeper positions is probably due to the displacement of the ignition source line (ie. the diesel spray) towards the lower wall away from the most central region of the chamber. That is, a burning zone which consumes the most gas phase fuel prior to wall burnout is the most effective. The depth of the injector is critical in obtaining this.

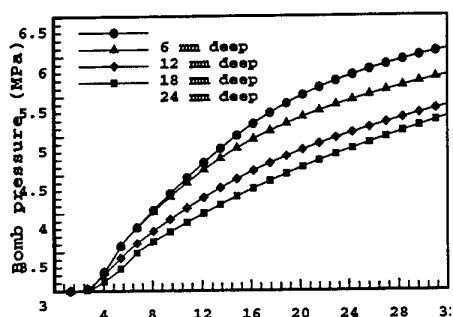


Fig. 13 Effects of injector depth on bomb pressure

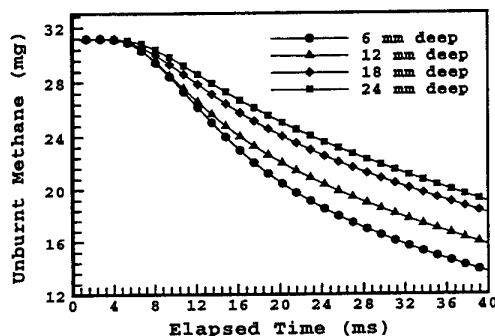


Fig. 14 Effect of injector depth on unburnt methane

6. CONCLUSIONS

The present work has highlighted the importance of the fundamental studies of the stimulated ignition of natural gas that occurs in DF engines at compression ignition conditions. This provides an understanding of the problems of the DF combustion and suggests some solution of these problems.

The combustion bomb has provided useful data for this study although it is difficult to obtain pre-ignition conditions, particularly temperature, which are at normal diesel engine levels. This is because the long period of heating of the NG/air mixture can cause inadvertent early ignition by surface hot spots. An improved apparatus, a moderately heated rapid compression machine, (RCM) is being examined to replace the combustion bomb. The 3D numerical model which incorporates a new system for sharing the combustion between the diesel spray and the pre-mixed NG works well. The computational output compared well with the experimental traces for a number of different injection parameters and injector configurations as well as pre-ignition conditions.

While further validation is required at higher initial pressures and temperatures, the 3D model has been used for parametric studies of the DF combustion of NG at the higher compression ignition conditions. In this simulation, the influence of injector characteristics have been examined. The study shows a beneficial effect on the overall combustion as injection pressure rises, with an increased number of smaller diameter holes and with an injector depth that locates the spray centreline furthest from any wall. The rate of burning of the gaseous fuel is increased due to the increase of ignition centres generated by well-distributed pilot fuel throughout the chamber.

REFERENCES

- 1 A.E. Felt and W.A. Steel, *SAE Trans.*, v.70, p. 644, (1962).
- 2 G.A. Karim, *Proc. Inst. Mech. Engrs.*, v.181 pt. 1 No. 20, pp 435-466, (1966).
- 3 O.B. Nielsen, B. Qvale, and S.C. Sorenson, *SAE Paper* 870589, (1987).
- 4 G.A. Karim, G.A., R.R. Raine, and W. Jones, *SAE Paper* 892140, (1989).
- 5 B. Hu, B.E. Milton and W. Krepl, *Proc. 3rd Int. Conf. On Comb. for a Clean Environment*, v.1, sect. 9, pp. 22-31, Lisbon, Portugal, (1995).
- 6 I.S. Choi and B.E. Milton, *Numerical Heat Transfer, Part A: Applications*, v.31, 7, , pp 725-743, (1997).
- 7 B. Hu, *PhD Thesis*, University of New South Wales, Australia, (1992).
- 8 M. Mbarawa, *PhD Thesis*, University of New South Wales, Australia, (1998).
- 9 I.S. Choi and B.E. Milton, *Proc. Int. Symp. On Advanced Comp. Heat Transfer*, pp. 166-175, ed. G. de Vahl Davis & E. Leonardi, Begell House, Cesium, Turkey, (1997).
- 10 S.V. Patankar, *Numerical Heat Transfer and Fluid Flow*, Hemisphere Publishing Corporation, (1980).
- 11 M. Mbarawa, R.T. Casey and B.E. Milton, *4th Asian-Pacific Int. Symp. on Comb. and Energy Utilization*, pp. 420-434, Bangkok, Thailand, (1987).
- 12 H. Hiroyasu, and K. Nishida, *SAE Paper* 890462, (1989).
- 13 H. Hiroyasu, T. Kadota, T. and M. Arai, *Combustion Modeling in Reciprocating Engines*, Plenum Press, ed. J. Mattavi and C. Amann, pp. 369-408, (1980).
- 14 H. Hiroyasu, M. Arai and M. Tabata, *SAE Paper* 890464, (1989).
- 16 W.E. Ranz and W.R. Marshall, W. R., *Chemical Engineering Progress*, V. 48, pp. 141-146, (1952).
- 17 A.P. Watkins. and D.M. Wang, *Proc. Int. Symp. on Diagnostics and Modelling of Comb. in I.C. Engines*, pp 243-248, COMODIA 90, Tokyo, Japan, (1990).
- 18 C.K. Westbrook. and F.L. Dryer, *Combustion Science and Technology*, V. 27, pp. 31-43, (1981).
- 19 C. Olikara and G.L. Borman, *SAE Paper* 750468, (1975).
- 20 B. Hu and B.E. Milton, *Proc. Int. Conf. on Fluid Eng., JSME Centennial Grand Conf.*, v.3, pp.1719-1724, Tokyo, Japan, (1997).

UNSTEADY HEAT AND MASS TRANSFER FOR MULTI-COMPONENT PARTICLE DEPOSITION IN THE MODIFIED CHEMICAL VAPOR DEPOSITION

K. S. Park

LG Cable Inc.

Email: kspark@cable.lg.co.kr; Fax: 82-343-56-1041

M. Choi

School of Mechanical and Aerospace Engineering

National CRI Center for Nano Particle Control, Institute of Advanced Machinery and Design

Seoul National University

Corresponding author: Email: mchoi@plaza.snu.ac.kr; Fax: 82-2-878-2465

J. D. Chung

National CRI Center for Nano Particle Control, Institute of Advanced Machinery and Design

Seoul National University

Email: jdchung@gong.snu.ac.kr; Fax: 82-2-887-8762

Keywords: MCVD, codeposition, unsteady, uniform deposition

ABSTRACT. A numerical analysis of unsteady heat and mass transfer for multi-component particle deposition in the Modified Chemical Vapor Deposition has been carried out. The earlier study showed that the optimized torch speed variation could be used to enhance the deposition uniformity of single component SiO_2 particle. However, this optimized torch speed resulted in the deterioration of GeO_2 deposition uniformity for multi-component $\text{SiO}_2/\text{GeO}_2$ deposition. Parametric studies varying three different operating conditions in time, maximum wall temperature, torch speed and in-take amount of GeCl_4 reveals that the uniformity of SiO_2 deposition is maintained by torch speed variation and that of GeO_2 is obtained by increasing the in-take flow rate of GeCl_4 in time.

1. INTRODUCTION

The Modified Chemical Vapor Deposition (MCVD) process is utilized to manufacture high-quality optical fibers [1]. In the process, a fire polished silica tube is rotated and heated by a slowly traversing oxy-hydrogen torch. A mixture of gases, such as silicon tetrachloride (SiCl_4), germanium tetrachloride (GeCl_4), oxygen (O_2) flow into the rotating silica tube and are heated to high temperatures. Chemical reactions occur and result in fine particles; e. g., silicon dioxide (SiO_2), germanium dioxide (GeO_2), etc. These particles move axially with the gases and are deposited on the inner wall of the tube due to thermophoresis; that is, from the net force that a suspended particle experiences in the direction of decreasing temperature in nonisothermal medium [2]. The deposited particles are consolidated into a glassy thin layer by sintering. When the torch completes its traverse to the end of the tube, one layer of deposition is obtained. By controlling the dopant chemical composition, desired refractive index profile is obtained. Germanium is the most common dopant used to increase the refractive index of SiO_2 to form a guiding core. After 10 ~ 40 layers are deposited, the tube is collapsed into a solid preform rod and then drawn into a long thin fiber.

The high-temperature chemical reactions, deposition and consolidation steps are interrelated and affected by the details of the thermal processing and control as well as by the specific chemical mixture used. Thus, most of the previous studies of the MCVD have been numerical analyses. The previous investigations focused on various aspects of the problems; thermophoresis [2], correlation between overall efficiency and minimum temperature [3], Laser-enhanced MCVD [4, 5], chemical kinetics and silica aerosol dynamics [6], tapered entry region reduction [7, 8], three dimensional effect [9, 10], codeposition of SiO_2 and GeO_2 [11], two torch model [12], oxidation of SiCl_4 and GeCl_4 and buoyancy [13]; measurement of deposited film thickness and tube wall temperature [14]. However, there has been relatively little attention on the processing control for the optimum performance such as tapered entry region reduction and uniform deposition thickness. The reason of intactness in the control of the processing conditions may be found on the quasi-steady assumption used in previous works. Recently, Park and Choi [15] extended their work to the unsteady analysis and found out that unsteady calculations significantly improved the prediction of SiO_2 particle deposition profile in the entire region by

comparing their results with the existing experimental study. They also examined the effects of torch speed variation on deposition performance for silica particles and identified the linearly varying torch speed case resulted in a much shorter tapered entry than the constant torch speed case. For the codeposition of silica and germania, very precise compositional and processing control is necessary to ensure the desired refractive index structures especially for multi-mode fiber manufacture, and optimum operating conditions will be considerably different from single component particle generation and deposition. Therefore, time dependent operating conditions such as torch speed, chemical gas flow rate and tube wall temperatures, etc. should be considered and, correspondingly, the unsteady analysis is prerequisite in its modeling.

In this paper, we extend our earlier work [15] to the unsteady analysis of multi-component (SiO_2 and GeO_2) MCVD. For the present unsteady calculation, the quartz tube is included in the calculation domain and the effects of chemical reactions for oxidations of both SiCl_4 and GeCl_4 and variable properties are also included. The time dependent operating conditions for the reduction of tapered entry and uniform deposition are also examined.

2. ANALYSIS

Figure 1 depicts the geometric configuration considered in this study. A mixture of reactants (SiCl_4 , GeCl_4 and O_2) is fed into a silica tube (reactor) as a fully developed laminar flow at the inlet. The mixture is heated by an external heat source and exothermic oxidations of SiCl_4 and GeCl_4 take place forming SiO_2 , GeO_2 and Cl_2 . Fractions of newly formed silica and germania particles are deposited onto the relatively low-temperature tube wall mostly by thermophoresis, while the rest exit the tube by convection.

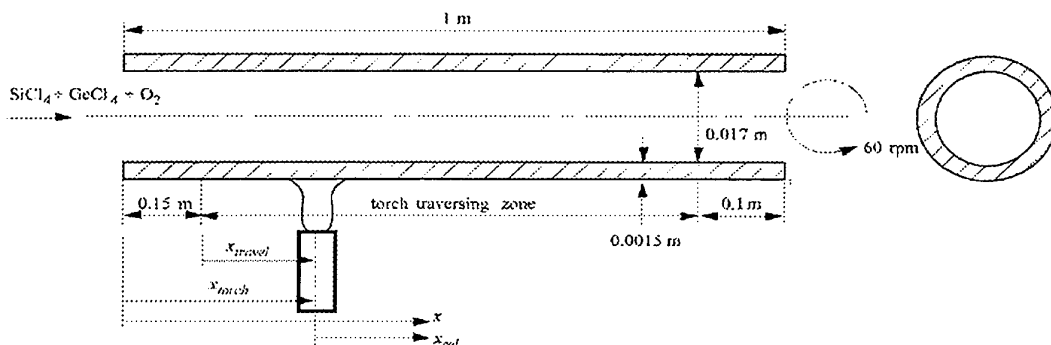


Fig. 1 Schematic diagram of the MCVD system

Since uniform deposition in the circumferential direction can be assumed for normal rotational speeds (60 ~ 120 rpm) [10] and the total moles in the gas phase is conserved throughout the MCVD process, the axisymmetric, two-dimensional unsteady governing equations can be written as

Continuity Eq.

$$\frac{\partial C}{\partial t} + \nabla \cdot C\bar{V} = 0 \quad (1)$$

Momentum Eq.

$$C \frac{\partial \bar{V}}{\partial t} + C\bar{V} \cdot \nabla \bar{V} = -\frac{1}{M} \nabla p + \frac{1}{M} \nabla \cdot \bar{\tau} \quad (2)$$

Energy Eq. for gas

$$CC_p \frac{\partial T}{\partial t} + CC_p \bar{V} \cdot \nabla T = \nabla \cdot k \nabla T + r_{sc} \Delta H_{sc} + r_{gc} \Delta H_{gc} \quad (3)$$

Energy Eq. for quartz tube

$$\rho C_p \frac{\partial T}{\partial t} = \nabla \cdot k \nabla T \quad (4)$$

Species Eqs.

$$C \frac{\partial X_i}{\partial t} + C \bar{V} \cdot \nabla X_i = \nabla C D_i \nabla X_i + R_i \quad (5)$$

where ΔH_i represents the reaction enthalpy of oxidation of species i (SiCl_4 , GeCl_4) and X_i and D_i denote mole fraction and diffusion coefficient of species i (SiCl_4 , GeCl_4 , Cl_2), respectively. The source terms, R_i in species equation are expressed as

$$R_{\text{SC}} = -r_{\text{SC}}, R_{\text{GC}} = -r_{\text{GC}}, R_{\text{CL}} = 2r_{\text{SC}} + 2r_{\text{GC}} \quad (6)$$

Kim and Pratsinis [11] and Powers [16] suggested the following equations for r_{SC} and r_{GC}

$$r_{\text{SC}} = (k_{\text{SC},0} + k_{\text{SC},1} C X_{\text{O}_2}) \exp(-E_{\text{SC}}/R_G T) C X_{\text{SC}} \quad (7)$$

$$r_{\text{GC}} = k_{\text{GC},0} \exp(-E_{\text{GC}}/R_G T) C^2 (X_{\text{GC}} X_{\text{O}_2} - \gamma Y_{\text{GO}} X_{\text{CL}}^2 / K_{\text{EQ}}) \quad (8)$$

where the particle phase is assumed to be an ideal solution ($\gamma = 1$) and particle surface reaction is assumed to be negligible.

Since relatively dilute suspensions in an excess oxygen flow are employed, the mixture gas properties are calculated as properties of the carrier gas, O_2 . These are given as a function of T and p using literature expressions for viscosity and diffusion [17], heat capacity [18] and thermal conductivity [19]. The details on the simulation conditions used for present MCVD process are summarized in Kim and Pratsinis [11].

The mass balance equation for SiO_2 and GeO_2 are written as

$$C \frac{\partial n_i}{\partial t} + C (\bar{V} + \bar{V}_T) \cdot \nabla n_i = \bar{r}_i \quad (9)$$

where \bar{V}_T denotes the thermophoretic velocity defined by $\bar{V}_T = -K(v/T) \nabla T$ [20] and n_i 's are moles of species i particles per mole of carrier gas. The boundary conditions are

$$x = 0, r \leq R_i :$$

$$u = 2V_0 \left[1 - (r/R_i)^2 \right], v = 0, T = T_0,$$

$$X_{\text{SC}} = X_{\text{SC},0}, X_{\text{GC}} = X_{\text{GC},0}, X_{\text{CL}} = 0, \quad (10)$$

$$n_{\text{SO}} = n_{\text{GO}} = 0$$

$$R_i < r \leq R_0 : \frac{\partial T}{\partial x} = 0 \quad (11)$$

$$x = L, r \leq R_i :$$

$$\frac{\partial^2(u, v, T, X_{SC}, X_{GC}, X_{CL})}{\partial x^2} = 0 \quad (12)$$

$$R_i < r \leq R_0 : \frac{\partial T}{\partial x} = 0 \quad (13)$$

$$r = 0 :$$

$$\frac{\partial(u, v, T, X_{SC}, X_{GC}, X_{CL}, n_{SO}, n_{GO})}{\partial r} = 0 \quad (14)$$

$$r = R_i :$$

$$u, v = 0, \frac{\partial(X_{SC}, X_{GC}, X_{CL})}{\partial r} = 0 \quad (15)$$

and continuity of temperature and heat flux

The localized heating by the torch is modeled as Gaussian distribution and dissipated by convection and radiation at the outer tube wall [12];

$$r = R_0 : q_{\max} \exp\left[-\lambda^2(x - x_{\text{torch}})^2\right] = k \frac{\partial T}{\partial r} + h(T - T_\infty) + \varepsilon \sigma (T^4 - T_\infty^4) \quad (16)$$

where x_{torch} is the torch location and h is the temperature-dependent heat transfer coefficient on the rotating cylinder [21]. Two parameters, λ and q_{\max} , control the width and the maximum value of the heating profile [12]. The emissivity of the quartz tube, ε , is calculated from a band approximation [22], with the assumption that the quartz is transparent below 4.5 μm wavelength and behaves like a black body above that.

In studies of optical fiber drawing, Homsy and Walker [23] and Paek and Runk [24] considered the effect of radiation in a silica solid rod by using the Rosseland diffusion approximation [22]. The same approximation is utilized in the present study:

$$k = k_{\text{cond}} + k_{\text{rad}} = k_{\text{cond}} + 16n^2\sigma T^3/3 \quad (17)$$

where the Rosseland mean absorption coefficient, \square , and the refractive index, n , take the values of 4 cm^{-1} and 1.5, respectively [23, 24].

The above set of governing equations subject to the given boundary conditions were solved in terms of the primitive variables by employing the finite volume technique along with power law scheme and SIMPLE algorithm [25]. The pressure correction equation is solved with the MCGS solver [26], and other discretized equations are solved with CGS solver [27]. Convergence is assumed when the summed residual over the domain falls below a prescribed tolerance (10^{-3}). More stringent convergence criteria did not reveal noticeable changes in the solution. After the solution converges, the deposition masses of SiO_2 and GeO_2 per unit area at the certain axial location are evaluated from the mass fluxes onto the inner surface of tube, as follows:

$$\delta m_i(x, t) = \int_0^t (-CM_i n_i K_v \partial \ln T / \partial r)_{r=R_i} d\tilde{t} \quad (18)$$

3. RESULTS AND DISCUSSIONS

In order to make a proper assessment of our numerical implementation, the limiting case for single component

SiO₂ deposition has been carried out for the comparison with the previous studies [14, 15]. The in-take flow rate of carrier gas, O₂, is 2 l/min and the flow rate of SiCl₄ and GeCl₄ is 3 mol/m³ and 1.9 mol/m³. Since overall efficiency can be expressed as a function of minimum temperature [3], a proper prediction of wall temperature is a prerequisite condition for a correct estimation of efficiency. Figure 2 shows the spatial wall temperature variation at several different times (i. e., different torch locations) using the relative coordinate that moves with the torch, $x_{rel} = (x - x_{torch})$. Reasonable agreement was obtained compared with quasi-steady experiment [14] at later times (i.e., larger distance of torch movement) and at early times, noticeable unsteady effects was found as significant difference between the present calculation and quasi-steady measurement proved. It is also noted that the previous calculation considering only the effect of SiCl₄ oxidation agrees very well with the present calculation considering both chemical reactions of SiCl₄ and GeCl₄. Therefore, the effect of GeCl₄ reaction on the wall temperature may be said to be small. The solid and dashed lines represent temperature distributions for the first pass and second pass of the torch traverse, respectively. The wall temperature ahead of the torch for the second pass is higher than that of the first pass, and there exists an axial region where the wall temperature increases ahead of the torch. This is a consequence of the residual heat from the first pass. This temperature increase coincides with experiment [14] and was also predicted by a two-torch quasi-steady model suggested by Park and Choi [12]. At early times, wall temperature distributions in the region behind the torch do not fall onto a single curve even when they are plotted using the relative moving coordinate, x_{rel} , and are much different from quasi-steady results. This means that the quasi-steady assumption cannot be used at early times. We also note that previous discrepancies in deposition profile between quasi-steady state predictions and measurements near the inlet region was significantly improved by using a full unsteady calculation for the case of single component SiO₂ particle deposition [15]. It is now extended to consider the unsteady heat and mass transfer for multi-component SiO₂ and GeO₂ particle deposition.

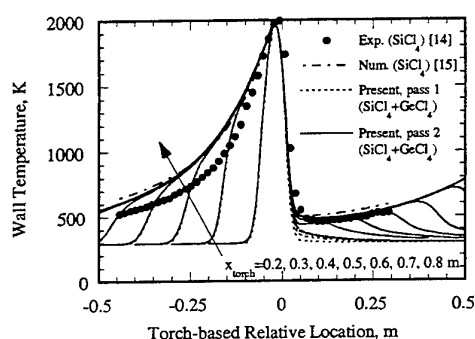


Fig. 2. Distribution of tube wall temperature with respect to the torch based relative axial coordinate for different torch location (different times)

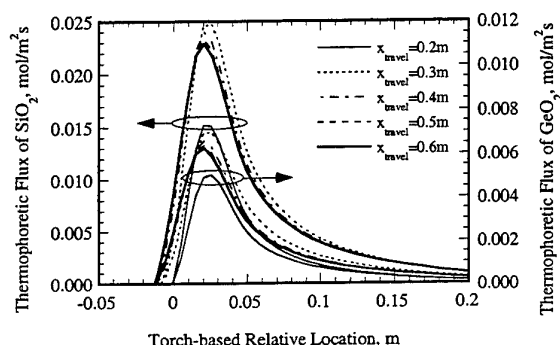


Fig. 3. Thermophoretic fluxes of SiO₂ and GeO₂ to the tube wall for different torch locations (different times)

Figure 3 shows the thermophoretic flux to the wall, defined as $\bar{V}_T C n_i$. \bar{V}_T is thermophoretic particle velocity and C and n_i are gas concentration and moles of species SiO₂ and GeO₂ per mole of carrier gas. The deposition efficiency is low at the beginning of torch traverse compared when torch moves enough to reach steady state. At the beginning of torch traverse, the narrow region of high wall temperature (shown in Fig. 2) causes this low deposition efficiency. Note that there is a maximum deposition efficiency at $x_{travel} = 0.3$ m before it reaches steady. The decrease of deposition efficiency beyond $x_{travel} = 0.3$ m is due to the increase of the minimum wall temperature ahead of torch. Figure 4 shows the wall temperature distribution ahead of the torch for different torch travel locations (or different times). The minimum wall temperature is about 435 K at the beginning of torch traverse and becomes steady near 500 K as the torch moves on. The effects of exothermic chemical reactions would cause the increase of the minimum wall temperature as the torch travels and similar effect was observed experimentally [14]. As the wall temperature becomes higher, the particle deposition is suppressed due to lower thermophoretic particle velocity. On the other hand, as the torch moves on, particle formation in a tube becomes more active, which would tend to increase the deposition flux. Therefore, there are two mechanisms of which each has the opposite effect; the increasing minimum temperature to reduce the deposition flux and the increasing particle formation to increase the deposition flux. Correspondingly, the maximum deposition flux

may exist as the torch moves. Note also that the broad range of particle deposition occurs, which should cause the undesirable tapered entry. This means that there would be the area of non-uniform deposition that is equivalent to the broad particle deposition area, even if quasi-steady state is reached.

Torch speed control was shown to be effective to result in a much shorter tapered entry for single component SiO_2 deposition than the constant torch speed case [15]. This may be also true for multi-component $\text{SiO}_2/\text{GeO}_2$ particle deposition. To examine the validity of torch speed variation on the enhancement of deposition performance, calculations for the same torch speed variation utilized previously as in single component SiO_2 deposition [15], which is linearly increased up to 120 s and then maintains uniform as 0.2 m/min, have been done for multi-component particle deposition case. Figure 5 shows the deposition profiles of SiO_2 and GeO_2 during three passes. The deposition masses of both SiO_2 and GeO_2 during the first pass are more than those during second or third pass because the minimum wall temperatures of the latters are approximately 200 K higher than the former due to the heat remained from the first pass. There is no difference between second and third passes, which indicates calculations for further passes are not necessary. For SiO_2 deposition, the uniformity has been much improved compared to the case of constant torch speed (bold solid line) as already confirmed by Park and Choi [15]. The reason of this improvement was that the deposited mass near the torch starting position increased due to the longer duration of torch heating for the case of linearly varying torch speed, and thus the tapered entry region was greatly reduced by less than 0.1 m. The uniformity of deposition of GeO_2 , however, becomes worse by the excessive particle deposition at the beginning. Note that for the constant torch speed case the deposition of GeO_2 comes steady earlier ($x \sim 0.35$ m) than SiO_2 ($x \sim 0.45$ m). because the activation energy of GeO_2 is lower than that of SiO_2 . Therefore, the strategy slowing down the torch speed for the enhancement of SiO_2 uniformity may cause excessive particle deposition of GeO_2 over a broad zone. Thus, the different characteristics in chemical reactions between SiCl_4 and GeCl_4 poses a difficulty in achieving both uniformity of SiO_2 and GeO_2 simultaneously by the use of only one control method, e.g., the variation of torch speed in time.

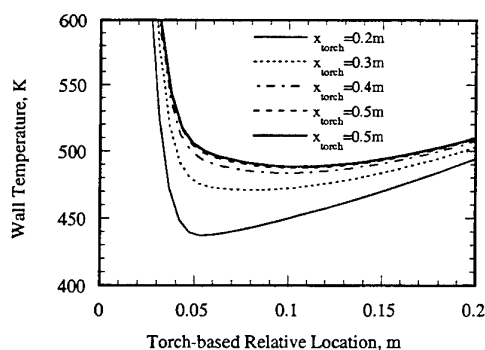


Fig. 4. The variations of minimum wall temperature for different torch locations (different times)

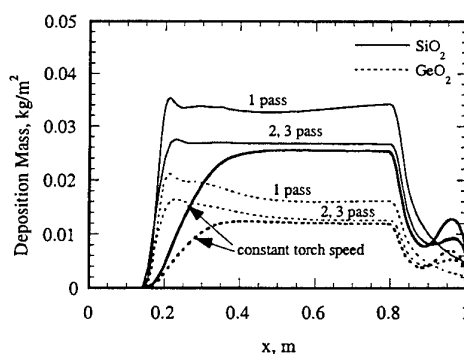


Fig. 5. Comparison of the deposition profiles of SiO_2 and GeO_2 between cases of variable torch speed (thin lines) and constant torch speed (bold lines)

To ensure the uniformity of both SiO_2 and GeO_2 , control strategy may need the variation of two parameters at least rather than changing only one parameter. For this purpose, parametric studies are conducted with varying three operating parameters, i. e., maximum wall temperature, torch speed, and in-take amount of GeCl_4 , independently or varying a set of two parameters simultaneously. The conditions for the base case are $T_{\max} = 1973$ K, $V_{\text{torch}} = 0.2$ m/min and $C_{\text{GC},0} = 1.9$ mol/m³. Case A is the variation of torch speed which is linearly increased from zero to 0.2 m/min for 120 seconds and then maintains uniform as 0.2 m/min after 120 s. Case B is similar to case A except for beginning the torch speed with an initial torch speed, 0.0667 m/min. Case C and D are the variations of maximum wall temperatures with the same torch speed variation as case A. Case C lowers the maximum wall temperature from T_0 by about 50 °C as torch travels while the case D raises the maximum wall temperature by about 50 °C from 1923 K at the starting position. Case E and F represent time dependent variations of in-take amount of GeCl_4 , which is linearly increased. The details on the variations of parameters used for each case are summarized in Table 1.

Figure 6 shows the deposition profiles of SiO_2 and GeO_2 for seven different cases. In case A, the enhancement of deposition uniformity of SiO_2 is quite clear compared with the base case but the deterioration of deposition uniformity of GeO_2 is also found as mentioned earlier. Slight change of torch speed profile (case B) makes it worse for the uniformity of both SiO_2 and GeO_2 . Thus hereafter the torch speed variation is fixed with that of case A, and then the change of another parameter has been studied to find uniform deposition of GeO_2 and SiO_2 . The effect of lowering the maximum wall temperature (case C) by 50°C would be negligible and resulted in almost same depositions as case A. Case D has been carried out to examine that lower maximum wall temperature at the starting position may reduce the reaction rate of GeCl_4 and decrease the deposition amount of GeO_2 at entry region where excessive deposition was made for case A. This has a positive effect to some extent for the deposition uniformity of GeO_2 . However, the low maximum wall temperature also reduces the reaction rate of SiCl_4 , and makes the non-uniform deposition profile of SiO_2 near the entry region. Both cases E and F where the in-take amount of GeCl_4 is linearly increased to suppress the initial high deposition of GeO_2 , yielded considerable enhancement of deposition uniformity on both SiO_2 and GeO_2 while case F resulted in not only the uniform GeO_2 deposition, but also higher deposition rate than case E. Thus the uniformity of deposition thickness of SiO_2 can be maintained by torch speed variation in time and that of GeO_2 may be simultaneously obtained by increasing the in-take flow rate of GeCl_4 as torch travels.

Table 1. Parametric studies for searching optimum operating parameters of time dependent maximum wall temperature, torch speed, and in-take amount of GeCl_4

	T_{\max} [K]	V_{torch} [m min ⁻¹]	$C_{\text{SC},0}$ [mol m ⁻³]	$C_{\text{GC},0}$ [mol m ⁻³]
Base	T_0	V_0	C_1	C_2
A	T_0	$\text{Min}[V_0 t/t_0, V_0]$	C_1	C_2
B	T_0	$\text{Min}[V_0(2t/t_0+1)/3, V_0]$	C_1	C_2
C	$-a_T(x_{\text{travel}}/x_{\text{sweep}})+T_0$	$\text{Min}[V_0 t/t_0, V_0]$	C_1	C_2
D	$a_T(x_{\text{travel}}/x_{\text{sweep}}-1)+T_0$	$\text{Min}[V_0 t/t_0, V_0]$	C_1	C_2
E	T_0	$\text{Min}[V_0 t/t_0, V_0]$	C_1	$a_x(x_{\text{travel}}/x_{\text{sweep}}-1)+C_2$
F	T_0	$\text{Min}[V_0 t/t_0, V_0]$	C_1	$b_x x_{\text{travel}}/x_{\text{sweep}}+C_2$

$T_0 = 1973\text{ K}$, $a_T = 50\text{ K}$, $x_{\text{sweep}} = 0.75\text{ m}$, $t_0 = 120\text{ s}$, $V_0 = 0.2\text{ m/min}$,
 $C_1 = 3\text{ mol/m}^3$, $C_2 = 1.9\text{ mol/m}^3$, $a_x = 0.475\text{ mol/m}^3$, $b_x = 0.665\text{ mol/m}^3$

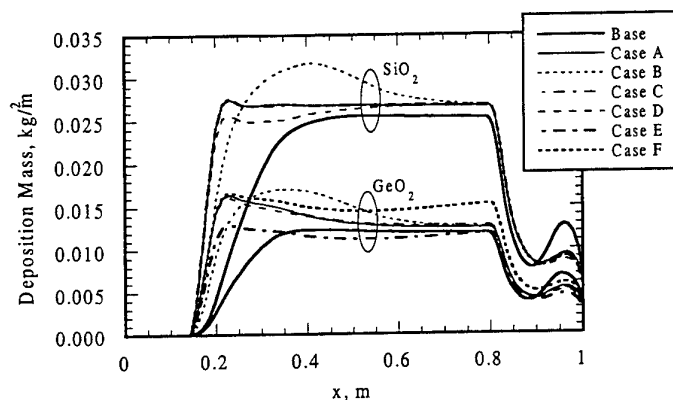


Fig. 6 Deposition profiles of SiO_2 and GeO_2 corresponding to the various operating parameters in Table 1

4. CONCLUSIONS

Unsteady heat and mass transfer analysis on the codeposition of SiO_2 and GeO_2 during the Modified Chemical Vapor Deposition Process has been conducted. The present unsteady analysis has been shown to be an effective and versatile tool to examine the effects of the time dependent variations of different operating parameters on deposition performance for enhancement of uniform deposition profile and short tapered entry region.

The tapered entry region for SiO_2 deposition can be reduced by varying the torch speed in time, that is, linearly increasing speed up to a certain time and maintaining at constant speed beyond that time. However, this optimized torch speed which was valid for SiO_2 deposition resulted in the deterioration of GeO_2 uniformity. Therefore, to ensure the uniformity of both SiO_2 and GeO_2 , a control strategy may need the variations of two parameters at least rather than changing only one parameter. Parametric studies varying three operating parameters in time, i. e., maximum wall temperature, torch speed, and in-take amount of GeCl_4 , independently or varying a set of two parameters simultaneously, have been conducted to find optimum operating conditions. The uniformity of deposition thickness of SiO_2 is sought by linearly varying torch speed and at the same time, GeO_2 uniformity can be obtained by increasing the in-take flow rate of GeCl_4 in time.

ACKNOWLEDGEMENTS

The part of this work was sponsored by Creative Research Initiatives Program funded by the Ministry of Science and Technology, Korea.

REFERENCES

1. J. B. MacChesney, P. B. O'Connor and H. M. Presby, *Proc. IEEE*, v. 62, pp. 1278-1279 (1974).
2. P. G. Simpkins, S. G. Kosinski and J. B. MacChesney, *J. Appl. Phys.*, v. 50, pp. 5676-5681 (1979).
3. K. L. Walker, F. T. Geyling and S. R. Nagel, *J. Am. Ceram. Soc.*, v. 63, pp. 552-558 (1980).
4. C. W. Wang, T. F. Morse and J. W. Cippola Jr., *ASME J. Heat Transfer*, v. 107, pp. 161-167 (1985).
5. T. F. Morse, D. DiGiovanni, Y. W. Chen and J. W. Cippola Jr., *J. Lightwave Technol.*, LT-4, pp. 151-155 (1986).
6. K. S. Kim and S. E. Pratsinis, *AIChE Journal*, v. 34, pp. 912-920 (1988).
7. M. Fiebig, M. Hilgenstock and H. A. Rieman, *Aerosol Sci. Technol.*, v. 9, pp. 237-249 (1988).
8. M. Choi and K. S. Park, *10th International Heat Transfer Conference*, v. 7, pp. 209-214 (1994).
9. M. Choi, Y. T. Lin and R. Greif, *ASME J. Heat Transfer*, v. 112, pp. 1063-1069 (1990).
10. Y. T. Lin, M. Choi and R. Greif, *ASME J. Heat Transfer*, v. 114, pp. 735-742 (1992).
11. K. S. Kim and S. E. Pratsinis, *Int. J. Heat Mass Transfer*, v. 33, pp. 1977-1986 (1990).
12. K. S. Park and M. Choi, *Int. J. Heat Mass Transfer*, v. 37, pp. 1593-1603 (1994).
13. S. Joh and R. Greif, *Int. J. Heat Mass Transfer*, v. 38, pp. 1911-1921 (1994).
14. J. Cho and M. Choi, *ASME J. Heat Transfer*, v. 117, pp. 1036-1041 (1995).
15. K. S. Park and M. Choi, *ASME J. Heat Transfer*, v. 120, pp. 858-864 (1998).
16. D. R. Powers, *J. Am. Ceram. Soc.*, v. 61, pp. 295-297 (1978).
17. R. C. Reid, J. M. Prausnitz and T. K. Sherwood, *The Properties of Gases and Liquids*, McGraw-Hill (1977).
18. J. M. Smith and H. C. Van Ness, H. C., *Introduction to Chemical Engineering Thermodynamics*, McGraw-Hill (1975).
19. R. H. Perry and D. Green, *Perry's Chemical Engineers' Handbook*, McGraw-Hill (1984).
20. L. Talbot, R. J. Cheng, R. W. Schefer and D. R. Willis, *J. Fluid Mech.*, v. 101, pp. 737-758 (1980).
21. B. Farouk and K. S. Ball, *Int. J. Heat Mass Transfer*, v. 28, pp. 1921-1935 (1985).
22. R. Siegel and J. R. Howell, *Thermal Radiation Heat Transfer*, Hemisphere (1992).
23. G. M. Homsy and K. L. Walker, *Glass Technol.*, v. 20, pp. 20-26 (1979).
24. U. C. Paek and R. B. Runk, *J. Appl. Phys.*, v. 49, pp. 4417-4423 (1978).
25. S. V. Patankar, *Numerical Heat Transfer and Fluid Flow*, Hemisphere (1980).
26. C.-J. Kim and S. T. Ro, *Numerical Heat Transfer*, v. 27B, pp. 355-369 (1995).
27. D. S. Kershaw, *J. Comp. Phys.*, v. 26, pp. 43-65 (1978).

THE BASIC STUDY ON BIOGAS STORAGE BY USE OF METHANE CLATHRATE

Iwane Fujii and Tohru Kimura

Meiji university, Department of Mechanical Engineering

Higashi-Mita, Tama-ku, Kawasaki 214-8571 Japan

Email: ce88220@isc.meiji.ac.jp; Tel/Fax: +81-44-934-7395

Keywords: biogas, methane clathrate, THF additive, CO₂ removal, energy storage

ABSTRACT. Nowadays our lifestyle is characterized by consuming the large amount of energy. However, energy sources as fossil fuels are limited. Taking into consideration the present condition, it seems to be important to secure new energy sources. One of the promising renewable energy sources is biogas, which is compound gas consisting mainly of methane (CH₄) and carbon dioxide (CO₂). It is normally formed with the decomposition of organic substances. Because of its low energy density, the gas is generally stored in high-pressure gas bomb. To store it in a condition of high density, it is also attempted to store methane in the form of clathrate. The clathration of methane requires normally high pressure and low temperature. If the clathration of biogas and methane could be achieved under the normal pressure and temperature, this would make the gases a very useful energy source. In this study, the clathration of methane under the normal pressure and temperature was first attempted by using Tetrahydrofuran (THF) as additive. Further, to realize the higher storage density of methane, CO₂ must be removed beforehand because not only methane but also CO₂ form clathrate. To achieve CO₂ removal, the possibility of absorption method using Monoethanolamine (MEA) is experimentally investigated, aiming efficient biogas utilization in final.

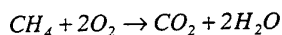
1. INTRODUCTION

In the state of increasing energy demand with economic growth the phenomena of global warming and the increase of negative inheritance such as radioactive waste compel us to reduce consumption of every kind of fossil fuel and to refrain from using nuclear energy. One of the promising means that could conquer such a deadlock is the utilization of renewable energy resources such as solar, wind and biomass. In general, however, utilization of these resources, especially solar and wind, is apt to be restricted by time and location, which are disturbing smooth spread of their application. On the other hand, biomass has no such restriction, because the material itself is one storing energy already. This property enables us to use the energy freely according to demand, which raises attraction of biomass energy more together with effect of CO₂ recycling. However, a drawback of biomass is quite troublesome handling in its use. To overcome this problem, biomass gasification and biogas generation are generally performed. However, gaseous fuels are generally inferior to liquid or solid ones in volumetric energy density. Liquefaction as LNG for example is one of the counterplans to cover this drawback at the sacrifice of much energy consumption. In addition, methane is considered to be stored as clathrate compound recently [1][2]. Although this way promises great step-up in energy storage density, there remain still many technical problems such as energy reduction for clathrate formation and prior CO₂ removal from biogas. In this paper experimental results concerning the solution of the above problems are presented. Furthermore, considering practical application of biogas storage by clathrate compound, system diagram which describes process from biogas generation to its usage via storage of the biogas is proposed.

2. CONVENTIONAL WAY OF METHANE STORAGE

2.1 Physical And Chemical Characteristics Of Methane

Biogas, together with natural gas, is widely used in our daily life. Needless to say, one of the main components of these gases is methane. Under atmospheric pressure and room temperature methane is in gaseous state, and its calorific value is approximately 38 MJ/m³. Strictly speaking, higher and lower heating values of the next exothermic reaction, namely,



are respectively 39.72 MJ/m³ and 35.80 MJ/m³, which represent fairly large generation of heat. Nevertheless, compared with those of the conventional liquid and solid fuels, these values are extraordinarily inferior. Therefore, though easy to ignite and handle, gaseous fuels, including biogas, are ill fitted for energy storage and

transportation especially due to low volumetric energy density. In fact, as seen from LNG, gaseous fuel is generally liquidized prior to its storage and transport. Methane liquefaction makes about a six hundredth volume state possible. As indicated in Fig.1, critical pressure and temperature of methane are respectively 4.64 MPa (45.71 atm) and 190.55 K (-82.6 °C).

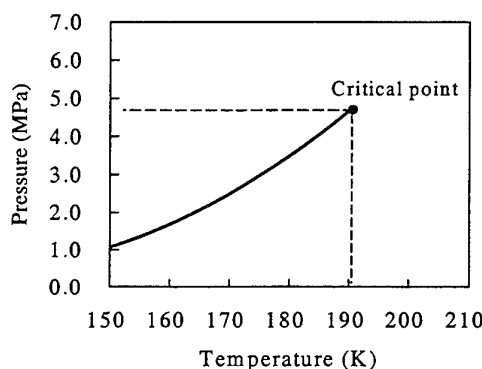


Fig. 1. Phase diagram of methane [3]

Further, the temperature of liquefaction under atmospheric pressure is around 111.15 K (-162 °C). These facts state that methane liquefaction implies a large energy consumption and a high cost for the liquefier. On the other side, increase of energy density is also practiced through pressurization of the gas with no liquefaction. Naturally, energy consumption in this case is much reduced as compared with the case of liquefaction. However, the final energy density attained here is insignificant when compared to liquefied methane, which can be easily imagined from the relation between pressure and gas density by Boyle – Charles's law. Hereupon, effective way of gaseous fuel storage with less energy consumption is keenly required.

3. BIOGAS STORAGE BY CLATHRATE

In addition to gas liquefaction and gas pressurization, hydrate formation could also offer a new way of efficient storage and transportation for gaseous fuel. Methane clathrate formed by methane and water is a kind of hydrate, which is recognized to be stored in large quantities at the sea bottom in certain location. Now, judging theoretically from molecular coupling structure of methane clathrate, methane of 9.66 mole combines approximately with water of 56 mole. In short, energy density attained by methane clathrate is approximately equivalent to the density of gaseous methane pressurized until 20 MPa (≈ 200 atm). Hence, this fact gives another way of methane storage having high energy density. Unfortunately, however, physical conditions necessary for forming methane hydrate are not always easy in practice, unless some artificial treatment is given. Therefore, it is main subject here to find new efficient way of biogas clathrate formation.

3.1. Effect Of THF Additive For Clathrate Formation [4]

Figure 2 shows schematic diagram of the experimental apparatus to prove the effect of Tetrahydrofuran (THF) on clathrate formation. The reactor whose vessel is made of pyrex is equipped with an agitator. Pressure gauge and several thermocouples are installed in the vessel to detect physical data. Testing procedure is as follows:

1. Water containing THF at a fixed rate is held in the holder.
2. Vacuum is created inside the reactor vessel, using vacuum pump.
3. After obtaining adequate vacuum state, the THF solution is transferred to the vessel by valve operation.
4. Successively, methane gas is also transferred there from the gas bomb until internal pressure of the vessel becomes a fixed.
5. The vessel is gradually cooled, stirring the solution by the agitator.
6. When temperature of the solution attains a certain temperature clathrate formation occurs.
7. At the time when clathrate formation is first recognized vessel's inside pressure and temperature of the solution are marked on the recorder.
8. The recorded values are respectively regarded as critical pressure P_c , and temperature T_c of clathrate formation under the specific test condition.

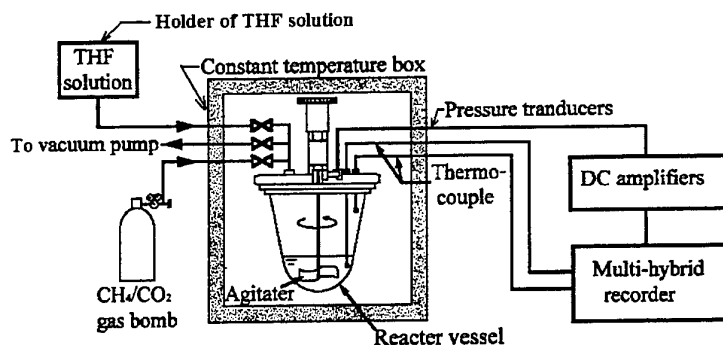


Fig. 2. Schematic diagram of experimental apparatus

In Fig.3 the relation between P and T is shown. The solid rhombic marks are experimental points obtained through similar successive tests mentioned above. The curve tracing these points is drawn according to the following consideration. Namely, as it is also seen for CO_2 hydrate, formation of methane hydrate is accompanied with heat release and heat absorption due to phase change. Here, if Clapeyron-Clausius equation is applied to the relation between the pressure P and the temperature T , we have:

$$\frac{dP}{dT} = \frac{\Delta H}{T v'} \quad (1)$$

under assumption that molar volume change of saturated vapor v' is much greater than that of the liquid. Further, application of equation of state for ideal gas, $P v' = RT$, transforms Eq.1, as:

$$\frac{dP}{dT} = \frac{P \Delta H}{RT^2} \quad (2)$$

which gives

$$\ln P = -\frac{\Delta H}{R} \cdot \frac{1}{T} + C' \quad (3)$$

where R is gas constant, and constant C' is concretely determined together with ΔH , if appropriate boundary conditions are set up.

On the other hand, if the testing points and the tracing curve are indicated on coordinates of $\ln P$ and $(1/T)$, value of ΔH can be determined from a slope of the straight line transformed from the curve. Consequently, using $R = 518.46 \text{ J}/(\text{kg} \cdot \text{K})$ for methane, $\Delta H = 1.2 \times 10^7 \text{ J/kg}$ is obtained for the case when molal ratio of THF to water, namely C , is 0.1. The another curve seen in Fig. 3 is a case of no THF additive, which is shown for reference. Needless to say, upper part of these lines is the domain where methane clathrate can be formed. The comparison of the both domains tells us that THF additive offers extreme facility for methane clathrate formation. The formed clathrate is a sherbet-like material, whose appearance can be seen in the left picture of Fig. 4. Its ignition is easily achieved only by bringing an open fire to it, and it burns as seen in the right picture.

As a next step, the effect of THF concentration on CH_4 clathrate formation can be seen from Fig. 5. Here, the horizontal axis C having unit of $[\text{mol/mol}]$ is, as is already explained, the molal ratio of THF against water. Experimental measurements were performed at constant pressure of 0.83 MPa, altering the value of C for each experiment and recording the value for T . From this figure it can be seen that THF shows the most marked effect when C is in the range of 0.05~0.1. Accordingly, the tests related to Fig. 3 become to be carried out under best setting of C .

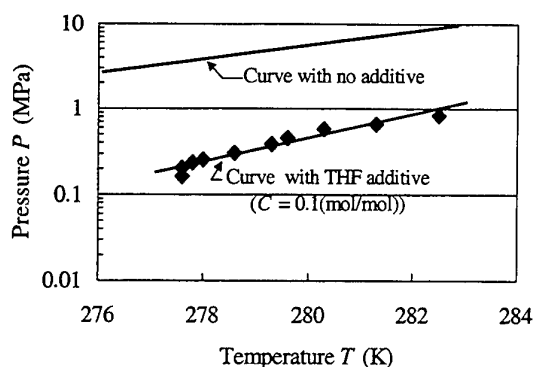


Fig. 3. Relation between P and T for methane clathrate formation

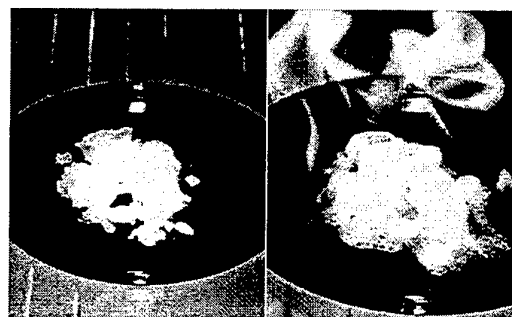


Fig. 4. Appearance of methane clathrate

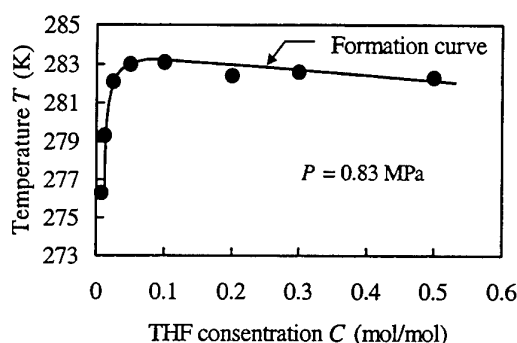


Fig. 5. THF concentration effect upon CH_4 clathrate formation

Now, we have paid our attention only to methane clathrate heretofore. However, considering that our ultimate interest is efficient usage of biogas, influence of CO_2 should be also investigated. Roughly speaking, biogas is said to be a compound gas of CO_2 and methane with content of about 60 %. Most of the residual being CO_2 , necessity for experiments determining the influence of CO_2 on methane clathrate formation appeared, which obliged us to do the relevant tests using artificial mixed gas. Then, if we denote molal ratio of CO_2 to CH_4 by κ , mixed gas samples of five kinds were prepared. κ value of these samples is chosen to be 0.1, 0.2, 0.3, 0.4 and 0.5. In addition, two more samples of $\kappa = 0$ and 1 were added. Needless to say, additional sample of $\kappa = 0$ is methane itself and another is CO_2 gas itself. However, intentional consideration of the unmixed gas is mainly for reference.

Experimental results related to these gas samples are shown in Fig. 6. The results for $\kappa = 0.2$ and 0.4 are omitted here to avoid confusion. Testing points for the mixed gases are distributed in the domain vaguely enclosed by testing points of CH_4 ($\kappa = 0$) and CO_2 ($\kappa = 1$). In addition, it can be easily noticed that with increase of κ value they shift entirely and gradually towards points of CO_2 . Furthermore, it can be seen that CO_2 clathrate can be easily formed even under the normal pressure and temperature provided that $C = 0.1$. Therefore, judging from these experimental results, easier formation of CO_2 clathrate will naturally change more or less the composition ratio of the mixed gas clathrate. Hereupon, gas analysis of dissociated gas of these clathrates was performed using gas-chromatography and the results are indicated in Fig. 7. By indicating simultaneously the values of gas-chromatography analysis and the original gas compositions on the same picture, it can be easily recognized that the content of CO_2 for the every mixed gas increases by clathrate formation. Hence, it is necessary to remove CO_2 in advance from biogas, if biogas is desired to be stored under higher energy density.

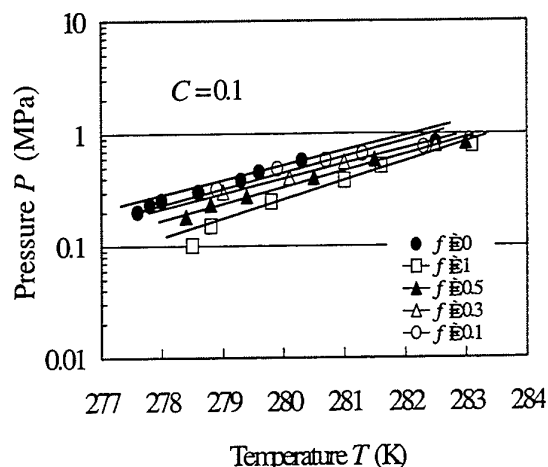


Fig. 6. Relation of P and T for clathrate formation of mixed gas of CH_4 and CO_2

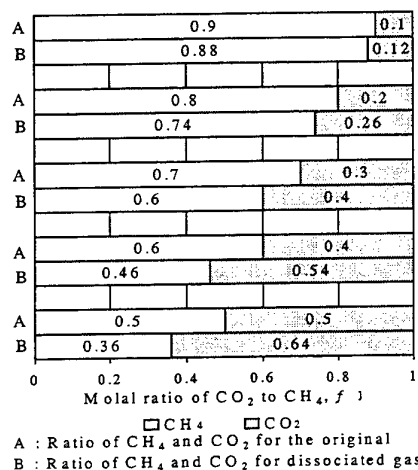
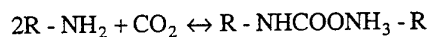


Fig. 7. Gas composition shift of mixed gas

3.2 Removal of CO_2 from Biogas [5]

Due to critical temperature difference of CO_2 and CH_4 biogas cooling may be a method of CO_2 removal from the gas. However, expected high energy consumption prevents us from practical application of this method. Under such circumstances alternative method by chemical absorption has been investigated. Concretely speaking, as it is known, monoethanolamine (MEA) reacts with CO_2 as follows:



where R is alkyl radical. Now, when surroundings is under room temperature, the above reversible reaction proceeds from the left to the right, absorbing CO_2 . On the other hand, under high surrounding temperature such as more than 100°C , the reaction proceeds conversely, releasing CO_2 . Hence, in addition to a small quantity of heat consumption MEA is said to have possibility of repeated use through its resuscitation. Furthermore, the material has no reactivity upon CH_4 at present. These convenient properties will make CO_2 removal by MEA more facile. Unfortunately, these natures are not necessarily confirmed yet completely. However, according to our experiments, the following natures of MEA are clarified:

1. Temperature lower than 70°C is recommended for CO_2 absorption process.
2. Existence of CH_4 in the mixed gas interrupts fairly active CO_2 absorption.
3. CO_2 absorption rate per unit time increases naturally with increment of contact area of MEA and the mixed gas.
4. Regardless of presence of CH_4 absorption by MEA, considerable absorption of CO_2 is confirmed under room temperature environment in final, which is checked by reaction of lime water and the released gas from CO_2 -rich-MEA, namely, MEA which is under CO_2 saturation.
5. Temperature more than 120°C is required to obtain active CO_2 release from CO_2 -rich-MEA.

On the other hand, in our confirmatory experiments MEA resuscitation is unsuccessful yet at present. Nevertheless, if CO_2 removal reactor by MEA from biogas is boldly designed with reference to the MEA natures already confirmed, a setup shown in Fig. 8 is proposed for the present.

4. EXPECTED BIOGAS STORAGE SYSTEM

Fundamental information necessary to set up biogas storage system could be obtained through our confirmatory tests. Under such situation, a system as shown in Fig. 9 can be considered as a biogas using system with ability storing biogas compactly, although there remain still unsolved problems such as reuse of THF and MEA resuscitation for instance.

In the system biogas is fundamentally utilized directly. However, the extra comes to be stored in clathrate form. Stored clathrate is naturally taken out according to demand and utilized for the purpose of many kinds. Due to comparatively rich energy density, its field of utilization is wider as compared with the case of gaseous. Usage as a fuel for a internal combustion engine may become as one of suitable example.

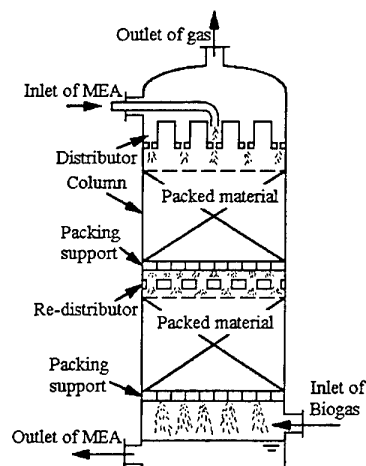


Fig. 8. Structure of packed column for CO₂ removal

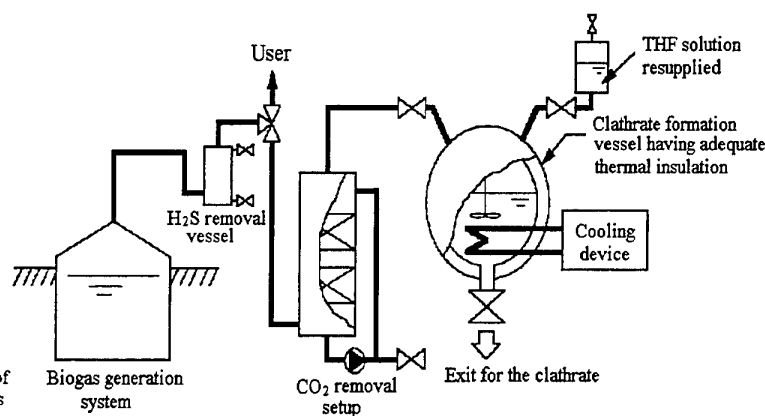


Fig. 9. Biogas storage system presently supposed

5. CONCLUSIONS

Summarizing the main results of this paper, the following items can be cited:

1. Addition of THF offers easier physical conditions for methane clathrate formation.
2. THF molal ratio added to water is recommended from 0.05 to 0.1 for methane clathrate formation.
3. Methane clathrate formation can be observed by adding THF additive even under slightly pressurized and reduced temperature environment from the normal surroundings.
4. Concerning hydrate formation for mixed gas of CH₄ and CO₂, the formation produces CO₂ concentration.
5. MEA is supposed to absorb selectively CO₂ from the mixed gas under room temperature.
6. CO₂ absorption rate per unit time by MEA is approximately proportional to contact area of MEA and the mixed gas.
7. MEA heating more than 120 °C releases actively the gas formerly absorbed.

Anyhow, these results might help to realize easy biogas storage further. If much biogas is stored compactly, biogas can serve, for example, as a alternative fuel of light oil for various farm appliances. However, to realize such a situation, there remains still more subjects to be investigated such as THF recovery and the reuse, check of MEA durability, practical high energy-conservative system design for the attendant provisions and so forth. Hence, it is quite expected that such subjects are faithfully worked out hereafter.

REFERENCES

1. S.Yokoi, et al, Formation equilibrium shift of methane hydrate, J. of the Chemical Society of Japan, Vol.4, (1993), pp. 389-392 (in Japanese).
2. I. Fujii, T. Kimura and H. Umeda, Study on biogas storage in the form of clathrate, Proc. of JSES/JWEA Joint Conf. (1997), pp. 417-420. (in Japanese).
3. A. S. Holmes, et al, Process improves acid gas separation, Hydrocarbon Processing, 61-5, (1982), pp. 131
4. I. Fujii and T. Kimura, Fundamental study on biogas storage in the form of clathrate, Proc. of JSES/JWEA Joint Conf. (1998), pp. 417-420 (in Japanese).
5. CPC, Proc. of JSES/JWEA Joint Conf. (1998), pp. 389-392 (in Japanese)
6. K. Onda, Gas absorption, Kagaku-Kogyosya, (1981).

INTERFEROMETRIC MEASUREMENTS OF GAS DIFFUSIVITY IN SUPERCRITICAL WATER

Katsuya Kuge, Kenji Yokota, Yusuke Murayama, Takahiro Honda,
Yukitaka Kato and Yoshio Yoshizawa

Research Laboratory for Nuclear Reactors

Tokyo Institute of Technology

Email: yyoshiza@nr.titech.ac.jp, Fax: +81-3-5734-2959

Keywords: supercritical, water, diffusion coefficient

ABSTRACT This study constitutes a part of attempt to develop a clean and high efficiency combustion system utilizing reactions in supercritical water. This study is aimed at establishing the measuring techniques of transport properties and observing techniques of reaction zone in supercritical water. First, the refractive index of water was measured because previous values were not available in supercritical region. The measurements were made at the temperatures from ambient temperature to 420°C and pressures from atmospheric pressure to 27MPa. The results show that the refractive index is constant in the experimental conditions within experimental errors. Next, the mass diffusivity of gas in supercritical water was measured. Nitrogen was used in this experiment to avoid the effects of reaction. The mass diffusivity of nitrogen in supercritical water was calculated from the fringe shift. The results show that the activation energy of the diffusion is as large as those of chemical reactions.

1. INTRODUCTION

Supercritical fluids are widely used as solvent extraction media and also as an environment for chemical reactions, due to the unique solvent characteristics of these fluids. Pure water is called in supercritical state when its temperature and pressure exceed 374.2°C and 22.1MPa, respectively. In the supercritical and near-critical regions, the density of water is a strong function of both temperature and pressure, leading to large changes in the physical properties particularly the solution behavior. Therefore, supercritical water oxidation is expected to be an advanced technology for clean combustion. But the properties in supercritical water are not fully known because of difficulties in experiments under high temperatures and pressures. The studies utilizing supercritical fluids as solvent for separation extraction have been often discussed since 1970's [1]. Supercritical water was demonstrated to be utilized also for decomposition of waste materials and toxic substances such as plastics, polychlorinated biphenyl and freon [2-4]. Combustion phenomena at supercritical condition are studied well also. Under supercritical condition, an observation of diffusion flame of oxygen and a mixture of methane and methanol [5, 6], reaction kinetic studies of hydrogen and carbon monoxide [7], and an analysis of diffusion flame structure [8] were discussed. A new energy system using a supercritical combustion and a coal highly utilization system using supercritical water are studying as national projects of Japan, which are organized by NEDO (The New Energy and Industrial Technology Development Organization).

Consistency of energy balance is an important criteria to realize these proposals for practical use, because large amount of heat and pump work energy are required to maintain a supercritical condition at high temperature and pressure. A work for ideal isotherm compression of air from atmosphere to 22MPa, which is supercritical pressure of water, is corresponded to 11-17% of the combustion energy of hydrogen or carbon with the stoichiometric amount of air. Then a balance between the required energy and the added value of performance of supercritical condition have to be considered. This study attempts to develop a clean and high efficiency combustion system utilizing reactions in supercritical water for decomposition of waste materials. Enhancement of combustion ability, which needs a realization of a formation of reaction zone under supercritical condition, is a practical subject. As the first step of this program, the mass diffusivity of gas in supercritical water was measured using a supercritical reactor installed with an optical interferometer.

2. EXPERIMENT

A supercritical water reactor and an optical interferometer was adopted in this experiment study. The experimental setup shown in Fig. 1(a) was composed of (1) a high pressure reaction cell in an electric furnace, (2) water supply and pressure regulation system, (3) gas supply system and (4) Mach-Zehnder

interferometer system. A He-Ne laser was used as the light source for of the interferometer. The reaction cell shown in Fig. 1(b) has 10cm^3 of inner volume and a couple of sapphire windows (5mm of diameter) which was used for the interferometric measurement. The cell temperature was controlled by an electric furnace monitoring a thermocouple at inner side of the cell. The cell was installed three ports for introductions of high pressured water and gas, and a discharge of them. The water was supplied by a high pressure plunger pump and controlled the pressure by a back pressure regulator. The gas was pressurized by a manual screw pump. The water and gas were supplied to the cell through pre-heating coils. The interferograms were recorded CCD camera and analyzed graphically by a personal computer.

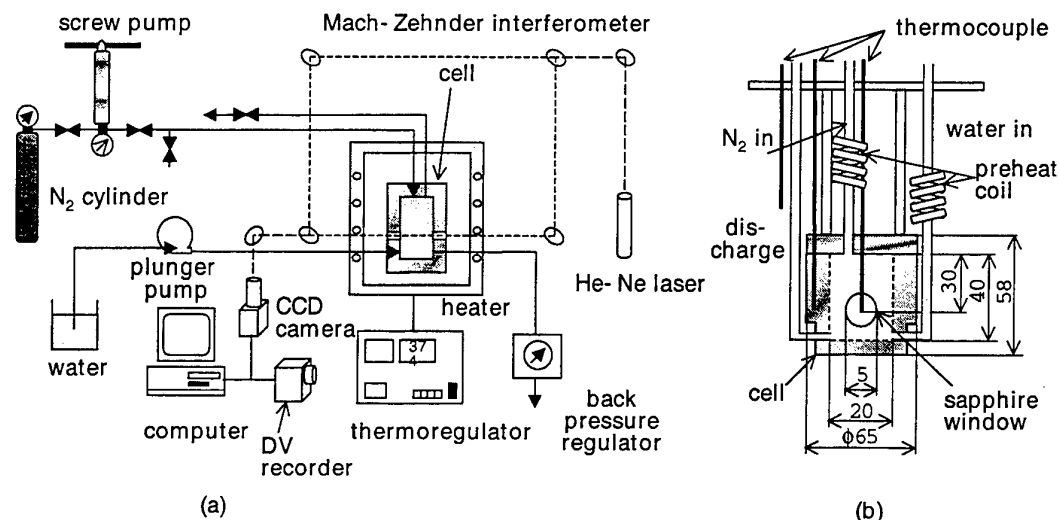


Fig. 1. Experimental apparatus

The mass diffusivity of a gas in supercritical water was mainly measured because an oxidizer for a practical supercritical combustion was supposed to be supplied in a gas state. It is considered to use air as a common oxidizer in supercritical water. Then, nitrogen gas is employed as an alternative of air for a model oxidizer gas in the diffusion experiment to avoid the effects of reaction. The interferometric fringes were observed from the interferograms experiment. Because fringes shifted depending on changes in density field, the mass diffusivity of nitrogen in supercritical water was calculated from the fringe shift.

3. RESULTS

Refractive Index Measurement of Sub-and Supercritical Water

The interferometric fringes analysis of the Mach-Zehnder interferometer needs a refractive index of a media. The refractive index of water at high-temperature and pressure was measured firstly in this study, because the index around supercritical condition had not reported enough. It is known that a refractive index is proportional to a density of a compressive media as follows.

$$n = 1 + K\rho \quad (1)$$

$$\Delta n = K\Delta\rho = \frac{h\lambda}{L} \quad (2)$$

$n[-]$, $\rho[\text{kg/m}^3]$, $h[-]$, $\lambda[\text{m}]$ and $L[\text{m}]$ show a refractive index, density of the media, shift amount of interferometric fringe, and optical length, respectively. The proportional constant, K , is called as Gladstone-Dale constant. The measured Gladstone-Dale constants for sub- and supercritical water are shown in Fig. 2. Symbols "E" and "J" in the figure show the constants under ambient temperature water at atmospheric pressure to 27Mpa, and a literature value for steam [11], respectively. The constants at ambient temperature independents from pressure, and are similar value to the vapor's one. Measured values at high- temperature and pressure were shown in the figure. These experimental values are also close to the atmospheric water's one.

Scattering of values at high-pressure and temperature would be affected from noises of the back pressure regulator control. Since the measured Gladstone-Dale constant in vapor, water and supercritical water are substantially the same values, the constant value of $0.33\text{cm}^3/\text{g}$ is employed as the unique value of water for the following discussion.

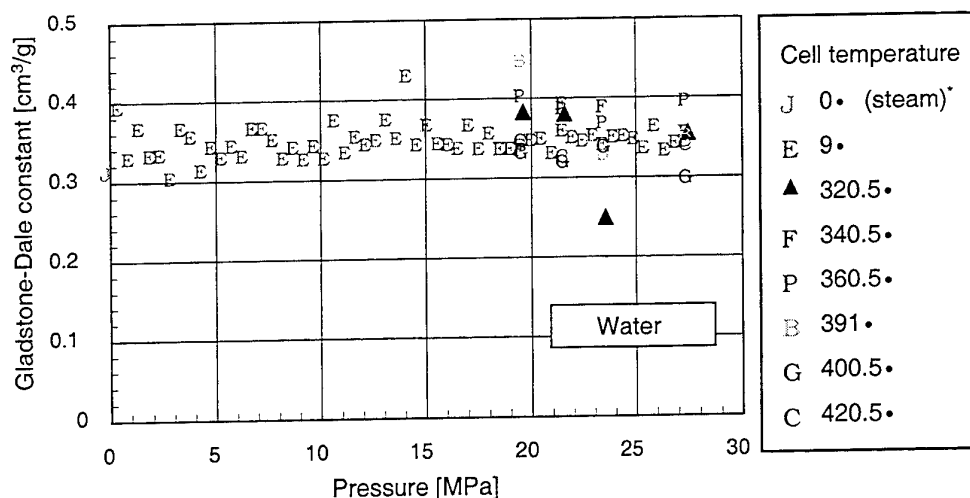


Fig. 2. Gladstone-Dale constants for water at sub- and supercritical phases *literature value [11]

Measurement of Diffusion of a Gas in a Supercritical Water

Diffusion speed of nitrogen into a supercritical water was measured. Nitrogen (N_2) which had pressurized and heated previously was introduced to the supercritical water reactor cell by the screw pump to observe the diffusivity of nitrogen in the water optically. The diffusion process observed through the sapphire windows of the reactor cell is shown in Fig. 3. An area in the circle and a black rectangle in the figure shows the cell inside the reactor cell is shown in Fig. 3. The interferometric fringes produced by the interferometer were observed in the circle. Fig. 3(a) shows supercritical water state at 400°C and 27.6 MPa before N_2 injection. When N_2 at a high temperature and pressure was injected into the cell, interferometric fringes once disappeared because of scattering the laser light by a random mixture phase of N_2 and water (Fig. 3(b) at 29 sec. after). The density field of N_2 became moderate around bottom and top parts, and interferometric fringes appeared again in Fig. 3(c) and (d). In a little while, the fringes become clear again in all area (Fig. 3(e) and (f)). After 15 min. at which the density change and fringes shift became moderate enough for measurement, the fringes shift rate (h) was measured and the diffusion coefficient was calculated.

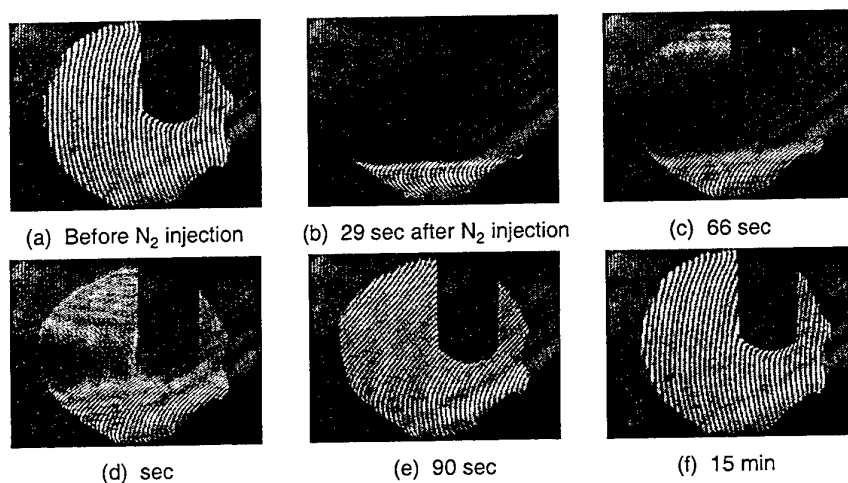


Fig. 3. Observation of nitrogen gas diffusion into a supercritical water at 400°C and 27.6 MPa

Calculation of Concentration of Nitrogen in a Supercritical Water

Nitrogen diffusion in a supercritical water was analyzed by the nitrogen concentration change measurement in the experimental cell. The process for nitrogen concentration calculation is shown as follows. Under the assumption that the nitrogen and water mixture is an ideal mixture, the relation between the index (n) and a nitrogen molar concentration ($x[-]$) is depicted as follows.

$$\begin{aligned} n &= xK_N\rho_{N0} + (1-x)K_H\rho_{H0} + 1 \\ &= xn_{N0} + (1-x)n_{H0} + 1 \end{aligned} \quad (3)$$

The subscripts of N, H and O shows nitrogen, hydrogen and an individual value. Then, molarity, c [mol/m³] is introduced in the equation.

$$n = K_N M_N c_{Nv} + K_H M_H \left(c_{H0} - \frac{c_{H0}}{c_{N0}} c_N \right) + 1 \quad (4)$$

The refractive index change rate is depicted as follows.

$$\frac{\Delta n}{\Delta t} = \frac{(n_{N0} - n_{H0})}{(Z-1)^2} \cdot \frac{Z}{\left(x + \frac{1}{Z-1} \right)^2} \cdot \frac{\Delta x}{\Delta t} \quad (5)$$

$$\text{since } Z = \frac{c_{H0}}{c_{N0}}$$

Then, the molar concentration change rate is shown as follows.

$$\frac{\Delta x}{\Delta t} = A(x+B)^2 \frac{\Delta h}{\Delta t} \quad (6)$$

$$\text{since } A = \frac{(Z-1)^2}{(n_{N0} - n_{H0})Z} \cdot \frac{\lambda}{L} \quad B = \frac{1}{Z-1}$$

$\Delta t=1\text{min}$ and measurement interval was 5min in this study, then, the change of x between time of $i-1$ to i is defined as,

$$x_{i-1} = x_i + \frac{5}{2} \left\{ A(x_{i-1}+B)^2 \frac{\Delta h}{\Delta t} \Big|_{i-1} + A(x_i+B)^2 \frac{\Delta h}{\Delta t} \Big|_i \right\} \quad (7)$$

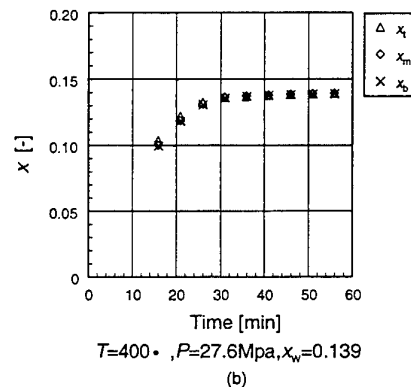
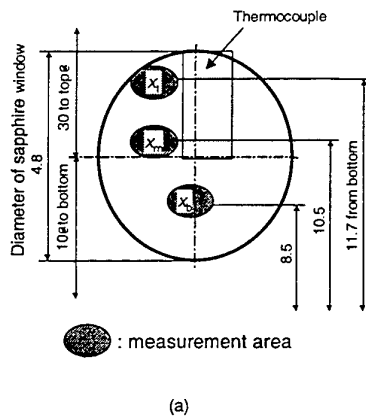


Fig. 4. Measurement of nitrogen concentration change. (a) Measurement areas, (b) measured concentration changes

An experimental concentration change was calculated from Eq. (7). The terminal nitrogen molar concentration, x_w , which is required for the calculation was measured experimentally by the measurement of discharged water amount from the cell by the nitrogen injection. The concentration changes were calculated from the measurement of the fringe shift amount, h , at some parts at the sapphire window which were top, medium and bottom parts shown in Fig. 4(a). The molar concentration changes at the three parts are shown in Fig. 4(b). The concentration changes to time show diffusion of nitrogen into the supercritical water. The concentration gradient between the three parts was not steep. Then, the concentration at the medium part, x_m , was employed for the following discussion as a representative experimental value.

4. DISCUSSIONS

Derivation of the Diffusion Coefficient

A diffusion coefficient of nitrogen to supercritical water was discussed using above experimental results. A diffusion model was set up for the discussion. Fig. 5 shows the initial condition of the model. It was assumed that after nitrogen injection the three phase zones, that is, a random mixture zone between H_1 and H_2 , pure nitrogen and water zone, are formed initially. Fig. 5 (b) depicts the initial phase structure in the cell, and Fig. 5 (a) shows the nitrogen concentration distribution at the structure. Then, it is presumed that a distribution between three phases proceeds to a uniform concentration according to the following equation based on the Fick's second law.

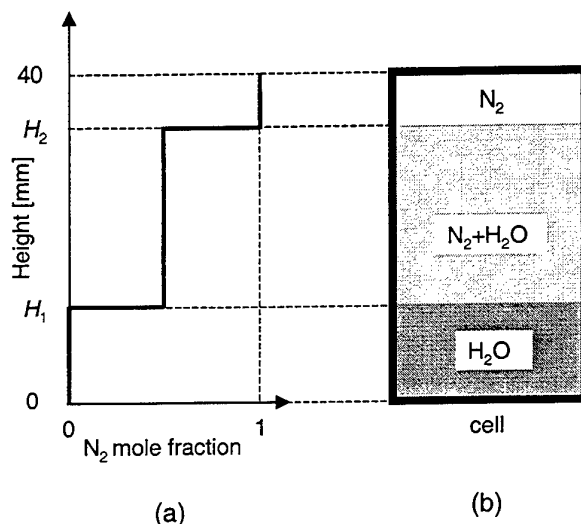


Fig. 5. Initial condition of simulation model. (a) initial nitrogen concentration distribution, (b) schematic diagram of initial phase structure

$$\frac{\partial c_N}{\partial t} = -\frac{\partial N_N}{\partial y} = D \frac{\partial}{\partial y} \left[\left\{ 1 + c_N \left(\frac{1}{c_{H_2O}} - \frac{1}{c_{N_2}} \right) \right\} \frac{\partial c_N}{\partial y} \right] \quad (8)$$

N [mol/m².s] and D [m²/s] shows a molar flux and a diffusion coefficient, respectively. $H_2=40$ mm was used the following discussion because the value was most fitted to the experimental results from a previous study. A nitrogen concentration distribution change in the cell was simulated from Eq. (8) by assuming a value of the diffusion coefficient. Then, the simulation results was compared with the experimental result statistically. Fig. 6 shows a relative error distribution between a simulation and an experimental result at $T=400^\circ\text{C}$ and $P=27.6\text{MPa}$, $x_w=0.139$. The error distribution shows as parameters of the diffusion coefficient, D , and the height of water phase, H_1 . The more an area becomes dark, the less the relative error becomes. $5.0\text{ mm}^2/\text{s}$ of D was the most appropriate value in this condition. Then, Fig. 7 shows the comparison between the experimental result and simulated result at the same diffusion condition with regard to x_m . The simulation result agrees well the experimental one.

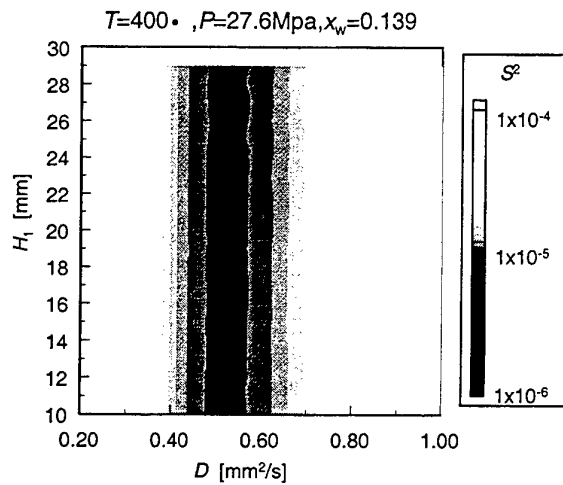


Fig. 6. Relative error distribution of the diffusion coefficient

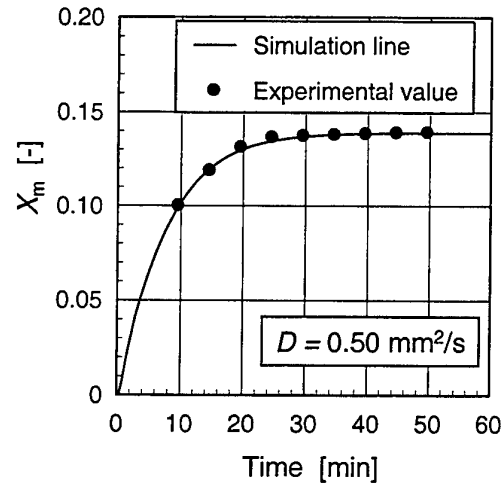


Fig. 7. Comparison of simulation result and measured value

Dependency of the Diffusion Coefficient to the Temperature and Concentration

Calculated diffusion coefficient for each experiment was derived by above procedure. The calculated values of D are shown against the terminal nitrogen concentration, x_w , with the cell temperature as a parameter in Fig. 8. The coefficient becomes larger at a higher temperature and a lower nitrogen concentration. Orders of diffusion coefficients of liquid and gas phases are generally 10^{-3} and 10^{-1} [mm^2/s], respectively. The diffusion coefficient of this study at supercritical condition was intermediate between liquid and gas phases' one.

The coefficient dependency on the cell temperature was discussed using Arrhenius' law defined as follows,

$$D = D_0 \exp\left(-\frac{Q}{RT}\right) \quad (10)$$

The activation energy of diffusion, Q , was 80-200 kJ/mol on these results. Q was as large as those of chemical reactions

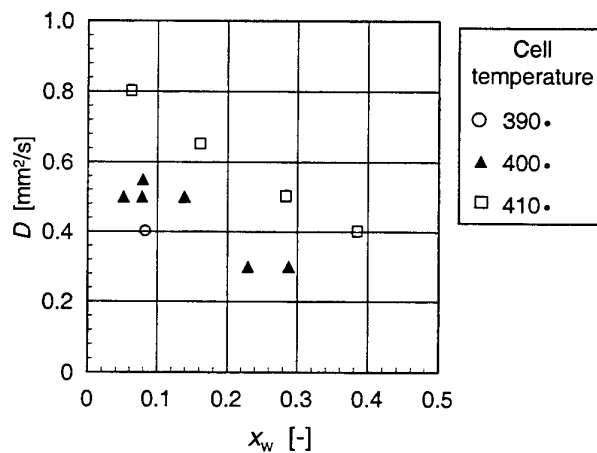


Fig. 7. Comparison of simulation result and measured value

5. CONCLUSIONS

1. The observation method of gas diffusion process in a supercritical water was demonstrated.
2. The Gladstone-Dale constant were measured widely at sub- and supercritical water. The G.-D. constant value remained constant in the wide condition including supercritical state.
3. The diffusion coefficient of nitrogen to supercritical water were obtained. The value of the coefficient was intermediate between gas and liquid's one. The activation energy of diffusion is as large as those of chemical reactions.

NOMENCLATURES

c: concentration [mol/m^3]	T: temperature [K]
D: diffusion constant [m^2/s]	t: time [s]
D_0 : frequency factor [m^2/s]	x : N_2 mole fraction [-]
H: height from cell bottom [m]	ρ : density [kg/m^3]
h: amount of passage of interferometric fringes	λ : wave length of laser beam [m]
K: Gladstone-Dale constant [m^3/kg]	
L: optical length [m], M: molecular weight [g/mol]	Subscripts
N: molar flux [$\text{mol/m}^2\text{s}$]	H: water
n: refractive index [-]	N: nitrogen
P: pressure [Pa]	w: terminal or whole
Q: energy of activation [J/mol]	0: independent
R: gas constant [J/kg K]	1: area of water
s^2 : relative error	2: area of mixture of water and nitrogen

REFERENCES

1. S. Saito, *The Science and Technology of Supercritical Fluids*, Sankyo Business Co. Ltd., 1996• @ (in Japanese).
2. M. Ajiri, et al., "Supercritical Fluids as a Reaction Medium", *Kagaku Kogaku Ronbunshu*, v. 23, pp. 505 (1997) (in Japanese).
3. T. Oe, et al., "Waste Water Treatment by SCWO", *J. of Japan Institute of Energy*, v. 76, pp. 868 (1997) (in Japanese).
4. T. Sugeta and T. Sako, "Decomposition of CFCs with Supercritical Water", *ibid.* pp. 874 (1997) (in Japanese).
5. W. Schiling and E. U. Frank, "Combustion and Diffusion Flame at High Pressures to 2000 bar", *Ber. Bunsenges. Phys. Chem.*, v. 92, pp. 631 (1988).
6. R. R. Steeper, et al., "Methane and Methanol Diffusion Flames in Supercritical Water", *J. Supercritical Fluids*, v. 5, pp. 262 (1992).
7. H. R. Holgate and J. W. Tester, "Oxidation of Hydrogen and Carbon Monoxide in Sub- and Supercritical Water: Reaction Kinetics, Pathways, and Water-Density Effects. 1 Experimental Results", *J. Phys. Chem.*, v. 98, pp. 810 (1994).
8. J. K. Bechtold & S. B. Margolis, "The Structure of Supercritical Diffusion Flames with Arrhenius Mass Diffusivities", *Combust. Sci. Tech.*, v. 83, pp. 257 (1992).
9. M. Fujie, et al., "Basic Combustion Experiments for Electric Power Generation with Supercritical Water Combustion", *64th Symposium of Japan Soc. Chem. Eng.*, I 215 (CD), Nagoya, Japan (1999) (in Japanese).
10. H. Hatano, et al., "A New Concept of Hydrogen Formation Process with Coal and Supercritical Water Reaction", *ibid.*, I 305 (CD), Nagoya, Japan (1999) (in Japanese).
11. *Handbook of Chemistry and Physics*, 56th Ed., CRC Press (1975).

BIODIESEL PRODUCTION USING WASTE COOKING OIL FROM RESTAURANT

D. Y. C. Leung

Department of Mechanical Engineering
The University of Hong Kong
Email: ytleung@hkucc.hku.hk

G.Y. Chen

Institute for Thermal Power Engineering
Zhejiang University
Email: enechen@emb.zju.edu.cn

Keywords: biodiesel, methy-ester, fatty acid, waste cooking oil, renewable energy

ABSTRACT. A large amount of waste cooking oil is generated by the restaurants in Hong Kong every day. Currently, there is no efficient way to dispose of this waste material, which are simply dumped into sewers. In 1997, the government collected about \$220M as sewage charges from the restaurant trade. This poses a heavy burden on the trade as well as on the government's wastewater treatment facilities. Biodiesel is a clean-burning fuel made from natural, renewable sources such as vegetable oils. The study on the feasibility of replacing diesel by biodiesel fuel is increasing in recent years due to the increasing pressure in reducing the emissions from diesel vehicles. Biodiesel is considered as a cleaner alternate fuel to substitute the diesel fuel in USA and many other countries in Europe. This paper presents our study on the biodiesel production technology using waste cooking oil generated from local restaurants. Different recipes to make biodiesel from waste oil are investigated and compared with those produced from neat vegetable oil. The effect of process parameters, such as mixing, reaction and washing times, heating temperature for filtration and separation, reaction temperature, incoming feedstock quality etc. on the quality of biodiesel produced will be discussed based on the preliminary data obtained.

1. INTRODUCTION

With the increasing demand in energy and the continuous reliance on fossil fuels, our world is facing the threat of shortage and exhaustion of these valuable resources. With the current fuel consumption trend, it is indicated that fossil fuels would be exhausted within the next 45 years for oil, 330 years for coal and 55 years for natural gas [1]. At the same time, human-beings, animals and plants are being subjected to health deterioration due to the increasing exhaust emissions from using different fossil fuels. Our world is becoming susceptible and vulnerable to the damage made by us. We have no choice but immediately take great strides to stop this trend, thus keeping our living environment sustainable. In the past several decades, many cities become modernized as a result of economic growth. One outcome of the modernization is the tremendous increase in exhaust emissions from road vehicles which account for great proportion of total emissions, especially in urban area. In this case, alternative fuels, especially those renewable like biodiesel, are therefore of great interest to lots of researchers, government officials, lawmakers and general people.

Hong Kong is a small metropolitan with very high population and vehicle density. Geographically Hong Kong is embraced by clusters of mountains and highrise buildings. Therefore, vehicle exhaust emissions in Hong Kong are more serious than any other regions as indicated by the daily reported roadside air pollution index. A government report [2] indicated that the major on-road emissions come from vehicles using diesel fuel and proposed all diesel taxis to switch to LPG fuel in the coming years. Apart from that other alternative fuels are also well considered. Of these, biodiesel is the one which receives increasing attention by the public. Biodiesel is a clean burning alternative fuel for diesel engine produced from renewable resources such as vegetable oils and animal fats. Chemically, it consists of mono alkyl ester (for example, methyl ester, ethyl ester) of long chain fatty acids derived from renewable lipid source. Biodiesel has several advantages as alternative fuel in the safety, toxicity and biodegradability aspects. Besides, it is advantageous to the environment. Some of these advantages are stated below:

- Particulate matter (respirable fraction) emissions, which is a human health hazard when breathed can be cut significantly;
- Greatly reduces the amount of carbon monoxide emitted from vehicles;
- Ozone forming potential of the hydrocarbon emissions of biodiesel nearly 50% less than that of petroleum fuel;
- Contains essentially no sulfur, therefore greatly reduces sulfur dioxide (and hence particulates) emission from diesel vehicles.
- A net gain of energy producing biodiesel;
- Biodegrades as fast as dextrose;
- Polycyclic aromatic hydrocarbons (PAH's) and nitrated PAH's, both of which are identified as carcinogenic compounds, can be reduced by 75% to 85% in engine tests.

Other Characteristics of biodiesel are listed as follows:

- Lubricity: it provides improved lubricity compared to conventional diesel fuel leading to decreased maintenance costs.
- Flexible blending: it can be mixed at any level with petroleum diesel. It has been demonstrated that 20% volume biodiesel blended with 80% volume petroleum diesel has similar fuel consumption, horsepower, and torque as petroleum diesel.
- Safety: Biodiesel is a fuel with higher flash point ($>100^{\circ}\text{C}$) than petroleum diesel, therefore it is safer to store and handle biodiesel.
- Minimum modification: Biodiesel does not require expensive modifications to engine or refueling facilities and mechanics do not have to be retrained.

A large amount of waste cooking oils (WCO) is generated by the restaurants in Hong Kong including traditional Chinese and Western style restaurants, and fast food chains like McDonald's and Kentucky. In 1997, the Hong Kong government collected about \$220M as sewage charges from the restaurant trade. Traditional way of disposing these WCO is not only expensive to the trade, but also increases the burden of sewage treatment and maintenance of sewers. The present study is initiated due to the above-mentioned facts and due to the potential benefits of converting WCO to biodiesel.

2. BIODIESEL PRODUCTION TECHNOLOGY

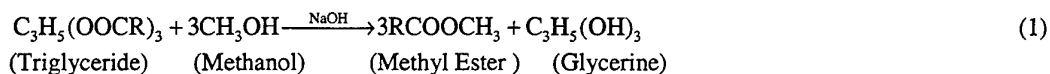
Up to now, plenty of researches have been conducted on biodiesel production using neat vegetable oils but very little of these studies is related to the use of waste cooking oil as raw material. Therefore, an overview of biodiesel production technology using neat vegetable oils or fats is made here, which is a very good reference to the present work. There are three basic routes to produce biodiesel from oils and fats:

1. Base catalyst transesterification with methanol.
2. Direct acid catalyzed esterification with methanol.
3. Conversion of oil to fatty acids, and then to methyl ester with acid catalysis.

The majority of the methyl ester produced today is done with the base catalyzed reaction because of the following reasons:

- Low temperature ($\sim 65^{\circ}\text{C}$) and pressure (20 psi) during conversion;
- High conversion (98%) with minimal side reactions and reaction time;
- Direct conversion to methyl ester with no intermediate steps;
- Exotic materials of construction not necessary.

In this paper, only the first method, i.e. base catalyst transesterification, is discussed. Transesterification is the process of reacting triglyceride with alcohol in the presence of a catalyst to produce glycerol and fatty acid esters [3]. In our study, methyl ester biodiesel is produced through transesterification reaction of a waste cooking oil with methanol in the presence of sodium hydroxide (catalyst). The chemical reaction is depicted below:

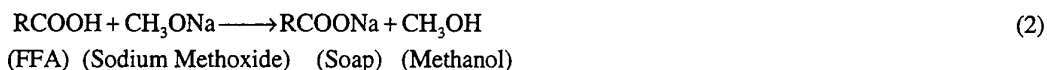


The stoichiometry of the above reaction requires three moles of methanol for every mole of triglyceride reacted. On a weight basis, this corresponds to adding methanol of about 10% by weight per unit mass of oil processed. However, to obtain high yields and reasonable reaction time, an excess of methanol is usually used. A variety of base catalysts have been used for this reaction including sodium hydroxide, potassium hydroxide, sodium methoxide etc. In current experimental conditions, only sodium hydroxide was used as the base catalyst.

3. CONVERSION METHODOLOGY

The procedure to complete the conversion of WCO into biodiesel is different from those generally used for neat vegetable oils and it consists of the following steps:

- 1) Filtration and separation: WCO is different in some physical and chemical properties from neat oils. It is normally contaminated with solid residue and other water soluble materials, which may influence the subsequent transesterification reaction. Therefore, a delicate filtration and separation process is necessary to filter the oil contaminants before conversion. Normally WCO is very viscous and it is recommended to heat it to about 60°C before filtration and separation. It should be noted that the quality of WCO varies from restaurant to restaurant and this makes the conversion process more difficult to control.
- 2) Removal of free fatty acids (FFAs): WCO has high levels of FFAs which are natural degradation products of oils. The FFAs are detrimental to the transesterification process as they can tie up catalyst through the formation of soaps, as shown in the reaction (2) below [4]:



In addition, soap formation in some cases may begin to form strong emulsion with methanol and oil, which is unbreakable and forms a cottage cheese looking products, and results in a more difficult phase separation of methyl ester and glycerol. To prevent this, caustic and water are added to the preheated WCO before carrying out the transesterification step.

- 3) Transesterification reaction. The methanol/sodium hydroxide mixture is charged into a reactor, either continuously or batch, and the filtered WCO is added. Excess methanol is normally utilized to ensure total conversion of the fat/oil to the esters. The catalyst of sodium hydroxide will first react with FFAs of the oil to form soap. There must be enough additional catalyst to catalyze the transesterification reaction.
- 4) Separation of methyl ester rich phase (Biodiesel) from glycerine rich phase. Once the reaction is completed, two major products exist: glycerine at the bottom and methyl esters on the top. Due to the density difference, the two are allowed to gravity separate and glycerine is simply drawn off from the bottom. In some cases, a centrifuge is needed to separate the two products.
- 5) Methyl ester purification. Once separated from the glyceride, the methyl ester rich phase is washed with water to remove residual catalyst, soaps, methanol and other water-soluble components, and then dried, and sent to storage. This is the biodiesel sample. The esters can be distilled under vacuum to achieve even higher purity.

4. EXPERIMENTAL SETUP

The main reaction facilities is shown in Photo 1 below. It consists of an electrically controlled mixer combined with a transesterification reactor of 2000ml. Figure 1 shows the schematic flowsheet detailing the biodiesel production process.

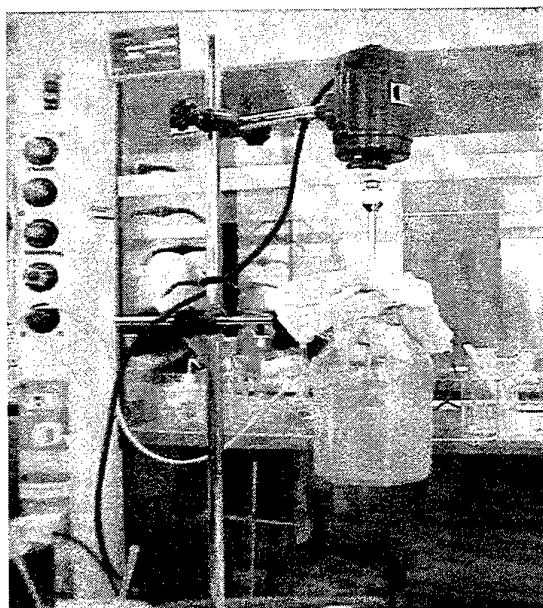


Photo 1. Main experimental facility

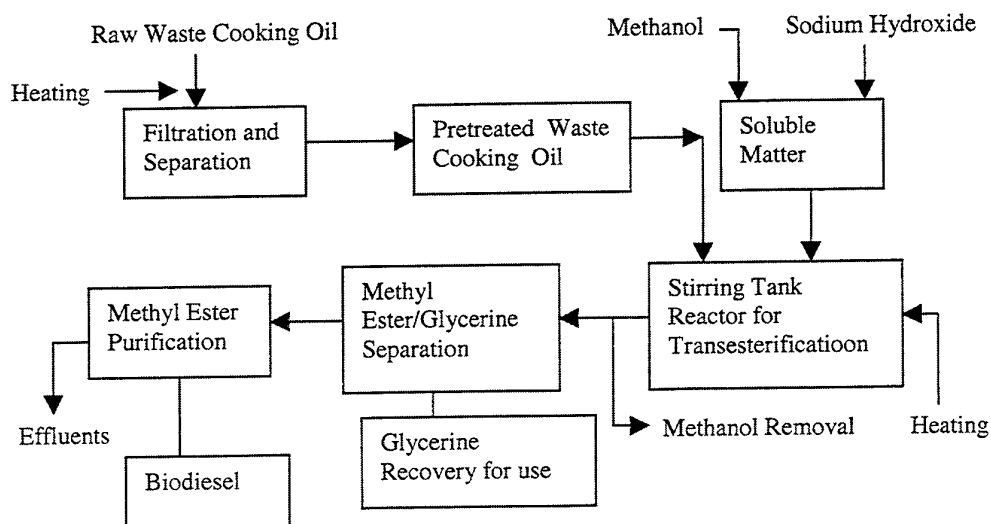


Figure 1. Schematic flowsheet for biodiesel production using waste cooking oil.

5. RESULTS AND DISCUSSIONS

The sample produced are shown in Photo 2, which indicates same recipes but different operating conditions and different oil feedstock. In the photo there are four samples of biodiesel produced referred as sample 1, 2, 3, 4 respectively from left to right. The operating conditions are: for sample 1, WCO as feedstock, no FFA removal before transesterification, methanol /WCO volume ratio is 1: 5, NaOH=1.0% by weight of total WCO used; for sample 2: WCO as feedstock, FFA removal, not enough NaOH pellets dissolved in Methanol, same recipe; for sample 3: WCO as feedstock, FFA removal, same recipe; for sample 4: NCO as feedstock, same recipe.



Photo 2. Four samples of biodiesel produced

The physical properties of the typical biodiesel produced using WCO and neat corn oil (NCO) is shown in Table 1 below, where the recipe is: for WCO, volume ratio of WCO to methanol is 5:1, 1.15% sodium hydroxide by weight of WCO used with a portion of it as a reagent for neutralization; for NCO, volume ratio of NCO to methanol is 6:1, 0.85% sodium hydroxide by weight of NCO used.

Table 1. Fuel-related Properties of Biodiesel Produced Typically

Properties	Test Methods	Unit	Biodiesel Using WCO	Biodiesel Using NCO
Flash point	D-93	$^{\circ}\text{C}$	<100	126
Water & sediment	D-2709	Vol. %	Nil.	Nil.
Kinematic viscosity	D-445	mm^2 / s	5.799	4.964
Sulfur content	D-429	wt. %	0.004	0.003
Copper Corrosion	D-130	3hrs@100 $^{\circ}\text{C}$	1B	1A
Cloudy point	D-2500	$^{\circ}\text{C}$	0	1
Cetane number	D-613		56	61
High heating value	Estimation	kJ/kg	38500	41000

Table 2 shows the corresponding data of No. 2 diesel fuel and ASTM standard for pure (100%) biodiesel. Based on Table 1 and 2, the following observations on the biodiesel fuel produced can be obtained:

- Contains a very low sulfur content, so emits little sulfur oxides.
- Has higher flash point than DF2 by near 70%, thus it is safer to store, use and transport than DF2.
- Meets the requirement of ASTM standard for pure biodiesel, thus can be directly applied to existed vehicles fueled with DF2 with no modification to the engine.
- Twice the kinematic viscosity as that of DF2. This may be a major contributing factor to the onset and severity of durability problem.

However, the flash point of biodiesel produced using WCO is non-ideal at current time. This may be contributed to non-thorough purification, not enough long time of storage and complete separation of biodiesel from some water-soluble matters.

Table 2. The Properties of Diesel Fuel and the Specification by ASTM Standard for Pure (100%) Biodiesel

Properties	Test Methods	Unit	Diesel fuel (DF2)[5]	ASTM Standard
Flash point	D-93	°C	74	100min.
Water & sediment	D-2709	Vol. %	<0.005	0.050max.
Kinematic viscosity	D-445	mm ² / s	2.98	1.9~6.0
Sulfur content	D-429	wt. %	0.036	0.05max.
Copper Corrosion	D-130	3hrs@100 °C	1A	No. 3B max.
Cloudy point	D-2500	0 °C	-12	no standard
Cetane number	D-613		49.2	40min.

Table 3 shows the analytical data obtained from other experimental conditions. Three runs were conducted with different recipes and mixing times. Run 1 used WCO as feedstock with methanol amount to 18% of WCO used. The mixing time was more than 2 hours. Runs 2 and 3 used NCO as feedstock with the same methanol quantity in the two runs (13%) but different mixing time (1.5 hours and 0 hour respectively).

Table 3. The Analytical Data Obtained Based on Other Experimental Conditions*

Properties	Test Methods	Unit	Run#1	Run#2	Run#3
Flash point	D-93	°C	<100	110	116
Water & sediment	D-2709	Vol. %	Nil.	Nil.	Nil.
Kinematic viscosity	D-445	mm ² / s	9.284	4.471	12.40
Sulfur content	D-429	wt. %	0.002	0.004	0.002
Copper Corrosion	D-130	3hrs@100 °C	1A	1A	1A

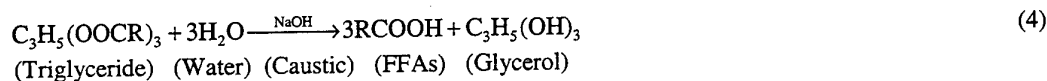
As can be observed the biodiesel produced using NCO fully meets requirements by ASTM standard for pure biodiesel, however, the quality of biodiesel produced using WCO under Run 1 and using NCO under Run 3 is not very satisfactory. For Run 1, there was enough mixing, but chemical recipe is non-ideal, probably due to the non-accurate estimation of FFAs content. In fact, the content of FFAs of WCO is difficult to determine precisely. By standard titration method of Joshua and Tickell [6], only an approximate range of FFAs in raw WCO can be obtained. This makes quality control of biodiesel more difficult. For Run 3, There was no enough mixing before transesterification. This indicates that the good mixing between methanol and sodium hydroxide before transesterification is very important in order to access to high quality of biodiesel. Further investigation regarding this point will be continued.

Reaction time for transesterification reaction has obvious effect on the quality of biodiesel produced. In general, reaction time of 1.5 to 2 hours is acceptable. In theory, the influence of Reaction time is positive, however, its influence may be neglected for more than 4 hours.

Water removal and washing is also important for the improvement of biodiesel quality. WCO, in general, contains a different degree of water. If not removed before transesterification, the soap forms emulsions with methanol and oil, preventing the reaction from occurring. The soap formation reaction is listed below [7]:



Also water contributes to formation of FFAs by the following route (Steehan et al, 1998):



The quality of biodiesel produced will be affected in the presence of the FFAs. After the transesterification reaction is finished, the raw biodiesel contains some salts, methanol and water-soluble matters, the presence of these compounds which degrades the biodiesel. Delicate water-washing biodiesel is at least two-step process with reasonable control volume of washing water used.

The incoming feedstock quality is crucial for the quality of biodiesel produced. From the data in Table 1 and 2, it is obvious that NCO has better quality of biodiesel produced than WCO. However, the quality of incoming WCO is uncontrollable, its influence on the quality of biodiesel produced can be reduced by delicate pretreatment such as filtration, separation and even by adding some additives.

It has been found that moderate heating together with vigorous mixing applied to transesterification of WCO with methanol and sodium hydroxide can result in faster reaction, and better separation of layers after reaction, and therefore upgrades the quality of resulting biodiesel produced. However, the heating temperature has an optimum range of 50~60 °C . If the heating temperature is too high, the evaporation of methanol accelerates and thus does harmful to the reaction.

6. CONCLUSIONS

Biodiesel produced from waste cooking oil or neat corn oil in our laboratory, in general, meets the requirement of ASTM standard for pure biodiesel, and thus can be directly applied to diesel engine as a substituted fuel. Biodiesel is more advantageous than conventional diesel fuel in lots of fuel-related properties. However, biodiesel still has great potential in improving its quality and production rate in order to meet the increasing demand for diesel engine and stringent environment protection requirements.

The efficient conversion of free fatty acids of waste cooking oils is indispensable to produce biodiesel of high quality with high yields. Therefore, one of our future work will be focused on this area. Of course, the test using biodiesel on diesel engine is also our major area of focus in the future.

ACKNOWLEDGEMENT

The project is supported by the CRCG of the University of Hong Kong .

REFERENCES

1. G. Y. Chen. The Mechanism Study of Biomass Pyrolysis. Ph. D. Thesis, Zhejiang Univesity, China, 1998.
2. PELB (Planning, Environment and Lands Bureau). A Proposal to Introduce LPG Taxis (a consultancy paper). Hong Kong Government, 1998.
3. C. L. Peterson, M. Feldman and R. Korus et al. Batch Type Transesterification Process for Winter Rape Oil. Applied Engineering in Agriculture, Vol. 7(6), 1991.
4. J. Steehan, V. Camobreco and J. Duffield et al. Life Cycle Inventory of Biodiesel and Petroleum Diesel for Use in an Urban Bus. Final Report, NREL/SR-580-24089 UC Category 1503, May, 1998.
5. C. L. Peterson, D. L. Reece and B. J. Hammond. Production and Testing of Ethyl and Methyl Esters. National Biodiesel Report, January~December, 1994.
6. J. Tickell and K. Tickell. From the Fryer to the Fuel Tank. GreenTeach Publishing, USA, 1998.
7. J. Fischer, and J. Conneman. Biodiesel in Europe 1998. International Liquid Biofuels Congress, Curitiba-Parana-Brazil, July 19-22, 1998.

THE EFFECTS OF CO₂ CONCENTRATION ON LIMESTONE DESULFURIZATION DURING O₂/CO₂ COMBUSTION*

Jianrong Qiu[#], Lizhi Zhang, Bo Feng, Jian Wu and Quanhai Wang

National Laboratory of Coal Combustion

Huazhong University of Science and Technology

Wuhan, Hubei 430074, P.R.China

Email: jrqi@public.wh.hb.cn, jianrong_qiu@263.net

Fax: 86-27-87545526

Keywords: CO₂, CaCO₃, desulfurization, O₂/CO₂ combustion, SO₂

ABSTRACT. Experimental studies on the decomposition and desulfurization of CaCO₃ have been performed at a TGA-FTIR analyzer and a combustion test furnace under O₂/CO₂ conditions and conventional combustion environment. The effects of CO₂ concentration on limestone decomposition, desulfurization product properties, limestone desulfurization efficiency were investigated. The desulfurization reaction mechanism was analyzed. Decomposition temperature of CaCO₃ under O₂/CO₂ environment is higher than that under air environment. The presented CO₂ constrains the decomposition of CaCO₃. At a given temperature, CaCO₃ decomposition ratio decreased as CO₂ increase. Moreover, the initial decomposition temperature increased. The reactive surface area of CaCO₃ decomposition samples in high CO₂ environment was larger than that in conventional conditions. Two-stage reaction mechanism of limestone desulfurization during pulverized coal combustion in O₂/CO₂ atmosphere was obtained. At low temperature, the reaction is: CaCO₃+SO₂→CaSO₄. CaCO₃ having lower reactivity than CaO reacts with SO₂ directly results in lower desulfurization efficiency compared with air atmosphere. At high temperature, the reaction is: CaCO₃→CaO+CO₂, CaO+SO₂→CaSO₄. Higher reactivity CaO under O₂/CO₂ than air environment reacts with SO₂ and formed CaSO₄ reduction reaction at high temperature is restrained under O₂/CO₂ resulted in higher desulfurization efficiency.

1. INTRODUCTION

CO₂ has gained the interest of the investigators all around the world, because it has been linked to global climatic warming. Coal combustion, one of the most main sources of CO₂, SO_x and NO_x emission, has been studied widely. Many clean coal technologies have been developed. O₂/CO₂ recycling combustion is a new coal combustion style developed in recent years [1-6]. This combustion style is expected to be one of promising systems on CO₂-recovery from pulverized coal firing power plants. In the system, pulverized coal is fired in a CO₂-based atmosphere. The combustion style use oxygen/recycled flue gas, CO₂ is used to institute the N₂ in combustion air and the amount of exhaust gas decreases because no nitrogen mixes into the combustion gas. Therefore, the boiler efficiency is improved due to the thermal loss reduction and the power consumption in the plant is also reduced. In addition, the CO₂ concentration in the flue gas is much higher (>95%) than that in conventional combustion style. Therefore, there is a high CO₂ recovery efficiency. Meanwhile, recent studies [2,3] on the industrial-scale combustion test facilities showed that NO_x emissions from O₂/CO₂ combustion system were reduced to about 25% when compared with conventional air-blown combustion. It is also found that there is higher desulfurization efficiency in this combustion system than that in conventional limestone desulfurization system. However, the mechanism of SO₂ removal in this combustion style is far from being understood. This paper focuses on the effects of CO₂ on limestone desulfurization in order to find the mechanisms of SO_x removal during O₂/CO₂ combustion.

2. EXPERIMENTAL

CaCO₃ Decomposition Experiment

CaCO₃ decomposition properties were measured continuously by TGA curves at different conditions. The experiments were carried out in a high-temperature thermobalance under standard conditions of 20k/min heating rate and 2 ml/min of gas flows(O₂+N₂ or O₂+CO₂) and about 20±0.001mg of sample were used. The heating

* This work is supported by the National Natural Science Foundation of China and Science Foundation of HUST

[#] The corresponding author

temperature ranged from room temperature to 850°C or 1000°C. The sample mass change and rate of weight loss were recorded continuously as a function temperature. The experimental conditions were displayed as following:

- Ej1: O₂(55%)+N₂(45%) 850°C(maintain 30min.);
 Ej2: O₂(20%)+N₂(80%) 1000°C(maintain 30min.);
 Ej4: O₂(20%)+CO₂(80%) 850°C(maintain 20min);
 Ej5: O₂(23%)+CO₂(77%) 1000°C(maintain 20min).

The initial temperature and corresponding temperature to maximum decomposition rate of CaCO₃ were obtained.

The pore diameters, pore areas and pore volumes of sample obtained under above different conditions were measured respectively in order to analysis the structure changes during CaCO₃ decomposition. The measurement was carried out with ASAP2000 accelerated surface area and porosity system. The system is applicable to measuring accelerated surface area, pore size, pore distribution and absorption. Measuring range of pore size is 5000A~17A. The isothermal absorption method was used in this experiment. Pure He was selected as the loaded gas and pure N₂ was selected as the absorption medium (analysis gas). The absorption temperature is 77K. The BET equation and BJH models were used to analysis the isotherm plot.

Limestone Desulfurization Experiment under O₂/CO₂ Condition

SO₂ removing by CaCO₃ was performed at a little combustion test furnace [6]. The goal of this experiment is to detect the effect of CO₂ on desulfurization efficiency and measure the final product composition. Experimental furnace includes horizontal tube furnace, thermocouple, and temperature controller and gas transportation unit. About 2g samples were placed at the middle of furnace. Samples were heated at 30K/minute progressively from room temperature to 900°C under air and O₂/CO₂ conditions respectively. As temperature approached to 900°C, SO₂ was injected into furnace and the temperature were maintained invariable for 30minutue to insure complete reaction. Then switch off the temperature controller, but keep invariable furnace atmosphere and SO₂ flow till samples were quenched. React products compositions and contents at each conditions were determined by D/MAX III B X-ray powder diffraction analyzer. The diffraction condition such as Cu target, Ni ray filter, 30 mA tube current and 30 kV tube voltage were used.

Limestone Desulfurization under O₂/CO₂ Condition during Coal Combustion

A coal named Heshan was selected. Coal analysis data is shown in Table 1. Ash chemical composition analysis is shown in Table 2.

Table 1. Coal Analysis

Proximate Analysis (%)				Ultimate Analysis (%)				
Moisture	Volatile	Ash	FC	C	H	O	N	S
3.02	15.03	51.41	30.53	33.45	1.97	4.72	0.64	4.79

Table 2. Coal Ash Analysis

SiO ₂	Al ₂ O ₃	Fe ₂ O ₃	CaO	MgO	K ₂ O	Na ₂ O	TiO ₂
54.46	28.30	4.50	1.88	1.21	2.34	1.14	1.80

Combustion experiment was carried out at the aforementioned furnace. Furnace was heated up to experimental temperature and kept invariable value, then injected into Air or O₂+CO₂, next, the mixture of coal sample and limestone was feed to the middle of furnace. Measter 2000 flue gas analyzer was used to measure the concentration of SO₂ and NO_x. Different temperature, CO₂, Ca/S were used. In addition, TGA-FTIR was used to detect SO₂ release process at Air and CO₂ environment in order to find the optimum temperature during limestone desulfurization at different atmosphere.

3. RESULTS AND DISCUSSION

Effects of CO₂ on Limestone Decomposition

Table 3 shows the results from CaCO₃ decomposition experiment.

Table 3. CaCO₃ Decomposition in Different Conditions

Conditions sample	Total weight loss		DTG		DTA	T _i
	(%)	(mg/min.)	(dw/dt) _{max} (°C)	(mg/min.)	T _{max} dw/dt (°C)	
Ej1	1	46.40	1.880	841	0.913	756
Ej2	2	45.67	1.930	862	0.816	758
Ej4	4	45.69	2.070	867	1.583	820
Ej5	5	45.62	2.130	870	1.234	784

It can be seen that the total sample weight losses are similar under different atmosphere. However, the initial temperature and corresponding temperature to maximum decomposition rate of CaCO₃ is increasing with increase of CO₂ concentration. Meanwhile, the decomposition temperature of CaCO₃ is higher in high CO₂ concentration than that in O₂ atmosphere or low CO₂ atmosphere. It means that the presented CO₂ constrains the decomposition of CaCO₃. The decomposition temperature of CaCO₃ is higher under high CO₂ environment than under air condition.

Figure 1 A) to D) show the pore structures and specific surface area of different CaCO₃ decomposition products

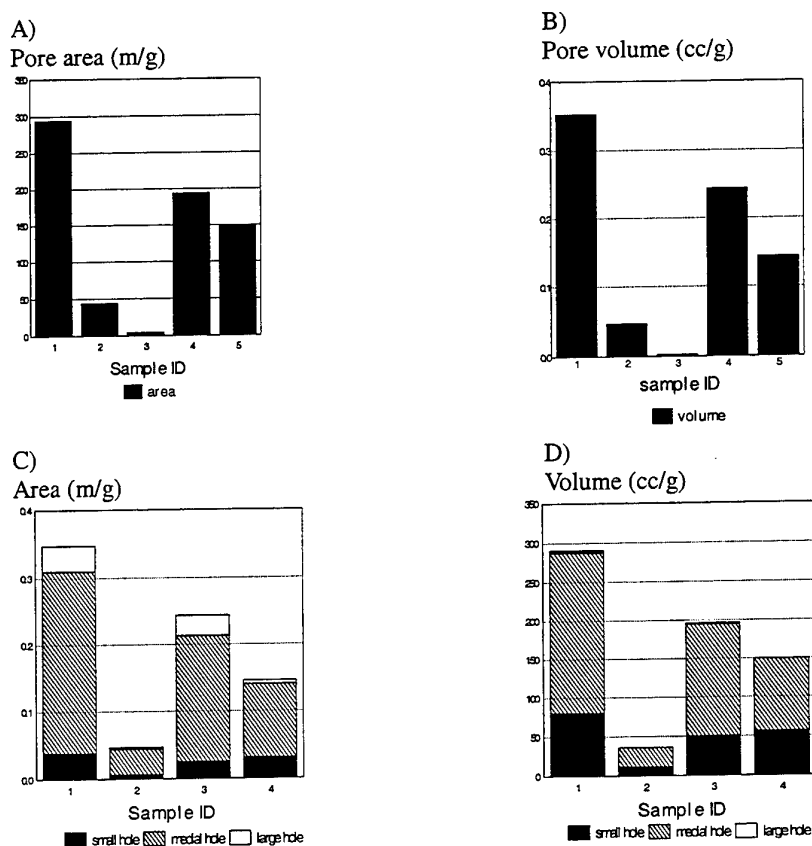


Fig. 1. Pore structure and specific of CaCO₃ decomposition products under different conditions

under different conditions. Sample 3 is the parent CaCO₃. It indicates from Figure 1 A) and B) that the pore

specific surface area of parent CaCO_3 is much smaller than any other samples, this is because CaO with loosed pore formed during CaCO_3 decomposition, therefore, pore structures of other samples are improved. However, there is a great difference between sample1 and sample 2, this is the result of the sintering of CaO under sample2 condition at high temperature, because that the sample1 was obtained at the final temperature of 850°C and sample2 was obtained at the final temperature of 1000°C , CaCO_3 decomposition was completed at about 820°C at N_2+O_2 atmosphere. The sintering of decomposed CaO decreased the specific surface area and pore volume. For sample 4 and sample5, CaO with multi-pore structure decreased as CO_2 increasing, hence, the specific surface and pore volumes of sample 5 and sample4 are smaller than that of sample1. It means that presented CO_2 constrain the decomposition of CaCO_3 . Meanwhile, compared sample 5 with sample 2, the sintering of CaO at 1000°C in high CO_2 concentration was not occur. It suggested that CaCO_3 decomposition delayed and the sintering of CaO was prevented at normal desulfurization temperature under CO_2 atmosphere.

Desulfurization Product Properties Under High CO_2 Conditions

Table 4 shows the CaCO_3 decomposition product composition measured by XRD method during limestone desulfurization at 900°C . Reactants were CaCO_3 and SO_2 . $\text{Ca/S}=2$.

Table 4. Main Products During Limestone Desulfurization Under Different Conditions

Combustion atmosphere	Main products				
		CaSO_4	CaCO_3	CaO	$\text{Ca}(\text{OH})_2$
	Air	20-40%	10%	40-50%	<10%
50% O_2 +50% CO_2		30-40%	50-70%		
10% O_2 +90% CO_2		30-40%	50-60%		

It can be seen that CaCO_3 reacted with SO_2 to form CaSO_4 at different conditions. At air environment, CaO was found as the presented products. It suggested that CaCO_3 decomposed at high temperature at air environment. At O_2/CO_2 environment, CaSO_4 increased compared with that at air environment, it means that the efficiency of SO_2 removing increased. Meanwhile, CaO was not found, it means that presented CO_2 constrain the decomposition of CaCO_3 . The reaction may be presented at middle temperature (around 900°C) as following style: $\text{CaCO}_3+\text{SO}_2\rightarrow\text{CaSO}_4+\text{CO}_2$. It is consistent with TGA experimental results.

Effect of CO_2 Concentration on Limestone Desulfurization Efficiency during Coal Combustion

Figure 2 plots SO_2 release concentration change after limestone desulfurization with time under air and 79% CO_2 +21% O_2 environments during coal combustion. In this experiment, $\text{Ca/S}=1.5$.

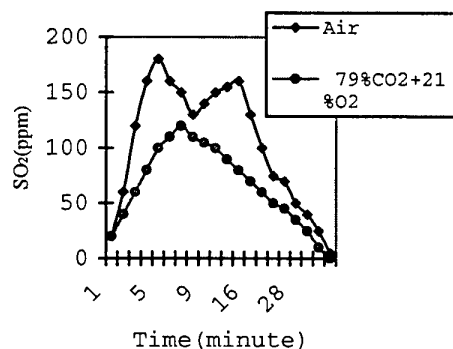


Fig.2. SO_2 release process at temperature of 960°C during limestone desulfurization

Figure 2 implies that SO_2 decrease more markedly when Nitrogen was substituted by CO_2 , which suggests that high CO_2 concentration increase limestone desulfurization efficiency. This can be explained by direct reaction of CaCO_3 with SO_2 partly under high CO_2 condition and presented CO_2 mitigates the sintering of CaO thereby improve the activity of CaO reacting with SO_2 .

Effect of Temperature on Desulfurization under High CO_2 Conditions

Figure 3 plots the change of SO_2 release concentration with time under 79% CO_2 +21% O_2 and air environment at

different temperature. Ca/S=3. When temperature increases from 900°C to 960°C, higher desulfurization efficiency is observed under high CO₂ environment. However, desulfurization efficiency has an inverse change tendency under air environment, which decreases with temperature increase.

This is the result that the sintering of CaO and formed CaSO₄ reduction at high temperature are restrained under high CO₂ condition compared with air environment [7], therefore, there is a higher desulfurization efficiency at relative high temperature under CO₂ condition.

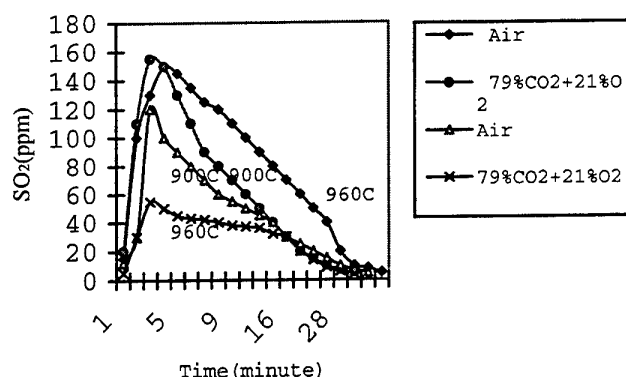


Fig.3. The effect of temperature on desulfurization efficiency under different environments.

Figure 3 also shows that at low temperature of 900°C, desulfurization efficiency is higher under air environment than CO₂+O₂ environment. It indicates that the desulfurization reactions under air environment occur as following: $\text{CaCO}_3 \rightarrow \text{CaO} + \text{CO}_2$, $\text{CaO} + \text{SO}_2 \rightarrow \text{CaSO}_4$. However, under CO₂+O₂ environment, the reactions may occur as following: $\text{CaCO}_3 + \text{SO}_2 \rightarrow \text{CaSO}_4$ at low temperature (<900°C at this experiment condition). CaO has larger specific surface area than CaCO₃ thereby has higher reactivity consequently its desulfurization efficiency is higher.

Meanwhile, under CO₂+O₂ environment, SO₂ release decrease markedly which means desulfurization efficiency improves remarkably when the temperature increase from 900°C to 960°C. Moreover, desulfurization efficiency is much higher comparing with air environment at the temperature of 960°C. It indicates that the limestone decomposition reaction as the first reaction, then CaO reacts with SO₂ during desulfurization at high temperature. The high efficiency is resulted by high reactivity CaO reaction with SO₂ and the CaSO₄ reduction decrease under CO₂ environment.

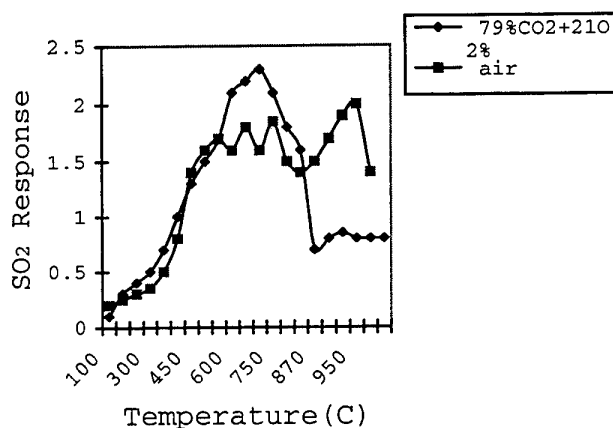


Fig.4. SO₂ Response change with temperature under air and O₂/CO₂ atmosphere

Limestone Desulfurization Process under High CO₂ Concentration

Figure 4 shows the SO₂ concentration response signal obtained from TGA-FTIR experiment change with temperature under air and O₂/CO₂ environment. Coal was heated continuously. The heating rate is 20°C/minute. As shown in the figure 4, at low temperature less than 880°C, SO₂ response is higher under O₂/CO₂ than air atmosphere which means former has lower desulfurization efficiency. However, when the temperature more than 880°C, the case is inverse. This result is consistent with the experiment result shown in Fig. 3. The difference of inflexion temperature is caused by different experiment conditions such as heating rate, sample weight etc. The change under different temperature certifies the two-stage reaction mechanism of limestone desulfurization during pulverized coal combustion in O₂/CO₂ atmosphere.

4. CONCLUSIONS

1. Decomposition temperature of CaCO₃ in O₂/CO₂ environment is higher than that in air environment. Presented CO₂ delayed the decomposition of CaCO₃ and mitigated the sintering of CaO at high temperature.
2. The reactive surface area of CaCO₃ decomposition samples in high CO₂ environment was larger than that in conventional conditions.
3. The reactive products were CaCO₃, CaSO₄, and Ca (OH)₂ in high CO₂ environment during limestone desulfurization at low temperature.
4. This investigation shows the two-stage reaction mechanism of limestone desulfurization during pulverized coal combustion in O₂/CO₂ atmosphere. At low temperature, the reaction is: CaCO₃+SO₂→CaSO₄. At high temperature, the reaction is: CaCO₃→CaO+CO₂, CaO+SO₂→CaSO₄.
5. The reaction mechanism of limestone desulfurization under air environment is: CaCO₃→CaO+CO₂, CaO+SO₂→CaSO₄. At low temperature, there is higher desulfurization efficiency under air environment compared with O₂/CO₂ environment. It is caused by the direct reaction of CaCO₃ having lower reactivity than CaO with SO₂ under O₂/CO₂ environment.
6. At relative high temperature, desulfurization efficiency is much higher under O₂/CO₂ environment compared with air environment. It is resulted by higher reactivity CaO under O₂/CO₂ than air environment reacts with SO₂ and formed CaSO₄ reduction at high temperature is restrained under high CO₂ condition compared with air environment.

REFERENCES

1. A.M.Wolsky, A new method of CO₂ recovery. 79th Annual Meeting of the Air Pollution Control Association, Minneapolis, Minnesota, June 22-27,1986.
2. N.Kimura, K.Omata, T.Kiga, S.Takano and S.Shikisima.The characteristics of pulverized coal combustion in O₂/CO₂ mixtures for CO₂ recovery. Energy Convers.Mgmt Vol.36, No.6, P.805-808, 1995.
3. T.Yamada, T.Kiga, M.Okawa, K.Omata, Characteristics of Pulverized-Coal Combustion in CO₂-Recovery Power Plant Applied O₂/CO₂ Combustion, ICOPE-97, Vol.2, 285-290. 1997
4. S.Y.Nakayama, T.Kiga and S.Miyamae, Pulverized Coal Combustion in O₂/CO₂ mixtures on a Power Plant for CO₂ Recovery. First International Conference on Carbon Dioxide Removal, March 1992, Amsterdam, Netherlands.
5. Koyata, K.T., Tanaka, T.Kiga and K.Suzuki, Pulverized Coal Combustion in O₂/CO₂ atmosphere. 8th International Pittsburgh Coal Conference. (1991)
6. Jianrong Qiu, Ph.D. Thesis, Huazhong University of Science and Technology. (1993 .)
7. Jianrong Qiu, Bo Feng. SO_x Reduction Mechanism during O₂/CO₂ Recycling Combustion. Proceeding of the 2nd Korea-China Joint Workshop on Coal & Clean Energy Utilization Technology, 71-82 (1998)

PYROLYSIS CHARACTERISTICS OF STRAW ON A PILOT-SCALE GASIFICATOR

Jinsong Zhou Zhongyang Luo Mengxiang Fan
Xiang Gao Chunjiang Yu Xinsheng Guo Kefa Cen
Departmental of Energy Engineering
Zhejiang University
Email: ccct@sun.zju.edu.cn; Fax: +86-571-7951616

Weihong Luo Dun Yang Xuefei Xu
Zhejiang Province Office for Rural Energy
Hangzhou, 310027, P. R. China

Keywords: biomass, gasification, moving bed

ABSTRACT. A novel pyrolysis technology of biomass with indirectly heating is carried out to produce medium energy gas. A pilot-scale gasificator has been build in the Institute for Thermal Power Engineering of Zhejiang University to investigate the pyrolysis characteristics of straw. The prospect of technologies to convert widely available straw into high quality gas fuel is very attractive. To utilize straw with high efficiency, medium energy gas and semi-coke are two main products in the pilot-scale gasificator. This gasificator can produce medium energy gas mainly through pyrolysis process. A series of related fundamental experiments have been made. The behaviors of straw pyrolysis, specially the effects of temperature had been research in detail. Through above experimental research, lots of valuable data had been collected. Those data are extremely useful to design the gasification part of biomass utilization project. The heating value of medium energy gas is 2800~3500 Kcal/Nm³. This gasificator can convert a wide range of biomass into medium-energy gas. In addition, a demonstration gasification system will be designed based on above experiments. The feedstock of this system is rice straw, which is the most common biomass residue in rural areas of China.

1. INTRODUCTION

With traditional fossil fuels (coal, oil and natural gas) becoming less and environment pollution caused by its wide use, the potential offered by biomass for solving some of the world's energy problem is widely recognized. In China, biomass fuel from agricultural residue such as rice husk, rice straw, wood and sugar cane et al are very abundant. According to the published figures, biomass accounts for about 16.8% of total energy and 70% of the peasant's living energy consumed in 1990. Direct using biomass for combustion in vast rural areas is convenient, but this causes low efficiency and emission problem. Therefore, it is imperative to find a new way to utilize biomass. Moreover, most of rural areas and small towns are facing shortage of gas and electricity when their economics are accelerating. Biomass pyrolysis technology is very optimal route to solve these problems. Easy utilization, low capital, flexible operation, good fuel adaptability and nearly zero emission of biomass pyrolysis technology is widely regarded as its advantage. Although some researcher proposed valuable introduction to biomass pyrolysis toward gas, but it is far from satisfactory because some of their opinions are contradictorily. Therefore, it is urgent to carry out a series of novel experimental studies for biomass pyrolysis. Regarding the real situation of Chinese rural areas, a novel scheme of biomass pyrolysis to generate medium heating value gas by heated indirectly is proposed, which is characterized by a biomass pyrolysis reactor coupling to a combustor burning recycled semi-coke. As a part of this biomass pyrolysis process, a pilot-scale gasificator had been build in Zhejiang University. A series of experiments are carried out in this gasificator with raw rice husk and rice straw as pyrolysis fuels. This paper reports experimental results and its analytic conclusions to pyrolysis process.

2. EXPERIMENTAL FUELS AND FACILITY

2.1 Experimental Fuels

Three kinds of fuels (Zhejiang late rice straw, rice husk and sawdust) were used in experiments because of their abundance in fuel feeding and easy pretreatment. The data are shown in Table 1. Compared to coal, their volatile content is very high, but ash content is moderate. Table 2 shows physical parameters of biomass fuels. Thermal

conductivity coefficient is very small with value only about $0.04\text{W}/(\text{m}\cdot^{\circ}\text{C})$, apparent density is small, only $1/6\sim 1/8$ of coal, and energy density is also small. All these show that biomass is not available to transport, it should be utilized locally in medium/small scale plant. In views of this point, pyrolysis is sure to be a good route

Table 1. The Analytic Data of Biomass Fuels

Biomass fuels	ultimate analysis					approximate analysis				heating value (kJ/kg)
	C_{ad}	H_{ad}	N_{ad}	S_{ad}	O_{ad}	M_{ad}	A_{ad}	V_{ad}	FC_{ad}	
rice straw	33.96	5.01	1.07	0.10	34.67	9.96	15.23	69.11	5.70	15175.2
rice husk	39.69	4.92	0.42	0.14	31.29	10.3	13.24	60.38	15.99	14784.7

Table 2. Physical Parameter of Three Kinds of Biomass Fuels

Items	Diameter (mm)	Geometry size (mm)	pack density (kg/m^3)	Heat transfer coefficient[$\text{W}/(\text{m}\cdot^{\circ}\text{C})$]	Energy density(Kj/m^3)
rice straw	0~4	$\Phi 2.5\times 10$	59.3	0.035	900
rice husk	0~3	$9\times 3\times 0.2$	122.9	0.036	1870

2.2 Experimental Facility and Procedure

The experimental research has been done using a electrical heating moving-bed reactor with inner length of 200mm, width of 110mm and height of 1500mm. The experimental system was composed of four parts, i.e. indirectly electrical heated furnace, pyrolysis reactor, on-line sample collected analyzer and gas condenser & collector. Fig. 1 shows a scheme of biomass gasification test system. In addition, Fig. 2 shows the pyrolysis reactor scheme.

After the reactor is heated up to a certain temperature, biomass like straw or rice husk are feed at intervals from the top of reactor while the feed rate is controlled by the pressure of gas outlet and gas flow rate. The temperature outside of reactor was maintained in the certain value like 700°C . Raw gas from the reactor was cooled below ambient temperature in the condenser with ice bath while a greater part of liquid produce including tar and water was separated from raw gas. The pressure inside reactor was slightly below zero to prevent from air leakage. The flow rate of fuel gas, which was taken out of the condenser by a vacuum pump, was adjusted by gas recycle. On the other hand, gas, liquid and semi-coke were sampled respectively from the bottom of the reactor, the bottom of the condenser and the outlet of gas storage. A more detailed description of the facility and experimental procedure is given in [1].

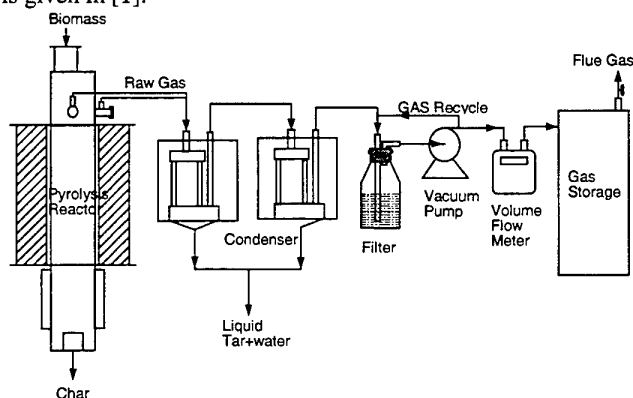


Fig. 1. The schematic of biomass gasification test system

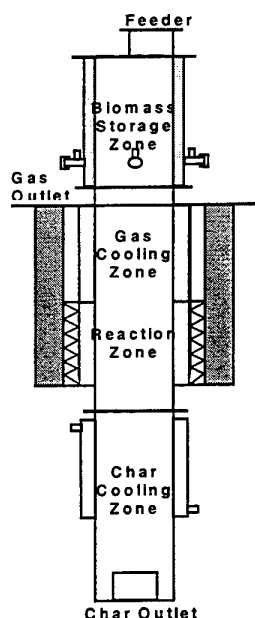


Fig. 2. The scheme of biomass pyrolysis reactor

3. EXPERIMENTAL RESULTS AND DISCUSSION

Although the biomass gasification process especially the pyrolysis process has been investigated widely [2-5], the experimental pyrolysis reactor has some new advantages. Tar content is decreased into a very low level because a biomass storage segment and gas-cooling segment are added on the top of reactor. The raw gas can be cooled below 100 °C after two segments while a considerable part of tar can be condensed or captured by cool biomass and decomposed thermally in the high temperature reactor. In addition, gas production rate will increase with liquid production rate decreasing. Thus, this process can overcome high tar yield in the normal upper-draft gasification and high outlet gas temperature in the normal downdraft gasification. In addition, high gas production rate will be expected as in the normal downdraft gasification. On the other hand, the gas production rate in this process is lower than that in the air gasification. However, the gas produced from biomass is isolated from air or oxygen so that the high heating value of gas will be expected when the biomass pyrolysis process is used in the reactor. Finally, there are so little good results from straw gasification presented by other researchers because of agglomeration problem. In the present biomass pyrolysis system, the agglomeration problem has been overcome by lower reactor temperature.

There are many factors influencing biomass pyrolysis behavior. The physical factor is relevant to heat transfer, mass transfer and fuel properties. Compared to physical factor, the chemical factor is more important, which involves a series of complicate prime and secondary thermolysis reaction. Gas, liquid and solid (gas, tar, water and semi-coke) are produced accompanying biomass pyrolysis, but its proportion is changeable due to change of reaction parameters including pyrolysis temperature, pressure, gas/solid residence time and biomass particle size, shape etc., however, temperature is a crucial parameter for biomass pyrolysis toward gas. Therefore, here only temperature is concerned in detail.

3.1 The Effect of Temperature on Gas, Semi-Coke and Liquid (Tar and Water) Yield

Gas, liquid and solid are produced during biomass pyrolysis process. In our experimental conditions, gas and solid are referred to pyrolysis gas and semi-coke drained from reactor respectively. Liquid includes condensed water and tar composed of a layer of black viscous colloid sticking to the wall of tube, oil colloid dissolved in water and lightly black colloid separated by oil-water separator. Fig. 3 shows the effect of temperature on pyrolysis product yield using rice straw as feedstock under the temperature from 650°C to 850°C. It shows that the gas yield is 0.25-0.32 Nm³/kg, increasing with pyrolysis temperature. The liquid yield and the semi-coke

yield reduce while the pyrolysis temperature increases.

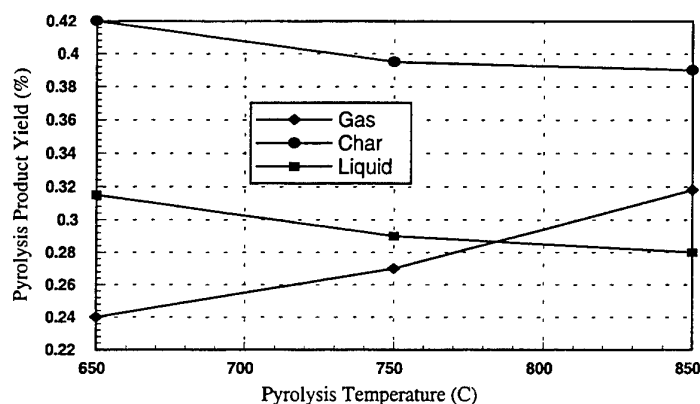


Fig.3. Pyrolysis product yield versus pyrolysis temperature

Compared with the results of small-scale experiments presented in [1], the trend is similar to that in the small-scale reactor. But the gas yield in the recent reactor is smaller than that in the small-scale reactor, which is in the range of 0.23-0.46 Nm^3/kg with temperature from 600°C to 900°C, under the same temperature. It can be explained that biomass resident time in the high temperature zone is not so enough that pyrolysis reaction is far from complete and a part of volatile still stay in the semi-coke. On the other hand, the semi-coke yield becomes larger than that in the small-scale reactor because a part of tar, which is condensed in the cooling zone, enters into the high temperature zone with cool biomass and then be decomposed thermally into coke. It raises the semi-coke yield as compared with the semi-coke yield in the small-scale reactor, which is from 0.37 to 0.32 Nm^3/kg .

3.2 The Effect of Pyrolysis Temperature on Heating Value of Gas

Fig. 4 shows heating value of sawdust pyrolysis gas versus temperature. From Fig. 4, we know that heating value of sawdust gas is increasingly linear with temperature increasing from 600°C to 800°C, but its slope is small. This indicates that it must be considered carefully to improve gas heating value by increasing temperature higher than 600°C. The above results are much more different from literature [2], where heating value of pyrolysis gas decreases with temperature increase from 700°C to 900°C due to decomposition of high heating value of CH_4 and other carbonhydrogens. In fact, 700°C is a turning point of secondary thermal decomposition. When temperature higher than 700°C, raw pyrolysis gas decomposes and produces H_2 and low quantities of CH_4 , C_2H_4 etc. When temperature higher than 800°C, CO and H_2 increase continuously and offset the negative effect caused by decomposition of some carbonhydrogen on gas heating value. Certainly, gas heating value will likely be decreasing when temperature is higher than 900°C due to strengthening decomposition of light carbonhydrogen.

3.3 The Effect of Temperature on Gas Composition

Fig. 5 shows sawdust gas composition versus temperature. In sum, with the temperature increase, H_2 always increases, CO decreases, but C_nH_m (containing C_2 or more) and CH_4 change at non mono-trend. C_nH_m and CH_4 increase with temperature increasing from 600°C to 800°C, then begin to decrease. This is different from literature [3,5]. In our experimental conditions, CO always increases. We do not investigate further high temperature (>900°C), however the literature [2] reported 900°C is a turning point of CO .

3.4 Pyrolysis Chareacteristics of Different Feedstock

The pyrolysis results of rice straw and rice husk are shown in Table 3. There are two and three tests respectively with rice husk and rice straw in the same condition of temperature, pressure and feed rate. The pyrolysis temperature is 750°C. During the straw pyrolysis test, N_2 content of sample 1, sample 4 and sample 6 are much higher than that of the others. It is suspected that air leaks into gas during sampling because of higher O_2 content in the same sample.

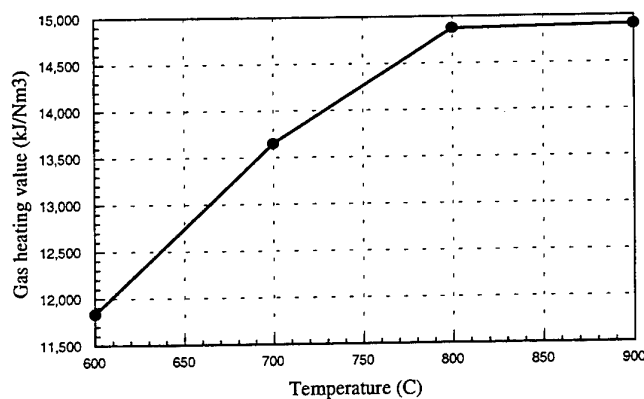


Fig. 4. Gas heating value versus temperature

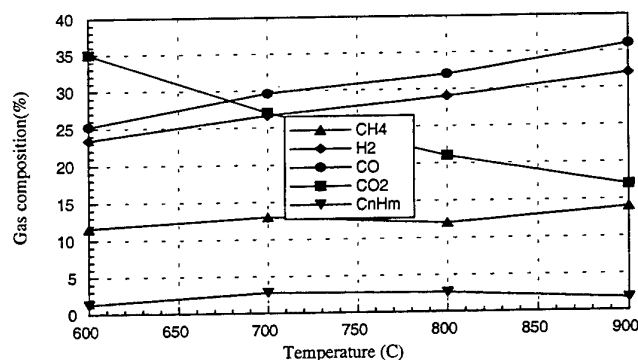


Fig. 5. Sawdust gas composition versus pyrolysis temperature

The composition and heating value of straw gas is very different from that of rice husk gas. The CO and CH₄ content in rice husk gas are much higher than that in straw gas. The heating value of straw gas is from 10920 to 11760 kJ/Nm³ and is smaller than that of rice husk gas which is from 16000 to 18000 kJ/Nm³.

Table 3. Gas Composition and Heating Value after Pyrolysis of Different Feedstock

	Rice Husk		Rice Straw					Test E
	Test A	Test B	Test C	Test D				
	Sample 1	Sample 2	Sample 3	Sample 4	Sample 5	Sample 6	Sample 7	
Composition								
H ₂	13.6	17.82	15.22	16.46	15.72	15.99	15.34	13.93
O ₂	1.92	1.40	6.49	1.07	1.83	3.31	1.54	4.86
N ₂	4.83	2.79	23.02	3.66	5.90	14.53	3.54	15.95
CO	33.50	34.27	17.74	27.24	26.20	21.12	28.95	22.96
CH ₄	20.67	21.48	10.35	13.24	12.84	11.16	13.79	13.26
CO ₂	20.78	15.08	24.97	35.14	34.90	27.87	34.12	25.67
C ₂ H ₄	3.46	5.64	0.79	0.97	0.65	0.85	0.78	1.29
C ₂ H ₆	1.24	1.52	1.42	1.89	1.96	1.29	1.94	2.09
LHV(kJ/Nm ³)	15980	18320	8978	11879	11260	9739	11979	11277

3.5 Heat Balance of Pyrolysis Process in the Pilot-Scale Reactor

It is known that the most of reactions in the biomass pyrolysis process are endothermic reactions. Although some

researchers paid more attention to the heat balance of pyrolysis reaction, the heat absorption during biomass pyrolysis process is far from sure. The proportion of heat absorption to the heating value of biomass is a very important parameter in the design of large-scale biomass pyrolyzer/gasifier. Table 4 shows the heat balance during pyrolysis reaction in the pilot-scale reactor using rice straw as feedstock. Test 1 and test 2 are under the same pyrolysis temperature which is 750°C.

Table 4. Heat Balance During Straw Pyrolysis Reaction in the Pilot-scale Reactor

	Biomass Feed Rate	Output of Heat	Absorption of Heat		heat absorption per unit weight of straw
		Heat supported by electricity	Heat elimination*	Heat absorbed by pyrolysis process	
Test 1	3.24 kg/h	6.32 kW	5.73 kW	0.59 kW	655 kJ/kg straw
Test 2	2.15 kg/h	6.05 kW	5.63 kW	0.42 kW	703 kJ/kg straw

Note: * The heat elimination of the total reactor can be attained by recording the electric power on the condition of empty reactor.

Therefore, the average proportion of heat absorption to the heating value of straw can be calculated heat absorption per unit weight of straw in Table 4, which is about 4.5 percent under the testing condition.

4. BIOMASS GASIFICATION SYSTEM SCHEME

A biomass gasification demonstration project will be based on research and development of biomass pyrolysis at Zhejiang University and Zhejiang Provincial Office for Rural Energy. Successful application of this technology will enable biomass resources to be used in the production of fuel gas, heat and fertilizer in the Chinese countryside. Take account of the scale of a typical village in East China or South China, the project can produce 200Nm³ medium energy gas per day, which can meet the need of 100 households. The feedstock of this system is rice straw, which is the most common biomass residue in rural areas of China.

Figure 6 is a simplified biomass gasification plant schematic.

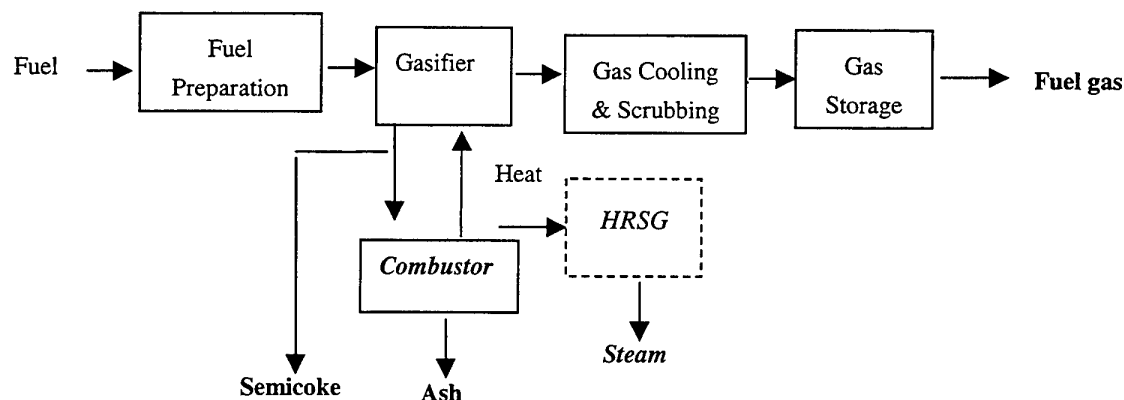


Fig. 6. A simplified biomass gasification system schematic

The two bed process takes advantage of the best features of both gasification and combustion by dividing the process between two units: the biomass pyrolyzer/gasifier (carbonizer), and the residual coke combustor. In the system, biomass are fed into a moving bed pyrolyzer/gasifier, where biomass pyrolysis occur at about 750 ~ 800°C, producing a crude gas with medium calorific value and semi-coke. Heat required for the pyrolysis reactions is supplied by the combustor.

The medium calorific value gases from the carbonizer are cooled and cleaned of dust by a condenser and a

scrubber. It will make tars content lower than the national standard. Once cleaned, this stream can be utilized as fuel gas. Simultaneously, the residual coke from the carbonizer is fed and burned in the combustor. This process product the hot flue gas, which heats the carbonizer by indirect heat transfer. A HRSG (Heat Recovery Steam Generator) cools the exhaust gases, eventually producing more steam for district heating.

The gasification process provides suitable fuel gas for community residents. Fine bottom ash and some of semi-coke can be used as a kind of fertilizer. It can overcome the shortcoming in the current process due to the large semi-coke yield.

5. CONCLUSION

The advantage of the updraft gasifier was adopted and utilized to the moving bed Pyrolysis reactor. The tar in the fuel gases can be condensed on the virgin biomass materials and enter into the pyrolysis zone with them, where the tar can be cracked into gases or polymerized into coke. So the tar content in gases reduced and semi-coke product and gases increased.

Pyrolysis temperature has a great influence on pyrolysis product yield. It is a good way for biomass pyrolysis to increases pyrolysis temperature when gas production is preferred. This pilot-scale gasificator can convert a wide range of biomass into medium-energy gas. The heating value of medium energy gas using rice straw as feedstock is 2800~3500 Kcal/Nm³. A novel pyrolysis technology of biomass with indirectly heating is carried out to produce medium energy gas. A pilot-scale gasificator has been built in the Institute for Thermal Power Engineering of Zhejiang University to investigate the pyrolysis characteristics of straw. The prospect of technologies to convert widely available straw into high quality gas fuel is very attractive. To utilize straw with high efficiency, medium energy gas and semi-coke are two main products in the pilot-scale gasificator. This gasificator can produce medium energy gas mainly through pyrolysis process. Based on the series of related fundamental experiments, a demonstration gasification system will be designed based on above experiments. The feedstock of this system is rice straw, which is the most common biomass residue in rural areas of China.

In comparison to coal, biomass has two decisive advantages: it is a renewable energy and it is a clean energy. So biomass is an important energy resource, both at present and from a future perspective. It is necessary to develop an effective and simple technique to convert biomass feedstock into medium-energy gas for civil use in rural areas. The project uses pyrolysis approach to product medium-energy gas. The gasification system is designed according to the principle of easy and economical operation. It has been proved to be feasible through extensive experimental research.

REFERENCES

1. X.S. Guo, Study of Reaction Properties on Biomass/Coal gasification and Combustion, *Master Dissertation in Zhejiang University* (1999).
2. Y. Wang, et al, *Solar Energy* v.49, pp. 153-158 (1992).
3. B.Y. Xu, et al, *Solar Energy* v.49, pp. 199-204 (1992).
4. L. Curas, et al, *Ind. Eng. Chem. Res.* V. 27, pp. 1775-1783(1988).
5. P. Liu, et al, "The Effect of reaction temperature on pyrolysis gas of two types of biomass fuels", *Session of Alternative fuels technology - Annual Meeting of Chinese Society of Engineering Thermophysics* (1997).

AERODYNAMIC SUPPRESSION OF COMBUSTION-DRIVEN PRESSURE OSCILLATIONS IN TECHNICAL PREMIXED COMBUSTORS

Dr.-Ing. Horst Büchner, Prof. Dr.-Ing. Henning Bockhorn

Engler-Bunte-Institut, Combustion Technology Division

Department of Chemical Engineering

Karlsruhe University

76128 Karlsruhe, Germany

fax: Germany +721661501

Dr.-Ing. Stefan Hoffmann

Division KWU WB TVF

Siemens Power Generation

45466 Mülheim a.d. Ruhr, Germany

Keywords: flame stability, flame/pressure oscillations, feedback mechanisms, control/suppression

ABSTRACT. In recent studies on feedback mechanisms leading to the formation and the sustainment of large amplitude pressure oscillations in industrial combustors (e.g. gasturbine combustors, industrial furnaces, etc.) by amplification of initially small-amplitude disturbances the interests are more and more focused on the periodical formation and combustion of coherent turbulent ring vortex structures, being an important characteristic of periodically modulated flows [1,2,3]. On one side, these structures are mainly responsible for the amplification of small-amplitude disturbances, while forming and combusting in-phase with the pressure oscillation in the combustion chamber, fulfilling Rayleigh's criterion. On the other side they make possible to control the amplitudes of combustion-driven pressure oscillations by aerodynamic means (secondary air injection), that can avoid the formation of reactive vortex structures and therefore, interrupt the feedback coupling between pressure oscillation, periodic flow field and periodic heat release. In the present paper experimental studies on the fluidodynamical conditions for the formation of coherent ring vortices are shown and furthermore, first test results of a new method for the suppression of large-amplitude pressure oscillations, driven by periodic ring vortex combustion, are presented, obtained from power plant gasturbine combustors.

1. INTRODUCTION

In highly-turbulent technical combustion systems like gasturbine combustors, industrial furnaces as well as in domestic applications (like gas- or oil-fired water heaters etc.) the formation of large-amplitude oscillations of the static pressure in the combustion chambers or downstream fluegas sections represents a considerable and serious problem for the manufacturers and operators. The complex interaction within a closed feedback loop between pressure oscillations, periodically modulated outflow of fuelgas/air mixture of the burner nozzle and the periodical, frequency-depending overall reaction and heat release characteristics of the flame leads at a proper timing of the processes to the formation of self-sustaining pressure oscillations. For the fully-developed instability the usually obtained high pressure amplitudes can damage the plant and cause flashback of the flame into the burner nozzle; furthermore, under unsteady operation conditions the emission characteristics (CO, NO_x, soot) are often considerably altered in comparison with the steady-state operation of the combustors. In order to avoid time consuming and therefore, cost-intensive trial and error means for the suppression or prevention of combustion-driven oscillations in technical combustors for all the reasons mentioned above, the physical understanding of the effective feedback mechanism causing the amplification of initially small-amplitude disturbances is an inevitable requirement for the solution of periodic flame instability problems.

In the present paper a feedback mechanism consisting of the generation and in-phase combustion of large-scale turbulent ring vortex structures, leading to a periodic, properly timed heat release rate of the flame to sustain the pressure oscillations under fulfillment of Rayleigh's phase criterion, is discussed, which could be identified doubtlessly to be responsible for the driving of pressure oscillations in various technical combustors in the thermal load range between 50 kW and 400 MW.

2. FLOW CONDITIONS FOR THE PERIODIC FORMATION OF TURBULENT VORTEX RINGS

In the figure below the feedback loop for the formation and the sustainment of flame-/pressure oscillations in a technical premixed combustor is shown.

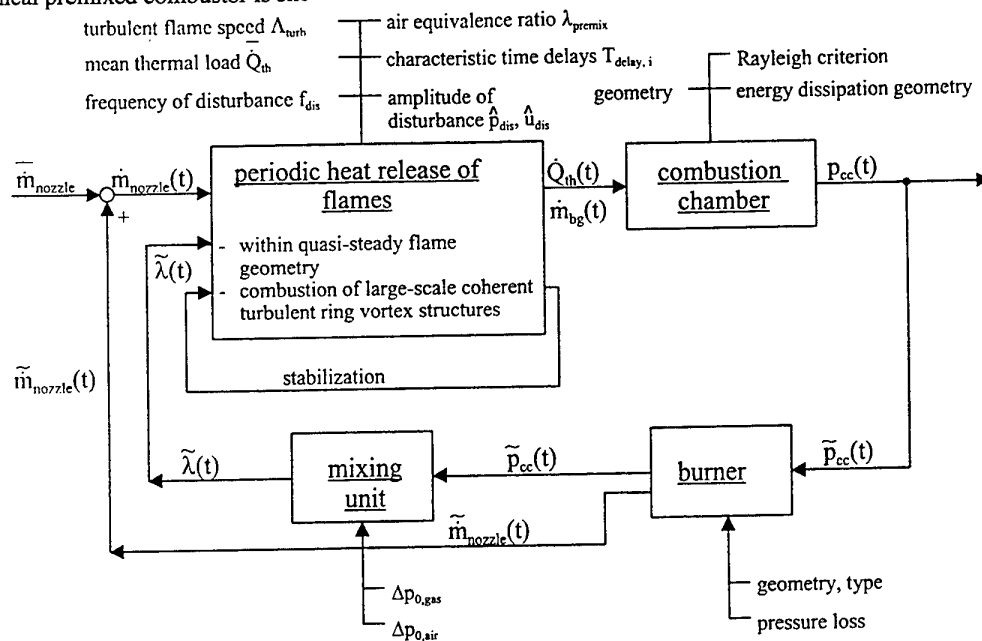


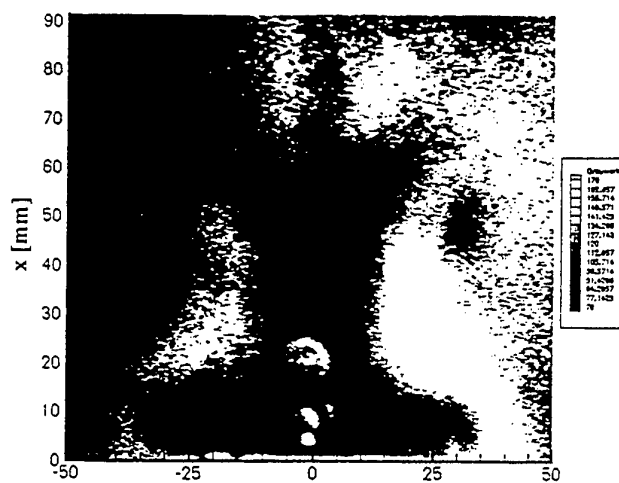
Fig. 1. Feedback loop for premixed combustors

If, for a better understanding, the influence of the static pressure oscillations in the combustion chamber on the fuelgas/air mixture formation can be neglected in a first approach, the remaining loop consists of the components burner - flame - combustion chamber. The periodic-unsteady static pressure in the chamber modulates the fuelgas/air mixture flow out of the burner nozzle periodically; for fully-developed oscillations amplitudes of the mixture massflow fluctuation at the nozzle exit can reach values up to 50 % of the mean massflow rate. After a characteristic time delay for the transport of the mixture elements from the nozzle exit to the main reaction zone of the turbulent premixed flame, for the heating-up of the mixture to ignition temperature and for the reaction kinetics the flame responds to the periodic flow disturbances with periodical changes of the overall heat release rate, connected with the formation of a periodical, unsteady production rate of exhaust gases, which both cause a rise of the static pressure in the combustion chamber again.

In experimental studies the frequency-depending reaction characteristics of forced-pulsated turbulent premixed axial jetflames and swirl flames were investigated [2]. Therefore, the mixture massflow rate of the unburnt fuelgas/air mixture was modulated sinusoidally in time with adjustable frequency and amplitude of pulsation using a pulsating unit [2] and the flame's response was measured simultaneously. It could be shown, that the periodic overall heat release can be realized by the flame in two different ways: By a periodic change of the reaction surface within quasi-steady flame geometry (flame is changing periodically its length) or by the periodic combustion of large-scale turbulent vortex rings, formed by the rolling-up of the free shear layer of the nozzle outflow.

To understand better the fluiddynamic conditions for the formation of these structures, in further isothermal studies the massflow rate out of different nozzles (generating turbulent axial and swirled jets) was pulsated in a well-defined way as described above under variation of the following parameters: mean massflow rate \bar{m}_{nozzle} , frequency of pulsation f_{puls} and amplitude of massflow pulsation \hat{m}_{nozzle} . The vortex formation and downstream motion in the traced flow was recorded using a laser-light sheet technique and a phase-locked CCD-camera, triggered with the rotation of the pulsating unit. By this way the formation process of the ring vortices for a given set of parameters could be studied in detail, because the structures could be "frozen" at different times t_v within the pulsating period t_p . The following figures show the development of a turbulent ring vortex from a pulsated, swirled jet for different times ($t_v/t_p = 0.2, 0.6, 1.0$).

$$t_v/t_p = 0.2$$



$$t_v/t_p = 0.6$$



$$t_v/t_p = 1.0$$

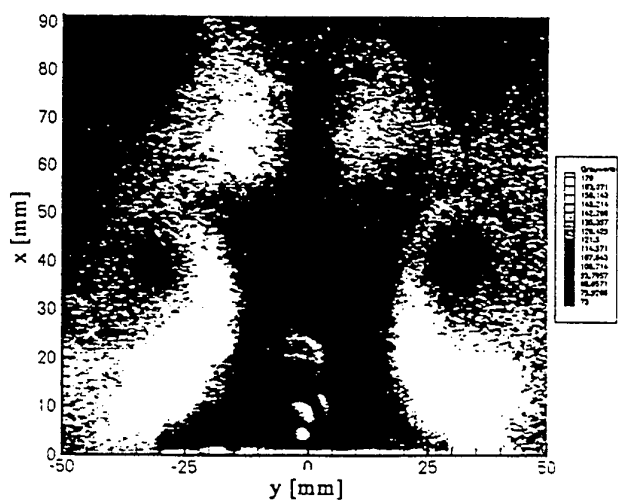


Fig. 2. Laser light-sheet measurements of ring vortex formation in pulsated isothermal flows

With the parameters, varied during the experiments, two dimensionless numbers can be formed to describe the fluidynamical conditions for the ring vortex formation: The Strouhalnumber Str

$$Str = \frac{d_{equiv} * f_{puls}}{u_{ax, vol}} \quad (1)$$

and the pulsation level Pu as the relative amplitude of pulsation

$$Pu = \frac{\hat{m}_{rms, nozzle}}{m_{nozzle}} \text{equiv} \frac{\hat{u}_{rms, ax}}{u_{ax, vol}} \quad (2)$$

In the following figure the results of the isothermal studies are given using the characteristic numbers Pu and Str defined above for a turbulent axial jet (two mean massflow rates or mean axial velocities $\bar{u}_{ax, vol}$) and two swirled jets with different swirl intensities, characterized by the theoretical swirl number $S_{0, th}$ ($S_{0, th} = 0.21$ and 0.79).

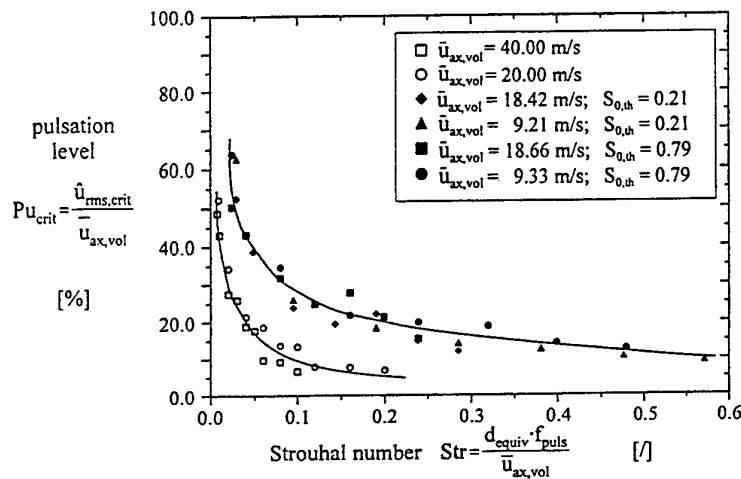


Fig. 3. Fluidynamical conditions for ring vortex formation at different nozzle geometries

For a given Strouhalnumber Str and sufficiently low pulsation levels Pu for both flow types (axial jet and swirl flow) no ring vortex formation in the nozzle near region could be detected. With increasing pulsation level Pu ring vortex formation first appeared for the pulsated turbulent axial jets, while the two swirled flows still remained within their steady-state flow geometry without ring vortices. For a further increase of Pu ring vortex structures also appeared for the two swirl flows with different swirl intensities (see fig. 3). Generally for both flow types at higher Strouhalnumbers Str the onset of ring vortex formation is shifted to lower values of Pu . With these results the ring vortex formation could be successfully predicted for geometrical similar nozzles under variation of the above mentioned operation conditions.

3. SUPPRESSION OF RING VORTEX FORMATION UNDER COMBUSTION CONDITIONS BY AERODYNAMIC MEANS

In the following part of the paper the results of a new method, meanwhile patented [4], for the suppression of flame-/pressure oscillations driven by the ring vortex mechanism explained above are shown. In technical premixed combustors the transition from stable combustion to complete unstable combustion with ring vortex formation can be achieved - at a given mean thermal load level - by reducing the air equivalence ratio λ_{premix} from high, fuel-lean values in the direction of stoichiometric mixture. At a particular, very good reproducible air equivalence ratio $\lambda_{premix, crit}$ the sudden onset of flame-/pressure oscillations starts under the formation of large-scale ring vortex structures, combusting in-phase with the pressure oscillations and sustaining them at a large-amplitude level.

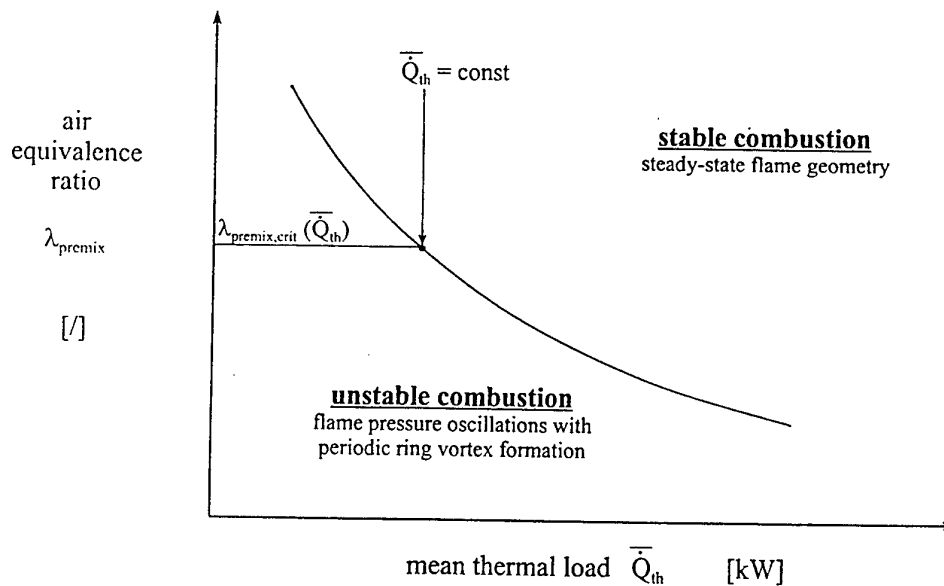


Fig. 4. Scheme for the onset of flame-/pressure oscillations in premixed combustors

When the combustion process starts to become unstable, initially small-scale ring vortices were formed, which react in-phase with the pressure oscillation. When the energy input per cycle added in this way is higher than the energy dissipation of the pressure oscillation with the amplitude level existing at this moment, the oscillation is amplified with the result of an increasing amplitude. Referring to fig. 1 the increase of the static pressure amplitude in the chamber $\hat{p}_{cc}(f_{\text{puls}})$ leads to an also increased amplitude of mixture massflow fluctuation at the burner nozzle $\hat{m}_{\text{nozzle}}(f_{\text{puls}})$ and - as a consequence of it - in the formation of larger ring vortex structures, containing more unignited fuelgas/air mixture to produce higher amplitudes of the heat release oscillations when combusting. After some cycles, where amplification takes place, the pressure oscillation is fully developed, characterized by constant pressure amplitudes.

Derived from this physical understanding of the amplification of initially small-scale disturbances it became clear, that a successful way to suppress or prevent large-amplitude pressure oscillations has to avoid the formation of combustible ring vortices. Therefore, the following method was developed and - after successful tests at different industrial premixed combustors - patented. The next figure shows in a scheme how this can be achieved on principle.

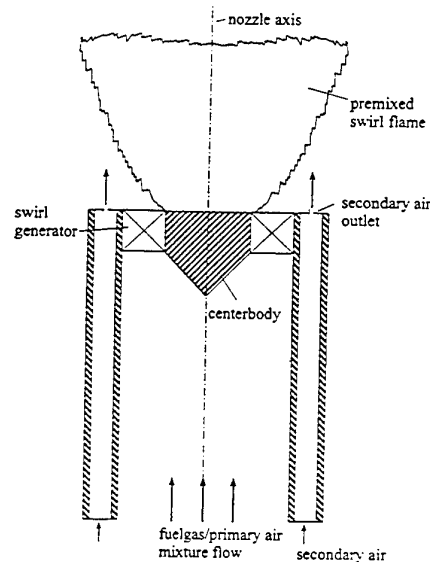


Fig. 5. Aerodynamic suppression of turbulent ring vortex structures by secondary air injection

The fuelgas/air mixture flow out of the burner nozzle is closely surrounded by a secondary air or inert gas flow, coming out from a continuous slot or from a sufficient number of drillings located concentrically to the burner nozzle and enclosing the nozzle flow respectively the flame. Due to the higher axial momentum of the secondary airflow the outer regions of the flame or the mixture massflow are accelerated by radial turbulent exchange and the formation of small-scale ring vortices is avoided. Simultaneously, the surrounding cold airflow suppresses the entrainment of hot fluegases during the rolling-up of the edges of the flame or the mixture massflow into the ring vortices and therefore, the mixture inside the ring vortices, consisting of the initial fuelgas/air mixture and secondary air instead of hot fluegases, is shifted outside the ignition limits, so that these structures are no longer reactive. In the following figure the suppression of vortex-driven pressure oscillation in a turbulent premixed swirl flame is demonstrated.

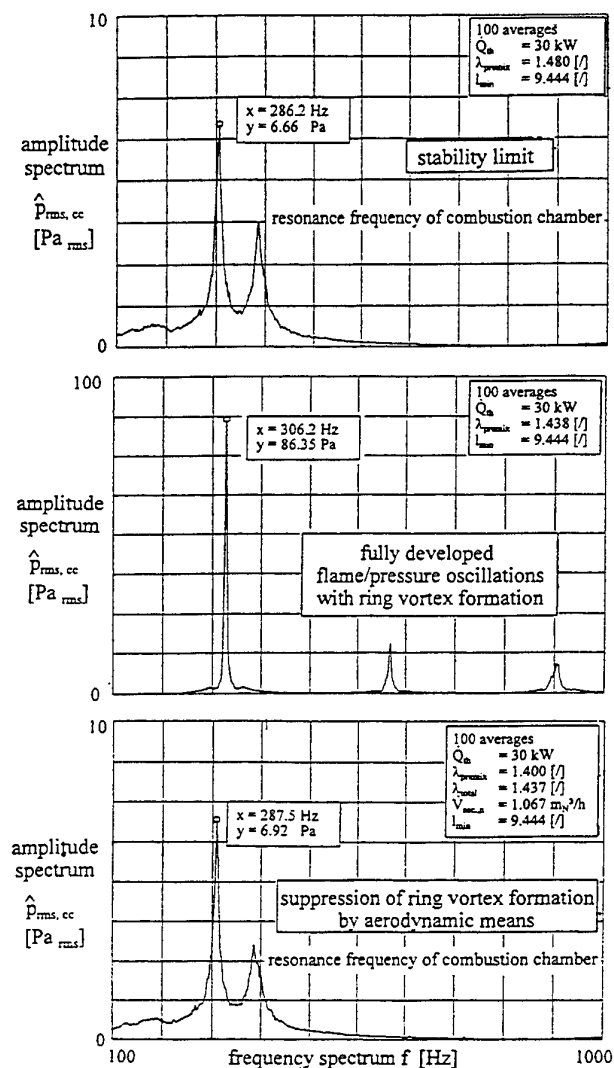


Fig. 6a-c. Effect of secondary air injection on the formation of reactive ring vortices

For a given air equivalence ratio $\lambda_{\text{premix,crit}}$ of 1.48 the flame is close to the stability limit (onset of flame-/pressure oscillations), but still stable and with steady-state flame geometry without ring vortices (fig. 6a). Referring to fig. 6b a further decrease of the excess air ($\lambda_{\text{premix}}=1.44$) leads to fully-developed pressure oscillations with 15 times higher amplitudes in the combustion chamber as before, driven by the ring vortex mechanism. The injection of secondary air with proper axial momentum and massflow rate (fig. 6c) results in a stable, steady-state combustion process for the same air equivalence ratio $\lambda_{\text{premix}}=1.44$, where before strong oscillations were obtained. The pressure frequency spectra in fig. 6a and 6c at stable, non-oscillating combustion are nearly identical, expressing the fact that with secondary air injection the amplification of initially small-scale disturbances by the ring vortex mechanism can be suppressed, but the initial level of disturbance, from which periodic ring vortex formation starts, remains unchanged.

After successful testing with premixed burners in the thermal load range between 30 kW and 200 kW the method of secondary air injection was implemented into a full-scale gasturbine burner for premixed combustion of natural gas with a maximum thermal load of 1 MW under atmospheric operation conditions and 20 MW in a fully-loaded test rig. Testing started in an atmospheric, non-loaded single-burner test rig at Karlsruhe University. With secondary air injection, using a very low air massflow rate, a considerable extension of stable burner operation was obtained for all thermal load levels tested. In figure 7 the increase of flame stability is quantified by the reduction of the air equivalence ratio $\Delta\lambda_{\text{premix,crit}}$, that is now possible without the onset of vortex-driven pressure oscillations in comparison with the stability limits of an original, unmodified gasturbine burner for equal operation conditions.

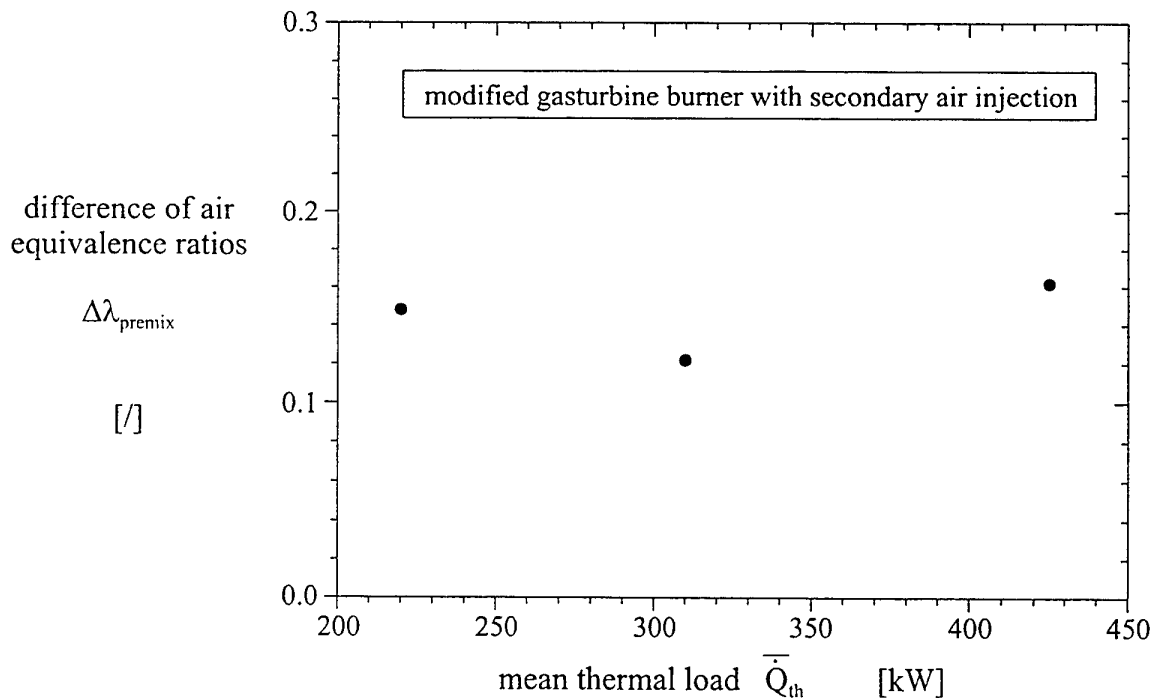


Fig. 7. Shifting of flame stability limits due to secondary air injection at different thermal loads

In figure 8 burner tests under gasturbine conditions (preheated combustion air, fully-loaded test rig) with and without secondary air injection are compared. For sufficiently high air equivalence ratios $\lambda_{\text{premix}} > \lambda_{\text{premix,crit}}$ at a given thermal load the original, unmodified burner is stable, although showing slightly higher rms-values of the chamber pressure than the burner with implemented secondary air injection. A decrease of the air equivalence ratio $\lambda_{\text{premix}} < \lambda_{\text{premix,crit}}$ leads to a sudden onset of large-amplitude pressure oscillations. In comparison to this result the modified gasturbine burner with secondary air injection allows a stable combustion process within the entire operation range with constant rms-values of the chamber pressure.

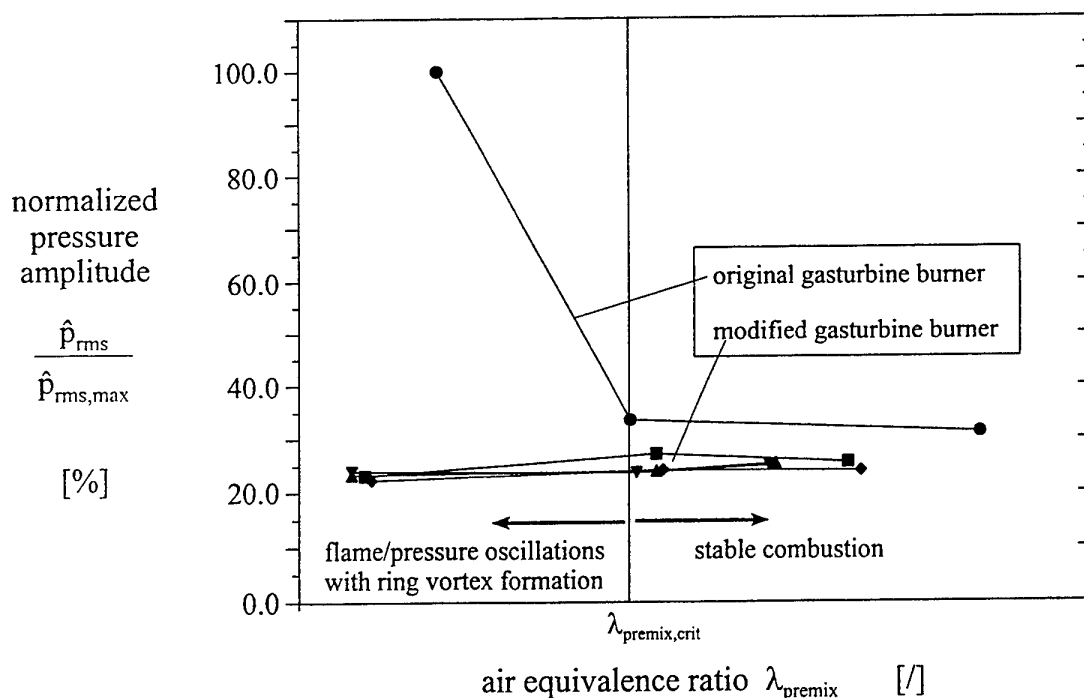


Fig. 8. Suppression of vortex-driven combustion instability for gasturbine operation conditions

4. CONCLUSIONS

In the present paper the formation and in-phase combustion of large-scale turbulent vortex rings, which have to be understood as an important amplification mechanism for initially small-scale disturbances, have been described and quantified in terms of the fluiddynamic conditions of the underlying mixture massflow modulation. In particular, the formation has been studied in dependence on the frequency of pulsation f_{puls} , on the amplitude $\dot{m}_{rms,nozzle}$ of the excitation and on the mean massflow rate \dot{m}_{nozzle} and the individual nozzle geometry, normalized in form of two dimensionless characteristics Str and Pu . With these results the prediction of ring vortex formation for different flow types (turbulent axial jet, swirl flows with various swirl intensities) and nozzle geometries is now possible. Furthermore, a new patented method for the aerodynamical suppression of combustable ring vortex structures by the injection of secondary air with properly adjusted axial momentum and massflow rate is successfully demonstrated for different industrial premixed combustors in the thermal load range between 30 kW and 400 MW.

REFERENCES

1. K.C. Schadow, E. Gutmark, T.P. Parr et al., "Large-Scale Coherent Structures as Drivers of Combustion Instability", *Combust. Sci. and Techn.*, Vol. 64, pp. 167-186 (1989).
2. H. Büchner, C. Hirsch and W. Leuckel, "Experimental Investigations on the Dynamics of Pulsated Premixed Axial Jet Flames", *Combust. Sci. and Tech.*, Vol. 94, pp. 219-228 (1993).
3. H. Büchner, W. Leuckel and A. Hilgenstock, "Experimental and Theoretical Investigations on the Formation of Self-Sustained Pressure Oscillations in a Low- NO_x Burner", 3rd Asian-Pacific Intern. Symp. on Combustion, Hong-Kong (1995).
4. H. Büchner, W. Leuckel et al., US Patent No. 5758587, June 2, 1998.

COMBUSTION AND EMISSION CHARACTERISTICS OF RESIDUAL OIL WITH ADDITIVE OF ORGANIC BARIUM

T. S. Lee

Aerospace Science and Technology Research Center
National Cheng Kung University, Taiwan
Email: lee@astrc.iaalab.ncku.edu.tw; Fax: (886)-6-2391915

M. J. Chen

Tai-power Company, Taiwan

Keywords: heavy oil combustion, additives combustion, organic barium additive

ABSTRACT. Combustion and emission characteristics of burning of No. 6 residual oil with the additive of 100ppm of organic barium are investigated in a can combustor test rig. The effects of the additive on the flame structure and formation of pollutant are examined at a fixed fuel air ratio of 0.02. With Beckman/Rosemount gas analyzer and Roseco engine smoke emission sampler, the exhaust pollutant and particulate were measured. Temperature distribution inside the combustor was employed to assess the flame structure. Emission of CO and particulate of the oil with additive combustion are found about 25% and 40% less than those of pure oil combustion. The emission of NO_x is, however, observed not much difference between two test cases. A longer and wider flame zone is found in the case of burning oil with the additive of organic barium.

1. INTRODUCTION

Burning heavy oil with fuel additives is an effective technique of reducing soot formation in a combustion system. Soot is the particulate matter resulting from incomplete combustion of hydrocarbon fuels. When present in sufficient particle size and quantity, soot in exhaust gases constitutes a black smoke. Soot formation is undesirable when it leads to environmental pollution or damages the performance of combustion equipment. The polynuclear aromatic hydrocarbons (PAH) absorbed on soot are known to be carcinogenic [1]. The prevention of soot emission is, therefore, an important constraint in the design and operation of combustion systems. Usually, turbine combustor performance is limited by the temperatures, which the construction material can withstand. Increased emissivity and higher radiative heat transfer caused by soot formation in the combustor can cause overheating and damage [2].

Soot formation can be broken down into three stages: soot particle nucleation, formation of spherical by agglomeration and surface growth and coagulation of spherical soot particles to form the characteristic chain-like structure [3]. While the above three stages are occurring, soot particles also undergo dehydrogenation.

Two of the most interesting hypotheses that are especially pertinent to the explanation of the effects of metal-containing fuel additives are based on radical and ionic polymerization. The hypotheses that positive ion serves as nuclei for carbon formation in flames and has been shown to predict the well-known chained structure of carbon particles and the uniform size of the spherical chain units. The alkyl derivatives of PAH are believed to be the first precursors, which may then grow by ionic or radical polymerization path way to high (>500 amu) molecular weight species to higher H/C ratio than to the final soot. This material then agglomerates and dehydrogenates to form solid carbonaceous particulate. The well known PAH which can be extracted from soot particles are believed to be the highly condensed and unreactive byproducts of the soot formation scheme.

The first use of flame additives to reduce soot formation was reported by Bartholome and Sachsse in 1949 [4]. Based on the tests performed in fuel-rich hydrocarbon flame, soot reductions as high as 75% were reported with the transition metal nickel. Additionally, the soot collected was observed to be 'more finely gained' when the additive was employed.

An extensive review of combustion additives for pollution control has been compiled by Krause et al [5]. The general conclusions are that fuel additives can be very effective for flyash and carbon particulate removal, less effective for polycyclic organic matter (POM), only very weakly effective against NO_x, and virtually no effect on total sulfur emissions, although SO₃ can be reduced. The effectiveness in reducing soot formation of the

barium fuel additives is believed to cause by following two mechanisms [3]:

(1) An ionic mechanism that occurs with barium fuel additives which ionizes extensively in the flame. The resulting barium ions act on natural flame ions (both molecular and particulate) to decrease the nucleation or coagulation rate. The result is a decrease of the amount of soot formed, or a shift of particle size distribution to smaller sizes that burn out more quickly.

(2) Barium-fuel additive undergoes a homogeneous reaction with flame gases to produce hydroxyl radicals which rapidly removed soot or gaseous hydrocarbons soot precursors. This action appears to occur throughout the flame, with significant decreases in flame radiation in the early flame zones.

Many authors have questioned the use of metallic fuel additives to reduce smoke emission on the grounds that metal oxides formed by the combustion of the additives may be more toxic than the soot itself [6,7]. Barium compounds are usually only toxic if water-soluble. The most common barium compound, barium sulfate, is insoluble and generally nontoxic. Typically, less than 25% of barium emitted by diesel engines is in the form of soluble barium compounds, usually barium carbonated [8]. The majority of the soluble barium compounds exist as solids.

The aim of the present work is to investigate the effect of organic barium fuel additive on a gas turbine combustion system. With same additive dosage of 100 PPM employed in a thermal power station, The NO₆ heavy-oil with additive was burnt in a pilot laboratory plant. The effect of fuel additive was analyzed by characterization of flame and the gaseous and solid emissions.

2. EXPERIMENTAL SET-UP

Combustion Equipment

This comparative study was intended primarily to delineate the effects of organic barium fuel additive on their pollutant emission characteristics of gas turbine combustion. Hence, the combustion chamber consisted of a can combustor of 2G-GTC85-3 and a downstream pipe with temperature and emission measurement taps on it. The combustion air was directed to pass through a pebble bed heater and heated to the test temperature in the range of 70°C~130°C. An orifice plate measured airflow rate.

The oil feeding system was designed for heavy oil injection by an air-assist atomizer. Oil and atomization air were heated before entering the oil gun by electric heaters. The oil gun was then placed along the axis of the air duct with the frontal plane of the atomizer aligned with the edge of the can combustor dome. The heated combustion air would assist to maintain the fuel temperature along the length of the gun immersed in the airflow. The actual injection temperature was measured by a small-diameter thermocouple placed on the inner tube of oil gun with its sensing tip near to fuel nozzle. The fuel supply condition was maintained at 7 bars and in the range of 110°C~140°C.

The residual oil used in the present study had the specification of ASTM NO.6 oil. The oil-soluble organic barium fuel additive was added at dosage of 100 PPM. With a mixer installed in the oil tank, the fuel was mixed continuously during test time.

Experimental Procedure

The experimental work was designed to investigate the effect of the additive on heavy oil combustion characteristics at same inlet conditions. Overall air /fuel mass ratio was maintained at 50 for both pure oil and with additive oil combustion. Combustor inlet air temperature was kept at the preset values of 65°C and 800°C.

Temperature distribution in the combustion chamber was measured by k-type thermocouples at two axial positions of $x=750\text{mm}$ and $x=1300\text{mm}$ (x was measured from fuel atomizer) and at two radial positions of $r=0$ and $r=R/2=64\text{mm}$. Gas composition measurements in the combustion tests were conducted with six on-line analyzers: O₂ (paramagnetic, Beckman/Rosemount Model 1775), CO₂/CO (N.D.i.r., Model 1864), NO/NO_x (chemiluminescence, Model 1951), unburned hydrocarbons, UHC, (f. i. d, Model 1400A) and SO₂ (Quintox gas analyzer). Before reaching the analyzers, the gas sample was conditioned through cooling, drying and filtering, so that it was perfectly clean and dry. The species concentrations were expressed as molar fractions on the dry

basis. The gas sample was extracted by a non-cooled stainless suction tube at positions of $x=750\text{mm}$ and $x=1300\text{mm}$ at $r=0\text{mm}$. Particulate concentrations in the flue gases were determined with a smoke emission sampler (Roseco Model 473B, as shown in Fig. 3). Iso-kinetic sampling conditions were maintained. The filter on which the particulate was collected and weighed before and after the measurements, giving the particle load in the gases. The filter was previously heated and dried so that errors due to the presence of water were avoided. The particulate sample was examined by optical microscopy to study their size and morphology. Fig. 4 shows the sampling probe.

3. RESULTS AND DISCUSSIONS

Flame Characteristics

With same fuel-air ratio condition as shown in Fig. 1, temperature history of burning with fuel additive at station $x=750\text{mm}$, TC1, shows similar to that of pure oil combustion as shown in Fig. 2. The temperature difference along axial direction, TC1-TC3 ($x=1300\text{mm}$), however, shows lower values for pure oil combustion cases as shown in Fig. 3. Longer flame lengths are thus observed in the cases of burning with fuel additive. The value of radial temperature difference, TC1 ($r=0$)-TC2 ($r=R/2$), was employed to estimate the flame width. A wider flame structure can be found in the case of burning with fuel additive as shown in Fig. 4.

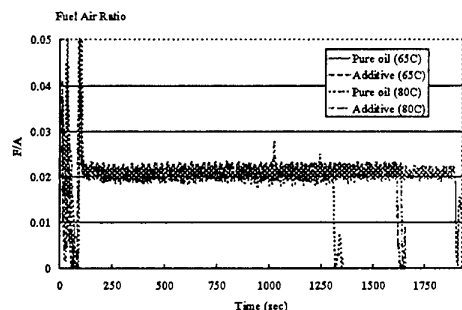


Fig. 1. Fuel air ratio

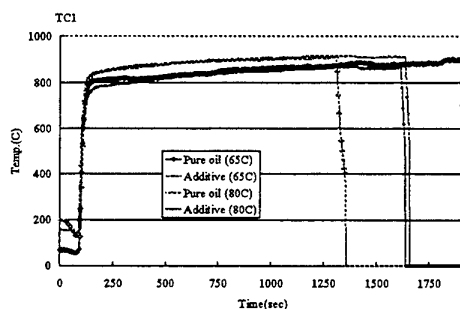


Fig. 2. Can-combustor temperature histories

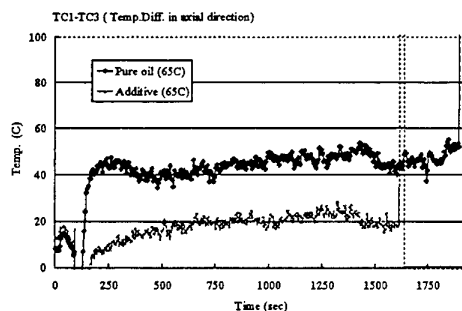


Fig. 3. Temperature variations in the axial direction

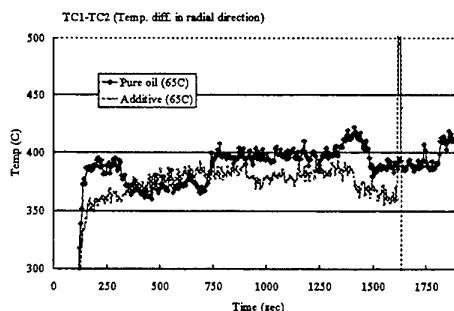


Fig. 4. Temperature variations in the radial direction

Pollutant Emissions

The levels of NO_x corrected to 15% O_2 , $\text{NO}_{x,c}$, are shown as in Fig. 5, in which slight lower values for cases of fuel additive combustion were observed. This is probably caused by the existence of wider flame structure. A better combustion efficiency could be achieved for fuel additive combustion case in which lower emission values of CO and same emission level of unburned hydrocarbons, UHC, were obtained as shown in Fig. 6 and Fig. 7, respectively. Emission of CO is found about 25% lower than the pure oil combustion. The pollutant of SO_2 , however, shows not much difference between the cases of pure oil and fuel additive combustion as shown

in Fig. 8.

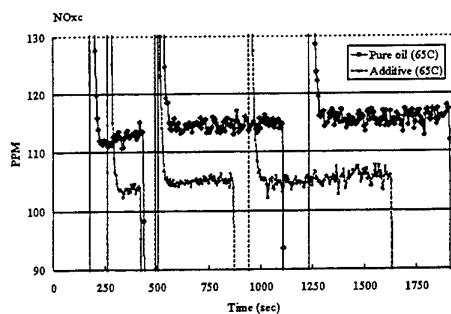


Fig. 5. NO_x emissions

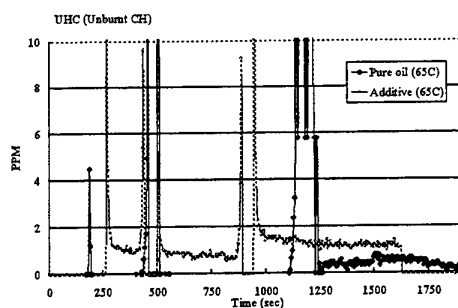


Fig. 6. Unburned hydrocarbons emissions

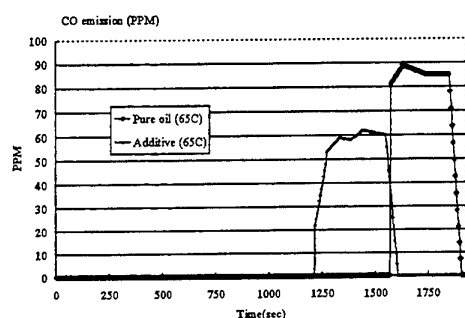


Fig. 7. CO emissions

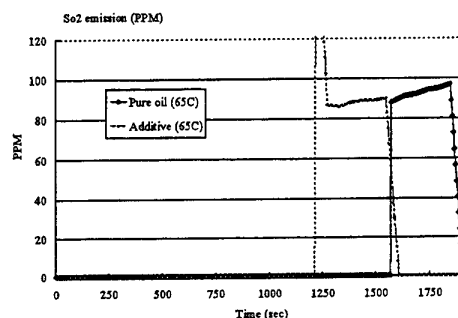


Fig. 8. SO₂ emission

The significant effect of the fuel additive on the soot formation can be found in Fig. 9. Particle load in the gases was obtained by weighting the filter pre- and posts test. About 40% reduction on the soot formation was obtained for the case of fuel additive combustion. Furthermore, by employing optical microscopy technique, smaller particle size distributions was also observed.

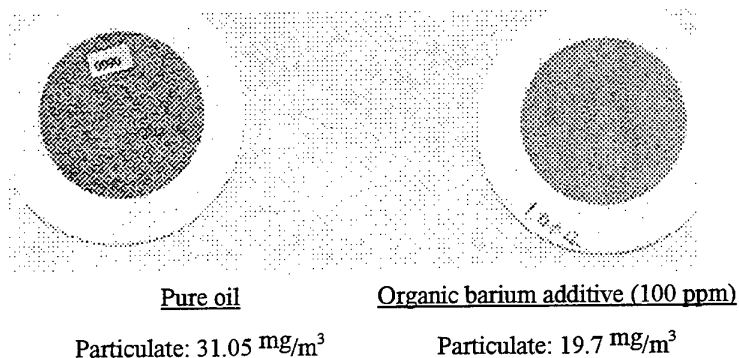


Fig. 9. Particulate samples ($T_{inlet}=65^{\circ}\text{C}$)

4. CONCLUSIONS

Combustion and emission characteristics of burning of No. 6 residual oil with additive of organic barium are

investigated in a can combustor test rig. With same additive dosage employed in a thermal power station, the effect of fuel additive was analyzed by characterization of flame and the gaseous and solid emissions.

With Beckman/Rosemount gas analyzer and Roseco engine smoke emission sampler, the exhaust pollutant and particulate are measured. Temperature distribution inside the combustor is employed to assess the flame structure. A longer and wider flame structure was observed for the case of oil with fuel additive combustion. The wider flame structure, and thus more uniform temperature distribution in the flame zone, causes emission of NO_x to decrease. About 7% decrease was found in the present study. Emission of CO and particulate of heavy oil with organic barium additive combustion are found about 25% and 40% less than those of pure oil combustion. The decrease of the amount of soot formed as well as the particle size distribution is believed to cause by the ionic mechanism of barium additive. The reduction of CO emission indicates the organic barium is also a combustion improver. The pollutant of SO_2 , however, shows not much difference between the cases of pure oil and with fuel additive combustion.

ACKNOWLEDGMENTS

The authors acknowledge the supports provided by the National Science Council, R.O.C. under the contract NSC 88-TPC-E-006-007.

REFERENCES

1. A. Dipple, *Chemical Carcinogens*, Am. Chem. Soc. (Ed. C. E. Searle), pp. 245, Washington, D.C. (1976).
2. L.H. Lenden and J.B. Heywood, *Comb.Sci.Tech.* 2, pp. 401 (1971).
3. J.B. Howard and J.K. Jr. William, *Prog. Energy Combust. Sci.* Vol. 6, pp. 263-276 (1980).
4. E. Bartholome and H.Z. Sachsee, *Electrochem*, pp. 53 ~ 326 (1949).
5. H. H. Krause, L.J. Hillenbrand, A. E. Wellar and D. W. Locklin, NTIS No. PB 264068, January (1997).
6. D.V. Giovanni, P.J. Pagni, R.F. Sawyer and L. Hughes, *Comb. Sci. Tech.*, 6, pp.107 (1972).
7. P.G. Pagni, L. Hughes and T. Novakovt, NTIS No. 25, AD769278 (1973).
8. D.W. Golothan, Diesel engine exhaust smoke: The influence of fuel properties and the effects of using a barium containing fuel additive. SAE Paper 670092, January (1967).

CONCENTRATED PRIMARY AIR ARRANGEMENT TO MAKE BITUMINITE BURNED BOILER SLAGGING - PREVENT AND LOW NO_x RELEASE

Hao Zhou, Zuohe Chi, Xiao Jiang Jiang, Kefa Cen

Department of Energy Engineering

Zhejiang University

Email: zhouhao@eed.zju.edu.cn; Fax: (086-571)7951616

Guojun Sun

Gansu Electric Power Test Institute

Fax: (086-931)2333985

Keywords: coal combustion, slag, NO_x release

ABSTRACT. In traditional pulverized coal tangential firing boiler design, the uniform air distributing burner is always adopted to burn bituminite with fine ignitability, so that good furnace flame coefficient of fullness and high coal powder burn-off rate can be obtained. But such assemblage also brings too concentrated heat release rate in burners' zone which leads to slagging while burning clinkering coal, the local high temperature zone and uniform air distribution also lead to high NO_x emission. In today's China, there are lots of tangential burning boilers without overfire air to decrease NO_x emission, to add OFA on the top of burner group is a difficult and expensive work which may also brings other problems. In this paper, an idea that the upper primary air is moved to lower location to provide room for OFA is developed, using the concentrated primary air arrangement plan combined with the horizontal fuel rich-lean combustion technology, the altitude and horizontal directions' two-region combustion is formed to make boiler slagging-prevent and low NO_x release. The test and numerical simulation are used to prove the scheme's feasibility, through analyzing the heat release rate in the burners' zone, the principle of choosing various zone's air excess coefficient is determined. Finally, the hot test illustrates the feasibility of the scheme.

1. FOREWORD

Bituminite produced in Gansu province has good ignitability and combustion performance, but it also has severe slagging property. In traditional pulverized coal tangential firing boiler design, the uniform air distributing burner group is always adopted to burn the bituminite, such as "second air- primary air -second air" scheme which leads to good furnace flame coefficient of fullness and high coal powder burn-off rate. But this scheme also leads to over-high temperature zone in the furnace, and causes problems such as serious slagging while burning clinkering coal, high emission of thermal NO_x and fuel NO_x.

In this paper, an idea that the upper primary air is moved to lower location to provide room for OFA is developed, using the concentrated primary air arrangement plan combined with the horizontal fuel rich-lean combustion technology, the altitude and horizontal direction's two-region combustion is formed to make boiler slagging-prevent and low NO_x release.

2. THE TRADITIONAL BURNING SYSTEM DESIGN FOR GANSU COAL

A 410t/h pulverized coal tangential firing boiler is investigated. The boiler is Π shaped arrangement, which burners are divided to three groups, using "second air-primary air-second air" arraying scheme illustrated in Fig.1. The designed and actual burning coal is typical Gansu bituminite which has good ignitability and high burn-off rate but also serious clinkering property. The ash's soften temperature is only 1185°C. Although the small imaginary tangential circle diameter is adopted and the heat release rate is kept lower limit value in design, the serious slagging always occurs in operation.

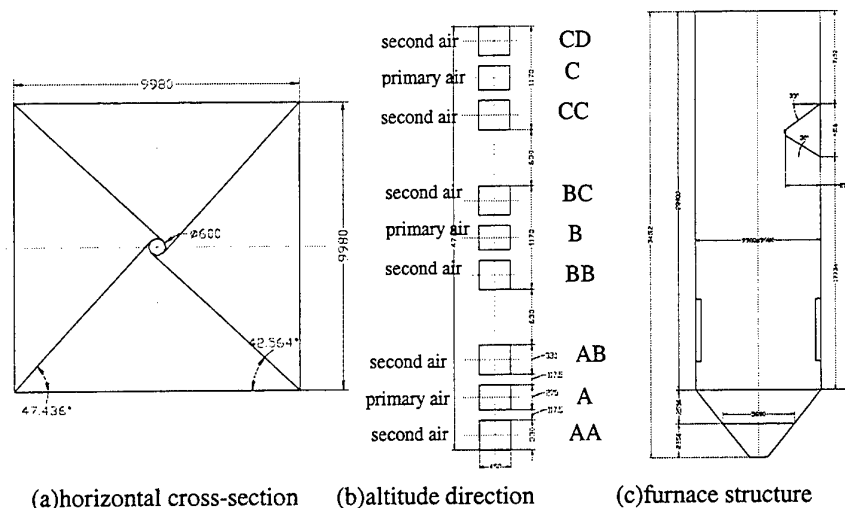


Fig.1. Burning system arrangement

3. HORIZONTAL FUEL RICH-LEAN COMBUSTION TECHNOLOGY DEVELOPED BY ZHEJIANG UNIVERSITY

Zhejiang University developed a set of horizontal fuel rich-lean combustion technology including a collision separation equipment which schematic diagram is shown in Fig.2, when the pulverized coal air mixture flow through the equipment, it is divided into fuel rich stream and fuel lean stream [1]. The important technical parameters of the separator are the height of the collision block, the collision angle of the block facing air flow, the distance between the block and the separate plate, the curve shape of the plate located at the opposite of the collision block. To improve the technology adaptability to coal quality and the boiler's load, the separation rate of the equipment is designed as adjustable by regulating the height of the collision block, the effect of regulating is illustrated in Fig.3.

After the air-coal flow is divided into rich coal stream and lean coal stream through the separation equipment, rich coal stream is guided to the side of burner facing the upstream flame and the lean stream is led to the other side of the burner, which forms the horizontal fuel rich-lean technology, for the lean coal stream has a concentration C/A of 0.1~0.2, forms a prevention layer around the waterwall to depress the waterwall slagging.

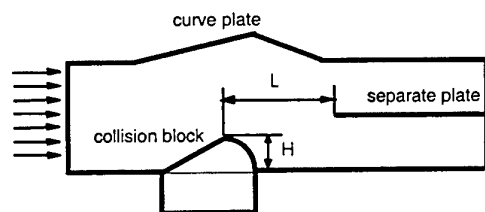


Fig.2. Schematic diagram of collision separation equipment

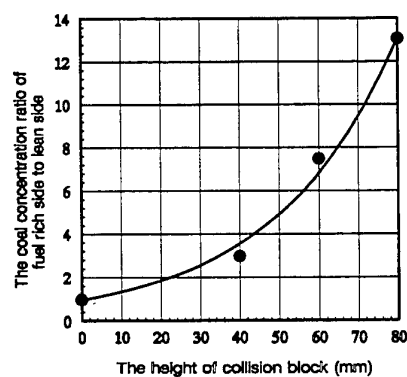


Fig.3 The coal concentration ratio of fuel rich side to lean side changed with the height of collision block

4. RETROFIT PLAN

A kind of combination burning system is developed which is based on the staged combustion technology and horizontal fuel rich-lean combustion technology, forming two region combustion in the altitude and horizontal direction. Horizontal two-region combustion scheme uses the horizontal fuel rich-lean technology, making the center zone of furnace as a high temperature, high heat release rate combustion zone while the near wall zone as a low flow velocity, low CO and solid phase concentration zone.

At the same time, the upper primary air is moved to lower zone (as illustrated in Fig.4) to form altitude direction's two-region combustion. Comparing the scheme which adds OFA to decrease NO_x release, the total height of the burner group will not be changed and the waterwall will be kept without retrofitted in this retrofit plan.

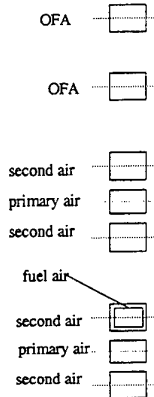


Fig.4. Schematic plan of moving upper primary air to lower location

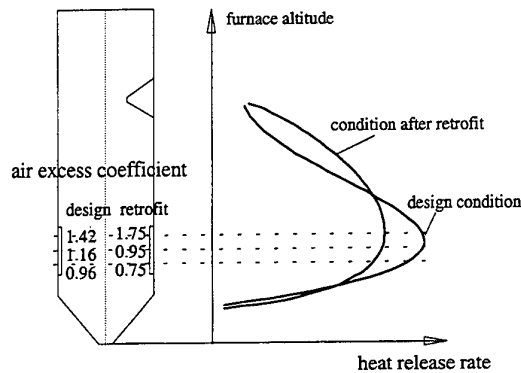


Fig.5. Air excess coefficient in burners' the zone and heat release rate in furnace

After the upper primary air being moved downward, the air excess coefficient of the lower furnace zone should be decreased to 0.75. The heat release rate of that zone also decreases which causes the temperature of that zone decreases too.

Altitude direction staged-combustion always increases the carbon burn-off rate, but when using the above retrofit scheme, the residence time of coal particle in furnace extends, so the burn-off rate can be controlled.

Moving the upper primary air burner to lower location just means the using of the primary air concentric arrange program in bituminite burned boiler. Someone may think it will increase the heat release rate of the lower zone of furnace, but considering the air excess coefficient control scheme, the heat release rate can be controlled, which is analyzed as follows.

5. THE FURNACE HEAT RELEASE ANALYZING

The burner's zone heat release $(q_A)_r$ represents the temperature level of burner's zone, which is an important parameter to prevent waterwall slagging. Which is expressed as:

$$(q_A)_r = \frac{BQ_{\text{net,ar,p}}}{3600uH_r} \quad (1)$$

where, B is the coal amount used per hour, kg/h; $Q_{\text{net,ar,p}}$ represents the coal's net calorific power, MJ/kg; u represents the circumference of the furnace, m; H_r is the total height of the burner group, m.

To various coal in China, the limited value of $(q_A)_r$ is different[4]:

$$(q_A)_r < (9.531 - 1.379 \ln R) \times 10^6 \quad (2)$$

where, R is the coal clinkering property factor.

$$R = 1.237B/A + 0.282 \cdot \frac{\text{SiO}_2}{\text{Al}_2\text{O}_3} - 0.0023 \cdot \text{ST} - 0.0189 \cdot G + 5.415 \quad (3)$$

Where, B/A is the amount ratio of alkali to acid of the ash; $\text{SiO}_2 / \text{Al}_2\text{O}_3$ represents the amount ratio of SiO_2 to Al_2O_3 ; ST is the soften temperature of the ash; G represents the silicium ratio.

Using the above formula (2), we can get the limited $(q_A)_r$ value of the boiler is $2.3 \text{ MW} / \text{m}^2$. Then we know if the upper primary air burner is moved to lower location as illustrated in Fig.4, and with the same coal heat release law, the burner's zone heat release $(q_A)_r$ will be double of that before retrofit, which will exceed the permitted range. To avoid such problem, the air excess coefficient in the lower half of the furnace should be kept as 0.75 to control the pulverized coal combustion velocity in the lower zone of the furnace.

6. NUMERICAL SIMULATION OF THE FLOW FIELD AND THE TEMPERATURE FIELD

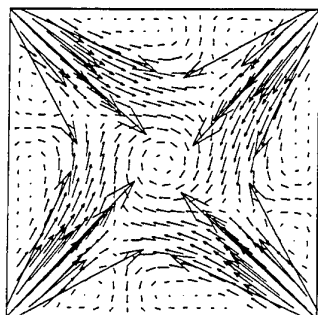


Fig.6. The flow field at B layer section after moving upper primary air downward

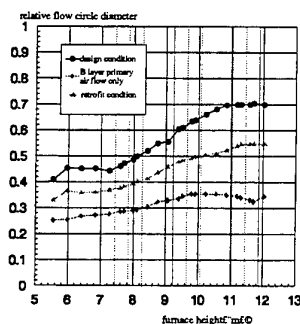


Fig.7. The relative circle diameter changes with furnace height

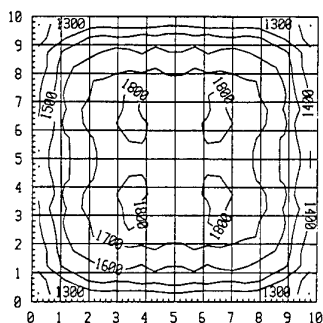


Fig.8. Cross-section temperature field at 15m height under design condition

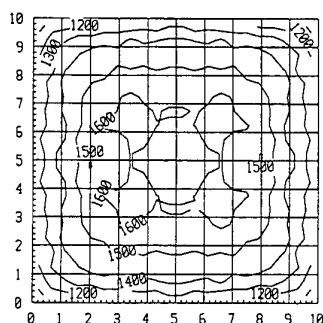


Fig.9. Cross-section temperature field at 15m height under retrofit condition

Using numerical simulation [2], the flow field of the middle primary air section of the furnace after retrofitting is calculated, as illustrated in Fig.6. Fig.7 illustrates the calculated results of the relative tangential circle in the furnace in the case of only middle primary air flow in the furnace, designed operation condition and condition after retrofit, it is clear that the relative flow circle diameter decreases after moving the primary air downward, it may be the results of the pulling down the spacing of the upper second air burners. The temperature field simulation results are shown in Fig.8 and Fig.9, which indicates the temperature of burners' zone decrease more than 100°C after retrofit.

7. HOT TEST OF RETROFIT SCHEME

Because of the complication the combustion process, only theoretical analyzing is not enough, hot test is done to prove the feasibility of retrofit scheme. Closing the upper primary air and using the upper two second air as overfire air, the load of upper burner is shared by the B and the A primary air burner, and the load of the A primary air burner is bigger than B, the boiler is under full load. The hot test results show that no slagging occurs in furnace and the flame is stable, the main steam temperature is rated and the highest furnace flame temperature decreases by 100°C than that in the design condition which is anastomotic with numerical simulation. And an important phenomenon is that the NO_x emission decreases 60% than design condition and.

8. CONCLUSIONS

- (1) Moving the upper primary air downward to form staged combustion in altitude direction and using the horizontal fuel rich-lean burner to realize the slagging prevention, NO_x emission decreasing.
- (2) Concentrated primary air arrangement to make bituminite burned boiler slagging-prevent and low NO_x release, the air excess coefficient controlling is important, through controlling the air excess coefficient in the various zone of the furnace to control the heat release rate is an effective way to prevent waterwall slagging, which decreases the NO_x emission.
- (3) In paper, the principle of the air excess coefficient controlling is given.
- (4) The numerical simulation method combining with the modeling test and hot test prove the feasibility of the concentrated primary air arrangement for slagging prevention and NO_x release decreasing.
- (5) To set adjusting means in concentrated primary air arrangement scheme is important, which can restore the burner group to the scheme of eight burners bearing full load, which is proved feasible in hot test.

REFERENCES

1. H. Zhou Z. Chi, etc. *Refurbishment of Low Quality Coal-fired Boiler Using horizontal Fuel Dense-thin Combustion technology*, Electric Power, vol.30, NO.6 (1997).
2. Z. Chi, H. Zhou, etc. *Prediction on the Flame-stability and Slagging-prevention with Concentric Firing System Using Computer-Simulation*, Proceedings of the CSEE, vol.18, No.2 (1998).
3. K. Cen, *Boiler Combustion Measurement Method and Technology*, Water conservancy and electric power press, (1987).
4. Y. Li, *Investigation on Methods Calculating Furnace Parameters for Large-capacity Boilers*, Power System Engineering, vol.11, No.4 (1995).

PREDICTION AND MEASUREMENTS OF CARBON COMBUSTION RATE IN CO_2/O_2 ENVIRONMENTS AND ITS RELEVANCE TO GREENHOUSE GAS RECOVERY

Weiping Yan

Department of Thermal Power Engineering
North China Electric Power University
Email: hdkyc@public.bdptt.he.cn; Fax: (86)312-5016595

Yanfeng Liu

Department of Thermal Power Engineering
North China Electric Power University
Email: lyf@bd-user.he.cninfo.net; Fax: (86)312-5016595

Keywords: carbon combustion rate, CO_2/O_2 environments, greenhouse gas recovery

ABSTRACT. In this work carbon combustion rates are predicted based on the proposed model for a variety of gas mixture conditions. An entrained-flow reactor was used to experimentally measure the overall combustion rate of pulverized-coal char in different gas temperature (from 1247 to 1575 K) with selected O_2 partial pressure balanced by CO_2 or/and N_2 . Discussions about some of the important influencing factors are also presented.

1. INTRODUCTION

Rising concern about global warming have focused attention on the need to reduce the atmospheric emissions of greenhouse gases from fossil fuel use. CO_2 released from fossil fuel combustion retain the major focus of attention in the search to reduce greenhouse gases due to the much larger quantities emitted. The novel CO_2 reduction technology involves fossil fuel combustion in a CO_2/O_2 medium, which has the advantage of producing a highly enriched CO_2 stream for removal and disposal from a variety of new or retrofit power generation applications[1].

Application of flue gas recycle combustion to power generation and CO_2 capture has been proposed and evaluated [2]. The mode of operation of a steam boiler employing an oxygen and flue gas recycling combustion process is shown schematically in Fig.1. Another important application is coal gasification in spout bed reactor by CO_2 stream[3]. Carbon reaction in air and in CO_2/O_2 medium are expected to show different behaviors which will have important implications in design of new concept coal combustion and gasification facilities including furnace, coal gasifier, coal burner, solid-gas flow and reaction, heater transfer in furnace and etc. One of those focuses is to acquire new knowledge on combustion rate of pulverized-coal char in O_2/CO_2 and important differences in comparing with the traditional reaction process in air environments.

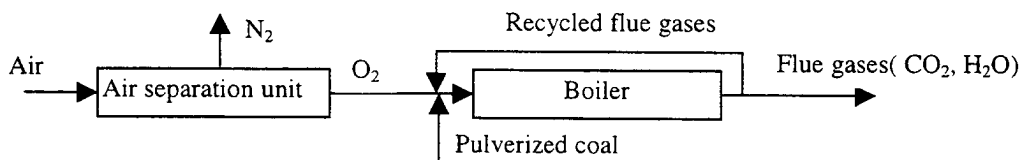
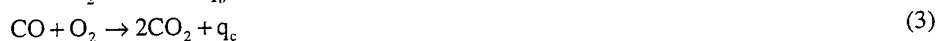


Fig.1 Schematic of the CO_2 recycle power plant system

In this work theoretical investigations on reaction rate of carbon particles are implemented based on a model that has been recommended in literatures [4]. Dependence of reaction rate on environmental temperature and medium with different CO_2/O_2 mole ratio are predicted. Calculated results of carbon particle temperature variation in the reaction process are also presented. The combustion rates of pulverized-coal char in O_2/CO_2 as well as in O_2/N_2 environments were experimentally studied in an entrained-flow reactor (EFR). The tested gas temperature were from 1247 to 1575 K with selected O_2 partial pressure. Preliminary discussion about the different carbon reaction rate in air and in CO_2/O_2 as well as its relevance in designing the novel combustion facilities for CO_2 recovery is given.

2. THEORETICAL MODEL

The carbon combustion model adopted in this work describes chemically and physically the reaction process of a single carbon particle in a static gas medium. The chemical reactions take into account the surface C-O₂ and C-CO₂ reactions together with the CO-O₂ reaction in gas phase (as shown in Eqs.1 to 3).



Through dimensionless and Zeldovich's transformation, the reaction system for single carbon particle can be described by the following components, as presented by Eqs.4 and 5.

$$L(\bar{Y}_P + \bar{Y}_F) = L(\bar{Y}_P + \bar{Y}_O) = L(\bar{Y}_P - \bar{T}) = L(\bar{Y}_N) = 0 \quad (4)$$

$$L(\bar{T}) = D_{ag} W_g \quad (5)$$

The energy conservation equation for a single particle in the reaction system can be expressed as

$$\left(-\frac{d\bar{T}}{dr} \right)_s + \bar{G}_c(1 - \bar{C}_s)\bar{T}_s + \epsilon \frac{R}{B_0}(\bar{T}_s^4 - \bar{T}_\infty^4) = Q\delta\bar{G}_{c(a)} + (Q-1)\delta\bar{G}_{c(b)} \quad (6)$$

Total combustion rate can be predicted as:

$$G_c = \bar{G}_c \times (4\pi\rho_\infty D_\infty r_s) \quad (7)$$

3. EXPERIMENTAL TESTS

The measurements on char combustion rate were performed in an electrically heated EFR, which has a 2m long corundum tube furnace with 50 mm inner diameter. The sieved char particles were fed through a water-cooled injector into the reaction zone. A water-cooled probe was used to collect and quenched the solid sample. Furnace wall and gas temperatures were continuously monitored by thermocouples positioned along the length of reactor. And gas temperatures can also be predicted by using a numerical simulation code. The ash tracing method was adopted to calculate the weight losses of samples due to solid reaction.

A typical Chinese anthracite, Yangquan coal, was choosed for the investigations. Approximate analyses gives 61.8% fixed carbon, 11.8% volatile matter, 1.4% moisture and 25% ash. The chars were prepared by heating at 800°C for one hour in a muffle furnace. The samples were sieved to a particle size fraction between 76 and 102µm. Test conditions in the experiments are shown in Table 1. The total volumetric flow rates through the reactor were kept as the same for all test conditions.

TABLE 1: Test conditions list.

Test No	O ₂ partial pressure (atm)	CO ₂ partial pressure (atm)	N ₂ partial pressure (atm)	Temperature Range (K)
1	0.3	0.7		1247-1575
2	0.21	0.79		1247-1575
3	0.1	0.9		1247-1575
4	0.21		0.79	1247-1575
5	0.1		0.9	1247-1575

4. PREDICTIONS BASED ON THE PROPOSED MODEL

Predictions on reaction rate of a carbon ball with diameter of $100\mu\text{m}$ are made based on the model and the selected chemical kinetic parameters taken from reference [5]. From Fig.2 to Fig.5 some preliminary conclusions can be drawn by comprising the predicted results in air and in CO_2/O_2 medium with different O_2 concentrations. It is indicate that below temperature of 1750 K the overall combustion rate in CO_2/O_2 medium with mole ratio of 79/21 is lower than in air. The overall reaction rate increases obviously with reduction of the CO_2/O_2 mole ratios. In temperature ranging from 1300K to 2000K carbon particle temperature is always predicted to be 50 to 200K higher in air than in CO_2/O_2 mixtures.

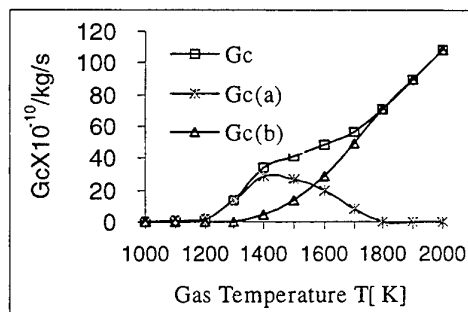


Fig.2. Variation of combustion rate with gas temperature in CO_2/O_2 medium

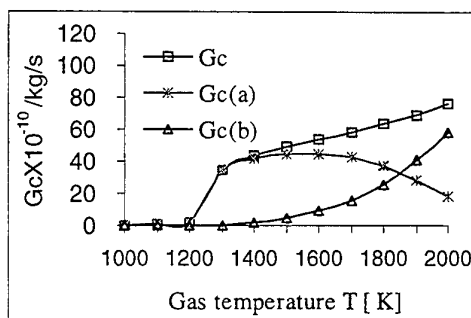


Fig.3. Variation of combustion rate with gas temperature in air

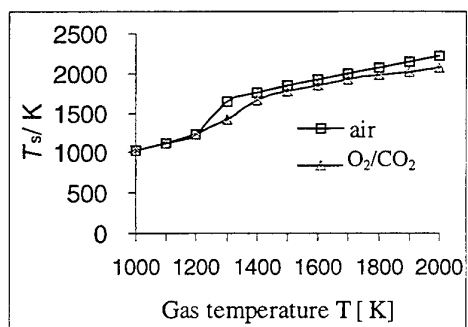


Fig.4. Variation of particle temperature with gas temperature

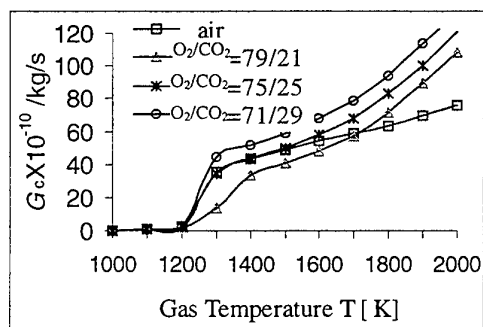


Fig.5. Comparison of variation combustion rate with gas temperature in CO_2/O_2 medium and in air

5. EXPERIMENTAL RESULTS

Fig.6 shows dependence of weight losses of coal char particles on the average gas temperature. Weight losses are ranged from 9% to 50%. For gas conditions listed as No2, No4 (equivalent to air) and No3, No5, although the O_2 partial pressure was kept as same level, the measured weight losses was lower in the O_2/CO_2 environmental conditions for all tested gas temperatures. With higher O_2 partial pressure in the gas mixtures the weight losses increased obviously. And when CO_2/O_2 partial pressure ratios was taken as 2.33 (condition No1), the measured weight loss in the O_2/CO_2 environment was approaching to that in air. Fig.7 shows the comparison of model prediction and measurement results, both are in reasonable agreement.

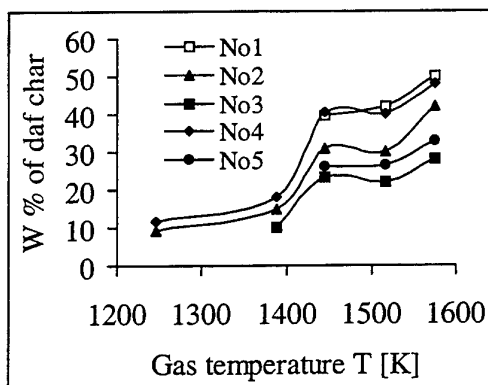


Fig.6. Dependence of measured weight losses on average gas temperature

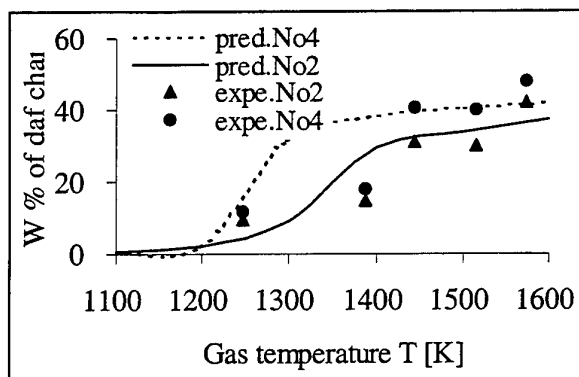


Fig.7. Comparison of predicted and measured results

6. PRELIMETARY DISCUSSION

Both the model prediction and experiment results have shown that below 1600K the overall combustion rate of coal char is lower in O_2/CO_2 than in O_2/N_2 (or air) environment at same environment gas temperature. The reasons could be contribute to following points:

- (1) Thermal properties for gas mixtures of O_2/CO_2 and O_2/N_2 are different. In particular gas diffusivity for O_2-CO_2 is lower than for O_2-N_2 . Thermal capacity of gas mixtures is higher for O_2-CO_2 . This would decrease the char particle temperature and lower the char combustion rate.
- (2) For the O_2/CO_2 environment, CO_2 gasification reaction has a comparative contribution to the char mass losses because of dominant proportion of CO_2 .

7. CONCLUSIONS

Based upon the selected chemical kinetic parameters, the measurement data are in general agreement with predicted results. Both the model prediction and experimental measurement results show that below 1600K the overall char combustion rates of coal char are lower in O_2/CO_2 than in O_2/N_2 environment at same environment gas temperature. With increasing of the O_2 partial pressure in gas mixtures, the overall char combustion rates increase significantly. When the CO_2/O_2 partial pressure ratios was taken as 2.33, the predicted combustion rate in the O_2/CO_2 environment was approximately the same as in air environments. The relevant thermal properties and gas diffusion are different for different gas mixtures and play an important role in char reaction process.

REFERENCES

1. A.M. Wolsky, et. al., Combust. Sci. And tech., V.67, PP.1-, (1989).
2. G.S. Booras, S.C. Smelser, et. al, Energy, V.16(11/12), PP.1295-, (1991).
3. T. Takematsu, and C. Maude, IEA Coal Research, (1991).
4. Makino, and C.K. Law, Proceedings, 21th Symposium(International) on Comb., The Combustion Institute, Pittsburgh, PA, PP.183, (1986).
5. Makino, Combustion and Flame, V.90, PP.143, (1992).

A DESULFURIZATION MATHEMATICAL MODEL AND A PILOT EXPERIMENT BY SPRAYING NaOH SOLUTION INTO DOWNSTREAM FLUE DUCT OF A COAL-FIRED INDUSTRIAL BOILER

Hesheng Zhang, Yongping Liu, Dezhen Chen

Thermal Engineering Department, Tongji University, Shanghai (200092)

E-mail: dezhen@infoworld.sh.cn

Keywords: dual alkali wet desulfurization, dual film mass transfer theory, desulfurization efficiency

ABSTRACT. In a wet desulfurization process NaOH solution is sprayed into flue duct, small droplets are then formed and react directly with gaseous SO₂ in FG. In this paper a two-phase mathematical model based on dual film mass transfer theory and boundary layer theory on the surface of droplet is proposed to describe the reacting processes between the gaseous SO₂ and a single droplet. Then according to the droplet diameter distribution function, a set of formulas to estimate the binding capability of droplets on SO₂ and to predict the desulfurization efficiency are established. Through numerical calculation, key factors such as pH value of droplets, the ratio of spraying NaOH solution volume to the volume of FG, etc. are analyzed and discussed. Additionally, a SO₂ removal pilot experiment is carried out on the flue duct of a coal-fired industrial boiler with steam capacity of 10T/h to test the SO₂ removal rate.

1. INTRODUCTION

Gaseous sulfur dioxide exhausted from coal-fired industrial boilers contributes a lot to air pollution. Wet scrubbers using dual alkali solutions as absorbents are widely used in industrial boilers to intercept sulfur dioxide from flue gases. Under high pressure alkaline NaOH solution is sprayed into the scrubber by a mechanical atomizer, the atomized alkaline droplets contact with gaseous sulfur dioxide directly, at the meantime, physical and chemical interactions are taking place and sulfur dioxide is absorbed. NaOH solution is commonly used as the spraying alkali because NaOH is more reactive than Ca(OH)₂, and the reaction production, namely, Na₂SO₄ or Na₂SO₃ can easily dissolve in water. The reacted solution discharged from scrubber is treated with lime in a settling pond and NaOH is formed again with calcium sulfate or calcium sulfite deposits in the pond. The reformed NaOH solution is set back to the scrubber.

2. MATHEMATICAL MODEL FOR A SINGLE DROPLET OF NaOH SOLUTION ABSORBING SULPHUR DIOXIDE IN FLUE GAS

A single droplet of alkali solution absorbs SO₂ according to the following step:

1. Gaseous SO₂ diffuse to outside surface of droplet through the gaseous boundary layer,
2. On the gas-liquid phase boundary surface, SO₂ dissolve in the liquid till equilibrium is reached.
3. The dissolved SO₂ dissociates into HSO₃⁻ and SO₃²⁻ ions, the ions then diffuse in the solution mainly as SO₃²⁻.
4. Na⁺ ion, which is formed as a result of NaOH dissociation, reacts with SO₃²⁻ in the solution. Their reaction can be described by the following equations :



According to dual film theory, there is a film on either side of the gas-liquid phase boundary layer in the process of convective mass transfer between the two phases. Ions penetrate the films by diffusion, and the diffusion process through the film consists of the main resistance of the mass transfer for both phases.

A droplet of NaOH solution in the spray mist can be divided into five zones as shown in Fig.1.

1. The most outside section with radius r larger than r_1 is the first zone ($r > r_1$), where the concentration of SO₂ equals to that in the bulk flow C_{sg} .
2. The second zone is the annular area with radius r in the range $r_1 \leq r \leq r_i$, this zone forms the gaseous boundary layer of the gas-liquid phase system.
3. The section within $r_i < r < r_f$ is the third zone, from which SO₃²⁻ ion diffuses to the reaction surface as a counterflow in the direction of r_f .

4. The section within $r_2 < r < r_f$ is the fourth zone, where Na^+ ion diffuses to the reaction surface in the direction of r_f .
5. The core with radius r less than r_2 is the fifth zone, where the concentration of alkali keeps its initial concentration value in the spray.

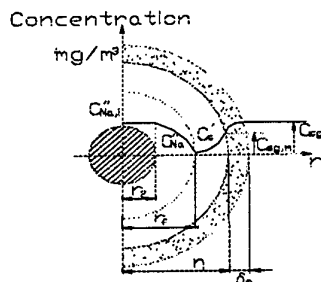


Fig. 1. The five zones division for a single droplet and ion concentration distribution in the direction of droplet radius

The meanings of the nomenclature specified in Fig. 1 are as follows: C_{sg} —gaseous concentration of SO_2 in the bulk flow around NaOH solution droplet, mg/Nm^3 ; $C_{sg,m}$ —concentration of SO_2 on the surface of NaOH solution droplet, mg/Nm^3 ; C'_s —concentration of SO_3^{2-} in the NaOH solution droplet, mg/Nm^3 ; C''_{Na} —concentration of Na^+ in the NaOH solution droplet, mg/Nm^3 ; $C''_{\text{Na},i}$ —initial Na^+ concentration in the NaOH solution, mg/Nm^3 ; r_f —the position of Na^+ and SO_3^{2-} reaction surface, m; δ_m —depth of boundary layer containing dissolved SO_2 , m; $r_1 = r_i + \delta_m$; r_i —radius of a certain droplet in the spray, m; r_2 —radius of the core that contains initial Na^+ concentration, m.

The governing equations are obtained on the basis of the following four assumptions:

1. There is no macroscopic movement of NaOH solution in the droplet, and there is no temperature gradient inside the droplet.
2. Heat of solution and heat of reaction is neglected.
3. Reaction rate of ions is far more rapid than their diffusion rate.
4. On the boundary surface of gas-liquid phases, dissolution of SO_2 equilibrium in the liquid is reached. Solubility of SO_2 in the NaOH solution droplet can be described by Henry's Law.
5. According to the above assumptions, together with help of quasi-stationary analytical method, SO_3^{2-} and Na^+ ion concentration distribution function in the droplet can be established as follows:

$$\text{For } \text{SO}_3^{2-}: \frac{\partial^2 C'_s}{\partial r^2} + \frac{2}{r} \frac{\partial C'_s}{\partial r} = 0 \quad (1)$$

$$\text{For } \text{Na}^+: \frac{\partial^2 C''_{\text{Na}}}{\partial r^2} + \frac{2}{r} \frac{\partial C''_{\text{Na}}}{\partial r} = 0 \quad (2)$$

$$\text{With boundary conditions: 1. At } r = r_f, C'_s(r_f, t) = 0, C''_{\text{Na}}(r_f, t) = 0 \quad (3)$$

$$\text{At } r = r_2, C''_{\text{Na}}(r_2, t) = C''_{\text{Na},i} \quad (4)$$

$$\text{At } r = r_i, \frac{\partial C'_s(r_i, t)}{\partial r} = \frac{h_m}{D'} (C_{sg} - C_{sg,m}) \quad (5)$$

where D' is diffusion coefficient of SO_3^{2-} in the droplet, m^2/sec . And h_m = convective mass transfer coefficient. According to Geankoplis [1], convection mass-transfer formula for spherical surface can be expressed as:

$$\text{Sh} = 2 + 0.75 \cdot \text{Sc}^{1/3} \cdot \text{Re}^{1/2} \quad (6)$$

where Sh is Sherwood number, $Sh = \frac{h_m \cdot d_i}{D}$; S_c is Schmidt number, $S_c = \gamma/D$; Re is Reynolds number, $Re = \frac{V_\infty d_i}{\nu}$; and D is molecular gaseous diffusion coefficient of SO_2 , m^2/sec ; γ is the kinematic viscosity of the gases.

On the boundary surface of radius r_i , dissolved SO_2 in the NaOH solution is in accordance with Henry's Law, which can be expressed as:

$$C_{sg,m} = \frac{H \cdot M_w}{R_u \cdot T \cdot \rho_d} C'_{s,m} \quad (7)$$

where H is Henry' law constant, $atm \cdot cm^3/(g \cdot mole)$; M_w is molecular weight of water, 18 g/mol; R_u is the universal gas constant equal to 1.987 cal/(g.mole.K); T is absolute temperature of flue gas, K; ρ_d is density of alkali solution, it can be well approximated by density of water g/cm^3 .

From which, solutions for equation (1) and (2) can be derived as follows:

$$C'_s = \frac{0.75 \cdot \left(\frac{D}{D'}\right) \cdot Sc^{1/3} \cdot Re^{1/2} \cdot C_{sg} \cdot \left(1 - \frac{r_f}{r}\right)}{2 \left(\frac{r_f}{r_i}\right) + 0.75 \cdot \left(\frac{D}{D'}\right) \cdot Sc^{1/3} \cdot Re^{1/2} \cdot \left(\frac{H \cdot M_w}{R_u \cdot T \cdot \rho_d}\right) \cdot \left(1 - \frac{r_f}{r_i}\right)} \quad (8)$$

and
$$C''_{Na} = C''_{Na,i} \cdot \frac{1 - r_f/r}{1 - r_f/r_i} \quad (9)$$

Mass flow rate of SO_3^{2-} and Na^+ through the two films on either side of the reaction surface can be expressed as:

For SO_3^{2-} : $\dot{m}' = -4\pi \cdot r_f^2 \cdot D' \cdot \frac{\partial C'_s(r_f, t)}{\partial r} \quad (10)$

For Na^+ : $\dot{m}'' = 4\pi \cdot r_f^2 \cdot D'' \cdot \frac{\partial C''_{Na}(r_f, t)}{\partial r} \quad (11)$

where D' and D'' are ion diffusion coefficients for SO_3^{2-} and Na^+ in the liquid respectively.

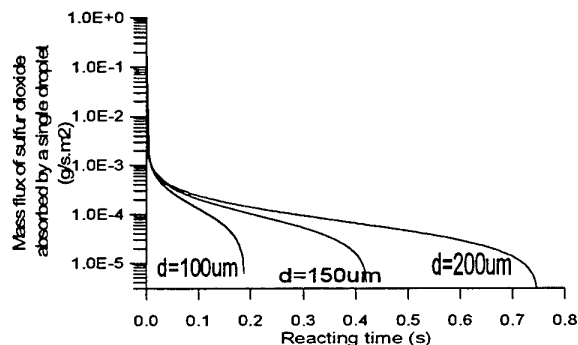


Fig. 2. Qualitative dependence of absorbed SO_2 mass flow rate on reaction time and droplet diameter (initial SO_2 concentration in the bulk flow is $C_{sg}=1200mg/Nm^3$, temperature is $T=90^\circ C$, pH value of droplet is 13).

Differentiating equation (8) and equation (9) referring to radius r and substituting the resulting differentials into the equation (10) and equation (11), together with the chemical reaction equation, the radius of reaction surface can be worked out and we obtain the expression for mass flow rate of SO_2 :

$$\dot{m}' = \frac{4\pi \cdot D' \cdot (\alpha \cdot C_{sg} + \beta \cdot \alpha \cdot \alpha_H \cdot C''_{Na,i}) \cdot r_2}{2 \frac{r_2}{r_1} + \alpha \cdot \alpha_H \cdot \left(1 - \frac{r_2}{r_1}\right)} \quad (12)$$

where $\alpha = 0.75 \cdot \frac{D}{D'} \cdot \text{Sc}^{1/3} \cdot \text{Re}^{1/2}$; $\alpha_H = \frac{H \cdot M_w}{R_u \cdot T \cdot \rho_d}$; $\beta = X \cdot \frac{M'}{M''} \cdot \frac{D'}{D}$; and X is stoichiometrical factor of chemical reaction; M' and M'' are molecular weight of SO_3^{2-} and Na^+ respectively.

From the equation (12) the reaction ability of alkali droplets absorbing SO_2 changing with diameter and reaction time can be obtained and shown in Fig.2.

3. THE TIME FOR NaOH USE-UP IN DROPLETS (Δt_s) AND THE DURATION TIME OF DROPLETS IN THE SCRUBBER (Δt_r)

With the reaction between NaOH and dissolved SO_2 proceeds in the droplet, radius of the core where concentration of NaOH in the solution keeps its initial value is decreasing. The dependence of radius r_2 on the reaction time can be determined according to mass conservation law:

$$-\frac{d \left[C''_{Na,i} \cdot \frac{4}{3} \pi \cdot r_2^3(t) \right]}{dt} = \frac{M''}{X \cdot M'} \cdot \dot{m}' \quad (13)$$

Initial condition: $r_2 = r_1$ when $t = 0$

The time needed for r_2 reaching zero is the use-up time of NaOH contained in the droplet which is noted as Δt_s . Now mass flow rate of SO_2 \dot{m} in the equation (13) is replaced by the expression (12) and the use-up time Δt_s can be derived as:

$$\Delta t_s = \frac{2r_1^2}{3D'} \cdot \frac{\left(1 + \frac{\alpha \cdot \alpha_H}{4}\right) \cdot C''_{Na,i}}{\frac{M''}{X \cdot M'} \cdot (\alpha \cdot C_{sg} + \beta \cdot \alpha \cdot \alpha_H \cdot C''_{Na,i})}, \text{ sec} \quad (14)$$

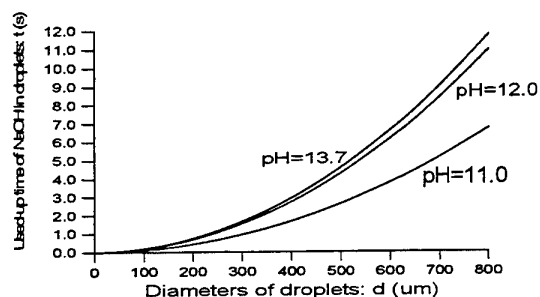


Fig.3. Use-up time Δt_s as function of droplet diameter and pH value (SO_2 concentration in the bulk flow is $C_{sg} = 1200 \text{ mg/Nm}^3$; temperature is $T = 90^\circ\text{C}$)

From Figure 3 it can be seen that use-up time Δt_s of NaOH increases with diameter of droplet and also with pH value of droplet.

In the SO₂ scrubber, the absorbed mass flow rate of SO₂ is influenced by mass transfer rate as well as duration time of droplets within the scrubber. It is assumed that duration time of droplet in the scrubber (noted as Δt_r) can be approximated by the ratio of scrubber volume to the volumetric flow rate of flue gas, namely as:

$$\Delta t_r = \frac{V_y}{Q_y}, \text{ sec} \quad (15)$$

where V_y is scrubber volume, (m³); and Q_y is volumetric flow rate of flue gas, (m³/sec).

When calculating the reaction ability of droplet for absorbing SO₂, use-up time Δt_u and duration time Δt_r should be estimated firstly for different droplets, and the smaller one of the two should be taken as reaction time.

4. MATHEMATICAL MODEL AND EFFICIENCY ESTIMATION FOR SO₂ REMOVAL WITH ALKALI SOLUTION

Alkali solution is sprayed into scrubber with pressure atomizer and mist is formed as a result of atomization. For per mass solution, the number of droplets with diameter not larger than d_i is noted as N(d_i), and the droplet diameter density distribution function is noted as n(d_i). Then N(d_i) is related to n(d_i) as:

$$N(d_i) = \int_{d_{\min}}^{d_{\max}} N_0 \cdot n(d_i) \cdot d(d_i) \quad (16)$$

where N₀ is total number of droplets in per mass solution, and d_{max}, d_{min} are the maximum and the minimum droplet diameters.

Expression for estimating SO₂ removal efficiency with an alkali spray can be derived on the supposition of the following:

1. The gas flow field in the scrubber be one dimension and steady-state.
2. In the flow process the alkali solution droplet will not coalesce or be crushed.
3. The droplets are well-distributed in the flue gas and their vaporization be neglected.

Considering a small increment of distance dx in the direction of flue gas flow, as shown in Figure 4, the absorbed mass of SO₂ by alkali solution spray can be estimated with the help of Equation (12):

$$dM_{\text{SO}_2} = \left[\int_{d_{\min}}^{d_{\max}} G \cdot N_0 \cdot \frac{4\pi \cdot (\alpha \cdot C_{\text{sg}} + \beta \cdot \alpha \cdot \alpha_H \cdot C''_{\text{Na,i}}) \cdot r_2}{2r_2/r_1 + \alpha \cdot \alpha_H \cdot (1 - r_2/r_1)} \cdot n(d_i) \cdot d(d_i) \right] dt \quad (17)$$

where G is mass rate of solution spray in the unit time, (L/sec).

The abatement of SO₂ concentration in this distance dx can be determined as:

$$-dC_{\text{SO}_2} = \frac{1}{Q_y} \cdot dM_{\text{SO}_2} \quad (18)$$

Let C_{so2,in} and C_{so2,out} indicate inlet concentration and outlet concentration of SO₂(mg/Nm³) in the scrubber; the SO₂ removal efficiency in the scrubber is determined by:

$$\eta_{\text{SO}_2} = \frac{C_{\text{SO}_2,\text{in}} - C_{\text{SO}_2,\text{out}}}{C_{\text{SO}_2,\text{in}}} \times 100\% \quad (19)$$

The calculated SO₂ concentration distribution in the direction of gas flow as a function of the mass flow rate G is shown in Figure 4.

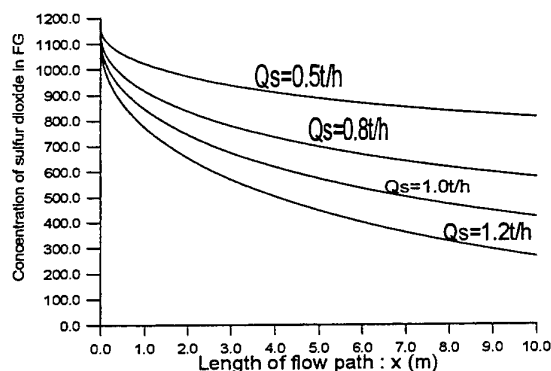


Fig.4. $C_{SO_2, in} = 1200 \text{ mg/Nm}^3$, $\text{pH} = 13.3$

4. PILOT EXPERIMENT DATA OF THE SO_2 REMOVAL EFFICIENCY WITH ALKALI SOLUTION SPRAY

The pilot experiment was carried out on a coal-fired industrial boiler with pressure of 1.25Mpa and capacity of 10t/h. Alkali solution was sprayed into the downstream flue duct. The end of the flue duct was connected with a wet dedustor using water spray to remove dust in the flue gas. Pressure atomizer was installed in the inlet of the flue duct. Temperature measuring and gas sampling points were arranged in the duct inlet and outlet. In order to prevent the condensation of steam vapor in the sampling process, electrical heating sampling pipe is used. Schematic of alkali solution system and measuring points arrangement is shown in Fig. 5.

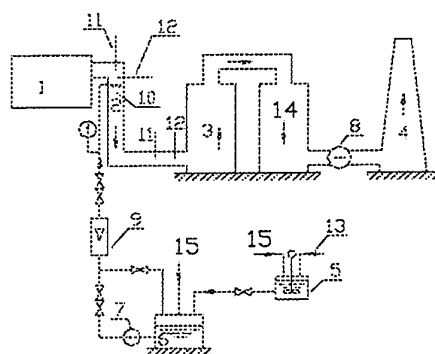


Fig.5. Schematic of alkali solution system and measuring points arrangement

(1—10t/h industrial boiler, 2—downstream flue duct, 3—wet fly-ash collector, 4—stack, 5—Alkali dissolution tank, 6—alkali solution storage tank, 7—alkali solution pump, 8—ID fan, 9—flowmeter for alkali solution, 10—pressure atomizer, 11—flue gas flue sampling system, 12—thermocouple, 13—alkali solution, 14—dewater tower, 15—water)

Flue gas velocity (noted as ω_y) in the duct was measured and the value was $\omega_y = 8.5 \text{ m/s}$ under the experimental conditions. The experimental data and calculated values of SO_2 concentration at the inlet and the outlet of boiler's downstream duct are listed in Table 1. The flow rate of spray solution was 0.3l/sec. Deviation between experimental data and calculated values is less than 5%.

When calculating desulfurization efficiency, the experimental data of SO_2 concentration at duct outlet should be converted into values on the basis of inlet excess air coefficient in FG to take into account the leakage of the duct. The experimental and calculated desulfurization efficiency curves under the condition of different alkaline solution pH values are compared in Fig. 6.

Table 1. Experimental Data Of SO₂ Concentration In The Duct Inlet And Outlet And Comparison With The Calculated Data

Sulfur content in the coal	S _{ar} (%)		0.75					1.05				
flow rate of spray solution	G (L/sec)		0.30					0.3				
Duct inlet	Oxygen level in the flue gas	O _{2,in} (%)	10.3					10.4				
	Excess air coefficient	α _{iv}	1.96					1.98				
	Flue Gas temperature	T _{in} (°C)	175					173				
	SO ₂ concentration	C _{SO₂,in} mg/Nm ³	869					1159				
	pH value of solution	pH	12.5	13.0	13.3	13.5	12.5	13.0	13.3	13.5	13.7	
Duct outlet	Oxygen level in the flue gas	O _{2,out} (%)	12.5	12.4	12.4	12.5	12.6	12.6	12.7	12.6	12.7	
	Excess air coefficient	α _{ovt}	2.47	2.46	2.46	2.47	2.5	2.5	2.53	2.5	2.53	
	Flue Gas temperature	T _{out} (°C)	95					94				
	SO ₂ concentration	C _{SO₂,out} mg/N ³	650	590	502	391	865	806	703	618	448	
	Converted into values on α _{in} basis	C' _{SO₂,out} mg/N ³	819	740	630	423	1092	1018	898	776	572	
Calculated SO ₂ concentration at duct outlet C _{SO₂,out} mg/N ³			834	758	648	518	1124	1049	940	813	600	
Deviation Δ%			1.76	2.37	2.81	4.99	2.83	3.03	4.49	4.44	4.59	

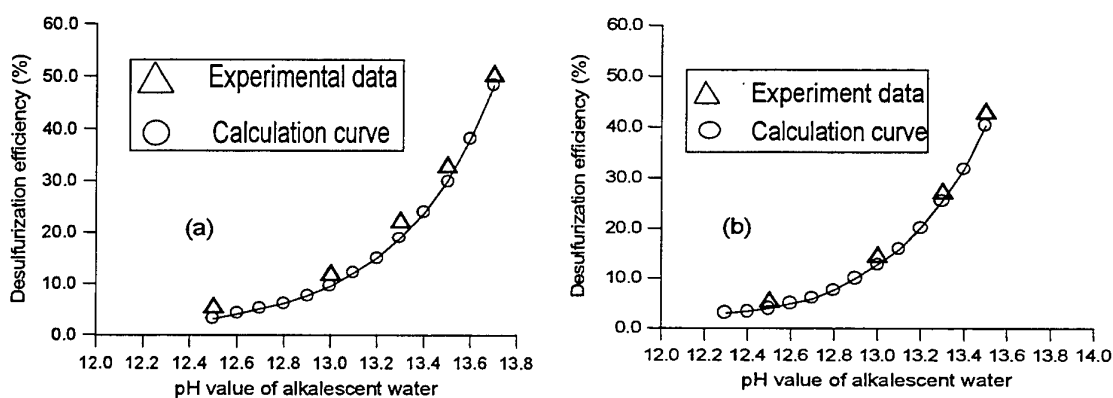


Fig.6. Comparison of experimental and calculated desulfurization efficiency under the condition of different alkalescent solution pH values (a) $S_{ar}=0.75\%$ (b) $S_{ar}=1.05\%$

6. CONCLUSIONS

1. Diameters of droplets formed as a result of atomization have a remarkable effect on desulfurization efficiency. In order to obtain a higher desulfurization efficiency, good atomization performance of the atomizer is requested and the mean diameter of droplets shall be less than 150 μ m.
2. Desulfurization efficiency can be improved by increasing spray flow rate. But excessive flow rate of spray will cause a heavy water entrainment in FG, thus a dehydration unit shall be installed before draught fan.
3. When the alkali solution spray is adopted for FG desulfurization, the pH value of alkali solution should be around 13.5 and the corresponding desulfurization efficiency is 35-40%.

REFERENCES

1. C.J. Geankoplis: "Mass Transport Phenomena". P.291, Holt Rinehart and Winston. Inc. New York. 1972.

EXPERIMENTAL STUDY ON COMBUSTION BEHAVIORS OF PETROLEUM COKE RESIDUAL OIL SLURRY

Xu Han, Zhenzhong Li, Jingwu Zhang

The State Engineering Technology Research Center of Combustion
of Power Plant, Shenyang, P.R.C, 110034

Email: npcclb@pub.sy.ln.cn; Fax: (086)-24-89347558

Xinyu Cao, Kefa Cen

Institute For Thermal Power Engineering
Zhejiang University, Hangzhou, P.R.C, 310027

Email: cws@sun.zju.edu.cn

Keywords: petroleum coke, slurry, combustion behavior

ABSTRACT. Petroleum coke residual oil slurry (POS) is a new kind of substitute fuel that is developed for burning oil boilers of power plant. It is a mixture of pulverized petroleum coke and residual oil. It can not only make good use of petroleum coke, but also save fuel oil in quality. The experimental study on combustion character of POS is done through a series of experiments on 0.4MW test facility in this paper. The experimental results show that POS with high concentration of 40% pulverized petroleum coke can be prepared, heated, transported and burned and the combustion efficiency is high. The parameters such as POS concentration, POS heating temperature, fuel load and oxygen content have high influences on combustion efficiency. In addition, discharge behaviors of pollutants such as NO_x, SO₂, and CO are also discussed when the POS is burned in the chamber.

1. INTRODUCTION

Petroleum coke is final after product of heavy oil that is deeply processed. The amount of petroleum coke has the increasing tendency to be used at home and abroad [1,2]. Whether petroleum coke can be used for fuel of boiler in power plant has becomes the key problem that is solved for increasing amount of petroleum coke. There are three ways when petroleum coke is used as the fuel of boiler for combustion at the present time. The first way is combustion of petroleum coke or mixing combustion of pulverized petroleum coke and coal [3]. The second way is mixing combustion of pulverized petroleum coke and heavy oil. The third way is combustion of slurry fuel that is a mixture of pulverized petroleum coke and residual oil [4]. Even though petroleum coke has a lot of advantages such as low price per heat value, low ash content and easy to grind, it will result in incomplete combustion and an unstable flame if burning petroleum coke directly in boilers because of its low percentage of volatile. In contrast to coal oil mixture (COM) and coal water slurry (CWS) that are used as oil substitute in many boilers, POS is convenient to be pipelined and be stored as fluid fuel. Furthermore, the heat value is higher than COM and CWS. Besides, the ash content in petroleum coke is very low, and it is unnecessary to change furnace bottom structure while retrofitting oil-fired boilers to POS-fired boilers.

The results of rheological experiments show that POS is a kind of non-Newtonian fluid and has high viscosity. Maximum concentration of petroleum coke and combustion characters for POS are different for different kinds of viscosity residual oil [5,6]. Therefore, it is necessary to study characters of the flow, heat transfer and combustion for POS. On the basis of investigations of the characters of preparation, rheology, flow, and heat transfer for POS, a series of experiments in a 0.4MW test facility are conducted to investigate the combustion characters of POS. Based on the experimental results, the various parameters that have influence on combustion and discharging behaviors are discussed.

2. EXPERIMENTAL SETUP

The experimental system for combustion of POS is shown in figure 1, which includes six parts: POS supply system, light oil igniting system, wind and gas system, cooling system, measurement system and chamber. The POS supply system consists of preparation apparatus, heating apparatus and transporting system. There is a screw mixer in the preparation apparatus, the mixer can disturb petroleum coke and residual oil fully and make the required POS. The heating system is a coiled-coil heater with mixing, which can heat POS a more

temperature before the chamber and satisfy the requirements for atomizing and transporting. The transporting system consists of a screw pump, which can overcome the flow resistance losses for pipe, pressure losses in heater and supply the pressure for atomizing. The measurement system includes color pyrometer, thermal-couple pyrometer, CYT oxygen scope, gas chromatograph, MSI flue gas analyzer and flue dust sample scope. In order to understand the combustion behaviors of POS, the measurements of temperature distribution for axial and radial directions, flue gas composition in chamber, flue gas composition and fly ash carbon content at the tail of gas flue are carried out. The different kinds of thermal parameters for the process of preparation, heating and transporting are also supervised and recorded so that stable operation of the system can be made in the experiment period.

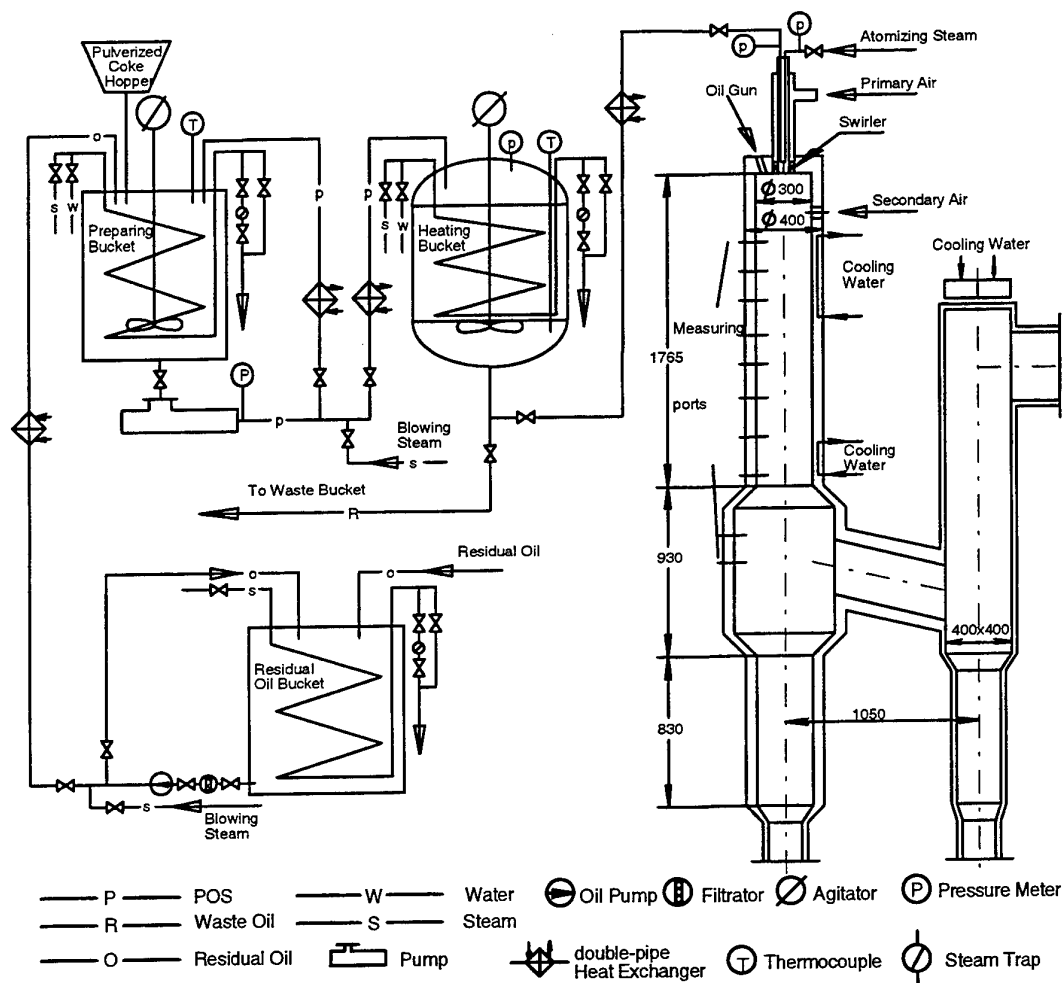


Fig.1 Experimental system of combustion

3. EXPERIMENTAL CONDITIONS

The fuels for experiments include the residual oil and POS with the 30% and 40% concentration of petroleum coke. The ultimate analysis and net calorific values of residual oil and petroleum coke are shown in Table 1. The SMD average diameter of pulverized petroleum coke is $45\mu\text{m}$, $R_{70}>84\%$, and the volatile matter of dry ash free for petroleum coke is 10.7%. Firstly, the comparing experiments between the POS with the concentration 40% of petroleum and residual oil was made. Then the experiments of different operating conditions (such as heating temperature of POS, load, and oxygen content, etc.) for POS with the concentration 40% of petroleum coke were also carried out.

Table 1. Fuel Character

Sample	Ultimate Analysis							
	W%	A%	C%	H%	N%	S%	O%	Q _{net ar} (J/g)
Petroleum coke (air dry)	/	0.04	86.13	11.6	0.71	0.74	0.82	43300 (high)
Residual oil (dry)	0.70	0.39	90.29	3.87	1.80	2.18	0.77	37267 (lower)

4. EXPERIMENTAL RESULTS

The efficiency of combustion is the major criterion that is used as evaluating combustion behavior for POS. The efficiency of combustion is determined by measuring unburnt CO loss q_3 and unburnt carbon loss q_4 . The experimental results show that combustion efficiency for residual oil is very high and as high as 99.8%. The unburnt carbon loss q_4 of POS is higher than that of residual oil because POS is difficult to be burnt out. Therefore, the combustion efficiency of POS is lower than that of residual oil. The experimental results also show that the combustion efficiency of POS for different operating conditions is between 92% and 97%, and the chemical heat loss q_3 of unburnt combustion is very low and is as low as 0.1% when POS is burnt. However, the mechanical heat loss q_4 of unburnt combustion is between 3.16% and 8.4%. From the analysis of the experimental results, it is necessary to investigate the parameters that have influence on q_4 and we can understand combustion behaviors of POS. It can be known from the results that the main factors influencing the efficiency are the coke concentration of POS, the excess air coefficient and the heating temperature of POS. The parameters that have influence on combustion efficiency and discharge behavior are discussed as followings.

4.1 Influence of Parameters on Combustion Efficiency

Fig.2 gives the influence of load on mechanical heat loss q_4 . As shown in Fig.2, unburnt carbon loss q_4 is increased slowly with the load of POS. The reason is that the particles of POS stays in chamber for longer time and can be burnt out more fully when the load is low. However, when the load is high, the particle of POS stays in chamber for shorter time and the combustion can not be burnt out fully.

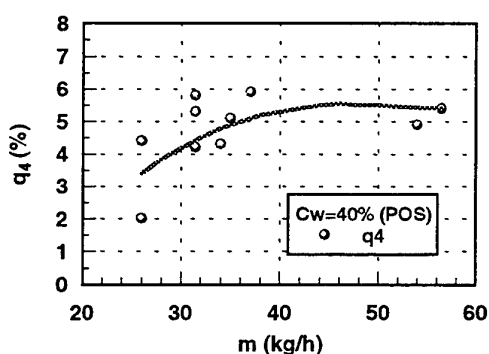


Fig.2 Variation of q_4 with the load

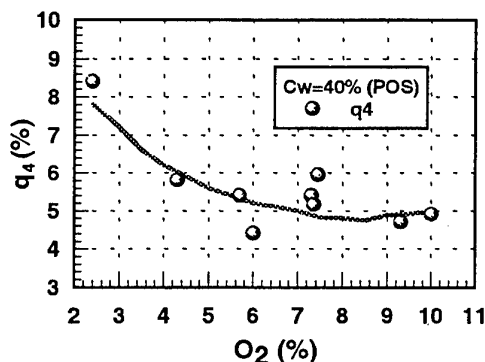


Fig.3 Influence of O_2 % on q_4

Fig.3 shows the variation of q_4 with oxygen content. It can be seen that as the oxygen content is increased, q_4 is decreased. When the oxygen content is lower than 6%, q_4 is decreased quickly with increase of oxygen content; when the oxygen content is larger than 6%, the oxygen content has no influence on q_4 . It can be obtained from the results that it is appropriate to control the oxygen content on 6% at the tail of gas flue, and the result is as close as burning coal and oil. This conclusion verifies that combustion behavior of POS is same as that of oil and coal. The effect of heating temperature for POS on q_4 is shown in Fig.4. It can be known that when heating

temperature is increased from 150 °C to 160 °C, mechanical heat loss of q_4 is decreased about 3%. The reason is that with the increase of the temperature, viscosity of POS is decreased and the performance of atomizing is improved. Therefore, 160 °C or more higher heating temperature for POS will be propitious to raising combustion efficiency.

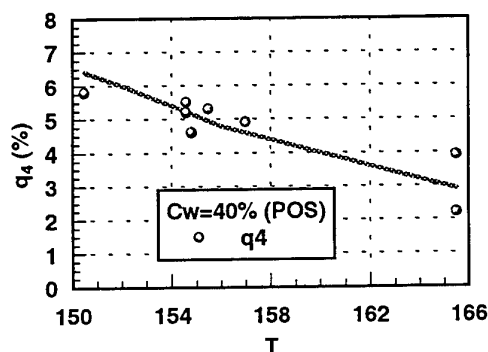


Fig.4 Influence of heating temperature on q_4

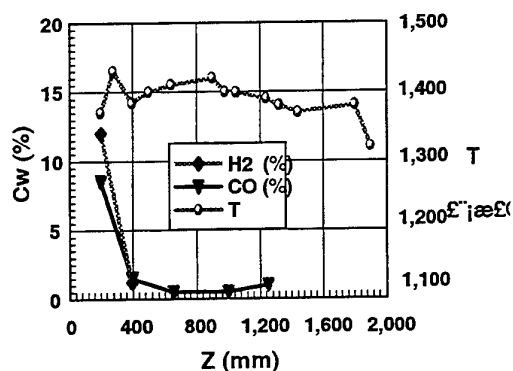


Fig.5 Distributions of axial temperature and flue compositions

4.2 Influence of Parameters on Process of Combustion in Chamber

Fig.5 gives the distributions of the axial temperature and the flue gas compositions in the chamber. It can be seen that the combustion process of POS can be divided into three phrases: preheating, kindling and homogenous combustion, burning of the petroleum coke residue. The axial temperature distribution in chamber is given in Fig.6 for POS with 40% concentration of petroleum coke and residual oil. It can be seen that the temperature of residual oil combustion is higher than that of POS in the former part of chamber; however, temperature of residual oil combustion is lower than that of POS in the latter part of chamber. The reason is that igniting and burning out of residual oil is quicker than POS and the combustion of residual oil is focus on former part of chamber. This results in higher temperature in the part of chamber. In the latter part of the chamber, residual oil has been burnt out, but the POS is still in combustion and this results in higher temperature for POS and lower temperature for residual oil. The axial temperature distribution in chamber is shown in Fig.7 for different loads of POS when other parameters such as oxygen content, heating temperature are kept same. Fig.7 shows that the temperature in chamber is increased with the load. As the POS is ignited and combusted in chamber, the difference of temperature at the first measuring location is increased from 50°C to 100°C at the end of the

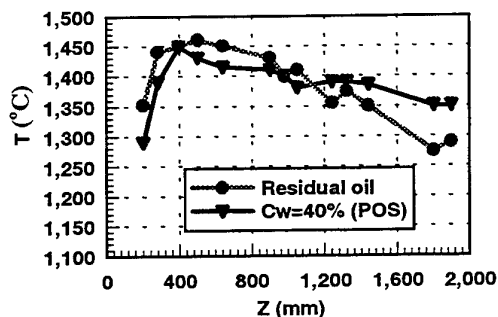


Fig.6 Comparison of axial temperature between POS and residual oil

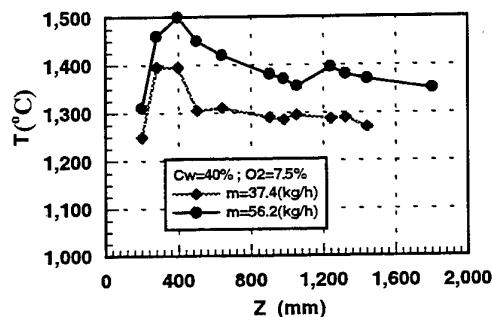


Fig.7 Influence of load on axial temperature

chamber. The maximum temperature for residual oil and POS in the chamber were 1397°C and 1496°C respectively. The experimental results show that the operating condition with higher load will be propitious to igniting and stable combustion in chamber. The variation of axial temperature distribution is given in Fig.8 for three different oxygen contents. It is seen that oxygen content has little effect on the temperature in chamber. As

the oxygen content is increased, both the maximum temperature and unitary temperature in the boiler are decreased. It is shown that when the oxygen content is larger than a specified value the temperature in the chamber will be decreased and this will have effect upon the igniting, combustion and formation of pollutants for POS and will have influence on thermal efficiency of boiler. The influence of third wind ration on the axial temperature distribution is given in Fig.9 when POS with 40% concentration of petroleum coke is burned in the chamber. It can be seen that the third wind ratio have effect on the combustion behavior of POS. When third wind ratio is 30%, the temperature in chamber before the location that is away from the burner 275mm is higher compared with the wind ratio 8%. At the locations from 275mm to 800mm, the temperature is lower compared with the wind ratio 8%. The temperatures in chamber are almost same for both two operating conditions after that location. It can be concluded from the experimental results that raising of third wind ratio can decrease the maximum temperature in chamber and this will be propitious to decreasing discharge of NO_x.

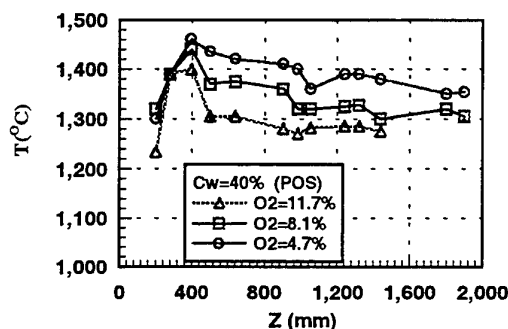


Fig.8 Effect of oxygen content on distribution of axial temperature

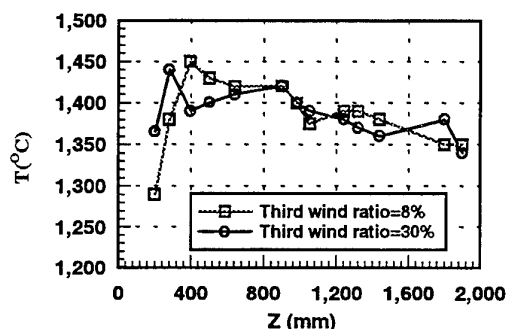


Fig.9 Influence of third wind ratio on distribution of axial temperature

4.3 Discharge Behaviors of Pollutants for POS Combustion

The pollution from the pollutants of fuel combustion has becomes more severe for the environments. The government has taken various methods to control the discharge of pollutants. It is essential to investigate the discharge behaviors of pollutants such as NO_x, SO₂ and CO when POS is burned. Fig.10 gives the variation of NO_x with the oxygen content when POS is burned in the chamber. It can be seen that the NO_x is increased with the increase of oxygen content. The NO_x becomes the highest value when the oxygen content is (10-13)%. When oxygen content is larger than 13%, the NO_x is decreased with the oxygen content. The experimental results also show that the discharge behaviors for POS with different concentration of petroleum coke are same as that of the pulverized coal and oil.

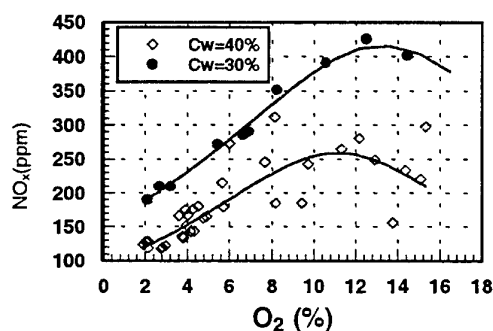


Fig.10 Influence of oxygen content on NO_x

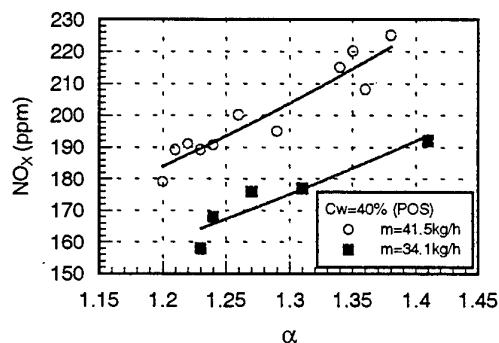


Fig.11 Variation of NO_x with excess air coefficient for different loads

Fig.11 gives the influence of the excess air coefficient on NO_x for the different loads. It is seen that NO_x is increased quickly when the load is increased from the 34.1kg/h to 41.5kg/h for given excess air coefficient. The reason is that the temperature of the combustion chamber is increased with the increase of the load and this

results in increase of NO_x.

Fig.12 show the variation of the SO₂ with oxygen content when 40% POS is burned in the combustion chamber. It can be seen that the oxygen content has no influence on SO₂. The experimental results also show that discharge of CO is mainly dependent on the oxygen content and has little relation with the temperature of the chamber and the load when POS is burned. Fig.13 gives the variation of CO with oxygen content for 30% and 40% POS. It can be known that when oxygen content is less than 3%, the discharge of CO is increased quickly and the discharge of CO is almost same when oxygen content is larger than 4%. Therefore, the discharge of CO can be lower if the oxygen content of the flue is controlled reasonably.

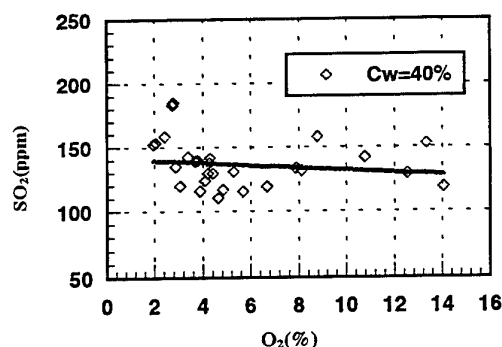


Fig.12 Relation between the O₂ and SO₂

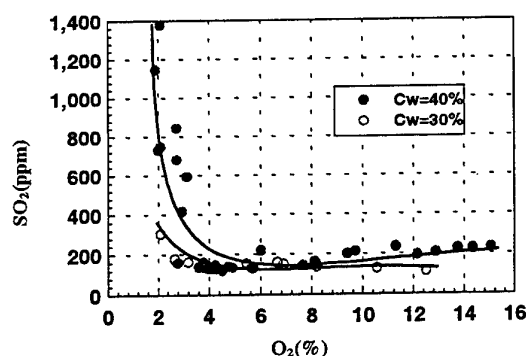


Fig.13 Influence of O₂ on CO

5. CONCLUSIONS

Experimental investigations were carried out to study the combustion behaviors of POS and residual oil through a series of experiments in the 0.4MW test facility. The experimental results show that POS with 40% concentration of petroleum coke can be in stable combustion. The parameters such as the concentration of POS, oxygen content, load and heating temperature of POS will have influence on the combustion efficiency of POS. The 40% of POS will be feasible for industrial application. The oxygen content should be controlled in specified ranges when POS is burned in chamber. In addition, the heating temperature of POS should be controlled in 160°C. The experimental data of preparation, transportation, heating, atomizing and combustion for POS will be basis on industrial amplifying design, and this will give the operating parameters for industrial experiments of POS.

REFERENCE

1. E.J. Swain, *Oil & Gas Journal*, v.6, pp1100-1105(1991).
2. Y.G. Zhou, *Boiler Technology(In Chinese)*, v.29, pp26-31(1998).
3. I.F. Abdulally, *Proceedings of International Conference on Fluidized Bed Combustion*, v2, pp753-762.
4. W.Y. Shou etc, *Proceedings of 22nd. International Technological Conference on Coal Utilization & Fuel Systems*, pp503-511, Florida, U.S.A(1997).
5. W.Y. Shou etc, *Proceedings of 22nd. International Technological Conference on Coal Utilization & Fuel Systems*, pp521-529, Florida, U.S.A(1997).
6. W.Y. Shou and X.Han, etc, *Proceedings of the International Conference on Energy and Environment*, pp364-370, edited by K.M.Chen, Shanghai, P.R.China(1998).

PRECESSION STROUHAL NUMBERS OF A SELF-EXCITED PRECESSING JET

J. Mi and G.J. Nathan

Department of Mechanical Engineering, University of Adelaide, SA 5005, Australia

Email: jemi@mecheng.adelaide.edu.au; Fax: +61 8 8303 4367

Keywords: Jet, precession, Strouhal number, nozzle

ABSTRACT. The self-excited precessing jet (PJ) nozzle has been the subject of research and development for industrial applications since the discovery of naturally occurring precession of a jet partially confined in a relatively large chamber [1]. In this paper we first report how the nozzle chamber length and the jet inlet Reynolds number influence the frequency (f_p) of jet precession and then seek a method of forming an appropriate Strouhal number of the precession which can effectively describe turbulent mixing in the flow downstream from the nozzle.

1. INTRODUCTION

Jet precession is the rotational motion of the entire jet with respect to an axis other than the jet's own centreline. Luxton & Nathan [1] discovered the naturally-occurring, or self-excited, precession of a jet within an axisymmetric nozzle chamber (see Fig. 1). This motion is a result of the breakdown of initial symmetry of jet due to some natural instability under specific conditions [2]. The precessing jet (PJ) flow has recently found application in industrial burners. Full-scale installations of commercial gas-firing PJ burner systems in rotary kilns used in the process industries have consistently demonstrated that NO_x emissions are reduced by typically 50% with fuel savings of about 5%, relative to the flames from the burners they replaced, e.g. [3-5].

The PJ burner technology has been under large-scale development since 1990 through a collaborative research and development program between the University of Adelaide, Australia, and Fuel & Combustion Technology International. The ongoing program includes work on the flow inside the nozzle chamber which generates the precession and outside the chamber in the region where combustion occurs [6,7]. In addition, a parallel investigation of the effects of precession on the mixing characteristics of a round jet whose precession is driven mechanically under controlled conditions [8-11]. A key finding of this work is that the Strouhal number of precession and the jet exit angle is a controlling parameter of the flow mixing. However, it is not appropriate to relate mixing characteristics of the flow which emerges from the mechanical nozzle to those from the fluidic nozzle. This is mainly

due to the lack of a proper definition of the precession Strouhal number for the latter case. The reason for the lack is that the effect of the fluidic nozzle geometry on the precession frequency has yet to be thoroughly investigated and also that the Strouhal numbers previously defined (e.g. [2,7]) are based only on the jet inlet conditions and the chamber dimensions which cannot describe the flow downstream from the chamber outlet.

The present work aims to address the above lack. For this purpose, we will first report how the chamber length and the jet inlet Reynolds number influence the frequency (f_p) of jet precession. Then, the precession Strouhal number in conjunction with the outlet conditions of the chamber will be sought for the study of turbulent mixing characteristics in the flow downstream from the nozzle. This work is an onset of the research program which is proposed to investigate both turbulent mixing and flame characteristics of the self-excited precessing jet.

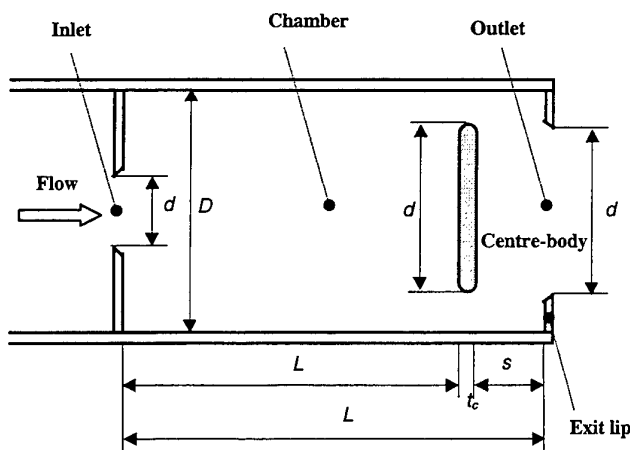


Fig. 1. Sketch of a PJ nozzle with relevant notations and definitions

2. EXPERIMENTAL DETAILS

The experimental facility includes a plenum chamber to which various nozzles can be attached (see Nathan et al. [2] for more details). The plenum is supplied with filtered and compressed air at pressures of up to 500 kPa at the room temperature. The jet exit velocity can be varied by changing the plenum pressure. The configuration of the PJ nozzle is shown in Fig. 1. In the figure, d_1 represents the inlet diameter, D the chamber diameter, L the chamber length, L_c the distance between the inlet exit and the centre-body, d_c the centre-body diameter, s_c the distance between the centre-body and the chamber exit lip, and d_2 the chamber outlet diameter. Three different-sized PJ nozzles were used for the study; their chamber diameters are 13.4 mm, 26.6 mm and 47.5 mm, respectively. The dimensions d_1 , L , L_c and the Reynolds number $Re_1 \equiv U_1 d_1 / \nu$ can be varied (within limit) in each nozzle. The precession frequency f_p was measured using a $5\mu\text{m}$ tungsten wire positioned near the chamber outlet. The wire was operated by in-house constant temperature circuit with an overheat ratio of 1.5. The signal from the circuit was offset, amplified and then taken by a spectrum analyzer (HP3582A). For some cases, the signals were digitised using a 16 channel, 12-bit A/D converter on a personal computer.

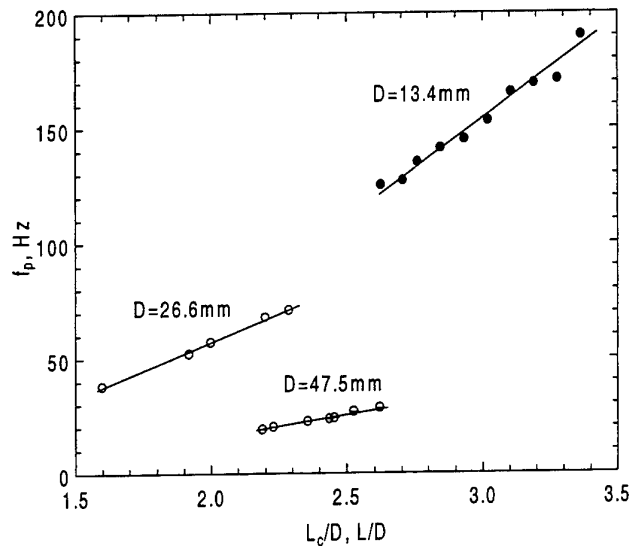


Fig. 2. Dependence of f_p on L or L_c . ●: $D = 13.4$ mm, $d_1/D \approx 0.19$, $d_2/D \approx 0.86$ & $Re_1 \approx 25000$; ○: 47.5 mm, 0.194 , 1 & 65000 ; ○: 26.6 mm, 0.19 , 0.82 , & 75000 .

3. EFFECTS OF CHAMBER LENGTH AND REYNOLDS NUMBER

Fig. 2 shows the dependence of the precession frequency f_p on $L^* = L_c/D$ (with a centre-body) and $L^* = L/D$ (without a centre-body). Experimental conditions for the measurements are given in the figure caption. Clearly, f_p increases linearly as L^* increases over a certain range of L^* . This feature applies to all PJ nozzles tested here and elsewhere and is thus generic.

Fig. 3 shows the dependence of f_p on the Reynolds number Re_1 , where Re_1 was varied by changing the inlet jet velocity U_1 for each nozzle. The experimental conditions are given in the figure caption. For each PJ nozzle, f_p increases with Re_1 or U_1 . As viewed from the six data sets, this variation appears linear and may be approximated by $f_p = C_0 + C_1 Re_1$, where C_0 and C_1 are experimental constants. These constants, as indicated in Fig. 3, depend strongly on the jet inlet geometry and, especially, the chamber size (D). That is, they are different from nozzle to nozzle. Interestingly, when the 47.5 mm nozzle was with a smooth contraction inlet but without a centre-body and the outlet lip, the best-fitted line of the data points approaches to the origin of the coordinates, i.e. $C_0 \approx 0$. If it is the case for all PJ nozzles without a centre-body and lips, then the scaled precession frequency may form a constant Strouhal number defined by $St \equiv f_p l_o / U_1$ when an appropriate length scale l_o is chosen.

4. PREVIOUS DEFINITIONS FOR St AND EXPERIMENTAL DATA

Nathan & Luxton [6] defined the Strouhal number (St_i) of jet precession based on the conditions at the inlet to chamber. They chose the height of the expansion step, $(D - d_1)/2$, and the inlet jet initial velocity U_1 , for configurations with a narrow range of chamber lengths, i.e.

$$St_i \equiv \frac{f_p \frac{1}{2}(D - d_1)}{U_1} \quad (1)$$

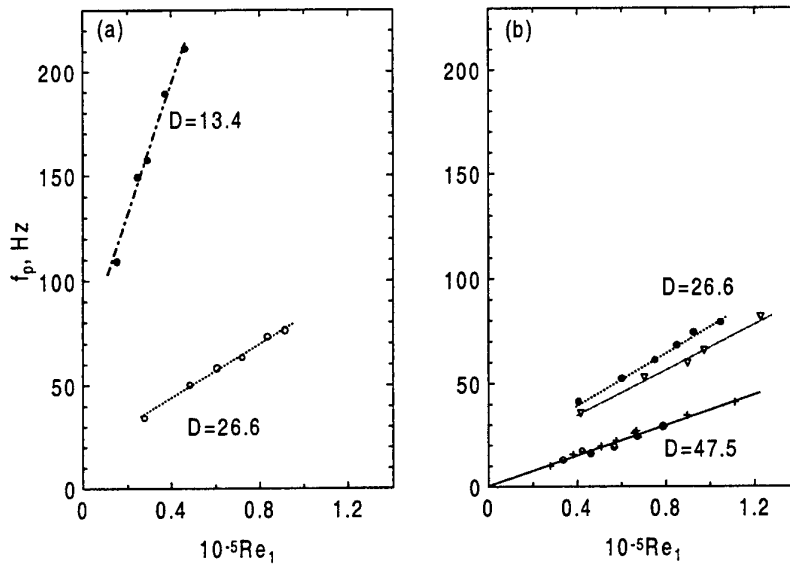


Fig. 3. Effect of Re_1 on f_p . (a) Orifice-type inlet ($L_c/D = 2.2$): \bullet , $D = 13.4$ mm; \circ , 26.6 mm. (b) Smooth contraction inlet: \bullet ($L_c/D = 2.2$), 26.6 mm and with inlet-lip; ∇ ($L_c/D = 2.2$), 26.6 mm and no inlet-lip; ψ ($L/D = 2.32$) and $+$ ($L/D = 2.49$), 47.5 mm and no lips.

Transposing the f_p data from Fig. 3, we obtained six data sets for the Strouhal number St_i against the Reynolds number Re_1 , which are plotted in Fig. 4. It is demonstrated that, for the 47.5 mm nozzle with no centre-body and no exit-lip, St_i is nearly constant (≈ 0.0045) and independent of Re_1 . By comparison, it decays slowly as Re_1 increases for the other two nozzles with a centre-body and the exit-lip. Further, since f_p depends strongly on L^* (Fig. 2), the St defined by (1) should be a function of L^* . This is confirmed in Fig. 5. Surprisingly, however, the data from the different nozzles lie well along the line $St = 0.0037L^* - 0.0046$.

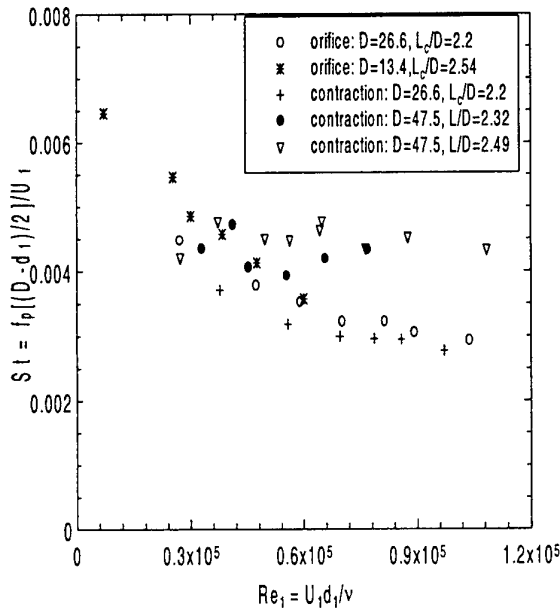


Fig. 4. Dependence of the Strouhal number St_i on Re_1 .

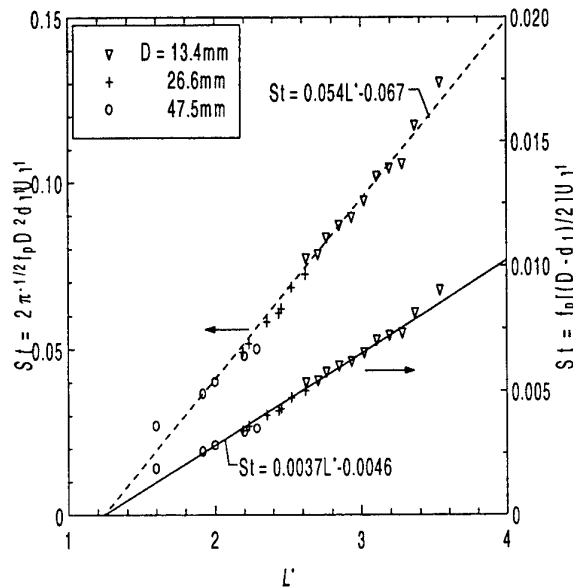


Fig. 5. Dependence of St_i on L^* , defined by Eq. (1) and Eq. (3).

Hill et al. [7] observed a large scattering of the values of the precession Strouhal number which is based on the characteristic dimensions $l_o = (D-d_1)/2$ [i.e. definition (1)], $l_o = d_1$ and $l_o = D$ for several different PJ flows fully confined within long ducts. This observation led them to seek other more appropriate length scales for the estimate of St. They used the initial momentum M of jet as the basis for the scaling of f_p , defining

$$St_i \equiv \frac{f_p \sqrt{\rho} D^2}{\sqrt{M}} \quad (2)$$

Definition (2) provided a good collapse of the St_i data obtained from the fully confined PJ flows. It should be noted that the length (L) of those very long ducts is no longer a factor influencing f_p of the jet, implying that St_i is not dependent on L . However, this scaling has yet to be checked for the PJ from a fluidic nozzle sketched in Fig. 1, for which L and/or L_c are critical in determining f_p . Note that the definition (2) is equivalent to

$$St_i \equiv \frac{f_p d_1}{U_1} \left(\frac{D}{d_1} \right)^2 \sqrt{\frac{4}{\pi}} \quad (3)$$

since $M = \rho U_1^2 (\pi d_1^2 / 4)$. The data for this St_i are also presented in Fig. 5. As expected, similar to the St_i defined by (1), this St_i also has strong dependence on the effective chamber length.

5. PROPOSED DEFINITIONS OF St FOR DOWNSTREAM TURBULENT MIXING

The previous definitions of the precession Strouhal number may be appropriate for the study on the flow within the chamber. However, they are inappropriate for characterising the turbulent mixing of the PJ flow downstream from the nozzle since they do not use the local characteristic length scale (l_2) and velocity scale (U_2) at the outlet plane of the nozzle chamber (see Fig. 6). To study mixing characteristics of the PJ, the "external" Strouhal number of precession should be defined, see Fig. 6, as

$$St_e \equiv \frac{f_p l_2}{U_2} \quad (4)$$

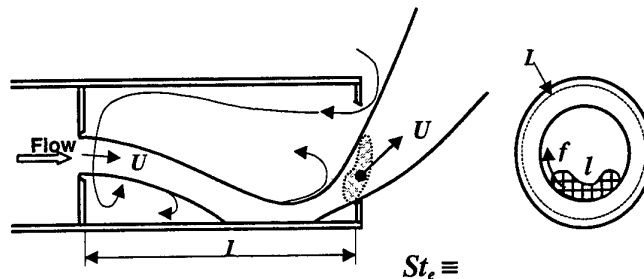


Fig. 6: Proposed definition of the precession Strouhal number along with a sketch

However, the scales l_2 and U_2 are difficult to measure by experiment. Under this situation, we will seek to advance understanding by exploring analytical expressions of (4).

For a free jet, with the initial diameter d_1 and velocity U_1 , the jet half-width $R_{1/2}$ and the centreline mean velocity U_c in the flow region sufficiently far downstream from the exit are expected to satisfy the relations

$$R_{1/2} \sim \left(\frac{L}{d_1} \right) d_1 \quad \text{and} \quad U_c \sim U_1 \left(\frac{L}{d_1} \right)^{-1}$$

where L is the distance from the virtual origin. When the jet is initially confined in a chamber over the distance L , these relations will be modified. Accordingly, it is logic by the dimensional analysis to propose that, for the PJ shown in Fig. 6,

$$l_2 \sim \left(\frac{L}{d_1} \right)^{n_1} d_1 \quad (5)$$

and

$$U_2 \sim U_1 \left(\frac{L}{d_1} \right)^{-n_2} \quad (6)$$

With (5) and (6), we can specify the definition (4) by

$$St_e = \frac{f_p d_1}{U_1} \left(\frac{L}{d_1} \right)^{n_1 + n_2} \quad (7)$$

Based on the fact that, in the far field, a confined jet develops downstream at a lower spreading rate and a higher decaying rate than does a free jet, we expect that the exponents $n_1 < 1$ and $n_2 > 1$. It follows that the approximation $(n_1 + n_2) \approx 2$ may be reasonable, although it should be determined by experiment. This results in the following expression

$$St_e = \frac{f_p d_1}{U_1} \left(\frac{L}{d_1} \right)^2 \quad (8)$$

Eq. (8) implies that the St_e depends strongly on the chamber length (L) of PJ nozzles. The experimental result of this St_e against L is shown in Fig. 7, which is transposed from the f_p data presented in Fig. 2.

6. DISCUSSION

We have examined the effect of the nozzle chamber length (L) and the jet inlet Reynolds number (Re_1) or velocity (U_1) on the jet precession frequency (f_p). It is shown that f_p increases approximately linearly as U_1 or $L^* = L/D$ (no centre-body) or $L^* = L_c/D$ (with a centre-body) increases. On the basis of this information, previous definitions of the precession Strouhal number, i.e. (1) and (3), have been tested. As shown in Fig. 5, there is strong dependence of those Strouhal numbers on L^* . Since definitions (1) and (3) for St_i are not appropriate for the study of turbulent mixing downstream from the nozzle, we have scaled the precession frequency f_p in a different way and formed the Strouhal number St_e defined by (7) and (8).

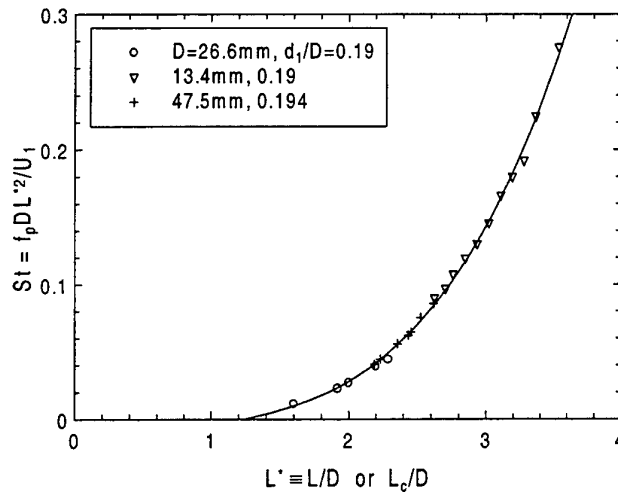


Fig. 7: The L^* -dependence of St_e defined by (8).

Using a mechanical precessing jet (MPJ), Schneider [8] and Mi et al. [9,10] have clarified that the precession Strouhal number

St is a controlling factor in determining the downstream development and mixing characteristics of the mechanical precessing jet (MPJ). In the regime of high St (when $St \geq$ the critical value St_{cr}), the MPJ has significantly different features from those for $St < St_{cr}$. This difference is also reflected in the MPJ flame [12]. However, the similar studies have yet to be conducted on the naturally precessing jet, due to the lack of a definition of St_e in the past. With the definition (8) of St_e , we have planned to investigate the effects of St_e and other parameters such as Reynolds number on turbulent mixing characteristics in the PJ flow and on the PJ

flame characteristics. Fig. 7 suggests that this St_e can be varied from 0.01 to 0.15 by changing the chamber length between $1.6D$ and $3.0D$.

ACKNOWLEDGEMENTS

The collaborative support of the Australian Research Council and Fuel & Combustion Technology Pty Ltd is gratefully acknowledged. Thanks also go to Dr G. Newbold and Mr. S.J. Hill for their helpful comments.

REFERENCES

1. R. E. Luxton, G. J. Nathan, and Luminis Pty Ltd, "Mixing fluids", *Int. Patent App. No* PCT/AU88/0014, Australian Patent Office (Priority date: April 1987).
2. G. J. Nathan, S.J. Hill, and R. E. Luxton, *J. Fluid Mech.*, v.370, 347-380 (1998).
3. C. G. Manias and G. J. Nathan, *World Cement*, March, 4-11 (1992).
4. C. G. Manias and G. J. Nathan, "Low NO_x clinker production", *World Cement*, May, (1994).
5. C. G. Manias, G. J. Nathan and D. S. Rapson, "Gyro-Therm: a new efficient low NO_x gas burner for product quality improvement" *ASEAN Federation of Cement Manufacturers*, Kuala Lumpur, April, 1995.
6. G. J. Nathan and R. E. Luxton, "Mixing Enhancement by a self-exciting, asymmetric precessing flow-field", *4th (Int.) Symposium on Transport Phenomena*, July 14-18, 1991, Sydney, Australia.
7. S. J. Hill, G. J. Nathan and R. E. Luxton, "Precession in axisymmetric confined jets", *Proceedings of the 12th Australasian Fluid Mechanics Conference*, v.1, pp.135-138, edited by R.W. Bilger, Sydney, Australia (1995).
8. G.M. Schneider, "Structures and turbulence characteristics in a precessing jet flow", *PhD Thesis*, Department of Mechanical Engineering, The University of Adelaide, Australia, 1996.
9. J. Mi, G.J. Nathan and R.E. Luxton, "Frequency spectra of turbulence in a precessing jet", *Proceedings of the 7th Asian Congress of Fluid Mechanics*, v. 2, pp.437-440, Allied Publishers Ltd, Chennai, India (1997).
10. J. Mi, R.E. Luxton and G.J. Nathan, "The mean velocity field of a precessing jet", *Proceedings of the 13th Australasian Fluid Mechanics Conference*, v.1, pp. 623-626, edited by M.C. Thompson and K. Hourigan, Melbourne, Australia (1998).
11. D.S. Nobes, "The generation of large-scale structures by jet precession", *PhD Thesis*, Department of Mechanical Engineering, The University of Adelaide, Australia, 1997.
12. G.J. Nathan, S.R. Turns and R.V. Bandaru, *Combustion Science & Technology*, v.112, pp.211-230 (1996).

RESEARCH METHOD OF RELATIVE CONTRIBUTION OF VOLATILE-N AND CHAR-N TO N₂O FORMATION BASED ON COAL / CHAR RESPECTIVE COMBUSTION EXPERIMENT: DISCUSSION ON EXPERIMENT AND CALCULATION

Liu Yu Li Qingyu Zhou Jimin Li Guanhua

Henan Electric Power Research Institute

No. 85 South Songshan Road, Zhengzhou 450052, P. R. China

Email: zxndi@public.zz.ha.cn; Fax: (0371) -7905513

Keywords: coal combustion, fluidized-bed, nitrous oxide (N₂O), volatile, char, relative contribution

ABSTRACT. During fluidized-bed combustion of coal, nitrogen in coal (coal-N) is divided into volatile nitrogen (volatile-N) and char nitrogen (char-N), which both make a contribution to N₂O formation. "Coal / char respective combustion experiment" is one of methods researching the relative contribution of volatile-N and char-N. Its main points are that two combustion experiments for coal and char prepared from the same coal are respectively performed to determine the contribution of coal-N and char-N, and the difference in contribution between both of them is taken as that of volatile-N, then the relative contribution is calculated. In this paper, the method is discussed in experimental technique and calculation of relative contribution. The char's properties and the distribution of coal-N between volatile-N and char-N can strongly be influenced by devolatilization temperature. The percentage of coal-N retained in char can decrease with increasing devolatilization temperature. Therefore, the char prepared at one given temperature is different from those prepared at other ones which are lower or higher than the given one. So the former char cannot take the place of the latter chars to be used in combustion experiment at other temperatures, and the temperature for char preparation should be the same as that for coal / char combustion experiment. The equipment for char preparation has notable influence on char's characteristics. Hence, the equipment for coal / char combustion should exactly be the same one as that for char preparation. It is demonstrated that the difference between percent conversion of coal-N and that of char-N could not be regarded as that of volatile-N. For the cases in which more than 90% of N in coal remains in char, the converted amount and percent conversion of N in char formed during coal combustion are larger than those of N in char prepared by coal pyrolysis and the latter char cannot be representative of the former one.

1. INTRODUCTION

N₂O (nitrous oxide) is a kind of atmospheric pollutant which can both enhance the greenhouse effect and deplete the ozone layer. During coal combustion, especially fluidized-bed combustion of coal at lower temperature of 800~900°C, a large amount of N₂O can be emitted. Hence, much research work [1-3] on N₂O emission from fluidized bed (FB) have been undertaken, and the source and formation-decomposition mechanism of N₂O as well as various factors influencing the amount of N₂O formed are understood to a large extent.

Research on mechanism of N₂O formation during fluidized-bed combustion of coal showed that N₂O is formed from nitrogen (N) in coal through a series of chemical reactions. During coal combustion, the evolution and combustion of volatiles in coal occur first, and then the char burns. Part of nitrogen in coal (coal-N) is released as volatile (volatile-N) and the rest remain in char (char-N). N₂O can be produced from both volatile-N (HCN and NH₃) through homogeneous gas-phase reactions and char-N through heterogeneous gas-solid reactions. Hence, both volatile-N and char-N make a contribution to N₂O formation. Some researchers [4-8] thought that most of N₂O are produced from volatile-N, but others [9, 10] thought that the contribution of char-N is larger than that of volatile-N. In these literatures, there are no unified experimental and assessment methods. Each researcher carried out experiment and data processing using the methods which they thought to be reasonable ones. According to experimental technique, the methods used in available literatures can be classified as two types: "coal / char respective combustion experiment" and "batch combustion experiment". In the former method, two combustion experiments for coal and char prepared from the same coal are respectively carried out to determine the contributions of coal-N and char-N, and the difference between both of them is taken as that of volatile-N, then the relative contribution is calculated and assessed. This method is used in literatures [4-7, 10]. In the latter one, a batch of coal is once only fed into a bed for combustion experiment and an appropriate indication is chosen to distinguish the volatile-burning stage from char-burning one. The contribution from each stage to N₂O formation

is used for assessing the relative contribution of volatile-N and char-N. This method is used in literatures [8, 9]. Pels *et al* [6] thought that interaction between heterogeneous and gas-phase pathway are unlikely and conversions of volatile-N and char-N can be assumed to be independent processes. Therefore coal / char respective combustion experiment is not unreasonable. Tullin *et al* [9] thought that in coal combustion experiment with continuous coal feed, the volatile and char reactions will simultaneously occur and secondary reactions between volatile and char can be expected. Hayhurst and Lawrence [8] doubted that whether the char prepared by coal pyrolysis can truly be representative of that formed during coal combustion. Thus it can be seen that there are different viewpoints about the coal / char respective experiment method. But analysis and discussion on this method has not been found in available literatures so far.

Research on the relative contribution of volatile-N and char-N to N_2O formation is valuable for understanding N_2O formation mechanism and developing effective technology to decrease the N_2O emission, while reasonable experimental and calculating method is very important for assessing correctly the relative contribution. The purpose of this paper is to discuss the method in several aspects including experimental technique and calculation of relative contribution with the help of experimental data, by way of calculation and demonstration.

2. MAIN POINTS OF THE METHOD

The main points of coal / char respective experiment include: char preparation, coal / char combustion experiments and assessment of relative contribution.

Char Preparation

Original coal is fed into pyrolysis equipment and is heated for devolatilization at one given temperature and in inert atmosphere (N_2 or Ar) for a given time with the result that char is prepared. Moreover, the char is thought to be able to represent that formed during coal combustion.

Combustion Experiment

Combustion experiments for coal and char are performed respectively. Coal or char is continuously fed into fluidized-bed combustor (FBC) and combustion experiments are performed at some temperature points over a wide range of temperature. The effluent gases are sampled and analyzed to determine the amounts of N_2O formed during coal or char combustion. The results of char combustion experiment is thought to be able to reflect the contribution of char formed during coal combustion.

Assessment of Relative Contribution

Assessment can be done through either comparison between concentrations of N_2O produced from coal and char combustion [7] or calculation using data of percent conversions of coal-N and char-N [4, 5, 6].

Assessment through comparison between N_2O concentrations. Concentrations (ppm) of N_2O formed from coal / char combustion experiments are measured respectively. The difference between the two concentrations is regarded as that from volatile-N. The ratio (%) of concentration of N_2O during char combustion to that during coal combustion is thought to be the relative contribution of char-N. Similarly, the ratio of concentration of N_2O from volatile-N to that during coal combustion is taken as the relative contribution of volatile-N.

Assessment through calculation using percent conversions. The percent conversion of coal-N or char-N, i.e. the ratio (%) of amount of nitrogen converted to N_2O to that of nitrogen in coal or char, is calculated respectively. The difference between the two percent conversions is regarded as the percent conversion of volatile-N and is calculated using Eq.(1):

$$F_v = f_{\text{coal}} - f_c \quad (1)$$

where f_v is the percent conversion of volatile-N (%), f_{coal} is the percent conversion of coal-N (%), and f_c is the percent conversion of char-N (%). The relative contribution of char-N and volatile-N can respectively be calculated using Eqs (2) and (3):

$$C_{\text{char}} = f_c / f_{\text{coal}} \quad (2)$$

$$C_{vm} = f_v / f_{coal} \quad (3)$$

where C_{char} and C_{vm} are the relative contribution of char-N and volatile-N (%), respectively.

Substitute Eq.(1) into Eq.(3), we can obtain

$$C_{vm} = (f_{coal} - f_c) / f_{coal} = 1 - f_c / f_{coal} = 1 - C_{char} \quad (4)$$

Eqs(5) and (6) are used in literature [10] for calculating relative contribution :

$$C_{char} = \frac{f_c \cdot N_{char}}{f_{coal} \cdot N_{coal}} \quad (5)$$

$$C_{vm} = 1 - C_{char} \quad (6)$$

where N_{coal} and N_{char} are nitrogen content in coal and in char, but dimension of them are not given in literature [10].

3. DISCUSSION ON THE METHOD

On Experimental Technique

On experimental temperature. It can be noticed from main points mentioned-above that in char preparation the process of coal pyrolysis (devolatilization) is conducted at one given temperature, but combustion experiments for coal and char are performed over a wide range of temperature. The temperature values of char preparation and coal / char combustion experiments quoted from some literatures are presented in Table 1. It can be found from Table 1 that temperatures in char preparation are much different from those in combustion experiments and the largest difference is as high as 400K [7].

Table 1. Experimental Temperatures and Equipments for Char Preparation and Coal / Char Combustion

literature	temperature [K]		equipment	
	char preparation	coal / char combustion	char preparation	coal / char combustion
[4]	1073	923~1273	FBC	FBC
[5]	1148	1048~1148	Φ30cm FB	Φ10cm FB
[6]	1073	973~1273	FB pyrolyser	FBC
	1173	973~1273	tube furnace	FBC
[7]	1373	973~1173	FB reactor	FBC
[10]	1123	973~1273	FBC	FBC

Research results [7, 11, 12] in recent years indicated that temperature in char preparation has significant influence on N content in char, the distribution of coal-N between volatile-N and char-N as well as amount of N_2O formed from char. Hayhurst and Lawrence [12] found that the temperature of fluidized-bed is one parameter with the largest effect on the amounts of N in the resulting char. The higher the temperature of bed, the more the percent of coal-N released into the volatile. It is also observed by Gulyurtlu *et al* [7] that for three kinds of coal with different volatile content, the percent of coal-N remaining in char after devolatilization will decrease with increasing the devolatilization temperature, as shown in Fig. 1. In addition, the amount of N_2O formed has a close relation with N content in fuel and will reduce with decrease of N content [13]. Amounts of N_2O formed from chars which are prepared from the same coal at different char preparation temperatures are presented in Table 2. It can be seen from the Table that for the same kind of coal, the higher the char preparation temperature, the less the amount of N_2O formed from the char. The reason is that the higher the char preparation temperature, the less the coal-N retained in char; and the lower amount of char-N can result in the less amount of N_2O from char combustion. A change of amount of N_2O formed means that of amount of char-N converted to N_2O .

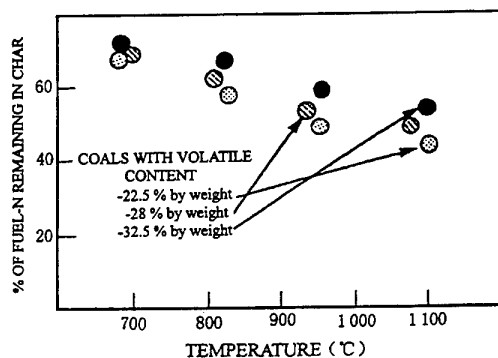


Fig. 1 Effect of devolatilization temperature on proportion of fuel-N. remaining in char prepared from different coal

In addition, other properties of char, such as porosity, surface area, reactivity as well as ability to adsorb and decompose N_2O , can also differ due to difference of char preparation temperature and can influence the conversion of char-N and formation of N_2O .

For this reason, the char prepared at one given temperature cannot be representative of those prepared at other ones which are lower or higher than the given one. When the char made at the given temperature is combusted at other ones the results of char combustion experiment cannot correctly reflect the contribution of char at these temperatures. Only upon condition that three temperatures for char preparation, char combustion and coal combustion are the same, the char prepared can be comparable to that formed during coal combustion and the char's contribution to N_2O formation at each experimental temperature can reasonably be reflected. Otherwise, not only can diversity in char's properties and amount of N_2O formed be caused, but also the amount of char-N converted to N_2O and assessment result of char's contribution can be influenced.

On experimental equipment. From Table 1 it can be found that in some research work the equipments for char preparation are not the same one as that for coal/char combustion experiment and not even the same type. Research results [14] indicated that for the chars prepared from the same coal type and at the same pyrolysis temperature but in different experimental equipments, there are large difference in their properties and amounts of N_2O formed when the chars are burnt. Table 3 presents the main properties of two chars prepared from the same coal as well as amounts of N_2O from the two char's combustion experiments, in which the combustion temperature was 1133K, the same as char preparation one. It can be seen from Table 3 that two chars prepared from two

Table 2. Amounts of N_2O Formed from Chars Prepared at Different Temperatures

char preparation temperature (°C)	amounts of N_2O formed during combustion at 800°C and 900°C (ppm)	
	800°C	900°C
900	68	34
1000	59	31
1100	52	27
1300	41	24

* Adapted from data in literature [7].

Table 3. Main Properties of Two Kinds of Chars Prepared in Two Different Equipments and Amounts of N_2O Formed

coal/char	char preparation equipment	Main analysis result (wt%)			combustion equipment	mounts of N_2O formed (ppm)
		N	VM	FC		
original coal		1.159	17.48	71.47		
char A	semi-industrial FBC	1.2	6.4	80.3	laboratory-scale FBC	67
char B	laboratory-scale FBC	0.94	4.8	81.9	laboratory-scale FBC	46

different fluidized-bed equipments were significantly different in contents of N, volatile matter (VM) and fixed carbon (FC) as well as amounts of N_2O formed. For char A and char B, the relative derivation of N-and VM-contents and amounts of N_2O formed were 22%, 25% and 46%, respectively. These results revealed that if char was prepared in different equipments, there must be some diversity in devolatilization process of coal, which can cause the diversity in char's properties. Still further, the conversion of char-N and amount of N_2O formed would be influenced due to the diversity of char's properties. Hence, the equipment for char preparation should exactly be the

same one as that for coal/char combustion experiment. Only in this way, both the devolatilization process of coal during coal pyrolysis (char preparation) and the volatile evolution process during coal combustion could conduct under the same equipment conditions and the experimental results are really acceptable.

On Assessment Method of Relative Contribution

On comparison between concentrations. This method deals only with the concentrations (ppm) of N_2O in effluent gas without relating those with N contents in coal and char, but N_2O concentration is related to amount of N fed into the bed. Under otherwise equal conditions, the more the amount of coal-N or char-N fed into the bed, the higher the concentration of N_2O formed. Unless the amount of char-N fed with char in char combustion experiment is exactly equal to that in char formed during coal combustion, the concentration of N_2O formed from coal combustion have no relation to that formed from char combustion. Certainly, the difference between the two concentrations cannot be representative of contribution of volatile.

On calculation using percent conversions. In this method, the percent conversions of coal-N and char-N are respectively drawn from two combustion experiments, and the percent conversion of volatile-N is calculated by a difference using Eq.(1). But it is not demonstrated in available literatures so far that whether the difference can be representative of percent conversion of volatile-N and whether the char prepared separately by coal pyrolysis can be representative of that formed during coal combustion. These problems would be discussed here.

During coal combustion, N in coal is divided into volatile-N and char-N. we take symbol N_{coal} for expressing the amount of N in 100 g of coal, and F_v and F_c for expressing the distribution coefficients of coal-N between volatile-N and char-N, i. e. the percentage of coal-N released as volatile (volatile-N/coal-N) and that retained in char (char-N/coal-N), moreover, $F_v + F_c = 100\%$, then the amounts of volatile-N and char-N can respectively be expressed as:

$$N_v = N_{coal} F_v \quad (7)$$

$$N_c = N_{coal} F_c \quad (8)$$

where N_v is amount of volatile-N (g), N_c is amount of char-N (g).

With the help of the percent conversions, the amounts of coal-, char- and volatile-N converted to N_2O can be calculated from:

$$N_{coal}' = N_{coal} f_{coal} \quad (9)$$

$$N_v' = N_v f_v \quad (10)$$

$$N_c' = N_c f_c \quad (11)$$

where N_{coal}' is amount of coal-N converted (g), N_v' is amount of volatile-N converted (g), and N_c' is amount of char-N converted (g).

If the char prepared from coal by pyrolysis could be representative of that formed during coal combustion with the percent conversion of the latter char being equal to that of the former one (f_c) and the percent conversion of volatile-N, f_v , could also be calculated from Eq.(1), after substituting Eq.(1) into Eq.(10), and Eqs (7)-(8) into Eqs (10)-(11), respectively, the N_v' and N_c' can further be expressed as:

$$N_v' = N_{coal} F_v (f_{coal} - f_c) \quad (12)$$

$$N_c' = N_{coal} F_c f_c \quad (13)$$

Theoretically speaking, the amount of coal-N converted to N_2O should be equal to the sum of amounts of volatile- and char-N converted to N_2O , i. e.

$$N_v' + N_c' = N_{\text{coal}}' = N_{\text{coal}} f_{\text{coal}} \quad (14)$$

For the results of combustion experiment using any type of coal and char made from that coal, the Eq(14) should be correct.

Main results of combustion experiments for two coals and chars prepared from the same coals are offered in Table 4, in which F_v , F_c , f_{coal} and f_c are included. Using Eqs (9), (12), (13) and data in Table 4 and taking 100 g of coal on a weight basis, the amount of coal-N (N_{coal}), distribution of coal-N between volatile-N and char-N (N_v and N_c) and

Table 4. Main Experimental Data of Two Coals and Chars^①

Coal type	N content in coal (wt% daf)	percent of coal-N released as volatile F_v (%)	percent of coal-N retained in char F_c (%)	percent conversion of fuel-N (%)		
				$f_{\text{coal}}^{\text{②}}$	$f_c^{\text{②}}$	$f_v^{\text{③}}$
DE10	1.4	5.3	94.7	33.1	11.6	21.5
DE53	0.6	23.2	76.8	10.9	1.6	9.3

①Data from literature[4];

②Data at combustion temperature of 1073K which is the same as the char preparation temperature;

③Calculated using Eq.(1).

amounts of fuel-N converted to N_2O are calculated and the results are presented in Table 5. It can be seen from Table 5 that for DE 10 coal, amount of N in 100 g of coal is 1.4 g, in which volatile-N and char-N account for 0.074 g and 1. 326 g, respectively. It can be calculated that the sum of amount of char-N converted and that of volatile-N converted is smaller than that of coal-N converted, i.e.

$$N_v' + N_c' = 0.016 + 0.154 < N_{\text{coal}}' = 0.463$$

For DE53 coal, similar result, $N_v' + N_c' = 0.013 + 0.007 < N_{\text{coal}}' = 0.065$, can be obtained.

Calculated results of other four types of coal are shown in Table 6, in which the sums of amounts of char - and volatile-N converted are all smaller than those of coal-N converted, as is the cases for Table 5.

Table 5. Calculated Results of Distribution of Coal-N between Volatile-N and Char-N as well as Amounts of Fuel-N Converted to N_2O (Based on 100 g of Coal Burnt)

coal type	amount of coal-N	distribution of coal-N		amounts of fuel-N converted to N_2O (g)			difference between N_{coal}' and N_c'
	N_{coal} (g)	N_c (g)	N_v (g)	N_{coal}'	N_c'	N_v'	
DE10	1.4	1.326	0.074	0.463	0.154	0.016	0.309
DE53	0.6	0.461	0.139	0.065	0.007	0.013	0.058

Table 6. Distribution of Coal-N between Char-N and Volatile-N as well as Amounts of Fuel-N Converted to N_2O (Based on 100 g of Coal Burnt)

coal type	amount of coal-N	percent of coal-N retained in char (%)	distribution of coal-N		amounts of fuel-N converted to N_2O			difference between N_{coal}' and N_c'
	N_{coal} (g)		N_c	N_v	N_{coal}'	N_c'	N_v'	
BE30	1.7	98	1.666	0.034	0.292	0.062	0.005	0.230
GB04	0.9	96	0.864	0.036	0.189	0.138	0.002	0.051
DE38	1.7	82	1.394	0.306	0.255	0.046	0.036	0.209
AU52	0.9	72	0.648	0.052	0.045	0.010	0.002	0.035

a) Original data are from literature [6] with the percent conversion omitted.

b) Calculating methods are the same as those in Table 5.

Whether the sum of N_v' and N_c' is always smaller than N_{coal}' for any type of coal ?
Adding up Eq.(12) and Eq.(13), we can have

$$\begin{aligned} N_v' + N_c' &= N_{coal} F_v (f_{coal} - f_c) + N_{coal} F_c f_c \\ &= N_{coal} f_{coal} [F_v (1 - f_c / f_{coal}) + F_c f_c / f_{coal}] \end{aligned}$$

From formula above, it can be found that only when $[F_v (1 - f_c / f_{coal}) + F_c f_c / f_{coal}] = 1$, the equation, $N_v' + N_c' = N_{coal} f_{coal} = N_{coal}'$, could be obtained.

Because $0 < f_c / f_{coal} < 1$ and $0 < (1 - f_c / f_{coal}) < 1$

Therefore $[F_v (1 - f_c / f_{coal}) + F_c f_c / f_{coal}] < F_v + F_c = 100\%$

i. e. $[F_v (1 - f_c / f_{coal}) + F_c f_c / f_{coal}] < 1$

so that $N_v' + N_c' < N_{coal}'$

Demonstration above shows that the sum of amounts of volatile-and char-N converted is always smaller than that of coal-N converted, whatever the coal type is. Synthesizing above-mentioned results in Tables 5 and 6 as well as mathematical demonstration, the Eq.(1) could not be considered to be an accurate formula for calculation of the percent conversion of volatile-N.

From Table 5, it can still be seen that for DE10 coal, the difference between amount of coal-N converted and that of char-N converted, i.e. $N_{coal}' - N_c'$, is 0.309 g. However, the amount of volatile-N, N_v , is only 0.074g. Even if all of it can be converted to N_2O , the amount converted is still smaller than the difference. Therefore, in addition to the volatile-N's contribution to the difference, there must be a contribution from char-N, which should be more than 0.235(0.309-0.074). Hence, for DE10 coal, the actually-converted amount of N in the char formed during coal combustion is far from being only equal to 0.154 and must be larger than 0.389 (0.154+0.235); Similarly, the percent conversion of N in the char is also larger than 29.3% (0.389/1.326), not to be only equal to 11.6% (the f_c in Table 4).

Similar to DE10 coal, for BE30 and GB04 coal in Table 6, the differences between amounts of coal-and char-N converted are also larger than the amounts of N in volatiles, hence the converted amounts of N in the char formed during coal combustion are also larger than those of N in the char prepared by coal pyrolysis. It can be noticed from Tables 4 and 6 that for the three coals, DE10, BE30 and GB04, percents of coal-N retained in chars are all more than 90%, with less than 10% of coal-N released as volatile. Therefore, we could consider with reason that when most of coal-N is distributed to char, the converted amount and percent conversion of N in char formed during coal combustion will be more than those of N in char prepared from coal by pyrolysis. This means that the char prepared separately by coal pyrolysis could not be representative of that formed during coal combustion, and Hayhurst and Lawrence's doubt as to the reasonableness of the former char in place of the latter one is quite reasonable. The above results indicate further that the percent conversion of volatile-N, f_v , cannot be calculated using Eq.(1).

4. COMPARISON WITH BATCH COMBUSTION EXPERIMENT

From above discussion, it can be noticed that the coal/char respective combustion experiment method could not be thought to be a perfect and reasonable one in both experimental technique and calculation of relative contribution. The present authors think that a reasonable experimental technique should be consistent with principles below:

- the temperature at which the char is prepared should be the same as that at which the combustion experiments for coal and char are performed.
- the equipment for the coal/char combustion experiment should exactly be the same one as that in which the char is prepared.

By comparison, "batch combustion experiment" method is consistent with above principles. In the method, the evolution and combustion of volatile as well as formation and combustion of char conduct continuously in the same

FB equipment and under the same operating conditions, without the necessity for coal/char respective combustion and without dealing with the reasonableness of char prepared by coal pyrolysis in place of that formed during coal combustion. The key to this method is how to most reasonably distinguish volatile-burning stage from char-burning one. In addition, the coal feed way in which a batch of coal is fed into bed is different from that in which coal is continuously fed into bed in actual boiler operation. It needs to be further studied how to deal with the diversity.

It should be added that in available literatures, the equipment used for combustion experiment are all the bubbling fluidized-bed (BFB), without circulating fluidized-bed (CFB) being used for experiment. Related experiment results [15] showed that for the same coal type and under otherwise equal conditions, the amount of N_2O produced from CFB is higher than that from BFB. The higher the recycle ratio, the higher the concentration of N_2O [5, 15]. These results indicate that the char unburnt out in return fly ash can make an important contribution to N_2O formation. Because of a large difference between CFB and BFB in operation, it is an important subject for us how to assess the relative contribution of volatile and char under CFB operating condition.

5. BRIEF SUMMARY

- (1) The char's properties, especially the distribution of coal-N between volatile-N and char-N, can significantly be influenced by the temperature and equipment for char preparation, hence, a reasonable experimental technique should be consistent with following principles:
 - the temperature for char preparation should be the same as that for coal/char combustion experiment;
 - the equipment for coal/char combustion experiment should exactly be the same one as that for char preparation.
- (2) The difference between percent conversion of coal-N and that of char-N can not be regarded as that of volatile-N.
- (3) For the cases in which more than 90% of nitrogen in coal remains in char, the percent conversion and converted amount of nitrogen in char formed during coal combustion are more than those of nitrogen in char prepared by pyrolysis. The latter char cannot be representative of the former one.
- (4) The research method based on coal/char respective combustion experiment could not be considered to be a perfect one and needs to be modified. Furthermore, research on relative contribution of volatile-N and char-N under CFB operating condition should be carried out.

REFERENCES

1. M. D. Mann, M. E. Collings and P. E. Botros, "Nitrous oxide emissions in fluidized bed combustion: fundamental chemistry and combustion testing", *Prog. Energy Combust. Sci.* Vol. 18, pp. 447~461(1992).
2. A. N. Hayhurst and A. D. Lawrence, "Emissions of nitrous oxide from combustion source", *Prog. Energy Combust. Sci.* Vol. 18, pp. 529~552 (1992).
3. J. E. Johnsson, "Formation and reduction of nitrogen oxides in fluidized-bed combustion", *FUEL*, volume 73, No. 9, pp. 1398~1415 (1992).
4. M. A. Wojtowicz, J. A. Oude Lohuis, P.J.J. Tromp and J.A. Moulijn, " N_2O Formation in Fluidized-Bed Combustion of coal", *Proceedings of 11th Int. Conf. on Fluidized-Bed Combustion*, ASEM, pp. 1013~1020 (1991).
5. E. A. Bramer and M. Valk, "Nitrous Oxide and Nitric Oxide Emissions by Fluidized-Bed Combustion", *Proceedings of 11th Int. Conf. on fluidized-bed Combustion*, ASME, pp. 701~707 (1991).
6. J. R. Pels, M. A. Wojtowicz, and J. A. Moulijn, "Rank Dependence of N_2O Emission in Fluidized-Bed Combustion of Coal", *FUEL*, Vol. 72, March, pp. 371~379 (1993).
7. I. Gulyurtlu, H. Esparteiro and I. Cabrita, " N_2O formation during fluidized bed combustion of chars", *FUEL*, vol. 73, No. 7, pp. 1098~1102 (1994).
8. A. N. Hayhurst and A. D. Lawrence, "The Amounts of NO_x and N_2O Formed in a Fluidized Bed Combustor during the Burning of Coal Volatiles and Also of Char", *COMBUSTION AND FLAME*, 105:341~357 (1996).

9. C. J. Tullin , A. F. Sarofim and J. M. Beer , "Formation of NO and N₂O Coal Combustion: The Relative Importance of Volatile and Char Nitrogen" , *Proceedings of 12th Int. Conf. on Fluidized Bed Combustion*, ASME, pp. 599~609 (1994).
10. Feng Bo , Yuan Jianwei, Lin Zhijie and Liu Dechang , "The Relative Importance of Char Nitrogen on the Formation of Nitrogen Oxides" , *Journal of Huazhong University of Science and Technology*, Vol. 25, Sup. II, pp. 108~111 (1997).
11. D. G. Gavin and M. A. Dorrington, "Factors in the conversion of fuel nitrogen to nitric and nitrous oxides during fluidized bed combustion" , *FUEL*, Vol. 72, March, pp. 381~383 (1993).
12. N. Hayhurst and A. D. Lawrence, "The Devolatilization of Coal and a Comparison of Chars Produced in Oxidizing and Inert Atmospheres in Fluidized Beds" , *COMBUSTION AND FLAME* 100:591~604 (1995).
13. Liu Hao , Feng Bo , Lu Jianxin and Lin Zhijie, "The Influence of Coal Properties on N₂O Generation during Combustion in a Circulating Fluidized Bed" , *Journal of Huazhong University of Science and Technology*, Vol. 23, No. 5, pp. 100~103 (1995).
14. Liu Hao , Lu Jidong , Feng Bo, Wang Jinghong, Liu Dechang and Lin Zhijie, "Influence of Non-homogeneous Reactions on N₂O Formation and Destruction during Combustion of Coal Char in a Circulating Fluidized Bed" , *Proceedings of the Chinese Society for Electrical Engineering*, Vol. 18, No. 4, pp. 237~240 (1998).
15. Liu Hao , Feng Bo, Lin Zhijie and Liu Dechang , "The Influence of Combustion Conditions on Nitrous Oxide Emission from CFB Combustion" , *Journal of Huazhong University of Science and Technology*, Vol. 23, No. 11, pp. 1~4 (1995).

EFFICIENT INTEGRATION OF FURNACES FOR ENERGY SAVING IN THE PROCESS INDUSTRY

P. Stehlík and Z. Jegla

Institute of Process and Environmental Engineering

Faculty of Mechanical Engineering, Technical University of Brno, Czech Republic

E-mail: stehlik@kchz.fme.vutbr.cz, jegla@kchz.fme.vutbr.cz, Fax: +420 5 41142373

Keywords: furnace integration, furnace design, Pinch Analysis, synthesis, optimization

ABSTRACT. A new method for an integrated design of process furnaces (especially tubular fired heaters) has been developed. This approach consists in bridging a gap between equipment (furnace) design and process design. It utilizes some principles from Pinch Analysis. The procedure for an efficient integration of furnaces is partly interactive and is based on three stages: (i) targeting, (ii) synthesis and (iii) detailed design. Its application is illustrated through examples - case studies for both grassroot design and retrofit. A substantial energy saving can be observed.

1. INTRODUCTION

Energy saving and emissions reduction can be considered as priorities in the process industries at present. Process tubular furnaces as large and complex items of industrial units are major consumers of energy in process plants. In the chemical and petrochemical plants it is approximately 75% of their total energy consumption. Moreover, the cost of the furnace system usually ranges between 10 and 30% of the plant total investment. From these and other reasons furnaces usually rank among the key pieces of equipment in various processes and their operation substantially influences energy consumption and emissions production. The aim of furnaces' designers and operators is to achieve an acceptable energy efficiency. It is not possible if the furnace is considered as "stand-alone". The furnace must be considered as a part of overall process using an integrated approach and an efficient technique based on process integration for solving this problem is necessary to be used. Pinch Analysis [1, 2] has emerged as one of the most effective methodologies in the field of process integration and is widely used among practising engineers. It is based on thermodynamic analysis and provides us with valuable information about heat fluxes in processes and in the field of an interaction between processes and utility systems. Using the approach called "targeting" we can find energy and capital requirements even before the detailed design. This method which has established itself as a highly versatile tool in process and heat exchanger design can be efficiently used in an integrated furnaces design.

This contribution is devoted to process furnaces (especially tubular fired heaters) integration into processes. Some basic ideas and principles were formulated in [3, 4] and in [5] later. However, it was found that a new methodology bridging existing gaps between modern targeting methods for furnaces based on Pinch Analysis and detailed design of furnaces should be developed. This methodology presented in the paper is partly interactive and is based on three stages of design: (i) targeting, (ii) synthesis and (iii) detailed design. It can be applied for both grassroot design and retrofit.

2. BASIC PRINCIPLES OF PROCESS INTEGRATION

Basic principles of process integration through Pinch Analysis are useful to be briefly explained for a better understanding the method for furnaces integration which has been developed.

Pinch Analysis

Energy saving in the process industry is not efficient enough without process integration. Process integration is considered as a systematic simultaneous design of an overall process as opposed to the design of individual items of equipment. By properly integrating the process, substantial energy and capital costs can be saved. Pinch Technology (and/or Pinch Analysis) provides a methodology which allows process integration to be conducted in a scientific and systematic manner and enables energy/capital trade-off to be made even before the design [1,2]. Pinch Analysis can be considered as a very efficient tool for reducing total costs (the sum of energy and

capital costs) not only in grassroot design but also in retrofit in the process industry. This methodology is widely used in industrial practice at present because it is „easy to understand“ and „easy to use“. The basic principles of Pinch Technology are based on thermodynamic analysis as mentioned above.

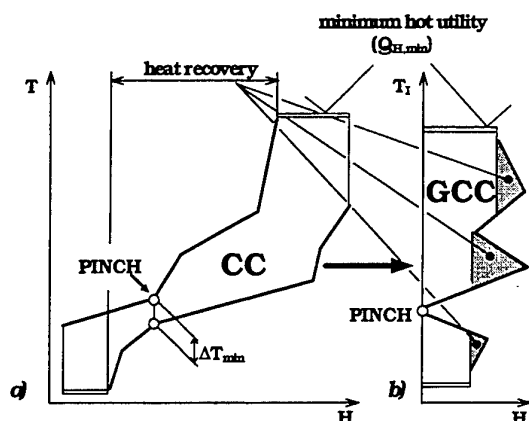


Fig. 1. Composite curves (CC) and grand composite curve (GCC)

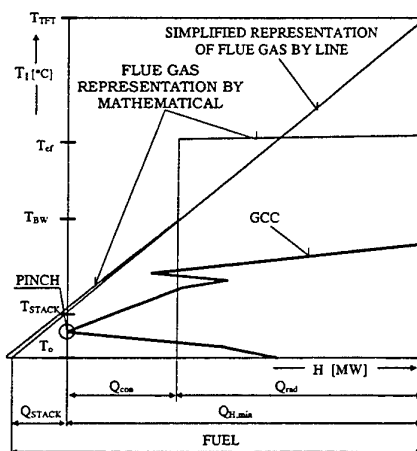


Fig. 2. Representation of furnace flue gas temperature vs. GCC

In each process, sources of heat (called hot process streams) and sinks (called cold process streams) can be identified from the flowsheet and from the material and energy balance of a process. Assuming a given temperature difference ΔT_{\min} we can plot composite curves (CC) in the form of a temperature/enthalpy diagram (T-H) as shown in Fig. 1a. ΔT_{\min} is normally observed at a particular point between the hot and cold composite curves which is called pinch and is of fundamental importance in design. The pinch point divides the overall system (process) into two subsystems - above the pinch (AP) and below the pinch (BP). From the thermodynamic point of view the AP subsystem can be considered as a heat sink and represents the minimum heat demand (minimum hot utility - $Q_{H,\min}$) e.g. for the purpose of crude oil pre-heat in the atmospheric distillation process and the BP subsystem can be considered as a heat source (on a lower temperature level) and the heat must be rejected (minimum cold utility - $Q_{C,\min}$). Furnaces are frequently used as hot utility systems. When the minimum hot utility $Q_{H,\min}$ is found by Pinch Analysis we can use e.g. flue gas from a furnace as hot utility. The composite curves tell us a greater deal about the process (the hot and cold composite curves represent all the hot and cold process streams, respectively). However, a better tool has been developed for an economic selection of utilities - the grand composite curve [1, 2]. The grand composite curve (GCC) reveals where heat is to be transferred between the utilities and the process and where the process can satisfy its own heat demand (shaded area in Fig. 1b).

Furnace Temperature/Enthalpy Profiles

A representation of flue gas as a straight line of constant heat capacity flowrate CP, linking the theoretical flame temperature T_{TFT} to the ambient temperature T_0 (Fig. 2), has been used successfully in process integration [3], although such a simple model has been justified in a rigorous manner only later [5]. This was done by using a simple mathematical model of furnaces described in [5,6] (see dashed curves in Fig. 2).

Flue gas leaves the furnace with stack temperature T_{STACK} . Heat released by combustion of fuel can be expressed as follows:

$$FUEL = Q_{H,\min} + Q_{STACK} \quad (1)$$

Q_{STACK} represents stack losses and $Q_{H,\min}$ is given by relation:

$$Q_{H,\min} = Q_{rad} + Q_{con} = Q_{abs} \quad (2)$$

While Q_{rad} is the heat absorbed in radiation chamber Q_{con} is heat transferred in convection sections of a furnace. Q_{rad} usually shares with 45 % to 55 % on FUEL. Therefore it can be expressed by relation:

$$Q_{rad} = k_R \cdot \text{FUEL} \quad (3)$$

where k_R is a coefficient of heat absorbed in the radiation chamber (efficiency of radiation chamber). In case of retrofit k_R can be evaluated for an existing furnace based on using the simple mathematical model [6].

3. PRINCIPLES OF FURNACES INTEGRATION

Process furnace and/or fired heater can probably be considered as an only equipment without completely developed rules of integration. It means that Pinch Analysis has not been applied in such a way that would reveal an optimum regime of operation, maximum achievable efficiency, appropriate fuel flowrate and acceptable investment cost provided emissions concentration below the permissible limit. Possibilities of furnaces integration based on Pinch Analysis can be specified as follows:

- optimization of stack temperature;
- optimum air preheating using exhaust flue gas, waste heat of process streams or both.

For an evaluation of optimum solution the capital/energy trade-off [1, 2] is applied.

Optimization of Stack Temperature

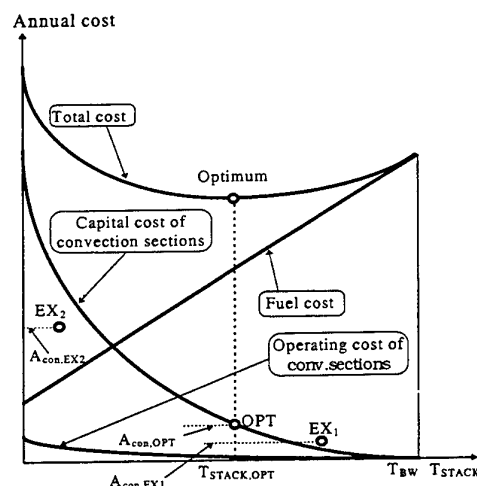


Fig. 3. Capital/energy trade-off for optimization of the stack temperature T_{STACK}

In case of furnaces heat of the flue gases can be utilized up to acid dew point T_{DP} . Let us define our target as minimum total costs (given by a sum of investment and operating (process fluid transport) costs for convective sections of furnace and costs for hot utility (fuel)) which are a function of the stack temperature T_{STACK} . Stack temperature can be found within the interval $T_{PINCH,hot}$ (temperature of hot streams in the pinch point) and bridgewall temperature (T_{BW}). In case $T_{DP} > T_{PINCH,hot}$, T_{DP} becomes the lower boundary of the interval [3]. The following procedure can be applied:

- The lower boundary of the stack temperature (T_{STACK}) interval $\langle T_{PINCH,hot} \text{ or } T_{DP} ; T_{BW} \rangle$ is determined and the area of convective sections (A_{con}) evaluated.
- A range of calculations for stack temperature T_{STACK} from the above interval follows.
- For each calculation (run) fuel burnt (FUEL) is evaluated as well as fuel cost.

- Then a simplified evaluation of heat absorbed in the radiation chamber (Q_{rad}) according to Eq. 3 is performed. Heat transferred in the convection sections (by cooling the flue gas from inlet temperature T_{BW} down to outlet temperature T_{STACK}) Q_{con} is determined using the Eq. 2.
- Area of convection sections A_{con} is evaluated and consequently capital and operating costs are calculated and then the total annual costs which are given by a sum of costs for hot utility (fuel) and capital and operating costs for convection sections.
- If the above steps are repeated many times a diagram showing the capital/energy trade-off vs. stack temperature can be drawn (see Fig. 3). The optimum stack temperature $T_{STACK,opt}$ related to the minimum total costs is found.

Detailed description of the above procedure can be found in [7]. Let us explain some constraints in case of retrofit. If we consider the point EX_1 (see Fig. 3) representing capital costs for existing area of convection sections $A_{con,EX1}$ we can find a scope for optimization because $A_{con,EX1} < A_{con,opt}$. In case of the point EX_2 results of optimization cannot be utilized because removing existing area is not an economic way of retrofit.

Optimization of Air Preheating

After determining the optimum stack temperature $T_{STACK,opt}$ we can start with air preheating optimization. Let us define our target as finding an optimum air temperature ($T_{air,opt}$) for minimum total costs for air preheating system. Fuel cost and investment cost for A_{con} are given, and $T_{STACK,opt}$ is necessary to be maintained and for utilizing preheating of air has to be higher than T_{DP} or $T_{PINCH,hot}$. Then the maximum heat available for air preheating can be expressed as

$$Q_{air} = CP_{fg} \cdot (T_{STACK,opt} - T_{DP}) = CP_{air} \cdot (T_{air,max} - T_O) \quad (4)$$

After evaluating $T_{air,max}$ we can undertake a number of calculations for T_{air} from the interval $\langle T_O ; T_{air,max} \rangle$. For each run the theoretical flame temperature T_{TFT} , enthalpy of air, heat supplied by fuel combustion and annual costs for hot utility are calculated.

The more air is preheated the more heat exchange area is necessary for air preheating. Air preheating is carried out using various types of heat exchangers (e.g. plate type heat exchangers, heat pipes, Ljungström exchangers, etc.). We consider plate type heat exchangers which are widely used because of their significant advantages (e.g. compactness, flexibility of design and dimensions, low pressure losses, low fouling, minimum maintenance, etc.). Area of air preheater, A_{air} , is evaluated from the equation for heat transfer:

$$Q_{air} = U \cdot A_{air} \cdot \Delta T \quad (5)$$

where ΔT is the mean temperature difference of the air preheater and U is the overall heat transfer coefficient which is dependent on the heat transfer coefficients of air and flue gas. The optimization of plate type air preheaters [8] is used for evaluating optimum investment, operating and geometrical parameters of air preheater with a given heat duty Q_{air} . Operating and capital costs for flue gas and air fans and capital cost for flue gas and air ducts are taken into consideration. While the optimization of air preheater [8] can be defined as an optimization of a local problem (equipment itself) then air preheating temperature optimization can be defined as an optimization of a global problem. An appropriate involving of air preheating optimization (local optimization problem) into the air preheat temperature optimization (global optimization problem) allows to achieve for each temperature T_{air} (from the above mentioned interval) all the cost and design data for air preheating system and fuel.

Principles of an optimum design of air preheaters. The principles are based on an interrelation of heat transfer and pressure drop in these heat exchangers and considering total costs for air preheating system as an objective function. Air preheating system which is considered for the optimization (local problem) is obvious from Fig. 4. Major cost components of a heat exchange system are as follows: capital, operating and maintenance costs of air and flue gas fans and capital and maintenance costs of the plate type air preheater. The relationship for the annual costs is:

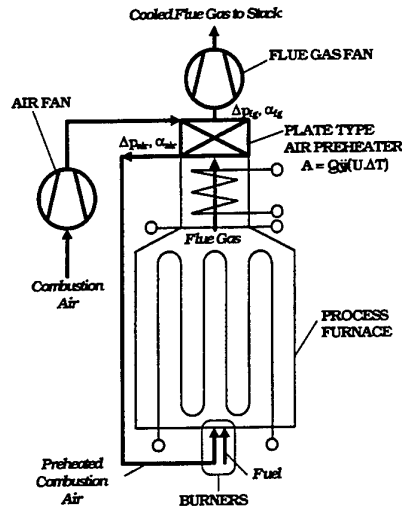


Fig. 4. Process furnace with preheating air

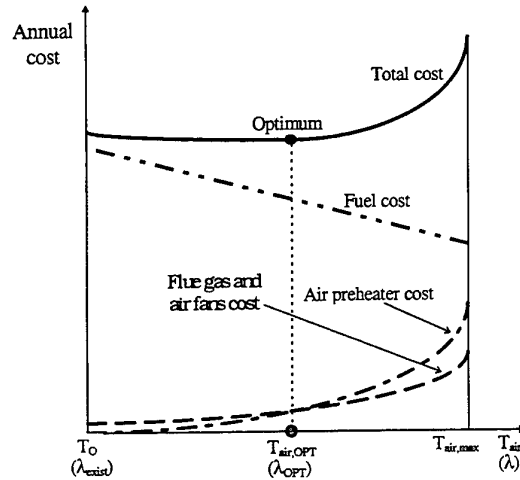


Fig. 5. Capital/energy trade-off for air preheating using furnace outlet flue gas heat

$$C_T = \frac{1}{e_f} [(1 + m_c) \cdot a_f \cdot C_C + \tau_B \cdot C_O] \quad (6)$$

Capital costs (C_C) are dependent on the air preheater area (A_{air}), and both the capital costs and operating costs are dependent on pressure drops Δp_{air} and Δp_{fg} . Using procedures from [9] we can obtain relations for pressure losses (both for air side and flue gas side) in the form as follows:

$$\Delta p = f(\text{thermophysical properties, geometry, flowrate, } \alpha) \quad (7)$$

Then the total costs can be expressed as a function of α_{air} and α_{fg} as follows:

$$C_T = f(\alpha_{air}, \alpha_{fg}) \quad (8)$$

From the necessary conditions for the extremum existence of the objective function

$$\frac{\partial C_T(\alpha_{air}, \alpha_{fg})}{\partial \alpha_{air}} = 0 \quad \text{and} \quad \frac{\partial C_T(\alpha_{air}, \alpha_{fg})}{\partial \alpha_{fg}} = 0 \quad (9)$$

the optimum heat transfer coefficients can be obtained. These values are substituted into the relation between α and Δp (Eq. 7) and optimum pressure drops Δp_{air} and Δp_{fg} and consequently the optimum dimensions of the air preheater and its new area A_{air} are evaluated.

Then the energy/capital trade-off for air preheating temperature optimization can be done (see Fig. 5). We can find an optimum temperature of preheated air $T_{air,OPT}$. For $T_{air,OPT}$ other important values as costs, operating and design data for air preheating system (air preheater, flue gas and air fans, fuel flow rate, NO_x emissions etc.) are evaluated. These parameters are used for the detailed design of a furnace. Details of this approach can be found in [7].

Air preheating optimization in case of retrofit. The theoretical flame temperature T_{TFT} can be considered as an indicator of tube heat flux density at the tube surface in the radiation chamber for the purpose of fuel consumption optimization. The principle of the procedure for optimization is to maintain the constant stack temperature $T_{STACK,opt}$ and the theoretical flame temperature T_{TFT} while the temperature of air preheating T_{air} is being increased. The values of this temperature range within the interval $\langle T_O, T_{air,max} \rangle$. Total costs are a sum of all the costs considered and the optimum values of air preheating temperature and air excess can be found. The air preheating optimization algorithm also involves an above mentioned procedure for optimization of plate type air preheaters which enables to evaluate optimum investment, operating and geometrical parameters of air preheater for a given duty Q_{air} . Based on minimum total annual cost the optimum value of air preheating temperature $T_{air,OPT}$ and the corresponding values of excess air λ_{OPT} (see Fig. 5), fuel flowrate and geometrical parameters and operating conditions of the air preheater can be identified [7]. (Values of excess air for the case of retrofit can be observed on horizontal axis in parentheses in Fig. 5.)

Utilizing waste heat of process streams for air preheating. Utilizing of heat which is to be rejected from hot process streams can contribute to both energy saving and cold utility reduction. Therefore the cold utility cost is involved in the capital/energy trade-off as well. This alternative can also be considered in a combination with using heat of exhaust flue gases for air preheating. All the feasible alternatives are necessary to be considered for an evaluation of the optimum air preheating system [7].

4. ALGORITHM FOR FURNACES INTEGRATION

An algorithm for furnaces integration consists of three main procedures: (i) targeting, (ii) synthesis, and (iii) detailed design of a furnace. Using targeting enables us to obtain important information about the process and especially the grand composite curve (GCC) which can be considered as an important tool for the furnaces integration. By targeting based on Pinch Analysis we can determine $Q_{H,min}$ and $Q_{C,min}$. If we want to achieve a furnace design of practical value it is necessary to combine process design with equipment design based on a collaboration with furnaces designers (selection of furnace type in case of grassroot design, identifying retrofit constraints), determining k_R , design of tube arrangement etc. Then the procedure for the synthesis which is based on methods for optimizing the stack temperature and air preheating is applied. This methodology also utilizes principles of targeting based on Pinch Analysis as described above. After completing the previous steps we can perform a detailed design based on the furnace simulation (calculation of heat transfer and fluid flow in the furnace) using computer code for simulation (e.g. the simple one [5, 6]) and then a detailed mechanical design. A simplified algorithm is obvious from Fig. 6.

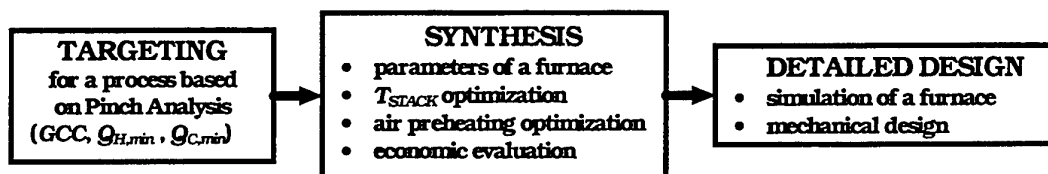


Fig. 6. Basic procedures in integrated furnace design

5. EXAMPLES - CASE STUDIES

Grassroot Design of Furnace for Gas Oil Hydrogenation Refining

A simplified flowsheet of the process is shown in Fig. 7 where the heat exchanger network (HEN) is symbolically represented by only one heat exchanger. Important values resulting from the targeting stage are as follows: $\Delta T_{min} = 21^\circ\text{C}$, $Q_{H,min} = 3244 \text{ kW}$, $Q_{C,min} = 4129 \text{ kW}$, $T_{I, PINCH} = 368^\circ\text{C}$. An interactive input into the furnace integration approach starts with the furnace design. A cylindrical radiation chamber with vertical tube coil and a horizontal convection section situated above it was selected. By applying the algorithm described above the optimum stack temperature for minimum total annual costs of convection sections $T_{STACK,opt} = 380^\circ\text{C}$ was found. Corresponding values of fuel flowrate and number of tube rows in the convection section were evaluated in addition to others

parameters. Then a system for preheating air was calculated ($T_{air,opt} = 270\text{ }^{\circ}\text{C}$) and detailed design of the furnace was performed. The furnace efficiency of 91.8 % was evaluated using a detailed simulation.

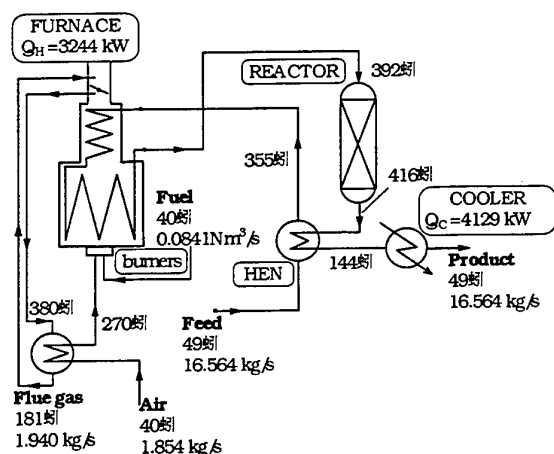


Fig. 7. Simplified flowsheet of gas oil hydrogenation refining

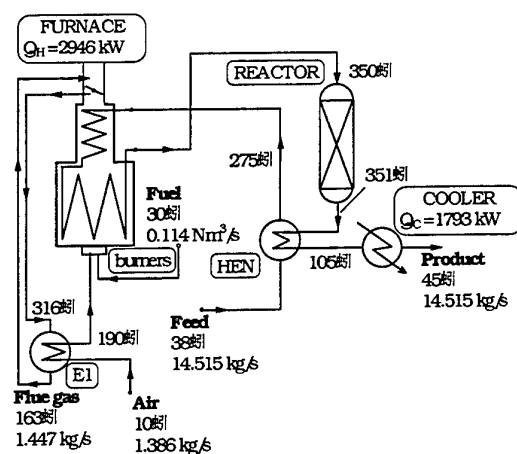


Fig. 8. Simplified flowsheet of the hydrogenation refining petrol plant after retrofit

Retrofit of Furnace from Process for Hydrogenation Refining Petrol

First, the existing state of the process was analyzed. Refinery management decided to replace the existing system for preheating air through utilizing steam as hot utility by a new one with the aim to save costs for energy and to match the more sweeping emissions limits. A limited cost for investment was available. Further, a minor retrofit of the furnace was considered to increase its efficiency. A type of fired heater was the same as in the previous case of grassroots design. It was found by applying the optimization of stack temperature that the results cannot be utilized because this type of retrofit would consist in removing a part of existing area from the convection sections (see point EX₂ in Fig. 3). However, the optimization of air preheating proved itself to be very useful. Then the computer program for furnaces simulation [5,6] was used for completing the retrofit design. A comparison of selected important parameters before and after retrofit is obvious from Table 1. It can be observed that an optimum utilization of flue gas exhaust heat for air preheating together with a minor change of operating parameters can bring approximately 20 % reduction of energy. A simplified flowsheet of the process after retrofit is shown in Fig. 8.

Table 1. Comparison of selected parameters before and after retrofit

Selected parameters	Before retrofit	After retrofit
Excess air λ [-]	1.15	1.254
Temperature of combustion air T_{air} [$^{\circ}\text{C}$]	140	190
Fuel flowrate V_{fuel} [m^3/s]	0.116	0.114
Furnace efficiency [%]	82.9	88.4
Total annual cost for fuel and steam [\$/yr]	159 840	128 250
Total annual costs for the new air preheating system [\$/yr]	-	5 820
Payback [months]	-	2.2

6. CONCLUSION

A method contributing to energy (fuel) saving in the process industry plants is based on process integration using Pinch Analysis. This approach combines principles of effective design of both processes and equipment. A

procedure for furnaces integration starts with process analysis and targeting procedure (based on Pinch Analysis). The targeting procedure is followed by synthesis and by a detailed design of the furnace. For the new partly interactive synthesis stage we have applied a combined targeting and optimization approach for the analysis of furnace subsystems. A complex synthesis procedure like this then enables to determine preliminary geometric parameters of these subsystems (like convective sections, air preheaters) in addition to an optimum regime of operation. Parameters obtained from the synthesis stage can be considered as the best input data for a detailed design of the furnace by using various software products. The benefit of this integration approach is illustrated through examples of both grassroot and retrofit design of furnaces.

NOMENCLATURE

a_f	annuity factor, 1/yr	$Q_{C,min}$	minimum cold utility, W
A_{air}	heat transfer area of air preheater, m^2	$Q_{H,min}$	minimum hot utility, W
A_{con}	area of convective sections, m^2	Q_{rad}	radiation chamber duty, W
C_C	capital cost, \$	Q_{STACK}	stack losses, W
C_O	operating cost, \$/hr	T	temperature, °C
C_T	total annual cost, \$/yr	T_{BW}	bridgewall temperature, °C
CP	heat capacity, $W.K^{-1}$	T_{DP}	dew point temperature, °C
e_f	equipment availability factor, -	T_{ef}	effective flue gas temperature, °C
FUEL	heat supplied by fuel combustion, W	T_I	interval temperature, °C
H	enthalpy, W	T_O	ambient temperature, °C
k_R	efficiency of radiation chamber, -	T_{STACK}	stack temperature, °C
m_c	maintenance costs ratio, -	T_{TFT}	theoretical flame temperature, °C
Δp	pressure drop, Pa	ΔT	mean temperature difference, °C
Q	heat, W	ΔT_{min}	minimum allowable temperature difference, °C
Q_{abs}	heat absorbed in a furnace, W	U	overall heat transfer coefficient, $W.m^{-2}.K^{-1}$
Q_{air}	heat used for air preheating, W	α	heat transfer coefficient, $W.m^{-2}.K^{-1}$
Q_{con}	convective sections duty, W	λ	excess air, -
		τ_B	plant attainment, hrs/yr

Indices

air	air	max	maximum value
C	cold utility	min	minimum value
exist	existing value	new	new value
fg	flue gas	opt, OPT	optimum value
H	hot utility	PINCH	value at PINCH point

REFERENCES

1. B. Linnhoff, D.W. Townsend, D. Boland, G.F. Hewitt, B.E.A. Thomas, A.R. Guz, and R.H. Marsland, *User Guide on Process Integration for the Efficient Use of Energy*, IChemE, Rugby, U.K. (1982), latest updated reprint (1994).
2. R. Smith, *Chemical Process Design*, McGraw-Hill (1995).
3. B. Linnhoff, and J. de Leur, "Appropriate Placement of Furnaces in the Integrated Process", *IChemE Symposium "Understanding Process Integration II"*, pp. 22-46, UMIST, Manchester, March (1988).
4. S.G. Hall, *Targeting for Multiple Utilities in Pinch Technology*, PhD Thesis, UMIST, DPI, Manchester, November (1989).
5. P. Stehlík, S. Zagermann, and T. Gangler, Furnace Integration into Processes Justified by Detailed Calculation Using a Simple Mathematical Model, *Chem. Eng. and Proc.*, v. 34, pp. 9-23 (1994).
6. P. Stehlík, J. Kohoutek, and V. Jebáček, Simple Mathematical Model of Furnaces and its Possible Applications, *Comp. & Chem. Eng.*, v. 20, pp. 1369-1372 (1996).
7. Z. Jegla, *Furnaces Integration into Processes for Energy Consumption Reduction*, PhD Thesis, Technical University of Brno, CZ, June (1999).
8. P. Stehlík, Z. Jegla and J. Kohoutek, Optimization of Plate Type Air Preheaters in Process Furnaces, *Proceedings of the 1997 National Heat Transfer Conference*, pp. 245-249, Baltimore, USA, August (1997).
9. W.M. Kays, & A.L. London, *Compact Heat Exchangers*, 3rd ed., McGraw-Hill, New York (1984).

THE BIOMASS PYROLYSIS FOR LIQUIDS IN CFB REACTOR

Dai Xianwen Xiong Zhuhong Wu Chuangzhi Chen Yong

Guangzhou Institute of Energy Conversion, CAS

Email: daixw@ms.giec.ac.cn; Fax: (020)-87608586

Keywords: biomass, CFB, fast pyrolysis, for liquids.

ABSTRACT. With the CFB as main reactor, an integrated facility was developed for the fast pyrolysis of biomass. To model the main chemical processes, the bed is divided into two zones according to the pyrolysis and secondary reaction. The pyrolysis of pine wood powder was processed by varying the bed temperature, particle size of wood powder and the feeder position. Based on the variation of the pyrolysis gas composition and the bio-oil ingredients, analysis of the experimental data highlights the important effects of temperature, heating rates and secondary reaction. The main technical problems during the experiment and the solution are also discussed.

1. INTRODUCTION

Because environmental pollution problems become increasingly serious, it is important to make use of the clean and renewable resource —biomass as substitution for fossil energy. On the other hand, biomass is just wastes before they can be treated and recycled, which will become pollutant to the environment due to landfill and pile-up or malignant sources which result in accident fire. The biomass pyrolysis for liquids is a promising technology. It offers a number of unique advantages of which the most significant is that a liquid is produced that can be stored and transported. Pyrolysis is thermal degradation either in the complete absence of oxidizing agent or with such a limited supply that gasification does not occur to an appreciable extent or may be describes as partial gasification. Moderate temperature about 500 °C, high heating rates of up to a claimed 1000 °C/s or even 10000 °C/s and very short residence time less 2s[1] are the perfect reaction conditions. In order to get these strict conditions, we uses the Circulating Fluidized Bed (CFB) as the main reactor.

2. EXPERIMENTAL STUDIES

2.1 Materials

Using quartz sand as circulating particle, the pyrolysis of pine wood powder for liquids was studied in CFB. The particle sizes of two wood powder samples were 0.38mm and 0.73mm. The proximate and ultimate analyses of the wood powder are summarized in Table 1. Since the wood powder has large amounts of volatile matter (70.7 Wt.%), pyrolysis of which for liquids is an efficient method for utilizing wood powder.

Table 1. Proximate And Ultimate Analysis Of Wood Powder

Proximate analysis	Wt. %	Ultimate analysis	Wt. %
Volatile matter	70.7	C	47.9
Fixed Carbon	21.2	H	7.0
Ash	2.3	O	41.4
Moisture	5.8	N	0.1
H.H.V(kJ/kg)	18032.5	S	0.3
		Ash	2.3

2.2 Facility

The Circulating Fluidized Bed (CFB) has been successfully used in many fields as an efficient, no bubble and high production capacity reactor [2]. Using the CFB as main reactor, we designed and constructed an experimental facility which included the heating, reaction, measurement and control devices. Its processing capacity is 5 kg/h.

A schematic of the apparatus is shown in Fig.1. The system has five components: (i) two variable speed rotary feeders at the different height along the CFB; (ii) a CFB reactor assembly with two cyclone separators; (iii) cooling system; (iv) combustion chamber; (v) gas circulating pump and preheating system. The CFB reactor was

constructed from the heat-resistant stainless-steel pipe of 100mm i.d, and the total height of this apparatus is about 3 m.

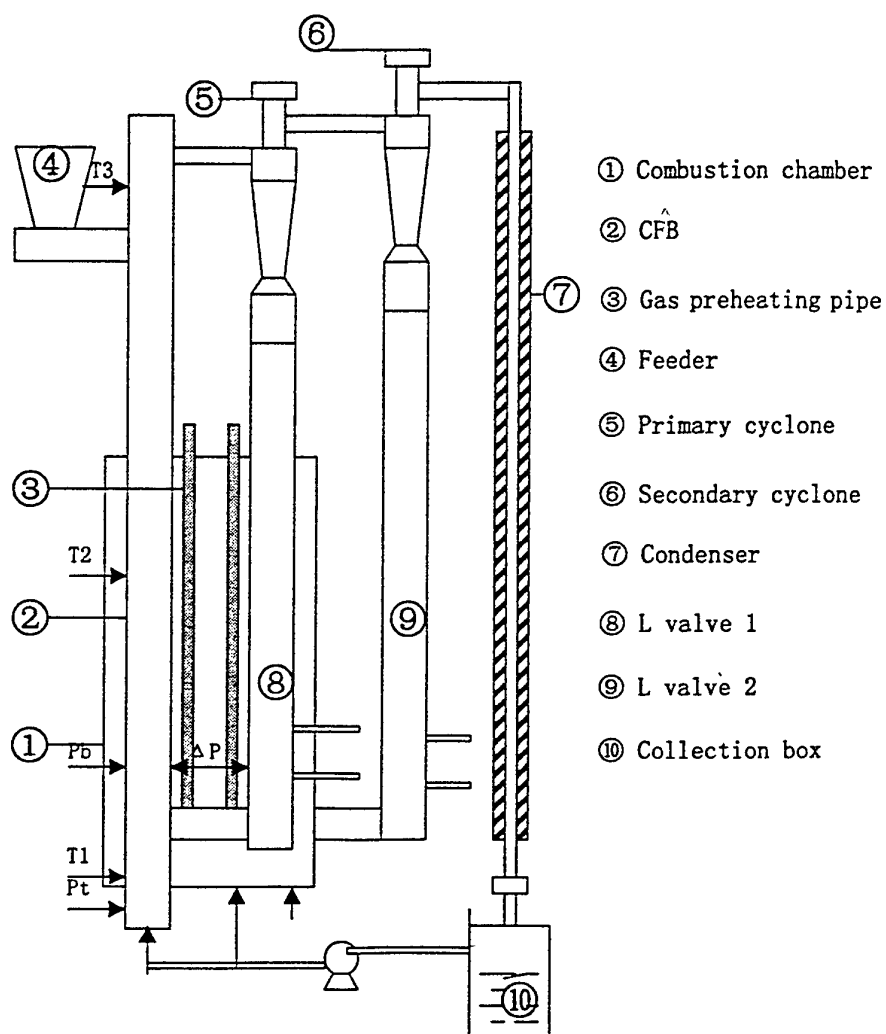


Fig. 1 Experimental apparatus

2.3 Experimental Procedure

Combustion chamber was the main energy source in this apparatus, in which the shredded charcoal powder was burned to provide heat for the whole system. The carrier gas (air firstly, then pyrolysis gas) was pumped into preheating pipe by the circulating pump to be heated, then it carried quartz sand to circulate in the CFB. When bed temperature rose to a proper degree, wood powder was fed by a rotary feeder with a variable speed motor from a sealed hopper. With favorable conditions of heat and mass transfer, the wood powder was pyrolyzed immediately and brought out of CFB quickly. After the quartz sand and pyrolysis char were separated by the two cyclones respectively, the pyrolysis vapours was quenched when it escaped through the condenser. Thus, we could collect the liquid product, bio-oil, and the non-condensable gases were extracted by the circulating pump. In order to study on the effects of temperature, heating rates and vapour residence time, we changed the reactor temperature, particle size of wood powder and the feeder position in the experiment.

3. CHEMICAL PROCESSES OF CFB

In a CFB, the bed could be divided into two zones according to the main chemical processes [3], which can be modelled as Fig.2.

3.1 Pyrolysis Zone

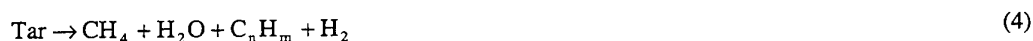
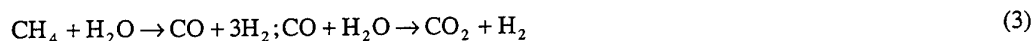
In this zone, feed was loaded into the bed and pyrolyzed very quickly. Since the feed particles were small and the heat exchanged rapidly, the heating rate was very high. For example, a small particle at 0.1-0.2mm diameter, could be heated at the rate of about 10^3 °C /s in an atmosphere at 1000 °C. In this zone, the main chemical process could be described as:



Temperature was another essential factor affecting the pyrolysis. Because the relatively high temperature was favorable to form more non-condensable gas and reduce the tar yield, so moderate and carefully controlled temperature was needed.

3.2 Reduction And Cracking Zone

After the feedstock pyrolyzed, further reactions took place before the pyrolysis vapours were quenched by the condenser: the tar cracked and the char was reduced. These processes produced more non-condensable gas such as CO and H₂. Some C_nH_m also cracked at the same time. The main reactions could be expressed as:



Char contributed to secondary cracking by catalysing secondary cracking in the vapour phase, rapid and complete char separation was therefore desirable. Since the vapour residence time influenced the yield and quality of the liquid product, the shorter this zone, the better.

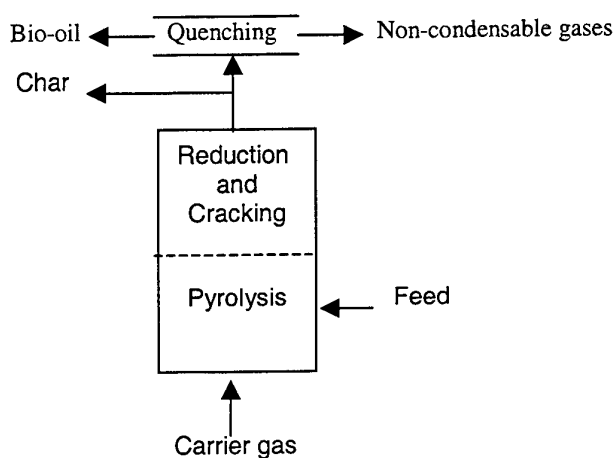


Fig.2. Model of the chemical processes of CFB

4. RESULTS AND DISCUSSIONS

4.1 The Composition of Gas Product

Although gas product was not the main research object, the variation of whose composition contributed to understand the mechanism of pyrolysis. The comparison of gas composition are shown in Table 2. And T = temperature ($^{\circ}\text{C}$), R = gas residence time (s), D = wood powder diameter (mm). The smaller the wood powder diameter provides more heating surface area, so it can be considered as the indication of the heating rate.

Table 2 shows that the composition of the gas product from CFBG is quite different from the gas sample obtained from the pyrolysis gas of our CFB after quenching. This difference is the very reflection of the different pyrolysis mechanism between biomass gasification and fast pyrolysis for liquids. The object of gasification is to get high quality gas product. Thus the high temperature of up to 900°C is wanted to enlarge the gas product and reduce the tar, while the relatively long residence time contributes to the secondary reactions including char reduction, tar cracking, shift reaction, etc. So the amount of CO_2 , CO , CH_4 and H_2 is far more, and the amount of C_nH_m is less in gasification. By contrast, The object of fast pyrolysis is to obtain more liquid product, which determines the operation conditions of moderate temperature and short residence time to increase the liquid production rate. Such operation conditions lead to the higher amount of C_nH_m and less amount of CO , CH_4 and H_2 which indicates that the degree of pyrolysis is not excessive.

Table 2. Comparison Of Gas Composition

Facility	Operation condition	gas composition (mol %)					LHV(MJ/m ³)
		H ₂	CH ₄	CO	CO ₂	C _n H _m	
CFB gasifier	D ₀ T ₀	24.62	13.16	29.03	29.21	3.98	13.56
Our CFB reactor	D ₁ T ₁ R ₁	1.89	2.7	13.48	49.13	32.8	23.71
	D ₁ T ₂ R ₁	3.01	2.68	18.28	39.74	36.29	26.65
	D ₁ T ₂ R ₂	7.01	4.41	24.13	36.35	28.1	23.23
	D ₂ T ₂ R ₁	2.16	2.13	15.68	41.8	38.23	27.26
	D ₂ T ₂ R ₂	5.51	4.32	20.37	37.25	32.55	25.39

Note: (1) $D_0 = 0.41$ mm, $D_1 = 0.38$ mm, $D_2 = 0.73$ mm, $T_0 = 920^{\circ}\text{C}$, $T_1 = 450^{\circ}\text{C}$, $T_2 = 550^{\circ}\text{C}$, $R_1 = 0.8$ s, $R_2 = 1.5$ s. (2) $\text{LHV} = (30.0 * \text{CO} + 25.7 * \text{H}_2 + 85.4 * \text{CH}_4 + 151.3 * \text{C}_n\text{H}_m) * 4.2$ (kJ/m³)

Table 2 also shows the difference of results at various operation conditions in our CFB reactor. The main trend is that the higher temperature and longer residence time lead to less CO_2 , more CO , H_2 , CH_4 varies slightly. The bigger particle diameter decreases the heating rate and favors the carbonization, so the amount of product gas are lower. The LHV is determined mainly by the amount of C_nH_m . It must be pointed out that only the changing trend of H_2 can definitely reflect the degree of secondary reactions. More H_2 suggests that secondary reactions take place more extensively. In contrast to the H_2 , other components will increase or decrease when the secondary reactions take place. Such features can be derived from the previous discussion of chemical processes. The gas composition according to different operation conditions is shown in Fig. 3.

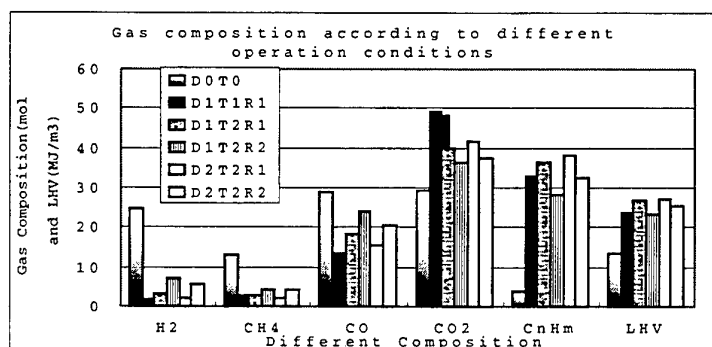


Fig.3. Gas composition according to different operation conditions

4.1 The Components Of Bio-oil

The bio-oil sample was separated into alkanes, aromatics, non-hydrocarbons and bitumen fractions, then the alkanes, aromatics and non-hydrocarbons were analyzed by HP 5972-II gas chromatography- mass spectrometry (GC-MS) system using the ligroin, benzene and ethanol as solvents respectively (Fig.4-Fig.6), the bitumen was detected by PE1725X infra-red spectrometry instrument (Fig.7). The weight percent of each fraction is shown in Table 3, and the main identified components are listed in Table 4.

Table 3. Weight Percent Of Each Fraction

Alkanes (Wt. %)	Aromatics (Wt. %)	non-hydrocarbon (Wt. %)	Bitumen (Wt. %)
31.04	13.47	39.10	16.39

Table 4. The Main Identified Components

Name of fraction	Retention time	Area % (To the specified fraction)	Compound name
Alkanes	22.87	1.715	Valencene
	23.19	0.805	1H-3a,7-Methanoazulene
aromatics	12.81	2.125	Naphthalene
	21.60	1.112	1,1'-Biphenyl
	22.67	1.864	Naphthalene,1,8-dimethyl-
	23.31	1.673	Naphthalene,2,3-dimethyl-
	24.49	1.030	Acenaphthylene
	30.04	1.974	9H-Fluorene
	37.52	6.537	Anthracene
	37.84	1.978	Phenanthrene
	41.60	2.333	Anthracene,2-methyl-
	41.78	3.165	Anthracene,9-methyl-
	47.06	2.313	Pyrene
	50.03	1.955	Phenanthrene,2,3,5-trimethyl-
	52.03	6.437	Phenanthrene,1-methyl-7-
	58.80	5.102	Chrysene
non-hydrocarbon	9.15	4.964	Phenol,2-methoxy-
	13.74	6.638	2-Methoxy-4-methyl phenol
	17.57	2.426	Phenol,4-ethyl-2-methoxy-
	22.79	1.604	Benzaldehyde,4-hydroxy-3-methoxy-
	23.10	2.235	Benzaldehyde, 4-hydroxy-3-methoxy-
	26.83	0.939	Ethanone,1-(4-hydroxy-3-methoxyphenyl)-
	45.13	3.209	Hexadecanoic acid
	50.63	5.518	9,12-Octadecadienoic acid(z,z)-
	51.58	1.600	Octadecanoic acid
	55.95	1.290	1-Phenanthrenecarboxylic acid
	60.25	31.517	1-Phenanthrenecarboxylic acid
	84.43	1.247	Stigmast-4-en-3-one

Table 3 shows that most compounds in bio-oil are non-hydrocarbons, then alkanes, aromatics and bitumen are relatively low. The percent of bitumen indicated the pyrolysis degree, more sufficient pyrolysis led to less bitumen. From table 4 and Fig.4-Fig.6, it can be concluded that the bio-oil is extremely complex and is composed of hundreds of compounds. The major constituents include phenol, phenanthrene, anthracene, naphthalene and some species of acid. Although a number of components are identified by the GC-MS, a number of species of interest are not identified due to (a) their low concentration levels below the MS detection levels and (b) the overlapping of certain species such as aromatics by phenols which are major constituents with excessive peak tailing. Due to the large amount of oxygen in bio-oil, the components of bio-oil are affected by oxydation severely.

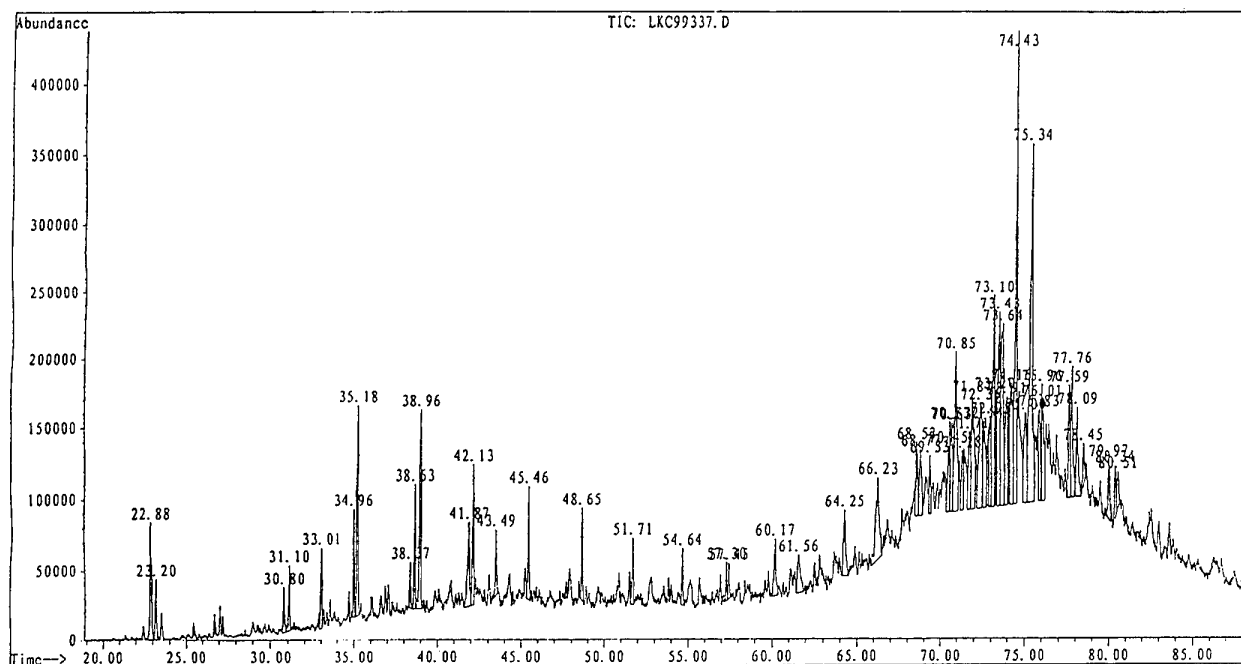


Fig.4. Gas chromatogram of alkanes fraction. Conditions: 30mx0.25mmx0.25 μ m, HP-5 capillary column; carrier gas, He; temperature program, 75°C (hold 5 min) to 285 °C @ 3°C/min (hold 40 min); injector and detector temperature: 280 °C. For identification of peaks see Table 4.

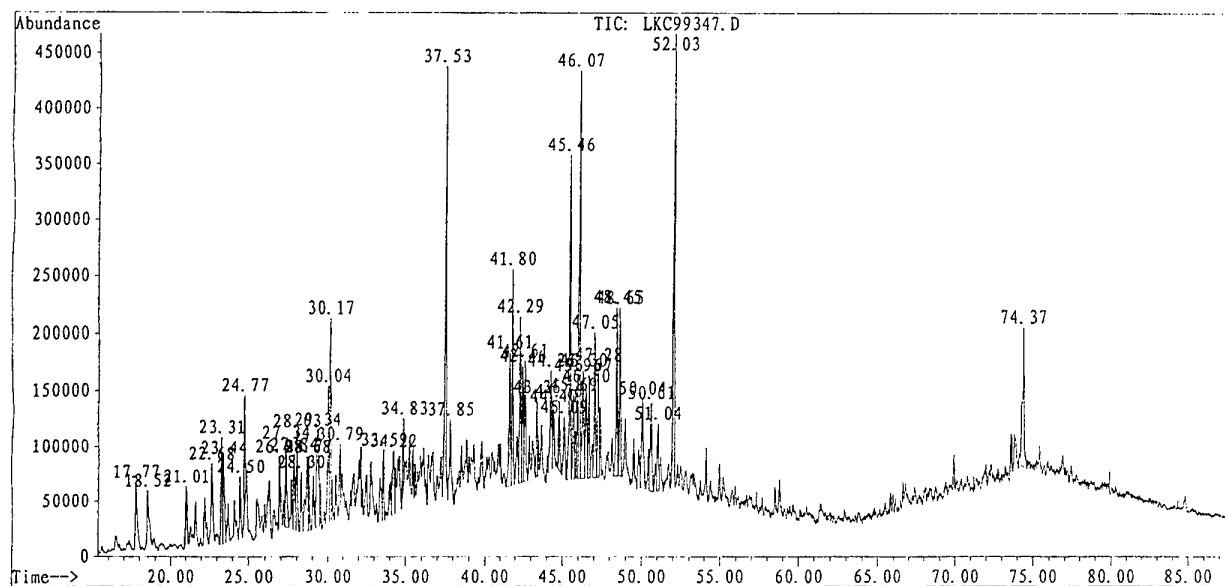


Fig.5. Gas chromatogram of aromatics fraction. Column and flow conditions as in Fig. 4.

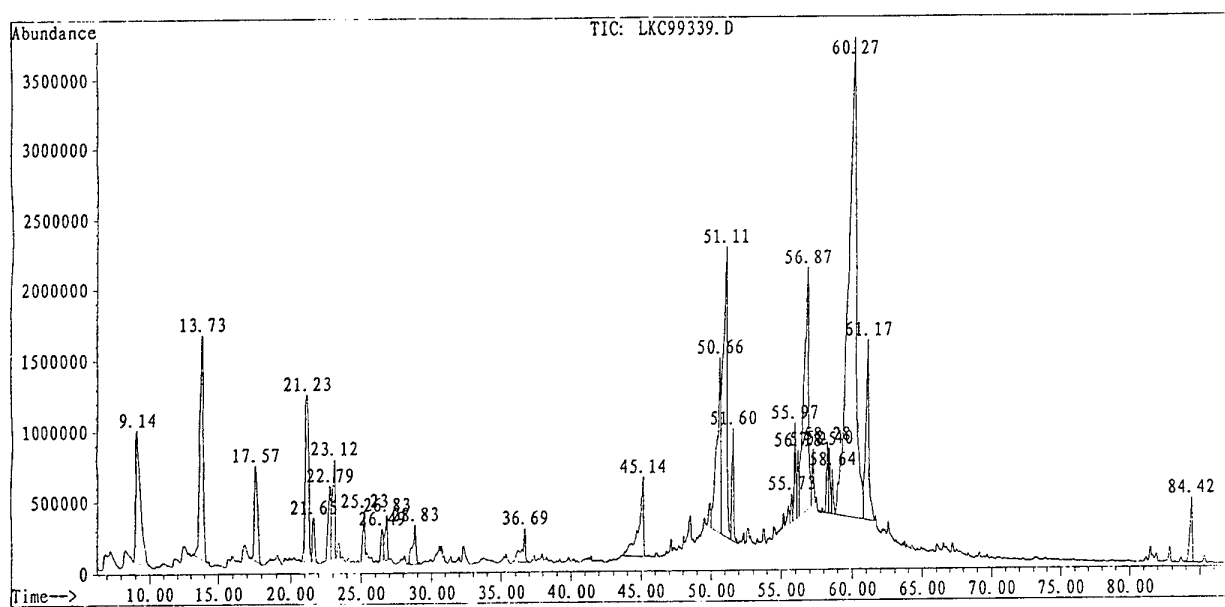


Fig. 6. Gas chromatogram of non-hydrocarbons fraction. Column and flow conditions as in Fig. 4.

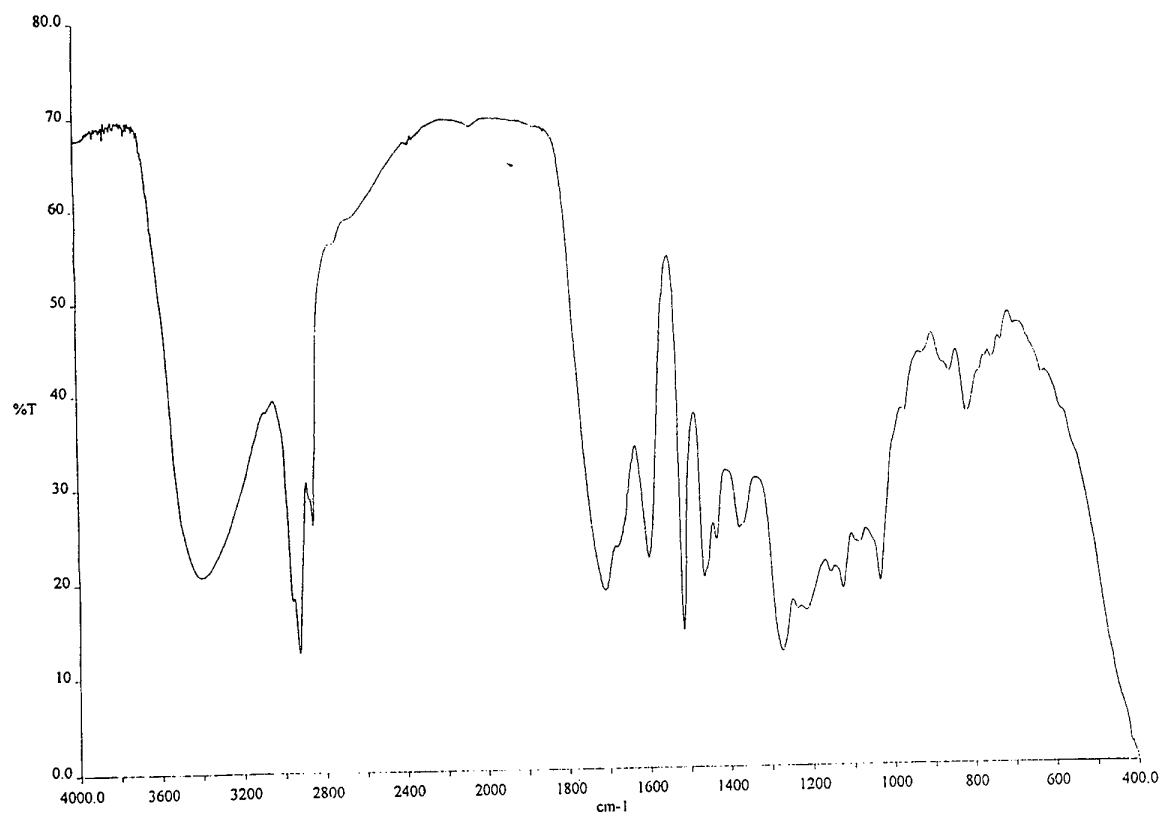


Fig. 7. Infra-red spectrometry of bitumen fraction (solvent: CHCl₃)

5. RECOMMENDATIONS

- (1) The CFB bed can be divided into pyrolysis and secondary reaction zones according to the main chemical processes. In order to obtain high quality bio-oil, the secondary reaction zone should be short enough.
- (2) The bed temperature, heating rates and the vapours residence time have the important effect on the pyrolysis gas composition and the bio-oil ingredients, so they must be controlled carefully.
- (3) The carrier gas preheating is important, and it is necessary to take steps to control the preheating temperature strictly. Using the combustion chamber and the electrical heating jacket to preheat together not only improves the utilization rate of the combustion chamber's heat and reduces the electricity usage, but also provides the convenience of controlling and regulating the temperature of carrier gas.
- (4) In order to quench the vapours quickly, an efficient cooling method is needed. Cooling the collected bio-oil firstly with ice water, then pumping the cooled bio-oil into condenser to cool the vapours directly has obvious effect. If it is hard to collect any bio-oil at the beginning, we can use any gauged water or alcohol alternatively, which would be removed from the final result.
- (5) The pipe clogging arising out of the mixture of tar and quartz sand is a serious problem and must be solved. An electrical heating jacket may be equipped from the CFB exit to the condenser to avoid the vapours 'condensation inside the pipes. Even though, it was necessary to pump the air into this system for a long time after the experiment to ensure the pyrolysis vapours and tar's burning up.

REFERENCES

1. "The Research Progress Of Biomass For Processes". pp.167-179, *Integrated Energy Systems in China*. Food and Agriculture Organization of the United Nations, 1994.
2. T.M. Knowlton, Hirsan. L-valves Characterized for Solids Flow. *Hydrocarbon Processing*. 1978: 149-156.
3. Jianzhi Wu, Bingyan Xu, Zhenfan Luo and Xiguang Zhou. Performance Analysis of a Biomass Circulating Fluidized Bed Gasifier. *Biomass and Bioenergy*: Vol. 3, No. 2, pp. 105-110, 1992.

STUDY ON THE THERMAL EFFICIENCY AND HEAT TRANSFER OF POST COMBUSTION FOR SMELTING REDUCTION FURNACE

Hsuan-Cheng Liu, Tsong-Sheng Lee, H.H. Chiu
Aerospace Science and Technology Research Center
National Cheng Kung University
Email: Jonathan @ Astrc.iaalab.ncku.edu.tw

Chun-Lang Yeh
Department of Aeronautical Engineering
National Huwei Institute of Technology
Email: clieh@sunws.nhit.edu.tw

Ling-Chia Weng
Industrial Technology
Research Institute
Email: 830183@cast.itri.org.tw

Keywords: post combustion, smelt reduction furnace, furnace simulation

ABSTRACT. The objectives of this smelting reduction furnace study are to understand the heat transfer, fluid mechanics and combustion process inside a smelting reduction furnace, to develop the parametric control for the combustion optimization and to minimum energy consumption for the smelting reduction. A cold flow analysis with k- ϵ turbulence model was used to investigate the velocity and pressure profiles inside the testing furnace, which provide the initial information for the combustion analysis. A finite rate/eddy-break-up model and mixture fraction/partial probability density function (PPDF) model are adopted and the results compared. Numerical simulations revealed that a stagnation region present on the top opposite to the exit of the non-symmetrical smelting furnace. The mean furnace temperature that calculated from PPDF model is higher than that predicted from eddy-break-up model. The future research topics are also presented.

1. INTRODUCTION

New iron making processes are being investigated for future iron making, because economic and environmental requirements for steel making are changing. A world wide effort has been undertaken to develop of an alternative iron making process that will have the positive feature of the blast furnace and in addition, it will overcome its major shortcomings by having the flexibility of using coal, quick operational response and lower capital investment [1]. One of the most promising new processes is based on the bath smelting of iron ore. Iron bath smelters are developed for operation with coal rather than coke and fine ores in place of pellets or sinter, which eliminates pretreatment steps [2]. A liquid iron pool is the reaction medium. Iron ore is dissolved and reduced in the bath and coal is charged into the reactor. Process gas (mainly carbon monoxide and hydrogen) is generated in the iron bath range and evolves into the furnace upper space. By injecting air or oxygen, the generated gas from the bath is oxidized. The degree of the post combustion than can be attained determines the energy efficiency of the process.

The main role of the post combustion operation is to supply the iron bath with the heat generation from the combustion reaction for energy source demanded by the endothermic reduction reaction occurring in the iron bath. Therefore, the post combustion plays an important role on the efficiency of the bath type smelting reduction process in the respect of reducing the consumption of the coal. To design an efficient post combustion operation, the understanding of the combustion phenomena occurring in the post combustion stage is necessary. Combustion is the heat and mass transfer phenomena accompanying with the fluid flows and chemical reactions.

Based on different considerations and applications, many designs of post combustion operations have been proposed in iron making process [3,4,5]. However, the development concept and the study issues are similar to each other. In 1997, Takahash [6] operated a 5-ton post combustion furnace. In his paper, an important parameter to increase the post combustion rate is to control the distance between the foaming slag and the

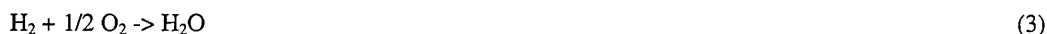
oxygen lance. Shin[7] published a paper about the post combustion rate increases with increasing the distance of the length between the oxygen lance and the slag zone. The China Steel Corporation recently proposes a testing pilot furnace design to investigate this new technology. A commercial numerical code, StarCD developed by Computational Dynamics Limits, is then used to simulate the post combustion phenomena inside the free board, which is above the foaming slag zone. Different locations of the oxygen lance, variations of the inlet mass ration and the preliminary calculation of the heat transfer efficiency are discussed.

2. MODEL DESCRIPTION

In this study, two-dimensional turbulence compressible flow model is considered. The mathematical models can be found in reference [8]. The governing equations can be expressed as

$$\nabla \cdot (\rho \bar{v} \Phi) = \nabla \cdot (\Gamma_{\Phi} \nabla \Phi) + S \quad (1)$$

where Φ is parameter that can be 1 for mass conservation equation, (U,V,W) for momentum equation, h for energy equation and (κ, ϵ) for turbulence equation. Γ is the exchange coefficient and S is the source term. The chemical compositions involved are CO, H₂, O₂, N₂, CO₂ and H₂O. All of these compositions are assumed to be gas type. Three steps chemical reaction are used:



And eddy-break up combustion model is assumed inside the free board, the slag zone is treated as a fixed surface with a fixed temperature flux into the free board. The test pilot furnace of China Steel Corp. consists of 2 layer oxygen injections with 300 mini-meter apart, two inlets for raw material and one exhaust gas outlet. The detail dimension of the furnace is shown in Figure 1.

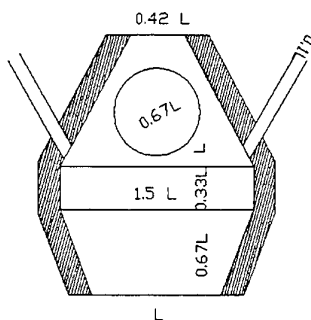


Fig. 1 Furnace model dimension

The 0.1L diameter material inlet is 1.42L above the slag zone and the center of the exhaust outlet with 0.67L diameter is 1.5L about the slag zone. Only certain amount of the 4.5ton/hr raw material is assumed to be injected through two material inlets. The rest of them are dropped down into the slag zone and gasified, then flux back to the free board for the post combustion. There are six oxygen injections in the first layer and four oxygen injections in the second layer of the lance. Two locations of the lance are chosen – 0.25L above the slag zone and 1L above the slag zone. The amount of the oxygen supply is calculated by using stichiometric ratio of the equation (2) (3) and (4) and subtracted total amount of the oxygen inside the raw material.

3. SIMULATION RESULTS

Several configurations of the inlet and outlet are investigated during the simulation of this particular furnace. In the first case the distance between first oxygen injection layer and the slag zone is chosen as the study

parameter. The second case focus on the effect of the reduction of oxygen to the combustion. Then the variation of the raw material ratio supplied through the material inlet and slag zone is used. At the last, the preliminary calculation of the post combustion rate (PCR) and the heat transfer efficiency (THE) is discussed.

3-1 Location of the Lance

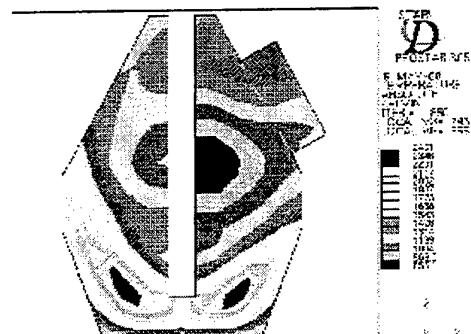


Fig 2 Temperature distribution for lance 0.25L above slag zone ($y=0.0L$)

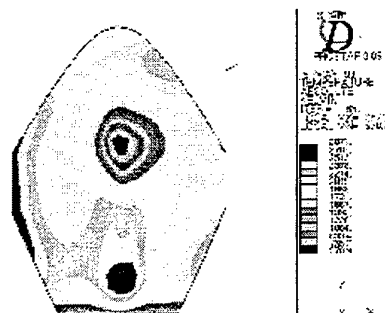


Fig. 3 Temperature distribution for lance 0.25L above slag zone ($y=0.67L$)

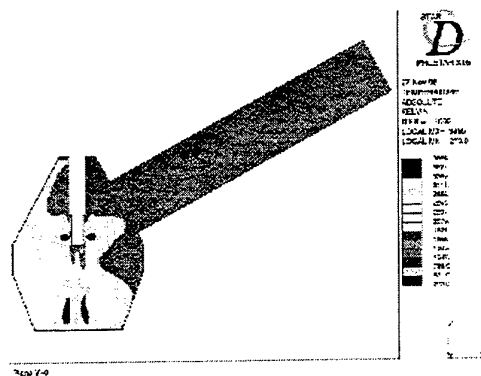


Fig. 4 Temperature distribution for lance 1 L above slag zone ($y=0.0L$)

In this study, oxygen lance is placed in two different height above the slag zone: 0.25 L and 1 L. Figure 2 and 3 shows the temperature distributions at the xz plane at $y = 0.0L$ and $0.67L$ for oxygen lance located at 0.25L above slag zone. As shown in Fig.2 the maximum temperature happened at the exit of the oxygen and is about $2450^{\circ}K$. The combustion zone propagates from the oxygen injector to the bottom of the free board, and hot spots are observed on the surface of the wall. At the top of the furnace, a stagnation zone is generated by the asymmetrical design of the exhaust gas outlet. As the xz plane moves $0.67L$ away from the center line along the y direction which shown in Fig.3, the maximum temperature increases up to $2875^{\circ}K$ at the injection of the oxygen lance. The temperature of the wall opposite to the exhaust outlet reaches $2700^{\circ}K$, which is not reality in the operation of the furnace. The reason for this high temperature generated along the surface of the wall is due

to the assumption of the slag zone inlet condition. Since the fixed surface of the slag zone is assumed and no any material/heat can be penetrated through it, the heat flux can only flow through the circulation of the flow field and then pass out from the exhaust outlet.

Figure 4 and 5 show the other configuration of the oxygen lance with 1L above the slag zone. In Fig.4, there are two ignition zone observed, one is around the oxygen lance and the other is around 0.1L above the slag zone.

The maximum temperature in this configuration is about 3885°K . Fig. 5 is 0.25L along y axis away from the center of the furnace. The maximum temperature is located 0.15L above the slag zone. The wall temperature is around 1800°K for this configuration. This is believed that there is enough space between the oxygen lance and slag zone for the combustion.

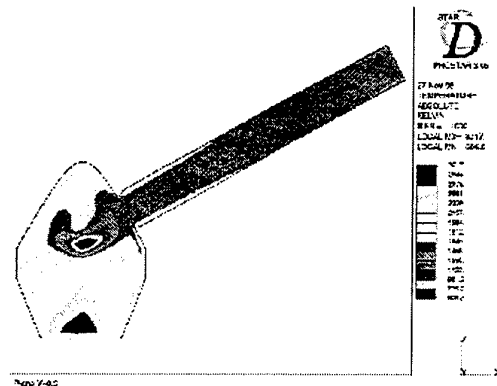


Fig. 5 Temperature distribution for lance 1 L above slag zone ($y=0.25L$)

Comparison of these two configurations, the increasing the distance between the lance and the slag zone increases the combustion rate. This also reported in Shin's paper too.

3-2 Variation of the Material Inlet Ratio

As seen from Fig. 4, two combustion zones are observed. From the energy point of view, the heat generated around the oxygen lance can hardly be used for the post combustion purpose. One suspicion is raised that the initial assumption of the raw material supply from the material inlet is more than expected. Reducing the material amount through the material inlet then is done for another simulation. Figure 6 shows the result with half amount of the material from the material inlet.

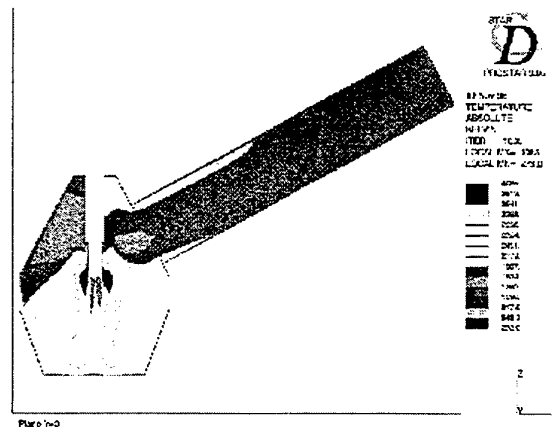


Fig. 6 Temperature distribution with half amount of material inlet

In Fig. 6 the combustion zone becomes one single area and ignition portion is around the oxygen injection. The maximum temperature for this case is 4085°K and that of whole combustion zone is around 2700°K .

3-3 Variation of Amount of Oxygen

As the ratio of the raw material will cause the combustion zone changes, a further study of the change of oxygen amount to the combustion effect is given in the section. Unlike the situation of section 3-2, the change of the oxygen supply did not effect on the shape of the combustion zone but on the maximum temperature inside the furnace. Fig. 7 shows the results of using different amount of the oxygen.

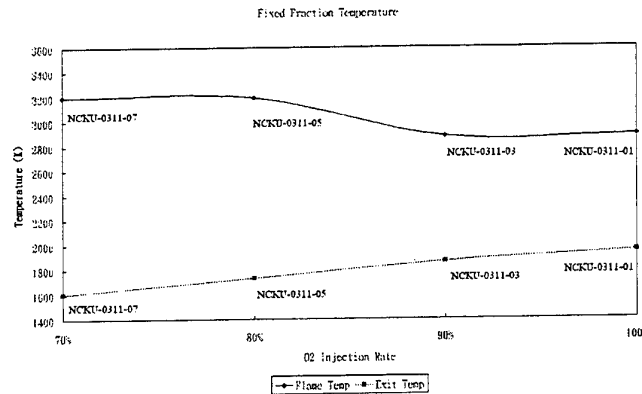


Fig. 7 Comparison of different oxygen inlet

In Fig. 7, NCKU-3011-01 stands for 100% of oxygen inlet and NCKU-0311-03, NCKU-0311-05, NCKU-0311-07 represent the 90%, 80% and 70% of oxygen inlet. The lowest ignition temperature happens at 90% of oxygen inlet, and the exhaust temperature decreases with the decreasing of the oxygen rate.

3-4 Preliminary Study of PCR and HTE

As definition in Katayama's paper [9], the post combustion ratio (PCR) can be expressed as

$$PCR = \frac{(CO\%) + (H_2O\%)}{(CO_2\%) + (CO\%) + (H_2O\%) + (H_2\%)} \times 100\% \quad (5)$$

and heat transfer efficiency (HTE) is

$$\eta = \left[1 - \frac{\text{super heat of exhaustgas}}{\text{heat generated by post combustion}} \right] \times 100\% \quad (6)$$

The mass fractions of the compositions for oxygen lance located at 1L are listed in table 1.

Table 1 Mass Fraction of Compositions

Material	CO	CO ₂	H ₂	H ₂ O
100%	0.328	1.94E-7	1.01E-8	0.407
50%	0.390	1.72E-7	1.12E-8	0.410

Substitution the values into equation 5, the PCR for first case is 55.3% and for reduced material through the material inlet is 51.3%. In this calculation, the amounts of H₂ and the CO₂ are negligible which is based on the assumption of the chemical reaction steps. Equation 4 forced most of the CO₂ and H₂ to form as CO and H₂O. There is a little trick in calculation of the HTE. From equation 6, the super heat of the exhaust gas is defined as the net heat through the slag surface. In this paper, the slag surface is assumed to be a fixed temperature inlet, which is also treated as the net heat between the interaction of the free board and the slag zone. The heat generated by post combustion is calculated by selected two certain distances above the slag zone, 0.04L and 0.08L and takes the average temperature and Cp. The average temperature for these two locations is 1509.8

1854.2. Average C_p are 2178.3 and 2578.6. Then the super heat can be calculated by using

$$\Delta H_{\text{super}} = C_p T_{\text{slag}} = 1165.8 \times 1773 = 2066963.4$$

The post combustion heat at $z = 0.05$ m and $z = 0.1$ m are

$$\Delta H_{PCz=0.04L} = C_p T_{PCz=0.04L} = 1509.8 \times 2178.3 = 3288797.3$$

$$\Delta H_{PCz=0.08L} = C_p T_{PCz=0.08L} = 1854.2 \times 2578.6 = 4781240.1$$

Such, the HTE can be obtained as $\eta_{z=0.04L} = 37.2\%$ and $\eta_{z=0.08L} = 56.8\%$.

4. CONCLUSION

1. Simulations of the post combustion process inside a smelting furnace indicate that the distance between the oxygen lance and the slag zone affects the combustion area and temperature distribution along the furnace wall. The higher oxygen lances the more efficiency that the post combustion can get.
2. The amount of the raw material vaporization near the material inlet dominates the flame location and the ignition temperature inside the furnace. For energy saving, the less amount of the raw material vaporization is needed in the material inlet.
3. Flame temperature not only controlled by the amount of the vapor of the raw material but also by that of the oxygen. Less oxygen will reduce the exhaust gas temperature and not necessary reduces the flame temperature.
4. Post Combustion ratio and heat transfer efficiency in this study are based on several assumptions, although these assumptions are not good at accuracy prediction of PCR and HTE. However, for the very beginning study of the bath type smelting furnace, 50% of PCR and 30-60% of HTE are very close to the operation data.
5. To achieve more reality simulation of post combustion process inside a smelting furnace, a good model of the slag zone is needed, specially the physical model for the interaction between the free board and slag zone.

REFERENCES

1. E. Aukrust and K. B. Downing, Proc. Ironmaking Conference, 1990, 49, 630-644.
2. C. L. Nassaralla, B. Sarma, A. T. Morales and J. C. Myers, Aspects of the Slag-Metal-Gas Reactions in Bath Smelting Reactors, Proc. Tukdagn Symposium, 1994, 61-71.
3. R. B. Smith and M. J. Corbett, "Coal-based Ironmaking," Ironmaking and Steelmaking, Vol. 14, No. 2, 1987, pp.49-75.
4. J. V. Keogh, et. al., "Hismelt Process advances to 100,000 t/y Plant," Proc. 50th Ironmaking Conference, 1991, ISS-AIME, pp. 635-649.
5. T. Ibaraki, et al., "Development of Smelting Reduction of Iron Ore," Iron and Steelmaker, Vol. 67, 1991, No. 12, pp.30-37.
6. K. Takahashi, Muroya, K. Kondo, T. Hasegawa, I. Kikuchi and M. Kawakami, "Post Combustion Behavior in in-bath Type Smelting Reduction Furnace," ISIJ International, Vol. 23, No. 1, 1992, pp. 102-110.
7. M. K. Shin, S. D. Lee, S. H. Joo and J. K. Yoon, "A Numerical Study on the Combustion Phenomena Occurring at the Post Combustion Stage in Bath-type Smelting Reduction Furnace," ISIJ International, Vol. 33, No. 3, 1993, pp.369-375.
8. A. Shinotake and Y. Takamoto, "Combustion and Heat Transfer Mechanism in Iron Bath Smelting Reduction Furnace," La Revue De Metallurgie – Juillet/Aout, 1993, pp.965-973.
9. H. Katayama, T. Ohno, M. Yamauchi, M. Matsuo, T. Kawamura and T. Ibaraki, "Mechanism of Iron Oxide Reduction and Heat Transfer in the Smelting Reduction Process with a Thick Layer of Slag," ISIJ International, Vol.32, No. 1, 1992, pp.95-101.

STUDY ON FLUID DYNAMIC CHARACTERISTIC IN THE ESP

Yang Wang Yun Zhang Zhenzhong Li Zhaoxing Feng

The State Engineering Technology Research Center of Combustion of Power Plant
No. 185 Huanghe Bei da Jie ,
Shengyang , Liaoning , 110034 , P. R. C

Keywords: simulating, ESP, efficiency, fly ash, power plant

ABSTRACT. The efficiency of fly ash separating of the electrostatic precipitator(ESP) in Yuan Bao Shan Power Plant has not reached the designed destination since being put into operation, that caused pollution the environment of that district severely and influencing the normal operating of the 600MW generating unit. Being aimed at this, we carried out a series of research work with the lab-scale facility. A few of new discoveries were found and the reforming scheme was drafted. The content of research work is stated in this paper.

1. INTRODUCTION

The number 2 boiler(1824t/h) in Yuanbaoshan power plant includes the rotated air preheater and the electronic precipitator(ESP) which is located in the end of the gas duct with the double trumpet shaped entrance boxes. The type of the ESP is 2x3x56x14x4x300. Through several years operation, a serious of problems was found. Those problems result in the decrease of efficiency of ash separating, induce the severe erosion of fan's scrub and pollute the environment around the district. According to the research work having been done, we realize that one of the main reasons is that the distribution of gas velocity in the electron area was obviously irregular. If the gas velocity is higher than normal, it would be difficult to discharge ash, but if the gas velocity is lower than normal, the ash would deposit on the negative electrode line (electrical corona) , that would reduce the current as a result, reduce the efficiency of ash separate[1]. It was proved by the tests in situ, the root-mean square of relative deviation of velocity (see eq.1) has not reached the demanded value of $\delta = 0.25$ required by the stand DL/T514-93. The detected result was $\delta = 0.31$ which indicated the state of gas distribution in the ESP. In order to find out the reason induce the problem and then solve it, we established a facility of lab-scale at The State Engineering Technology Research Center of Combustion of Power Plant. A lot of research work aimed at the fluid-dynamic characteristic (especially in the entrance boxes) had been done in the facility.

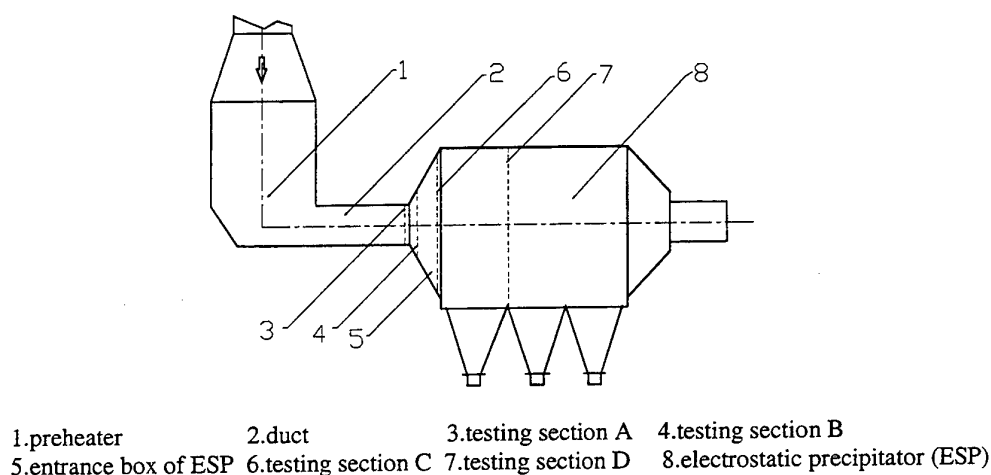


Fig.1. Lab-scale experiment facility

The main stages of research were the following: The first, performed a lot of cooling fluid dynamic response experiments in the precipitator model for searching the problems on the related aspect. The second, in order to draft of prime schemes for transforming the ESP, the reasons resulting in the problems was analyzed according

to the fluid dynamic theory. The third, On the basis above, performed the optimizing experiments to confirm the final scheme of reforming the structure of the ESP and the related duct.

The system structure of the lab-scale experiment facility is illustrated in Figure 1. In the trumpet shaped entrance box, there were four sections installed with current regulation plank, and one section installed with U shaped plank (see Fig 3). In order to simulate the entrance condition, the models of air preheater and the duct to the ESP was added into the system.

2. SIMULATING CALCULATION [2]

2.1. Criterion Eu

Because the prime reform schedules of the ESP during research stage were based on ensuring the resistance to be relatively stationary, it was not necessary to measure the static pressure of the fluid, and the criterion Eu could be ignored.

2.2. Criterion Re

Because the velocity of the gas in the ESP was lower, it was difficult to reach the second self-simulating zone, so we adopt the same Re value in module as that in the real plant.

2.3. Geomitry Analogy

The scale from the module to the real plant was 1:8.

2.4. Criterion Stk

In the principal of insuring the Stk value were the same between the module and real plant, the diameter of the ash should be 55.3 μ m. The ash from Shenyang power plant was used in the experiment instead of the ash of Yuanbaoshan power plant.

2.5. Criterion Fr

The air mass needed in the lab-scale experiment facility calculated according to the criterion Fr was smaller than that based to the criterion Re. In order to increase the quality of fluid simulating, the effect of Fr was ignored. The Fr is chiefly representative the influence of gravity. Because the ratio of inertia force and gravity force to the ash particle was great, so it was reasonable to ignore the effect of gravity force, and then the criterion Fr could be ignored.

3. THE CONTENT AND ANALYSIS OF EXPERIMENTS

3.1 Method of Experiments

The experiments was divided into two parts, there were aerodynamic and air-solid two-phase flow dynamic experiment. The root-mean square of relative deviation of velocity of some sections was tested in aerodynamic experiments [1,3]. It was defined as:

$$\delta = \left[\frac{1}{nm} \sum_{i=1}^n \sum_{j=1}^m \left(\frac{u_{ij} - u_{av}}{u_{av}} \right)^2 \right]^{1/2} \quad (1)$$

where: m and n represent the row and column number of the points on the tested section respectively, u_{ij} represents the velocity on the intersectional point of i-th row and j-th volume on the tested section, u_{av} represents the average velocity of the tested section. The density distribution of particles was tested with camera-computer image treatment system(CCITS) in the two-phase flow dynamic experiment.

3.2.The Performance Characteristic Of Original Structure

3.2.1. Aerodynamic experiment. Four sections were selected for testing the velocity distribution in the model as illustrated in Figure 1. Section A was located in the start section of entrance box. Section B was located in the section behind the first current regulation plank, Section C was located in the section behind the fourth current regulation plank, and Section D was located in the electric zone. The distance of the two nearest testing points on the same section along the row direction was 100mm, and that on the other direction was the same.

Table 1. The Result of Aerodynamic Experiment On Original Structure

Section	A	B	C	D
δ	0.13	0.26	0.12	0.11

The result of testing was presented in Table 1. From the aerodynamic experiment result of above, the function of the gas current regulation plank could be clearly presented. Because there were a long straight duct before the entrance box of ESP, the gas velocity on section A was uniform. It was due to the fluid spread suddenly, the value of δ on section B was increased to 0.26 although there was first current regulation plank before section B. But the value of δ was greatly decreased to 0.12 through the other three current regulation planks, and that of section C was 0.11. So, it was proved that the current regulation planks did have the important function and ability to make the gas velocity into the ESP to be uniform.

3.2.2. Air-solid two phase flow experiment. From the result of the experiment, it was found that there was a dense fly ash spray formed in the entrance box, as illustrated in Figure 2. The dense fly ash spray formed on the duct bottom ahead of the ESP would breakdown the first current regulated plank partly before the section B in the entrance box of ESP. In the mean time, the fluid velocity would increase in that part. And that sped up the erosion of the current regulated planks. So the uniform velocity filed of fluid between the electron boards was disturbed. This situation was proved by the result of the inspection against the real plant (the current regulated planks were broken down within about two months of operation in the real plant).

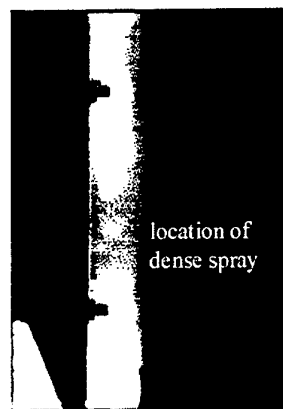


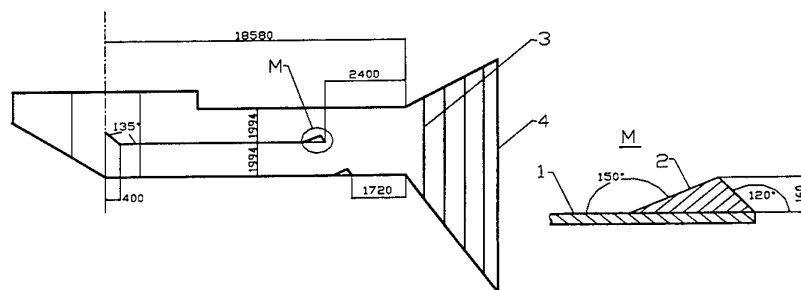
Fig.2. The image of dense spray formed in original structure near section B

It was obviously that the efficiency of the fly ash separating would decrease after losing the efficacy of current regulated planks with the value of $\delta > 0.25$ of the fluid between the electron boards. In order to ensure the value of $\delta < 0.25$ of the gas between the electron boards during demanded period, some reformation must be done to avoid the severe partly erosion of the current regulated planks.

3.3. Study On Reform Scheme

3.3.1. Reform scheme. Through the experiment study on the model of original structure of ESP, it was regarded that the main reasons led to the forming of dense fly ash spray in the entrance of ESP may be as follows:

1. There was direction change of gas flow with 90° angle below the air preheater as illustrated in Figure 1. A part of particles, especially the bigger ones, were threw away to the bottom of the horizontal duct.



1. separate plate
2. disturbing object
3. current regulation planks(four)
4. U shaped plank

Fig.3. The optimal reform scheme in the duct

2. The relatively thick boundary layer on the duct bottom ahead of the ESP had kept or developed the dense fly ash spray formed on the bottom of the duct. The principal of forming the boundary layer will be discussed later.

A series research work had been done towards the problem of the partly erosion of the current regulated planks. The optimal reform scheme was drew up as illustrating in Figure 3. Firstly, install a horizontal separate plate along the duct from the central line of air preheater exit to the position before exiting the duct. The duct was divided into two separate parts on an equal footing by the separate plate, and so did the gas with fly ash from the preheater. Thus, the fly ash density of the dense fly ash spray would decrease. On the other hand, the disturbing object was installed on the end of the horizontal plat and the duct bottom respectively as illustrated in Figure 3. The dense fly ash spray would be defused by disturbing objects before entering the entrance box of ESP.

3.3.2. Aerodynamic experiment. The result of testing was presented as Table 2. It was proved that the values of δ in the entrance box and electron filed were not influenced by the reform of duct compared with the related data in Table 1. The efficiency of ash separating by the ESP would not decreased due to the reforming scheme in the horizon duct.

3.3.3. Air-solid two-phase flow dynamic experiment. Fig. 4 is one of the images obtained during the experiment with CCIT system. It was illustrated that there were no significant dense fly ash spray formed in the entrance box of the ESP. This reform scheme would be efficiency to destroy the dense fly ash spray in the real plant. Thus, the severe partly erosion would be avoided. That extended the usage life of the current regulated planks and ensured the needed efficiency in the required continuous operating period of the ESP. The scheme of reforming the structure like Figure 3 of the duct was adopted by Yuan Bao Shan Power Plant. It was said by the technologist in Yuan Bao Shan that the situation of reformed plant was very well.

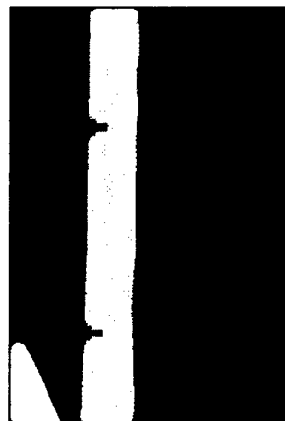


Fig.4. The image of density distribute in reformed structure near section B

Table 2 The Result of Aerodynamic Experiment on Reformed Structure

Section	A	D
δ	0.12	0.12

4. THE THEORETICAL ANALYZE OF THE FORMING OF DENSE FLY ASH SPRAY

4.1. Calculation On The Boundary Layer [4]

On the real plant, the velocity of the gas in the horizontal duct between the air preheater and ESP was nearly 10m/s. The particles would be in the suspended status. It is impossible to deposit on the bottom of the duct owing to gravity. So, the chief reason why the dense fly ash spray exists is the boundary layer on the duct bottom. Boundary layer is combined with stratum boundary layer and turbulent boundary layer as illustrate in Figure 5. The point of conversion from stratum to turbulent would be confirmed by the value of Re_x , normally in the range of $5 \times 10^5 \sim 3 \times 10^6$.

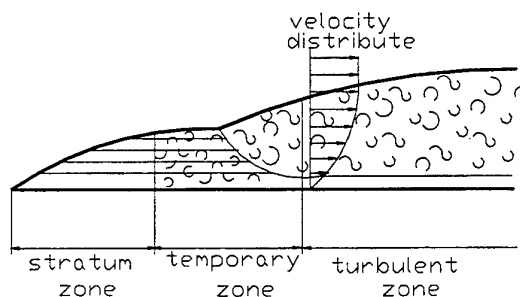


Fig.5. The composition of theoretic boundary layer

$$Re_x = VX/v$$

(2)

where, V represents the velocity of the gas(m/s), X represents the distant from a certain point to the start point on the plank(m), ν represents the kinematic viscosity of the gas(m²/s).

In the calculation, the interfering to the initial condition by the air preheater was ignored, and it was supposed that the fluid space was limitless on the up direction. In the horizontal duct of the real plant, if $Re_x=5 \times 10^5$, $\nu=25.66 \times 10^{-6}$ m²/s, $V=9.06$ m/s, than $X=1.4$ m . It is demonstrated that the part of stratum boundary layer is very short compared with the length of the whole plank of 18m. The boundary layer on the bottom of the duct can be considered as the turbulent boundary layer. So, the theory about the turbulent boundary layer can be applied to calculate the thickness of the boundary layer on the bottom of the duct approximately as the following equality.

$$\delta=0.37X(\nu/VX)^{1/5} \quad (3)$$

According to eqn(3), the maximum thickness on the end of the duct($X=18$ m) would be 0.29m. The practical thickness of the boundary layer in the duct would be thinner than 0.29m due to the ignored factors.

4.2. The Reasons of the Particle Concentration in the Boundary Layer

The chief reasons of forming the dense fly ash spray due to the existing of boundary layer are presented as follows:

1. There was direction change of gas flow with 90° angle below the air preheater as illustrated in figure 1. A part of particles, especially the bigger ones, were threw away to the bottom of the horizontal duct.
2. The diffusion coefficient of the gas in the main stream is greater than that in the boulder layer. So it is difficult for the particles moving from the boundary layer to the main stream, but it is easy on the opposite direction. The relatively thick turbulent boundary layer on the duct bottom ahead of the ESP had kept or developed the dense fly ash spray formed on the bottom of the duct.
3. Because of the inertia, most of the particles forming the dense fly ash spray would not keep pace with the spread gas in the entrance box of ESP, and impact on the current regulated planks directly.

It is clearly that the boundary layer must be destroyed before entering the entrance box of ESP in order to diffuse the dense fly ash spray.

5. CONCLUTIONS

It was proved that the current regulation planks did have ability to make the gas velocity into the ESP to be uniform under the normal conditions.

One of the chief problems induced the decrease efficiency of the ESP was that, there was a dense fly ash spray formed. That broke down the current regulated plank partly in the entrance of ESP rapidly, and the uniform velocity of fluid between the electron boards was disturbed.

The reform scheme as illustrated in figure 3 would be efficiency to destroy the dense fly ash spray in the real plant. Thus, the severe erosion partly would be avoided. That extended the usage life of the current regulated plank and ensured the needed efficiency in the required continuous operating period of the ESP.

REFERENCES

1. T.Y. Tan, Technology of Precipitator Industry, Press of Architecture Industry in China, 1984.8 (in chinese).
2. Z.G. Li, Simulating, Press of Nation Defence Industry, 1982.12 (in chinese).
3. J. P.Gooch, Journal of the Air Pollution Control Association, February 1975, Volume 25, No.2.
4. Shandong Engineeering college, Engineering Hydromechanics, Power Industry Press, 1980.7 (in chinese).

A STUDY ON THE ELECTRON-EMITTING CHARACTERISTICS IN NHTHPESP

Gu Zhongzhu Cai Song Liu Xiaoguo Wei Qidong Yong Yaping Cao Zhonghua

Thermoenergy Engineering Research Institute

Southeast University

Nanjing, 210096, P.R.China

Email: Songcai @ seu.edu.cn

Keywords: non-corona, temperature, pressure, electron-emitting characteristic, precipitator

ABSTRACT. This paper provides the results of experimental investigations on the electron-emitting characteristics of the Non-corona High Temperature and High Pressure Electrostatic Precipitator (NHTHPESP). The tests were carried out on the pilot NHTHPESP equipped with an oil-fired combustor which uses a kind of light diesel oil as fuel. Conclusions with respect to the influence of different operating parameters on the thermal emission properties of the emitter are drawn. The performance of NHTHPESP is also investigated.

1. INTRODUCTION

The application of new technologies in power plants, such as PFBC, results in great efficiency. On the other hand, there are a few problems to solve, including the ash-removing of coal-boiler flue gases at high temperature and high pressure. The use of Corona Electrostatic Precipitators (CESP) for collecting fly ash from pulverized coal combustion is a conventional method in power plant environmental control. In these devices, the ash is charged by the ions formed through the corona effect on the high voltage emitting electrodes, and the charged ash is collected by grounded plates under the action of the electric field. Due to the high voltage causing corona, the application of CESP would, under high temperature and high pressure, come up against many difficulties, such as electricity insulation, the stability of operation, etc.

The NHTHPESP is a new dust-removing technique invented by the Thermoenergy Engineering Research Institute of Southeast University. It utilizes the thermoelectrons emitted by some particular materials to charge dust particles, instead of the corona discharge in traditional CESP. The charging section is one of the key components in the NHTHPESP. Whether the dust particles can get sufficient electronic charge depends on if the emitter used as the negative electrode can continually and steadily emit enough electrons. In this presentation, the effect of different variables on the thermoelectron emission properties is investigated and the results of precipitation tests for evaluating the performance of NHTHPESP are also provided.

2. DESCRIPTION OF THE PILOT FACILITY

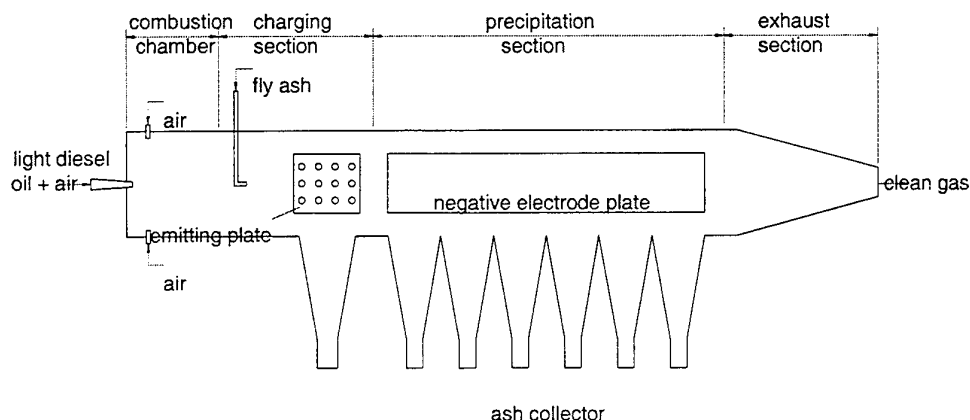


Fig.1. The diagrammatic sketch of the pilot NHTHPESP

The pilot NHTHPESP, whose characteristics are described in Table 1, was conceived as a versatile unit that allows testing different variables, with which to analyze the precipitator's properties in various conditions. It is equipped with an automatic control system of the most important operating parameters, such as gas flow, temperature, pressure, voltage, etc. The facility includes three chief components (see Fig.1). In order to make the study more close to industrial reality, the oil-fired combustor was used to supply the high temperature and high-pressure flue gas circumstances for the research. In charging section, 18 emitters which will give off electrons when heated by the exterior are uniformly distributed on the two sides of a steel plate called emitting plate. The plate hung in the middle of the passage is used as negative electrode and the grounded duct wall parallel to that as positive one. To obtain adequate emission current density, a small amount of voltage is applied between the two electrodes. When the flue gas stream mixed with dust particles (the coal-boiler fly ash of Nanjing Xiaguan Power Plant) pass through the emitting zone, the particles will capture the electric-charges from the emitters. In precipitation section, those charged particles are removed by the effect of the strong electric field force.

Table 1. Design characteristics of the pilot NHTHPESP

Combustion Chamber Dimensions		Length (mm)	1200
Diameter (mm)	250	Width (mm)	70
Length (mm)	400	Height (mm)	140
Configuration of Charging Section		Negative Electrode Plate Dimensions	
Length (mm)	640	Length (mm)	940
Width (mm)	70	Width (mm)	80
Height (mm)	140	Thickness (mm)	12
Emitting Plate Dimensions		Operating Conditions	
Length (mm)	400	Temperature (°C)	300-800
Width (mm)	90	Pressure (MPa)	0.1-0.6
Thickness (mm)	12	Gas flow (Nm ³ /h)	48.7
Emitter Dimensions		Charging section voltage (Kv)	0.2-3
Diameter (mm)	21.4	Precipitation voltage (Kv)	12
Thickness (mm)	4		
Configuration of Precipitation Section			

3. RESULTS AND DISCUSSION

V-I Characteristics

The V-I curves corresponding to different temperature and pressure conditions are shown in Fig. 2, where it is clear that the thermal emission current density increases with the growth of the charging section voltage, which is similar to what happens in CESP. Increasing the temperature also causes the rise of the current density, showing that the electron-emitting properties of NHTHPESP can be improved by raising the temperature of flue gases. Contrary to this, the current density decreases when pressure goes up. As is shown in Fig. 2. (d), the current density corresponding to 0.6Mpa, 3000v and 850°C is at least of the order of one more than that of the CESP which has been founded so far, indicating that the electricity insulation problem in NHTHPESP is easily solved because of the low operating voltage, and the dimensions can also be greatly decreased.

Influence Of Temperature

Fig.3 illustrates the characteristics of the emission current density as a function of temperature. There is a little current when the temperature of the emitter is lower than 700°C, and the current density increases abruptly when the temperature is more than 700°C. As a result of that, it is believed that the critical emitting temperature, above which a large quantity of electrons are given off, is about 700°C. In addition, comparing the I_d -t curves obtained at both operating pressures, the curve B from 0.1MPa indicates a considerable increase in slope with respect to the curve A corresponding to 0.6Mpa, showing the influence of temperature on the emission current is smaller at high pressure than that at low pressure.

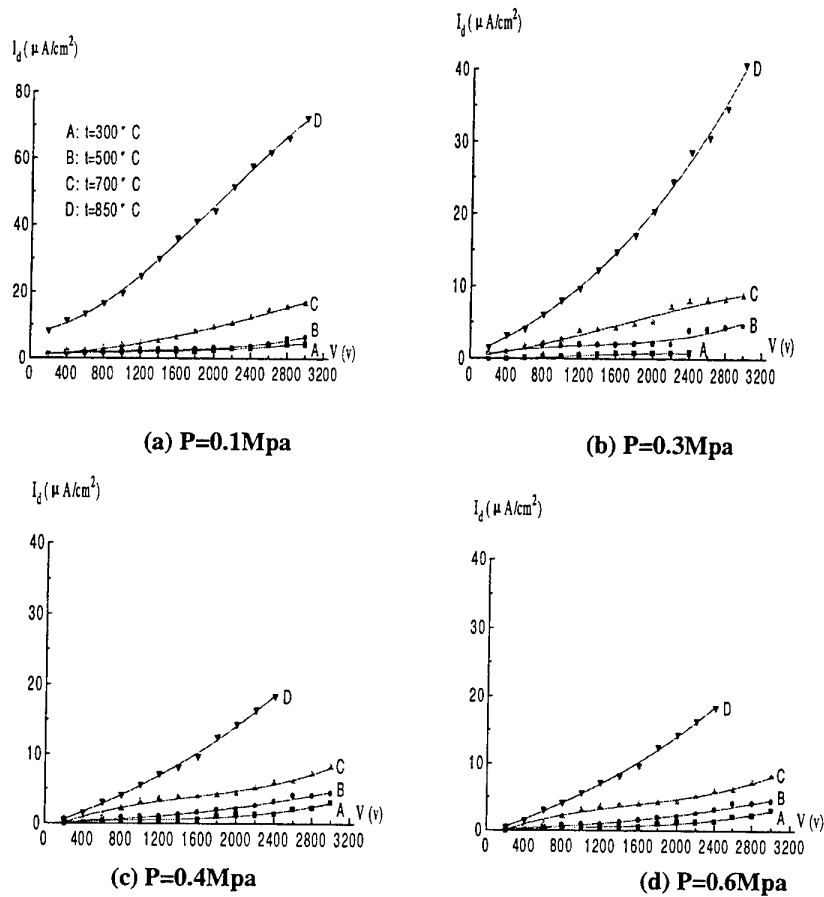


Fig.2. V-I characteristics for various experimental conditions

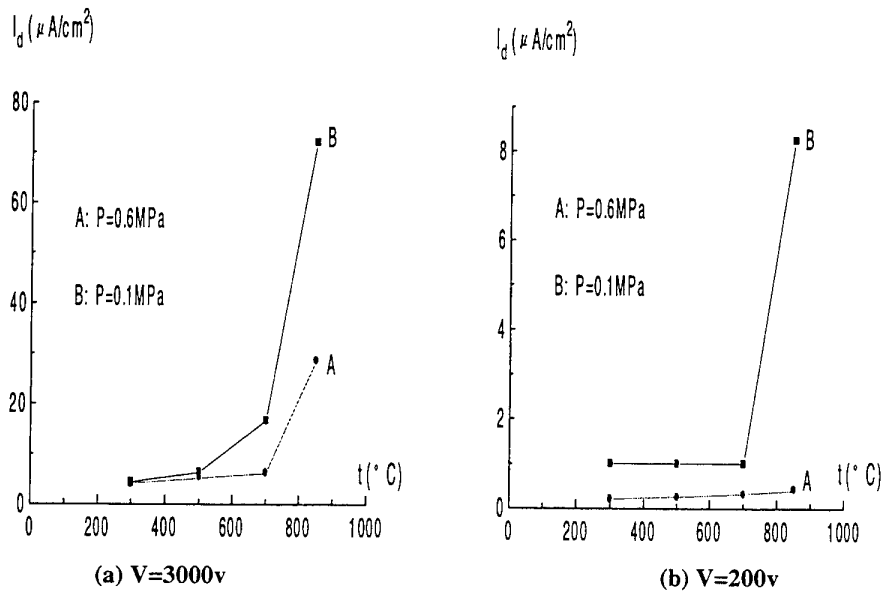


Fig.3. Influence of temperature on the emitting properties

Influence of Pressure

The influence of pressure on the emission current density is shown in Fig.4. At low pressure, the current density declines rapidly with the rise of the operating pressure. Then, the curves begin to reduce their slope gradually. Also, comparing the I_d - P curves produced by both operating temperatures, that corresponding to 300°C presents considerable reduction in slope with respect to that from 850°C, indicating that the effect of pressure on the emission current is greater at high temperature than that at low temperature.

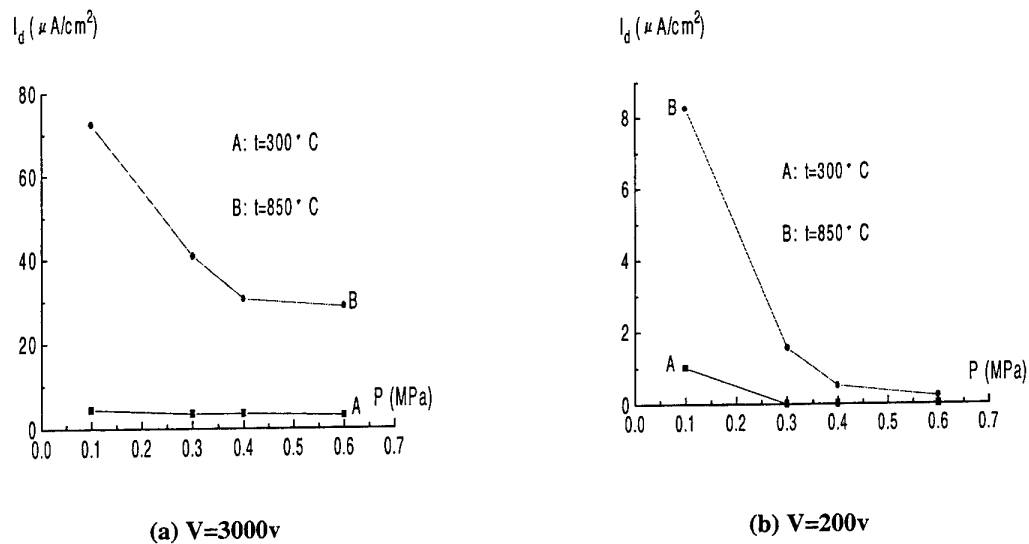


Fig.4. Effect of pressure on the emission current density

Stability of the Cathode Emission Property

The performance of NHTHPESP is significantly dependent on whether the emitter can continually and steadily give off electrons. Fig.5 shows the characteristics of the current density from the emitting plate as a function of time at 0.6 MPa and 850°C. The emission current density decreases abruptly at initial stage, and then the

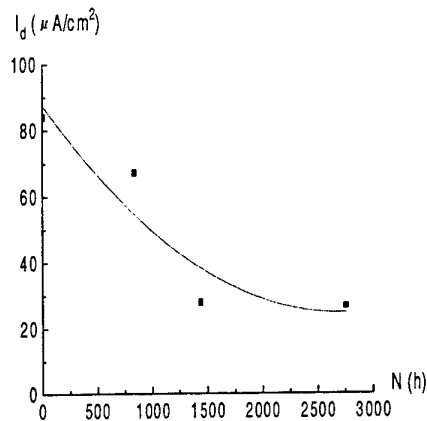


Fig.5. Variance of the emitting property with time

curve begins to reduce its slope, showing an apparently asymptotic tendency toward stabilization with the growth of time. The sudden decline in the emission current at early stage is mainly due to the inevitable changes in the physical and chemical properties of emitter, which result in the drop of its emitting ability. With the increase of time, the material properties tend to be stable and therefore the emitter gives off electrons steadily at

the constant operating conditions. From Fig.5, it is also founded that the current density from emitter, in spite of a considerable decline at beginning, is still about $28\mu\text{A}/\text{cm}^2$ at stable state, which is 10 times higher than that of common CESP. As a result, it is believed that the Non-corona Electrostatic Precipitator can work effectively at high temperature and high pressure conditions for a long time.

Performance of NHTHPESP

In order to investigate the practicality of NHTHPESP, the ash collection tests were carried out on the pilot facility (see Fig.1 and Table1). The experimental conditions are shown in Table2. Fig.6 illustrates that the ash collection efficiency goes up with the increase of temperature, due to the rise of the emission current density in

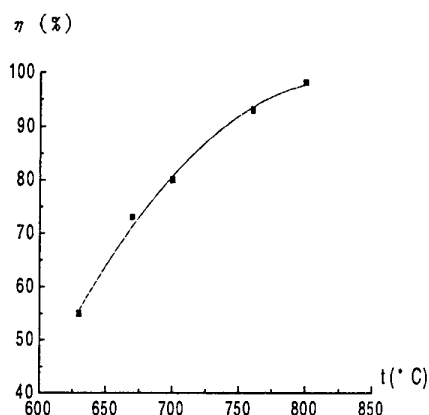


Fig.6. Variance of efficiency with temperature for 12Kv(precipitation section voltage)

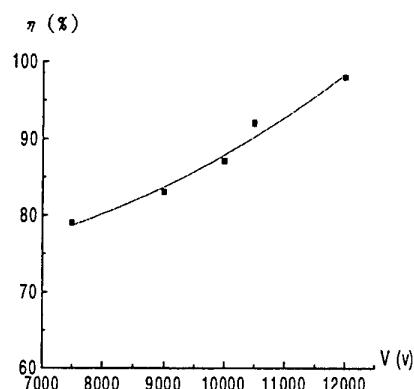


Fig.7. η -V curve for 850°C

Table 2. Operating Conditions For Ash Collection Test

Pressure (Mpa)	0.6	Gas velocity (m/s)	1.0
Charging section voltage (Kv)	3	Temperature (°C)	300-800
Gas flow (Nm ³ /h)	48.7	Precipitation section voltage(Kv)	7.5-12

this case. As is shown in Fig.7, the efficiency can be increased through raising the precipitation voltage, which is similar to what happens in CESP. Also, from Fig.6 and Fig.7, it is confirmed that the Non-corona Electrostatic Precipitator is specially suitable for high temperature occasions, and in spite of high pressure(0.6Mpa), its efficiency is more than 90% so long as the temperature is above 750°C.

4. CONCLUSIONS

The influence of various operating parameters on the electron-emitting characteristics of the emitter material and the performance of NHTHPESP are investigated experimentally. The results founded from the experiments are summarized as follows:

- 1) Temperature has a great influence on the emitting properties. There is a little emission current density when the temperature of the emitter is lower than 700°C, and it increases abruptly with the rise of temperature as the temperature is above 700°C.
- 2) The significant decrease of the emission current density due to the increase of the pressure is observed at various conditions. The effect of the voltage applied between the emitting plate used as negative electrode and the positive plate on the emission current is also considerable.
- 3) The emitting material developed is practical in high temperature and high- pressure occasions.
- 4) The Non-corona Electrostatic Precipitator is available under high pressure. It is especially suitable to high temperature situations.

REFERENCES

1. Q.D. Wei, "The Study of Non-corona High Temperature Electrostatic Precipitation", 27th Symposium of Engineering at Aspects of Magneto Hydrodynamics, June 27-29, 1989, Reno, Nevada, Session 3,3.3-1
2. B. S. Choi, and C. A. J. Fletcher, "Computation of Particle Transport in an Electrostatic Precipitator", *Journal of Electrostatics* 40&41 (1997) 413-418
3. B. Navarrete, L. Canadas, V. Cortes, and L. Salvador, "Influence of Plate Spacing and Ash Resistivity on the Efficiency of Electrostatic Precipitators", *Journal of Electrostatics* 39 (1997) 65-81
4. T. Barbarics, H. Igarashi, A. Ivanyi, and T. Honma, "Electrostatic Field Calculation Using R-functions and the Method of Characteristics in Electrostatic Precipitator", *Journal of Electrostatics* 38 (1996) 269-282

A STUDY OF THE MOVING GRANULAR BED FILTER REMOVING DUST FROM HOT GAS FOR IGCC AND PFBC-CC SYSTEMS

Shisen Xu

Thermal Power Research Institute

State Electric Power Corporation of China, Xi'an 710032, P.R. China

Email: xss98@pub.xaonline.com; Fax: 86-29-3236151-2309

Keywords: dust removal, moving bed filter, hot gas cleaning

ABSTRACT. Hot gas cleanup is a key technology of improving efficiency for IGCC and PFBC-CC systems. This paper is a study of the moving granular bed filter that is one of the greatest potential technologies for hot gas dust removal. The flow process and filtration mechanisms of the moving granular bed filter were studied, and filtration characteristics were described. Experimental studies on high temperature dust removal on the test system of the moving granular bed filter without screen had been done. The relationship between the filter characteristics and main affecting factors were found. The study showed that the moving granular bed filter can remove particles from hot gas continuously, and lead to high efficiency after optimized. This study will provide a basis for the moving granular bed filter for applications in hot gas cleanup.

1. BACKGROUND

The Integrated Coal Gasification Combined Cycle (IGCC) and the Pressurized Fluidized Bed Combustion-Combined Cycle (PFBC-CC) have high efficiency and low emission, so they are one of the most promising clean coal power generation technologies in 21st century. Hot gas cleanup is a key technology to improve efficiencies of IGCC and PFBC systems, but it has not been commercialized now[1]. Hot gas cleanup systems are concerned with the control of particulate, H₂S (or SO₂), NH₃ and alkali metal in synthetic gas (or flue gas) at high temperatures and pressures(HTHP). The paper studies on dust removed from hot gas.

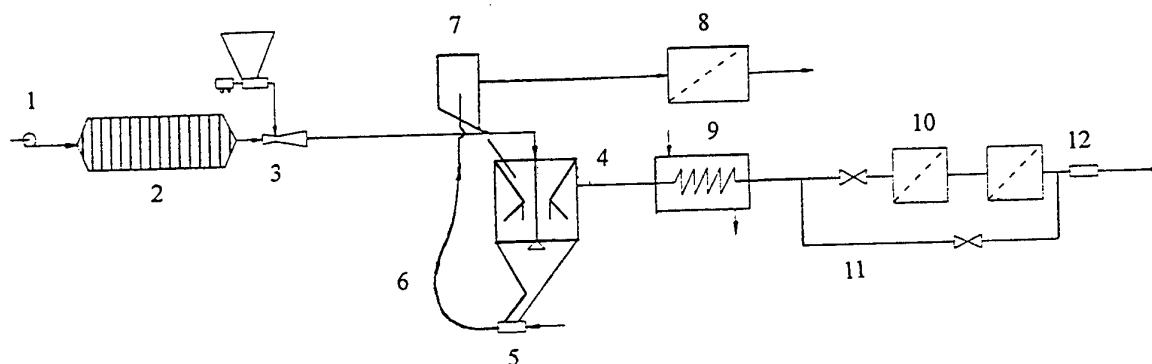
Hot gas cleaning must meet both gas turbine specifications and environmental standards. Maximum gas turbine inlet concentrations are considered to be approx. 10 mg/m³_{STP} for particles larger than 5 μm and 1 mg/m³_{STP} for particles larger than 10 μm [2,3]. This specification is more stringent than environmental standard, so hot gas dust removal must meet gas turbine specification. There are many techniques under development for hot gas dust removal, such as cyclones, electrostatic precipitators(ESPs), wet scrubbers, metal filters, ceramic candle filters and moving granular bed filters(MGBF) [4]. Among these techniques, ceramic candle filters and moving granular bed filters have the greatest potentials. Ceramic candle filters can remove most particles larger than 5 μm, but its filter elements suffer from microcrack formation during high temperature testing due to thermal and mechanical fatigue. Apart from these problems, chemical attack on ceramic filter materials or composites by alkali metals, steam and trace elements may be problems for long-term use. MGBF has good performance at HTHP, and the possibility of continuous regeneration in MGBF systems makes granular bed filtration an attractive option for continuous gas cleaning purposes. However, MGBF is far from optimal: the complexity of the solids handling and filter material cleaning system, effects of operation facts and structure facts on filter performance. This paper researched on optimizing structure and operating parameters to improve MGBF's performance by an experimental study.

2. EXPERIMENTAL SYSTEM

Fig.1 is the high temperature dust removal experimental system of MGBF without screen. The diameter of the filter was 0.45m and the height of the filter was 1.50m. The gas stream between 30 to 300 m³_{STP}/h could be used as filter gas flow, which corresponded to filter velocities between 0.066 to 0.66 m/s. There were four distributor legs for the filtration media flowing into the filter to make the bed well-distributed.

A high temperature electric heater could heat the airflow from 20°C to 900°C. An aerosol generator was used to produce a dust-laden airflow that was fed to the filter. Dust concentration could be 50 mg/ m³_{STP} to 30 g/ m³_{STP}. The bed material recirculation and regeneration system consisted of an injector driven by pressurized air, a pneumatic conveying line, an inertial separator and a dust collector. The filter material was collected in a recollect vessel. The transport air flowed through a dust collector, and went out of the system. The clean gas out

from the filter was cooled to 70~80°C, then flows through a sampling collector. Used by the SKC-2000 optical particle counter, the inlet and outlet particle size distributions were analyzed.



1. Air inlet 2. Heater 3. Aerosol generation 4. MGBF 5. Injector 6. Pneumatic conveying line
7. Inertial separator 8. Dust collector 9. Cooler 10. Sampling collector 11. By pass line 12. Flow meter

Fig.1. The high temperature dust removal experimental system of the moving granular bed filter

3. RESULTS OF OPTIMIZATION TESTS

3.1 The Parameters of the Optimization Tests

The parameters of the optimization tests were as follows.

The filter bed material: Silicon Carbide and Al_2O_3
The gas flow rate: 50~150 $\text{m}^3_{\text{STP}}/\text{h}$
The dust concentration: 10 $\text{g}/\text{m}^3_{\text{STP}}$
Test temperature: 600°C

The size of the material: 1~2mm
The bed transport rate: 0~1.5kg/min
The dust size: <100 μm
Test pressure: atmospheric

3.2 Effects of Some Facts on the Filter Pressure-Drop

Fig.2 shows the effects of the length of the gas inlet tube under the bed material surface on the filter pressure-drop. The experimental results show that the filter pressure-drop increases with the increasing length of the inserted inlet tube. The pressure-drop is 4kPa with a 400mm inserted length.

Fig.3 is the test result for the bed transport rate affecting the filter pressure drop at a given inserted length of 200mm. The experimental results show that the filter pressure drop decreases as the bed transport rate is increased, but it didn't profit for the filter efficiency.

Fig.4 shows the effect of dust concentration in gas on the filter pressure drop. Fig.5 shows that the filter's critical fluidized velocity is about 0.9m/s at 1.0kg/min bed transport rate.

3.3 The Selection Characteristics of the Filter Efficiency for the Particle Size

Figs. 6-10 are the experimental data on the effect of operating parameters on the filter efficiency. These tests show the following results.

1. The grading filtration efficiency is a function of particle size. There is a lower efficiency range (80%~90%) on all test curves, which correspond to 0.5~1 μm particle sizes. The grading filtration efficiency increases for particles smaller than 0.5 μm , because the diffusion separation mechanism is more important for very small particles. The grading filtration efficiency can reach to 98.5~99.5% for particles larger than 10 μm , but for particles larger than 1 μm and smaller than 10 μm , which are dominated by inertial impaction, interception and gravitation mechanisms, the filtration efficiency decreases quickly with decreasing particle

size.

- The total efficiency of the filter increases 0.4 percent as the dust concentration increases from $0.5 \text{ g/m}^3_{\text{STP}}$ to $1.5 \text{ g/m}^3_{\text{STP}}$, and the grading filtration efficiency for small particles increases due to inertial impaction and agglomeration.
- The valley of test curves is more obvious and moves toward right varying with the increase in gas flow rate increase. It means that the grading filtration efficiency for small particles decreases with the increase in gas flow rate.

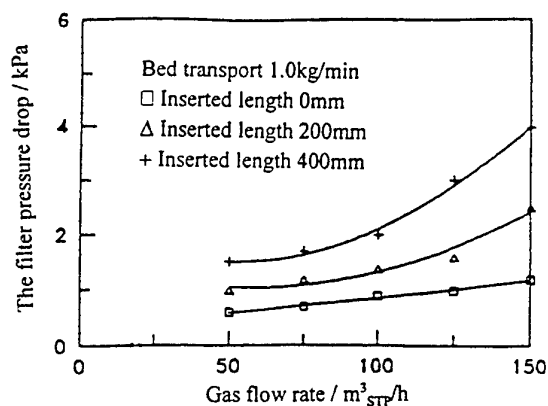


Fig.2. The length of the gas inlet tube under the bed surface affecting the filter pressure drop

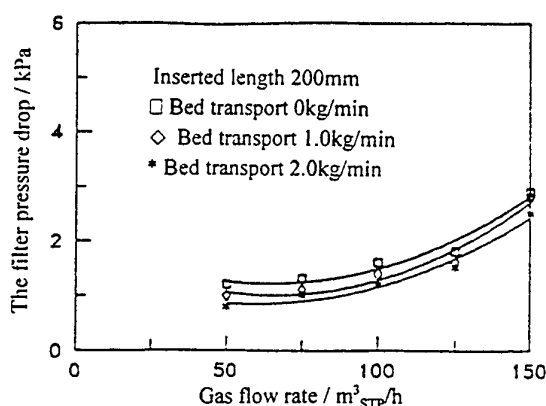


Fig.3. The bed moving rates affecting the filter pressure drop

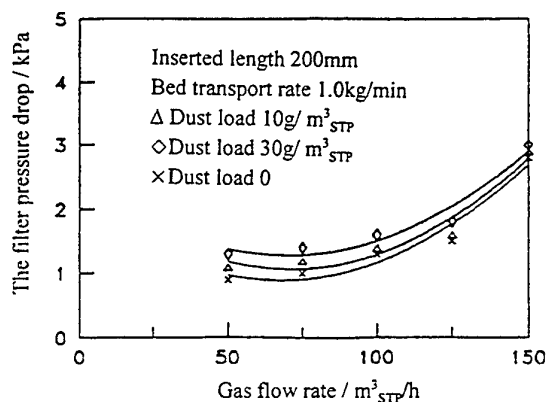


Fig.4. The dust concentration in the gas affecting the filter pressure-drop

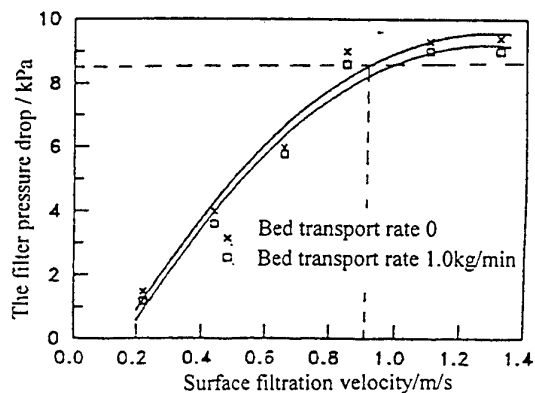


Fig.5. The experiment of the filter critical fluidized velocity

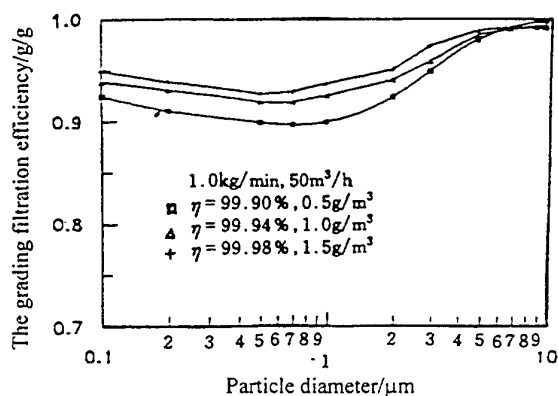


Fig.6. The filtration efficiency of MGBF

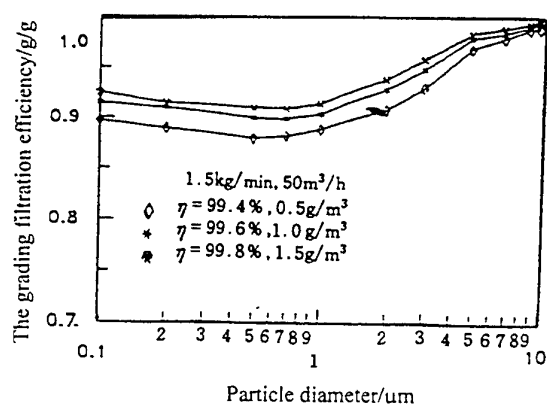


Fig.7. The filtration efficiency of MGBF

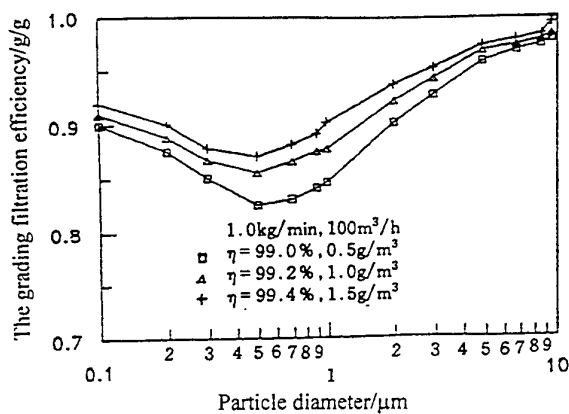


Fig.8. The filtration efficiency of MGBF

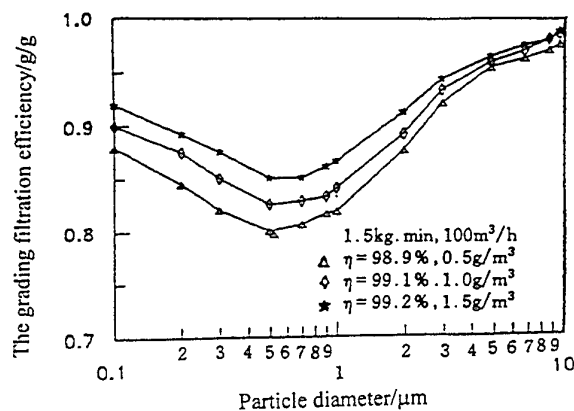


Fig.9. The filtration efficiency of MGBF

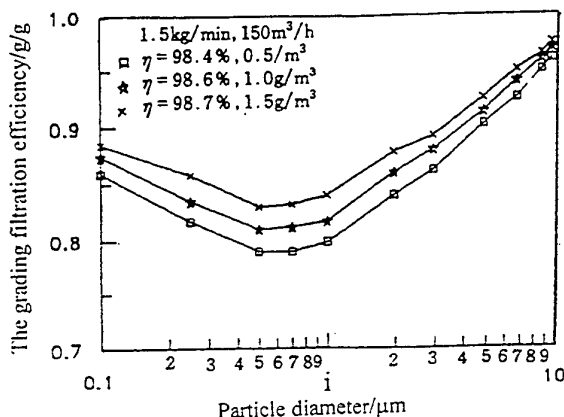


Fig.10. The filtration efficiency of MGBF

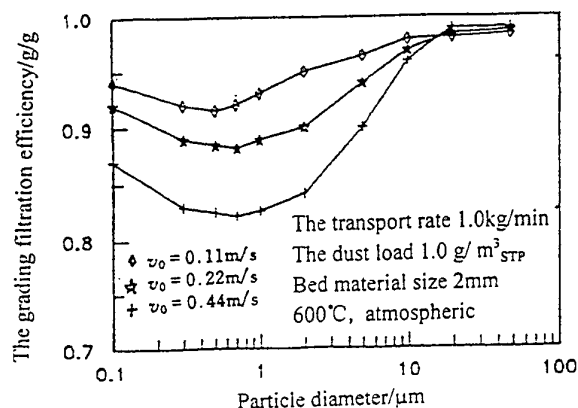


Fig.11. The effect of the filtration velocity on the grading filtration efficiency

3.4 The Effect of the Filtration Velocity on the Filtration Efficiency

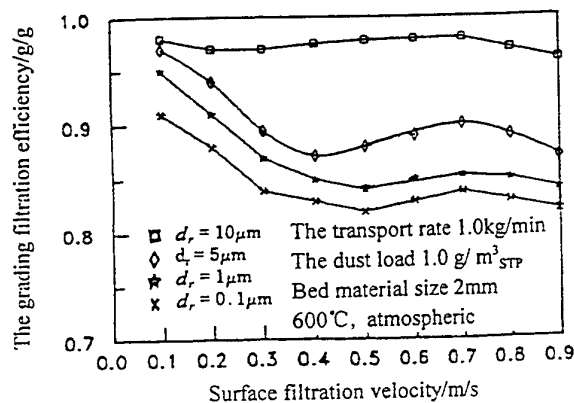


Fig.12. The effect of the filtration velocity on the grading filtration efficiency

The surface filtration velocity is an important factor affecting the performance of MGBF. Fig.11 is the test result of the effect of the surface filtration velocity on the grading filtration efficiency. For $5\mu\text{m}$ particles, the grading filtration efficiency decreases from 99.0% to 89% as the surface filtration velocity increases from 0.11m/s to 0.44m/s. The grading filtration efficiency has not change much for the particles larger than $10\mu\text{m}$ particles in the

specifically velocity range. The reason is that the penetration ratio increases but the inertial impaction also increases at higher filtration velocity for particles larger than 10 μ m. However, if the velocity increases beyond the specifically velocity range, the grading filtration efficiency decreases too.

Fig12 shows the effect of the surface filtration velocity on the grading filtration efficiency. For 10 μ m particles, this test result is similar to Fig.11. For 5 μ m particles, the test curve has an obvious valley, which is due to the inertial impaction and interception and the porosity of the bed both increasing at larger velocity. For 1 μ m and 0.1 μ m particles, the diffusion is the main mechanism, so the curves of the filtration efficiency vs. the filtration velocity are smooth.

4. CONCLUSIONS

The following conclusions can be drawn:

1. A necessary condition of MGBF without screen is that the surface filtration velocity must be lower than the critical fluidized velocity, which is 0.9~1.0m/s for this test facility. The test shows that MGBF can get the high efficiency and the reliable filtration performance at 0.11~0.44m/s filtration velocity.
2. After optimized, the total quality filtration efficiency of MGBF can approach 99.5~99.9%. The grading filtration efficiency could be larger than 99.6% for the particles larger than 10 μ m, but may be 95.0~98.5% for the particles smaller than 10 μ m.
3. There is a valley on the test curves of the grading filtration efficiency, which corresponds to 0.5~1.0 μ m particles. For applying to IGCC and PFBC system, MGBF should focus on improving the efficiency for 1.0~10 μ m particles.
4. The grading filtration efficiency decreases with the increase in surface filtration velocity. The effect of the surface filtration velocity on the grading filtration efficiency is obvious for particles smaller than 10 μ m, but is little for the particles larger than 10 μ m. There is a optimal filtration velocity for MGBF, the lower velocity will lead to the higher efficiency and higher cost, or conversely, the higher velocity will lead to the lower efficiency and lower cost.

REFERENCES

1. J. Stringer, D.B.Meadowcroft, "A Review of Hot Gas Clean Up Requirements for Coal Fired Gas Turbines", *Trans. I. Chem. E.* 68B, PP.181-194 (1990).
2. S.S. Xu, "The status and development of hot gas cleanup for IGCC and PFBC", *Thermal Power Generation*, v.1, pp.3~9 (1995).
3. "Coal Gasification for IGCC", IEA report (1992).
4. S.C. Saxena, R.F. Henry, W.F. Podolski, "Particulate removal from HTHP combustion gases", *Prog.Energy Combustion Sci.* 11(3)pp.193-251 (1985).

THE SENSITIVITY OF PRESSURIZED FLUIDIZED BED COMBUSTION OF CHAR TO IN-BED PROCESSES AND THEIR PARAMETERS

Yongbin Cui and John F. Stubington

CRC for Black Coal Utilization

School of Chemical Engineering and Industrial Chemistry

University of New South Wales

Sydney 2052, Australia

Email: z2125202@student.unsw.edu.au; Fax: (612)-9385-5966

Keywords: pressurized fluidized bed combustion (PFBC), modeling, in-bed char combustion

ABSTRACT. A mathematical model of our batch-fed PFBC was developed incorporating the processes of char oxidation and secondary fragmentation during char combustion, but assuming that the loss of carbon by elutriation was negligible compared with the carbon consumption by oxidation. A sensitivity analysis was carried out to determine the important parameters in the model prediction of carbon loading.

1. INTRODUCTION

Pressurized Fluidized Bed Combustion (PFBC) is a commercial clean coal technology utilizing combined gas turbine and steam turbine cycles to increase the efficiency of electricity production from coal. Preliminary assessment of Australian coals showed that they should be suitable for use in PFBC [1, 2], although low combustion efficiency was identified as a potential disadvantage. The elutriation of unburned char from PFBC is the main cause of combustion inefficiency and may also contribute to the 'sticky ash' problems in the ceramic hot gas filters by causing combustion and increased temperature in the filter cake. Attrition rates from atmospheric pressure fluidized bed combustion are proportional to the bed carbon loading [3], so we are investigating the in-bed char combustion in PFBC to predict this in-bed carbon loading to enable extrapolation of the elutriation data from our laboratory-scale PFBC to industrial-scale.

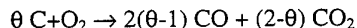
The mathematical model of in-bed char combustion processes was developed to predict the carbon loading of a batch of uniformly-sized coal particles fed to our laboratory-scale PFBC rig. A sensitivity analysis has been carried out to rank the parameters in the model, and the more important parameters will be investigated further experimentally in order to improve the model prediction of carbon loading.

2. MODELING OF IN-BED CHAR COMBUSTION IN PFBC

2.1 Model Assumptions

Several assumptions were made during the model development:

1. Char combustion includes two sub-processes – char oxidation and secondary fragmentation;
2. Char is non-swelling and acts like a shrinking sphere during char oxidation;
3. Plug flows occur in both emulsion and bubble phases;
4. Elutriable amount of carbon is negligible;
5. The overall reaction for carbon oxidation is expressed as follows



6. Char oxidation is an n th order reaction with respect to O_2 ;
7. Both local mass transfer and char surface reaction control the burning rate of carbon during the combustion of char particles;
8. There is no temperature gradient in char particles at any time during the combustion process;
9. Char is uniformly distributed throughout the emulsion phase.

2.2 Model Development

2.2.1 Char oxidation submodel. The transfer of oxygen between bubble and emulsion phases includes

two steps – interphase transfer and local transfer from emulsion phase to the surface of char particles. The interphase transfer between bubble phase and emulsion phase can be expressed:

$$-U_b \frac{dC_b}{dy} = K_{be}(C_b - C_{em}) \quad (1)$$

where U_b is bubble velocity, C_b and C_{em} are oxygen concentrations in bubble and emulsion phase, respectively. K_{be} is the effective interphase mass transfer coefficient calculated with Sit's correlation [4]:

$$K_{be} = \frac{U_{mf}}{3} + \left(\frac{4D_g \epsilon_{mf} \bar{U}_b}{\pi D_b} \right)^{1/2} \quad (2)$$

Char oxidation rate, r_c , defined as the mass of carbon consumed per second per unit external surface area of the char particle (mol/m^2), can be related to the local transfer of oxygen and the apparent kinetics as follows:

$$r_c = \theta k_g (C_{em} - C_p) = k_s C_p^n \quad (3)$$

where C_p (mol/m^3) is the oxygen concentration on the external surface of the char particle, k_g (m/s) is the local gas mass transfer coefficient ($Sh = k_g d/D$), θ is the ratio of carbon moles to O_2 moles consumed during char oxidation, n is apparent reaction order, and k_s is external surface area-based reaction rate constant.

Based on the method of Smith [5], k_s can be calculated from the intrinsic reaction rate constant (k_i) and char properties as follows:

$$k_s = \left(\frac{2S_E D_E k_i}{m+1} \right)^{0.5} \quad (4)$$

$$k_i = A T_p^m \exp(-E/RT_p) \quad (5)$$

where m is true reaction order, $n=(m+1)/2$, A is pre-exponential factor, E is activation energy and T_p is char particle temperature, S_E is the effective pore area for combustion per unit volume, D_E is the diffusion coefficient of oxygen within the solid carbon. A , E , S_E and D_E are char-related. In this work, S_E has been taken as $2.28 \times 10^7 \text{ m}^2/\text{m}^3$, and D_E is calculated with the method of Miccio [6] using a median pore diameter (volume) of $3.33 \mu\text{m}$, based on the properties of one Australian coal char produced under PFBC conditions.

An oxygen balance on an infinitesimal height of the whole bed, assuming negligible diffusion in the axial direction, gives:

$$U_{em} \frac{dC_{em}}{dy} + U_b \epsilon_b \frac{dC_b}{dy} + \frac{\sum_{i=1}^{n_i} N_{d_i} k_{s,d_i} \pi d_i^2 C_{p,d_i}^n}{\theta A_V H_f} = 0 \quad (6)$$

where n_i is the number of boxes for storing char particles with different diameters, N_{d_i} is char particle number with a diameter of d_i , k_{s,d_i} is the apparent reaction rate constant of a char particle with a diameter of d_i , and C_{p,d_i} is oxygen concentration on the external surface of a particle with a diameter of d_i .

Bed hydrodynamics are described by the modified two-phase model of Cai [7, 8]. U_{mf} is calculated with Grace's correlation [9]:

$$Re_{mf} = \sqrt{27.2^2 + 0.0408Ar} - 27.2 \quad (7)$$

The temperature of a char particle with a diameter of d is calculated by solving the steady-state energy balance:

$$r_c H_r - h(T_p - T_b) - \sigma \epsilon_{char}(T_p^4 - T_b^4) = 0 \quad (8)$$

where H_r is the heat of reaction (J/mol carbon) calculated from the formation enthalpies of products and reactant gas, h is the heat transfer coefficient (W/m²K), T_p is char particle temperature (K) and T_b is bed temperature(K), ϵ_{char} is the emissivity of char particle and is taken as 0.85 [10].

Char oxidation-induced char diameter change can be calculated as follows:

$$-\frac{dd}{dt} = \frac{24\delta^3 k_s C_p^n}{1000\rho_{char} x_c} \quad (9)$$

where d_v is volume diameter, d is surface diameter, $d_v = \delta d$, δ is a proportionality factor, and x_c is carbon weight fraction in char.

2.2.2 Secondary fragmentation submodel. Similar to the work by Chirone [11] at atmospheric pressure, two statistical functions are used to determine which particle will break at any moment as well as the size distribution of the fragments generated. A symmetric normal distribution function, $F(d_b)$, was used to determine the probability density on a numerical frequency fraction basis for a char particle of size d_b to break into fragments. Based on the similarity hypothesis [12], the size distribution of the fragments from particles of different sizes is expressed by a single distribution function $f(d_f/d_b)$:

$$f_n(d_f/d_b) = a(d_f/d_b)^m(1 - d_f/d_b)^n \quad (10)$$

From our preliminary experiments, the number of char particles as a function of combustion time t , when $t/t_b < 0.5$, can be expressed as:

$$\frac{N}{N_0} = 1 + A_1 \frac{t}{t_b} + A_2 \left(\frac{t}{t_b} \right)^2 \quad (11)$$

where N is the char particle number at time t , N_0 is the initial char particle number at the start of char combustion ($t=0$), t_b is the burnoff time of char particles for a certain initial char particle diameter and A_1 & A_2 are constants for that initial char particle diameter. Parameters t_b , A_1 and A_2 are coal-specific.

2.2.3 Calculation method. Char oxidation and secondary fragmentation were assumed to occur in series in every Δt . For char oxidation, equations 1,3,6,8 and 9 were solved simultaneously to predict particle temperatures, the overall rate of carbon combustion, and particle size distribution as a function of time after injection of the batch of uniformly-sized char particles to the rig. For secondary fragmentation, char particles were randomly chosen to break up based on $F(d_b)$ and $f(d_f/d_b)$. Fragmentation stops when the total char particle number equals that predicted by equation 11 at time t , and then char particle size distribution was recalculated. Surface diameter and volume diameter were used for char oxidation and fragmentation, respectively.

3. SENSITIVITY ANALYSIS

The sensitivity of char loading, defined as char weight at time t divided by initial char weight, to various model input parameters is examined using 2mm or 5mm char under our experimental conditions: 850°C, 1.6MPa, 0.9m/s and 3% O₂. Each of these parameters was varied while all the other parameters were held constant. From the results of our preliminary experiments, there is no secondary fragmentation when char diameter is less than

2mm, so the influence of secondary fragmentation was checked with 5mm char and other parameters were analyzed with 2mm char.

3.1 Mass Transfer Coefficient

The correlations of Prins [13] and Agarwal [14] were recommended for the prediction of local mass transfer coefficient in FBC under atmospheric pressure [15]. Afterwards, Coehl [16] developed another model which was tested at pressure in the range 1 to 5 bar and at a temperature of 1223K [17]. When $n=1$, $\theta=1.5$ and Barbosa's correlation for heat transfer coefficient [18] were used, the influence of Prins' and Coelho's correlations on char loading was as shown in Fig.1. The maximum char loading difference between the two lines in Fig.1 is 0.110.

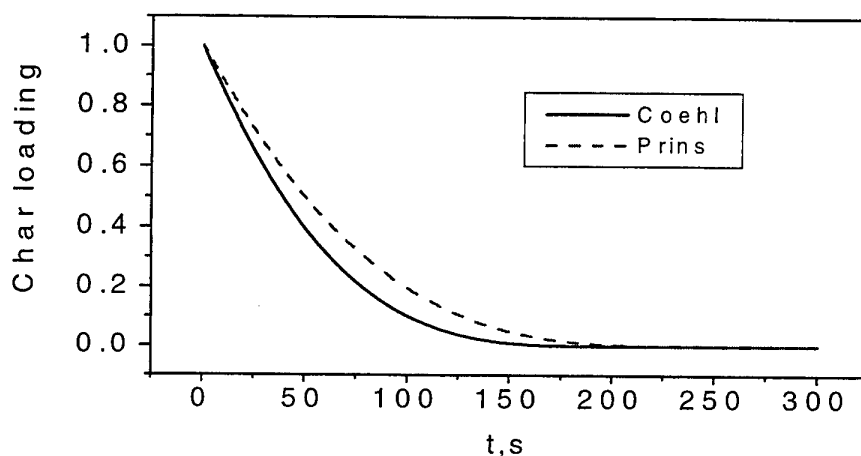


Fig.1 Influence of local mass transfer coefficient on char loading

3.2 The Ratio of Carbon to Oxygen Moles Consumed Within the Boundary Layer (θ)

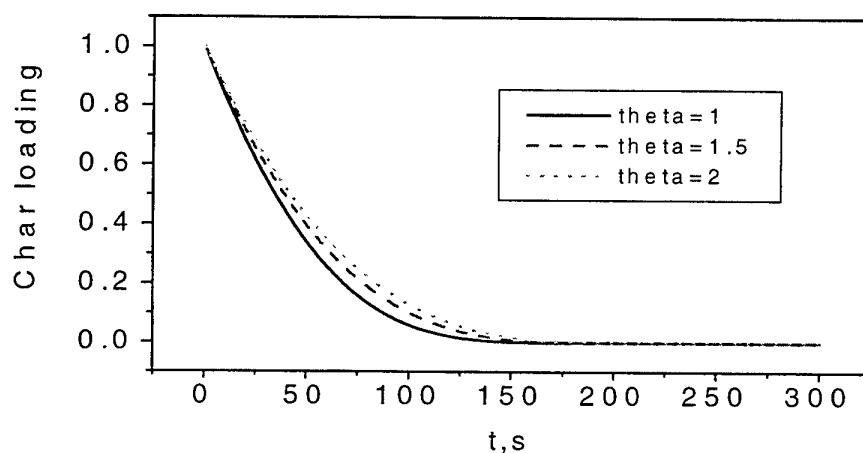


Fig.2 Influence of theta on char loading

The value of θ directly influences the reaction heat released during char oxidation and char particle temperature, which affects char oxidation rate and the local mass transfer rate of oxygen near the external

surface of char particles. Therefore, the influence of θ on in-bed char loading was investigated. Using Coelho's model for local mass transfer [16], Barbosa's correlation for heat transfer coefficient [18] and taking n as 1, three values of θ (1, 1.5, 2) were examined as shown in Fig.2. The maximum char loading difference between the lines in Fig.2 is 0.093.

3.3 Apparent Reaction Order

Using chars produced at 850°C, 1.6MPa, 0.9m/s in our hot rig, the intrinsic reactivity at 1.6Mpa was measured by PTGA. The activation energy was 169KJ/mol, but reaction order was not measured. Using the model, the influence of different apparent reaction orders and corresponding pre-exponential factors on char loading was compared (Fig.3), with Coelho's model for local mass transfer [16], Barbosa's correlation for heat transfer coefficient [18] and $\theta=1.5$. The maximum char loading difference for different values of n in Fig.3 is 0.081.

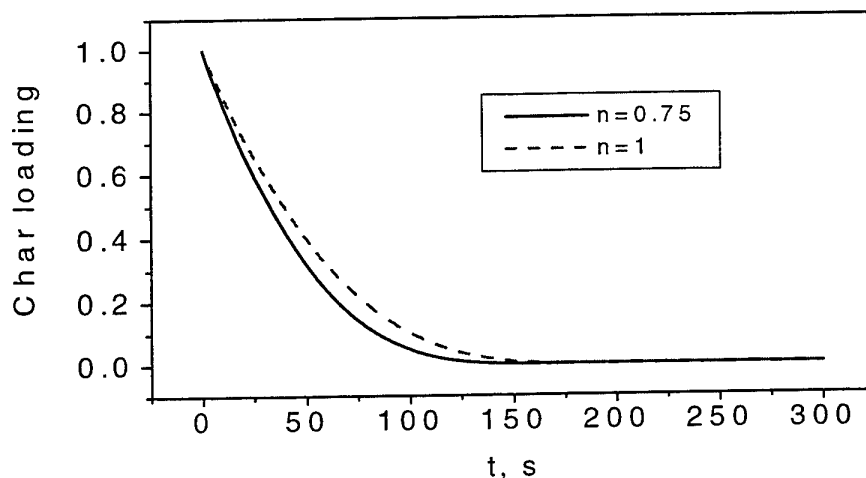


Fig.3 Influence of reaction order on char loading

3.4 Different Correlations for Heat Transfer Coefficient

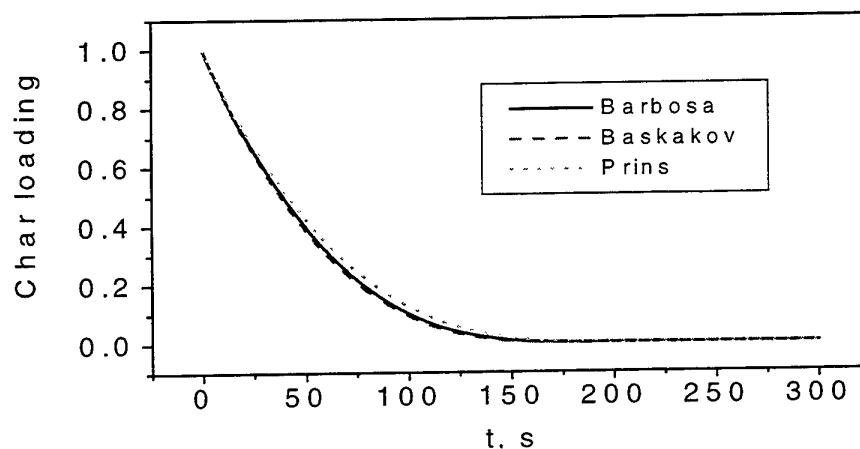


Fig.4 Influence of heat transfer coefficient on char loading

Three correlations [13, 18, 19] for heat transfer coefficient were compared as shown in Fig.4, with Coelho's model for local mass transfer [16], $n=1$ and $\theta=1.5$. The maximum char loading difference for different correlations in Fig.4 is 0.040.

3.5 Secondary Fragmentation

Fig.5 shows the influences of secondary fragmentation on char loading, using Coelho's model for local mass transfer [16], Barbosa's correlation for heat transfer coefficient [18], $\theta=1.5$ and $n=1$. The values of parameter A_1 and A_2 in equation 11 were obtained for one Australian coal char. The maximum char loading difference between the two lines in Fig.5 is 0.073.

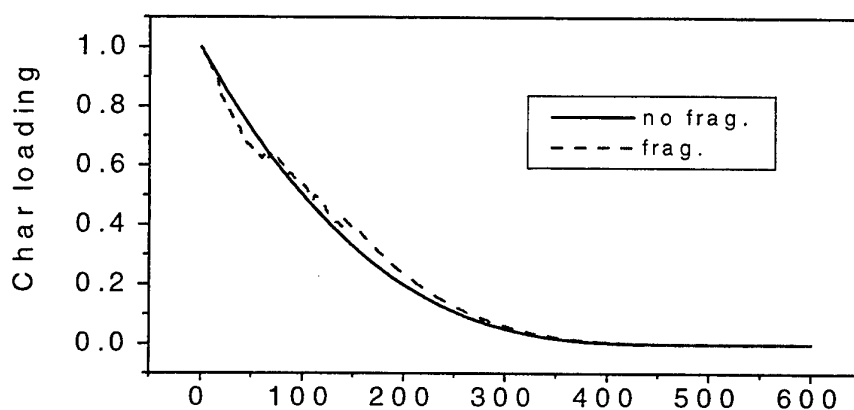


Fig.5 Influence of secondary fragmentation on char loading

Based on the influence of each parameter on in-bed char loading above, these parameters were ranked in priority order: local mass transfer coefficient, theta, reaction order, secondary fragmentation and heat transfer coefficient.

4. CONCLUSIONS

A mathematical model was developed to simulate the in-bed char combustion in our batch-fed PFBC. Using sensitivity analysis of parameters in the model with respect to in-bed char loading, these parameters were ranked in priority order as follows: local mass transfer coefficient, the ratio of carbon to oxygen moles consumed within the boundary layer, reaction order, secondary fragmentation and heat transfer coefficient. The more important of these parameters will be investigated further experimentally in order to improve the model prediction of in-bed char loading.

ACKNOWLEDGMENTS

The authors wish to acknowledge the financial support provided by the Cooperative Research Centre for Black Coal Utilisation, which is funded in part by the Cooperative Research Centres Program of the Commonwealth Government of Australia. The authors thank Mr. Alan Wang from UNSW, Mr. David Murphy and Mr. Naranjin Sharma from Pacific Power for their invaluable efforts in construction, assembly, commissioning and operation of the facility.

REFERENCES

1. J.F. Stubington, "Preliminary Evaluation of Australian Coals for Pressurized Fluidized Bed Combustion", *Proceedings of the 1st Annual Conference of CRC for Black Coal Utilization*. Brisbane, Australia. pp. 6. (1997).

2. K.M. Laughlin and K.M. Sullivan, "Evaluation of Australian Coals for Pressurized Fluidized Bed Combustion", (1997).
3. I.T. Lau, "Char Particle Reaction and Attrition in Fluidized Bed Combustors: Modeling and Measurement", in *Canada Centre for Mineral and Energy Technology (CANMET)*. Department of Chemical Engineering, University of Ottawa. pp. 297. (1995).
4. S.P. Sit and J.R. Grace, *Chemical Engineering Science*, v. 36, pp. 327-335 (1981).
5. I.W. Smith, "The Combustion Rates of Coal Chars: A Review", *Proceedings of the 19th Symposium (International) on Combustion*. The Combustion Institution, Pittsburgh, PA. pp. 1045-1065. (1982).
6. M. Miccio and M. Poletto, "The Effect of System Pressure on Char Combustion in Fluidized Beds: Model Predictions", *Proceedings of the 11th International Conference on FBC*. pp. 1233-1243. (1991).
7. P. Cai, *et al.* "A Generalized Method for Predicting Gas Flow Distribution between the Phases in FBC", *Proceedings of the 12th International Conference on FBC*. San Diego, California. pp. 991-1002. (1993).
8. P. Cai *et al.*, *Powder Technology*, v. 80, pp. 99-109 (1994).
9. J.R. Grace, *Canadian Journal of Chemical Engineering*, v. 64, pp. 353 (1986).
10. I.B. Ross, M.S. Patel and J.F. Davidson, *Transaction Institute of Chemical Engineers*, v. 59, pp. 83-88 (1981).
11. R. Chirone, P. Salatino and L. Massimilla, *Combustion and Flame*, v. 77, pp. 79-90 (1989).
12. T.W. Peterson and M.V. Scotto, *Powder Technology*, v. 45, pp. 87-93 (1985).
13. W. Prins, PhD thesis, "Fluidized Bed Combustion of a Single Carbon Particle", University of Twente, The Netherlands. (1987).
14. P.K. Agarwal, W.J. Mitchell and R.D. La Nauze, *Chemical Engineering Science*, v. 43, pp. 2511-2521 (1988).
15. P.K. Agarwal and R.D. LaNauze, *Chemical Engineering Research and Design*, v. 67, pp. 457-480 (1989).
16. M.A.N. Coelho and J.R.G. Guedes de Carvalho, *Chemical Engineering Research and Design*, v. 66, pp. 178-189 (1988).
17. J.R.G. Guedes de Carvalho, A.M.F.R. Pinto and C.M.C.T. Pinho, *Transaction Institute of Chemical Engineers*, v. 69, pp. 63-70 (1991).
18. A.L. Barbosa, D. Steinmetz and H. Angelino. "Heat Transfer around Spherical Probe at High Temperature in a Fluidized Bed", *Proceedings of the International Symposium of the Engineering Foundation, Fluidization VIII*. TPURS, France. pp. 145-152. (1995).
19. A.P. Baskakov, "Heat Transfer in Fluidized Beds :Radiative Heat Transfer in Fluidized Beds of Inert Material", in *Fluidization*, J.F. Davidson, R. Clift, and D. Harrison, Editors. Academic Press: London. pp. 465. (1985).

CARBON ELUTRIATION FROM PRESSURISED FLUIDIZED BED COMBUSTION OF AUSTRALIAN BLACK COALS

Alan L. T. Wang and John F. Stubington

Co-operative Research Centre (CRC) for Black Coal Utilisation and
School of Chemical Engineering and Industrial Chemistry,
University of New South Wales, Sydney 2052, Australia
Email: a.wang@unsw.edu.au, Fax: (61-2) 93855966

Keywords: PFBC, coal combustion, efficiency, carbon elutriation, attrition

ABSTRACT. A batch-fed bench-scale pressurised fluidized bed combustion (PFBC) facility was built at UNSW to research the in-bed processes generating fine char particles during PFBC of Australian black coals. Measured carbon elutriation varied from coal to coal and the results agreed qualitatively with large-scale PFBC performance, allowing definition of satisfactory and unsatisfactory performance criteria. For both of the tested coals, the carbon elutriation rate decreased during burnout due to the decrease of in-bed carbon loading. The specific carbon attrition rates were constant at the early stage of burnout when the in-bed char particles were larger (about $>2\text{mm}$) and then increased at the later stage of burnout. Carbon elutriation in PFBC was correlated tentatively with crucible swelling number (CSN), although the range of values of CSN needs to be extended. Carbon elutriation in PFBC did not correlate with volatile matter for the 5 Australian coals investigated, in contrast with previous PFBC pilot plant studies. The higher swelling coal produced a significantly larger average macro-pore diameter after devolatilisation in PFBC, which caused greater attrition of fine char from the particle surface during the char burnout stage.

1. INTRODUCTION

Pressurised fluidized bed combustion (PFBC) is the first of the Clean Coal Technologies to be commercialised for large-scale electricity generation from coal. PFBC technology is combined cycle technology providing increased efficiency of electricity generation from coal at a competitive cost. Typically, the efficiency advantage is around 3-4 percentage points higher than a conventional steam power plant with commonly used steam conditions, which corresponds to about a 10% fuel saving[1]. Despite the low inlet gas temperature of 850°C to the gas turbine, ABB Carbon's standard 425 MW_e P800 plant achieves an efficiency of 44-45% based on the lower heating value of the coal and 0.02 bar condenser pressure[2]. In 1997, ABB Carbon quoted a typical greenfield capital cost of \$US 1000/kW for their P800 unit[2]. In Japan, Mitsubishi Heavy Industries have built an 85 MW_e PFBC power plant. Currently, a few larger PFBC plants (360 MW_e and 250 MW_e) are under construction in Japan and scheduled for start-up between 1999 and 2002. Australian Black coals have been fired in all the Japanese PFBC power plants and in the Japanese PFBC research Programs. Also, the new larger commercial PFBC plants now under construction in Japan will certainly be firing Australian coals, so it is essential that we understand the behaviour of Australian coals in this new technology to support their marketing into Japan.

Unburned carbon elutriation is the main cause of combustion inefficiency in PFBC technology, and may also contribute to the 'sticky ash' problems in the ceramic filters by causing combustion and increased temperature in the filter cake[3]. The main objectives of this project are to characterise Australian black coals under industrial PFBC conditions, investigate the mechanisms of generation of elutriable fine chars and study the influences of coal and char properties on carbon elutriation in PFBC.

2. EXPERIMENTAL

PFBC Facility at UNSW

A novel bench-scale PFBC combustor has been constructed at UNSW, designed specifically to research PFBC of coal with the aim of understanding the influence of coal on combustion performance in industrial-scale plant. This facility has identical conditions in the bed to those used industrially (1.6MPa, 850°C & 0.9m/s fluidizing velocity) to ensure that the local environment around each coal particle matches that in an industrial PFBC. Batch experiments provide time-resolved data on coal devolatilisation and char combustion to allow

investigation of the mechanisms occurring during these processes. The exhaust gas is analysed continuously for O_2 , CO , CO_2 and hydrocarbons as a function of time after coal injection. The elutriated carbon particles undergo minimal freeboard combustion and are collected in one of two cyclones over any desired period of time during the experiment, for subsequent analysis. The facility allows quenching of the combustion at any time by switching to pure, non-preheated nitrogen as the fluidizing gas and the sand bed then may be removed from the rig for collection and characterisation of the partially burnt char particles. Fig. 1 is a schematic diagram of the PFBC facility and further details are available elsewhere[4,5].

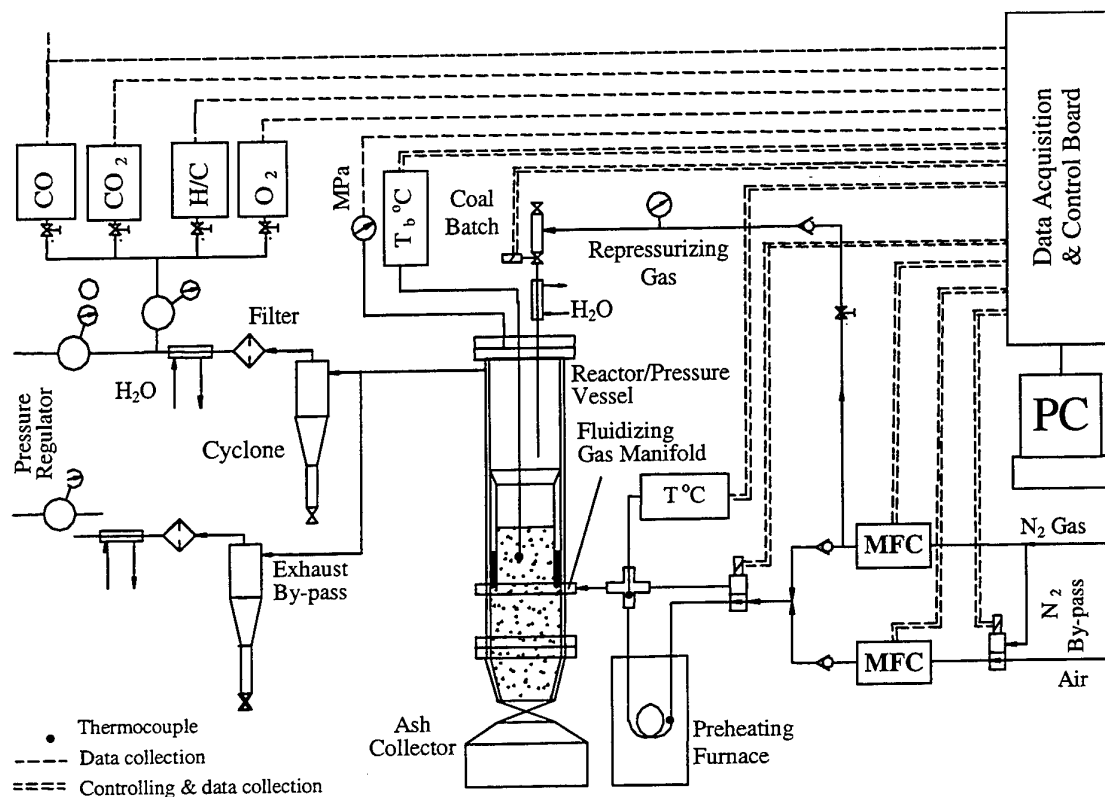


Fig. 1 Schematic of UNSW's bench-scale batch-fed PFBC facility

This PFBC facility was designed to duplicate the in-bed processes of coal/char combustion and attrition in industrial-scale PFBC plant but did not attempt to duplicate freeboard processes. Any freeboard combustion of elutriated char was deliberately minimised by utilising the shortest possible freeboard height, by cooling the freeboard wall (by direct contact with the ambient atmosphere) and by cooling the cyclone (by external water-cooling). Experiments in this facility therefore investigated only the processes by which fine unburnt carbon was generated in the bed, uncompromised by any subsequent combustion of fines, which may occur in industrial PFBC plant. The elutriated material was predominantly coal ash, from SEM elemental analyses of elutriated particles collected in the cyclone. The rate of elutriation from the sand bed alone was negligible compared to that for coal injection experiments. Carbon elutriation was measured as the loss on ignition at 815°C in air from the cyclone fines, which was typically 20-40% of the elutriated material. This carbon elutriation is expressed in Fig. 2 as a percentage of the carbon fed in the coal batch, since this ratio is directly related to combustion inefficiency.

The effects of rig operating parameters on the carbon elutriation during the complete devolatilisation and char burnout process were first estimated using a factorial experimental design with a single coal. Results of the factorial experiments found that feed coal particle size and oxygen concentration had the most significant effects

on carbon elutriation, whereas system pressure had only a minor effect and coal batch size had a negligible effect. Standardised experimental conditions were then chosen for the coal comparison experiments reported below and are summarised in Table 1.

Table 1 Standardised Operating Parameters for Carbon Elutriation Experiments

Bed temperature (°C)	850
Mean bed particle size (mm)	1.3
Fluidizing velocity (m/s)	0.9
Coal particle size (mm)	4-4.75
Oxygen concentration (%)	7
System pressure (MPa)	1.6
Coal batch size (g)	1

Coal Analysis

Five Australian black coals were chosen, covering a range of proximate Volatile Matter (VM) (and hence a range of Fuel Ratios), with some differences in swelling properties for similar VM; since VM was reported to correlate with pressurised fluidized bed combustion efficiency[6] and swelling behaviour was reported to correlate with atmospheric pressure fluidized bed combustion efficiency[7]. Chars devolatilized in the PFBC rig were subjected to Hg porosimetry to determine the pore size distribution in the macro- and larger meso-pore range.

Table 2 Analyses of Australian Black Coals Studied and Typical Carbon Mass Balances

Coal		A	B	C	D	E
Proximate Analysis (a.d.):	Moisture (%)	1.7	3.0	1.9	1.3	1.6
	Ash (%)	18.5	8.2	7.7	11.5	10.6
	Volatile Matter (%)	28.4	29.7	40.5	19.9	34.2
	Fixed Carbon (%)	51.4	59.1	49.9	67.3	53.6
	Fuel Ratio = FC/VM	1.81	1.99	1.23	3.38	1.57
Crucible Swelling Index		0.5	0.5	1.5	1.5	2.0
Ultimate Analysis (d.af):	Carbon (%)	89.3	82.9	85.8	90.9	84.7
	Hydrogen (%)	5.1	4.5	5.8	4.5	5.3
	Nitrogen (%)	2.2	1.9	1.8	2.1	1.6
Carbon Mass Balance (%)		96.85	98.1	97.94	98.34	98.19
Mean Pore Diameter of Devolatilized Chars (μm)		0.041	0.077	0.087	0.041	0.174

3. RESULTS AND DISCUSSION

Carbon Mass Balances

Excellent carbon mass balance closure was observed for the complete burnout experiments, with the results shown in Table 2. The carbon in the exhaust gas was determined by integration of the CO and CO₂ versus time curves from the on-line analysers. This result provides confidence that the loss on ignition method for measuring carbon elutriation was satisfactory.

Carbon Elutriation During Complete Burnout

Unburnt carbon elutriation was measured for the complete combustion process, with the results shown in Fig. 2. Excellent reproducibility of results is evident from the repeat experiments performed. Different coals exhibited substantial differences in carbon elutriation in this standardised experiment. Coal E was similar to the coal which gave high char carryover in the pilot-scale facility of ABB Carbon in Sweden and the results reported

here are the first replication of that unsatisfactory behaviour. Coal B exhibits significantly lower carbon elutriation than Coal E in our standard test and has been fired successfully in the 70 MW_e Wakamatsu demonstration plant in Japan. These comparisons with larger-scale PFBC performance show that results from our bench-scale facility do correlate with such larger-scale PFBC performance and provide benchmarks against which to assess the performance of other coals.

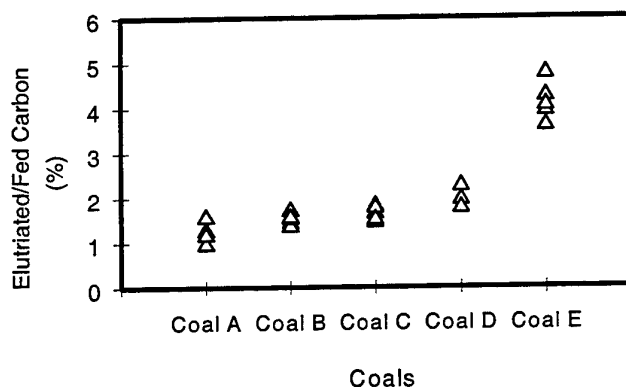


Fig. 2. Carbon elutriation from PFBC for 5 Australian black coals (1.6MPa, 850°C, U=0.9m/s, 7% O₂, coal particle size: 4~4.75mm)

For our standard test, a carbon elutriation less than 1.6% of the carbon fed in the coal would be satisfactory, since this is the average of the results for Coal B. On the other hand, a carbon elutriation greater than 4.2% would definitely be unsatisfactory, since this is the average of the results for Coal E. Results between 1.6 & 4.2% cannot yet be categorised since insufficient large-scale data are available, so should conservatively be considered as unsatisfactory until further data becomes available. On this basis, coals A, B and C would be satisfactory; whereas coals D and E would not be recommended for PFBC firing.

Fixed Carbon Elutriation During Devolatilisation And Char Combustion Stages

The elutriated carbon collected by the cyclones is in the form of solid char. The exhaust gas analyses had negligible levels of hydrocarbons [4], showing that volatile matter was released and essentially burned to completion within the combustor. Hence, volatile matter did not contribute to the measured carbon elutriation, which must have come only from the fixed carbon. Therefore, the following data on carbon elutriation were compared to the proximate fixed carbon by expressing the carbon elutriation as a percentage of the fixed carbon fed in the coal batch (Fig. 3).

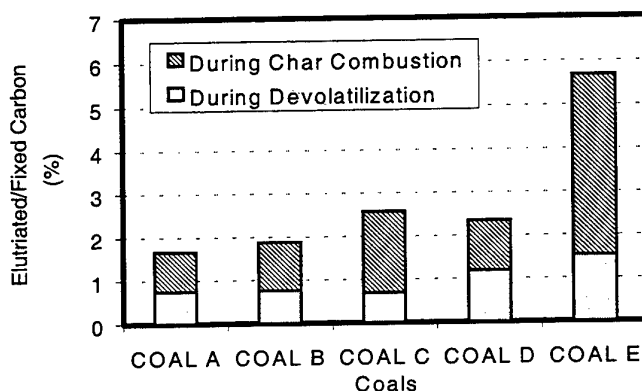


Fig. 3. Carbon elutriation contributions from coal devolatilisation and char combustion stages (1.6 MPa, 850°C, U=0.9m/s, 7% O₂, coal particle size: 4~4.75mm)

The devolatilisation time was estimated at 28s for the coal particle size used. Further experiments were performed under the same standardised experimental conditions, but the exhaust gas was diverted from the first to the second cyclone 30 seconds after injection of the coal batch into the bed. In this way, elutriated carbon was collected in one cyclone during the devolatilisation stage and in the second cyclone during the char burnout stage from a single experiment. The relative contributions to fixed carbon elutriation during the devolatilisation and char combustion stages are presented in Fig. 3, in which the ranking of coals C and D in terms of total elutriation have changed from Fig. 2 due to the substantially higher fixed carbon content of coal D. For coal E, the higher carbon elutriation comes predominantly from the char burnout stage and may be attributed to the significantly larger macro-pore size of its char (Table 2), which enhances attrition on the char particle surface in the bed.

Fixed Carbon Elutriation Rate

To understand coal behaviour for PFBC technology, coal B (satisfactory coal) and coal E (problem coal) were studied and compared. The rate of carbon elutriation for coals B and E was measured in further experiments. After injecting the coals, the exhaust gas was directed through the bypass exhaust line and cyclone until the start of the measurement period, at which time the exhaust gas was directed through the measurement exhaust line and cyclone for a sampling period of 15 or 30 s, before switching back to the bypass line. The experiment was repeated for different start times throughout the complete burnout time. Dividing the measured carbon elutriation by the sampling period gave the average carbon elutriation rate over the period. The elutriation rates of fixed carbon fed in the coal batches were plotted as a function of time, expressed as the ratio of time to burnout time, t/t_b (Fig. 4). The rate of fixed carbon elutriation was greater during devolatilisation than during char combustion, and decreased with burnout time as the char burnout proceeded. At all times, the rate of carbon elutriation was greater for the problem coal E than for the satisfactory coal B.

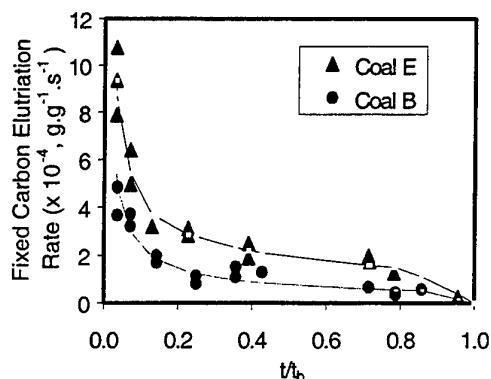


Fig. 4 Elutriation rate of fixed carbon during burnout from PFBC (1.6MPa, 850°C, 7% O₂, U=0.9m/s, coal particle size: 4~4.75mm)

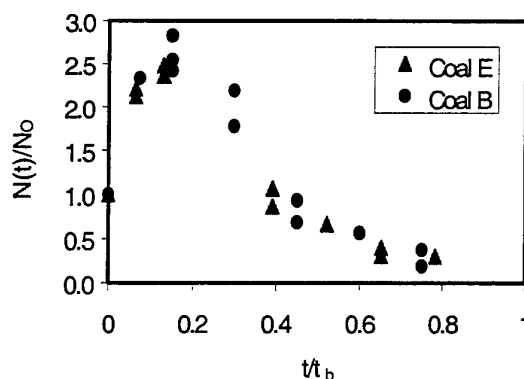
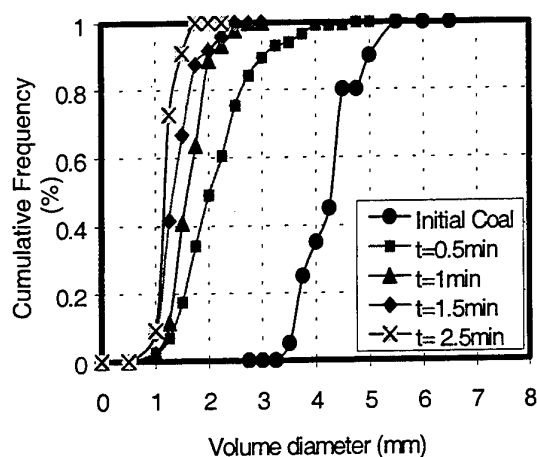


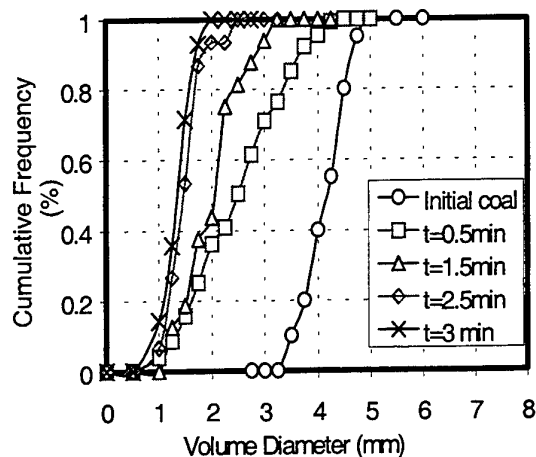
Fig. 5 In-bed coal char particle number variation during burnout in PFBC(1.6MPa, 850°C, U=0.9m/s, 7% O₂, coal particle size: 4~4.75mm)

In-Bed Coal Char Particle Size Reduction

During burnout, the reactions were quenched at various times. The in-bed char particles were recovered from the bed after cooling by sieving with a 1.4 mm aperture sieve and then picking out by hand as many as possible of the smaller char particles remaining in the sand. The number of particles in the bed compared to the initial number of coal particles in the batch, $N(t)/N_0$, shown as a function of burnout time in Fig.5, increased during devolatilization due to primary fragmentation and then decreased as the combined result of secondary fragmentation and burnoff of smaller particles. The coal char particles were analysed by image analysis and Fig. 6 compares the particle size distributions of the original coal with the devolatilized char and partially burnt char at various stages for both coals B and E. As a result of fragmentation, the median particle diameter decreased sharply and, although the fragmentation behaviours of coals B and E were similar (Fig.5), the greater particle swelling behaviour of coal E resulted in substantially larger char particle sizes after devolatilization for coal E than for coal B.



(a) Coal B



(b) Coal E

Fig. 6. In-bed char particle size reduction and distributions at various stages during burnout (1.6MPa, 850°C, 7% O₂, U=0.9m/s, coal particle size: 4–4.75mm)

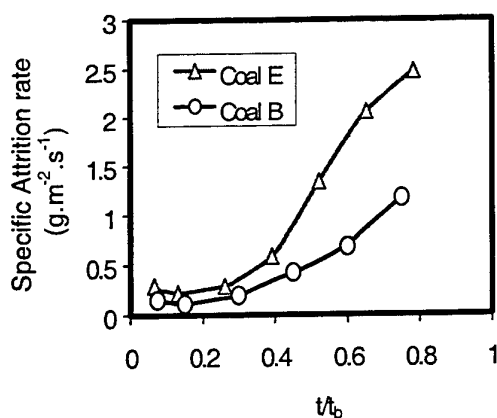


Fig. 7. Specific carbon attrition rate during burnout in PFBC (1.6MPa, 850°C, 7% O₂, U=0.9m/s, coal particle size: 4–4.75mm)

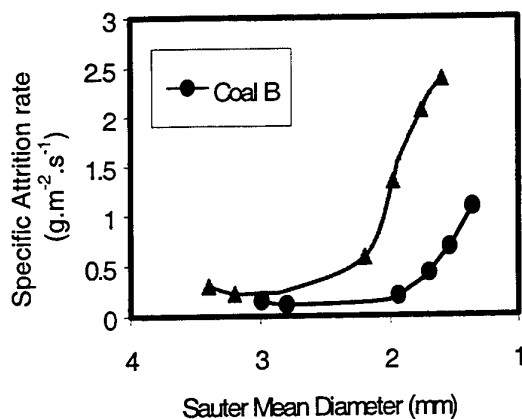


Fig. 8. Influences of char particle size on specific carbon attrition rate during burnout in PFBC (1.6MPa, 850°C, U=0.9m/s, 7% O₂)

Specific Carbon Attrition Rate During Coal Burnout

Attrition is the phenomenon by which fines are abraded from the surface of the parent particle by wearing against bed solids and combustor walls [6]. Carbon attrition is the main mechanism of generation of elutriable fine char particles in PFBC. The post-combustion of attrited carbon was minimized by the design of the shallow bed, short air-cooled freeboard and water-cooled cyclones. Accordingly, the measured values of the rates of carbon elutriation were the effective rates of formation of carbon fines, or the carbon attrition rates, for the coal batch fed. The total external surface area and the Sauter mean diameter of in-bed char particles were calculated from the char particle size distribution curves (Fig.6) and the particle numbers (Fig.5) at different times during burnout. The specific carbon attrition rates (the carbon attrition rate per unit external surface area per second) were then calculated and plotted as a function of time (Fig. 7) and mean char particle diameter (Fig. 8).

Although the carbon elutriation rate of coal E is much higher than that of coal B (Fig. 4), the greater external surface area of coal E (due to its significantly greater swelling behaviour) made the specific carbon attrition rates closer to each other for coals E and B within the early stage of burnout.

The specific carbon attrition rates for both coals B and E were nearly constant when the coal char particles were large at the earlier stage of burnout, but increased when the char particle sizes decreased. The higher specific attrition rate at the later stage of burnout may be attributed to: (1) percolation fragmentation of the smaller char particles in the batch; and (2) the growth of detachable asperities because the better external O_2 mass transfer for the smaller char particle could enhance the O_2 penetration into the char particle and the development of porous structure within the surface layer. This result confirmed the conclusion from the factorial experiment that feed coal particle size had the most significant effect on carbon elutriation. The specific attrition rate of coal E was substantially higher than that of coal B for the smaller char particles in PFBC and the increase started at a larger Sauter mean char particle diameter.

Correlation of Fixed Carbon Elutriation with Coal Properties

Carbon elutriation from this study did not correlate with the volatile matter (or Fuel Ratio) of the parent coal, in contrast with previous work on Northern Hemisphere coals. Combustion inefficiency data from the Grimethorpe PFBC facility were correlated inversely with VM [7], whereas the highest carbon elutriation was observed for the intermediate VM coal E in this work. Lower carbon elutriation was observed for the other coals, with VM both lower and higher than coal E.

Fig. 9 shows that the carbon elutriation from PFBC did correlate with the crucible swelling number (CSN) of the parent coal, as was also reported for pilot-scale trials in atmospheric pressure fluidized bed combustion of four Canadian coals [8]. However, the range of values of CSN in this work was narrow (0.5 – 2.0) compared with the Canadian work (0 – 7) and should be extended before such a correlation could be employed as a predictive tool.

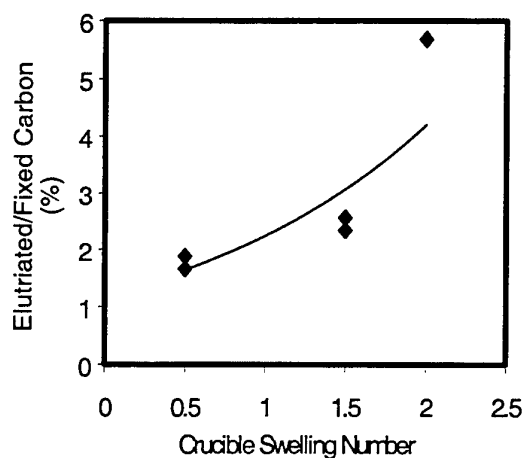


Fig. 9 Correlation of Fixed Carbon elutriation with Crucible Swelling Number

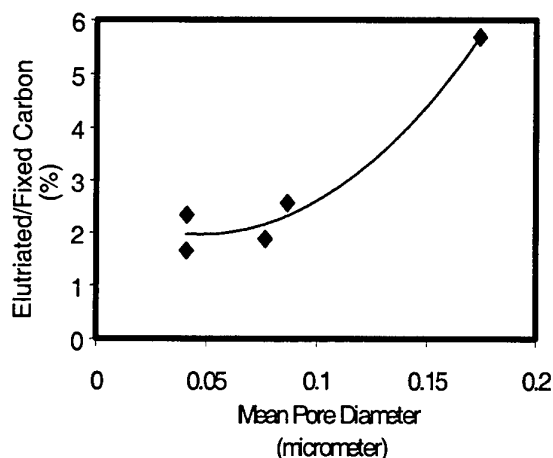


Fig. 10 Correlation of Fixed Carbon elutriation with average pore diameter

Correlation of Fixed Carbon Elutriation with Char Properties

Devolatilised chars were prepared by burning batches of coal particles for 30 s in the PFBC facility under the standardised conditions and then quenching the reaction by switching to ambient temperature nitrogen as the fluidizing gas. These chars were analysed by Hg porosimetry to determine their porosities and pore sizes. The devolatilised char porosities correlated with VM as expected, but not with the carbon elutriation. Fig. 10 shows that the carbon elutriation, expressed as a percentage of the Fixed Carbon, correlated well with the average pore diameter. This measurement method does not interrogate the smallest pores, so the average diameter plotted in Fig. 10 indicates only the macro-pores and the larger meso-pores in the char[9]. This correlation with macro-pore size but not with porosity agrees with the conclusion of Kantorovich and Bar-Ziv for non-uniform oxidation of Spherocarb[10]. Oxidation occurs throughout all the pores near the particle's external surface with the dominant contribution from the much larger surface area of the meso- and micro-pores, whereas attrition occurs when the diameter of the macro-pores near the particle's external surface becomes sufficiently high for fragmentation of the large-scale porous structure.

4. CONCLUSIONS

The bench-scale facility at UNSW allows measurement of the unburnt carbon elutriation from coal combustion in PFBC. These measurements correlate with the differing performance of various coals in larger-scale plant and provide an indication of the potential problem of carbon carryover in industrial PFBC installations. This unburnt carbon carryover is the main source of combustion inefficiency and also may cause problems in the hot-gas ceramic filters proposed for advanced PFBC plant.

Both devolatilisation and char combustion stages contribute to carbon elutriation. However, a greater amount of carbon elutriation occurred for the problem coal during char combustion than during devolatilisation. Although a higher rate of carbon elutriation was observed during devolatilisation, the longer time-scale required for char burnout gave greater cumulative carbon elutriation during this stage. The specific carbon attrition rates were constant at the early stage of burnout when the in-bed char particles were larger and then increased at the later stage of burnout. The specific attrition rate of coal E was substantially higher than that of coal B for the smaller char particles in PFBC. Carbon elutriation does not correlate with the Volatile Matter of the Australian coals studied, in contrast with combustion efficiency correlations in the literature. Carbon elutriation from PFBC of 5 Australian black coals did correlate with crucible swelling number, as reported for AFBC of 4 Canadian coals, and with the average pore diameter determined from Hg porosimetry of chars devolatilised under PFBC conditions. However, further work is necessary to extend the range of values of CSN from the narrow range studied here, before such correlation could be used as a predictive tool.

ACKNOWLEDGEMENTS

The authors acknowledge the financial support provided by the Cooperative Research Centre for Black Coal Utilisation, which is funded in part by the Cooperative Research Centres Program of the Commonwealth Government of Australia. The authors thank Mr. David Murphy and Mr. Naranjin Sharma of Pacific Power for their invaluable assistance in construction, assembly, commissioning and operation of the facility and Dr. Allen Lowe of Pacific Power for his guidance.

REFERENCES

1. P. Alnhem and J. Lofe, *The PFBC Power Plant: A Competitive Alternative*, in Power-Gen '96 International: 9th International Conference & Exhibition for the Power Generating Industries, Orange County Convention Center, Orlando, Florida, USA, 1996, 169-197.
2. S. Jansson and L. Anderson, *Pressurised Fluidised Bed Power Plants*, in Indo-European Seminar on Clean Coal Technology and Thermal Power Plant Upgrading, New Delhi, 1997, IX.2.1 to IX.2.8.
3. J. F. Stubington, *Research necessary to predict the performance of Australian black coals in Pressurised Fluidized Bed Combustion technology*, Report to the CRC for Black Coal Utilisation on project 5.5, UNSW, Sydney, 1997, pp. 25.
4. A. L. T. Wang and J. F. Stubington, *Characterisation of Australian black coals for pressurised fluidized bed combustion*, in 8th Australian Coal Science Conference, Australian Institute of Energy, UNSW Sydney, 1998, 261-266.
5. J. F. Stubington, A. L. T. Wang and Y. Cui, *Understanding the behaviour of Australian black coals in Pressurised Fluidized Bed Combustion*, in 15th International Conference on FBC, ASME, Savannah, Georgia, USA, 1999, pp. 16.
6. R. Chirone, M. D'amore, L. Massimilla, A. Mazza, "Char attrition during the batch fluidized bed combustion of a coal" *AIChE J.*, vol.31, No5, 812-820, 1985.
7. J. M. Wheeldon, J. M. *et al.* *Experimental results from the Grimethorpe PFBC facility*, in 8th International Conference on Fluidized Bed Combustion, DOE/METC, Houston, Texas, 1985, 317-335.
8. H. A. Becker, R. K. Code and J. R. Stephenson *Pilot Scale Trials on Atmospheric Fluidized Bed Combustion of a Western Canadian Sub-bituminous Coal (Highvale)*, Technical Report QFBC.TR.87.3, Queen's Fluidized bed Combustion Laboratory, Dept. of Chemical Engineering, Queen's University at Kingston, 1987, pp. 39.
9. N. M. Laurendeau, *Prog. Energy Comb. Sci.* 1978, 4, 221-270.
10. I. I. Kantorovich and E. Bar-Ziv *Combustion and Flame* 1998, 113, 532-541.

MEASURES FOR EMISSION CONTROL IN FLUIDIZED BED COMBUSTION OF SEWAGE SLUDGE

Markus Saenger, Joachim Werther

Chemical Engineering I

Technical University Hamburg-Harburg

Email: werther@tu-harburg.de; Fax: ++49-40-42878-2678

Georg Hiller

Sewage Sludge Treatment Plant Ulm-Steinhaule

Wischernstrasse 10, D-89073 Ulm, Germany, Fax: ++49-731-9797260

Keywords: sewage sludge, incineration, emissions, fluidized bed

ABSTRACT. In the present paper work is reported which was carried out at the Technical University Hamburg-Harburg (TUHH) in connection with the retrofitting project of the sewage sludge incinerator of the city of Ulm. In order to keep the emission limits under a variety of operating conditions different primary measures of emission control were examined at TUHH's pilot-scale bubbling fluidized bed combustor (150 mm diameter, height of combustion chamber 9m). In the first phase of the investigations it was shown that the emissions of the pollutants CO and NO_x measured at the test rig compare well with those measured at the existing large-scale combustor if operating conditions were chosen according to similarity rules. The main part of the work consisted then of a systematic investigation of the various means to influence the combustion process and the pollutants generating and reducing reactions inside the combustion chamber. In particular, the influences of predrying of the sludge, excess air ratio, staging of the combustion air and flue gas recirculation were investigated. Furthermore, the influence of a mixing element in the freeboard on the emissions was examined. The results which are described in detail in the paper have given valuable advice for the design of the new incinerator. The knowledge of the various influences and interdependences will furthermore allow the operator to choose suitable measures to minimize the emissions and keep the regulation limits under all possible operating conditions.

1. INTRODUCTION

Due to the annual increase in the production of sewage sludge in the developed countries its disposal is becoming increasingly difficult. Currently, four standard disposal routes for sludge exist namely landfilling, use as a fertilizer on agriculture land, dumping into sea and incineration. Incineration has become one of the main disposal outlets of sewage sludge in many developed countries and some newly industrialised nations. Already, incineration takes 24 % of the sludge produced in Denmark, 20 % in France and 15 % in Belgium [1]. In the USA and Japan, 25 and 55 % of the sludge produced, respectively, is incinerated [2]. It is expected that 38 % of the sludge produced by the member states of the European Union will be incinerated by the year 2005 [1]. In 1996, 2.7 million tons dry matter of sewage sludge were produced in Germany 45% of which were used as fertilizers in agriculture, 12% for recultivation and landscaping works, 11% for landfill, 10% for composting and 19% were incinerated [3].

At present, 21 sewage sludge incineration plants are existing in Germany and one more is in the commissioning phase. The combusted sludge is either wet if auxiliary fuel e.g. oil or gas is used or predried if an autothermal combustion is practised. Mono-combustion of sewage sludge is effected predominantly in combustors with fluidized beds (17 of the total 21 plants). Most of them burn semi-dried sludge with a dry matter content between 32 and 50 wt.-%.

An important aspect for consideration during sludge incineration is the control of the emissions of gaseous pollutants, especially CO, N₂O and NO_x. The potential for N₂O and NO_x emissions is high during the combustion of sewage sludge due to its high contents of nitrogen. The nitrogen content of sewage sludge is generally in the range 6-8 wt.-%, referred to water-and-ashfree conditions (waf) [4] but can be as high as 10 wt.-% (waf) [5]. The N₂O and NO_x emissions depend on nitrogen contents of the fuel [6,7].

Much information is currently available concerning the N_2O and NO_x emission characteristics of dry sludge [8-11] as well as for wet sludge [4,8,12,13]. It was found that dry sludge exhibits NO_x and N_2O emission characteristics similar to those of coals. High concentrations of NO_x (800-1200 mg/m³) and N_2O (300-400 mg/m³) were obtained from sewage sludge granulates due to the high nitrogen contents [9-11]. NO_x and N_2O increased with increase in excess air ratio whereas increasing the combustion temperature led to an increase in NO_x and a decrease in N_2O . Furthermore, reduction of N_2O and NO_x could be achieved through application of staged combustion whereas SNCR (i.e. NH_3 injection) was effective for NO_x control. Unlike dry sludge, wet sludge was found to exhibit totally different NO_x and N_2O emission characteristics [8,12,13]. Very low NO_x emissions (<200 mg/m³) were measured from wet sludge, although the nitrogen content was higher than for the dry sludge. Furthermore, combustion parameters such as combustion temperature and excess air ratio as well as emission reduction strategies (e.g. staged combustion and SNCR) had little effect on the emissions. The low NO_x emissions from wet sewage sludge incineration were validated by the NO_x emission data collected from large-scale incineration plants in Germany, burning wet sludge [14].

The above mentioned differences in the NO_x and N_2O emission behaviour of dry and wet sewage sludges and the growing interest in large-scale combustion of semi-dried sludge have currently stimulated research on the combustion of semi-dried sewage sludge. The fundamental research question is whether semi-dried sludge would behave like wet sludge or dry sludge. In the present paper work is reported which was carried out at the Technical University Hamburg-Harburg (TUHH) in connection with the retrofitting project of the sewage sludge incinerator of the city of Ulm which incinerates semi-dried raw sludge. The first fluidized bed sludge incinerator at Ulm started operation in 1972 and was one of the first municipal sewage sludge incinerators in Germany. The one which is needed to be retrofitted now was built in 1979. The question was which primary measures should be installed to reach low CO , NO_x emissions to keep the German emission limits of the 17th regulation of the Federal Immission Protection Law (17th BImSchV). This regulation is applicable to waste incineration and sets as emission limits the daily mean value for CO of 50 mg/m³ (dry, std. conditions) and for NO_x of 200 mg/m³ (dry, std. conditions) respectively. The N_2O emission characteristic was also investigated although there is no emission limit in Germany at the moment.

2. EXPERIMENTAL

The incineration of the semi-dried sewage sludge from Ulm was conducted in TUHH's pilot-scale bubbling fluidised bed combustor of which the flow diagram is shown in Fig. 1. The required fluidised bed (150 mm in diameter and 9 m high) the flow diagram of which is shown in Fig. 1. The required combustion temperature was maintained through electrical heating of the walls of the combustor. The test unit has the necessary facilities for automatic and continuous recording of combustion parameters such as temperatures, pressure drops, combustion air and fuel flow rate as well as facilities to feed wet sludge, solid, liquid and gaseous fuels. The height of the unit was chosen such as to ensure that the mean gas residence times can be adjusted to be similar to those applied in large-scale plants.

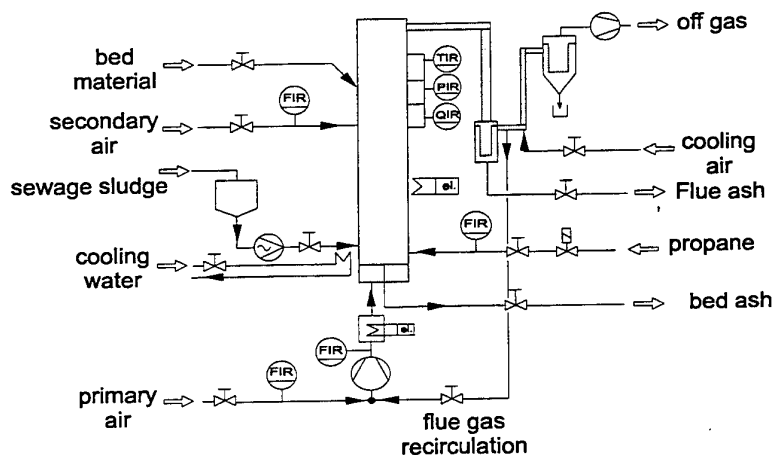


Fig. 1. A flow diagram of the pilot-scale bubbling fluidised bed combustor at TUHH

The combustor has several sampling ports along the freeboard. The details of the experimental set-up for gas sampling and analysis have been previously reported [8,12,13]. The gas sample is withdrawn from the centre line of the combustor and sucked through an electrically heated filter and sampling line by means of a gas pump. It is then directed into a cooler where it is dried before it is supplied to the various analysers at a rate of 60 l/h. Components of the flue gas such as O_2 , CO_2 , H_2O , CO , NO , NO_2 , N_2O , NH_3 and SO_2 can be analysed.

In the first phase of the investigations it had to be shown that the emissions of the pollutants CO and NO_x measured at the test rig compare well with those measured at the existing large-scale combustor if operating conditions were chosen according to similarity rules. To calculate the operation conditions in the pilot-scale plant typical operation conditions at the combustor in Ulm were recorded and evaluated. The main difference in geometry is that the bed region at Ulm's plant is conical and at TUHH's plant it is cylindrical. At Ulm the superficial velocity in the bed decreases slightly with height although the volume of the gas passing the bed increases because of the evaporation of water from the burnt sludge. In the pilot plant there is an increase of the gas velocity in the bed. To have nearly the same residence times as at Ulm's combustor the superficial velocity in the freeboard of the pilot-scale plant (including the water vapor from sludge) was calculated to 2 m/s which corresponds to a superficial velocity at distributor level of 1.3 m/s.

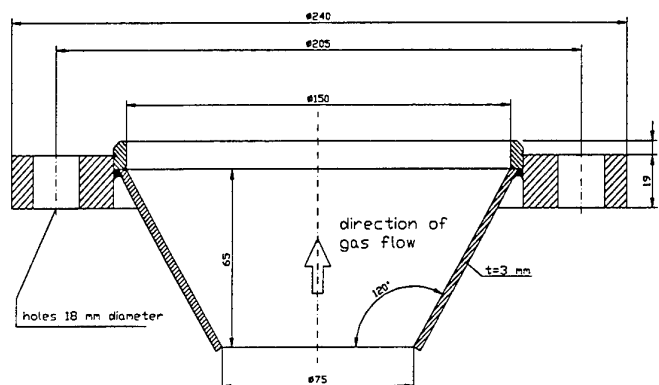


Fig. 2. Details of the mixing element installed in the bubbling fluidised bed test rig

An important feature of modern incinerators is a reduction in the cross-sectional area in the upper section of the freeboard (e.g. sludge incineration plants at Ulm, Hoechst AG and Dordrecht, the Netherlands). The Ulm plant has a rectangular freeboard of a cross-sectional area of 15.6 m² with a cylindrical outlet chute of a cross sectional area of 2.8 m². The purpose of such furnace configuration is to provide intense mixing of the reactants in the freeboard by creating turbulence. To simulate this effect, a simple metal funnel (Fig. 2) which reduced the area for the passage of the gas to one quarter of the tube's area was installed in the test unit at 7000 mm above the distributor plate. The geometry, residence times, temperatures and gas velocities at both plants are summarized in Fig. 3. At TUHH's plant a static bed height of 540 mm was used. The sludge was fed directly into the bed at 380 mm above the distributor plate. The measurement ports were located at 6500 mm (Q1), 7500 mm (Q2) and at 9100 mm (Q3) above the distributor. The ultimate and proximate analysis of the municipal raw sludge is given in Table 1.

Table 1. Proximate and ultimate analysis of the burnt sludge

semi-dried sludge			
proximate		ultimate (wt.-%, waf)	
water, wt.-% raw	68	C	47.8
ash, wt.-% wf	31	H	7.68
volatiles, wt.-% waf	90	O	38.4
NH_3 -N, wt.-% waf	0.9	N	4.6
LCV, kJ/kg - raw	4,408	S	0.77
- wf	13,775		

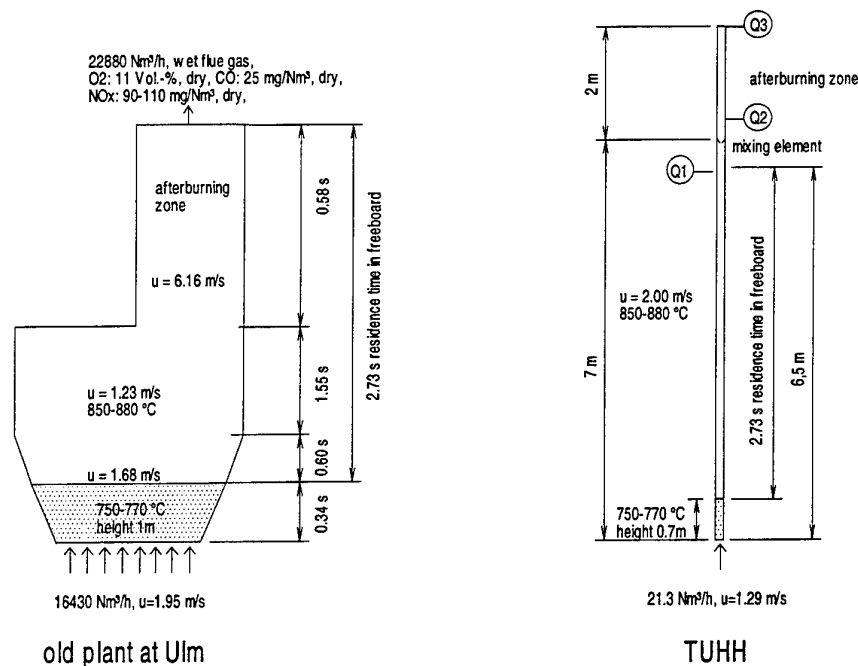


Fig. 3. Adaptation of the operating conditions of the pilot-scale plant to those of the large-scale combustor

3. RESULTS

Comparison of the Emissions From the Large Scale with Those from the Pilot-Scale Plant

The operation conditions for the first test were chosen as described above. The aim was to show that it is possible to scale down the plant at Ulm and to reach the same emissions at the small plant at TUHH. It is known that the bed material has catalytic effects on the NO_x emissions. Therefore used bed material of the large-scale combustor was used in this test. As discussed above the superficial velocity at the distributor level in the small rig was lower compared to that in the big plant. To prevent a defluidization in the bottom bed the original bed material was reduced in size by milling from a mean diameter of around $1774 \mu\text{m}$ to $820 \mu\text{m}$. The bed temperature was around 830°C and the freeboard temperature around 870°C . The oxygen concentration in the off gas was 11 vol.-%. The gas concentrations were measured at 7500 mm above distributor. That means that the gas residence time in the small plant was slightly higher as in the old large-scale combustor but the effect of the reduction in the cross-sectional area was included. As shown in Table 2 the emissions from both plants are nearly the same. After successfully finishing this first step the major part of the work was to find the best emission reduction measures for the retrofitting of the plant. For this further investigations a finer quartz sand ($d_{p50}=483\mu\text{m}$, $u_{mf,20^\circ\text{C}}=19 \text{ cm/s}$) was used as bed material.

Table 2. Comparison of emissions from both plants for similar operating conditions (for Ulm different sets of data are presented which are felt to be typical by the operator)

	Large-scale plant at Ulm				Pilot-scale plant at TUHH
O_2 [vol.-%, dry]	9.6	10.1	11.5	9.1	11.3
CO [mg/m^3 , dry, std. conditions]	12	24	42	16	42
NO_x [mg/m^3 , dry, std. conditions]	125	168	247	195	185
H_2O [vol.-%]	33.1	29.1	28.0	31.1	28.0

Effect of the Mixing Element on the Emissions

The analysis of the CO concentrations along the plant indicates that the mixing element has indeed improved the combustion quality. As is shown in Fig. 4 the measurement signals obtained at a port located at 6500 mm i.e.

upstream of the mixing element exhibited large fluctuations of CO concentrations with extreme peaks and an average concentration clearly above 50 mg/m³. However, sampling from locations downstream of the mixing element (7500 mm and 9100 mm) showed that the signal fluctuations were much less and that the average concentration was reduced to about 20 mg/m³. A significant improvement of the combustion efficiency was thus achieved by this comparatively simple means.

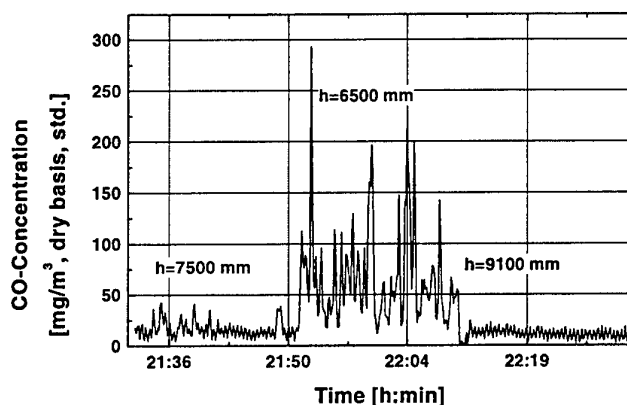


Fig. 4. Time-resolved signals of CO concentrations before and after the mixing element (the mixing element is located at h=7000 mm above the gas distributor)

In general, low CO-emissions can be achieved if the temperature is high enough and the gas residence time at this temperature level is sufficient. Both conditions are regulated by the 17th BImSchV by requesting a minimum temperature of 850°C and a flue gas residence time of at least 2 seconds after the last air supply.

NO_x Emissions as a Function of Excess Air Ratio

Fig. 5 shows the results of the emissions of NO_x. The data were obtained on different days. For comparison, the results of NO_x emissions from wet and dry sludge samples obtained from Werther et al. [12] are also included. The NO_x emissions are given as a function of oxygen concentrations in the flue gas (i.e. excess air ratio). The excess air ratio was varied by adjusting the mass flow of the sludge while maintaining a constant combustion air supply. The gas sample was withdrawn at the top of the plant. The bed temperature was around 830 °C whereas the freeboard was maintained at around 870 °C. Unlike for wet sludge for which propane had been used as supplementary fuel [8,12], no support fuel was required for the experiments with semi-dried sludge.

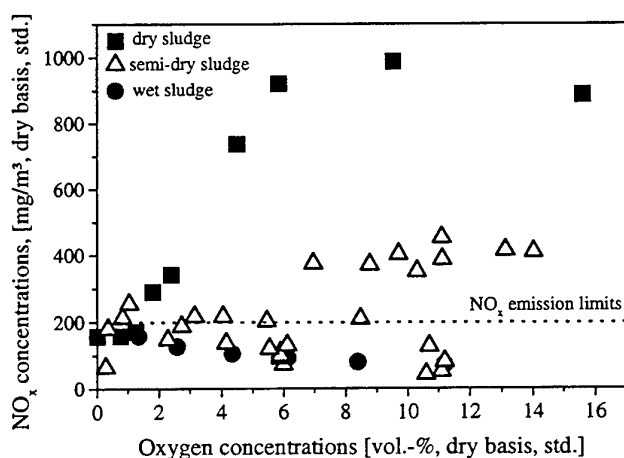


Fig. 5. NO_x emissions as a function of oxygen concentrations – comparison with those of wet and dry sludge samples [12]

It can be seen that the NO_x emission characteristics of semi-dried sludge samples are closer to those previously obtained for wet sludge samples. The NO_x levels are slightly higher than those of the wet sludge but much lower than those of the dry sludge. It is not possible to deduce the NO_x trend as a function of the oxygen concentrations. At low oxygen concentrations (0-6 vol.-%), NO_x appears to decrease with increase in O_2 , as exhibited by wet sludge samples. However, above 6 vol.-% O_2 , the trend is not clear due to the high fluctuation of NO_x emissions. Another important conclusion from these results is that, whereas it is possible to meet the NO_x limits of 200 mg/m^3 when burning wet sludge using single-stage combustion, this appears not to be guaranteed during the combustion of semi-dried sludge especially within the normal range of operating conditions (i.e. 6-11 vol.-% O_2).

N_2O Emissions as a Function of Excess Air Ratio

In Fig. 6 the N_2O emissions from semi-dried sludge as a function of oxygen concentrations in the flue gas is depicted. Here too, the data represent different samples of the same sludge collected and burnt on different days. Included in Fig. 6 for comparison, are the measurements from three different wet sludge samples previously reported by Werther et al. [8] and Ogada [4]. Compared with those obtained for wet sludge, the combustion of semi-dried sludge gave lower N_2O . N_2O concentrations less than 250 mg/m^3 were measured with semi-dried sludge compared with $500 - 700 \text{ mg/m}^3$ measured with wet sludge. Another observation is that, similar to wet sludge, there appears to be no dependence of N_2O emissions on oxygen concentrations in the flue gas.

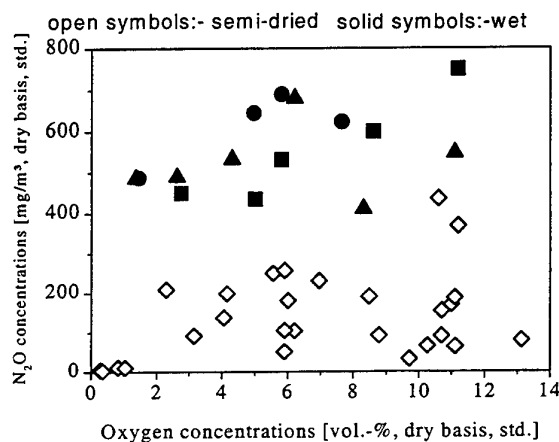


Fig. 6. Comparison of N_2O emissions from semi-dried sludge with those from wet sludge obtained from Werther et al. [8] and Ogada [4] (open symbols - semi-dried sludge, solid symbols - wet sludge)

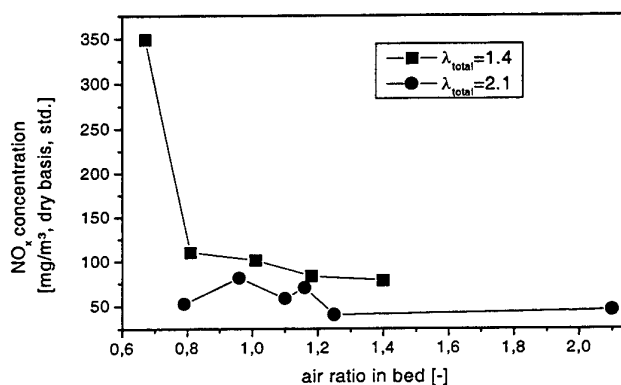


Fig. 7. Emissions of NO_x as a function of excess air ratio in the bed (Combustion temperature 850°C , staged combustion with $\lambda_{\text{total}} = 1.4$ and 2.1 , gas concentrations measured at Q3)

Staged Combustion

The experiments with staged combustion for conditions with 6 vol.-% ($\lambda_{\text{total}}=1.4$) and 11 vol.-% oxygen ($\lambda_{\text{total}}=2.1$) in the flue gas show that using staged combustion does not improve the NO_x emissions for the burnt sludge (Fig. 7). There is a tendency that with increasing air ratio in bed the NO_x emissions decrease. A strong increase in NO_x emission was observed when lowering the bed air ratio from 0.8 to 0.7 in the case with 6 vol.-% oxygen in off gas. In general the emissions in the case with $\lambda_{\text{total}}=2.1$ are lower than in the case with $\lambda_{\text{total}}=1.4$. This emission characteristic is similar to that of wet sludge obtained by e.g. Ogada [4].

The influence of using secondary air on the N_2O emissions is much more significant (Fig. 8). There is a strong minimum in the cases with 11 vol.-% oxygen in flue gas when operating the pilot plant with a bed air ratio around 1.2. It can be seen that N_2O decreased from 438 to 77 mg/m^3 . In the second case with 6 vol.-% oxygen in flue gas the N_2O concentration decreases with increased bed air ratio but on a higher level than in the previous case.

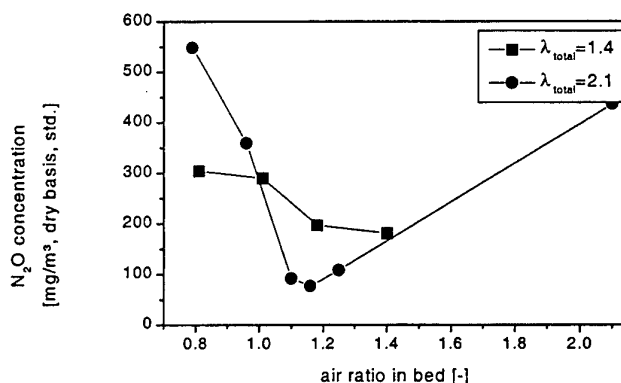


Fig. 8. Emissions of N_2O as a function of excess air ratio in the bed (Combustion temperature 850 °C, staged combustion with $\lambda_{\text{total}}=1.4$ and 2.1, gas concentrations measured at Q3)

Recirculation of Flue Gas

Flue gas recirculation is a proven method for the reduction of NO_x emissions in coal combustion. Recirculating part of the flue gas lowers the partial pressure of oxygen in the fluidized bed and leads to a higher CO level which favors the destruction of NO. Fig. 9 shows results of measurements in the pilot plant. The NO_x emission is plotted against the percentage of flue gas recirculated for different oxygen concentrations in the flue gas under conditions of single- and two-stage combustion, respectively. The fluidizing velocity was kept constant for each set of experiments which means that the fuel mass flow had to be reduced with increasing percentage of recirculated flue gas since the flue gas is replacing combustion air.

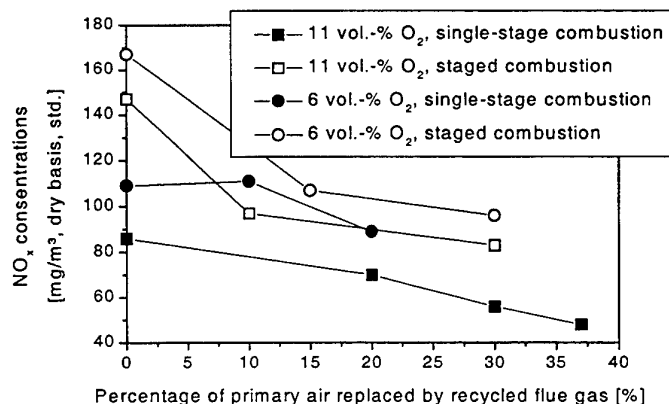


Fig. 9. Effect of flue gas recycling on the emissions of NO_x (combustion temperature 850 °C)

During single-stage combustion carried out with an excess air ratio of 1.4, (6 vol.-% in flue gas) only a mild decrease in NO_x was obtained. NO_x decreased from about 110 to 90 mg/m^3 as the ratio of recycled flue gas was increased from 0 to 20 %. During experiments carried out at excess air ratio of 2.1 (11 vol.-% oxygen in the flue gas), rapid reduction was obtained with both staged and single-stage combustion. NO_x decreased from 86 to 48 mg/m^3 (during single-stage combustion) as the ratio of recycled flue gas was increased from 0 to 37 %. During the staged combustion (excess air ratio in bed around 1), NO_x decreased from 147 to 83 mg/m^3 as the ratio of recycled flue gas was increased from 0 to 30 %. The measurements indicate that flue gas recirculation may be used as an efficient mean to "fine-tune" the NO_x emissions if there is a tendency for the emissions to exceed the legal limits. Industrial operating experience supports this conclusion. Another advantage of using flue gas to replace primary air is the opportunity to reduce the load of the combustor without changing the bed velocity and the fluidizing conditions.

4. CONCLUSIONS

In the first phase of the present investigations with burning a predried municipal sewage sludge it was shown that the emissions of the pollutants CO and NO_x measured at the test rig compare well with those measured at the existing large-scale combustor if operating conditions were chosen according to similarity rules. The main part of the work consisted then of a systematic investigation of the various means to influence the combustion process and the pollutants generating and reducing reactions inside the combustion chamber. In particular, the influences of predrying of the sludge, excess air ratio, staging of the combustion air and flue gas recirculation were investigated. Furthermore, the influence of a mixing element in the freeboard on the emissions was examined.

On the basis of these investigations the following proposals for the retrofitting of the fluidized bed combustor at Ulm in which predried municipal sludge is incinerated were made:

1. The emission limits can be fulfilled with single-stage combustion. Staged combustion has no positive effect on NO_x emissions.
2. The recirculation of flue gas to replace part of the primary air is a powerful tool to reduce NO_x emissions. It will be sufficient to replace up to 15 or 20 % of the primary air by recirculated flue gas.
3. The afterburning section is a important feature to control CO. Because of the reduction of cross-sectional area at its entrance the superficial velocity is increased and the gas mixing is improved which leads to a better burnout of CO and unburned hydrocarbons. The burnout depends on the temperature. To reach a sufficient high temperature a gas burner may be installed at the entrance of the afterburning section.
4. The emission of N_2O can be neglected if the freeboard and/or the afterburning section is operated at temperatures higher than 900 °C.

REFERENCES

1. J. E. Hall and F. Dalimier, Waste management - *Sewage Sludge: Survey of Sludge Production Treatment, Quality and Disposal in the EC*, EC Reference No: B4-3040/014156/92 (1994).
2. U. Loll, *Entsorgungspraxis-Spezial* v.8, p. 3 (1989).
3. S. van Riesen and F. Bringewski, Press release 1/1998, Abwassertechnische Vereinigung e.V., Hennef, Germany (1998).
4. T. Ogada, PhD Thesis, Technical University Hamburg-Harburg, Germany (1995).
5. M. Wirsum, PhD Thesis, University of Siegen, Germany (1997).
6. I.A. Gulyurtlu, *Fuel*, pp. 253-257 (1995)
7. E. Hampartsoumian and B.M. Gibbs, *J. Inst. of Energy*, p.403 (1984)
8. J. Werther, T. Ogada and C. Philippek, *J. Inst. Energy*, p.93 (1995)
9. U. von Raczeck., PhD Thesis, Technical University Hamburg-Harburg, Germany (1992)
10. B. Vogel, S. Lindau and U. Busse, *Wissenschaft und Umwelt*, p.105 (1992)
11. H. Hanssen, Diploma Thesis, Technical University Hamburg-Harburg, Germany (1991)
12. J. Werther, T. Ogada and C. Philippek, Proceedings, 13th International Conference on Fluidised Bed Combustion, p. 951, edited by K.J. Heinschel, Orlando, Florida, USA (1995)
13. C. Philippek, T. Knöbig, and J. Werther, Proceedings, 14th International Conference on Fluidised Bed Combustion, p. 983, edited by F.D.S. Preto, Vancouver, Canada (1997)
14. Anonymous, ATV Arbeitsbericht, *Korrespondenz Abwasser*, p. 1299 (1996)

Y. Coal Combustion

ENVIRONMENTAL CONTROL OF TOXIC METAL AIR EMISSIONS FROM THE COMBUSTION OF COAL AND WASTES

**Jost O.L. Wendt, Sheldon B. Davis,
Thomas K. Gale and Wayne S. Seames**
Department of Chemical and Environmental Engineering,
University of Arizona, Tucson, AZ 85721
Email: wendt@u.arizona.edu; Fax: +(1) 520-621-6048

William P. Linak
Air Pollution Technology Branch
National Risk Management Research Laboratory
U.S. Environmental Protection Agency,
Research Triangle Park, NC 27711
Email: linak.bill@epa.gov; Fax +(1) 919-541-0554

Keywords: toxic metals, combustion, incineration, sorbents

ABSTRACT: The emission of toxic metals from combustion of fossil fuels and wastes is an important global environmental issue. Toxic metals, such as arsenic, selenium, mercury, chromium, lead and cadmium are present in coals and in many municipal and industrial wastes. This paper is concerned with the partitioning of these metals during combustion, and with the mitigation of their effect on the environment using high temperature sorbents. The paper is divided into three parts. First, the partitioning of arsenic and selenium during coal combustion in a 17kW laboratory down-fired furnace is discussed and appropriate mechanisms identified. Second, the speciation of mercury and chromium during combustion is addressed, through special experiments on a 73kW refractory lined combustor. Third, experimental results on the sorption of individual and multiple metals on sorbents are presented. These sorbents were kaolinite and lime, and were injected directly into flue gas containing lead and cadmium metals, which had vaporized in the main flame. Results suggest that toxic metals from coal and waste combustion can be associated with lime or kaolinite sorbents, and that for some multiple metal mixtures, designer sorbents containing calcium, aluminum, and silicon might be useful to capture them and render them environmentally benign.

1. INTRODUCTION

Toxic metal emissions pose a problem in both fossil fuel and waste combustion [1-3]. Toxic metals can be classified either as non-volatile (Ba, Be, Cr, Ni), or as semi-volatile (Sb, As, Cd, Pb) or as volatile (Hg, Se), depending on their volatility at stack temperatures [1]. This paper focuses on the volatile metals, mercury (Hg) and (Se) and the semi volatile metals, arsenic (As), lead (Pb) and cadmium (Cd). The fates of selenium and arsenic are investigated as they relate to the combustion of pulverized coal. Both metals occur in many coals around the world, and arsenic can reach major concentrations in certain Chinese coals. Mercury speciation, a major issue in both fossil fuel and waste combustion, is investigated through special tests in which a clean flame is doped with a mercury salt. Lead and cadmium are discussed insofar as their emissions can be diminished through reaction of the metal vapor on sorbents such as kaolinite or lime. Cadmium and lead can vaporize in the combustion zone, subsequently to nucleate and form a difficult-to-collect fume. The fact that both lead and cadmium vaporize may allow solid substrates, such as kaolinite and lime, to react with metals vapors and render them in water insoluble forms. This process may be used to scavenge these metals preventing subsequent gas-to-solid transformations that would result in sub-micron particle formation.

In Fig. 1 are shown the possible mechanisms, which control the partitioning of toxic metals during combustion. These metals may be introduced as aqueous solutions, hydrocarbon fluids or solids, or as solids, municipal wastes and sludges. For pulverized coal, metal partitioning follows the route through porous char, where the metal may be contained extraneously in excluded mineral matter fragments, or in may be contained in inherent occlusions of mineral matter within the char matrix, or in may be organically bound directly to the organic matrix. The initial occurrence of the metal may well have a significant bearing on the subsequent partitioning routes it will follow as it passes through the combustion process. Of special interest in this paper are the routes that prevent toxic metals being emitted from the stack in the sub-micron form.

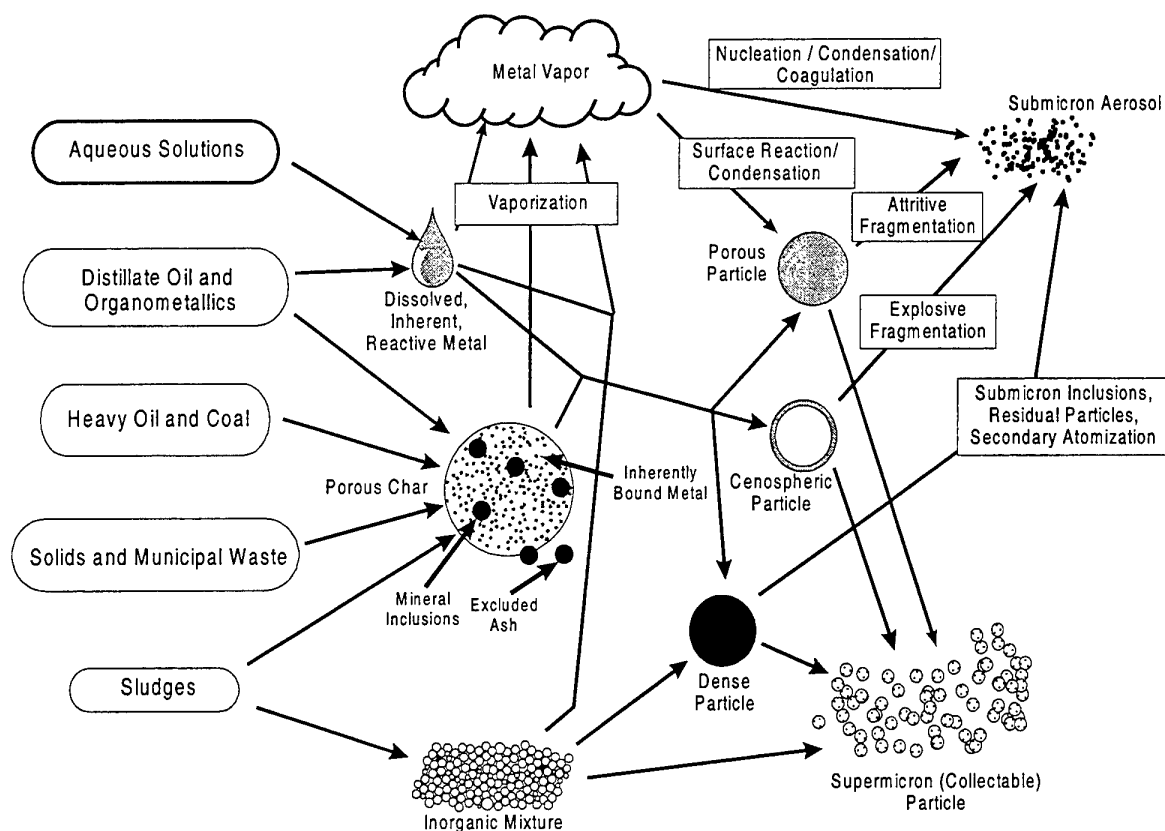


Fig. 1. Toxic metal partitioning paths

2. EXPERIMENTAL APPROACH

The approach followed was to introduce the appropriate metal into a combustion chamber, and, except in the case of mercury speciation, to infer its partitioning mechanisms through size segregated analyses of the ensuing particulate matter in the exhaust. For mercury speciation, the wet chemical method developed by Ontario Hydro [4], was used.

Experimental data presented here were obtained from two different laboratory combustion rigs. One rig at EPA was a 59 kW (actual), 82 kW (maximum rated) horizontal tunnel combustor which has been described elsewhere. This refractory-lined research combustor was designed to simulate the time/temperature and mixing characteristics of practical industrial liquid and gas combustion systems. Natural gas fuel, aqueous metal solutions, gas dopants, and combustion air were introduced into the burner section through an International Flame Research Foundation (IFRF) moveable-block, variable-air, swirl burner. Further details regarding the experimental combustor can be found elsewhere [5,6]. The other rig, located at the University of Arizona, consisted of a 7-meter tall, 12kW downflow combustor. Details can be found elsewhere [7,8]. Like the EPA furnace, this facility was also designed to have a time and temperature history similar to a full-scale system, yet, it was well defined and could be considered one-dimensional. In both systems, metals could be introduced into a natural gas flame, through an atomizer in the form of the aqueous stream. Metal salts were dissolved in distilled water in a quantity such that the concentrations of each metal on an elemental basis are 100ppm in the flue gas. In this paper, all the pulverized coal results reported were obtained from the 17kW University of Arizona (UA) down-fired furnace, while mercury and chromium speciation data were gleaned from the 59kW EPA refractory lined furnace. Results describing the metal /sorbent interactions reported here are taken from data from the UA furnace. Here, kaolinite or lime sorbents were introduced as powders suspended in nitrogen through a port downstream of the combustion zone.

Particulate samples were taken by the isokinetic sampling and size segregation system shown on Fig 2. The samples were drawn into a sampling probe, immediately mixed with a controlled amount of nitrogen. The nitrogen immediately quenched the stream and stopped all subsequent reactions. The diluted sample was directed immediately to an impactor, which performed the size segregation on the particles. A variety of impactors were used. The atmospheric pressure Andersen impactor allowed segregation onto nine stages while the Micro Orifice Uniform Deposition Impactor allowed better resolution for the smaller particle size range. The Berner low-pressure impactor (BLPI) is the experimental centerpiece for much of the data presented here and is also shown on Fig 2. Whereas conventional cascade impactors operate at atmospheric pressure under which separations are performed purely by varying the gas velocity through successively smaller orifices, the BLPI, by operating at low pressures, is able to take advantage of the compressible flow properties and can attain much smaller particle cut-off diameters than atmospheric impactors.

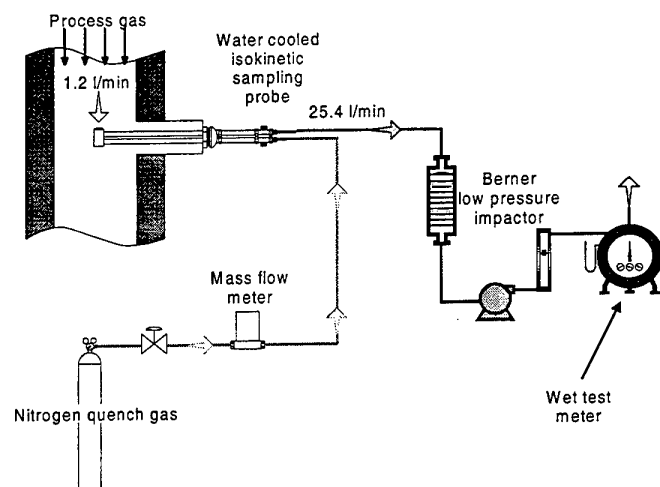


Fig. 2. Schematic of sampling and LPI size segregation system

The BLPI is composed of eleven stages having aerodynamic cut-off diameters ranging from $15.7\mu\text{m}$ to $0.0324\mu\text{m}$. The stage is composed of an orifice plate above a substrate and a substrate holder. The substrate is held in place by a ring, which also acts as a spacer between the orifice plate and the substrate. The flow rate through the BLPI is regulated by the last orifice plate, which acts as a sonic orifice. The absolute pressure after this final orifice plate is approximately 8 kPa. A full description of this apparatus and its performance can be found in reference [9].

The mode within the particle size distribution in which the metal of interest escapes is used to infer pertinent mechanisms controlling its fate. For example, the efficacy of reactive capture of toxic metals by sorbents can be determined by determining how sorbent addition shifts the particle size distribution (PSD) containing the metal. Previous work [7,8] has shown that when metal vapors are sampled they appear as a very fine nuclei fume at about $0.1\mu\text{m}$ diameter.

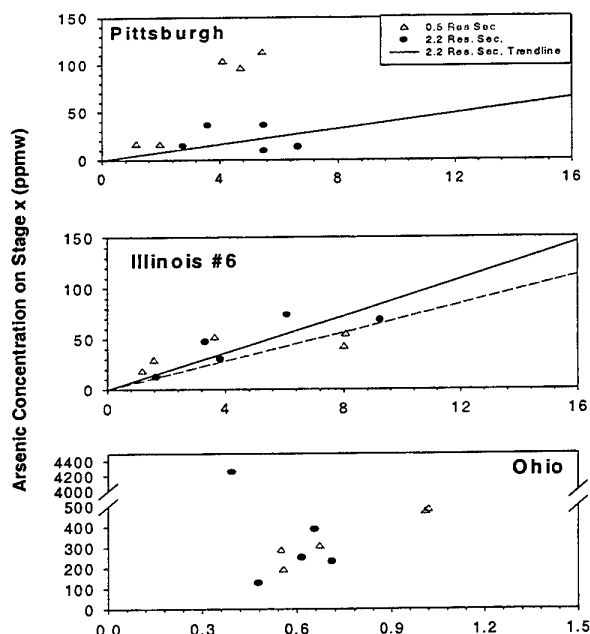


Fig. 3. Arsenic/calcium correlation for three US coals

3. RESULTS

Arsenic and Selenium During Pulverized Coal Combustion.

The fate of arsenic and selenium during coal combustion is discussed here in the context of the mechanism pathways shown in Fig 1. Experiments were conducted on the University of Arizona 17 kW laboratory combustor, in which pulverized coal was burned in a self-sustaining mode. Experimental results, not shown here for lack of space, have established [10] that most of the arsenic in fly ash from pulverized coal combustion is contained in particles less than $1\text{--}2\text{ }\mu\text{m}$, which is in the fine particle range. However, although arsenic is a semi-volatile metal, there is little evidence that arsenic vapors form arsenic rich nuclei in the exhaust. Rather, arsenic is associated with calcium, when that metal is present in coals. Fig 3 shows the correlation between arsenic and calcium for three US coals. The upper two panels show good correlation between these two elements for samples taken at the exhaust (2.2 s residence time), but not necessarily closer to the flame at 0.5s residence time. The lower panel, for the Ohio coal, does not show a correlation between arsenic and calcium, suggesting that any association between these elements is weak for that coal. The two coals in the upper panels contained sufficient calcium to react with the available arsenic. The Ohio coal in the bottom panel did not contain enough calcium for sorption of the arsenic available. These data suggest that arsenic will follow calcium, and that the ensuing particle size segregated speciation is determined by the aerosol mechanisms followed by the calcium.

Analogous selenium data are shown on Fig. 4 and show that selenium is rapidly associated with calcium early in the flame. This is true even for the low calcium Ohio coal, and indicates that calcium reacts more rapidly with selenium than it does with arsenic. For all three coals, selenium is associated with calcium, very early in the combustion process, at 0.5 sec residence time. Calcium is clearly a very important metal in determining the ultimately partitioning of both arsenic and selenium.

Mercury Speciation

Elemental mercury accumulation on the planet earth is a global issue. However, emission of oxidized mercury becomes a local environmental issue. Speciation of mercury is important, since oxidized mercury is soluble and thus removable from stack gases. Fig. 5 shows results from 73kW natural gas flames doped with $\text{Hg}(\text{NO}_3)_2$ such that 100 ppb Hg in the stack gas was produced at a fuel/air stoichiometric ratio (SR) of 1(fuel lean), or 140 ppb Hg at $\text{SR}=0.8$ (fuel rich). Chlorine and SO_2 levels were 500 ppm and 1000 ppm, respectively, at $\text{SR}=1.2$. The Ontario Hydro Method was used for Hg

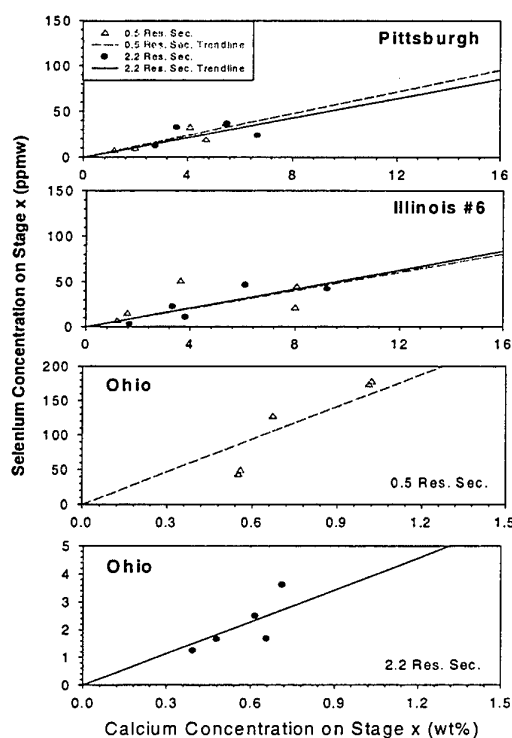


Fig. 4. Selenium/calcium correlation for three US coals

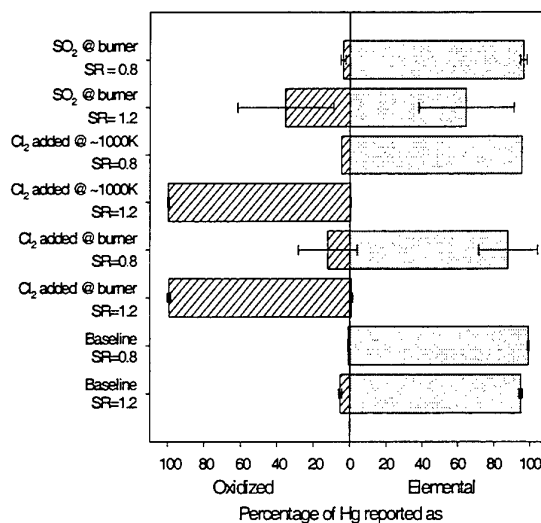


Fig. 5. Mercury speciation - doped gas

analysis, and the sample was withdrawn at a temperature of 640K. The data show that chlorine added as Cl_2 to the air stream at the burner, allowed almost complete conversion of mercury to the ionic form. Note that less than 1ppm Cl_2 can be expected to leave the flame with the remainder probably converted to HCl . It is not surprising that similar results were obtained when chlorine was added to the flue gas downstream. Slight oxidation was also observed with addition of SO_2 . However, only elemental Hg was observed in the absence of additives, and under all rich conditions, with or without Cl_2 or SO_2 additives.

Chromium Speciation and PSD.

Speciation of chromium is an important issue, since the hexavalent form of chromium is much more harmful to human health than is the trivalent form, which is quite environmentally benign. Fig. 6 shows results from the EPA 59kW refractory lined furnace, in which hexavalent and trivalent forms of chromium, CrO_3 and $\text{Cr}(\text{NO}_3)_3$, were added to distilled water and sprayed into a gas flame. Due to Cr^{III} digestion problems, the analysis of total chromium is quite difficult; a caustic fusion method was employed as described in Reference [11]. Clearly at these conditions, the initial form of chromium has a large influence on the particle size distribution (PSD) emitted, while it appears to have no influence on the speciation of chromium. The fraction of chromium that is generated as hexavalent chromium is very small, and less than 1% in the absence of chlorine. In further experiments, hexavalent chromium formation is enhanced by chlorine (to 5% fraction emitted) but greatly diminished by sulfur. In fact, the addition of sulfur can completely suppress the formation of hexavalent chromium in combustion systems.

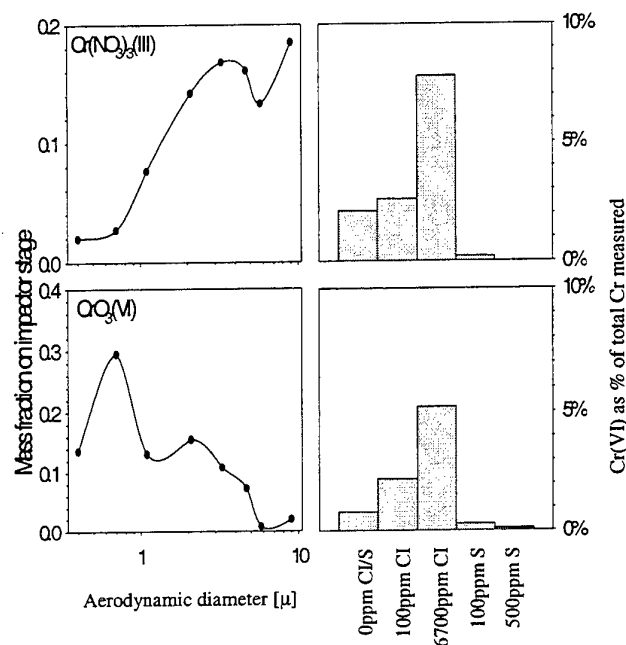


Fig. 6. Chromium wastes: effects of inlet speciation (Cr^{6+} versus Cr^{3+}) on outlet PSD and speciation

Reactive Scavenging of Hot Toxic Metal Vapors by Sorbents.

The efficacy of reactive capture of toxic metals by sorbents can be determined by determining how sorbent addition shifts the particle size distribution (PSD) containing the metal. Previous work [8] has shown that metal

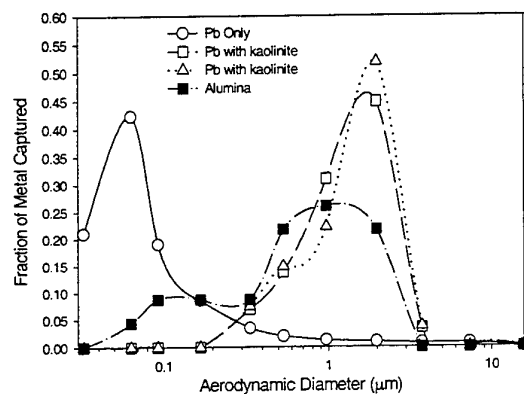


Fig. 7. Lead capture by kaolinite in a single metal/sorbent system.

vapors appear as a very fine particles ($\sim 0.1 \mu\text{m}$ aerodynamic diameter) when extracted by the sampling system described earlier. Further, there is insufficient time within the sampling system for significant coagulation to occur. Discrimination between physical condensation and reactive scavenging is more difficult. The former process cannot occur above the metal dewpoints, and, at the concentrations encountered here, generally requires a greater external surface area than that afforded by the sorbent injection rates here. In this paper, we restrict ourselves to three systems: 1) lead capture by kaolinite and lime, 2) cadmium capture by kaolinite and lime, and 3) mixtures of lead and cadmium interacting with kaolinite sorbent.

Pb/kaolinite and Pb/lime systems. Figures 7 and 8 show the changes in lead aerosol size distribution when kaolinite (Fig 7), and hydrated lime (Fig 8), are individually injected at ~1450K. Samples were taken at the bottom of the furnace (~900K), below the dewpoint of the metals.

Without sorbent, the sampled lead aerosol has a predominant size of 0.1 μ m (Fig 7), suggesting a freshly coagulated aerosol of lead nuclei. Upon introduction of kaolinite powder, the lead PSD shifts by over a factor of 10 in particle size, and (except for a fine aluminum tail) appears to correlate with the aluminum PSD, which is represents the injected sorbent powder. With lime injection (Fig 8), no change in the lead aerosol psd is discerned. Clearly lead is almost completely reactively captured in Fig 7, whereas, only a small portion is scavenged (most probably by physical condensation) by lime in Fig 8. Therefore, comparison of Figs 7 and 8 allows reactive scavenging and simple physical condensation processes to be distinguished in samples taken after the metal dewpoint. At the metal and sorbent concentrations used here, reactive scavenging is demonstrated by the data in Fig. 7, while other forms of interaction are demonstrated in Fig. 8 (although partial reaction cannot be completely ruled out, unless samples are also taken above the dew point).

Cd/kaolinite and Cd/lime systems. Figs. 9 and 10 show the analogous data for cadmium capture on kaolinite (Fig. 9) and cadmium capture on lime (Fig. 10) where each experiment consisted of injection of one metal and one sorbent at a time. Fig. 9 shows that cadmium is partially captured by kaolinite, but substantially more so than lead was captured by lime. The coarse cadmium peak is believed to represent partial scavenging, rather than physical condensation because of the large fraction of cadmium that was transferred to the coarse particle size. Results below support this conclusion.

Multiple metals, Pb and Cd, interacting with kaolinite.

Experiments were performed in which the flue gas contained 100-ppm lead vapor together with 100-ppm cadmium vapor. Dew points for lead and cadmium were very close and lay within 25K of each other. Hence times for reaction between metal vapor and sorbent are the same for both metals. Results are shown on Figs 11 and 12, a comparison of which clearly demonstrates that lead is preferentially reactively scavenged by kaolinite. Essentially all of the lead follows the coarse aluminum mode, whereas essentially none of the cadmium is now affected by the kaolinite. Additional experiments in which the multi-metal mixture was exposed to lime sorbent showed that, as expected, the lime captured the cadmium, but not the lead. These data are not presented here.

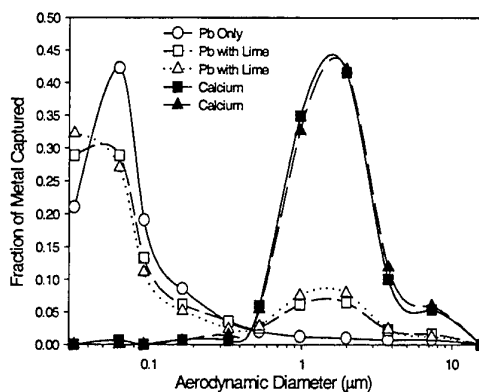


Fig. 8. Lack of lead capture by lime in a single metal/sorbent system.

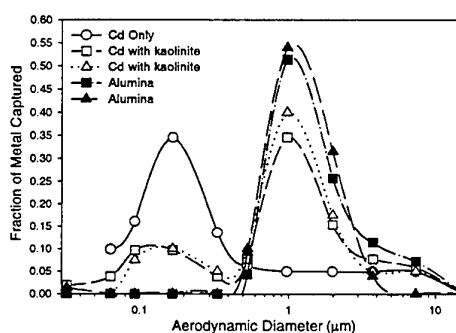


Fig. 9. Cadmium capture by kaolinite (single metal, single sorbent).

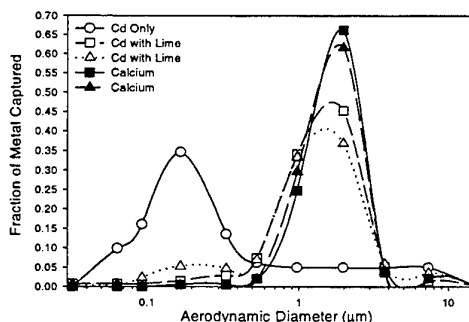


Fig. 10. Cadmium capture by lime (single metal, single sorbent)

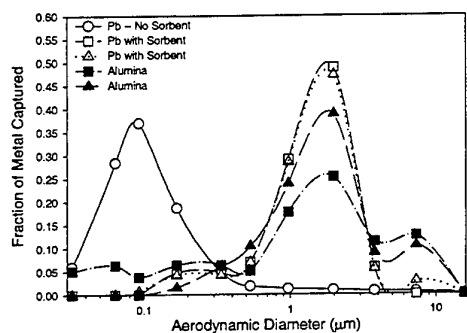


Fig. 11. Lead capture by kaolinite in a multi-metal Pb-Cd/single sorbent system

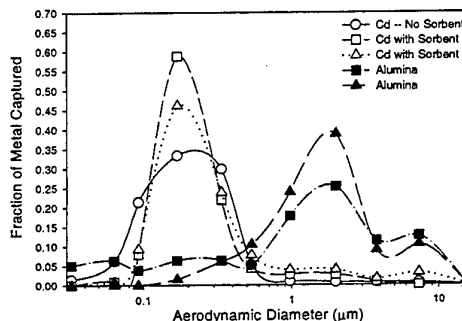


Fig. 12. Cadmium capture by kaolinite in the multi-metal Pb-Cd, single sorbent system

4. CONCLUSIONS

Arsenic and selenium from pulverized coal appear to be associated with calcium when there is sufficient calcium present in the coal. When calcium levels are low, as in the Ohio coal, there is no correlation between arsenic and calcium, although there is a correlation between selenium and calcium. Selenium and calcium appear to react rapidly in the combustion zone, while arsenic and calcium react more slowly downstream in the post flame region.

Mercury speciation, oxidized versus elemental, seems to be profoundly influenced by chlorine, especially molecular chlorine. Results suggest that oxidized mercury can only be found under lean combustion conditions. Chromium in the exhaust appears primarily as trivalent chromium, with less than 1% present as hexavalent chromium, which is mutagenic. The outlet valency form appears to be independent of the form that was fed to the furnace. The outlet PSD depended strongly on the initial form fed to the furnace.

Emissions of toxic metals, which constitute an environmental problem in the combustion of waste and fossil fuels, can possibly be managed through the injection of commercial sorbents, such as kaolinite and lime. Kaolinite is very effective at reactively scavenging lead vapor, and moderately effective at capturing cadmium, provided there is little competition for reactive sites. When both lead and cadmium are present, the kaolinite scavenges lead preferentially to the cadmium. The situation is reversed for lime as a sorbent. Lime captures cadmium very effectively but is ineffective for lead. These data suggest that effective designer sorbents for multiple metals might consist of mixtures of kaolinite and lime, for example. Additional work is required to determine the pertinent kinetics, to develop models necessary for optimization, and to evaluate the total environmental impact of the products produced.

ACKNOWLEDGEMENTS

The authors acknowledge financial support of this research by NEDO, a Japanese government agency, under their co-operative international program on energy and environmental research. They also acknowledge the sponsorship by the U.S. Environmental Protection Agency under Grant R 825389-01, and by the U.S. Department of Energy under Contract DE-AC22-95PC95101. The authors acknowledge the assistance rendered by Dr. Ichiro Naruse of Toyohashi University, Japan, by Dr. I. Olmez of MIT, Cambridge, USA. for performing the neutron activation analysis, and by Jeffrey Ryan, of EPA. for the mercury and chromium analyses. The authors also acknowledge the assistance of the many undergraduate students who worked in the University of Arizona combustion group during the performance of this research.

REFERENCES

1. W.P. Linak and J.O.L. Wendt, *Prog. Energy Combust. Sci.*, 19:145-185 (1993)
2. T. Abbas; P.G. Costen,; and F.C. Lockwood, *Twenty-Sixth (International) Symposium on Combustion*,

3. pp. 3041-3058, The Combustion Institute, Pittsburgh, PA.(1996)
4. J.O.L. Wendt, *Twenty-Fifth (International) Symposium on Combustion*, pp. 277-289, The Combustion Institute, Pittsburgh, PA. (1994)
5. T.D. Brown, D.N. Smith, R.A. Hargis, and W. J. O'Dowd, *J. AWMA*, 49(6), 628-640(1999).
6. W.P. Linak, R.K. Srivastava, and J.O.L. Wendt, *Combust. Sci. and Technol.*, 101, 7-27(1994).
7. W.P. Linak, and J.O.L. Wendt, *Combust Sci and Technol*, 134(1-6), 291-314 (1998)
8. S.B. Davis, and J.O.L. Wendt, "Quantitative Analysis of High Temperature Toxic Metal Sorption Rates Using Aerosol Fractionation" in press to *Journal of Aerosol Science and Technology*, November 1998.
9. S. B. Davis, T. K. Gale , J.O.L. Wendt, and W.P. Linak, *Twenty Seventh (International) Symposium on Combustion*, pp 1785-1791, The Combustion Institute (1998)
10. R. Hillamo and E. Kauppinen, *Aerosol Sci Technol*, 14: 33-47 (1991).
- 10 J.O.L. Wendt, and W.S. Seames "The Partitioning of Arsenic, Selenium, Cadmium, and Cesium during Pulverized Coal Combustion in a 17kW Downflow Combustor", Invited Keynote Paper, *4th International Symposium on Coal Combustion*, August 18-21, 1999, Beijing, P.R. China.
11. W.P. Linak, J.A. Ryan, and J.O.L. Wendt, *Combust. Sci. and Technol*, 116-117, pp 479-498 (1996).

LARGE UTILITY BOILERS BURNING LOW GRADE COALS WITH HIGH EFFICIENCY AND CLEAN ENVIRONMENT

Jim Zhou

Power Generation Group

Babcock & Wilcox

Email:zhouj@pww.mcdermott.com; Fax: 330-860-6590

Keywords: low grade coal, combustion, environment

ABSTRACT. Low grade coals, such as anthracites and semi-anthracites as well as lean coals, contain lower volatile matter (VM), while the moisture and ash content are sometimes high. The conventional boilers and burners firing pulverized coal can not handle such fuels well due to the difficulties of ignition, flame stability and carbon conversion. The boiler efficiency generally is low and unburned carbon in the fly ash is high. The boiler load turn down range is poor while the minimum load without oil support is high. To successfully burn such fuels, enhancing ignition and flame stabilization and a longer residence time in a furnace are the key technical issues. These steps can be realized by burner design and its arrangement; furnace design and its configuration; as well as a combustion system type and its application. Depending on the coals as fired and combustion system adopted, the burner could be a straight jet or swirl type. The burner arrangement also could be corner or wall firing, even a roof downshot firing with W-shape flame. The downshot-firing furnace as approved is suitable for firing anthracite. The environmental concerns burning low VM coals are more serious compared to the case of burning high-grade coals (bituminous). Its NO_x emission level is much higher than bituminous. The available technologies for De-NO_x during the combustion stage are too sensitive to coal quality, and are still under development and improvement. At the current stage in China, most of the downshot firing with W-shape furnaces are 300-350 MW in capacity. Most fuels as fired are blends of anthracites and lean coals. Larger capacity downshot W-flame furnaces are under development. Most of lean coals firing units in China have adopted corner firing technology. Performance on minimum load without oil support of such units should be improved.

1. INTRODUCTION [1,2]

China has abundant low grade coal deposits. As being proven, 17% of coal resource are anthracites, lean or meager. These coals contain considerably low volatile matter (VM) while the ash and moisture can be high. The sulfur might be high for some kinds of low VM coals as well. According to Chinese government directives regarding the energy policy, the Utility Industry is restricted to burning high volatile bituminous and fuel oil, but encouraged to utilize low grade coals, including low volatile bituminous (lean coals, 16-18% VM); semi-/ anthracites (VM less than 14%) and even mining refuse. To successfully burn such fuels, enhancing ignition, flame stabilization and a longer residence time in a furnace are the key technical points.

Since the 1960s, the Chinese Utility Industry has worked with Chinese Research Institutes, Design Institutes and Universities to have conducted anthracite burning tests at utility boilers, which are tangentially firing furnaces and originally were designed to fire bituminous. The anthracite burning test at YongAn PP is the most famous test conducted. A Chinese report concluded the past R & D activity: "Generally speaking, due to the low volatile content (usually 10% and below, min. down to 3-4%), the ignition becomes difficult, and the flame reveals unstable, and resulting into a large amount of unburned carbon loss (usually 8-10%, max. to 15-16% min. to 6-7%). The boiler efficiency is low (typically 71-86%). The minimums load without oil support is high. Auxiliary fuel oil is needed to stabilize the flame, and the supporting oil amount is around 10-25% of total furnace heat input". Those researches for 30 years have collected considerably useful experiences in burning low volatile coals. However, a Chinese type mature furnace burning low grade coal is still under development.

Since the middle of 1980s, several downshot W-flame boilers were imported into China firing low volatile blending coals. Commercial operated units demonstrated that the overall boiler performance of those units is good. Boiler efficiencies of these units are all over 90%. The achievements highlight a new way to utilize low volatile coals, and

attract more Chinese users' interest. For the past several years, these downshot firing projects increased, and the unit capacity also increased to 600 MW.

Babcock & Wilcox have supplied the first 2-downshot units to China in 1990. Then others followed in next few years. Due to its energy policies of different nations in the world, except China only Spain has more downshot units firing local anthracites.

2. COAL RANKING CLASSIFICATION

International Classification Standard.

Utility industry ranks low-grade coal mainly per its volatile matter content (VM). The common classification standard is the ASTM D-338, which ranks coal per its dry and mineral free base VMdmf amount:

If	$8\% < \text{VM dmf} \leq 14\%$	Semi-anthracite
	$2\% < \text{VM dmf} \leq 8\%$	Anthracite
	$\text{VM dmf} \leq 2\%$	Meta-anthracite

ASTM D-338 ranks bituminous or other coals per its dry and mineral free base high heating value HHV dmf. The VM dmf and HHV dmf are calculated by Parr correlation as follows:

$$\text{VMdmf} = 100 - 100 (\text{FC} - 0.51\text{S}) / [100 - (\text{M} + 1.08\text{A}) + 0.55\text{S}]$$

$$\text{HHVdmf} = 100 (\text{HHV} - 50\text{S}) / [100 - (1.08\text{A} + 0.55\text{S})]$$

Note: items in the right of Parr Correlation are so-called A inherent moisture base \approx values.

Chinese Utility Industry Standard

Chinese Utility recommends to use "AVAWST" for coal ranking, which adopts the dry and moisture free base volatile content as main index and heating value as sub index for ranking. Per this standard, there is no semi-anthracite in classification. Readers might refer to this standard for details.

3. IMPACTS OF HIGH ASH CONTENT (PHYSICAL CHARACTERISTICS)

The ash content of a low VM coal usually is considerably high (around 15-20%). It could rise to as high as 30% due to supplying mine changes. Sometimes the moisture might be high as well.

During a new boiler design, B&W has developed a method to evaluate the impacts of ash content and its components on boiler performance. The B&W method, which evaluates the slagging and fouling tendencies, is mainly based on the ratio of acid oxides and base oxides and alkaline oxides in ash. Per evaluation, furnace size or volumetric heat release rate, heating surface arrangements, sootblower number and arrangement will be determined. During boiler operation, if the coal as fired contains more ash than the design coal, it could cause additional impacts on boiler operation and performance. Due to the high, no heating value inert in coal as fired, the coal heating value is lower than that of design coal. To achieve a certain load with the same heat input from fuel to furnace, the amount of raw coal being pulverized needs to be increased. If the capacity margin of a pulverizer is not big enough, the boiler output might be limited. The problem might be solved by losing fineness requirement as trade in for mill capacity and load demand. However, the unburned carbon loss will considerably increase. The ash shell surrounding coal particles increases the resistance of oxygen diffusion to the char core, and worsens the char burnout process. The unburned carbon loss increases. Fly ash deposit on the heating surfaces increases and worsens heat transfer of heating surface. The frequency of sootblowing increases for surface clearing, and the tempering water amount will increase.

Note the above discussion excludes the impacts of slagging due to lower ash fusion temperatures caused by ash component change of coal as fired. Due to a higher ash content, the erosions of convective heating surface, burner nozzle

and coal duct become more severe, resulting in a shorter parts wear life.

4. LOW VM COAL'S KINETIC CHARACTERISTICS AND IMPACTS [2,3]

The combustion behavior of low VM coals might be concluded by these *three difficulties* : difficulties on ignition, flame stabilization, and high carbon conversion of char residue. These "*three difficulties*" will greatly impact on designs of furnace configuration; burner selection and its arrangements; as well as the boiler performance as designed.

Ignition

A common problem to fire low VM coals is the ignition; i.e. the coal-air jet, leaving the coal nozzle and entering the furnace, is not easily ignited. It needs more external heat sources to support and to provide sufficient heat. The heating-up process of coal particles needs a longer time for volatile releasing. The ignition process will be usually delayed if there are no enhancing steps. The common criteria evaluating the coal ignition characteristics is the so-called "ignition temperature". It is widely used, and may be determined by the weight loss profile of a coal sample in TGA. The ignition temperature of anthracites is usually considerably higher than that of bituminous. The ignition temperature range of most anthracites is around 900-1000C while the range of bituminous is 650-750C. An index called T15C is also used to evaluate the ignition process. At the temperature of T15C, the coal sample temperature increasing rate achieves 15 C per minute due to oxidation (combustion). In China, a correlation based on coal proximate analysis to predict the ignition characteristics is proposed. The TGA weight loss profile of a coal sample (B&W named it as burning profile) was used to evaluate the ignition characteristics by B&W first. A paper describing this method was published at ASME Annual Proceedings of 1967. Fig. 1 shows a sample of burning profile. The ordinate represents the sample weight loss rate while abscissa is the temperature. The heating rate of a TGA furnace typically remains under constant, so the abscissa can be read as time. Curves in Fig. 1 represent different coal weight loss. From Fig.1, readers can clearly find that:

- 1) The starting temperature of quick weight loss of anthracite is much higher than the temperature of bituminous. For less VM of coal sample contents, the profile curve on Fig.1 will move towards to right. The rapid weight loss of a sample may be interpreted as the start of combustion. The temperature corresponding to the inflection point of a weight loss curve is read as the "ignition temperature".
- 2) The maximum weight loss rate of anthracite is lower than the rate of bituminous. It means that the burning rate of anthracite is smaller than that of bituminous.
- 3) After the curve peak, the weight loss curve of bituminous decays faster than anthracites. It indicates that the burnout process of anthracite char residue is slower than bituminous.

The heating history of coal particles from coal nozzle into actual utility furnace is quite different than the case in TGA furnace. There is magnitude difference on heating rate. The behavior of volatile release under a rapid heating up process is considerably different with TGA's process. It has been reported in many literatures. Therefore, the ignition temperature obtained from TGA provides relative information only. It is found that ignition temperatures obtained from different TGA devices might give different values for a same type of coal.

B&W has accumulated a lot of burning profile data of North American coals. B&W has also collected many ignition information of those coals from utility boilers. By comparing a burning profile of an unknown coal to ignition information in our database, the ignition characteristics of an unknown coal can be predicted.

The heat released by volatile burning greatly supports the ignition process of char residue. The anthracite can not provide sufficient heat to ignite the char on time due to its low VM content, its delayed releasing and burning, and possibly a lower volatile heating value. To overcome the ignition difficulty, it is necessary to take steps to enhance the ignition by adding more external heat sources. These steps of enhancing ignition may be achieved by furnace configuration, burner type, pulverizing and combustion air system designs and their arrangements.

Flame Stabilization

A continued flame torch after ignition should be retained and is another key issue to burn low VM coal. If the flame

becomes unstable or lost, it will cause a furnace pressure fluctuation. In a serious case, it might cause a furnace explosion. Whether the flame can be stable, depends on a dynamic balance between the coal jet velocity and the flame propagation velocity. The factors impacting the flame propagation velocity are mainly dependent on the following 4 factors:

- 1) VM content. The flame propagation velocity of a coal jet is mainly dependent on VM amount and its heating value of coal as fired. Higher VM content and its heating value are favorable to form a higher flame propagation velocity.
- 2) Air/fuel ratio (coal concentration). Within a typical range of coal-air jet concentration of utility boilers, a dense coal jet is favorable to form a high flame propagation velocity.
- 3) Mean size of pulverized coal particles. Within a common size distribution range of utility boiler operation, finer size distribution is good for high flame propagation. It will also reduce the dependency of flame propagation velocity on VM.
- 4) Ash content. A negative impact of ash content on flame propagation was observed. With an increase of ash content, flame propagation velocity might reduce.

In conclusion, the most important factor impacting flame stability is the VM content and its quality, which is a nature of coal as fired, and can not be changed. The coal jet concentration and pulverized coal size are operation factors, and can be adjusted.

Burnout Process of Char Residue

The reactivity of a low VM coal char residue is normally lower than that of high VM coals. The specific area of char residue available for oxidation is smaller due to less porosity. The oxidation of char is a heterogeneous type reaction. The thicker ash shell surrounding the char core increases the resistance of oxygen to char external surface. Therefore the burning rate of low VM char is normally smaller than that of bituminous char. In order to achieve a reasonable and acceptable carbon conversion, the residence time of char residue in a furnace needs to be longer. Increasing the furnace height and adopting special furnace configuration to achieve a longer residence time in furnace are common ways. Increasing combustion air turbulence at burnout stage of char, improving the diffusion of oxygen to char surface, and properly increasing overall excess air are other common steps.

Combustion Behavior of a Blended Coal

Utility industry usually burns very low VM coals by blending some percentages of lean coal. B&W experience indicates that the combustion behavior of a blended coal is normally worse than a single specie coal with an equal VM content. In China, all of the operating low VM firing downshot units and most of the lean coal firing units burn blended coals. The weighted mean VM amount of a blended coal can not directly be used to evaluate its combustion characteristics. An equivalent VM amount of a blended coal should be used. This equivalent VM of a blended coal varies with blending ratio, and it is normally smaller than the weighted mean value of volatile matter by blending coal species.

5. TECHNICAL SOLUTIONS FOR BETTER BURNING LOW VM COALS [1,4,5]

Low VM coal firing demands more external ignition heat sources to support ignition. These heat sources include the heat brought back by recirculating high temperature flue gas; the heat from flame torch and furnace arch and walls by radiation; and the heat carried in by the coal-air jet itself with a higher combustion air temperature. Per approximately estimating, the recirculating flue gas is a very effective way, and it can provide the most external heat for ignition. High temperatures of coal-air jet and secondary air entering to furnace reduce the dependency of ignition on other external sources. The technical solutions of enhancing ignition are the applications of the above steps alone or in combination.

Steps For Enhancing Ignition

- 1) Increasing Coal/Air Jet Temperature, Primary Air (PA) Exchange

Increasing the temperature of coal/air jet entering the furnace can greatly reduce the demand on external ignition heat resources. Its strong effect on enhancing ignition has already been known, and applied in bin system (indirect) firing for many years. The indirect firing system has a limitation to apply a higher temperature PA as dry and carrier medium due to the mill operation and pipe safety concerns. If the PA temperature is increased by air exchange just

at furnace front, it can avoid negative impacts of high temperature PA. Almost all types of burners burning anthracites have applied the principle.

B&W's PAX burner, developed 15 years ago, does apply this principle. The PAX burner adopts a mechanically simple, rather low resistance, internal air exchange device. Fig. 2 illustrates the structure. When a low temperature PA stream enters into the burner elbow, the PA stream is separated due to the centrifugal force. A certain amount (say around 45-55%) of colder air and 10% fine coal in the stream are separated, and flow out the burner. The 90% pulverized coal, together with the rest of air (55-45 %) in the stream continues forward to the coal nozzle where it merges with a hotter air stream from the secondary air (SA) windbox. The mixed air-coal temperature in the coal nozzle tip is boosted to approximately 350-400 F, depending on the SA temperature and colder air amount replaced by hot air. The concentration of the air-coal mixture in the PA stream into the furnace might be increased too, depending on the amount of replacing air. The PA separation and replacement can also be done by an external cyclone device at the furnace front. Some vendors adopt this method. The cyclone separation is mainly to increase the coal-air jet concentration for ignition enhancing.

2) Increasing Hot Flue Gas Recirculation Back to Burner Front

This is the most effective step for enhancing ignition. Not only a sufficient amount of high temperature flue gas back to coal nozzle tip, but also a preferred recirculation zone (size, shape and location) is critical. Compared to other type burners such as slots or round straight jet, the multi-coaxial jet type swirl burner has great advantages on this task. B&W PAX burner applies dual co-axial swirling jets for burner secondary air registration. It not only meets a certain recirculation request, but also creates a sufficient jet momentum to penetrate deeply for further char burnout. Fig. 3 shows the PAX burner secondary air register sketch. B&W names the duals SA zone register as XCL, an aXial Control Low-VM swirling type register. The SA combustion air enters the burner through a sliding drum, then splits into two streams to outer and inner SA air zones. In the outer air zone, there are a set of fixed vanes and a set of adjustable vanes with only a set of adjustable vanes in the inner air zone. The adjustable vanes are operated by a push-pull mechanism. The inner vanes are mainly designed to control the recirculation of hot flue gas while the outer vanes are designed to control depth of penetration and further mixing for char burnout. The combination of proper swirling created by the outer and inner air jets results in a proper high temperature recirculation zone to enhance ignition. With different burner settings, the size, shape and location of recirculation zone can be controlled to meet variations of coal quality as supplied. The airflow measurement device in each burner provides better burner balancing among the burners in a same compartment windbox. This controlled Air Mixing Feature of PAX is unique.

3) Increasing Radiation Heat

Lining refractory on furnace walls to reduce heat absorption and to increase furnace temperature level will provide more radiation heat to support ignition. This also is a very common method. The lining areas of a furnace could be the lower furnace shelf, and partial or whole areas of vertical walls of lower furnace. The lining covered areas are depended on the ignition characteristics of coal as fired and the minimum load required. The furnace wall lining might sometimes increase the slagging potential for some strong slagging tendency coals. This could be limited by a proper burner arrangement eliminating flame impingement to furnace wall, a proper registering combustion air to avoid the reducing environment near furnace wall, and proper selection of furnace volumetrical heat release rate. To do so, the slagging concern will be greatly reduced.

4) Proper Furnace Type

Depending on the coal as fired, conventional wall firing (opposed or corner) generally might be suitable for lean coal firing, while downshot firing with a W-flame shape furnace is favorable to anthracite firing due to its longer residence time. One Japanese boiler works adopts tangential firing with a U-shape flame tilting down to increase resident time for anthracite burning. There is no commercial unit applying this working principle so far. Fig. 4 is the furnace sketch with refractory lining locations of a B&W downshot furnace.

5) Applying More Fine Pulverized Coal

Adopting high fineness reduces the time for pre-heating to promote VM quick and early release and burn. For anthracites, 85%-90% passing 200 mesh is commonly applied.

Steps for Flame Stabilization

This can be achieved by either increasing flame propagation velocity of the coal-air jet or by properly selecting a nozzle velocity.

- 1) Increasing the jet concentration to have a higher flame propagation velocity. B&W experience reveals that the air/coal mass ratio in PA jet should maintain 1.8 or below for semi-anthracite while further lower for anthracite. B&W PAX and other types of low VM burners have a dense feature. Separating an entering coal/air jet being dense and lean jets by mechanical or centrifugal methods is a common step. The finer particle in jet will also help the flame propagation.
- 2) Flame Containing Device. A bluff body type flame-containing device is typically considered. China has a lot of practice in this area. B&W also has similar experiences.
- 3) Properly Select Design Nozzle Velocity. In order to contain the flame and not being blown off, the PA velocity must be reduced to a certain range. Per B&W experience, the nozzle design velocity should be properly limited within 15-16 m/s. If coal is much worse, the velocity might be reduced further to 13-14 m/s.
- 4) Increasing PA temperature entering the furnace and refractory lining on burner zone of furnace walls as well as properly arranging operating pulverizers and burners can also help flame stabilization. With a certain boiler load, keeping a higher load on operating burners (less mills in service) will also help flame stabilization. Corner firing can not easily achieve this. The B&W PAX burner can be operated around its half load with a stable flame.

Steps for Better Burnout

A longer residence time in a furnace for a high carbon conversion can be achieved by a proper furnace configuration (type and height). Enhancing the char oxidation reactivity by a strong turbulence, increasing excess air to improve the oxygen diffusion to char core surface, as well as grinding coal more fine to have higher specific char-oxygen reaction area are the technical steps being considered.

- 1) A longer residence time in furnace. A proper furnace type is mainly selected by the expected boiler performance and fuel. If the fuel as fired is anthracite or semi-anthracite and boiler efficiency is still expected to pass 90%, B&W will recommend adopting a downshift-firing furnace with W-shape flame. If the residence time in furnace is 3 seconds or longer, the unburned carbon loss is expected to be around 2.5%-3.0% firing anthracite. For the lean coal firing, a wall-firing furnace with a sufficient furnace height might be good enough.
- 2) Air staging. A sufficient downshot momentum is a key issue for a longer residence time and a better turbulence at burnout stage for a downshot furnace. B&W adopts the staging airports to admit staging air to the furnace. Others use the holes (openings) through furnace membrane wall as the stage airport. The angle of staging air jet is recommended to be parallel to the furnace hopper slope. The staging air amount is recommended to maintain main combustion zones excess air to close to or slightly greater than the theoretical air. The staging air velocity might be selected close to the velocity of secondary air. Fig.4 shows the arrangement.
- 3) Higher Overall Excess Air. The overall excess air burning semi-or anthracite is suggested to be higher than 25%. The worse the coal quality, the higher overall excess air to apply.
- 4) Proper pulverizing system and combustion system. Any improvement on overall fineness should, in general, help the char burnout. The coarse particles portion is only a very small portion of entire particle size distribution, but it makes a large contribution to overall unburned carbon loss due to its difficulty for burnout. The overall fineness of a ball mill might be better than a medium speed spin mill, especially the portion passing 200 mesh. Users often favor ball mills. However, the coarse portion (passing 50 -70 meshes) of a ball mill is normally larger than a medium speed spin mill. This is easy to be neglected by users.

6. THE NO_x EMISSION CONCERNS BURNING LOW VM COAL [4]

The major pollutants from utility boilers burning fossil fuels are NO_x and SO_x. The environment issue is a global

concern. The De-NO_x regulation in China has just been executed since 1997 (ref. to GB 13233-1996, Chinese Regulation). Only new boilers after 1997 with capacity greater than 1000 t/h steam (300-350 MW) will be mandated to comply. Chinese standard takes one limit for all types of boilers regardless the coal type. The limit is 650 mg/NM³ (0.53lb/MBtu). EPA NO_x limit is 738 mg/NM³ (0.6 lb/MBtu) for most types of boiler and fuels.

NO_x Formation and Its Harmfulness

The combustion of pulverized coal, fuel oil and gas produces nitric oxide (NO), a major pollutant. Pollutants of secondary importance formed between Nitrogen and Oxygen are nitrogen dioxide (NO₂) and nitrous oxide (N₂O). The sum of NO, NO₂ and N₂O are termed as "NO_x". The NO_x causes the photochemical smog and destroys the ozone to pollute the air. NO_x per its formation mechanisms during combustion, could be distinguished as Thermal NO_x, Prompt NO_x, and Fuel NO_x. The molecular nitrogen in combustion air is related to the formation of the thermal NO_x and prompt NO_x; while the elementary nitrogen situated in fuel, mostly existing as organic components, contributes the fuel NO_x. Based on the fuel as fired, the total amount of NO_x formed during combustion might have more or less percentages of thermal NO_x in total NO_x. Cleaner fuels such as natural gas and light oil will produce more percentages of thermal NO_x in total NO_x while pulverized coal with high VM and heavy oil might produce higher fuel NO_x within the total. At a moderate furnace temperature (1700 K), the total NO_x level in the exhaust flue gas for a typical pulverized coal unit varies from 615-1435 mg/NM³ (300-700 ppm @ 6 % O₂) firing bituminous coal.

High NO_x Emission Burning Low VM Coals

The NO_x levels firing low VM coal are much higher compared to firing bituminous, and are as high as 1400-2000 mg/NM³ (700-1000 ppm @6 %O₂). It greatly exceeds the allowable NO_x upper limit of NO_x regulation (650 mg/NM³ or 317 ppm @ 6 % O₂).

7. PROBABLE WAYS OF NO_x REDUCTION BURNING LOW VM COALS [4]

Existing De-NO_x Technologies at Combustion Stage

The low NO_x burner, as the main solution to reducing the NO_x emission, is widely applied firing coal, gas or oil. The working principle of a low NO_x burner is to delay the mixing of air and fuel, and reduce the oxygen availability at the early stage of combustion, as well as create a local fuel rich zone by separation. A 30% NO_x reduction will be expected by low NO_x burners only, compared to the case without NO_x control.

Combustion air staging is suitable for all kind of fuels, and normally applied in combination with low NO_x burners. It splits the combustion air to two or more routes, the majority through burners and minority through staging airports. The working principle is to control oxygen availability under different combustion stages. In combination with low NO_x burners, a 50% NO_x reduction may be expected, compared to no control.

Other low NO_x Combustion Technologies include flue gas recirculating and reburning. The first one is mainly suitable to burn clean fuels by reducing flame peak temperature. The reburning technology stages fuel into the furnace. Sizing the furnace to make a lower burner zone heat release rate reduces thermal NO_x formation by a lower furnace temperature. However, it has a negative impact on ignition of low VM coals.

Applications of Existing Low NO_x Technologies and its Limitations

The available low NO_x combustion technologies were developed based on fuels burned, good quality high VM bituminous, oil or natural gas. Existing low NO_x combustion steps are often contrast to steps for enhancing ignition burning low VM coals. With some improvements, the existing low NO_x combustion technologies might be applied to burn low VM to achieve a lower NO_x.

- 1) Deep air staging. The stoichiometry at the main combustion zone might be further reduced to 0.90-0.95 to form a slightly reducing atmospherical environment. It is favorable to reduce NO_x formation if slaging can be prevented by burner aerodynamics.

- 2) Vent air application. If the coal concentration of vent air can be adjusted to close to the reburning requirement, it might receive some positive effect on NO_x reduction. This is an idea being further developed.
- 3) Properly select the burner zone heat release rate to reduce the thermal NO_x emission.
- 4) Improving burner air register to form local fuel-rich effect to receive NO_x reduction.

8. CONCLUSIONS

The utility industry in China, after a recent slow down, will still remain in a fast growth for a considerably long period due to economic growth and a low per capita of power. Utilizing local low-grade coals is the nation's energy policy. The clean and efficiency burning of low grade coals not only produces the electric power demanded by economic growth, but also reduces emissions. The overall performance of existing downshot firing units is generally good. The ignition is quick, flame is stable and unburned carbon is low and acceptable. As an example, B&W units in China achieved: [1,5]

- 1) The guaranteed 40% MCR minimum load without lighter support burning average 11% VM (received bases) design coals can be easily achieved.
- 2) Demonstrating a great fuel flexibility. The coal quality as burned is often worse (~10% VM) than the design coal (11%VM). In early 1996, 75% Yang Quan Anthracite with 25% Shou Yang lean had been fired for a few months. In 1998, 100 % anthracite was burned. For all of these cases, ignition is fast, and combustion is good.
- 3) Achieved a high boiler efficiency and low unburned carbon loss. The carbon in fly ash of these two units remains at low levels of 6-8%. In 1994, the boiler performance tests indicated that the carbon in fly ash was around 5-6% equivalent 1.80-2.0% unburned carbon loss. With an upgraded burner, register newly designed by B&W, the carbon in fly ash had further reduced down to 4-5% as average and minimum to 3.5%.

The performances of lean coal wall firing units are fair. The minimum load, and the unbalanced FEGT remain to be solved. The combustion technologies firing low VM coals need more research and development to extend applications and to satisfy environment regulations. The following areas, as author opinion, might be considered first:

- 1) Further understanding the fundamentals burning low VM coals. This research might include ignition and flame stabilization as well as kinetics of char reactivity.
- 2) Furnace numerical modeling. This will provide more information on sizing a larger capacity furnace firing low-grade coals, such as downshift firing unit.
- 3) Technical solutions of low NO_x combustion for low-grade coal firing should be developed as early as possible.
- 4) Utility industry will need more large boilers with super critical parameters. Due to the furnace shape of a downshot firing boiler, the super critical once through design for a downshot furnace still has difficulty. The furnace with vertical internal ribbed tube walls (UP) might be an idea for consideration.

REFERENCES

- 1) J. Zhou and G.Xue, "Burning Anthracite and Low Volatile Coals", Proceedings of the 11th CEPSE, Kuala Lumpur, Malaysia (1996).
- 2) J Zhou, "Utilizing Local Fuel Resources with High Efficiency and Clean Environment", WEC Asia Pacific Regional Forum, Beijing China (1997).
- 3) J. Zhou, Int. Electric Power For China, V. 3, pp.40-44 (1997).
- 4) J. Zhou, "Combustion Technologies of Low Grade Coals with High Efficiency and Clean Environment", Proceedings of Int. Symposium on Clean Coal Technology, pp.408-416, Xiamen, China (1997).
- 5) J. Zhou "Burning Anthracite @ B&W Downshot Units & Burner Upgrading", Proceedings of 15th Int. Pittsburgh Coal Conference, Pittsburgh, USA (1998).

9. FIGURES

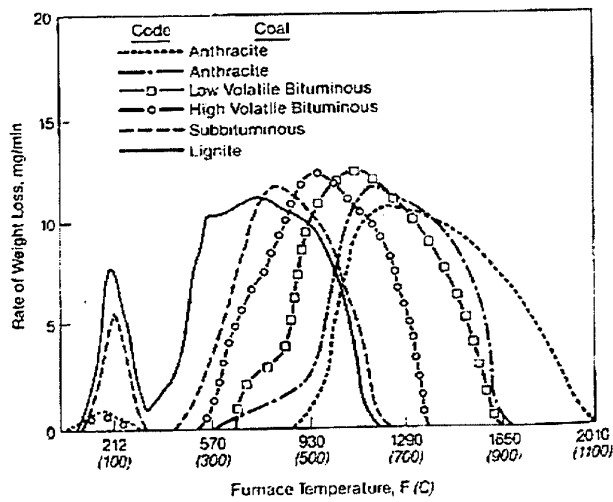


Fig. 1 Burning Profile of Coals @ TGA

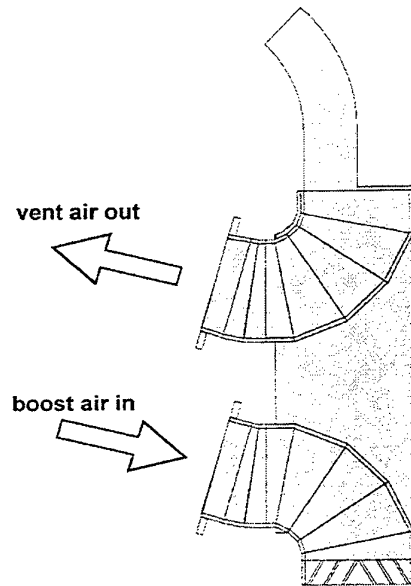


Fig. 2 PA Exchange Device

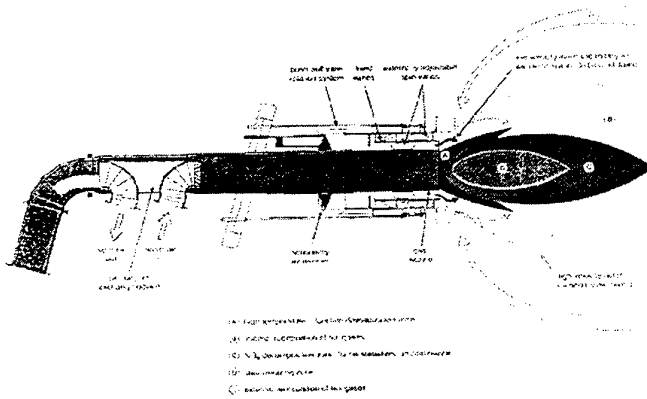


Fig. 3 PAX Burner with XCL Register

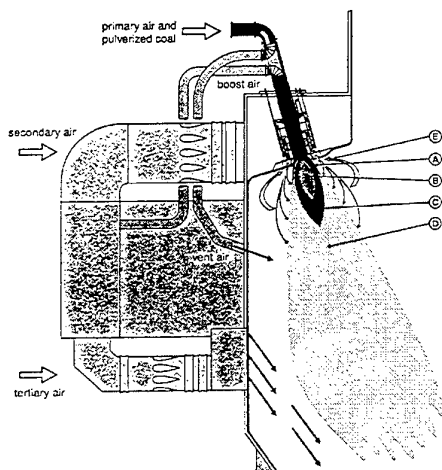


Fig. 4 Downshot Furnace and Refractory Factory

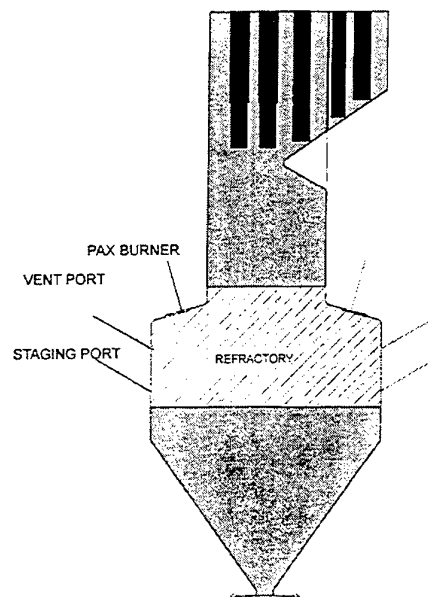


Fig. 5 Arrangement of PAX Burner, Vent Air and Staging Air.

APPLICATION AND RESEARCH OF THE AUTOMATIC ADJUSTABLE PULVERIZED COAL DISTRIBUTOR

Wei Dong Bai, Yong Yun, Zhen Dong Shu, Qing Guang Zheng

The State Engineering Technology Research Center of Combustion of Power Plant

Email: yunyun@hotmail.com; Fax: (086)-024-89347226

Keywords: combustion, low-load stable burning, dense/sparse burner, boiler, distributor

ABSTRACT. With the increasing tasks of load down operation of the power station units in China, the capacity of the boiler's low-load stable burning is more necessary. This paper proposes a new type automatic adjustable pulverized coal distributor (AAPCD) and mainly introduces the stable burning principle of this distributor and its application in the direct-fired system in boilers with fan mills. The dependence of the characters of the automatic adjustable pulverized coal distributor on the air and coal powder flows by means of a lot of commercial tests. The results show: being applied in domestic lignite boiler of 670 t/h, this AAPCD can adjust the distribution of the air and coal powder when the boiler is running; achieve effective control of distribution of them, increasing the capacity of the boiler's low-load stable burning without oil which usually used in China while the boiler works in a low-load condition from 70% down to 45%, so we can lower the load greatly. Because the combustion of the fuel is divided into two parts--over dense combustion and over sparse combustion in boiler, the emission of NO_x is less than 350ppm, the unburned carbon loss is decreased by 1.958%, So it effectively increases the thermal efficiency and improves the capacity of low-load operation.

1. INTRODUCTION

The boiler of the capacity 670t/h mentioned in this paper is a homedesign and homemade single-drum superheat/reheat natural circulation steam generator in super-high pressure, matching 200MW turbine-generator unit. The boiler is Π form layout and closed with membrane wall. There are a front-screen superheater at upper furnace and a back-screen superheater at exit of furnace. The convective superheaters, the reheater's hot section, the reheater's cool section, the economizer and the air heater are arranged in series.

The means of control for regulating superheater steam temperature is spray attemperator using secondary feedwater, for reheater steam temperature, mainly by spraying feedwater. It is a dry bottom boiler with straight flow burners at six corner and tangential firing. High temperature flue gas, hot air and warm air compose the moisture-free medium of the fan mill direct blow system.

Through a long term of operating, it has been found that the exit gas temperature of this type boiler is high, superheater steam temperature and reheater steam temperature is overproof. The amount of the water spray for attemperator is large. Especially when types of coals have a great variation, steam temperatures change largely, spray attemperators are out of work, often resulting in failure of superheater and reheater, severely affect reliability and economy of the generator's operation. On the other hand, with the development of power industry, it's inevitable for the high-capacity and high parameters generators to serve for peakload unit, so it's necessary for large units to have the capacity of low-load burning without oil, but the capacity of this type of boiler is bad, it has generally to use oil to improve combustion situation when the load is below 70%. Thus it not only greatly increasing the cost of electric power generation, but also not conform to the national energy policy. The State Engineering Technology Research Center of Combustion of Power Plant (NPCC) has developed AAPCD and applied it to many power plants. With a number of industrial tests and long-time operations, it shows that the furnace exit gas temperature can be effectively adjusted by this equipment, attemperator spray and possibility of superheater's failure reduced. The load can be lowered to 50% without burning oil.

2. OPERATING PRINCIPLE OF AAPCD

AAPCD is a new type of combustion adjustor. It has two parts: (1) pulverized coal concentrator, which are mounted at the entrance of the primary air duct of every burner. By centrifugal effect of pulverized coal flow through bent pipe, pulverized coal flow can be separated into dense part and sparse part (ratio of dense/sparse is 3.65), then make the absolute concentration of pulverized coal flow no less than 0.47kg/kg (max is 0.88kg/kg). Therefore, it can reduce the ignition heat and formation of nitrogen oxide. The ignition heat of dense phase is

little, so it's easy to be ignited and combusted, The unit's adaptability to various coals is wider, the capacity of variable load is perfect. (2) the main body of AAPCD which is mounted at the exit of separator above fan mill. The parameters like power of generator, speed of coal feeder, pressure of turbine's regulating stage, status of mills and so on, are automatically detected. By means of changing the angles of cascades of distributor, coal flow in the three levels of primary air will be altered. The results are: heat flux along furnace can be adjusted and position of flame core and water circulation can be improved, so we can achieve low-load stable burning without oil.

3. MODIFICATION OF EQUIPMENT

No.3 boiler of a power plant is 670t/h fired with local lignite and fan mills direct-fired system. It has six mills around furnace.

The following are designed parameters:

Rated load: 670t/h
SH steam temperature: 540°C
RH steam exit temperature: 540 °C
Exhaust gas temperature: 167 °C
Furnace exit gas temperature: 1060 °C

SH steam pressure: 13.72Mpa
RH steam exit pressure: 2.5Mpa
Boiler efficiency: 89.7%
Coal consumption: 185.6t/h

After starting up, it was found that furnace exit gas temperature was higher than designed value, causing reheater temperature going up, even failure. The capacity of low-load stable burning is bad. When the load below 70%, oil must be used to aid combustion, this severely affect reliability and economy of the generator's operation.

Considering above situation, NPCC modified the pulverized system: adding AAPCD. In order to obtain wider versatility, the vanes can rotate forward and backward, the zero angle is defined as the vanes parallel to the air flow (normal to ground). Forward rotating vanes will force more pulverized coal to flow to the lower primary air pipes, while backward rotating to upper pipes. So we can adjust furnace exit gas temperature, increase boiler efficiency and achieve low-load stable burning.

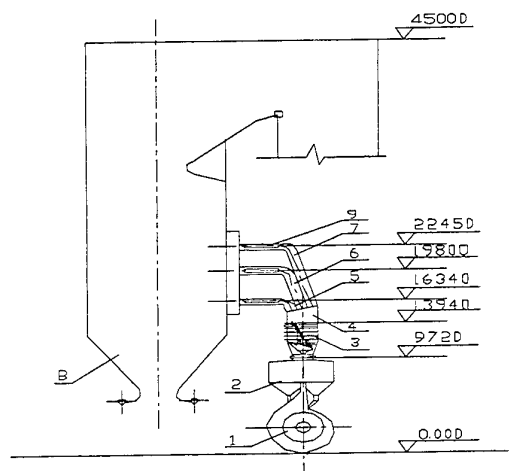


Fig. 1 Schematic drawing of the firing system

- | | |
|---------------------------|---------------------------|
| 1. Fan mill | 2. Mill separator |
| 4. Distributor exit | 5. Lower primary air pipe |
| 7. Upper primary air pipe | 8. Furnace |

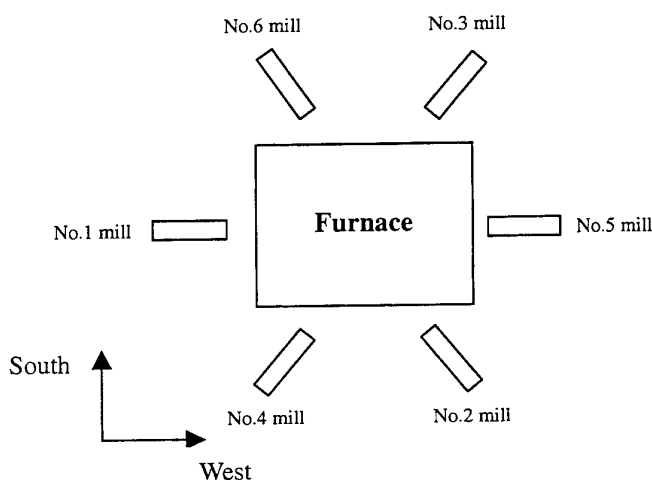


Fig. 2 Arrangement plan of mills

- | |
|--|
| 3. Pulverized Coal distributor |
| 6. Middle primary air pipe |
| 9. Horizontal orifice plate concentrator |

After mounting the equipment, we did some tests about low-load stable burning. The result showed that AAPCD can effectively control the distribution of pulverized coal among upper, middle and lower burners, adjust

pulverized coal flow and its density in burners, and can adjust flame center height continuously. In meantime, because of the concentrating effect of the horizontal orifice plate concentrator, which is mounted at the entrance of primary air pipe, every flow into furnace is divided into two streams. The upper stream is dense, the lower sparse, the ratio of flow rates is 3.65. Therefore, we can achieve dense/sparse burning and stable burning in single burner. Furnace exit gas temperature decreases markedly, attemperators spray of SH and RH decrease greatly, suction pressure of furnace is normal, basically reach the goal.

4. TEST CONDITION

During the test, the fuel was blended coal from local lignite and small coal pits with mass ratio of blending 8:2. Analysis of the blended coal is seen in Table 1. The test was divided into three conditions according to power generation load: 205MW, 140MW and stable limit load without oil. In every condition, measurements began after three hour's stable combustion. In order to get the effect of the distributor of AAPCD on the characters of distribution of air and coal powder, vanes are located at $+15^\circ$, $+7.5^\circ$, 0° , -7.5° and -15° respectively under 205MW condition, then measured the air flow, pulverized coal flow, temperature field in furnace, flue gas concentration etc. The unit was made such a way as sliding pressure operation during low-load test in order to stabilize operation. The rate of load descent was 1.5—3.0MW/min before 140MW for run No.1, No.3, No.5 and No.6 mills, when dropped to limit load, run No.1, No.3 and No.5 mills(see Figure 2), continued to lower load as long as there is no unstable condition occurred in combustion.

Table 1. Coal Analyses

No.		Symbol	Units	Design coal	205MW	140MW	100Mw
1	Low heating value	$Q_{ar.net}$	MJ/kg	13.304	12.27	12.51	12.85
2	Volatile matter(dry)	V_d	%	---	33.35	32.07	30.15
3	Volatile matter, (dry ,ash free)	V_{daf}	%	46.77	47.8	45.94	44.53
4	Moisture (rec)	W_{ar}	%	24	30.4	30.52	27.73
5	Ash(rec)	A_{ar}	%	32.88	21.05	20.97	23.34
6	Ash(dry)	A_d	%	---	30.24	30.19	32.3

5. TEST RESULTS AND DATA ANALYSIS

Low-load test began at 205MW, passed 140 MW, ended 90MW at minimum, stable burning can be maintained at 100MW ultimately. Test data were shown in Table 2

Table 2 Test Data

No.	Variable	Unit	19: 30	22: 00	0: 15
1	Unit power	MW	205	140	100
2	Drum pressure	MPa	14.16	13.7	10.7
3	Main steam pressure	MPa	13.37	13.3	10.4
4	Main steam temperature(east / west)	$^\circ\text{C}$	542/542	540/540	537/537
5	Main steam flow rate	T/h	610	430	332
6	RH steam tem(east / west)	$^\circ\text{C}$	542/540	538/538	533/533
7	RH steam pressure (east / west)	MPa	2.1/2.1	1.5/1.5	1.16/1.16
8	Feed water pressure	MPa	15.6	14.5	11.2
9	Feed water temperature	$^\circ\text{C}$	238	220	205
10	Feed water flow rate	t/h	618	440	311
11	Air inlet temperature	$^\circ\text{C}$	42/42	42/49	47/41
12	Exhaust gas tem(east)	$^\circ\text{C}$	174/172	163/165	154/151
13	Exhaust gas tem(west)	$^\circ\text{C}$	164/173	160/154	147/154

14	Inlet pressure of draft fan (east/west)	Pa	-2610/-2790	-1680/-1540	-1370/-1270
----	---	----	-------------	-------------	-------------

5.1 Distribution Character of Air Flow Rate

Under the condition of 205MW during both the air flow rate and pulverized coal flux being stable, vanes were put in five angles as above in turn, air rate was measured in every angle. In order to eliminate the errors caused by fluctuation of ventilation quantity in the mill, we divided actual measured air flow in each primary air pipe by mill's ventilation quantity, the relationship between air flow rate ratio in upper •middle and lower primary air pipe with the angles was what we need. Fig.3 shows that with the vanes move forward, air flow in upper primary air pipe decreases, lower increases, middle changes a little; with the vanes move backward, upper primary air pipe increases, lower decreases, middle change still a little.

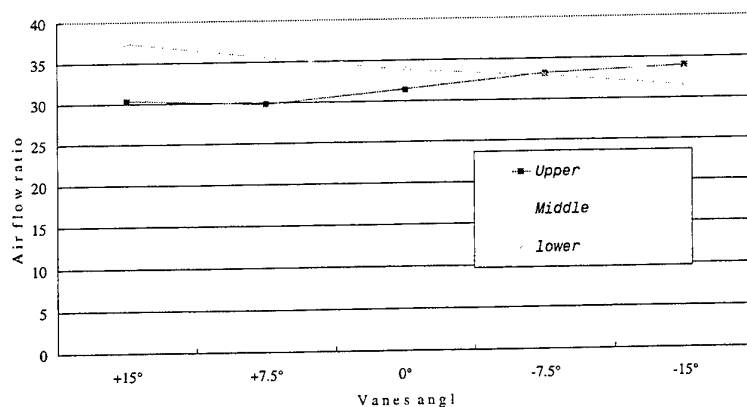


Fig.3 Distribution character of air flow

5.2 Distribution Character of Pulverized Coal Flux

At the same condition as described in 4.1, vanes were put in five angles as above in turn, pulverized coal flux was measured in every angle. In order to eliminate the errors caused by fluctuation of ventilation quantity in the mill, we did the same thing as above, the mass flow fraction in upper, middle and lower of the primary air pipe changed with angles. Fig.4 shows that with the vanes move forward, pulverized coal fraction in upper primary air pipe decrease markedly, lower increase, middle has increasing trend; with the vanes move backward, pulverized coal fraction in upper primary air pipe increases markedly, lower decreases markedly too, middle has decreasing trend.

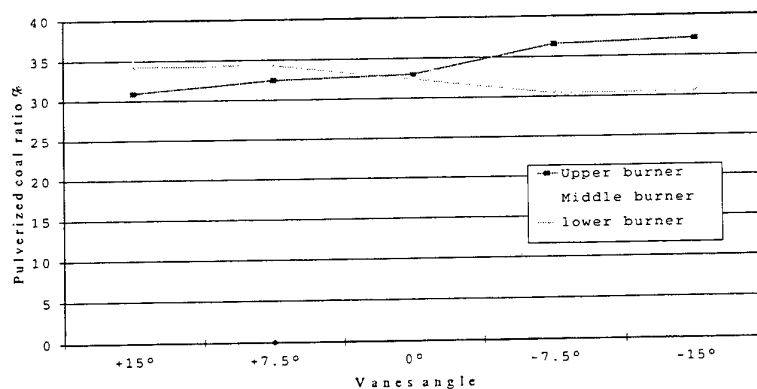


Fig. 4 Distribution character of pulverized coal

5.3 Mass Flow Ratio of Dense / Sparse

At 205MW condition, during the same situation as above and with the vanes in zero angle, pulverized coal mass flows in dense side and sparse side in each primary air pipe were measured, respectively. The result shows: All of the mass ratios of pulverized coal in dense/sparse in each primary air pipe are greater than 2.0, average 3.65, Average absolute concentration in dense side is greater than 0.47kg/kg, max. 0.88kg/kg.

5.4 Change of Gas Temperature in Furnace

Lowered unit load from 205MW(0 degree), passed 140MW(+7.5 degree),to 100Mw(+15 degree) after stable running several hours at each load, we measured temperature field in furnace with radial pyrometer, see Fig.5, Fig.6 and Fig.7.

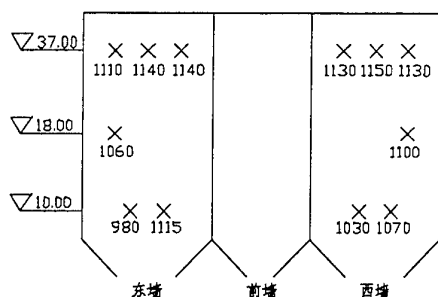


Fig.5 Temperature field in furnace, 205MW

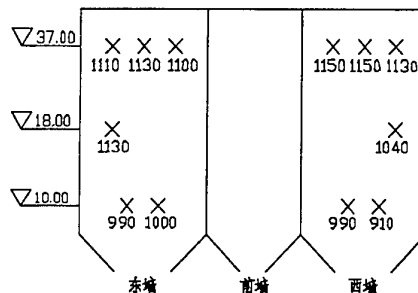
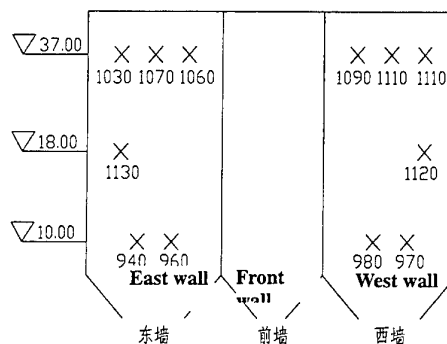


Fig.6 Temperature field in furnace, 140MW

Temperature profiles show us: at 140MW, temperature distribution and temperature level in furnace are better than that of 205MW. The reason is when vanes angle of AAPCD is 0 degree at 205MW, pulverized coal flux in the upper burner is larger than that in the lower, and the upper burners are closer to furnace exit. So coal particles in the upper burner have shorter residence time in furnace. They have left furnace before completing combustion. At 140MW, vanes angle of AAPCD is +7.5 degrees, pulverized coal flux in the upper primary air pipe decreases, lower increases; lower burners are farther from furnace exit, so particles residence time is long. They have much time to complete combustion. Fig.7 Temperature field in furnace, 100MW combustion. This can be confirmed with combustible matter content in fly ash. For the same reason, at 100MW, vanes angle of AAPCD is +15 degrees, pulverized coal flux in the upper primary air pipe continues to decrease, the lower increases more, so flame core drops down, unburned carbon loss gets small. The furnace exit gas temperature drop 10 °C -40 °C, the max temperature drops from 1150 °C to 1130 °C.



5.5 Change of Unburned Carbon Loss

With the load dropping, vanes angle of AAPCD begins to rotate forward, force the coal flow to move to lower burners. As the result, coal particles residence time becomes long, this reduces combustible matter content in fly ash, but with flame core dropping, combustible matter content in furnace slag increases somewhat. The combustible matter content in fly ash is 1.73% at 205MW, 1.6% at 140MW and 1.5% at 100MW. At the same time, the contents in furnace slag are 2.7%, 3.24% and 4.21%, respectively. Accordingly, unburned carbon loss are 1.077, 1.017 and 1.109. At 205MW, unburned carbon loss reduces about 1.956 after mounting the AAPCD. (Shown in Fig.8.)

5.6 Change of Emission

As a part of AAPCD, the concentrators can allow burners to achieve dense/sparse burning, so emission of nitrogen oxide decreases effectively. AT 205MW, exhaust gas temperature is 174 °C, O₂ content is 7.3%, NO_x emission is 330ppm, SO₂ emission is 310ppm, CO is 18ppm; At 140 MW, exhaust gas temperature is 165 °C, O₂ content is 6.2%, NO_x emission is 240ppm, SO₂ emission is 320ppm, CO is 18ppm; At 100 MW, exhaust gas temperature is 154 °C, O₂ content is 8.8%, NO_x emission is 314ppm, SO₂ emission is 287ppm, CO is 7ppm. See

Fig.9.

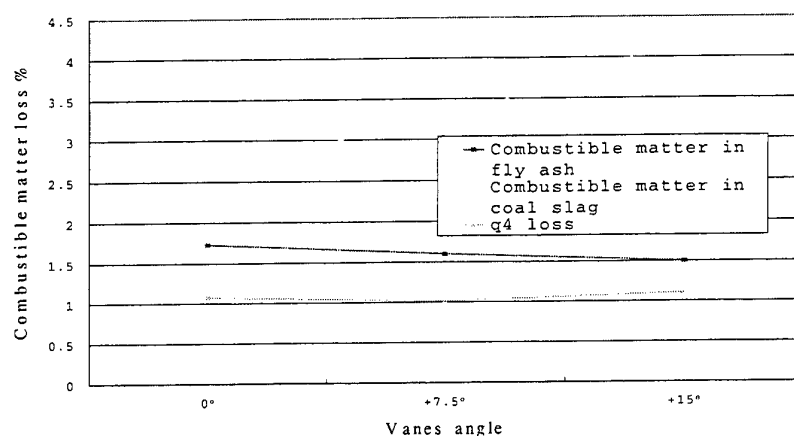


Fig. 8 Change of unburned carbon loss

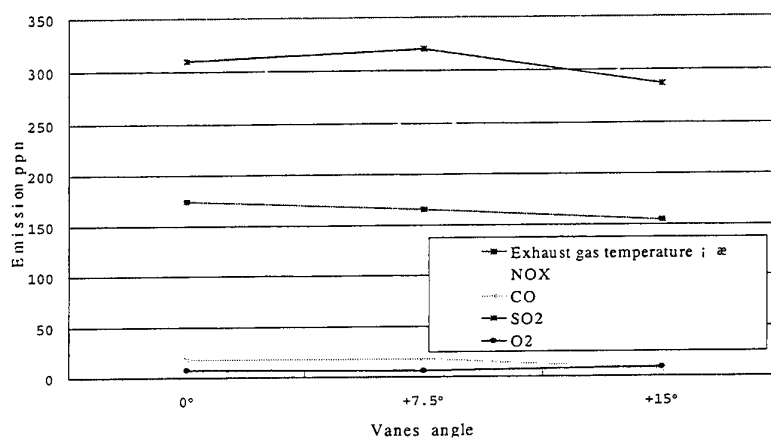


Fig. 9 Change of emission

5.7 Change of Steam Temperature and Attemperators Spray

During low-load test and making the unit sliding pressure operation, the turbine runs stable. There is no shock noise at steam control valve. Unit operation parameters are seen in Table.2, amount of spray water are shown in Table.3.

Table 3 Consumption of Spray Water

No.		unit	205MW(east/west)	140MW(east/west)	100MW(east/west)
1	Primary attemperator	t/h	13/17	9/10	7/6
2	secondary attemperator	t/h	10/8	7/8	5/4
3	Reheating attemperator	t/h	8/8	6/5	0/0

The rates of spraying amount of this three attemperators are: 12t/h, 7t/h and 11.8t/h. The amount decreased markedly after installation of AAPCD. But there are some differences in amounts between primary attemperator and secondary attemperator, the reason is that eddy of flue gas at furnace exit has not been avoided in tangential firing system.

CONCLUSION

Industrial tests and running practice proved that AAPCD can effectively adjust pulverized coal flow along height of the furnace, change flame core level, adjust gas temperature of the furnace exit, reduce attemperator water spray and superheater failure opportunity.

AAPCD can realize coal dense/sparse burning (Mass ratio of coal dense/sparse is 3.65) and bring coal ignition time forward. Unburned carbon loss is reduced, so boiler's efficiency will be improved, low-load stable ignition and burning can be realized and ensured.

After mounting the AAPCD equipment, boiler can burn stable without oil at 100MW condition, the capacity of variable load increases markedly, saving a lot of oil, emission of nitrogen oxide is smaller than 350ppm, it's good to improve atmosphere environment.

AAPCD can adjust vanes angle automatically according to mills' condition • exit gas temperature from furnace • generator power and so on, it's can be remote controlled and manual controlled.

REFERENCE:

1. W. Bai. Cold mold test about pulverized coal concentrator of fan mill direct-fired system at Tongliao power plant, Proceedings of the 3rd northeast modern boiler technical conference, 1996, Shenyang, Liaoning S & T Press (In Chinese), pp.52 - 59
2. Y. Hu, New type burner, Xian Jiaotong University Press(In Chinese).1993

STUDY ON ASH DEPOSITION CHARACTERISTICS OF DIFFERENT TYPES OF COALS

Miki Shimogori

Thermal Power Research Department
Babcock-Hitachi K.K.Kure Research Laboratory
Email: shimogori-m@krl.bhk.co.jp; Fax: 81-(823)-22-9504

Noriyuki Ooyatsu

Thermal Power Research Department
Babcock-Hitachi K.K.Kure Research Laboratory

Noboru Takarayama

Thermal Power Research Department
Babcock-Hitachi K.K.Kure Research Laboratory

Akira Baba

Thermal Power Research Department
Babcock-Hitachi K.K.Kure Research Laboratory

Keywords: pulverized-coal combustion, ash deposition, heat flux

ABSTRACT. Understanding ash-deposition mechanism and factors decreasing heat flux through a heat-transfer surface is useful for operating pulverized coal-fired boilers efficiently and reliably. We studied ash-deposition process through a monitoring test using a portable device, and confirmed that it generally consists of three main stages: formation of a powdery ash layer, particle impact and sticking, and deposit growth. We also studied an effect of ash deposition on heat-flux decrease for three types of coals through up to about 100-hour combustion tests in a large-scale test furnace. Powdery ash layers, formed during the tests for two of the coals, decreased the heat-flux dramatically. Our analysis of the ash samples showed that for one of the coals, a large amount of Na and K vapor condensed on the surface of the layers, and for the other coal, the layers contained a high percentage of fine ash particles under 10 μ m.

1. INTRODUCTION

Using low-rank coals, while enabling economic operation of pulverized-coal power plants, can cause excess ash deposition within a boiler, reducing boiler efficiency and possibly causing tube rupturing and falling deposits that might damage the hopper. Our goal is to develop a model for predicting ash-deposition characteristics; this model shows the decrease in heat flux caused by ash deposition on the surfaces of water walls - heat-transfer tubes - used in coal-fired boilers. During the past decade, considerable advances have been made in developing models to predict ash behavior [1 - 3] involving empirically obtained slagging and fouling indices based on ash components. However, many years' experience of burning many kinds of coal in practical boilers has shown that coals reducing boiler efficiency severely are not limited to low-quality coal that components can form large ash deposits. We have investigated the ash-deposition mechanism with a portable device that allows us to observe the deposition during the burning of various grades of coal. We clarified the factors that reduce boiler efficiency.

2. EXPERIMENTAL

We did two kinds of tests in a same furnace. The one is to study ash deposition mechanism with a portable device for monitoring ash deposition, the other is to study the effect of ash deposition on heat flux.

Portable Device for Monitoring Ash Deposition

We have developed a portable device (Fig. 1) for monitoring ash deposition process. This device enables us to study the deposition mechanism by watching each step of ash deposit formation through windows in the test section. Our device consists of the (1) induced-gas section, (2) test section, (3) air-cooled probe, (4) gas-cooling section (water spray, water tank, and pump), and (5) induced-draft fan. We attached this device to a port in the

side of the furnace and drew hot gas into the test section using the induced draft fan. After passing through this section, the hot gas was cooled by the water spray in the gas cooling section, then returned to the furnace through the another port. To collect deposited ash, air-cooled probe— a 60-mm-long stainless-steel tube with a 45mm-diameter—was set in the test section perpendicular to the gas flow. The thermocouple sensor was positioned in a recess cut into the probe wall to fastened to a metal surface from the inside of the probe to monitor a metal temperature controlled by adjustment of air flow rate. The gas temperature at the test-section inlet, upstream from the probe, depends on the gas velocity and the position where the device was set. Gas and particles approached the probe at a velocity 3 to 10 m/s. The gas temperature was 850 to 1200°C, and the temperature near the probe's outer surface was 450 to 650°C.

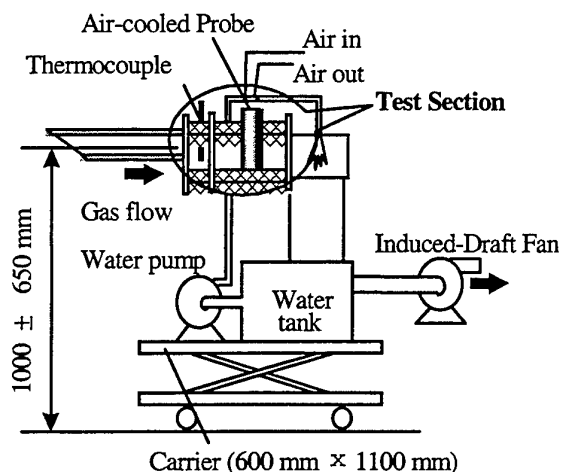


Fig. 1 Portable device for monitoring ash deposition

Large-Scale Test Furnace Used to Study the Effect of Ash Deposition on Heat Flux

We use vertical large-scale test furnace to investigate the decreases in heat flux caused by ash deposition on a water-cooled probe inside the furnace. The deposition behaviors of three types of coals were studied. The furnace size was 6m in height and its heat input was 2 MW (Fig. 2).

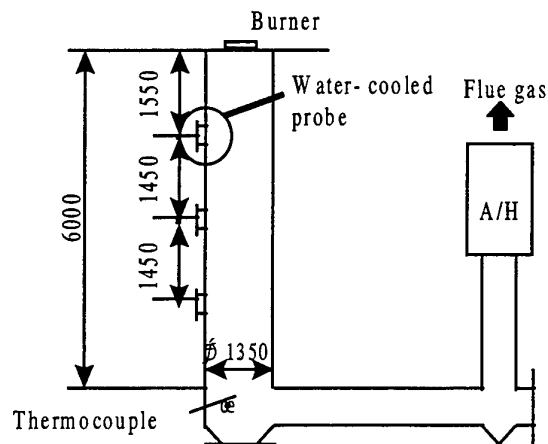


Fig. 2 Large-scale test furnace

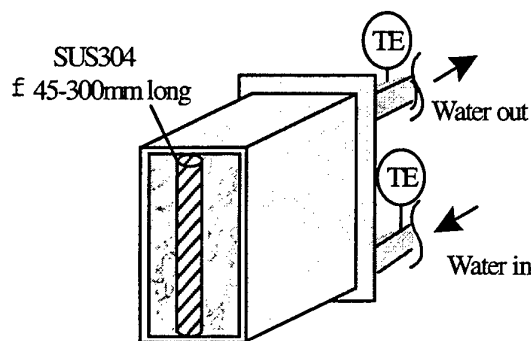


Fig. 3 Water-cooled probe

The water-cooled probe (Fig. 3)—a 300-mm-long stainless steel tube with 45-mm diameter—held in a housing that extended from the side of the furnace 1.5 m below the top inner surface. The probe was vertically aligned with the gas flow. We used the same probe for the three tests. Before the next test, we removed the ash sample completely and cleaned the probe surface.

We measured the furnace-exit gas temperature with a thermocouple inserted from the side of the furnace 1.5m from the furnace's bottom inner surface. The tests were conducted in a large-scale test furnace and lasted about 100 hours. Experimental conditions are given in Table1.

Properties of tested coals are listed in Table 2-1 and Table 2-2. Coal A was a typical sub-bituminous coal that contained only 1.7% ash. Coals P and W were bituminous coals.

Table 1. Experimental Conditions

Heat input	2 MW
Burner stoichiometry	0.9
O ₂ concentration at the furnace exit	3.5%
Furnace-exit gas temperature	1200°C
Coal fineness	75% of the coal particles were smaller than 75µm

Table 2-1. Coal Characteristics

	Heat Value (kcal/kg)	Ash (%)	Volatile matter (%)	Fixed carbon (%)	C (%)	H (%)	O (%)	N (%)	S (%)
Coal A	6240	1.7	46.9	52.4	72.7	5.5	18.9	1.1	0.2
Coal P	7220	5.2	43.6	51.0	75.6	5.2	11.3	1.7	0.7
Coal W	6770	11.1	43.5	45.4	70.2	5.5	11.2	1.3	0.7

Table 2-2. Inorganic Analysis of Coals

	SiO ₂ (%)	Al ₂ O ₃ (%)	Fe ₂ O ₃ (%)	CaO (%)	TiO ₂ (%)	MgO (%)	SO ₃ (%)	Na ₂ O (%)	K ₂ O (%)
Coal A	42.3	21.2	13.6	8.4	0.8	2.4	7.8	0.7	1.3
Coal P	52.3	24.0	11.5	2.1	1.0	2.6	1.6	1.3	2.2
Coal W	51.7	32.3	5.2	2.8	2.5	0.7	1.9	0.5	0.4

3. RESULTS

Monitoring the Process of Ash Deposition

We monitored the process of ash deposition of coal X which was a typical sub-bituminous coal (fuel ratio 1.7, ash content 7%) from Indonesia. The form of ash deposit on the heat-transfer surface of the metal probe changed remarkably over 2 hours. As soon as the induced-draft fan was turned on at the start of the test, hot gas drawn from the furnace lighted the inside of the test section, and the probe surface became white because of a powdery ash layer. After the first 10 to 20 minutes of the test, a portion of the layer was deformed. Then, not only sticky particles but also dry particles were captured on the layer and deposit grew. Once the layer covered the probe surface, the ash-surface temperature increased. As thickness and temperature increased further, the fraction of incoming particles that remains sticky on the surface also increased, accelerating deposit growth. When ash-surface temperature exceeds ash-melting temperature, deposit surface changes to slag. However, in this case it did not. After the 2-hour test, pourous deposit, which we call pourous clinker, was formed with a thickness of 4 cm on the probe surface. Ash was deposited in three main stages: formation of a powdery ash layer, particle impact and sticking, and deposit growth. We analyzed chemical components of porous clinker for each part: the powdery layer near the probe surface, the middle part, and the surface of the porous clinker itself. The analysis showed that the powdery layer included high percentages of Na and K compared with other parts of the clinker.

Decrease in Heat Flux for Different Types of Coals

We calculated heat flux through the water-cooled probe from the inlet and the outlet temperatures of the cooling water. Although the inlet temperature was kept stable, the outlet temperature decreased with the increase of ash deposition, then became stable. We found different ash samples on the probe surface after each test. The porous clinker layer covered the surface only after the test of coal W. The white powdery layer covered the surface with a thickness of 2-3mm after the test of Coal A. A flesh-colored layer, on which several black molten particles adhered, covered the surface after the test of Coal P. Heat flux values through the probe were $3.5\text{--}4.5 \times 10^5$ kcal/m²h at the beginning of the tests, and decreased to about 1.5×10^5 kcal/m²h, then became stable for the cases of Coals A and W (Fig. 4). The heat-flux values before and after the decrease, which were $3.5\text{--}4.0 \times 10^5$ and 1.5×10^5 kcal/m²h in our test, seemed to depend on experiments: furnace sizes, test conditions, and so on.

The point we have to make clear is the effect of coal types on heat-flux decrease during combustion. We tested Coal P only for 4 hours, because it was enough to see the behavior of heat-flux decrease as a line. On the other hand, in the case of Coals A and W, about 40 to 60-hours tests were necessary to study them. The slope of heat-flux decrease was remarkable in the case of Coal P. Coal A contained only 1.7% ash, which is about 1/10 that of Coal W (11.1% ash), however, the slopes of Coals A and W were almost the same. In the case of Coal A, heat-flux values scattered because of the particles which adhered to the probe surface and are removed at the first stage of the test.

To investigate the factors causing the heat-flux drop, we analyzed three ash samples from Coals A, P and W (Fig. 5). The chemical analysis showed that the ash sample of Coal A contained higher percentage of Na and K (Na 1.9%, K 1.8%) than the coal before burning (Na 0.7%, K 1.3%). The amount of contained Na and K in coal depends on each coal type. Fig. 5 shows the ratios of the amount of Na and K in ash samples to those in the coals before burning. In case of Coal A, the ratios for Na and K were 2.7 and 1.4. In the cases of Coals P and W, both ratios were lower than 1. We also measured particle-size distribution of ash samples. Percentages of ash particles smaller than $10\mu\text{m}$ were 27%, 45% and 5% for Coals A, P and W, respectively.

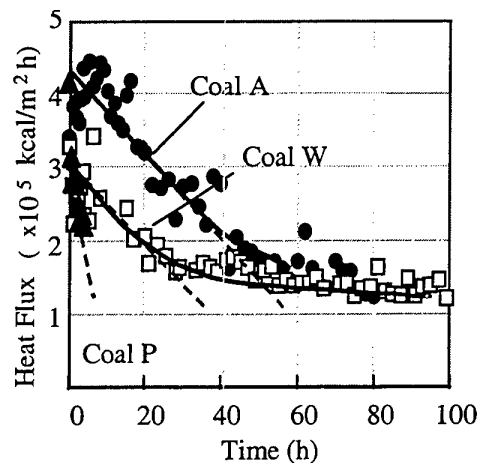


Fig. 4 Heat-flux decrease of three types of coals

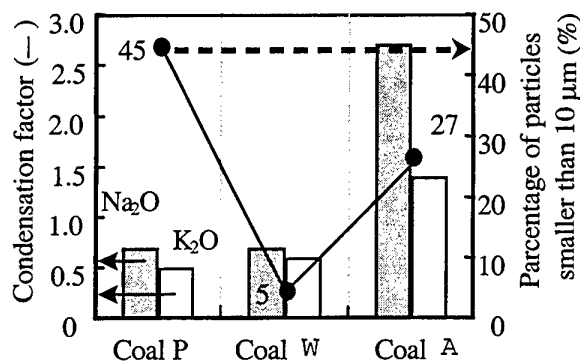


Fig. 5 Analysis of ash samples

4. DISCUSSION

Ash-Deposition Mechanism

We believe the ash-deposition follows the mechanism shown in Fig. 6. Various components that evaporated during combustion may have condensed either on a cool heat-transfer surface, or on entrained particles. This effect is called fick diffusion. Condensed vapors—most likely Na and K—may have made the heat-transfer surface and surfaces of entrained particles sticky. Similarly, steep temperature gradients in the gases close to the heat-transfer surfaces are the main cause of particle capture. This effect, called thermophoresis, is significant when the temperature of the heat-transfer surface is roughly 1000°C or higher [1].

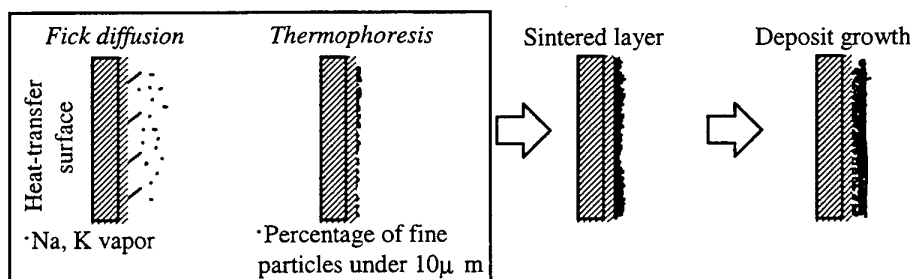


Fig. 6 Ash deposition mechanism

We observed during our monitoring experiment that as soon as the hot gas was drawn to the test section, the powdery ash layer covered the probe surface. In this case, both fick diffusion and thermophoresis seemed to occur. After 10 to 20 minutes, a portion of the ash-surface was deformed. The behavior of both the ash surface on the probe and the impacting particles suggested that they were sticky, so we think both fick diffusion and thermophoresis accelerated ash deposition. The deposition process depended largely on the formation of the powdery ash layer in the first stage of the test. Once the layer was formed on the heat-transfer surface, it

hindered heat transfer through the probe surface, causing the ash-surface temperature to rise close to the gas temperature. When the ash-surface temperature in the test section was higher than the ash-deformation temperature, the ash-surface became sticky. Thus, formation of the powdery layer on the heat-transfer surface during the first stage accelerated the ash deposition.

Effect of Ash Deposition on Heat Flux for Three Types of Coals

We expected the porous clinker layer that formed when we burned Coal W to decrease heat flux remarkably as the deposition thickness increased. However, our results did not show this. We calculated initial rates—slopes—for each coal from the lines of heat-flux decrease. The ash contents were 1.7%, 5.4%, and 11.1% for Coals A, P, and W, respectively. To evaluate the effect of ash deposition on heat flux for each coal, we ignored the effect of ash content by using divided initial rates by the percentage ash content. The ratio of three divided rates was 10:5:1 for Coals A, P and W. This result means that such a powdery ash layer on heat transfer surface as we found for Coal A and Coal P has a significant effect on heat flux.

The next question is what was the origin of the decreased heat flux. The powdery ash layer that directly caused the heat-flux drop was mainly due to fick diffusion—condensation of Na and K vapors—and thermophoresis. Because Na and K in coal easily evaporate during combustion, the effect of fick diffusion becomes stronger in coals with high Na and K contents. The Na and K contents in ash samples of Coal A were 2.7 and 1.4 times the corresponding contents in the coal before burning. This means that Na and K vapors were condensed on the probe surface or entrained and/or deposited particles, and that ash deposition of Coal A was caused mainly through fick diffusion. In the case of Coal P, Na and K vapor did not seem to condense, but the percentage of fine particles under 10 μ m in the ash sample was high (45%). This means that ash deposition of Coal P accelerated mainly through thermophoresis.

5. CONCLUSIONS

We studied the ash-deposition mechanism with a portable device used to monitor the deposition process. Ash was deposited in three main stages: formation of a powdery ash layer, particle impact and sticking, and deposit growth. We found that the powdery layer, which appears to be mainly formed through fick diffusion and thermophoresis, is the key to controlling the deposition process. To study the effect of ash deposition on the heat-flux, we tested three types of coals with different ash contents—Coals A, P, and W—in a large-scale test furnace. We found two main types of ash samples—powdery ash and porous clinkers—on the water-cooled probe after the tests. A porous clinker layer was formed only when Coal W was burned. We divided the initial rates (the changes in heat flux at the beginning of combustion before the rates saturated) for the heat-flux decrease by the percentage ash content for each type of coal. This eliminated the effect of the ash content on the heat flux. The ratio of these calculated values was 10: 5: 1 for Coals A, P, and W. In other words, Coals A and P, which produced a powdery ash layer, caused a greater decrease in the heat flux than Coal W, which produced a porous clinker layer. The three types of coals also differed in their Na and K content. Our analysis showed that Na and K were condensed in the ash layer from Coal A, and that the layer from Coal P contained a high percentage (about 45%) of fine ash particles smaller than 10 μ m. Ash deposition was accelerated by the large amount of Na and K evaporated then condensed in the ash layers during combustion of Coal A, and by the high percentage of fine particles produced during combustion of Coal P. However, the precise impact of these two factors on the formation of the powdery ash layer is not clear, nor are the relative roles of fick diffusion and thermophoresis in the formation. We are now developing statistical models to clarify these points.

REFERENCES

1. Gordon Couch, *Understanding slagging and fouling in pf combustion*, IEA Coal Research, London (1994).
2. T.F Wall and S.P. Bhattacharya, *Prog. Energy Combust. Sci.* Vol 19, pp.487-504, Pergamon Press, Oxford (1993).
3. L.Y. Huang and J.S. Norman, *Fuel*, Vol.75, pp.271-279, Elsevier Press, Oxford (1996).

ADVANCED TECHNOLOGY ON COAL-FIRED POWER GENERATION SYSTEMS

Akinori TAGISHI and Shozo NAKAMURA

Thermal Power Division, Hitachi, Ltd.

E-mail: a_tagishi@cm.power.hitachi.co.jp fax: 81-294-23-6784

Keywords: coal, power generation, USC, PFBC, IGCC

ABSTRACT. From a viewpoint of location of power stations, much is expected to thermal power generation systems. At present LNG (liquefied natural gas) is less expensive than coal, hence utilization of coal is not necessarily advantageous. However, diversifying usable fuels is necessary from a viewpoint of energy risk. Consequently, coal is expected to play a major part in the near future.

This coal-fired power generation will be supported by the following three key technologies:

- (1) Pulverized coal-fired power generation with USC (Ultra-Super Critical) steam plants which will continue to be developed as the main coal application technology for 20 or more years.
- (2) PFBC (Pressurized Fluidized Bed Combustion) power generation emphasizing both sulfur removal from the furnace and improved efficiency.
- (3) IGCC (Integrated coal Gasification Combined Cycle) power generation for clean coal usage with higher efficiency.

Hitachi intends to continue work in these areas in the future. Hitachi will strive to realize, as early as possible, practical applications of the advanced technologies on coal-fired power generation systems.

1. INTRODUCTION

Coal-fired power generation is aimed specifically towards the effective utilization of coal which is an abundant source worldwide by improving the existing technology. The advanced technologies on coal-fired thermal power generation which are able to develop coal utilization with high efficiency and low-environmental-load will be applicable to needs both to reach legally binding long-term CO₂ emission reduction target at the third Session of the Conference of the parties to the United Nations Framework Convention on Climate Change (COP-3) held in Kyoto December, 1997 and COP-4 held in Buenos Aires November, 1998.

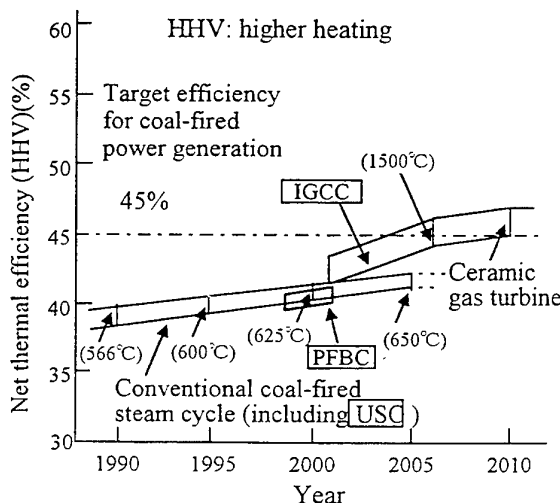


Fig. 1 Prospects for the improvement of the efficiency of coal-fired power generation

The research and development for various types of advanced coal-fired thermal power generation systems are

being conducted and these systems are expected to be put into practical use in the near future as shown in Fig. 1. In order to improve the efficiency of coal-fired thermal power generation systems, Hitachi is promoting both the research and development and the verification of its main equipment for advanced coal-fired thermal power generation as shown below:

- (1) The development of 12Cr steel for attaining steam temperatures of 630~650°C in the USC (Ultra-Super Critical) steam condition power plant.
- (2) The verification of the equipment for the 250MW commercial PFBC (Pressurized Fluidized Bed Combustion) combined cycle plant using of 4MWth test facility and mock-up model.
- (3) The research and development on the IGCC (Integrated coal Gasification Combined Cycle) which is regarded as the most promising thermal power generation systems.

2. ADVANCED COAL-FIRED THERMAL POWER GENERATION

The technologies on advanced coal-fired thermal power plant (USC, PFBC and IGCC) will contribute to improve thermal efficiency and to decrease CO₂ emission to environment. It is expected that USC, PFBC and IGCC will realize high thermal efficiency in this order and be put into practical use in the reverse order. The USC is based on PCF (Pulverized Coal Furnace) technology experience. The PFBC is now under construction for commercial plant. The IGCC is now in the stage of designing demonstration plant.

2.1 USC Power Plant

In the 1950s, USC (Ultra-Super Critical) technology was tested at the No.6 unit of the Phiilo Power Plant and the No.1 unit of the Eddystone Power Plant in the U.S. The specifications of the No.6 unit were 31.0 MPa-621/566/538°C, 125MW, while for the No.1 unit these were 34.5 MPa-649/566/566°C, 325MW. Although austenitic alloys were used in the high-temperature sections of these turbines, difficult operation was experienced due to structural difficulties caused by the large thermal expansion coefficient. The higher steam conditions temporarily declined and then the supercritical steam condition of 24.1MPa-538/538°C or 538/566°C has been adopted as the standard since benefits due to high capacity of concurrent thermal power plants were able to maintain their economic feasibility.

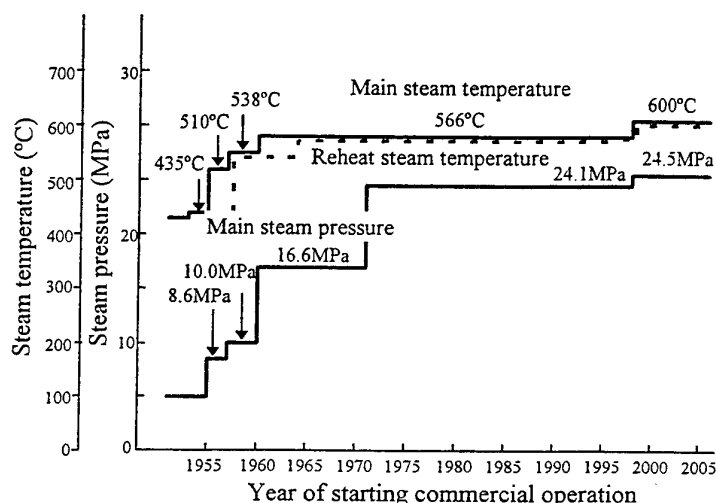


Fig. 2 Advances in turbine steam conditions

However, in a recent attempt to develop environmentally friendly power plants, efforts are again being made toward higher temperature steam conditions. The key technology is development of heat resistant ferritic steels. The new 12Cr steel is being developed as a high pressure rotor material for main steam and reheat steam. New materials are also being developed for the rotating blades. In addition to the conventional CrV casting steel with B, 9Cr cast and forging steel are also being developed for casing materials. By the use of these new materials, the steam conditions of the 1000-MW turbines at the Unit No.2 of Tohoku Electric Power Co., Inc. in

Haramachi which is currently in operation July, 1998 have been improved to 24.5 MPa-600/600°C as shown in Fig. 2.

Furthermore, a joint project between the Electric Power Development Co., Ltd. (EPDC) and the plant constructors backed by government financial assistance, is currently being made progress to assess the capability of a future USC plant with steam conditions of 30 MPa/630~650°C. The most important issue in this project is the evaluation of new 12Cr steels for application in the future USC plants [1].

The rotor shaft is the most important component in a turbine. Hitachi has developed the following rotor shaft, material HR1100 (10.5Cr-1.2Mo-W-V-Nb), for use in the 1000-MW-class commercial power plants. Furthermore, addition of Co and B as well as an increase in the W content results in a new rotor shaft material HR1200 (11Cr-W-Co-Mo-V-Nb-B), which shows a remarkably higher strength in creep examinations. The structural deterioration of the rotor shaft by creep can be controlled by decreasing the content of C. However, segregation during solidification in large ingots should be carefully controlled because HR1200 contains W, Mo, and B. The homogeneous structure of HR1200 is obtained by adopting the electro-slag remelting (ESR) process for the steel making process. Crack formation during upsetting is another problem in the process because the addition of Co and B causes an extreme hardening of the rotor shaft which results in deformation at elevated temperatures. The control of proper heating and forging enables to manufacture sound rotor shafts. Fig. 3 shows a comparison of the creep-rupture strengths for HR1100 and HR1200 as a function of temperature. The applicable temperatures of 600°C and 650°C are estimated to be the stress level of 100MPa for the creep-rupture strength after an exposure time of 100,000 hours for HR1100 and HR1200 respectively. It can be concluded that HR1200 is applicable for steam temperatures, between 630 and 650°C [2].

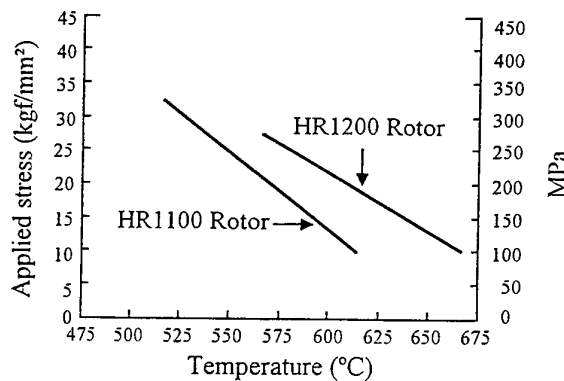


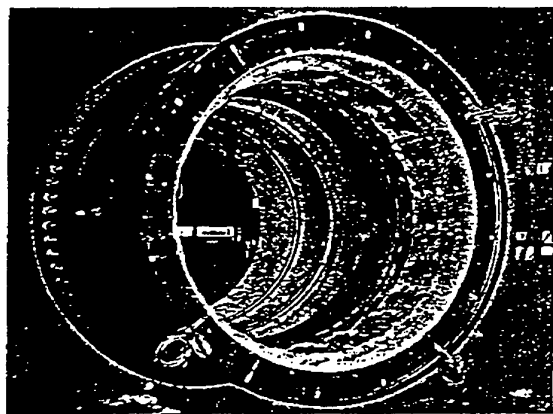
Fig. 3 Comparison of the applicable temperatures for HR1100 and HR1200 rotor shafts, in terms of creep-rupture strength

2.2 PFBC Power Generation

A system diagram of the 250-MW Osaki PFBC plant owned by the Chugoku Electric Power Co., Inc., for operation in 1999 is shown in Fig. 4. The Osaki PFBC plant has a combined cycle arrangement with a gas turbine and a steam turbine, producing an output of approximately 15% and 85% of the total electricity respectively. It also contains a pressurized fluidized-bed combustion boiler which generates steam to drive the steam turbine, where the gas from the boiler is directed to a gas turbine through a two-stage multi-cyclone. A limestone added to the bed materials contributes to reduce sulfur emissions during combustion. The boiler consists of two vessels containing two furnaces and the gas turbine which is a single shaft F7EA-P (Updated version of the GE Type F7EA). The reliability of the main component for the Osaki PFBC plant was verified by several models and newly developed analysis methods.

The basic fluidized specific properties of the furnace was evaluated on the basis of a 1/5 scaled model experiment. The fluctuating load on the in-bed tubes was evaluated by an actual-sized model. It was confirmed that the fuel dispersion is good enough for better combustion performance in the actual furnace.

Fig. 4 Main flow chart for the Osaki PFBC plant



1718

confirmed by an actual-sized model test using actual PFBC boiler ash. The cyclone for the Osaki PFBC plant is a two-stage system with twelve multi-cyclones. The efficiency of the multi-cyclones was verified in a 1/5 scaled model test by comparing its result to the efficiency of a single cyclone.

The internally heat-insulated single-wall pipings, of 2540mm diameter applicable to a high-temperature environment was adopted. The multi-cyclones located outside the pressure vessel requires more space for the high-temperature gas pipings. Several actual high-temperature gas piping models verified their reliability and non-existence of undesirable hot spots. An example of their models is shown in Fig.5.

2.3 IGCC Power Generation

In IGCC power generation, a syngas consisting mainly of carbon monoxide is refined and used as the fuel for a gas turbine for combined power generation. The characteristics of the individual system components are as follows.

In coal gasification, either air or oxygen can be used as the oxidizing agent, although the development of systems using oxygen is now advancing faster. Since syngas contains dust and impurities which are harmful to the downstream equipment, it needs to be refined. This is also important from the viewpoint of controlling environmental pollution. As a means to refine syngas, attempts have been made to develop a hot-gas refining technology. Since this technology has not yet been completed, it is feasible to use the wet-type gas refining process which is already employed in chemical plants.

In the wet-type gas refining process, dust is first removed and then the syngas is washed for desulfurization. From the viewpoint of minimizing the heat loss in wet-type gas refining, an oxidizing system using oxygen is more advantageous than an oxidizing system using air because it allows for the reduction of the syngas flow rate.

The lower part of the gasifier is held at a high temperature for the molten slag to fall to the bottom. The upper part of the gasifier is cooled by recycled gas to lower the syngas temperature, in order to prevent the char from sticking to the wall, heat exchanger, or other internal components. Hitachi has developed an ingenious system to further reduce the flow rate of recycled gas. In this system, the oxidizing agent is supplied in two stages, the lower stage for melting slag and the upper stage for gasifying coal and lowering the gas temperature as shown in Fig. 6. Since the calorific value of syngas is relatively low (about 10,460 kJ/Nm³), the gas turbine requires bleeding to maintain a proper balance of flow rate. In the air separation unit, the high-pressure bleed air is separated into oxygen and nitrogen. The oxygen is fed into the gasifier, and the nitrogen into the turbine, where the nitrogen is also effective for reducing the emissions of NO_x. Thus, an integrated system is effective for improving the efficiency of IGCC power generation.

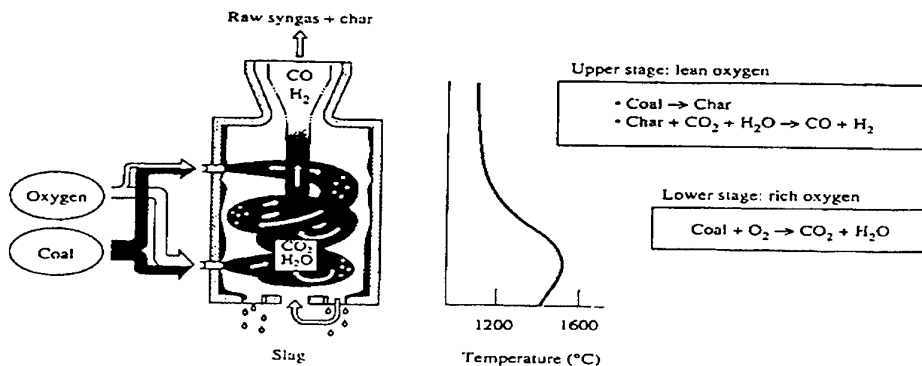


Fig 6 Concept of a single-chamber, two-stage gasifier

At Hitachi, the serious development of a coal gasifier began with the testing of the HYCOL (Hydrogen-from-

Coal Process Development) gasifier (coal feed rate: 50 t/d) at Sodegaura from 1988 through 1993. The gasifier was operated continuously for 1000 hours on a stable basis, demonstrating the reliability of the oxygen-oxidizing system [3]. With respect to the gas turbine, the operating tests of a 12.5-MW unit installed at the Nakoso pilot plant were studied from 1985 through 1995. Stable combustion with a fuel of low calorific value and stable operation combined with bleed air (a closed system in which gas turbine bleed air is fed into the gasifier and the fuel generated in the gasifier is returned to the gas turbine) were demonstrated [4].

Hitachi is now designing and constructing the EAGLE plant which is coal-gasification pilot plant for fuel cells and has an upgraded version of the HYCOL gasifier (coal feed rate: 150 t/d) as shown in Fig 7. It will be commissioned in 2000 under the direction of EPDC. For commercialization of large-scale IGCC, plant integration technology and plant reliability shall be improved and established by promoting demonstration plant project furthermore.

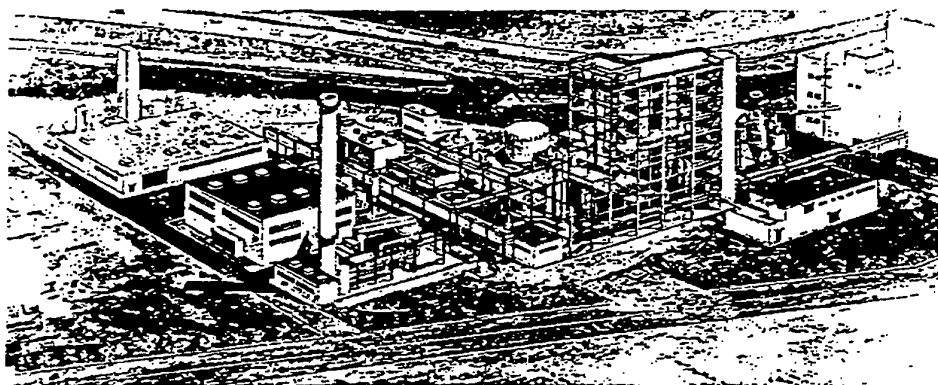


Fig. 7 Conceptual diagram of the EAGLE plant
(Coal-gasification pilot plant for fuel cell)

3. SUMMARY AND CONCLUSIONS

Various technologies developed for coal-fired thermal power generation have been described. On the one hand the demand for electrical power is ever increasing whilst on the other, there is a growing demand for power generation systems which are environmentally friendly. From the viewpoint of the location of power stations, much is expected to thermal power generation systems. Since LNG is less costly than coal at present the utilization of coal is not necessarily advantageous. However, diversifying usable fuels is necessary from the point of view of preventing energy risk. Consequently coal is expected to play a major part in the near future. The development of advanced coal-fired power generation technology will be made more progress:

- (1) The USC plant may increase its steam temperature to 630~650°C by installing the new 12Cr steels, which satisfy the required strength at elevated temperatures as well as the cost performance. The USC technology will be able to realize the most reliable and less expensive thermal power generation with more plentiful experience and larger unit capacity for twenty or more years than before on the basis of the conventional and established PCF thermal power generation technology even with the FGD (Flue Gas Desulfurization) facility which is the expensive and inevitable equipment for desulfurization. However, the net thermal efficiency of the USC power plant can not exceed 41~42% till an unpredicted break-through technology will be attained.
- (2) The PFBC power generation plant will be able to accomplish high reliability and performance by promoting the various tests. The PFBC technology without the FGD, that is, direct desulfurization in PFBC boiler using limestone will be needed to realize more reliability, less expensive cost and larger unit capacity for wide-spread commercialization. The PFBC technology will not be playing a major part in

thermal power generation in Japan. This is because the conventional PCF power generation will be able to realized almost the same performance as the PFBC power generation.

- (3) The IGCC will be able to utilize effectively various kinds of coals. If the reliability and cost competitiveness of the IGCC will be improved in the future, the IGCC will prove to be the most promising technology. The IGCC technology will be expected to play a major part in the thermal power generation after approximately 2020 with assumption of the first commercial plant for operation in 2010 in Japan. This is because the IGCC technology will have the higher net thermal efficiency of 44~48% and more flexibility for utilizing low grade-quality coal than the USC and the PFBC.

These advanced technologies in coal-fired thermal power generation will extend the utilization of coal energy and improve the efficiency of energy conversion with less undesirable emission to environment. These will contribute to make coal-energy more affordable and available, more readily usable and more environmentally compatible.

REFERENCES

1. T. Kikuchi et al., "Development of Ultra Super Critical Plant," Proc. 5th Symposium of JSME (1996), pp. 7-12, in Japanese.
2. R. Kaneko et al., "Development of Steam Turbine Material at Target Temperature 650°C," The Thermal and Nuclear Power 46, No.9 (1995), pp. 60-69, in Japanese.
3. M. Takagi et al., "Success of Entrained Bed Coal Gasification Development of HYCOL Pilot Plant," The Hitachi Hyoron 76, No. 10 (October 1994), pp. 705-710, in Japanese.
4. K. Wada et al., "Development of Gas Turbine for Air-Blown Gasification," ASME Paper 96-GT-88 (1996).

PROSPECT OF COAL PYROLYSIS UNDER HYDROGEN-RICH GASES

Baoqing Li and Hongqiang Liao

State Key Laboratory of Coal Conversion

Institute of Coal Chemistry

E-mail: libq@ms.sxicc.ac.cn; Fax: (+86)-351-4048967

Keywords: pyrolysis, coke-oven gas, synthesis gas, desulfurization, denitrogenation

ABSTRACT. Pyrolysis of Chinese high sulfur bituminous coal and lignite under hydrogen-rich gases such as real coke-oven gas (COG) and synthesis gas (SG) is carried out at pressures of 0.1-5 MPa with heating rate ranging from 5-25 K/min up to final temperature 923K in a fixed-bed reactor. The results are compared with those in pyrolysis under hydrogen and nitrogen. Higher pressure and slower heating rate are helpful to increase the quality and quantity of tar and to improve the removals of sulfur and nitrogen. Compared with hydrolypyrolysis (HyPy) at the same total pressure, the conversions and tar yield from pyrolysis with COG and SG are always lower than those from HyPy, but the yields of BTX and Desulfurizations are almost equal. At the same hydrogen partial pressure, all the yields of tar, BTX, PCX and naphthalene, and desulfurization from pyrolysis with COG and SG increase significantly with enhancing unwanted water. The results reveal that there are interactions among H_2 , CH_4 and CO in pyrolysis under COG and SG. This study demonstrates that pyrolysis under hydrogen-rich gases may provide a possible way for effective conversion of high sulfur coal.

1. INTRODUCTION

Coal is readily available and abundant source of energy and important chemical industry materials. About 75% of total energy consumption come from coal in China and 80% of coal are consumed by combustion. In addition, about 30% of coal reserves are high sulfur coal, which is mainly located in the southwest of China. Direct combustion of coal without any treatment has caused a serious pollution. Low efficiency and severe pollution are the major problems for coal utilization in China. Due to the lack of resources of petroleum and natural gas, it is an important subject to convert coals, especially high sulfur coals, cleanly and effectively into liquid fuel and SNG. Hydrolypyrolysis (HyPy), i.e., pyrolysis under hydrogen pressure, can remove most sulfur in coal as H_2S , leaving the char with low sulfur content. The main product is SNG in HyPy operated under high temperature, while oil under mild one. Both oil and SNG have huge market in China. The main problem for HyPy is use of the costly pure hydrogen. The possible candidates are coke-oven gas (COG) and synthesis gas (SG). In China the major resource of town gas comes from coke-oven and there are many chemical fertilizer plants with small scale, which are spread to most countries and most of them will be closed soon. The feasibility study of coal pyrolysis under COG instead of hydrogen in HyPy showed that more profits can be obtained when the pyrolysis plant is combined with coke-making plant. Thus, pyrolysis under hydrogen-rich gas may provide a new way to convert coals, especially for high sulfur coals, more cleanly and efficiently into oil and SNG. In this paper yields of products and compositions of oils from pyrolysis of coal under real COG and SG, and the desulfurizations and denitrogenations are investigated in detail and the possible synergetic function among H_2 , CH_4 and CO is discussed.

2. EXPERIMENTAL

Pyrolysis experiment was carried out by using Chinese Yanzhou high sulfur bituminous coal and Xianfeng lignite in a fixed-bed reactor with COG, SG, H_2 and N_2 at heating rate of 5-25K/min, final temperature ranging from 773K to 923K and pressure range of 0.1-5MPa. Details of the reactor have been given elsewhere[1]. The coal was ground to 170-350 μm and the analysis was given in Table 1. The compositions of real coke-oven gas and synthesis gas were given in Table 2.

Table 1 Analysis of Coal

	Proximate analysis(wt%, ar)			Ultimate analysis (wt%, daf)				
	M	V	A	C	H	N	S	O(diff.)
Xianfeng	18.5	39.6	2.4	68.7	5.0	2.2	0.3	23.8
Yanzhou	1.5	41.4	3.7	79.3	5.0	1.2	3.1	11.4

Table 2 Compositions of the Reactive Gas

	H ₂	CH ₄	CO	N ₂	CO ₂	C ₂ H ₄	C ₂ H ₆	C ₃ H ₆	H ₂ S(ppm)
COG	60.9	20.7	6.9	7.8	1.8	1.5	0.5	0.07	32.0
SG	64.9	2.4	31.6	0.5	0.6	--	--	--	--

The main components of oil from pyrolysis of Xianfeng lignite were determined by GC/MS and the contents of sulfur and nitrogen in char and oil obtained from pyrolysis of Yanzhou coal were analyzed by Vario EL Elemental Analyzer (Germany). The removals of sulfur and nitrogen were calculated by the following expressions:

$$\text{Des. \%} = \left\{ \frac{S_{t, \text{coal}} - S_{t, \text{char}}}{S_{t, \text{coal}}} \right\} \times 100 \quad (1)$$

$$\text{Den. \%} = \left\{ \frac{N_{t, \text{coal}} - N_{t, \text{char}}}{N_{t, \text{coal}}} \right\} \times 100 \quad (2)$$

All the results presented are expressed in weight per cent of coal (daf).

3. RESULTS AND DISCUSSION

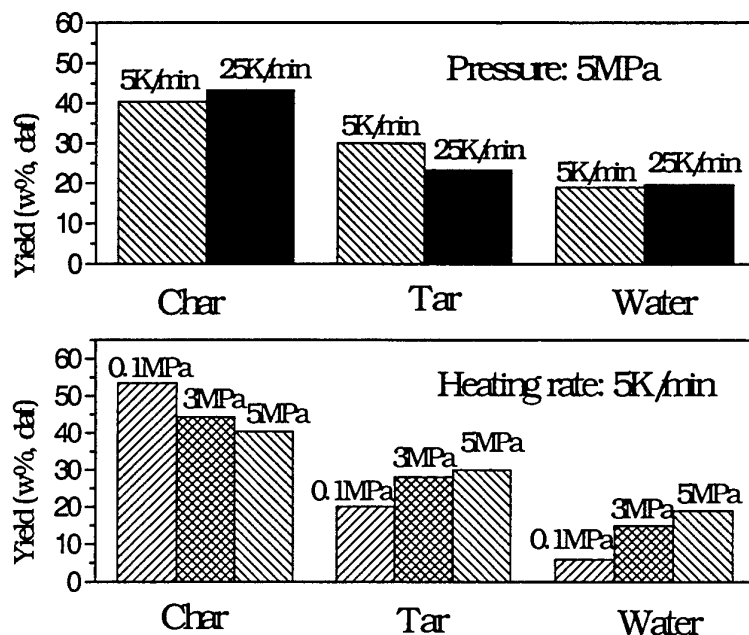


Figure 1. Effect of pressure and heating rate on the yields of products from pyrolysis of Xianfeng lignite under COG (Final temperature: 923K)

Influences of Pressure and Heating Rate

Effect on the yields of products and compositions of oil. The yields of products and the main components of oils from Xianfeng lignite pyrolysis under COG at pressures of 0.1 ~ 5 MPa with a given heating rate of 5~25 K/min and the final temperature of 923 K were given in Figure 1 and Figure 2. It can be seen that increasing pressure and decreasing heating rate enhance the coal conversion, oil yield and the yields of BTX, PCX and naphthalene. It shows the same conclusions as other reports about the effect of pressure and heating rate on hydropyrolysis [2-4] due to the extending of hydrogenation reaction.

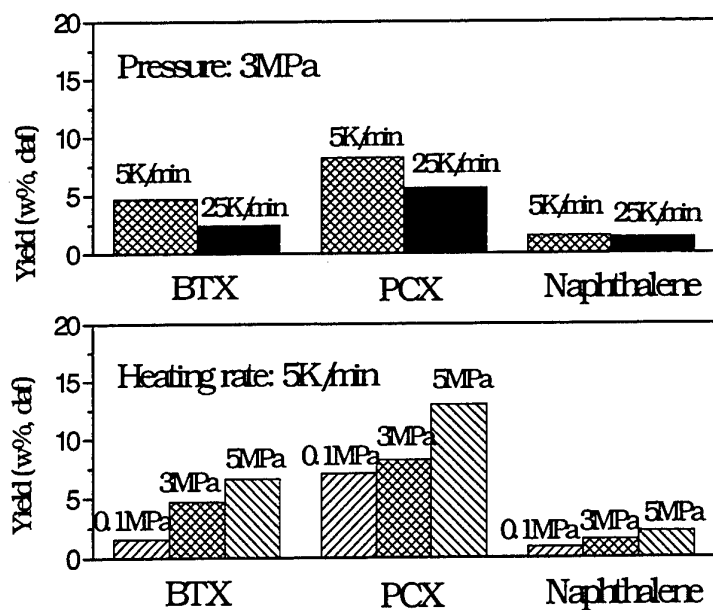


Figure 2. Effect of pressure and heating rate on the yields of main compositions of tars from pyrolysis of Xianfeng lignite under COG (Final temperature: 923K)

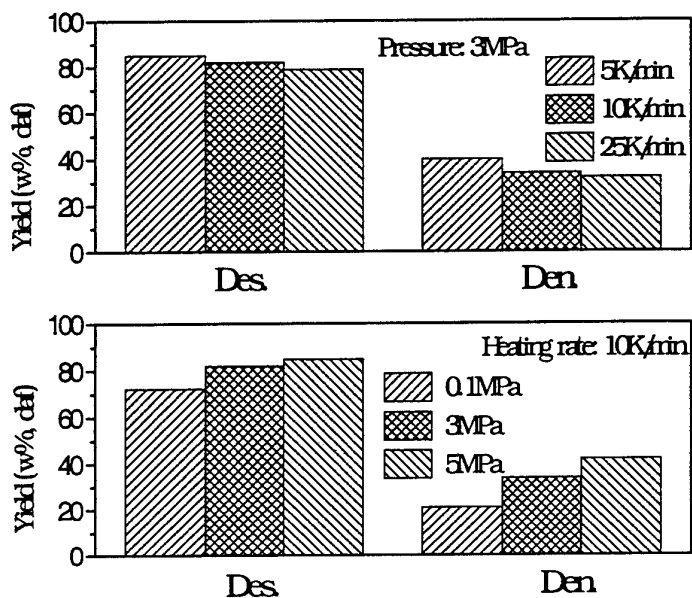


Figure 3. Effect of pressure and heating rate on the desulfurizations and denitrogenations in pyrolysis of Yanzhou coal under COG (Final temp.: 923K)

Effect on the desulfurization and denitrogenation and the distributions of sulfur and nitrogen. The desulfurizations and denitrogenations and the distributions of sulfur and nitrogen in products from pyrolysis of Yanzhou high sulfur bituminous coal under COG with different pressure and heating rate were given in Figure 3 and 4. Increasing pressure and decreasing heating rate, the desulfurizations and denitrogenations are improved,

the sulfur removed is mainly transferred into gas, sulfur in tar is almost a constant, while the nitrogen removed is mostly into tar, and the nitrogen in gas weakly changes with pressure and heating rate.

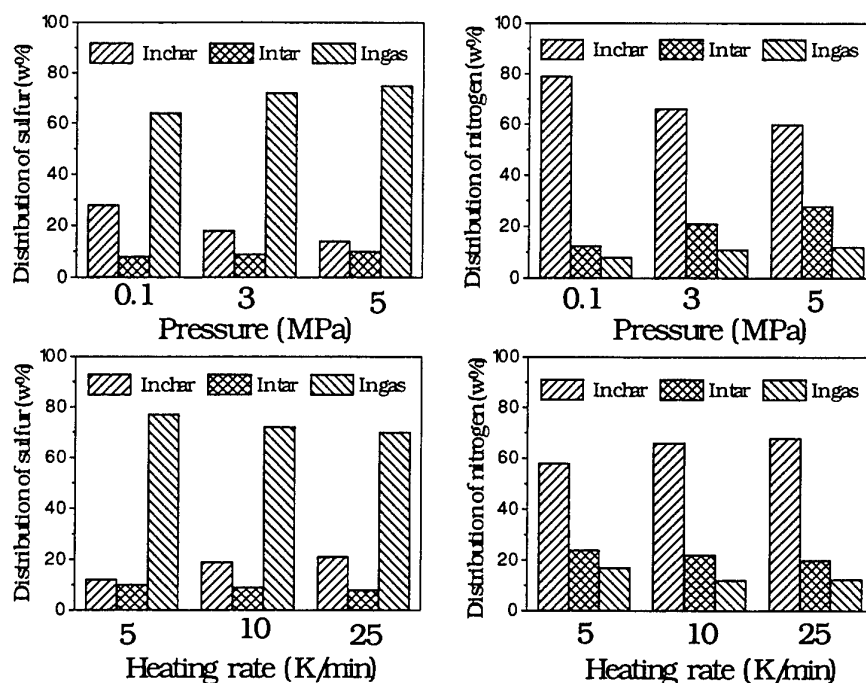


Figure 4. Distributions of sulfur and nitrogen in products from pyrolysis of Yanzhou coal under COG with different Pressure and heating rate (Final temperature: 923K)

Comparison Among Different Reactive Gases

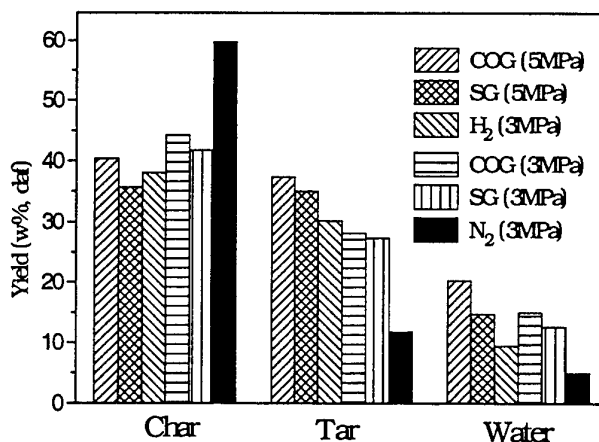


Figure 5. Yields of products from pyrolysis of Xianfeng lignite under different reactive gases (Heating rate: 5K/min up to 923K)

Comparison of product yields. The yields of products from pyrolysis of Xianfeng lignite under different reactive gases at the same total or hydrogen partial pressure with a given heating rate of 5K/min up to final temperature of 923K were given in Figure 5. At the same total pressure(3MPa), the yields of char, tar and water are the orders of N₂ > COG > SG > H₂, H₂ > COG > SG > N₂ and COG > SG > H₂ > N₂, respectively. Compared with hydropyrolysis (HyPy) at the same hydrogen partial pressure (3MPa), in coal pyrolysis with

5MPa COG and SG, the yields of tar increased. However, the unwanted water obviously increased too. All of these indicated that using coke-oven gas instead of pure hydrogen in hydrolysis can obtain higher tar yields at the same hydrogen partial pressure, however, the total conversion and tar yield are always lower than those from hydrolysis at the same total pressure. It shows that there is a synergetic action among H_2 , CH_4 and CO in COG and SG during coprolysis with coal, and the action leads to more tar and water. Perhaps, the interaction between CO and H_2 in COG leads to increasing of unwanted water from coal pyrolysis with COG[5].

Comparison of main compositions of tar. The yields of main compositions of tars from pyrolysis of Xianfeng lignite under different reactive gases at the same operating conditions as **Comparison of product yields**, were showed in Figure 6. At the same total pressure (3MPa), the orders of yields are $COG > H_2 > SG >> N_2$ for BTX, $H_2 > SG > COG > N_2$ for PCX and $COG > H_2 > SG >> N_2$ for naphthalene. While, the yields of BTX, PCX and naphthalene from coal pyrolysis at the same hydrogen partial pressure are always the order of $COG (5MPa) > SG(5MPa) > H_2(3MPa)$. All of these results indicated that the synergetic action among H_2 , CH_4 and CO is beneficial for the yields of BTX and naphthalene in COG and for PCX yield in SG. This improved the competitive capability of the new process of co-pyrolysis of coal with hydrogen-rich gas.

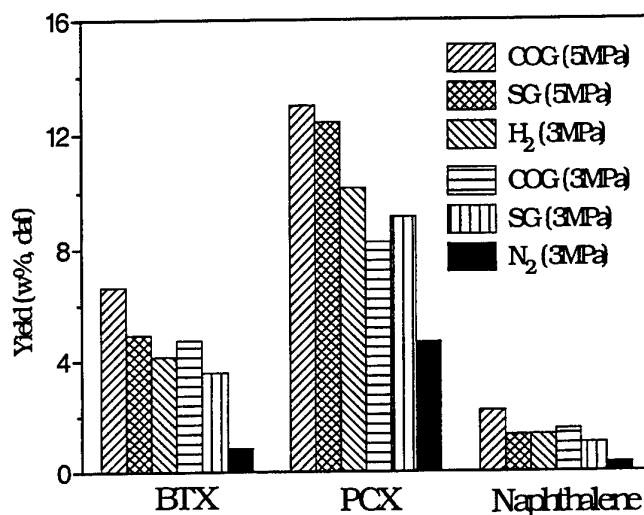


Figure 6. Yields of main compositions of oils from Xianfeng lignite pyrolysis with different reactive gases (5 K/min up to 923K)

Comparison of desulfurization and denitrogenation and the distributions of sulfur and nitrogen. Desulfurization and denitrogenation in pyrolysis of Yanzhou high sulfur coal under different gases were given in Figure 7. At the same total of pressure 3MPa , the orders are $N_2 < COG \approx SG \approx H_2$ for desulfurization and $N_2 < COG < SG < H_2$ for denitrogenation. Desulfurizations and denitrogenations in coal pyrolysis with COG, SG and H_2 are about 20% and 10~20% higher than those under N_2 , respectively. At the same hydrogen partial pressure, desulfurization under COG(5MPa) is about 4.5% higher than that under H_2 (3MPa), while the denitrogenation is about 3.5% lower.

Table 3 showed the distributions of sulfur and nitrogen in products from pyrolysis of Yanzhou coal with COG, SG, H_2 and N_2 . The distributions of sulfur in char, oil and gas from coal pyrolysis at 3MPa under hydrogen-rich gases(COG, SG and H_2) are about 20%, 10-12% and 67- 70% and the distributions of nitrogen are 60-70%,22-29% and 7-13%, respectively. The results indicated that the distribution of sulfur in coal pyrolysis with hydrogen-rich gases is mainly in gas phase, while most of nitrogen was still retained in char, and the nitrogen removed from coal is mainly into oil. Compared with pyrolysis of coal under hydrogen -rich gases, in coal pyrolysis under N_2 , the distributions of sulfur and nitrogen in char are always higher, and they are lower in oil for the low oil yield. All of these results demonstrated that nitrogen is much harder to remove than sulfur, and the sulfur even in heterocyclic form can be also transferred into H_2S during hydrolysis of Yanzhou coal[6]

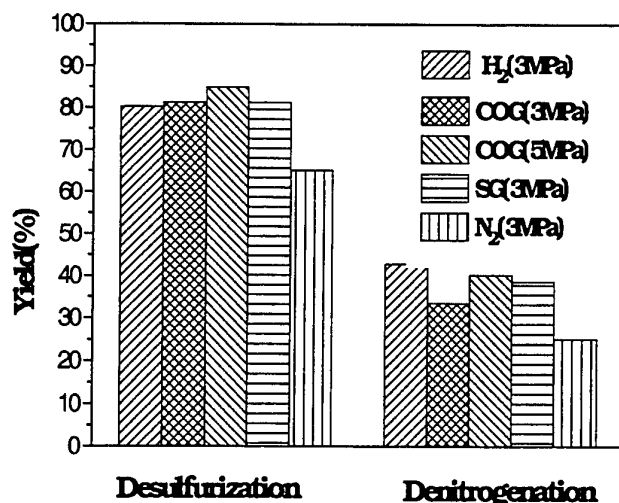


Figure 7. Desulfurizations and denitrogenations in pyrolysis of Yanzhou coal under different reactive gases (10 K/min up to 923K)

Table 3 The Distributions (wt%, daf) of Sulfur and Nitrogen in Products from Pyrolysis of Yanzhou Coal with Different Gases (10;æ/min, up to 650;æ)

Gases	In Char		In Oil		In Gas(diff.)	
	N	S	N	S	N	S
COG _(3MPa)	70.3	19.7	23.0	9.8	6.7	70.5
COG _(5MPa)	62.9	16.0	29.0	10.8	8.1	73.2
SG _(3MPa)	64.7	19.7	22.4	10.2	12.9	70.1
H ₂ _(3MPa)	59.5	20.5	28.8	12.2	11.7	67.3
N ₂ _(3MPa)	79.3	38.6	9.6	6.1	11.1	55.3

4. CONCLUSIONS

The results reported show that using COG and SG replace pure hydrogen in HyPy can get more tar with high light oil and char with low sulfur. Co-pyrolysis of coal with hydrogen-rich gas is a competitive process in China. However, the unwanted water is also high in this process. How to decrease water and increase water will be the further problem in this process.

ACKNOWLEDGMENTS

Financial support by New Energy and Industrial Technology Development Organization (NEDO, Japan), the Shanxi Foundation of Natural Science and the Shandong Foundation of Natural Science is gratefully acknowledged.

REFERENCES

1. H. Liao, B. Li, and C. Sun, J. Fuel Chem. Technol. (Chinese), 1997, **25**, 104
2. R. Cypres, W. Mingels, J-P. Lardinois, A. Laudet, and H. Masson, 'Feasibility Study of theHyPy of Coal', Commission of the European Communities , EUR14110, Luxembourg 1992
3. M. Steinberg, and P.T. Fallon, Hydrocarbon Proc. 1982,92
4. M. Steinberg, P.T. Fallon, and M.S. Sundaram, Annual Technical Report US DOE/CH/ 0016-1402, Brookhacen National Laboratory 1983, 953
5. C.J. Lafferty, S.C. Mitchell, R. Garcia, et al. Fuel,1993,**72**,367
6. C. Sun, B. Li, and C.E. Snapy, C.E.J. Fuel, Chem. Technol. (Chinese), 1997, **25**,353

AN EXPERIMENTAL RESEARCH AND NUMERICAL SIMULATION ON INFLUENCE OF COAL QUALITY ON BOILER COMBUSTION PERFORMANCE

Xiang Jun*, Sun Lushi, Zou Zuqiao, Li Min, Cheng Xiaohui, Sun Xuexin

National Laboratory of Coal Combustion

Huazhong University of Science and Technology, Wuhan 430074, PRC

Email: xiangjun01@hotmail.com; fax: (86)-27-87545526

Keywords: coal quality; combustion experiment; mathematical modeling

ABSTRACT. This paper deals with an experimental study on the influence of coal quality on NO_x emission and unburned carbon in flying ash. Chinese lean coals (fixed carbon content varied from 50%-70%) have been fired in a tangentially full scale boiler (300Mwe power unit, 1024t/h boiler). In furnace NO_x emission and unburned carbon in flying ash concentrations have been measured synchronously with different combustion condition. Identical trends in NO_x emission as a function of coal analysis content and excessive oxygen content have been obtained. NO_x emission was found to be proportional to the fuel nitrogen content of the coals. Coal quality characteristic, especially fix carbon content and ash content have been studied on the influence of boiler burnout performance. A relationship has been found between operation condition and unburned carbon in flying ash content. Additionally, a three-dimensional mathematical model for pulverized coal combustion has been developed which describes coal combustion, including volatile devolatilization and char burnout, and radiation heat transfer in full scale furnace. The model can predict the levels of velocity, temperature, oxygen, and carbon in ash. It can predict accurately the influence of coal quality on combustion status in the furnace, and numerical simulation is more useful as a tool to investigate the influence of coal type on furnace performance related to differences in furnace design.

1. INTRODUCTION

The influence of coal quality on furnace combustion performance has been investigated experimentally in the past [1-6]. Some results on the influence of coal quality on carbon in ash levels and NO_x formation has been found. These studies are almost conducted in a pilot scale furnace, and the results can only present the right trends. A comparison of coal quality influence between a full scale and a pilot scale furnace has been investigated with considerable success, and a one-dimensional engineering model was applied [7]. This model is too simple to predict the influence of coal quality on the temperature profile, NO_x formation and carbon in ash content. Most of the experiments have been conducted with bituminous coal on testing furnace performance. Although low NO_x burner and over fire air (OFA) are introduced in the furnace, as we know, the NO_x emission content of the furnace fired anthracite or lean coal is higher than fired bituminous coal relatively. An experimental research to investigate the influence of coal quality on furnace combustion performance is crucial significance.

2. EXPERIMENTS

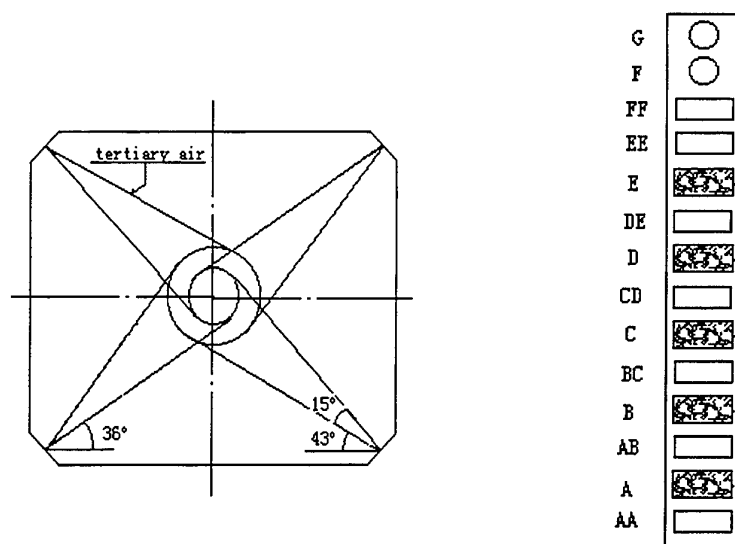
The experiments have been performed in a tangentially fired full scale boiler and a pilot scale test furnace. A brief description of the test facilities is given below.

Qingshan Power Station Unit 12

Qingshan power station unit 12 is a 300Mwe tangentially fired boiler with a large furnace of 11.76×11.858m diameter and 53m height. A wide ranged (WR) burner which include 7 secondary air ports, 5 primary air ports and 2 tertiary air ports is arranged on each corner of furnace. The original designed coal is Henan lean coal. Coal is ground with four roller mills with rotating classifiers. The burner arrangement is shown in Fig.1.

Drop-Tube Furnace

Drop-tube furnace is 800mm long, 40mm internal diameter. The primary air ratio is 10%. The secondary air is heated to 573k by electric preheater and then blow into furnace. The temperature in the combustion region of furnace is 1423k, and the particle residence time is around 1.5s. The burner is located at the top of the furnace and fires downward.



A,B,C,D,E : the primary air port ; AA,AB,BC,CD,DE,EE,FF : the secondary air port;
F,G : the tertiary air port

Figure 1 The burner arrangement of Qingshan boiler

Two coals were tested in both full scale furnace and the pilot scale test rig. The results of the ultimate analysis and size analysis are given in Table 1.

Table 1 Coal ultimate analysis (wt%) on dry basis and size analysis

coal type	C	H	O	N	S	Moisture	ash	heating value(kJ/kg)	R90
1	74.17	3.19	1.15	1.47	0.28	0.50	19.24	26830	13%
2	62.66	2.80	2.79	1.08	0.47	0.72	29.48	20820	14%

A brief description of the test program in the power plant and pilot scale test rig is given below.

- (1) The above two coals were supplied to the power plant and the test rig in order to test the relationship between coal type and combustion performance. The secondary air flow was varied to study the influence of combustion condition on the NO_x emission and unburned carbon.
- (2) During all the measurements, NO, NO₂ and O₂ concentrations were monitored continuously. Flying ash were withdrawn from the furnace exit by a water-cooled solids sampling probe.

3. RESULTS AND DISCUSSION OF EXPERIMENTS

Characteristic of Nitrogen Oxide Formation

The influence of coal quality. Figure 2 shows the NO_x emission as a function of coal type in the two test furnaces. It is necessary to state that the operation condition of qingshan unit is 100% continuous maximum ration (CMR) during the experiments. The result discussion is given below:

- (1) The data show that combustion of the coal type 1 results in the highest amount of NO_x followed by the coal type 2. The difference of NO_x emission between the coal type 1 and 2 can be explained by the higher nitrogen content of the coal type 1 if the influence of ash content on combustion process can be ignored under the condition of burnout completely. The coal nitrogen is evolved and oxidized to NO_x when it is mixed with the secondary air. It is reasonable that a larger fraction of the coal nitrogen results in higher NO_x

mixed with the secondary air. It is reasonable that a larger fraction of the coal nitrogen results in higher NO_x emission. An increase from 1.0 wt% coal-N to 1.5 wt% resulted in about 150mg/m³ more NO_x being produced. Good agreement has also been obtained between the NO concentrations and the coal-N content by Chen et al. Who investigated 48 coals and concluded that an increase from 1.0 wt% coal-N to 2.0 wt% resulted in roughly 50% more NO_x being produced [8].

- (2) Because of lower temperature (1423k) and shorter residence time (around 1.5 s), the NO_x formation of the drop-tube furnace is lower relatively. Both power station and pilot scale test rig show the same trend in the NO_x concentration with coal type.
- (3) The pulverized coal (PC) air flow is injected into furnace with dense and dilute coal-air jets when a WR burner is adopted in qingshan unit. A WR burner may improve performance of ignition, stabilize combustion and reduce NO_x emission. The principle of low NO_x formation with WR burner is similar to air staged combustion. The staged combustion may decrease in the oxygen concentration in the early stage of combustion, and make the main combustion region in a condition of fuel-rich. This may lead to lower combustion intensity and decrease in peak value of temperature. The coal-N may decompose to HN, HCN, CN and NH₃ et al. which can compound each other and reduce NO to N₂ in the fuel-rich combustion region. The formation of thermal-NO_x and fuel-NO_x may decrease remarkably as a result.

The influence of excess air. Figure 3 shows the relationship of O₂ levels and NO_x concentration. The data show that NO_x emission increase initially and then decrease slightly along with the increase of excess oxygen. The phenomenon may be explained below. The amount of oxygen supplied increases on the region of combustion with the higher amount of air blowing into the furnace. This may enhance the combustion intensity and result in a high flame and furnace temperature. Local high temperature and sufficient oxygen may not only produce high amount of thermal-NO_x formation but also provide oxidizing conditions for coal nitrogen transforming to fuel-NO_x. But the furnace temperature on the combustion region may decrease if the amount of excess air continuously increases. This may restrain the combustion intensity and combustion rate and result in low amount of thermal-NO_x formation. In a word, the total NO_x emission may increase and then decrease a bit with amount of excess air.

Performance of Burnout

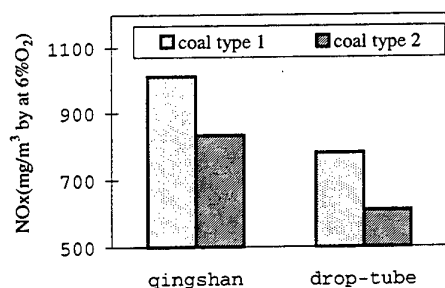


Figure 2 The relationship of coal type and NO_x emission

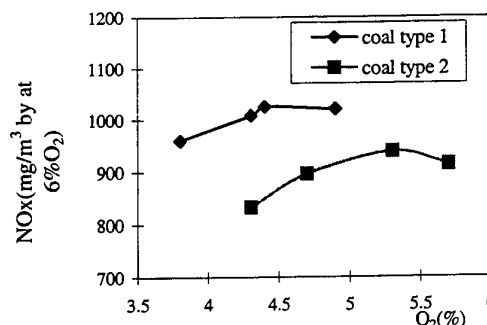


Figure 3 The relationship of O₂ levels and NO_x emission

The unburned carbon in flying ash is similar when coal type 1 and 2 have been fired in qingshan boiler under the same operation condition. Figure 4 shows the unburned carbon in flying ash as a function of unit load. The data clearly show that the unburned carbon in flying ash may rise gradually when the operation condition of boiler deviates from the CMR. It shows that qingshan boiler may have a high performance of burnout when the coal with the high ash content, low heating value has been fired and unburned carbon in flying ash is less than 5%. Meanwhile, it also states that the influence of ash content on performance of PC particle burnout may not be remarkable when ash content is less than 30% in the coal. So it may have an optimum operation condition related to the coal type and the specific combustion device used to ensure high combustion efficiency and low pollution.

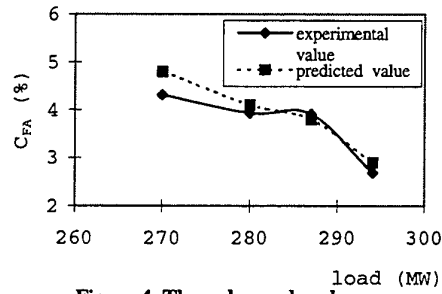


Figure 4 The unburned carbon as a function of unit load

4. MATHEMATICAL MODEL

Gas Turbulent Flow

The $k-\varepsilon-g$ turbulence model is used, the gas phase conservation equations in three dimensions can be expressed in following form:

$$\frac{\partial}{\partial x_i}(\rho u_i \phi) = \frac{\partial}{\partial x_i}(\Gamma_\phi \frac{\partial \phi}{\partial x_i}) + S_\phi + S_{p\phi}$$

here, ϕ represents gas velocities u_i , species mass fractions f , enthalpy h , kinetic energy of turbulence k and its dissipation rate ε , and square root of pulsation g , etc.. S_ϕ is the source term in the gas phase and $S_{p\phi}$ is the source term due to the particle phase. Γ_ϕ is dissipation coefficient. The source terms and exchange coefficients used are shown in Table 2.

Table 2 The source terms and exchange coefficients

ϕ	Γ_ϕ	S_ϕ	$S_{p\phi}$
1	0	0	0
u_i	μ_e	$\frac{dp}{dx_i} + \rho g_i + \frac{\partial}{\partial x_i}(\mu_e \frac{\partial u_j}{\partial x_j})$	$-\frac{d}{dt}(\mu u_{pi})$
k	$\mu_e / 0.9$	$G_k - \rho \varepsilon$	0
ε	$\mu_e / 1.22$	$(1.44 G_k - 1.92 \rho \varepsilon) \frac{\varepsilon}{k}$	0
f	$\mu_e / 0.7$	0	$-\frac{dm_p}{dt}$
g	$\mu_e / 0.7$	$-2\rho g \frac{\varepsilon}{k} + 2.8\mu_e (\frac{\partial f}{\partial x_i})^2$	0
h	$\mu_e / 0.7$	$-Q_R$	$-\frac{d}{dt}(m_p h_p)$

Here, $G_k = \frac{1}{2} \mu_e \left(\frac{\partial u_i}{\partial x_j} + \frac{\partial u_j}{\partial x_i} \right) \left(\frac{\partial u_i}{\partial x_j} + \frac{\partial u_j}{\partial x_i} \right) + G_B$,

$G_B = (u_i / 0.7)(g/\rho)(\partial \rho / \partial z)$, $\mu_e = C_\mu \rho k^2 / \varepsilon$, $C_\mu = 0.09$

Here, μ_e is effective viscosity, $\mu_e = \mu_t + \mu$, μ_t is turbulent flow viscosity, μ is laminar flow viscosity. G_k represents turbulence generation term.

Particle Dynamics Equation

This program accurately models the particle trajectories in a furnace by a stochastic method. The turbulent velocity is determined by making a random selection from the probability density function of velocity. Based on the Lagrangian approach, each particle size class is tracked through the gas field, and particle random trajectories and changing process are calculated. The particle momentum equation is:

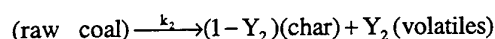
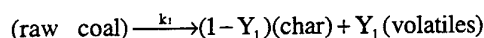
$$m_p \frac{du_{ip}}{dt} = 0.5 C_D \rho_g A_p (u_{ig} - u_{ip}) |u_{ig} - u_{ip}| + m_p g_k$$

u_{ip} and u_{ig} are instantaneous velocity of particle and gas. m_p is particle mass. ρ_g is local density of gas. A_p is particle surface area, g_k is gravity, C_D is the resistance coefficient and is a function of Reynolds number.

Pulverized Coal Combustion Model

Devolatilization and combustion of the volatile takes place in the gas phase through heating of the particle. The remaining char particle subsequently burnout at a chemical or diffusion controlled rate.

The particle devolatilization is modeled by considering a pair of parallel first order reactions:



These two reactions are competitive, and the reaction rate coefficient k_1 and k_2 are given by Arrhenius expression. So, the particle devolatilization rate is

$$\frac{dY_v}{dt} = k_1 Y_1 + k_2 Y_2$$

Following devolatilization, char burnout is controlled by the rate of oxygen diffusion to the particle and the rate of chemical reaction at the surface. The mass change of a particle due to char burnout is given by

$$\frac{dM_p}{dt} = \pi k_t \rho_p d_p^2 V_{ox}$$

Where, the overall rate k_t is given by the combination of chemical and diffusion rate terms

$$k_t = 1/(1/k_d + 1/k_c)$$

Energy Transport

In a pulverized coal combustion furnace, heat transfer mainly depends on thermal radiation. Discrete Transfer (DT) method is adopted here for the calculation of thermal radiation. This method bases on heat flux model solution method, and combines features and advantages of the Zone and Monte Carlo model solution method. So this method is suitable for practical application to projects.

The fundamental equations for the thermal radiation may be expressed as

$$\frac{dI}{ds} = -(K_a + K_p + K_s)I + \frac{\sigma}{\pi} (K_a T^4 + K_p T^4) + \frac{K_s}{4\pi} \int_0^{4\pi} I d\Omega$$

where, I is the radiant intensity in the direction of Ω . S is the distance in the Ω direction. K_a and K_p is the gas and particle absorption coefficients. K_s is the particle scattering coefficient.

For pulverized coal, the total energy balance equation can be expressed as:

$$\frac{d}{dt} (M_p C_p T_p) = C_p T_p \frac{dM_p}{dt} + Q_{pc} + Q_{pr} + Q_{pb}$$

where Q_{pc} , Q_{pr} and Q_{pb} represent heat transfer by conduction, thermal radiation and chemical reaction.

5. RESULTS AND DISCUSSION OF NUMERICAL SIMULATION

The physical models outlined above have adopted in the 3-dimensional combustion numerical simulation in the furnace. Figure 5 shows the distribution of temperature at plane section of burner B (see Fig.1) under the condition of CMR in qingshan boiler, and Figure 6 shows the distribution of oxygen. The data show that the program can simulate accurately the condition of combustion in the furnace.

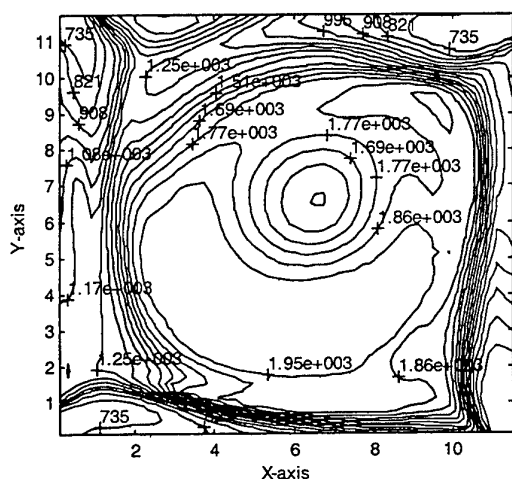


Figure 5 the distribution of temperature (CMR) at plane section of burner B

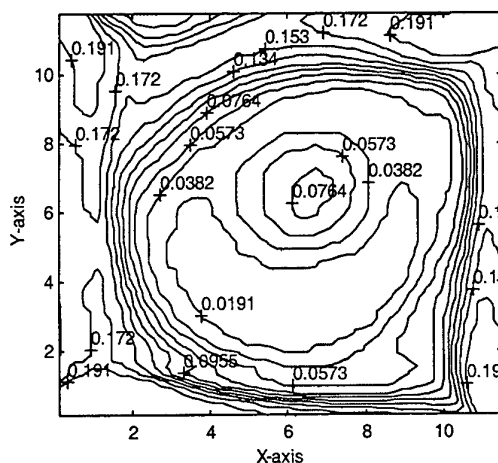


Figure 6 the distribution of oxygen (CMR) at plane section of burner B

The unburned carbon in flying ash can be predicted when the practical operational parameters have been inputted into the program. Figure 4 shows the result. The data show that the trend predicted is similar to the experimental value. It fails to predict the influence of ash content on burnout of PC particle because the obstruction of ash shell to char burnout has not been taken into account in volatile devolatilization model and char burnout model. But it can predict quantitatively the influence of volatile content on contribution of temperature in the furnace and the performance of char burnout.

As we know, the size of PC particle may affect remarkably the boiler performance of combustion. Figure 7 shows the relationship of PC particle size and unburned carbon in the flying ash.

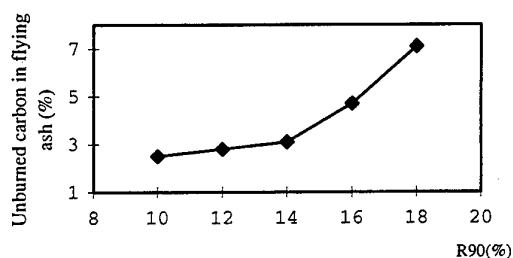


Figure 7 Unburned carbon in flying ash as a function of PC particle size

6. CONCLUSIONS

1. The coal quality may affect remarkably the boiler performance of combustion. An increase from 1.0 wt% coal-N to 1.5 wt% results in about 150mg/m³ more NO_x being produced.
2. NO_x emission increase initiative and then decrease slightly along with the increase of excess oxygen.
3. The staged combustion may reduce significantly the NO_x emission. A WR burner may improve performance of ignition, stabilize combustion and reduce NO_x emission. Meanwhile, the emission of NO_x is still high although low NO_x combustion technology has adopted in the boiler fired lean coal.
4. The result of experiments show that the influence of ash content on performance of PC particle burnout may not be remarkable when ash content is less than 30% in the coal.
5. The data clearly show that the unburned carbon in flying ash may rise gradually when the operation condition of boiler deviate the CMR. The experiment show that it may has an optimum operation condition related to the coal type and the specific combustion device used to ensure high combustion efficiency and low pollution.
6. The pilot scale test rig which was able to reproduce qualitatively the NO_x emission for the two coals is a powerful tool in the prediction of NO_x emission from full scale boilers.
7. The model of the 3-dimensional numerical simulation of combustion can predict the levels of velocity, temperature, oxygen in the furnace and carbon in ash levels. It can predict accurately the influence of coal quality on combustion status in the furnace, and numerical simulation is more useful as a tool to investigate the influence of coal type on furnace performance related to differences in furnace design.

REFERENCES

1. H. Maier, H. Spliethoff, Kircherer, etc. Fuel, vol.73, pp.1447 (1994).
2. J.P. Smart, and Nakamura, etc. J. Inst. Energy, vol.66, pp.99 (1993).
3. M.E.J. Morgan, Inst. Energy, vol.63, pp.3 (1990).
4. T. Abbas, Costen, etc. Combust. Sci. Tech., 93, 73 (1993).
5. W.A. Fiveland, and Latham, etc. Combust. Sci. Tech., 93, 53 (1993).
6. U. Schnell, Kaess, etc. Combust. Sci. Tech., 93, 91 (1993).
7. Robert Pieter van der Lans, etc. Fuel, Vol.77, No.12, pp.1317-1328 (1998).
8. S.L. Chen, M.P. Heap, etc. In the 19th Symp. (Int.) on Combustion, Pittsburgh, pp.1271 (1982).
9. D.B. Spalding, Combustion and Mass Transfer, Pergamon Press (1979).
10. L.D. Smoot, Prog. Energy Combust. Sci., Vol 10, No. 22, p.229 (1984).
11. G.D. Raithby, Skew Upwind, Comput. Meths. Appl. Mech. Eng. Vol.9, pp.153-164 (1976).
12. F.C. Lockwood, and N.B. Shen, in Twenty-fifth Symposium (International) on Combustion. The Combustion Institute, pp.503 (1994).
13. F.C. Lockwood, Mahmud. In Proceedings of the Eighth Annual International Pittsburgh Coal Conference, P.41 (1991).
14. Ubhayakar et al. Sixteenth Symposium (International) on Combustion, pp.427-436 (1977).
15. W. Smith, Nineteenth Symposium (International) on Combustion, pp.1045-1065 (1982).
16. A.S. Jamaluddin, J.S. Truelove and T.F. Wall, Combust. and Flame, vol.62, pp.85 (1985). Combust. Sci. Tech., 93, 73 (1993).
17. M.M. Baum and P.J. Street, Combust. Sci. and Tech. Vol.3, pp.231 (1971).

Authors Index to Volumes 1-4

Ahmad, G.E.	751	Cen, K.F.	1586
Ahn, J.	212	Cen, K.F.	1603
Ahn, Y.	557	Chai, L.H.	343
Akisawa, A.	759	Chan, A.M.C.	408
Akisawa, A.	1145	Chan, C.K.	1508
Allcock, H.R.	1483	Chan, C.K.	1515
Altraide, A.	191	Chandratilleke, T.T.	191
Amazouz, M.	917	Chang, L.J.	1002
Amazouz, M.	1084	Chazly, N.E.	826
An, E.	355	Chen, C.T.	636
An, E.	367	Chen, D.Z.	1595
Anderson, R.	1033	Chen, G.H.	910
Ando, D.	1226	Chen, G.H.	1048
Antohi, C.	866	Chen, G.J.	588
Aoki, H.	748	Chen, G.Y.	1553
Aoyama, S.	843	Chen, H.P.	1496
Aoyama, S.	852	Chen, J.	1397
Arlabosse, P.	923	Chen, M.J.	1581
Asano, H.	1122	Chen, Q.H.	379
Asano, H.	1438	Chen, T.K.	393
Assassa, G.M.R.	766	Chen, T.K.	416
Baba, A.	1710	Chen, X.	270
Bae, S.C.	1153	Chen, Y.	1427
Bai, Q.	521	Chen, Y.	1433
Bai, W.D.	1703	Chen, Y.	1632
Bartoli, C.	247	Chen, Z.H.	355
Behnia, M.	873	Chen, Z.H.	367
Benali, M.	917	Chen, Z.H.	598
Benali, M.	1412	Chen, Z.Q.	505
Benning, L.	1483	Chen, Z.Q.	529
Bhattacharyya, S.	1353	Cheng, K.	1212
Bi, Q.C.	393	Cheng, P.	505
Bi, Q.C.	438	Cheng, P.	529
Bingue, J.P.	1266	Cheng, P.	1192
Bockhorn, H.	1573	Cheng, X.H.	1728
Boral, A.A.	888	Cheng, Y.C.	1476
Borisov, I.	422	Cheung, C.S.	1397
Borzenko, V.I.	512	Cheung, F.B.	888
Bossi, L.	239	Cheung, F.B.	1289
Buchner, H.	1573	Chi, Y.	1333
Bull, S.R.	18	Chi, Z.H.	1586
Cai, J.Y.	416	Chiu, H.H.	1640
Cai, S.	1651	Cho, H.K.	384
Cannon, A.M.	1483	Choi, M.	1532
Cao, X.Y.	1281	Chou, C.S.	474
Cao, X.Y.	1603	Chou, T.C.	1257
Cao, Z.H.	1651	Chow, A.	680
Carrere-Gee, C.	923	Chua, H.T.	1145
Casey, R.T.	1524	Chung, B.T.F.	581
Cen, K.F.	1281	Chung, J.D.	1532
Cen, K.F.	1333	Chung, K.C.	636
Cen, K.F.	1566	Chung, S.K.	229

Ciocan, V.	866	Garner, S.D.	1007
Cote, R.	1084	Gavotti, N.	539
Cui, W.Z.	379	Gerlach, C.	1273
Cui, Y.B.	1662	Gerlach, C.	1296
Cunnington, G.R.	613	Goldstein, R.J.	206
Da Veiga, V.R.	1114	Gong, L.H.	1198
Dai, X.W.	1632	Gopinath, A.	1170
Davis, S.B.	1686	Gori, F.	239
Deeb, S.E.	826	Grandum, S.	860
Deng, P.G.	1217	Groll, M.	708
Deng, X.H.	1217	Groll, M.	957
Denner, H.D.	1212	Groll, M.	1130
Diaz, G.	940	Gu, F.	1305
Ding, L.S.	650	Gu, Z.Z.	1651
Dong, Y.X.	980	Guo, F.Z.	1203
Druck, H.	740	Guo, F.Z.	1208
Du, D.X.	658	Guo, T.M.	588
Du, D.X.	665	Guo, X.F.	1433
Du, J.H.	490	Guo, X.Q.	588
Dubble, E.H.	1007	Guo, X.S.	1566
Duluc, M.C.	127	Guo, Y.C.	1508
Eder, A.	1273	Guo, Y.C.	1515
Eder, A.	1296	Guo, Z.	658
Eisen, S.	1366	Guo, Z.Y.	118
El-Kotb, M.	826	Guy, C.	1412
Elphick, I.G.	408	Hahne, E.	740
Eschenbacher, J.F.	262	Hamada, K.	843
Fagguani, S.	247	Han, B.	206
Fan, M.X.	1566	Han, P.	270
Fan, W.C.	1340	Han, X.	1603
Fedkin, M.V.	1483	Hara, T.	1178
Fei, Q.	1002	Haruki, N.	695
Feng, B.	1560	Haruki, N.	723
Feng, Y.	1208	Haruki, N.	852
Feng, Z.	643	Haruki, N.	1138
Feng, Z.X.	1646	Hatabaka, M.	288
Fiebig, M.	598	Hawlander, M.N.A.	451
Francois, M.X.	127	He, K.X.	680
Francois, M.X.	1164	Hein, D.	1347
Fridman, A. A.	96	Hetsroni, G.	72
Fridman, A.A.	1266	Hetsroni, G.	255
Fu, H.L.	497	Hiller, G.	1677
Fu, X.Y.	1033	Hirashima, M.	564
Fudym, O.	923	Hirata, M.	57
Fujii, I.	1540	Hirata, Y.	628
Fujii, T.	1122	Hisazumi, Y.	1122
Fujii, T.	1438	Ho, C.J.	881
Fujioka, K.	628	Hoffmann, S.	1573
Fujita, Y.	521	Hofmann, M.A.	1483
Fujiyoshi, M.	1404	Holden, C.	680
Fushimi, J.	399	Honda, T.	1546
Gale, T.K.	1686	Horibe, A.	695
Ganzha, V.L.	688	Horibe, A.	723
Gao, X.	1566	Horibe, A.	852

Horibe, A.	1138	Kashiwagi, T.	759
Hosatte, S.	1084	Kashiwagi, T.	1145
Hoshi, A.	796	Kato, Y.	1546
Hsiau, S.S.	474	Katsuta, M.	1153
Hsieh, S.S.	1015	Kaviany, M.	32
Hsu, C.T.	505	Kawaguchi, Y.	716
Hsu, C.T.	731	Kellam, E.C.	1483
Hu, G.	1333	Kennedy, L.A.	96
Hu, W.	279	Kennedy, L.A.	1266
Huang, J.	1002	Khalatov, A.	422
Huang, S.H.	821	Khattab, N.	826
Huang, X.	355	Kida, T.	1138
Huang, X.	367	Kim, M.	557
Huang, X.Y.	497	Kim, M.O.	384
Hugron, I.	1412	Kim, M.S.	965
Hui, C.K.P.	1090	Kim, Y.J.	295
Hussien, H.M.S.	751	Kimura, M.	843
Hwang, I.J.	295	Kimura, T.	1540
Hwang, Y.W.	965	Klein, H.P.	1130
Hyuga, T.	521	Komiya, A.	873
Ichimiya, K.	184	Koo, J.H.	1289
Inaba, H.	695	Koyama, S.	445
Inaba, H.	723	Kudra, T.	917
Inaba, H.	852	Kuge, K.	1546
Inaba, H.	1138	Kumagai, S.	399
Inada, T.	860	Kuo, J.T.	474
Inatomi, Y.	302	Kurosaki, Y.	84
Ipek, O.	778	Kuwahara, K.	149
Ishizuka, M.	321	Kuwahara, K.	445
Iwai, H.	161	Kuznetsov, A.V.	896
Izumi, M.	399	Kwan, M.K.	731
Jang, K.J.	1015	Kwanka, K.	1347
Jebali, F.	127	Ladevie, B.	482
Jegla, Z.	1624	Ladevie, B.	923
Jeong, U.C.	295	Lam, W.C.	1404
Jerbi, F.J.	1164	Lazarescu, C.D.	866
Jiang, X.J.	1586	Lecomte, D.	923
Jiang, Y.	788	Lee, B.D.	650
Jiang, Y.	804	Lee, J.S.	212
Jiang, Y.	1059	Lee, L.	1098
Jiang, Y.	1066	Lee, S.C.	613
Joko, M.	262	Lee, T.H.	384
Jones, J.C.	1313	Lee, T.S.	1581
Jordan, M.	1273	Lee, T.S.	1640
Jung, I.S.	212	Leong, K.C.	497
Kage, H.	932	Leung, D.Y.C.	1427
Kakimoto, K.	302	Leung, D.Y.C.	1553
Kalabin, E.V.	328	Leutz, A.	759
Kameda, K.	1138	Li, B.Q.	1433
Kaneda, M.	302	Li, B.Q.	1722
Kang, Y.B.	788	Li, C.F.	255
Kang, Y.B.	804	Li, G.H.	1615
Kang, Y.M.	430	Li, H.B.	1433
Kasagi, N.	972	Li, H.P.	270

Li, J.	335	Ma, W.M.	1305
Li, M.	1728	Ma, Z.	581
Li, P.W.	716	Ma, Z.Y.	1333
Li, Q.	1203	Machida, K.	843
Li, Q.	1208	Madadnia, J.	349
Li, Q.Y.	1615	Makino, T.	604
Li, R.	355	Malysenko, S.P.	512
Li, R.Y.	367	Mandel, H.	740
Li, X.Z.	1212	Martiny, M.	221
Li, Y.D.	1420	Maruyama, S.	873
Li, Z.	658	Matsuno, Y.	932
Li, Z.W.	1388	Matsushita, M.	843
Li, Z.Y.	177	Mayinger, F.	1273
Li, Z.Z.	1603	Mayinger, F.	1296
Li, Z.Z.	1646	Mayinger, F.	1366
Liang, J.T.	1184	Mayinger, F.	1379
Liao, G.X.	1340	Mbarawa, M.	1524
Liao, H.Q.	1722	McClain, R.L.	940
Lin, F.	1388	Mei, Y.G.	980
Lin, G.T.	821	Meng, X.Z.	459
Lin, H.H.	821	Meng, X.Z.	1159
Lin, J.Y.	1041	Mertz, R.	708
Lin, R.	1360	Mertz, R.	957
Lin, W.Y.	1508	Mettawee, E.S.	766
Linak, W.P.	1686	Meyer, J.P.	1076
Ling, S.C.	1446	Meyer, J.P.	1105
Liu, B.M.	451	Meyer, J.P.	1114
Liu, C.	373	Mi, J.	1609
Liu, C.Y.	497	Miller, A.	1033
Liu, D.C.	1496	Milton, B.E.	1524
Liu, H.	1420	Mo, J.	680
Liu, H.C.	1640	Mohamad, M.A.	751
Liu, H.T.	1468	Morford, R.V.	1483
Liu, X.G.	1651	Morin, M.	1412
Liu, Y.	1305	Mosyak, A.	72
Liu, Y.	1615	Mosyak, A.	255
Liu, Y.F.	1591	Mujumdar, A.S.	910
Liu, Y.P.	1595	Mujumdar, A.S.	932
Liu, Y.W.	1212	Murayama, Y.	1546
Liu, Z.L.	1360	Mutaf-Yardimci, O.	96
Liu, Z.T.	1397	Nagayama, G.	672
Liu, Z.Y.	1054	Nakabe, K.	262
Lloyd, A.C.	138	Nakamura, S.	1715
Lorenzine, M.	247	Nakata, T.	695
Lou, H.	1241	Nathan, G.J.	1609
Lu, G.Q.	1192	Negishi, K.	564
Lu, S.S.	860	Neo, E.C.	161
Lu, Y.Z.	1054	Ng, K.C.	1145
Lubiez, J.V.	1164	Ng, M.L.	1476
Luo, W.H.	1566	Nguyen, T.H.	349
Luo, Y.	416	Nguyen, T.V.	1453
Luo, Y.H.	393	Nie, J.H.	177
Luo, Z.Y.	1566	Nigmatulin, R.	110
Lvov, S.N.	1483	Nishio, S.	360

Nobuchika, K.	695	Schmidt, B.	708
North, M.T.	573	Scholz, K.H.	1500
Novellani, M.	466	Schulz, A.	221
Nursubyakto	191	Seames, W.S.	1686
Ofner, B.	1366	Sen, M.	940
Ogura, H.	932	Serizawa, A.	643
Oido, K.	628	Shao, H.	279
Oka, M.	813	Sharkawy, A.E.	826
Okada, S.Y.	604	Sheen, P.J.	949
Olaru, I.	866	Shen, B.X.	1496
Oliveira, A.A.M.	32	Sheng, X.L.	650
Ooyatsu, N.	1710	Shevtsov, S.	422
Osa, N.	445	Shi, M.H.	905
Ota, T.	199	Shiah, S.W.	888
Ozoe, H.	288	Shih, Y.C.	1289
Ozoe, H.	302	Shimogori, M.	1710
Pacheco-Vega, A.	940	Shoji, M.	335
Paitoonsurikarn, S.	972	Shu, Z.D.	1703
Pan, Y.K.	910	Smid, J.	474
Pao, H.P.	1446	So, R.M.	169
Park, G.	557	Soudarev, A.	1500
Park, G.C.	384	Stehlik, P.	1624
Park, G.C.	430	Stubington, J.F.	1662
Park, K.S.	1532	Stubington, J.F.	1669
Peng, X.F.	343	Sugimto, K.	1438
Petit, P.J.	1076	Sugiyama, T.	1024
Polasek, F.	539	Sumathy, K.	774
Poslushny, G.	1500	Sun, C.C.	1257
Prechtl, P.	1379	Sun, C.Y.	588
Qiu, J.R.	1560	Sun, G.J.	1586
Qiu, Y.	980	Sun, H.	650
Que, X.C.	279	Sun, J.Y.	1041
Quitard, M.	482	Sun, L.S.	1728
Raghavan, G.S.V.	1090	Sun, S.J.	1404
Ramsden, V.	349	Sun, X.X.	1728
Ren, B.Z.	1002	Suzuki, A.	759
Ro, S.T.	965	Suzuki, H.	1024
Rong, S.X.	588	Suzuki, K.	161
Rozenblit, R.	72	Suzuki, K.	262
Sadhal, S.S.	229	Suzuki, Y.	972
Saenger, M.	1677	Swanepoel, W.	1105
Saha, B.B.	1145	Swift, G.W.	2
Saito, T.	84	Syred, N.	422
Saitoh, T.S.	796	Tadrist, L.	466
Saitoh, T.S.	1226	Tagawa, T.	288
Saitoh, T.S.	1233	Tagawa, T.	302
Sanchez, J.G.	1098	Tagishi, A.	1715
Santini, R.	466	Takahashi, K.	873
Sato, K.	695	Takarayama, N.	1710
Sato, M.	748	Takeguchi, S.	1153
Satoh, I.	84	Tan, G.H.	881
Saveliev, A.V.	96	Tanaka, H.	360
Saveliev, A.V.	1266	Tao, W.Q.	177
Saxena, S.C.	688	Tian, F.J.	1433

Tomiyama, S.	695	Wu, J.	1560
Toriyama, K.	184	Wu, X.P.	1340
Trinh, E.H.	229	Wu, Y.Z.	1212
Tsai, H.H.	474	Wyczalek, F.A.	1327
Tsai, Y.C.	1015	Xiang, J.	1728
Tsuchimoto, N.	1438	Xiao, L.Q.	835
Tsuruta, T.	672	Xin, M.D.	379
Vanhorn, S.R.	1321	Xing, K.Q.	373
Vesely, S.	1500	Xiong, F.	701
Vigneault, C.	1090	Xiong, Z.H.	1632
Vinogradov, E.	1500	Xu, B.Y.	1427
Vitali, J.A.	1321	Xu, S.S.	1657
Wakabayashi, H.	604	Xu, X.D.	1198
Wako, Y.	748	Xu, X.F.	1566
Wang, A.L.T.	1669	Xu, X.Y.	1433
Wang, B.X.	343	Xu, Y.Q.	1305
Wang, B.X.	490	Yabe, A	716
Wang, B.X.	665	Yabe, A	860
Wang, C.Y.	1460	Yabe, T.	1153
Wang, D.Q.	459	Yamada, N.	1233
Wang, F.	1333	Yamagishi, F.	695
Wang, J.	598	Yamanaka, T.	1024
Wang, J.C.	680	Yamashita, T.	1438
Wang, J.F.	1048	Yan, J.H.	1333
Wang, L.B.	980	Yan, W.M.	949
Wang, N.N.	1250	Yan, W.P.	1591
Wang, Q.H.	1560	Yan, Z.D.	1397
Wang, Q.W.	177	Yang, B.C.	821
Wang, S.	118	Yang, B.C.	1289
Wang, S.P.	835	Yang, D.	1566
Wang, X.	905	Yang, H.	1212
Wang, X.	1122	Yang, H.M.	1305
Wang, X.	1489	Yang, K.	199
Wang, X.S.	1340	Yang, K.T.	940
Wang, Y.	1646	Yang, L.W.	1184
Wang, Z.G.	459	Yang, S.M.	310
Wang, Z.G.	1159	Yang, X.L.	1433
Wang, Z.N.	701	Yao, B.	1340
Watanabe, C.	445	Yao, Q.	1281
Watanabe, M.	335	Ye, X.H.	270
Wei, C.Y.	1333	Yeh, C.L.	1640
Wei, Q.D.	1651	Yin, X.L.	1427
Wei, X.J.	1483	Yokota, K.	1546
Wendt, J.O.L.	1686	Yokota, M.	852
Weng, L.C.	1640	Yokoya, S.	335
Werther, J.	1677	Yong, Y.P.	1651
Whitaker, S.	482	Yoshikawa, H.	199
Willers, E.	1130	Yoshino, H.	1241
Wittig, S.	221	Yoshizawa, Y.	1546
Wong, H.	621	You, L.X.	1468
Wu, C.Z.	1427	Yu, B.F.	459
Wu, C.Z.	1632	Yu, B.F.	1159
Wu, F.	1217	Yu, C.J.	1566
Wu, G.T.	1002	Yu, H.L.	355

Yu, H.L.	367	Zhu, N.	316
Yu, J.	445	Zhu, W.X.	1184
Yu, S.M.	1250	Zhu, Y.Q.	804
Yu, W.P.	905	Zhu, Y.X.	788
Yu, X.L.	1397	Zhu, Y.X.	1059
Yue, D.T.	1002	Zou, Z.Q.	1728
Yun, Y.	1703	Zubkov, P.T.	328
Zakharov, Y.	1500	Zuo, Z.J.	573
Zeng, D.L.	373	Zuo, Z.J.	1007
Zhang, G.	379		
Zhang, H.	621		
Zhang, H.	701		
Zhang, H.S.	1595		
Zhang, H.X.	1048		
Zhang, J.W.	1603		
Zhang, L.	1198		
Zhang, L. Winston	989		
Zhang, L.Z.	1066		
Zhang, L.Z.	1560		
Zhang, S.H.	1489		
Zhang, S.Z.	1048		
Zhang, W.	1203		
Zhang, X.	860		
Zhang, X.L.	355		
Zhang, X.S.	997		
Zhang, Y.	910		
Zhang, Y.	1646		
Zhang, Y.H.	980		
Zhang, Y.P.	788		
Zhang, Y.P.	804		
Zhang, Y.P.	1059		
Zhang, Y.P.	1066		
Zhang, Z.J.	490		
Zhao, C.Y.	169		
Zhao, L.F.	1489		
Zhao, L.J.	910		
Zhao, T.S.	438		
Zhao, T.S.	529		
Zhao, Z.L.	1427		
Zheng, J.X.	393		
Zheng, L.	1360		
Zheng, Q.G.	1703		
Zhou, H.	1586		
Zhou, J.	379		
Zhou, J.	1694		
Zhou, J.H.	1281		
Zhou, J.M.	1615		
Zhou, J.S.	1566		
Zhou, L.P.	997		
Zhou, Q.T.	701		
Zhou, T.H.	1468		
Zhou, X.Y.	1483		
Zhou, Y.	1184		
Zhou, Z.J.	1281		